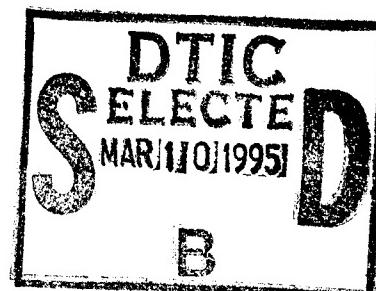


# NAVAL POSTGRADUATE SCHOOL

## Monterey, California



**SYSTEMATIC AND INTEGRATED APPROACH TO  
TROPICAL CYCLONE TRACK FORECASTING PART 1.  
APPROACH OVERVIEW AND DESCRIPTION OF  
METEOROLOGICAL BASIS**

by  
Lester E. Carr III  
Russell L. Elsberry

December 1994

Approved for public release; distribution is unlimited

Prepared for: Naval Postgraduate School  
Monterey, CA 93943  
Office of Naval Research  
Code 322MM, Arlington, VA 22217

19950308 153  
CC

Naval Postgraduate School  
Monterey, California 93943-5000

Rear Admiral T. A. Mercer  
Superintendent

This report was prepared for the Joint Typhoon Warning Center (JTWC) at the Naval Pacific Meteorology and Oceanography Center (NPMOC) West Guam and for the Alternate JTWC at NPMOC, Pearl Harbor, HI. Funded was provided by the Office of Naval Research Marine Meteorology Program.

Reproduction of all or part of the report is authorized.

This report was prepared by:

*Lester E. Carr III*

Lester E. Carr, III, CDR, USN  
Assistant Professor of Meteorology

*Russell L. Elsberry*

Russell L. Elsberry  
Professor of Meteorology

Reviewed by:

*R. Haney*

Robert L. Haney, Chairman  
Department of Meteorology

Released by:

*P. J. Marto*

Paul J. Marto,  
Dean of Research

# REPORT DOCUMENTATION PAGE

*Form Approved  
OMB No. 0704-0188*

Public reporting burden for this collection of information is estimated to average 1 hour per response, including the time for reviewing instructions, searching existing data sources, gathering and maintaining the data needed, and completing and reviewing the collection of information. Send comments regarding this burden estimate or any other aspect of this collection of information, including suggestions for reducing this burden, to Washington Headquarters Services, Directorate for Information Operations and Reports, 1215 Jefferson Davis Highway, Suite 1204, Arlington, VA 22202-4302, and to the Office of Management and Budget, Paperwork Reduction Project (0704-0188), Washington, DC 20503.

<b>1. AGENCY USE ONLY (Leave blank)</b>			<b>2. REPORT DATE</b> January 1995	<b>3. REPORT TYPE AND DATES COVERED</b> Interim 1/94 - 12/94	<b>4. TITLE AND SUBTITLE</b> Systematic and integrated approach to tropical cyclone track forecasting Part I. Approach overview and description of meteorological basis	<b>5. FUNDING NUMBERS</b>
<b>6. AUTHOR(S)</b> Lester E. Carr, III, and Russell L. Elsberry						
<b>7. PERFORMING ORGANIZATION NAME(S) AND ADDRESS(ES)</b> Naval Postgraduate School Department of Meteorology 589 Dyer Rd., Room 254 Monterey, CA 93943-5114			<b>8. PERFORMING ORGANIZATION REPORT NUMBER</b>			
<b>9. SPONSORING/MONITORING AGENCY NAME(S) AND ADDRESS(ES)</b> Office of Naval Research Code 322 MM 800 N. Quincy Arlington, VA 22217-5000			<b>10. SPONSORING/MONITORING AGENCY REPORT NUMBER</b>			
<b>11. SUPPLEMENTARY NOTES</b> The views expressed in this report are those of the author and do not reflect the official policy or position of the Department of Defense.						
<b>12a. DISTRIBUTION/AVAILABILITY STATEMENT</b>  Approved for Public Release; Distribution Unlimited				<b>12b. DISTRIBUTION CODE</b>		
<b>13. ABSTRACT (Maximum 200 words)</b> A systematic and integrated approach to tropical cyclone (TC) track forecasting is proposed. The approach is based on the premise that TC forecasters can improve upon dynamical track forecasts generated by numerical models and other objective guidance, if the forecasters are equipped with: (i) a meteorological knowledge base of conceptual models that organizes a wide array of scenarios into a relatively few recurring, dynamically-related situations; and (ii) a knowledge base of numerical model TC forecast traits and objective aid traits that is organized around the meteorological knowledge base. The approach is systematic because it includes a methodology for consistently applying the two knowledge bases to generate the official track forecast. The approach is also integrated because the meteorological knowledge base includes motion-relevant characterizations of environment structure, characterizations of TC structure (intensity and size), and motion-affecting alterations of the environment structure caused by various interactions between the TC and the environment.						
<b>14. SUBJECT TERMS</b> Tropical cyclone track forecasting Tropical cyclone motion					<b>15. NUMBER OF PAGES</b> 273	<b>16. PRICE CODE</b>
<b>17. SECURITY CLASSIFICATION OF REPORT</b> UNCLASSIFIED	<b>18. SECURITY CLASSIFICATION OF THIS PAGE</b> UNCLASSIFIED	<b>19. SECURITY CLASSIFICATION OF ABSTRACT</b> UNCLASSIFIED	<b>20. LIMITATION OF ABSTRACT</b>			

13. ABSTRACT (continued) :

This report constitutes Part I of the Systematic Approach, and provides an overview of the approach and a detailed development of the meteorological knowledge base. This development draws heavily from recent Office of Naval Research and other agency research in the literature by distilling and organizing various key concepts into cohesive, operationally-relevant insights into TC motion. To make the knowledge base more comprehensive, a number of additional concepts, tools, and techniques are introduced.

The various conceptual models of the meteorological knowledge base are illustrated using case studies that include U. S. Navy Operational Global Atmospheric Prediction System (NOGAPS) analyses, satellite imagery, and TC best tracks prepared by the Joint Typhoon Warning Center (Guam). Background dynamical concepts and process on which the various conceptual models are based are included in a number of appendices. In addition, these appendices help to make this report an essentially stand-alone reference manual for TC track forecasting.

Accession For	
NTIS GRAAM	<input checked="" type="checkbox"/>
DTIC TAB	<input type="checkbox"/>
Unannounced	<input type="checkbox"/>
Justification	
By _____	
Distribution _____	
Availability Codes	
Distr	Avail and/or Special
R'	

## TABLE OF CONTENTS

	<u>Page</u>
<b>List of Tables</b>	vi
<b>List of Figures</b>	vii
<b>Acknowledgments</b>	xii
<b>1. Introduction</b>	1
<b>a. Forecast process review</b>	1
(1) Ideal forecast approach	1
(2) Approximations to the ideal approach	3
<b>b. Forecast process deficiencies</b>	5
<b>c. Objectives and format</b>	10
<b>2. Approach overview</b>	12
<b>3. TC-Environment conceptual models knowledge base</b>	16
<b>a. Organization</b>	19
<b>b. Environment structure</b>	24
(1) Synoptic Patterns	24
(a) Standard (S) Synoptic Pattern	24
(b) North-Oriented (N) Synoptic Pattern	28
(c) Monsoon Gyre (G) Synoptic Pattern	32
(d) Multiple Tropical Cyclone (M) Synoptic Pattern	37
(2) Synoptic Regions	41
(a) Regions within the Standard (S) Synoptic Pattern	41
(b) Regions within the North-Oriented (N) Synoptic Pattern	46
(c) Regions within the Monsoon Gyre (G) Synoptic Pattern	50
(d) Regions within the Multiple TC (M) Synoptic Pattern	53
<b>c. Tropical cyclone structure</b>	57
(1) Tropical cyclone intensity	57
(a) Intensity conceptual models	57
(b) Steering level selection for NOGAPS charts	58
(c) Intensity forecasting	59

	<u>Page</u>
(2) Tropical cyclone size	59
(a) Proposed TC wind distribution model	60
(b) Wind distribution model application	61
(c) Tropical cyclone size forecasting	68
(d) TC size conceptual models	69
d. TC-Environment transformations	72
(1) Beta-effect propagation (BEP)	73
(a) BEP model description and impact	73
(b) BEP model illustration	76
(2) Vertical wind shear (VWS)	82
(a) Preliminary VWS model: Development and description	82
(b) VWS model impact	87
(3) Ridge modification by large TC (RMT)	91
(a) RMT model development and description	91
(b) RMT model impact	96
(c) RMT model illustration	98
(4) Monsoon Gyre-TC Interaction (MTI)	109
(a) Background	109
(b) MTI model description and impact	118
(c) MTI model illustration	118
(5) Tropical Cyclone Interactions (TCIs)	131
(a) TCIs model description and impact	132
(b) TCIs model illustration	136
(6) Summary	177
(a) Utilization guidelines	177
(b) Transformation indicators	178
e. Knowledge base overview	183
(1) Methodology	183
(2) TC track characterizations	183
4. Conclusion to Part I	189
APPENDIX A: Historical Review of TC Forecasting at JTWC	191
APPENDIX B: Summary of TC Intensity Effects on TC Motion	193

	<u>Page</u>
<b>APPENDIX C: A Proposed TC Tangential Wind Distribution Model</b>	198
<b>APPENDIX D: Beta Effect Propagation (BE) Background and Preliminary Development</b>	217
<b>APPENDIX E: Background for Vertical Wind Shear VWS) Model</b>	235
<b>APPENDIX F: Preliminary Development of the Proposed Ridge Modification by a Large TC (RMT) Model</b>	244
<b>APPENDIX G: Preliminary Development of the Monsoon Gyre-TC Interaction (MTI) Model</b>	254
<b>REFERENCES</b>	268

## LIST OF TABLES

<u>Table</u>	<u>Page</u>
3.1 Environment structure conceptual models	20
3.2 TC intensity and TC size conceptual models	20
3.3 TC-Environment transformation conceptual models	21
3.4 TC-Environment characterization of ST Yuri (1991)	185
3.5 As in Table 3.4, except for TY Seth (1991)	186
3.6 As in Table 3.4, except for TS Verne (1991)	186
3.7 As in Table 3.4, except for TY Owen (1989)	187
3.8 As in Table 3.4, except for TY Nancy (1989)	187
3.9 As in Table 3.4, except for TY Nat (1991)	188
B.1 Optimum steering levels for Atlantic TCs (Dong and Neumann 1986)	194

## LIST OF FIGURES

<u>Figure</u>	<u>Page</u>
1.1 Schematic of TC surface wind distribution	3
1.2 Schematic of "ideal" integrated approach to TC forecasting	6
1.3 Schematic of "historical" approach to TC forecasting	7
1.4 JTWC initial position and forecast error histograms	9
2.1 Flowchart of systematic approach	13
3.1 Track of TY Abe (1990)	17
3.2 Analyses for TY Abe	18
3.3 Overview of the three groups of conceptual models	22
3.4 Transitions in environmental structure	23
3.5 Standard (S) synoptic pattern conceptual model	25
3.6 Analyses for ST Yuri (1991), TYs Ed and Flo (1990), and TY Amy (1991)	27
3.7 North-oriented N1 and N2 synoptic pattern conceptual models	29
3.8 Analyses for TY Steve (1990) and TY Vernon (1990)	30
3.9 Model streamfunction field for monsoon gyre	32
3.10 Model streamfunction field including TC vortex	32
3.11 Analyses for ST Yuri (1991), TY Sarah (1989), and TS Tip (1989)	33
3.12 Monsoon Gyre (G) synoptic pattern conceptual model	34
3.13 Satellite imagery of G Pattern monsoon gyre	35
3.14 Analyses for TS Doug, TY Ellie, and TS Gladys (1991)	36
3.15 Multiple TC (M) synoptic pattern conceptual models	38
3.16 Analyses for TYs Yancy and Zola in 1990, ST Seth and TS Verne in 1991, TY Ed and ST Flo in 1990, and TY Nat and ST Mireille in 1991	40
3.17 Standard (S) pattern conceptual model with synoptic regions added	42
3.18 Tracks of TY Ed (1990) and TY Amy (1991)	44
3.19 Tracks of ST Flo (1990) and TS Verne (1991)	45
3.20 Analyses for TY Ed and ST Flo (1990), and ST Seth and TS Verne (1991)	46
3.21 North-oriented (N) pattern conceptual models with synoptic regions added	47
3.22 Tracks of TYs Steve and Vernon (1990)	48
3.23 Analyses for TS Luke and ST Mireille (1991), and TYs Ofelia and Percy (1990)	50
3.24 Tracks of ST Mireille (1991) and TY Percy (1990)	51
3.25 Monsoon Gyre (G) pattern conceptual models with synoptic regions added	52
3.26 Track of TY Ellie (1991)	52
3.27 Track of TS Doug (1991)	53
3.28 Multiple (M) TC pattern conceptual model with synoptic regions added	54
3.29 Track of ST Seth (1991)	55
3.30 Tracks of TYs Yancy and Zola (1990)	56
3.31 Values of $R_{850}$ as a function of TC formation latitude and 850 mb wind radii	63
3.32 850 mb winds for TS Robyn (1993)	65
3.33 Satellite imagery for TS Robyn	66
3.34 Satellite imagery for different TC sizes	67

<u>Figure</u>	<u>Page</u>
3.35 Tangential wind speeds in composite TC (Frank 1977)	69
3.36 Satellite imagery as in Fig. 3.34 for later periods	70
3.37 Beta-induced propagation speeds	74
3.38 Environmental transitions within S pattern owing to BEP	75
3.39 Superposition of BEP and steering to get TC motion	75
3.40 Analyses during TY Ed (1990)	78
3.41 Track of TY Hattie (1990)	79
3.42 Analyses during TY Hattie	80
3.43 Track of TY Kit (1981) and wind structure	84
3.44 Imagery during TY Kit	85
3.45 TC structure changes induced by (VWS)	87
3.46 Environment structure transitions related to VWS	88
3.47 Track of ST Ruth (1991)	89
3.48 Imagery during ST Ruth	90
3.49 Track of ST Yuri	92
3.50 Analyses during ST Yuri	93
3.51 Analyses during ST Yuri continued	94
3.52 Environment transitions induced by RMT	97
3.53 Track of TY Page (1994)	99
3.54 Analyses during TY Page	100
3.55 Imagery during TY Page	101
3.56 As in Fig. 3.54 and 3.55 continued	103
3.57 Track of ST Yvette (1992)	105
3.58 Imagery during ST Yvette	106
3.59 Analyses during ST Yvette	107
3.60 As in Fig. 3.59 continued	108
3.61 Track of TY Hal (1988)	110
3.62 Histogram of cases of sudden poleward track changes	110
3.63 Sudden poleward track changes 1989-1991	112
3.64 Track and surface gale areas around TY Orchid (1980)	114
3.65 Analyses during TY Abe and TY Becky (1990)	114
3.66 Imagery during TY Abe and TY Nathan (1990)	116
3.67 Analyses during TY Nathan	117
3.68 Environment transition induced by MTI	119
3.69 Tracks for TY Sarah and TS Tip (1989)	121
3.70 Analyses during TY Sarah and TS Tip	122
3.71 Imagery during TY Sarah and TS Tip	124
3.72 Tracks of TY Ivy and TS Joel (1991)	127
3.73 Analyses during TY Ivy and TS Joel	129
3.74 Imagery during TY Ivy and TS Joel	130
3.75 Tracks and relative motion diagram for TYS Owen and Nancy (1989)	133
3.76 As in Fig. 3.75, except for TYS Odessa and Pat (1985)	133
3.77 Environment transitions induced by TCI1 transformation	135

<u>Figure</u>	<u>Page</u>
3.78 Tracks for ST Seth and TS Verne (1991)	137
3.79 Analyses during ST Seth	138
3.80 As in Fig. 3.78 continued	139
3.81 As in Fig. 3.80 continued	141
3.82 Relative rotation diagram for ST Seth and TS Verne	142
3.83 Imagery for ST Seth and TS Verne	144
3.84 Tracks of TY Orchid and TY Pat (1991)	145
3.85 Analyses during TY Orchid	146
3.86 Relative rotation diagram for TYs Orchid and Pat	148
3.87 Imagery during TYs Orchid and Pat	148
3.88 Analyses as in Fig. 3.85 continued	149
3.89 Tracks of TYs Owen and Nancy (1989)	151
3.90 Imagery during TYs Owen and Nancy	152
3.91 Imagery as in Fig. 3.90 continued	153
3.92 Track of TS Peggy (1989)	154
3.93 Analyses during TYs Owen and Nancy (1989)	155
3.94 Analyses as in Fig. 3.93 continued	156
3.95 Analyses as in Fig. 3.93, except at 250 mb	157
3.96 Surface analysis during TYs Owen and Nancy	158
3.97 Schematics of upper-level streamlines during monsoon gyre situations including multiple TCs	160
3.98 Imagery of a monsoon gyre with TYs Odessa, Pat, and Ruby	162
3.99 Tracks of TYs Colleen and Brian (1992)	163
3.100 Analyses during TYs Colleen and Brian	164
3.101 Imagery during TYs Colleen and Brian	166
3.102 Analyses as in Fig. 3.100 continued	167
3.103 Tracks of TS Luke, ST Mireille, and TY Nat (1991)	169
3.104 Analyses during TY Nat, TS Luke, and ST Mireille	171
3.105 Imagery during TY Nat, TS Luke, and ST Mireille	172
3.106 Analyses as in Fig. 3.104 continued	173
3.107 Imagery as in Fig. 3.105 continued	174
3.108 Analyses as in Fig. 3.106 continued	175
3.109 Relative rotation diagram for TY Nat and ST Mireille	177
3.110 Sequence of steps for combining TC structure and environment structure	184
B.1 Forecast errors in Atlantic TS and Hurricanes for different steering levels	194
B.2 Optimum steering levels for Australian TCs	196
B.3 Track and imagery for TS Lewis (1990)	197
C.1 Wind radii for Tsui <i>et. al.</i> (1992) statistical model	199
C.2 Radial profiles of tangential winds from Weatherford and Gray (1988)	200
C.3 Inflow layer of Hurricane Frederic from Frank (1984)	203
C.4 Tangential winds from Eqs. (C-11) and (C-12)	205
C.5 Tangential wind at 10°N from Eq. (C-11) for varying $R_o$	207
C.6 As in C.5, except for 15°N	207

<u>Figure</u>	<u>Page</u>
C.7 As in C.5, except for 20°N	208
C.8 As in C.2, except stratified by eye size	209
C.9 As in C.2, except stratified by intensity	210
C.10 As in C.5, except for constant $V_m$ and $R_m$	212
C.11 As in C.5, except with radius of $17.5 \text{ m s}^{-1}$ wind speed fixed	212
C.12 As in C.5, except with $R_o = 700 \text{ km}$	213
C.13 Tangential winds for TY Bill (1981)	214
C.14 As in C.13b, except for TY Kit (1981)	214
C.15 Model tangential wind profiles during intensification with $R_o$ held fixed	215
C.16 As in C.15, except for increasing $R_o$ during initial intensification	216
D.1 Streamfunction for linear model of Chan and Williams (1987)	218
D.2 As in D.1, except for nonlinear model	218
D.3 Asymmetric streamfunction from Fiorino and Elsberry (1989)	220
D.4 Conceptualization of perturbation damping mechanism of Carr and Williams (1989)	222
D.5 Illustration of damping mechanism of Carr and Williams (1989)	223
D.6 Asymmetric vorticity in Shapiro and Ooyama (1990) model	223
D.7 Tangential winds and tracks from Fiorino and Elsberry (1989)	224
D.8 As in D.7, except varying outer tangential wind profile	224
D.9 Tangential wind profiles for angular momentum model	225
D.10 Vortex tracks for angular momentum model wind profiles of D.9	227
D.11 As in D.10, except for $R_o$ fixed, and latitudes of 10°, 15°, and 20°	228
D.12 Predicted streamfunction fields for initial wind profiles of D.9	229
D.13 As in D.12, except for same cases in D.11	231
D.14 Vortex translation speeds versus time for angular momentum profiles	232
D.15 Maximum beta-induced propagation speeds for TC sizes of 300 - 1000 km	234
D.16 As in D.14, except for $R_o$ fixed and latitudes of 10°, 15°, and 20°	234
E.1 Low-level and 200 mb streamlines from Sadler (1975)	236
E.2 Analyses for TY Page and ST Owen (1990)	238
E.3 Track for ST Owen (1990)	239
E.4 Track and analysis for TY Yunya (1991)	240
E.5 Imagery for TY Yunya (1991)	241
E.6 Imagery for ST Omar and TS Polly (1992)	242
E.7 Tracks for ST Omar and TS Polly (1992)	243
F.1 Initial tangential wind profiles for TC and monsoon gyre	244
F.2 Predicted streamfunction fields for TC-only and MG-only experiments	245
F.3 Predicted streamfunction and vorticity fields for MG-only experiment	246
F.4 Relative sizes of subtropical ridge and peripheral anticyclone	247
F.5 Relative vorticity in large-scale wave train (Lau and Lau 1990)	248
F.6 850 mb wind fields from Lau and Lau (1990)	250
F.7 Kinetic energy conversion diagram from Lau and Lau (1992)	251
F.8 Meridional wind components in wave train (Chang et al. 1994)	252
F.9 As in F.2, except with linear zonal wind shear	253

<u>Figure</u>	<u>Page</u>
G.1 Predicted streamfunction for TC 400 km east of MG	255
G.2 As in G.1, except with TC southeast or northeast of MG	257
G.3 PVA and NVA regions relative to TC in a MG	258
G.4 Predicted isotachs corresponding to G.1	260
G.5 As in G.1, except with TC collocated with MG	260
G.6 Predicted tracks for TC to east or to west of MG	262
G.7 As in G.6, except for TC positions in poleward and equatorward quadrants	263
G.8 As in G.6, except for various MG intensities	265
G.9 As in G.6, except for various TC intensities	266
G.10 As in G.6, except for various MG sizes	267

**Acknowledgments.** This research has been sponsored by the Office of Naval Research Marine Meteorology Program. The authors gratefully acknowledge the crucial assistance and many valuable contributions made by personnel at the Naval Pacific Meteorology and Oceanography Center West Guam/Joint Typhoon Warning Center and the Naval Pacific Meteorology and Oceanography Center Pearl Harbor, Hawaii. Appreciation is extended to CAPT D. Mautner and CAPT J. Etro for their support of this research and for making available personnel and facilities at NPMOC West Guam/JTWC during the development of this research. Many thanks to LCDR E. Petzrick, Deputy Director JTWC, for tremendous logistical and administrative support during the first author's visits to Guam. Capt. D. Mundell, USAF, prepared a very thorough critique of the manuscript, and Mr. F. Wells, Mr. C. Guard, Dr. M. Lander, and Mr. E. Fukada provided numerous valuable comments and suggestions. NOGAPS analyses were provided by the Fleet Numerical Meteorology and Oceanography Center, and modelling computations by the authors were made at the Naval Postgraduate School Church Computer Center. Prof. R. T. Williams provided valuable advice on the design of the modelling experiments. Mark Boothe provided comments on the manuscript, which was expertly typed in several versions by Mrs. Penny Jones.

## 1. Introduction

The purpose of this report is to describe the basic approach and advocate the adoption of a new systematic and integrated approach (hereafter referred to as simply the systematic approach) to tropical cyclone (TC) track forecasting. The systematic approach is intended to address some deficiencies in the current forecasting process, and to promote continuing improvements by providing a suitable framework for incorporating anticipated future advances in understanding and technology. Although the discussion of deficiencies is centered around procedures and techniques used at the Joint Typhoon Warning Center (JTWC), the authors believe that the underlying issues are generally applicable to TC track forecasting in any region of the world. Thus, this discussion should not be misconstrued as being critical of JTWC vis-a-vis other warning centers. Part I first provides an introductory description of the entire approach, and then describes extensively the meteorological framework or knowledge base of conceptual models that the forecaster may use to create a comprehensive and dynamically-based mental picture of the present TC forecasting situation. Although the meteorological framework is developed using examples selected from the western North Pacific and analyses from the U. S. Fleet Numerical Meteorology and Oceanography Center (FNMOC), it is believed to be generally applicable with minor modifications to TC forecasting in other basins. Part II will describe application of the systematic approach to the JTWC forecast problem and will address specific objective guidance that may not be available at other centers. It is anticipated that applications for other TC basins will be developed in future reports in this series.

The remainder of this introduction section first develops the concept of an "ideal TC forecast approach" that accounts for the inherently interconnected nature of the track, intensity, and wind distribution components of the TC forecasting problem. A review of the historical approach to TC forecasting reveals limitations in understanding and technology that prevented application of the ideal approach. Identification of the sources and nature of current procedural and knowledge base deficiencies then provides the motivation for the systematic approach.

### *a. Forecast process review*

1) Ideal forecast approach. From the perspective of most users of TC warnings, the goal of tropical cyclone (TC) forecasting is to predict accurately the temporal evolution of the areas of significant surface winds and heavy precipitation. The precipitation issue will not be considered here. The ideal TC wind-area prediction would accurately specify at any time the horizontal distributions of wind areas expected to cause high seas and damaging winds, perhaps in categories of minor, major, and severe. The wind speed threshold for the area in which high seas are generated is roughly the gale force ( $17 \text{ m s}^{-1}$ ) isotach. The wind speed thresholds for the three damage categories are roughly the storm force ( $24 \text{ m s}^{-1}$ ), 100-kt ( $50 \text{ m s}^{-1}$ ), and 130-kt ( $65 \text{ m s}^{-1}$ ) isotachs (Fig. 1.1). From a user perspective, the primary concern is the accuracy of forecast times of these threshold wind speeds for a particular

location. However, forecasters usually think in terms of TC track, intensity, and size<sup>1</sup>, which correspond to the movement of the wind circulation center, the maximum wind speed near the circulation center, and the radius of gale-force wind speeds relative to the center, respectively.

Traditionally, characterizations of the accuracy of TC forecasts have focussed primarily on track forecast error. However, error in forecasting the evolution of a significant wind area is a complex combination of the track, intensity, and size forecast errors. For example, even if the intensity and size of a midget typhoon were to be precisely forecast, a relatively small cross-track forecast error might lead to an extreme overestimate of surface winds for a location near the forecast track. Conversely, an accurate intensity and track forecast accompanied by a size forecast that fails to account for substantial growth of the extent of gale-force winds will lead to a large underestimate in wind speed at a location forecast to be on the periphery of the TC. The key point is that the track, intensity, and size forecasts are inextricably linked from the perspective of impact on the user.

The track, intensity, and size components of a TC forecast are also dynamically interdependent. For instance, TC movement is primarily a result of environmental "steering" vertically averaged over some depth of the troposphere. Since the vertical extent of the TC circulation increases with intensity (due in part to vertical momentum transport by convective clouds), environmental steering must be computed over a deeper layer as a TC intensifies (cf., Velden 1993). Thus, TC intensity affects motion. However, the environmental flow that advects the TC has a spatially variable vertical wind shear that tends to inhibit intensification in inverse proportion to the shear magnitude. As a result, the TC track affects how it intensifies, and how it intensifies can affect where it goes. A number of studies have shown that the size of the TC affects its propagation relative to the environmental steering (cf., Chan and Williams 1987; Fiorino and Elsberry 1989). In addition, a large TC may significantly modify its environment (Carr and Elsberry 1994). Thus, the present size of a TC and any subsequent changes in size can affect motion. Although little is known about how and why TCs change size, it is not unreasonable to expect that the TC track may have an effect on size evolution.

Since TC movement, intensification, and size evolution are closely linked from both user-impact and dynamical perspectives, an "ideal TC forecast approach" may be defined as

---

<sup>1</sup> As noted by Merrill (1984), two different and not necessarily consistent measures of TC size exist: (i) the average radius of the outer closed surface isobar (ROCI); and (ii) the average radius inside of which surface wind speeds exceed a certain threshold. Beginning in 1992, JTWC adopted the gale-force threshold to determine the outermost wind radius reported in JTWC warnings (the 30-kt threshold was used previously). A new definition of TC size based on the mid- and lower-tropospheric wind field relevant to tropical cyclone motion will be introduced later.

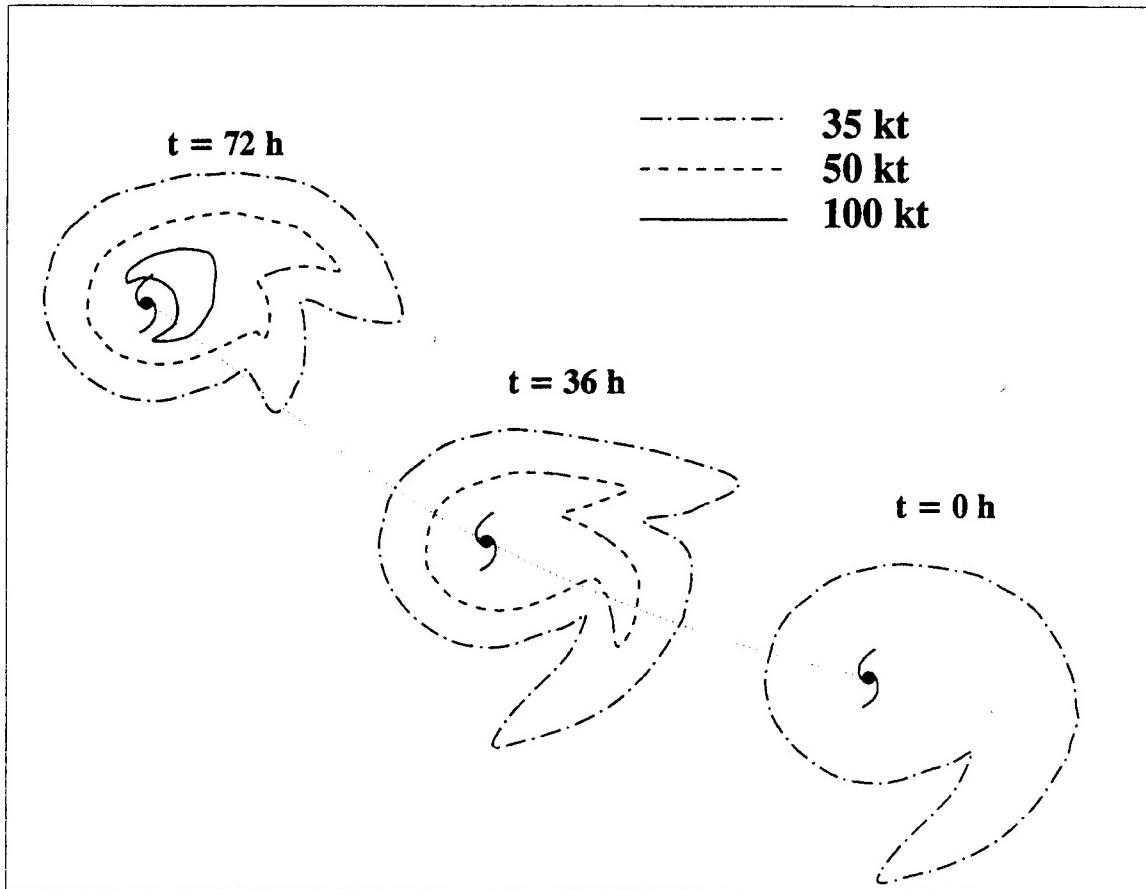


Fig. 1.1 Schematic of a hypothetical 72-h evolution of a TC surface wind distribution.

a fully integrated solution for the time evolution of the 3-dimensional TC circulation. The traditional TC track, intensity, and size forecasts may then be considered as three partial representations of the total forecast solution. Although the ideal forecast approach cannot be attained, two approximate realizations may be conceived that involve different proportions of technology and human reasoning.

2) Approximations to the ideal approach. One predominantly technological approximation would be to develop a numerical prediction model that: (i) accurately represents all physical processes relevant to the evolution of the TC wind field on say a 72-h time scale; (ii) provides adequate resolution over the domain necessary to resolve the smallest and largest atmospheric circulations expected to have a significant impact on this evolution; (iii) is integrated on a sufficiently powerful computer to provide the forecasts within a few hours; and (iv) is provided atmospheric and oceanic data on appropriate spatial

and temporal scales to define accurately the initial conditions. This purely numerical approach is characterized as essentially technological since no forecaster reasoning or understanding of the meteorological phenomenon would be required, except perhaps to interpret the forecast for users.

Even if advances in computer technology would allow requirements (ii) and (iii) to be approached, it is not clear that present representations of all the physical processes are adequate. Recall that the TC is a turbulent and nonlinear circulation that must have some limit of predictability. However, the seemingly insurmountable deficiency is the inadequacy of the data base required to define the initial conditions in (iv), despite the anticipated availability of unmanned aerial vehicle reconnaissance (Holland *et al.* 1992; Langford and Emanuel 1993) that would partly address the data problem. Thus, it is the authors' opinion that such a purely numerical approximation to the ideal forecasting approach will not be fully realized for the foreseeable future.

A second method for approximating the ideal forecasting approach would be to use human reasoning and understanding of the meteorological phenomenon to compensate for a numerical TC prediction model that provides integrated, but insufficiently accurate, forecasts (Fig. 1.2). In effect, the numerical TC prediction is an input and the official forecast is the output of the human reasoning process. Equal sizes of the circles in Fig. 1.2 imply an equal importance should be given to the individual track, intensity, and wind distribution sub-problems. However, the degree of human involvement in the individual track, intensity, and size aspects of the total TC forecast problem would be inversely proportional to the amount of skill of the numerical prediction in that aspect. The thin two-way arrows in Fig. 1.2 indicate careful attention should be given to the dynamical interdependence of the sub-problems. In this idealized approach, human reasoning consists of two fundamental processes that are applied in the following order:

- (i) developing a comprehensive meteorological picture of the current TC track, intensity, and size forecast situation by using available meteorological understanding to evaluate and interpret the TC-environment scenario depicted by the numerical guidance; and
- (ii) estimating the likely biases in the numerical guidance forecasts of TC track, intensity, and size based on a knowledge of the performance of the guidance in past situations that are meteorologically related to the picture developed in (i) above.

Such a man-machine approach would be considered successful if it results in official TC forecasts that improve upon numerical TC prediction forecasts sufficiently to satisfy user requirements for threshold wind predictions.

The general concept of this second approach has necessarily been the one adopted by forecasters. However, since a need to forecast TCs existed long before any numerical prediction capability existed, various objective techniques (typically for TC track prediction

only) were used as inputs into the forecasting process instead of integrated numerical prediction models. Because initial efforts to predict TC evolution began when the level of dynamical understanding was comparatively low, extreme simplifying assumptions were made during objective technique development and in the human reasoning process to make the TC forecast problem tractable. The authors contend that the history of overly simplified approaches to TC forecasting has had a long-term impact on the nature of the forecasting process, and has resulted in a current approach that has significant deficiencies. A brief review (Appendix A) of the evolution of the TC forecasting process at JTWC identifies the nature and source of these deficiencies, and serves as a backdrop for the systematic approach set forth in this report. The forecast technique summaries and references cited in the Annual Tropical Cyclone Reports<sup>2</sup> published by JTWC form the basis for the discussion in Appendix A.

#### *b. Forecast process deficiencies*

In contrast to the integrated man-machine mix approach shown in Fig. 1.2, the present approach to TC forecasting has historically evolved to a situation characterized in Fig. 1.3. The primary inputs into the track forecasting process are an abundance of objective track forecasts, perhaps one or two low-skill (e.g., analogs or persistence and climatology) objective intensity forecasts, and no objective wind distribution forecasts. In contrast to Fig. 1.2, the non-integrated track and intensity objective inputs are characterized by separated rectangles in Fig. 1.3. The different circle sizes emphasize that much forecaster attention and reasoning is directed toward the track forecast, some to the intensity forecast, and comparatively little to the wind distribution forecast. Another difference from Fig. 1.2 is the inadequate accounting for the interdependence of the track, intensity, and wind distribution sub-problems. Rather, the present forecasting process tends to be a unidirectional progression through the track, intensity, and wind distribution sub-problems. The reasoning approach presently used by forecasters may be summarized as follows:

- (i) the TC track forecast is primarily determined based on environmental steering concepts with insufficient consideration given to intensity and size influences;
- (ii) the track forecast then influences the intensity forecast (e.g., via movement relative to upper-level features affecting outflow, recurvature versus straight track, and encounters with land, high/low vertical wind shear regions, warm/cool water, tropical/non-tropical air);
- (iii) the intensity forecast influences the wind distribution forecast (i.e., determines the existence and radii of the 100-kt, 50-kt isotachs, and to some extent, the 35-kt isotach); and

---

<sup>2</sup> Called Annual Typhoon Reports prior to 1980, and Annual Tropical Storm Reports prior to 1958.

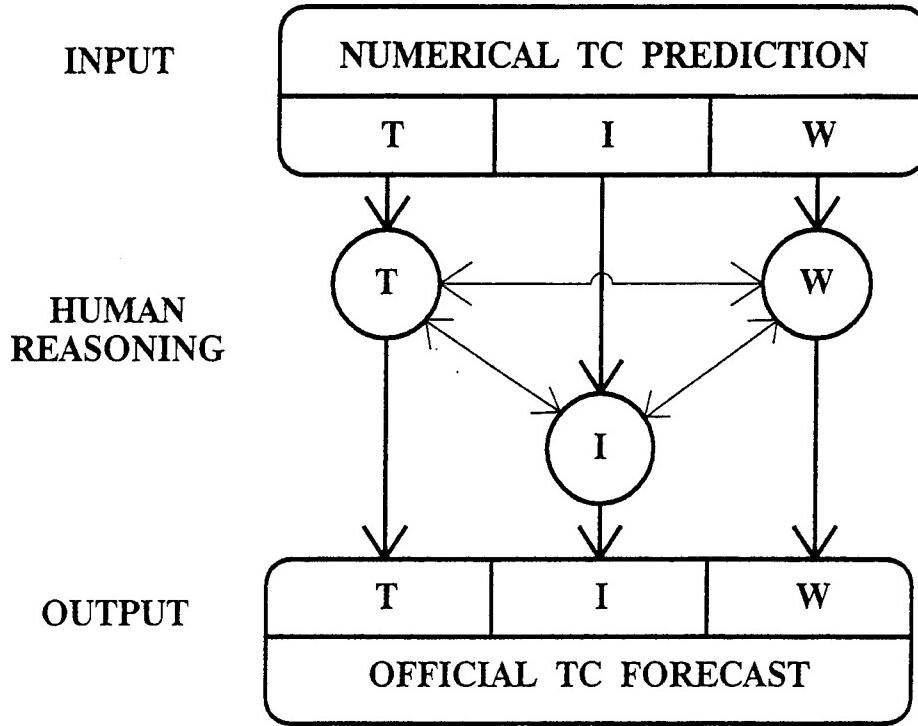


Fig. 1.2 Schematic of an "ideal" integrated approach to TC forecasting. Track, intensity, and wind forecasts from an integrated, but insufficiently accurate numerical TC prediction is used as input into a human reasoning process (circles) that fully addresses the integrated (thin two-way arrows) nature of the track (T), intensity (I), and wind distribution (W) components of the complete TC forecast problem.

- (iv) the track forecast influences the wind distribution (via the influence of translation speed, and determining what adjacent synoptic features influence the shape of the 35-kt isotach).

Notice that the only significant feedback (dashed arrow in Fig. 1.3) is the effect of intensity on the optimum steering level/layer, (e.g., JTWC forecasters typically use the shallow-, medium-, and deep-layer mean steering models as the TC intensifies).

The authors believe that this basic approach (Fig. 1.3) has not substantially changed since the 1950's, despite significant advances in the sophistication of objective motion forecast guidance, and recent improvements in understanding. The historical approach is inherently deficient because it places a disproportionate emphasis on the effect of the environment and importance of the track forecast, as well as being primarily a unidirectional

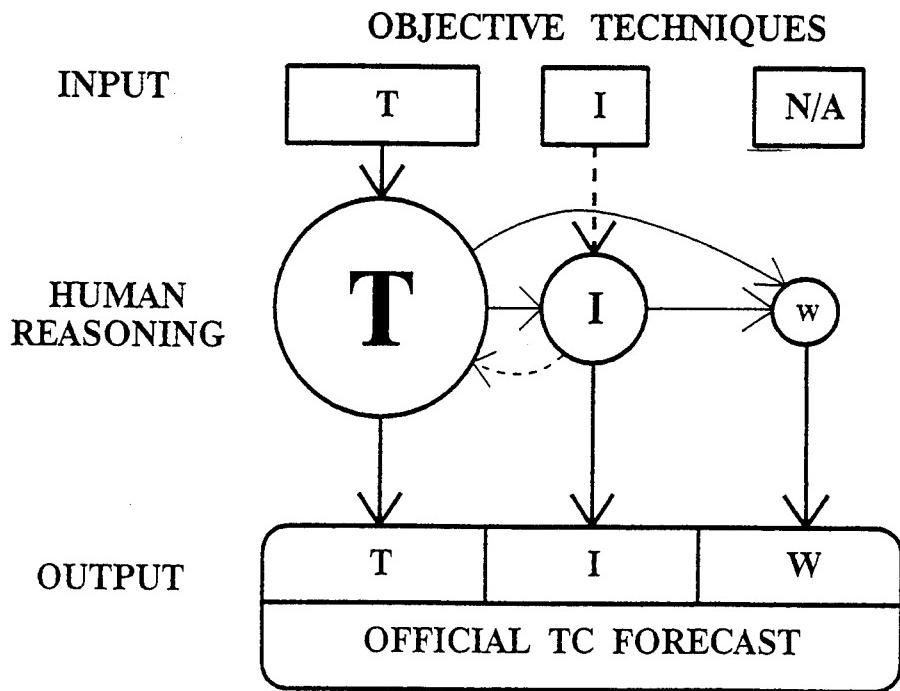


Fig. 1.3 As in Fig. 1.2, except for schematically portraying the "historical" approach to TC forecasting. Non-integrated (separated rectangles) objective techniques providing mostly track forecasts serve as input into a human reasoning process that is track-dominated (unequal circle sizes) and unidirectional (one-way thin, solid arrows).

forecast methodology. Furthermore, a case can be made that efforts to compensate for the large forecast errors arising from such an over-simplified forecasting approach have had an adverse impact on objective technique development and on the evolution of the forecast process. These problems are briefly identified below to further clarify the issues that an improved forecasting approach must address.

Two advantages of statistical techniques for track prediction are that no systematic errors should be present (given a sufficiently large sample), and the errors are minimized in a least squares sense. During model development, selection of the predictors may have been guided by real physical associations that were revealed by partial correlations between the potential predictors and predictands (TC motion). However, operational forecasters only have the output track from the statistical model, which then tends to become a "black box." An undue emphasis or dependence on these statistical techniques (to avoid biases and minimize errors over the season) may shift the focus of the forecaster away from dynamical considerations. As these statistical models have become increasingly complex, any insights they might give the forecaster into the dynamics of the TC forecast problem become more

obscure. Despite their practical utility, the widespread use of statistical models has contributed to making the present approach to TC forecasting excessively empirical, rather than dynamical.

An inherent deficiency of the statistical techniques is the inability to treat the outlier situations that contribute to "busted" forecasts, which lead to degraded customer confidence. This deficiency may be addressed by stratifying the database to account for variations in TC location, intensity, and synoptic situations (e.g., at JTWC two statistical-dynamical aids called CSUM and JT92 are used for TC motion prediction). However, the wide combinations of possible TC and environmental structures limit the gains attainable by such an approach.

In a similar vein, undue dependence on numerical model guidance may contribute to an overemphasis on environmental factors in TC track forecasting. Because numerical prediction models do much better at representing the evolution of the environment than the structure of the TC, they perform relatively well for the bulk of situations in which the environmental steering dominates. However, these models perform poorly in the important minority of situations where TC-environmental interaction(s) are important (Carr and Elsberry 1994).

Due in part to the above characteristics of statistical and numerical models, distributions of official track forecast errors for an entire season are distinctly skewed toward larger forecast errors, which may be as much as three times the mean (Fig. 1.4). Although warning centers characterize their performance on the basis of seasonal means (e.g., 107, 205, 305 n mi at 24, 48, 72 h for JTWC in 1992), it is the long "tail" of large forecast errors that place the users of TC warnings at risk.

Various subjective associations have been tested to compensate for the failure of objective guidance to forecast situations that depart significantly from the mean, and the tendency for objective guidance to have residual systematic errors. Some examples include: pattern-typing studies, such as Xu and Gray's (1982) association of various 500 mb patterns with fast, slow, and looping TC motion; Guard's (1983) association of TC intensity trends during recurvature with 200 mb wind patterns; and Weir's (1982) association of TC acceleration during recurvature with 200 mb wind patterns.

A large and generally undocumented body of empirical associations (commonly called "thumb-rules") have also naturally arisen out of operational experience. Typical examples of these thumb-rules include: (i) a particular objective technique is the "best" aid for a certain track type (e.g., recurving vs. straight); (ii) the direction and magnitude of objective track forecast biases depend on TC location in the environment (i.e., below, on, or above the subtropical ridge axis); and (iii) intensification rate is proportional to the number of outflow channels.

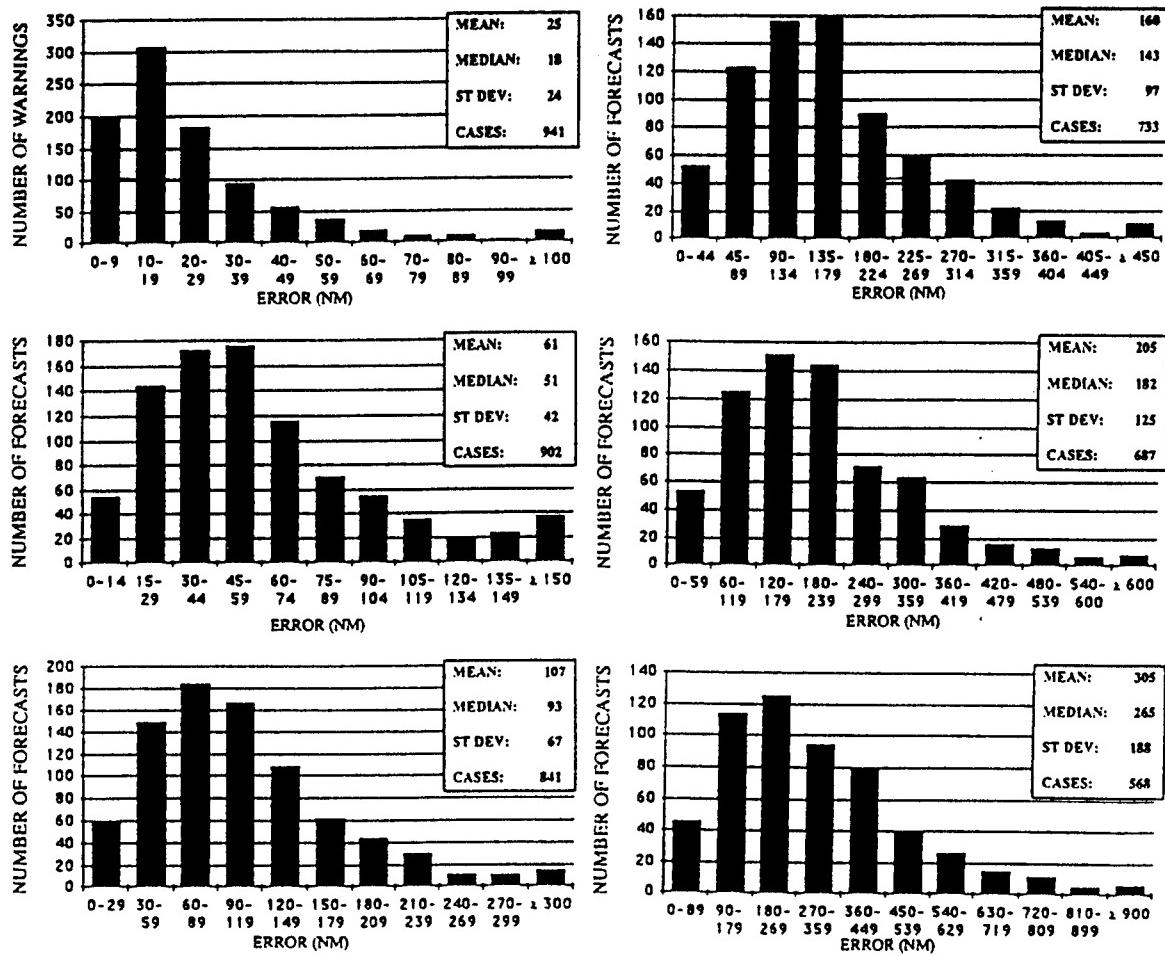


Fig. 1.4 JTWC initial position errors (upper left), and 12-h (middle left), 24-h (lower left), 36-h (upper right), 48-h (middle right), and 72-h (lower right) track prediction errors during 1992 for the western North Pacific.

The principal problem is not so much the validity of these thumb-rules, as it is the lack of proper documentation, and the lack of a systematic, consistent framework for using them. Thus, the application of thumb-rules varies from warning center to warning center, and even forecaster to forecaster and thus is often not consistent in time. As a result, the temporal consistency of official forecasts also may be degraded, and may not improve upon objective forecasts as expected (Elsberry and Dobos 1990).

In summary, the principal weaknesses in the current approach to TC forecasting are:

- insufficiently integrated and balanced treatment of the track, intensity, and wind distribution sub-problems;

- (ii) an environment-driven perspective that does not sufficiently account for significant interaction of the TC with its environment;
- (iii) excessive reliance on empirical techniques and thinking so that dynamical reasoning is underemphasized; and
- (iv) an insufficiently systematic and standardized approach, which results in degradation of forecast temporal consistency.

The proposed systematic approach will address to some extent all of the above deficiencies.

*c. Objectives and format*

The principal objective of the systematic approach to TC track forecasting is to overcome the problems described above. The approach implements the concept in Fig. 1.2 to the extent possible based on current understanding of TC evolution, and employs a framework that will facilitate incorporation of future insights. This systematic approach is designed to enable the TC forecaster to formulate an official TC track forecast that improves upon the numerical model (henceforth the FNMOC global model called NOGAPS will be used) track forecast by systematically applying forecaster reasoning to the forecast problem. The systematic approach is also integrated because expected departures of NOGAPS analyses and forecasts of TC intensity and wind distribution from actual conditions are taken into account in the formulation of the official track forecast.

Significant advancements in the understanding and modeling of TC motion and structure/structure change dynamics have occurred over the past decade as a result of the U. S. Office of Naval Research Tropical Cyclone Motion Accelerated Research Initiative (Elsberry and Abbey 1992; Elsberry 1994) and the U. S. National Oceanic and Atmospheric Administration (NOAA) research programs. However, these research results are scattered among many journals and technical reports, and are often in forms not immediately useful to the forecaster. Thus, an additional objective of the systematic approach has been the collection, organization, and incorporation of such research into the framework of Fig. 1.2. Summaries of research results will often be put in the Appendices to not unduly interrupt the description of the systematic approach. The reader is referred to these Appendices as necessary to understand the concepts utilized in the systematic approach.

Because current understanding of TC evolution is not complete, and is relatively weak in the intensification and size change aspects, the present approach can only incompletely accomplish the degree of integration suggested by Fig. 1.2. However, by creating an approach framework in which the integrated nature of TC track, intensity, and wind distribution as well as TC-environment transformations are emphasized, a natural outcome of this report will be to draw attention to areas in which additional research is needed.

The systematic approach is intended to offer the TC forecaster a practical problem-solving methodology. Since a comprehensive treatment of the total TC forecast problem is such a large and complex undertaking, an overview of the systematic approach is presented in Section 2. Section 3 will then provide detailed explanations of some conceptual models on which the systematic approach relies. Part II will illustrate the three major phases of the approach as it is intended to be applied at JTWC. A proof-of-concept demonstration of the systematic approach for selected historical examples will also be given in Part II, which closes with suggestions for additional research to implement fully the proposed systematic approach.

## **2. Approach overview**

The systematic approach is organized into three phases: Numerical Guidance Analysis, Objective Techniques Analysis, and Official Forecast Development (Fig. 2.1). As noted in the introduction, one of the major problems facing the forecaster is how to organize and logically apply all the available data, techniques, and dynamical concepts to solving the TC forecast problem. The systematic approach addresses this concern by organizing each forecast phase into resource, knowledge base, and process components. Resources are defined to be the raw materials that the forecaster may use to answer certain questions relevant to the forecast phase. Knowledge bases are defined to be the bodies of understanding that enable the forecaster to utilize the available resources in answering questions relevant to the forecast phase. The processes are defined to be a logical sequence of steps that assist the forecaster in accomplishing tasks by applying the knowledge bases to the resources within each phase in a consistent manner.

In accordance with the concept of Fig. 1.2, the principal resource to be used by the forecaster during the Numerical Guidance Analysis Phase is the standard set of analysis and forecast fields generated by the numerical TC prediction model serving the warning center, which for JTWC is provided by FNMOC's NOGAPS. Numerical products from other NWP centers could also be used with NOGAPS, but this aspect will not be discussed here. Additional resources that will be used to evaluate the likely veracity of the numerical guidance include various manual analyses produced by JTWC and satellite imagery.

The Numerical Guidance Analysis Phase employs two important knowledge bases. The first (which is the primary focus of Part I) is a comprehensive set of conceptual models to assist the forecaster in characterizing the TC-environment situation. This characterization is admittedly related to the environmental pattern typing schemes that have been unsuccessful in the past. However, the difference here is the inclusion of conceptual models that relate TC motion to: (i) TC structure (both intensity and size); and most importantly to (ii) TC-environment transformations, by which environmental patterns (and thus the attendant steering) may be significantly altered by the presence of the TC. The second knowledge base (which will be described in Part II as it applies specifically to JTWC for the western North Pacific) is a set of the traits and biases of the numerical TC prediction model organized in accordance with the conceptual model knowledge base.

The Numerical Guidance Evaluation Process of the first phase in Fig. 2.1 assists the forecaster to accomplish the two principle tasks in the human reasoning process described in Section 1.a.2. The first task is to use the TC-environment conceptual model knowledge base to develop a comprehensive understanding of the meteorological context in which the TC forecast problem is set *as depicted by the numerical guidance*. The second task is to use the numerical model traits knowledge base to estimate the extent to which the numerical guidance characterization of the TC-environment evolution and the associated TC motion will depart from reality. The importance and the separate purposes of these two tasks must be understood (and carried out) by the forecaster. It is essential that the forecaster

## SYSTEMATIC APPROACH FLOWCHART

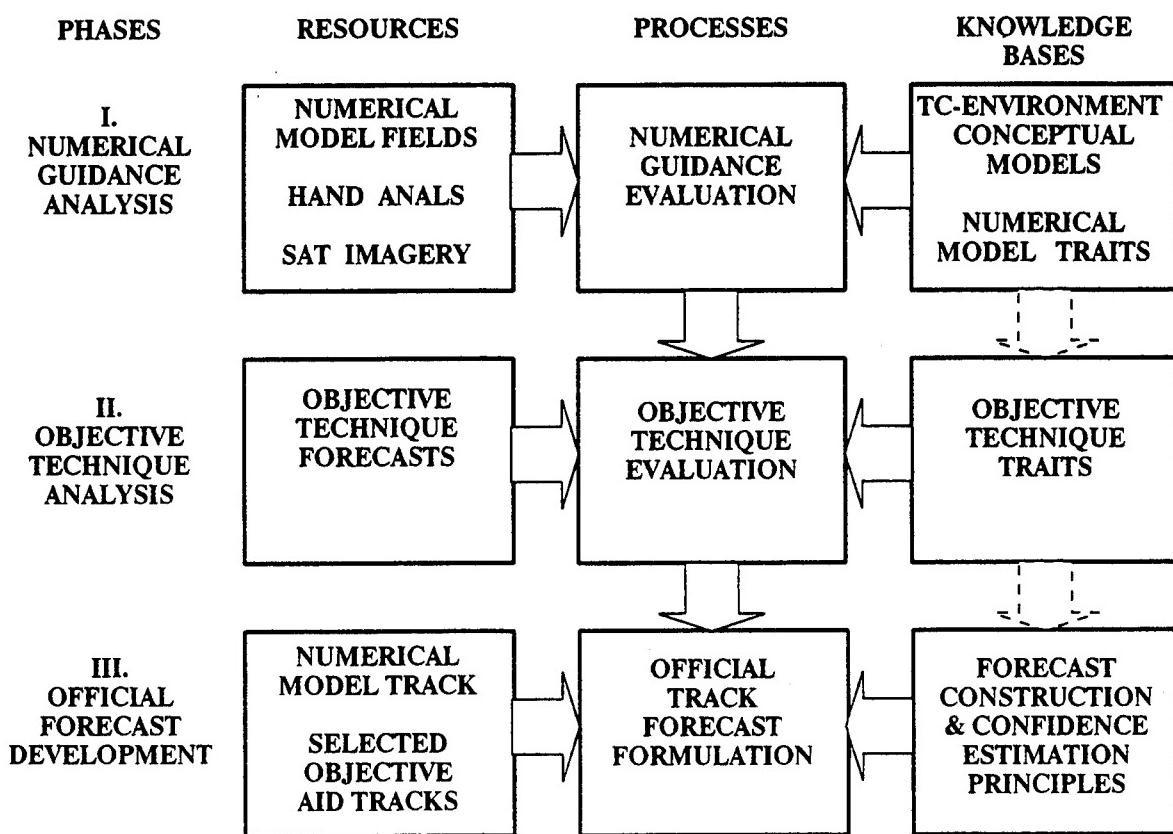


Fig. 2.1 Schematic flow chart of the three phases (left side) and inputs (top) in the schematic and integrated approach to TC track forecasting.

formulate an independent assessment of the meteorological situation. Even though the NOGAPS analysis is being used as the first step in the assessment, and the NOGAPS-predicted track is considered the first-order solution, the "value-addition" by the forecaster lies in the step-by-step reality check (first task) and modification of the numerical model guidance (second task). For example, if the NOGAPS model guidance has recently been good or bad, the forecaster must not fall into the trap of assuming that the accuracy of NOGAPS guidance will be the same in the present situation, and thus simply continue to follow or ignore the model guidance (called meteorological cancer). The essence of the systematic approach is to provide the framework for formulating the independent assessment of the synoptic context necessary to do the reality check at each stage in Fig. 2.1 and adjust

the numerical and other objective guidance accordingly.

The principal resource for the Objective Techniques Analysis Phase in Fig. 2.1 is the present and recent forecasts of the various objective techniques, which are primarily track techniques used by the warning center. It is emphasized that for the purposes of the systematic approach, the term objective technique is restricted to mean those simplified statistical, climatological, steering, or numerical models that are designed to forecast TC track (occasionally intensity). By contrast, sophisticated numerical prediction models, such as NOGAPS, are separately treated in the systematic approach (*i.e.*, Numerical Guidance Analysis Phase) because they provide an inherently (although inaccurate) integrated forecast of TC evolution.<sup>3</sup> The principal knowledge base of this phase is the expected traits/biases of the objective track forecasts, organized in accordance with the TC-environment conceptual model knowledge established in the first phase.

The Objective Techniques Evaluation Process of the Objective Techniques Analysis Phase in Fig. 2.1 assists the forecaster in accomplishing three tasks. The first task is to confirm, or modify as applicable, the expected TC-environment evolution forecast by the numerical guidance. The degree to which the objective technique forecasts are employed in this way will in general vary inversely with how well the recent numerical guidance has been, or is expected to perform for the present scenario. The second task is to estimate the biases expected for the objective track forecasts, using the objective technique traits knowledge base, and in light of the TC-environment picture determined during the Numerical Guidance Analysis Phase. Notice that these first two tasks are analogous to the two tasks of the Numerical Guidance Evolution Phase. The third task is to select a subset of objective technique tracks that are most consistent with the TC-environment evolution predicted by the numerical guidance, and thus will be considered with the numerically-predicted TC track in formulating the official forecast.

The resources of the Forecast Formulation Phase, the third and final phase in Fig. 2.1, are the TC tracks predicted by the numerical guidance and the subset of objective technique tracks determined from the Objective Technique Evaluation Phase. The knowledge base consists of a number of forecast construction and confidence estimation principles. The Official Track Forecast Formulation Process assists the forecaster in accomplishing two tasks. The first task is to construct an Expected Forecast Envelope from the numerical guidance track and subset of objective technique tracks, incorporating the expected track biases derived from the previous two phases. The second task is to construct the official TC track forecast that is based on the objective tracks from the Expected

---

<sup>3</sup> Another numerical prediction model called OTCM is also available at JTWC. However, because of its coarse vertical (3 layers) and horizontal resolution (205 km), crude TC specification, and use of analytic heating to maintain TC, OTCM will be treated as an objective track forecast technique for the purposes of the systematic approach.

**Forecast Envelope.** This task is accomplished by employing the dynamical and synoptic insights gained in the first two phases, and using various weighting and blending techniques. Due to the inherently integrated nature of the numerical guidance, the numerically-predicted TC track will generally be given precedence over the objective technique tracks when formulating the official forecast. In certain situations, the numerically-predicted track may be highly inaccurate, or unavailable (e.g., for weak, non-developing TCs that cannot be tracked objectively). In these cases, the tracks from the other objective techniques must be given more emphasis. The purpose of the systematic approach in Fig. 2.1 is to provide the forecaster with a step-by-step technique to follow for choosing the best guidance on which to base the official track forecast. The greatest benefit of the systematic approach, and the largest potential value-addition by the forecaster, is to recognize and to improve the forecasts in these cases in which the numerical guidance is not accurate.

The organization of this two-part report has been guided by the structure of the systematic approach flow chart in Fig. 2.1. Because the TC-Environment Conceptual Models knowledge base, the Numerical Model Traits knowledge base, and the Objective Technique Traits knowledge base all require rather extensive development and documentation, separate sections of this report will be devoted to each knowledge base. The application of the TC-Environment Conceptual Models knowledge base involves only the first aspect of the human reasoning process (see Fig. 1.2 and related discussion). Because this knowledge base is so extensive and influences all aspects of the Systematic Approach process, the remainder of Part I will describe this knowledge base.

Part II of this report will then describe the Numerical Model Traits and Objective Technique Traits knowledge bases. Part II then continues with a broader step-by-step application of the entire systematic TC forecast approach that is illustrated with several proof-of-concept demonstrations.

### 3. TC-environment conceptual models knowledge base

Some introduction is necessary to the NOGAPS analyses used here to illustrate the conceptual model. The Numerical Guidance Analysis Phase employs NOGAPS fields at the 850, 500, and 200 mb levels, and occasionally at the 700 mb level, may be used. The bulk of the analysis and interpretation is based on NOGAPS fields at the 500 mb level, which has historically been regarded as the best single level for depicting environmental steering. Justification for choosing 500 mb as the best single level for motion-related pattern interpretation is provided in Section 3.c.1), in which a set of conceptual models is defined based on relationships between intensity and steering.

The authors suggest that streamline and isotach analyses of NOGAPS wind fields provide the most effective indication of the direction of environmental steering influencing most TCs (exceptions are primarily in vertical wind shear cases described in Section 3.d; see also the TC intensity in Subsection 3.c.1). A particularly striking example involves Typhoon Abe during the period from 1200 UTC 26 August to 0000 UTC 28 August 1990. As Abe's direction of motion changed from north-northeast to west-northwest (Fig. 3.1), the associated 12-h NOGAPS streamline/isotach analyses (Fig. 3.2a-d) each had a closed, crescent-shaped 30-kt isotach to the right of the direction of TC motion at the time of the analysis. Notice how the 30-kt isotach smoothly rotated counter-clockwise in agreement with Abe's turn during the period. Thus, the 500 mb isotach pattern in the vicinity of the TC will be used here to provide a qualitative indication of the near-term direction of motion of the TC based primarily on the steering concept that is implied in the analysis. Similarly, the analogous isotach patterns in the NOGAPS 500 mb forecast wind fields can be used to provide a quick visual check on the longer-range *NOGAPS-predicted* steering of the TC.

The direction of environmental steering may also at times be estimated by comparing the JTWC working best track<sup>4</sup> TC position relative to the center of the NOGAPS-analyzed circulation. Whereas the JTWC position of Abe nearly coincides with the center of the NOGAPS in Fig. 3.2a, the JTWC positions are displaced 1° to 2° from the closed 30-kt isotach side of the NOGAPS circulation centers in Figs. 3.2b-d. When these position discrepancies are systematic, they may be attributable to the steering flow of the background environment. Such a steering flow tends to shift the wind center of a vortex to the left (relative to the direction of steering) of the vorticity center (which determines the JTWC position since it is based on satellite imagery). The magnitude of the center shift is proportional to the steering speed and the radius of maximum winds, and inversely proportional to the maximum winds of the vortex. The dependence on steering speed explains the small position discrepancy in Fig. 3.2a since the 6-h past motion of Abe was

---

<sup>4</sup> The JTWC working best track is the series of continually updated storm positions that has been updated as new fixes were received. That is, it reflects the best estimate of the present (warning) storm position and a smoothed representation of the prior track.

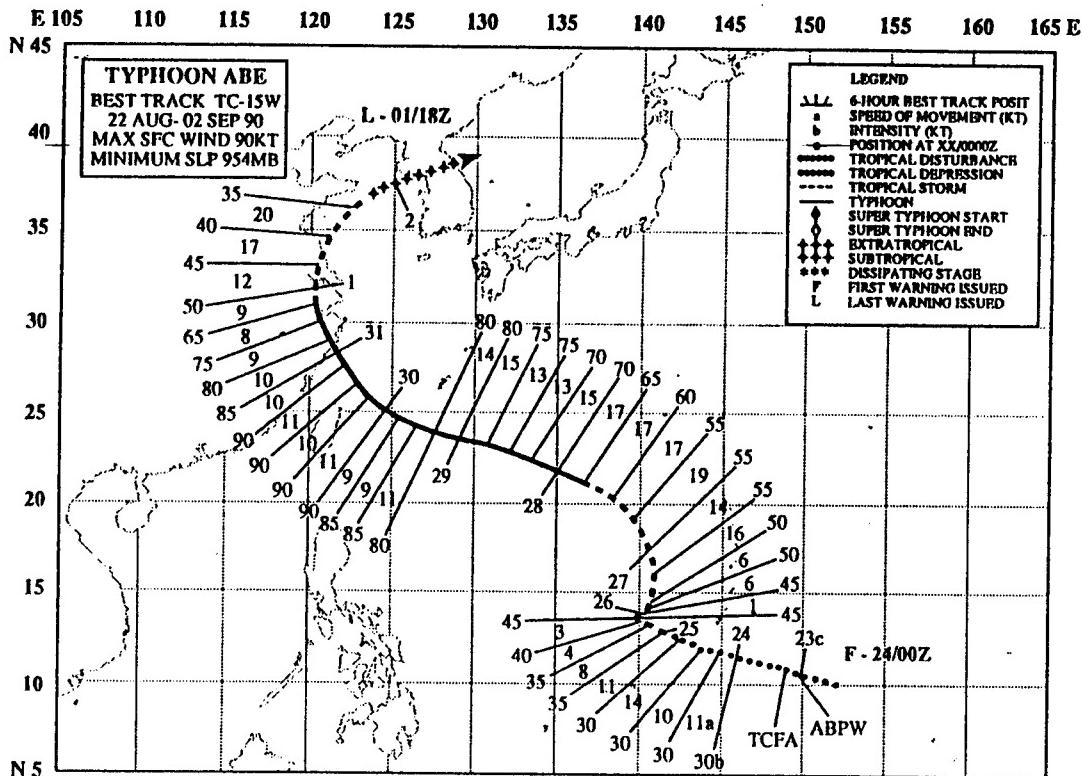


Fig. 3.1 Joint Typhoon Warning Center best track for Typhoon Abe 22 August to 2 September 1990. Positions at 0000 UTC are indicated along the track with intensities (kt) indicated at the end of radials extending from intermediate 6-h positions, storm translation speeds over 6 h are indicated between these radials (see inset for explanation of symbols).

only 6 kt (Fig. 3.1), and the larger displacements were at later times when Abe was moving at 14-17 kt.

Such steering-induced separations of vortex wind and vorticity centers would normally be small in a mature TC because the radius of maximum winds is small and the maximum wind speed is high. However, the center separation is usually evident in the NOGAPS analysis owing to the relatively coarse T79 resolution prior to June 1994, which artificially inflates the radius of maximum winds and reduces the maximum wind speed.<sup>5</sup> This second method for estimating the direction of NOGAPS-analyzed steering may be particularly

<sup>5</sup> A cursory examination of recent T159 NOGAPS resolution analyses indicates that the 1° to 2° lat. separation between the JTWC storm position and the analyzed circulation center still occur.

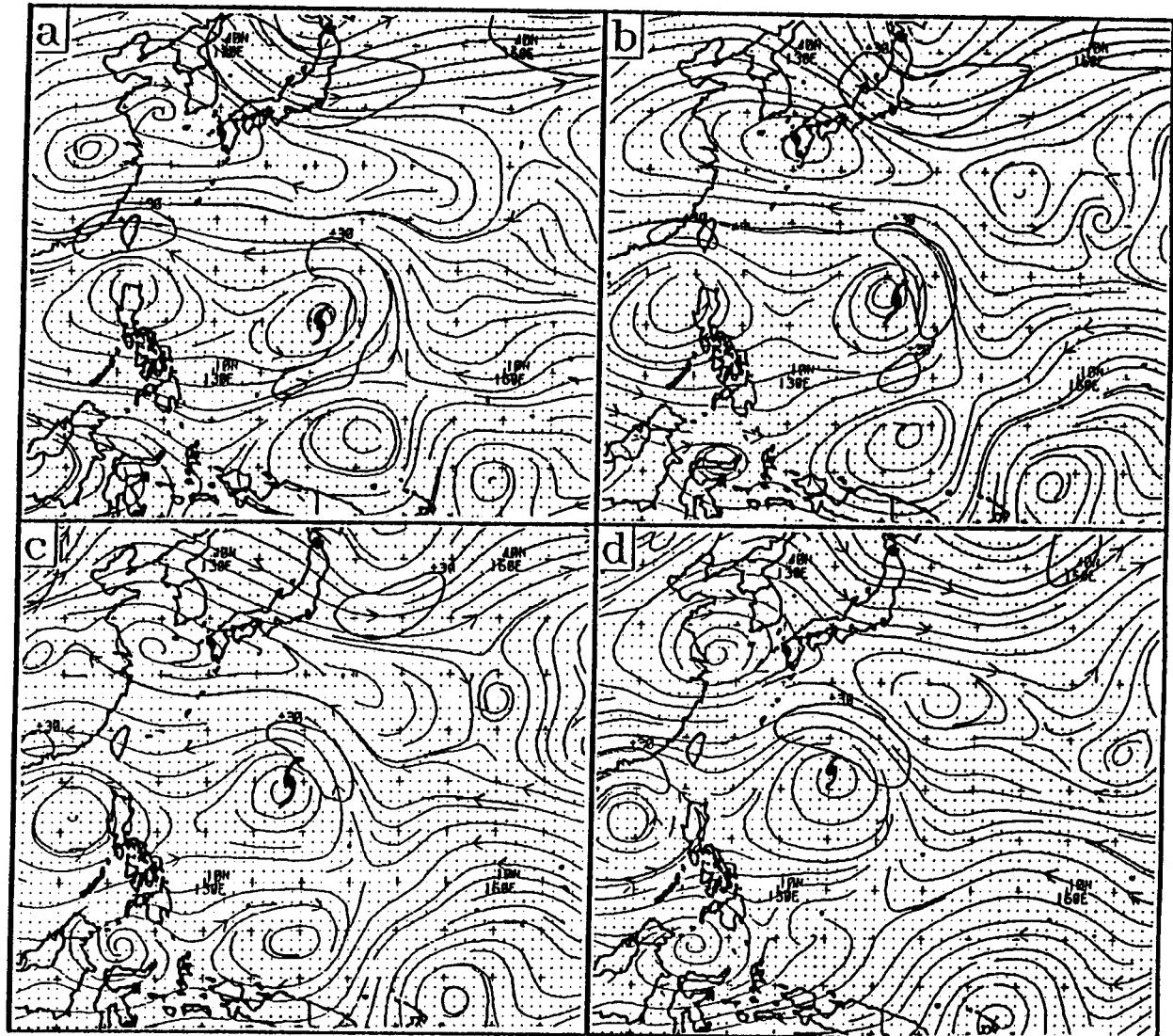


Fig. 3.2 NOGAPS 500 mb streamline and isotach analysis at (a) 1200 UTC 26 August 1990, (b) 0000 UTC 27 August 1990, (c) 1200 UTC 27 August 1990, and (d) 0000 UTC 28 August 1990. The TC symbol denotes the position of Typhoon Abe. The isotachs (thick lines) begin at 30 kt, and the contour interval is 20 kt.

useful when no 30-kt isotach is present or the complexity of the 30-kt isotach pattern makes interpretation difficult.

In principle, the direction of the streamline flow over the JTWC working best track position should give the best indication of 500 mb steering since the measurement occurs at the vorticity center of the TC. However, inaccuracy in the JTWC position arising from fix errors can complicate interpretation. In practice, the best estimate of steering may result from a subjective consensus of the two methods.

#### *a. Organization*

A set of TC-environment conceptual models has been developed to assist the forecaster in formulating a comprehensive understanding (or mental picture) of how the mutual influence of the TC and its environment may determine TC motion. The inherently complex nature of TC forecast scenarios has necessitated a rather broad array of conceptual models. Since this TC-environment conceptual model knowledge base is effectively the heart of the systematic approach, it is crucial that provision be made to facilitate efficient and consistent utilization of this large knowledge base in an operational setting. Thus, a system has been developed that: (i) organizes the individual models into related groups of models; and (ii) establishes general principles for how the model groups interact and change with time. An introduction of this system is provided first, before addressing the details of the synoptic framework.

The set of conceptual models is organized into three general groups:

- **Environment Structure:** characterizations of environmental flows, excluding the symmetric circulation of the TC being forecast, and without any TC-environment interactions (Table 3.1);
- **TC Structure:** characterizations of the intensity and size of the symmetric TC (Table 3.2); and
- **TC-Environment Transformations:** characterizations of one- and/or two-way advections or energy exchanges between the TC and the environment (Table 3.3).

Within the **Environment Structure** group (Table 3.1), the conceptual models are further organized into two subsets based on scale:

- **Synoptic Patterns:** classifications of the large-scale environment surrounding the TC based on the existence and orientation of various synoptic features such as cyclones, anticyclones, ridges, and troughs.
- **Synoptic Regions:** identification of smaller areas within the synoptic patterns where certain characteristic directions of environmental steering may be expected to occur.

**Table 3.1 Environment structure conceptual models organized by four Synoptic Patterns and various Synoptic Regions that appear in the synoptic patterns.**

SYNOPTIC REGIONS	SYNOPTIC PATTERNS			
	Standard (S)	North-oriented (N)	Monsoon Gyre (G)	Multiple Tropical Cyclone (M)
Dominant Subtropical Ridge (DR)	X		X	
Weakened Subtropical Ridge (WR)	X			
North-oriented (NO)		X	X	
Accelerating Mid-latitude Westerlies(AW)	X	X	X	
Multiple TC Southerly Flow (SW)				X
Multiple TC Northerly Flow (NF)				X

**Table 3.2 TC intensity and TC size conceptual models within the TC structure. Intensities are characterized in terms of maximum wind speed ( $v_m$ ) in kt. See discussion in Subsection 3.b.2 for explanation of definitions of TC sizes.**

#### TC INTENSITY

- (XL) Exposed Low-level Circulation
- (TD/TS) Tropical Depression/Storm ( $25 \leq v_m \leq 60$ )
- (TY) Typhoon ( $65 \leq v_m \leq 100$ )
- (IT) Intense Typhoon ( $v_m \geq 105$ )

#### TC SIZE

- (M) Midget TC
- (S) Small TC
- (A) Average TC
- (L) Large TC

**Table 3.3 TC-Environment transformation conceptual models defined in the Systematic Approach**

<b>Basic <math>\beta</math>-effect Propagation (BEP)</b>
<b>Vertical Wind Shear (VWS)</b>
<b>Ridge Modification by large TC (RMT)</b>
<b>Monsoon gyre-TC Interaction (MTI)</b>
<b>Tropical Cyclone Interactions (TCIs)</b>

Within the **TC Structure** group (Table 3.2), the conceptual models are organized into two subsets based on TC Intensity and TC Size. The TC Intensity categories (with the exception of the Exposed Low-level Circulation category) have standard definitions. Thus, they need no further introduction here. By contrast, no standard definitions of TC size are currently available, and basic research has shown that is not just the extent of the TC wind field, but also the magnitude of the outer tangential winds, or TC strength, that influences TC motion. Thus, a proposed system will be introduced in Subsection 3.c.2 that provides dynamically meaningful definitions of the TC size categories shown in Table 3.2.

An overview of the various groups and subsets of conceptual models within the complete TC-environment conceptual framework is provided by Fig. 3.3. Notice that the Environment Structure, TC Structure, and TC-Environment model groups are distinct components of the TC-environment description. Each Synoptic Region in which the TC occurs is defined as a subarea of a Synoptic Pattern, which is denoted by nesting the Synoptic Region portion within the Synoptic Patterns portion of the TC-environment description. By contrast, the intensity and size of the TC are denoted in Fig. 3.3 as separate aspects of TC Structure. Subject to certain conditions, various combinations of TC Structure (*i.e.*, size and intensity) and Environment Structure (*i.e.*, pattern and region) may be contributing (solid arrows) to TC-Environment Transformations, which in turn act (dashed arrows) to alter those combinations of TC Structure and Environment Structure, and thus affect TC motion. This feedback between the TC and Environment Structure portions of the TC-environment description is considered an essential aspect of real TC motion behavior, and thus is a key element of the systematic approach.

Although Fig. 3.3 provides a "snap-shot" of the TC-environment description at any time, the difficult aspect is to indicate how the Environment Structure or TC Structure component will change with time as a result of TC-environment transformations or other mechanisms. TC structure changes arising from TC-environment transformations or other mechanisms must proceed smoothly through the respective sets of TC structure conceptual models in Table 3.2. For example, a tropical depression can only become an intense typhoon by proceeding through the tropical storm and typhoon stages of intensity. Similarly, a midget TC can only become a large TC by first proceeding through the small and typical TC size categories.

## COMPLETE CONCEPTUAL PICTURE

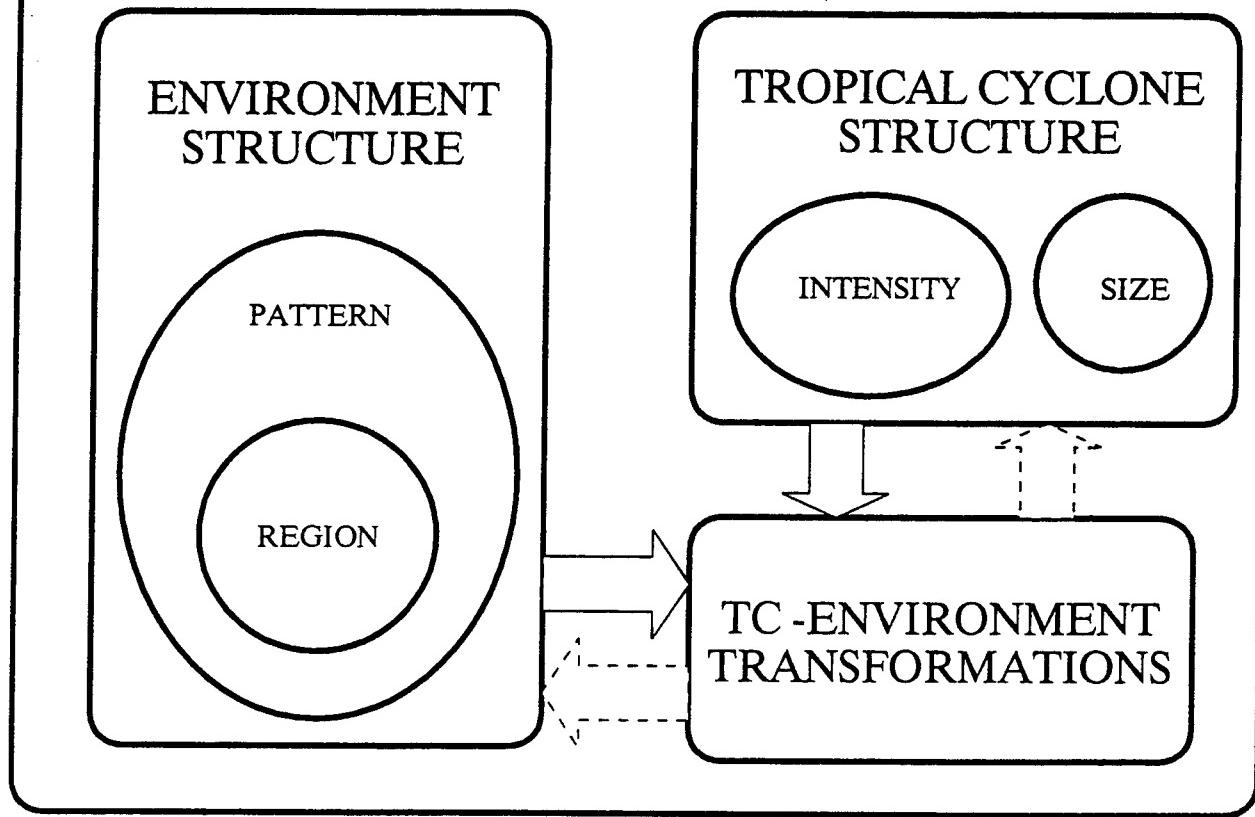


Fig. 3.3 Overview of the three groups of conceptual models in the Systematic Approach with transformations indicated by the arrows.

By contrast, environmental changes that result from TC-environment transformations or other mechanisms are inherently more complex phenomena since the Synoptic Pattern and Synoptic Region conceptual models are not independent. That is, some regions are associated only with certain patterns (Table 3.1). Thus, changes in the Environment Structure (dashed arrow in Fig. 3.3) imply a change from one pattern/region combination to another, which will be referred to as an "environmental transition," and the impetus for the transition will be referred to as a "transitional mechanism." These transitional mechanisms (Fig. 3.4) will include not only TC-environment transformations, but also phenomena that do not depend on the TC being forecast, such as simple environmental steering of the TC through some patterns, and evolution of the large-scale environment. Notice that environmental transitions may result in just a change of TC region within the same pattern (Fig. 3.4a), or may result in a change in both the pattern and region (Fig. 3.4b).

## ENVIRONMENT TRANSITIONS

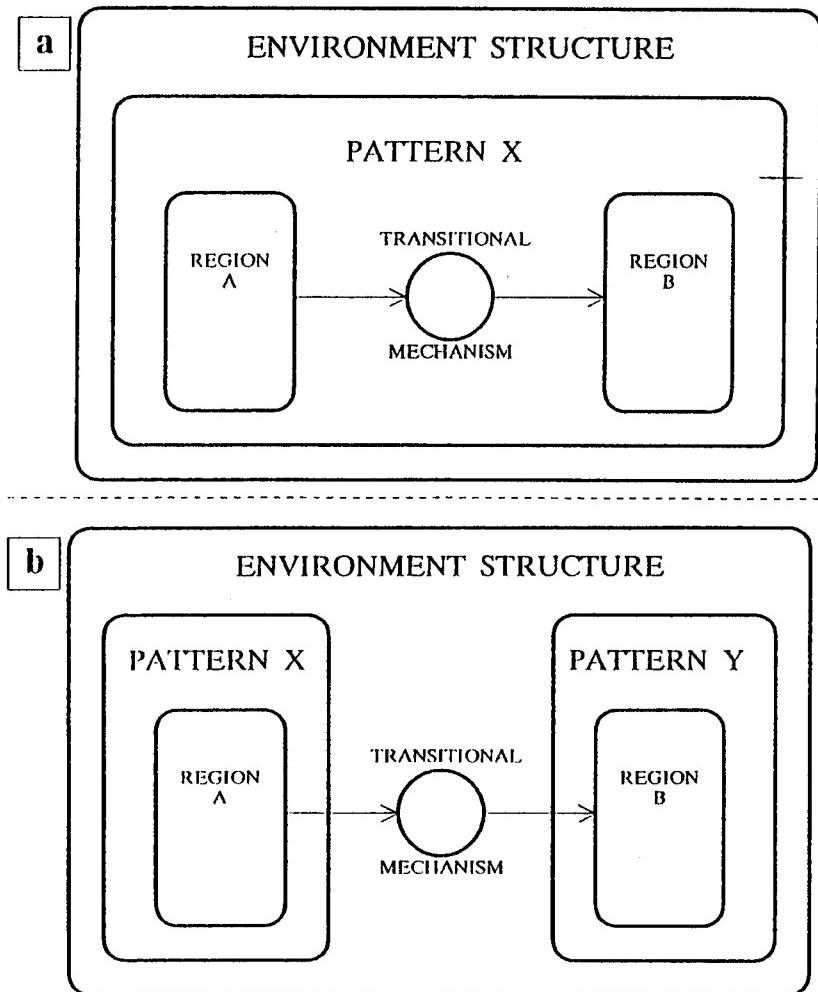


Fig. 3.4 Environment transitions in which the environment structure with respect to the TC changes due to a Synoptic Region change (a) within the same Synoptic Pattern X, or (b) a Synoptic Pattern change as well.

Environment transitions typically are accomplished over a period of one to several days, which is significantly longer than the 12-h period between successive global model analysis and prognostic fields. During these transitions, the structure of the environment may not be described particularly well by a single pattern and region. The term "transition state" will be used to describe these situations in which the environment of the TC is evolving from one pattern to another. Similarly, the term "transition zone" will be applied when the present location of the TC within a single persistent pattern is best described as being between two adjacent regions.

In summary, the complete TC-environment conceptual framework, with a wide array of individual models and provision for complex interactions and transitions among those models, is clearly complex. Such complexity is necessary to give the systematic approach the

capacity to address the wide variety of TC motion scenarios. It is emphasized that only a relatively small subset of models and associated environmental transitions apply for any particular forecast situation. Specifically, a conceptual description of the TC-environment situation affecting TC motion at any time will usually consist of: (i) one synoptic pattern, or a transition state between two synoptic patterns; (ii) one synoptic region, or a transition zone between two synoptic regions; (iii) one TC size class; (iv) one TC intensity class; and (v) one principal transitional mechanism (e.g., TC-environment transformation, etc.) that is acting to change TC structure and/or change environment structure (i.e., cause pattern and/or region transitions).

The following subsections develop the TC-environment conceptual framework following the order of the above discussion. Section 3.b describes the Synoptic Pattern and Synoptic Region conceptual models of Environment Structure, and Section 3.c covers the Intensity and Size models of TC Structure, and Section 3.d covers the TC-Environment Transformation models.

b. *Environment Structure*

1) Synoptic Patterns. The following subsections introduce each of the conceptual models of the Environment Structure group using a schematic, and then provide examples using NOGAPS streamline and isotach analyses primarily at 500 mb. The structure and orientation of the mid-tropospheric subtropical ridge is the prominent feature in many of the conceptual models. The term "ridge" will hereafter be understood to mean "mid-tropospheric subtropical ridge," unless another ridge such as a midlatitude or subequatorial is intended.

a) Standard (S) Synoptic Pattern For the environmental Synoptic Pattern surrounding the TC to be classified as Standard (S), the axis of the ridge circulation influencing the steering of the TC must be approximately zonally-oriented. In an idealized S Pattern (Fig. 3.5) an east-west oriented ridge separates tradewind easterlies that are equatorward of midlatitude westerly flow. The ridge structure may be modulated by a principal midlatitude trough that produces a col region (usually called a "break") in the ridge equatorward of the midlatitude trough. The idealized S Pattern also has a cyclonic circulation with a zonally-oriented axis to the equatorward of the tradewind easterlies. This circulation will usually represent the monsoon trough.

Notice that TC symbols and concentric circles have been placed at various positions in Fig. 3.5 to indicate where the TC circulation may be found relative to the ridge. Although pattern orientation relative to the TC is important, by definition the circulation of the TC being forecast is excluded. An experienced forecaster will mentally remove the TC circulation from the NOGAPS fields. However, a filter would be required for an automated version of the systematic approach.

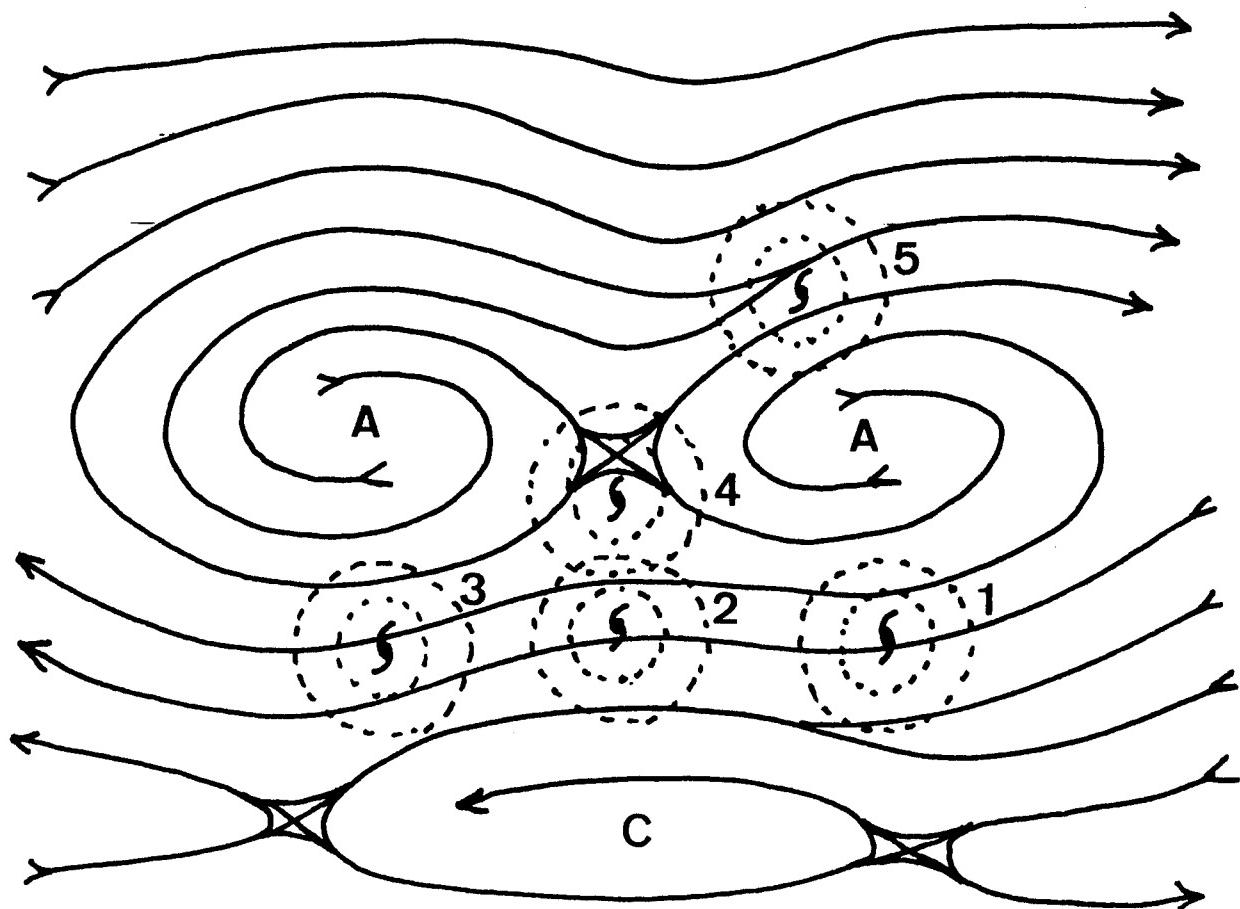


Fig. 3.5 Schematic of the Standard (S) Synoptic Pattern conceptual model. TC symbols and dotted concentric circle denote possible positions for TCs within the S pattern.

Although the S Pattern pictorial is for a single instant in time, connecting sequences of the TC symbols gives the general sense of the basic types of TC tracks that may occur. TC symbol sequence 1-2-3 represents that straight or "straight-runner" track, and sequence 1-4-5 represents the recurvature or "recurver" track. However, this assumes that the S Pattern is not transitioning to another pattern (e.g., due to the influence of TC-environment transformations).

The possible TC positions in Fig. 3.5 are distinct from the idealized monsoon trough. However, it is recognized that large TCs do not clearly separate from the monsoon trough early in their lifecycle; rather, the large TC and monsoon trough tend to temporarily move together. This situation is ignored in defining and recognizing the S Pattern, and does not affect the utility of the definition because it is assumed that the ridge structure will dominate TC motion as long as the large-scale environment conforms to the S Pattern and TC-environment transformations are not expected.

The idealized S Pattern in Fig. 3.5 is intended to be a basic template for the most common organization of TC environment. Thus, it must be adapted to conform to particular synoptic situations; e.g., by a shift in latitude or longitude. During the summer monsoon season, the S Pattern appears farther poleward so that the cyclonic feature represents the monsoon trough. During the fall and summer transition seasons, the S Pattern will appear farther equatorward, and hence the cyclonic feature typically will represent a near-equatorial trough. During the NH winter, the S Pattern will be shifted even farther equatorward so that the near-equatorial trough is along the equator and becomes a buffer zone.

Important and frequently observed variants of the S Pattern include:

- (i) absence of a significant break in the ridge in the general vicinity of the TC;
- (ii) different latitudes of the east and west ridge circulations so that the ridge axis has a west-southwest to east-northeast or west-northwest to east-southeast orientation; and
- (iii) unequal meridional extent of the ridge circulations on either side of the main break in the ridge.

The first variant produces predominantly easterly steering, and may result in prolonged and nearly westward TC motion if the S Pattern persists and no significant TC-environment transformations are taking place. The remaining two variants produce steering that deviates significantly from easterly, and may result in significant increases or decreases in latitude while the TC is equatorward of the ridge axis.

An example of a S Pattern variant (i) is the 25 November 1991 analysis in the vicinity of Supertyphoon Yuri (Fig. 3.6a). An unbroken, nearly east-west oriented, and meridionally-uniform ridge circulation extends from the Southeast Asia to the dateline. Yuri is located well south of the center of the ridge circulation, and is still closely connected with the monsoon trough. An example of a S Pattern variant (ii) is the 13 September 1990 analysis in the vicinity of Typhoon Ed (Fig. 3.6b). Because the ridge to the east is at a higher latitude than the ridge to the west, an anomalous TC track that is south of west may be anticipated. An example of a S Pattern variant (iii) is the 10 July 1991 analysis in the vicinity of Typhoon Amy (Fig. 3.6c). Whereas the ridge circulation over China to the west of the ridge break is rather small, the ridge circulation southeast of Japan to the east of the ridge break is quite broad. Such a tapered ridge tends to steer the TC to the west-northwest, apart from any TC propagation. The 17 September 1990 NOGAPS analysis in the vicinity of Typhoon Flo (Fig. 3.6d) is an example of a S Pattern with a complex ridge structure that has elements of both variants (ii) and (iii) since the ridge circulation east of Flo is broader and at a higher latitude than the ridge circulation to the west.

In Fig. 3.6b, notice a disturbance to the southeast of Ed that later becomes

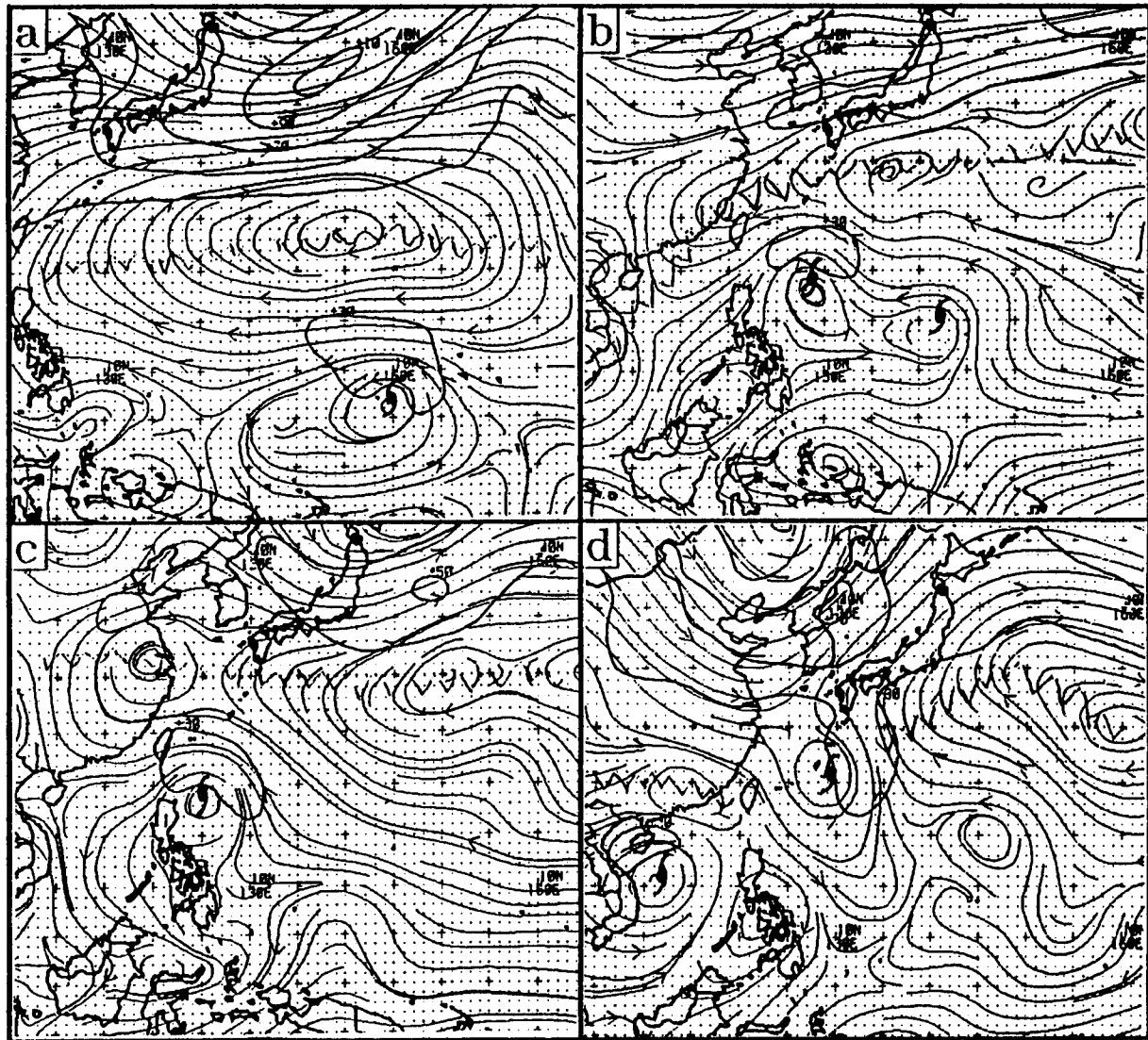


**Fig. 3.6** NOGAPS 500 mb streamline isotach (kt) analyses at (a) 0000 UTC 25 November 1991, (b) 1200 UTC 13 September 1990, (c) 0000 UTC 18 July 1991, and (d) 1200 UTC 17 September 1990. The TC symbols denote the positions of (a) Supertyphoon Yuri, (b) Typhoon Ed (west) and Supertyphoon Flo (east), (c) Typhoon Amy, and (d) Typhoon Ed (west) and Supertyphoon Flo (east).

Supertyphoon Flo. At this time, the circulation of Flo is too weak and is not correctly positioned to set up the Multiple Tropical Cyclone (M) pattern discussed later. Thus, both Ed and Flo share the same S pattern. In other situations with two TCs that are farther apart, each TC may be associated with a separate pattern (see Fig. 3.11c-d and related discussion)

b) North-oriented (N) Synoptic Pattern The conditions for classifying an environmental Synoptic Pattern as North-oriented (N) are: (i) a significant break in the ridge must be present poleward of the TC; and (ii) a prominent, and primarily north-south oriented, ridge to the east of the ridge break that also extends significantly equatorward of the latitude of the TC. Such an anomalous ridge structure to the east of the TC can arise from either a TC-independent or TC-dependent situation:

N1: TC-independent development of a reverse-oriented (RO) monsoon trough as defined by Lander (1994; personal communication); or

N2: one of the following TC-environment transformations (Table 3.3): (i) modification of the ridge by a large TC (RMT; see Subsection 3.d.3); or (ii) interaction of a monsoon gyre (MG) and a TC involving the coalescence of the TC and MG (MTI; see Subsection 3.d.4).

In the idealized N1 Pattern in Fig. 3.7a, the monsoon trough is depicted as an unbroken feature, despite the removal of the TC circulation. The southwest to northeast orientation of this monsoon trough is distinctively different from the climatological west-northwest to east-southeast orientation of the summer monsoon trough (cf., Elsberry 1987; Fig. 3.18a). Lander views this "reverse-oriented" monsoon trough as one of several modes of deviation from the climatological mean, and he notes that such a trough typically persists for several weeks. The key feature for designating this pattern of the N type is the anomalous ridge circulation to the east, which has an orientation that roughly parallels the monsoon trough. As suggested by the numbered sequence of TC symbols in Fig. 3.7a, TCs typically form in the generally poleward flow between the trough and ridge features, proceed on a roughly poleward track, and recurve at a higher than normal latitude.

An example of a N1 Pattern is the NOGAPS analyses for the period 0000 UTC 23 July to 1200 UTC 30 July 1990 (Fig. 3.8a-d). During this week, the monsoon trough east of the Philippines maintains a remarkably consistent southwest to northeast orientation. The ridge circulation to the east of the monsoon trough roughly parallels the orientation of the trough, and builds in both meridional and zonal extent. During this period, Typhoons Steve and Vernon formed in the vicinity of the monsoon trough and moved north to northeastward.

The dynamics of the evolution of the monsoon trough into a southwest to northeast orientation with accompanying ridging to the east and southeast has not been addressed in the literature. Carr and Elsberry (1995) noted the tendency in a nondivergent, barotropic

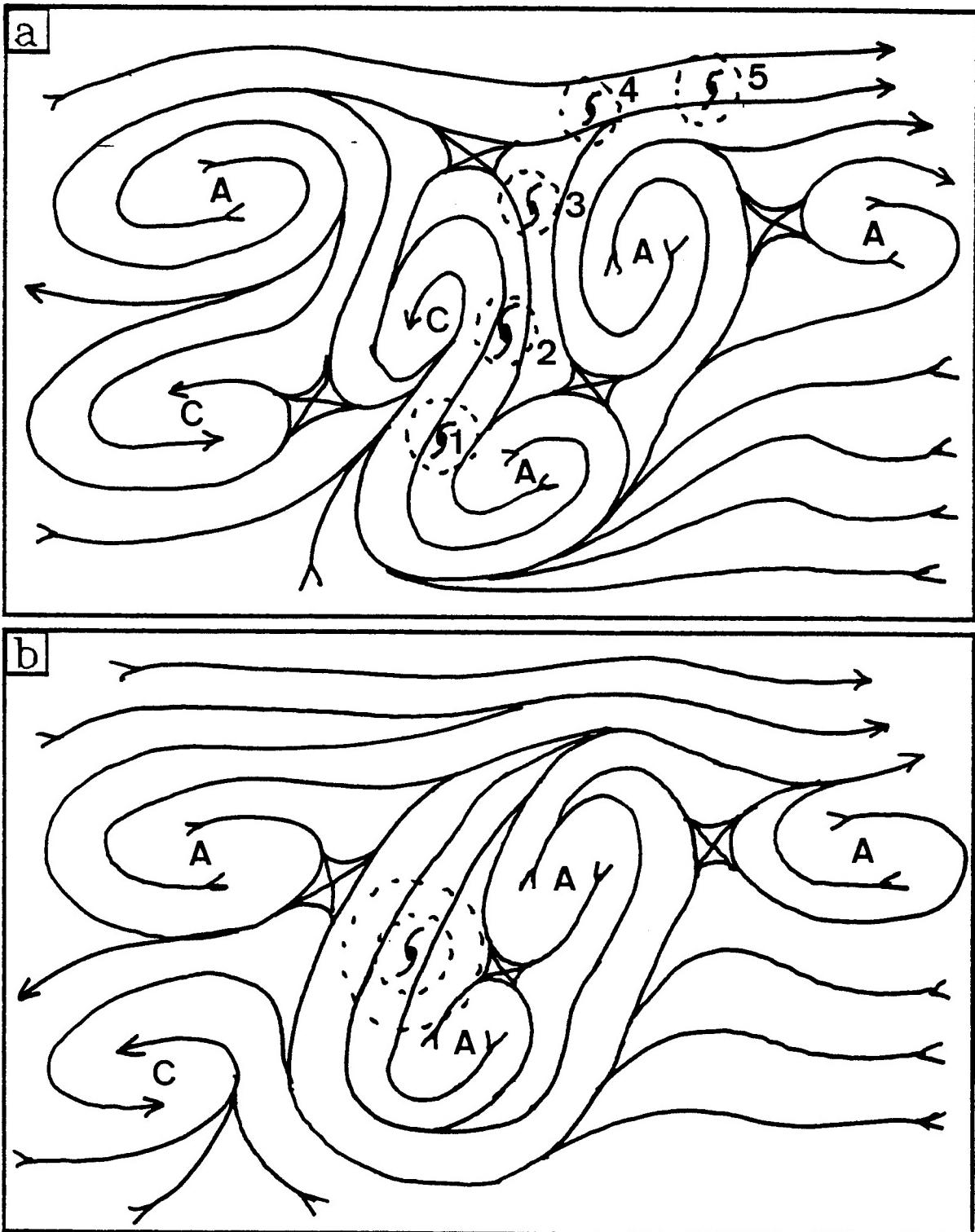


Fig. 3.7 As in Fig. 3.5, except for North-oriented Synoptic Patterns (a) N1, and (b) N2.

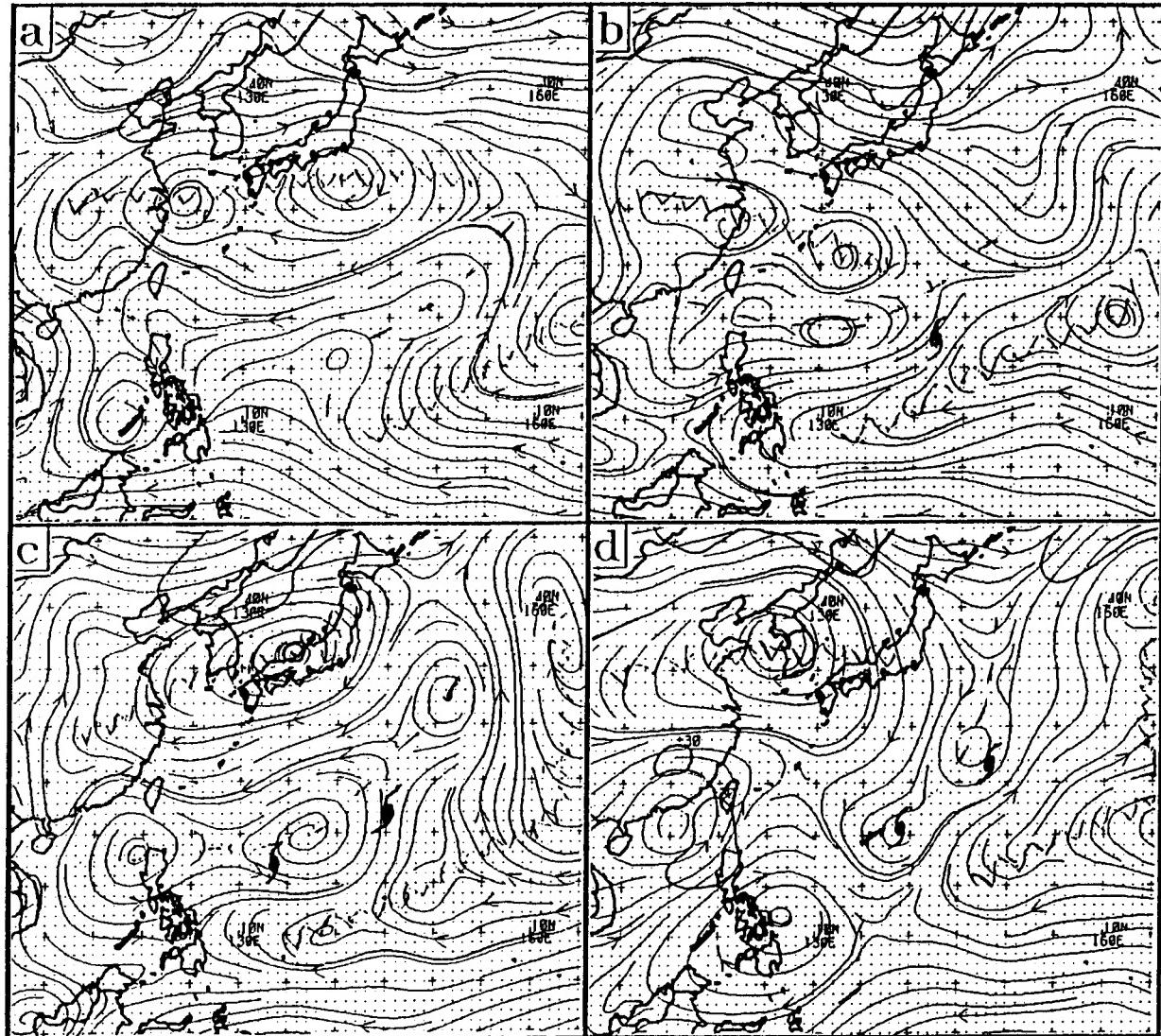


Fig. 3.8 NOGAPS analyses as in Fig. 3.6, except for (a) 0000 UTC 23 July, (b) 1200 UTC 25 July, (c) 0000 UTC 28 July, and (d) 1200 UTC 30 July 1990. The TC symbols denote the positions of (b) Typhoon Steve, and (c)-(d) Typhoons Steve (north) and Vernon (south).

model for large vortices representing the monsoon trough to disperse into northwest-southeast oriented wave trains via  $\beta$ -induced Rossby wave-like energy propagation (Fig. 3.9). When a TC-scale vortex is added 800 km to the east of the monsoon gyre center (Fig. 3.10a), the TC remains distinct from the gyre, and by 48 h the gyre has evolved into an elongated trough/ridge pair (Fig. 3.10b) that has a southwest-northeast orientation on a scale that resembles the monsoon trough pattern in Fig. 3.8. Although these barotropic simulations of Carr and Elsberry need to be confirmed with more realistic baroclinic simulations, they provide a preliminary dynamical basis for the structure of the N1 Pattern (Fig. 3.7a).

The N2 Synoptic Pattern may be distinguished from a N1 Pattern by the presence of one large TC as opposed to a southwest to northeast monsoon trough with one or more smaller TCs embedded in it. In the idealized N2 Pattern (Fig. 3.7b), the removal of the large TC or the coalesced MG-TC leaves a monsoon trough that is restricted to the southwestern portion of the pattern. Another important dissimilarity is that the TC position in the N2 Pattern tends to be at a particular location relative to the anomalous eastern ridge circulation(s), whereas the TC position in the N1 Pattern can be anywhere in the southerly flow between the trough and the anomalous ridge. Thus, the N2 Pattern *tends to move poleward with the large TC or coalesced MG-TC.*

An example of a N2 Pattern associated with a large TC occurred in conjunction with Supertyphoon Yuri. On the 28 November 1991 (Fig. 3.11a), Yuri is centered near 14°N, 141°E, and the axis of the anomalous ridge to the east is between an anticyclone near 19°N, 156°E and a buffer eddy near 1°S, 148°E. Over the next 24 h (Fig. 3.11b), all three circulations move west and north while maintaining the same approximately triangular orientation.

Two concurrent examples of a N2 Pattern associated with interactions between monsoon gyres (MG) and TCs occurred in conjunction with Typhoon Sarah and Tropical Storm Tip. On 10 September 1989 (Fig. 3.11c): (i) Sarah has already coalesced with the MG just to the northeast of Luzon; (ii) although anomalous ridging is evident to the southeast, the expected anomalous ridging to the northeast of Sarah is obscured by the presence of the MG associated with Tip; and (iii) anomalous ridging is clearly evident to the east of the MG and Tip. On 11 September 1989 (Fig. 3.11d): (i) the ridging to the northeast of Sarah has become more discernable as Tip moves north; and (ii) the N2 pattern associated with Tip has clearly moved north with Tip in agreement with the conceptual model (Fig. 3.7b). Although, this example illustrates how two concurrent and sufficiently distant TCs may be associated with two distinct patterns, the distinction may be partially blurred somewhat by pattern overlap.

As in the case of the N1 Pattern, the dynamics associated with the development and maintenance of the N2 Pattern is not well-understood. The work of Carr and Elsberry (1995) provide a preliminary basis for how N2 Patterns can arise via barotropic vorticity

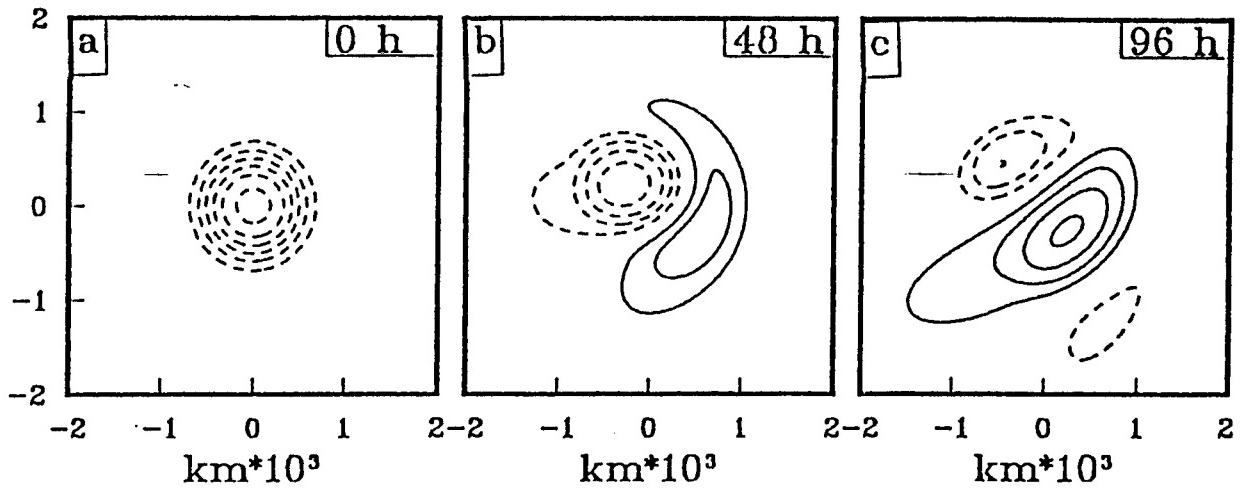


Fig. 3.9 Nondivergent, barotropic model streamfunction fields of a large cyclonic vortex representing a monsoon gyre. Contour interval is  $1 \times 10^{-6} \text{ m}^2 \text{ s}^{-1}$ , the negative (positive) contours are dashed (solid), and the zero contour has been suppressed for clarity (after Carr and Elsberry 1995).

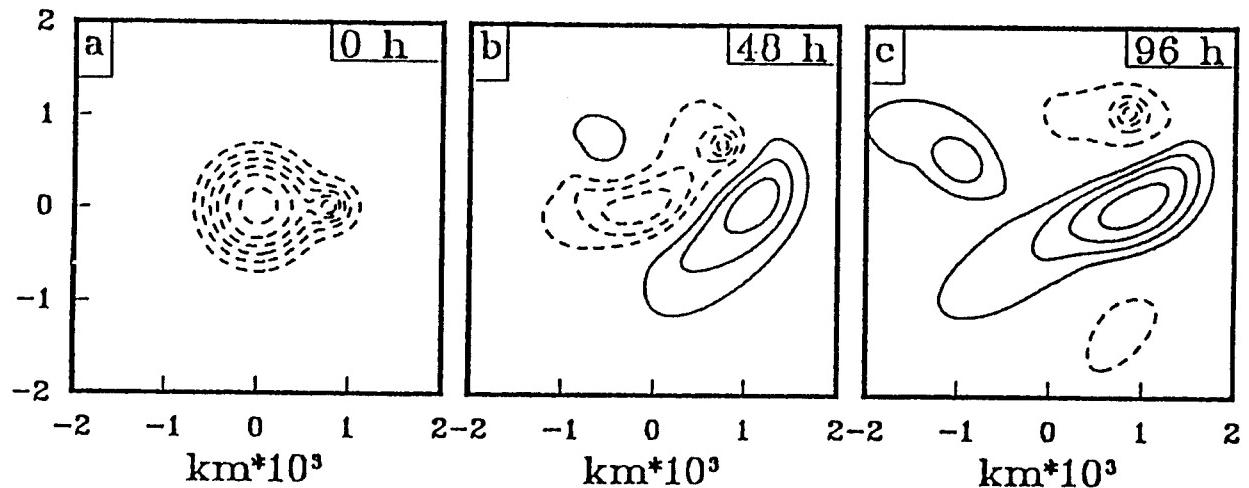


Fig. 3.10 As in Fig. 3.9, except with a TC-scale vortex added 800 km east of the monsoon gyre-scale vortex (after Carr and Elsberry 1995).

advections. Because the N2 Pattern is intimately tied to the TC-environment transformations RMT and MTI (Table 3.3), further discussion will be deferred to Subsections 3.d.3 and 3.d.4, respectively.

c) Monsoon Gyre (G) Synoptic Pattern The TC environment will be classified as a Monsoon Gyre (G) Synoptic Pattern (Fig. 3.12) whenever: (i) there is present in the vicinity of the TC a particular type of monsoonal circulation that will hereafter be termed a

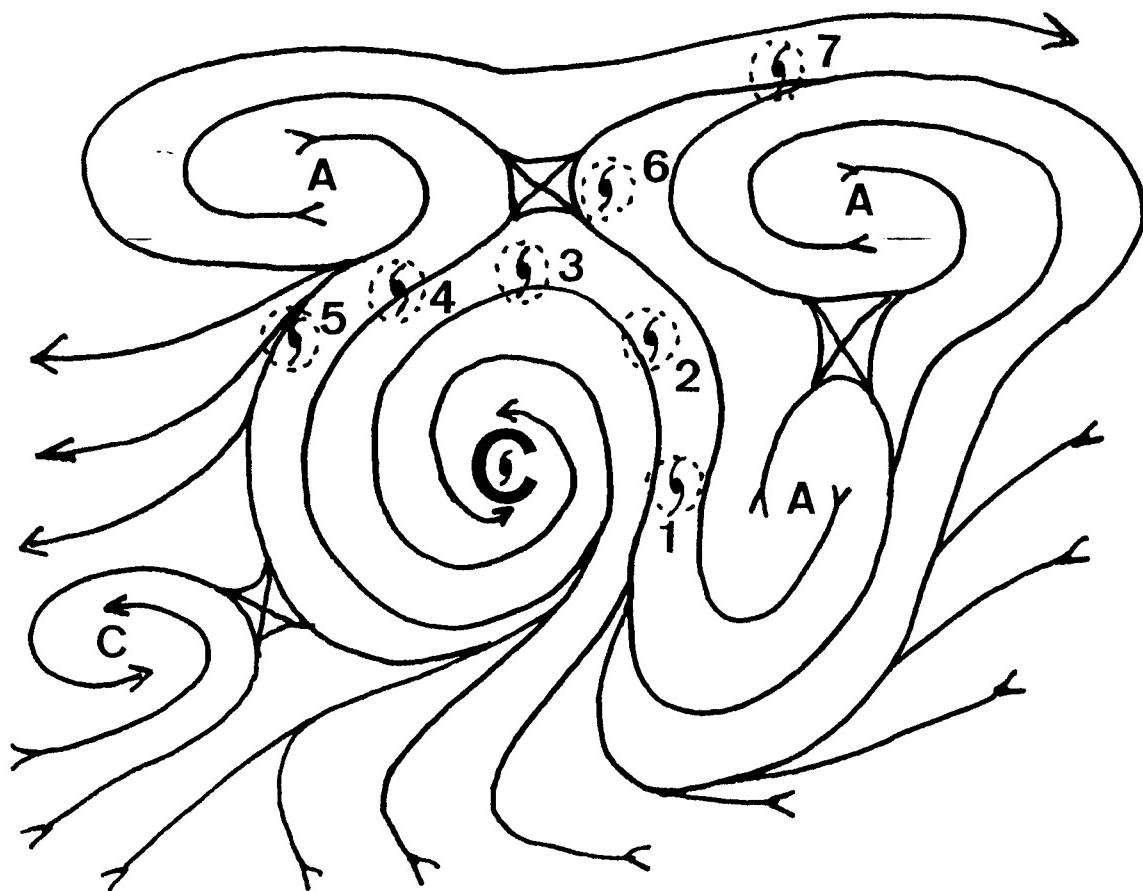


Fig. 3.12 As in Fig. 3.5, except for Monsoon Gyre (G) Synoptic Pattern. The large "C" denotes the center of the gyre.

cyclonically curved band of deep convection; and (iv) may serve as a favorable environment for the generation of midget or small TCs, or may develop a central convection region and become a particularly large TC. Herein, the term MG will include monsoonal vortices (ATCR 1992) that are larger and weaker than the TC with which they are associated, but are somewhat smaller, weaker, and more frequently occurring, than the large MG as defined by Lander. In addition, the systematic approach will allow for merger of the MG with a TC via the MG-TC Interaction (MTI; recall Table 3.3) transformation, whereas Lander discusses only genesis/advection of small TCs by the MG, and evolution of the MG into a large TC.

The G Pattern model depicted in Fig. 3.12 has a prominent north-south oriented ridge circulation to the east of the MG. Because the prominence of this ridge tends to depend on the scale of the associated MG, MGs that are somewhat smaller than the size suggested by Fig. 3.12 will tend to have weaker ridges on the eastern periphery. Thus, as with the other Synoptic Pattern conceptual models, the forecaster must recognize that actual G Patterns depicted in NOGAPS analyses may vary somewhat from the idealized schematic.

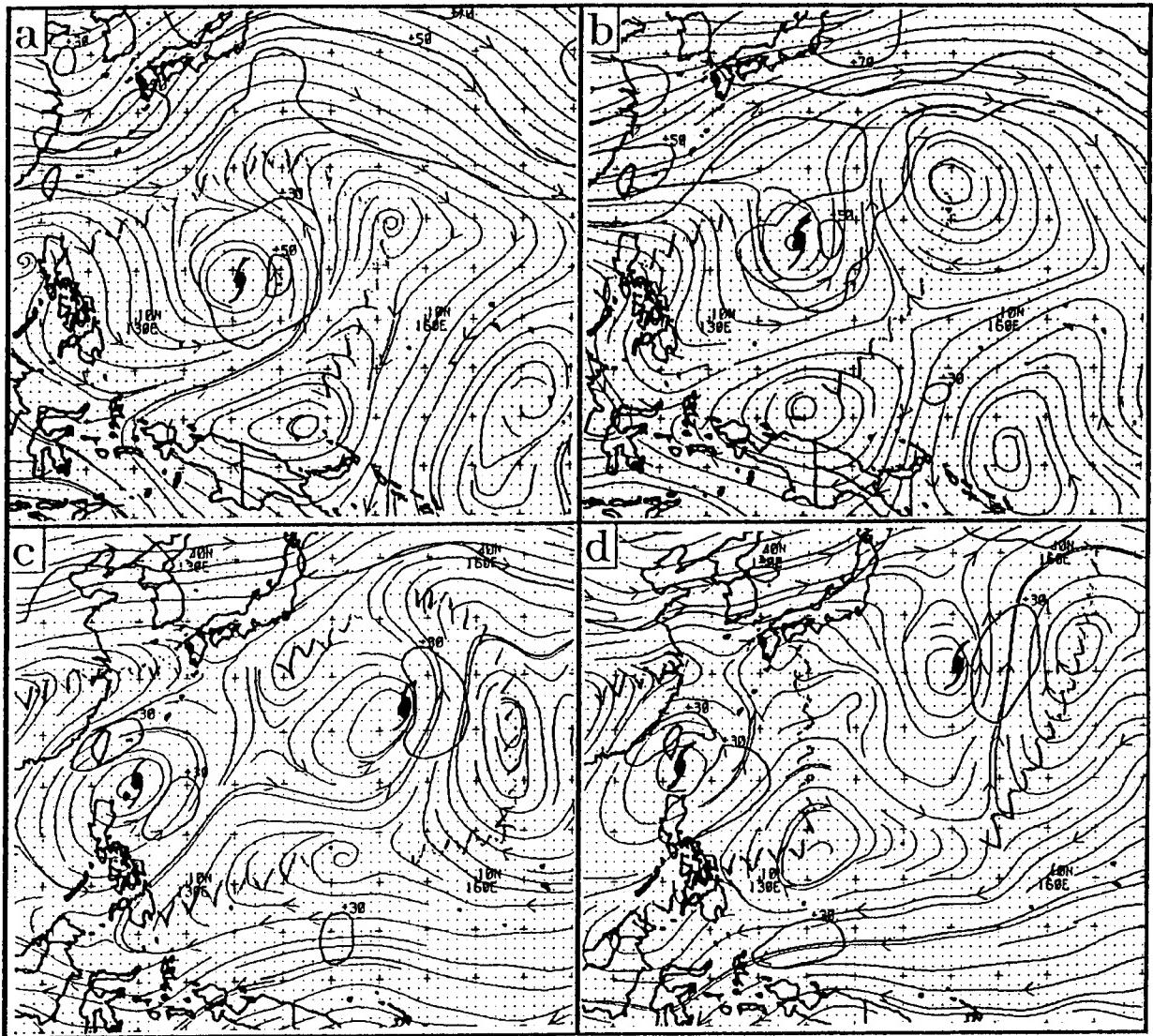


Fig. 3.11 NOGAPS analyses as in Fig. 3.6, except for 0000 UTC on (a) 28 November 1991, (b) 29 November 1991, (c) 10 September 1989, and (d) 11 September 1989. The TC symbols denote the position of (a)-(b) Supertyphoon Yuri, and (c)-(d) Typhoon Sarah (west) and Tropical Storm Tip (east).

monsoon gyre (MG); and (ii) the TC has a position relative to the MG as suggested by TC symbols 1-7 in Fig. 3.12. For the purposes of the systematic approach, the term MG will be applied more broadly than in Lander (1994), who restricted its usage to a feature that: (i) occurs roughly once per year during July through September; (ii) is organized as a large, but relatively weak, cyclonic vortex; (iii) produces an approximately circular, 2500 km diameter depression in the contours of sea level pressure, and typically is accompanied by a

Extensive, deep convection occurs in the confluent region between the large MG and the ridge to the east (Fig. 3.13), and this convection tends to be wrapped around the large MG, and take on a characteristic "fish-hook" shape. Arakawa (1952) was evidently referring to the G Pattern confluent area when describing a "convergence area in the subtropics," that was the preferred location for the formation of midget or small typhoons. Such formations are illustrated in Fig. 3.12 by the relatively small circulations around the TC symbols. The curvature of the large convective band would tend to focus subsidence near the MG center, which may partially explain the extensive area of suppressed cloudiness approximately within the radius of maximum winds of the MG.

After forming in or near the confluent region, a small TC will tend to move around the large MG and enter the east-northeasterly steering between the MG and the ridge circulation to the northwest (TC symbol sequence 1-2-3-4-5). An alternate path (especially for a larger TC) is to continue northward and recurve through the break in the ridge (TC symbol sequence 1-2-6-7). The TC symbol at the MG center represents two possible evolutions. First, the MG may evolve into a very large TC if an inner area of convection develops and the circulation tightens around the center with associated central pressure falls and reduction of the radius of maximum winds. Second, a TC at locations 1 through 4 may

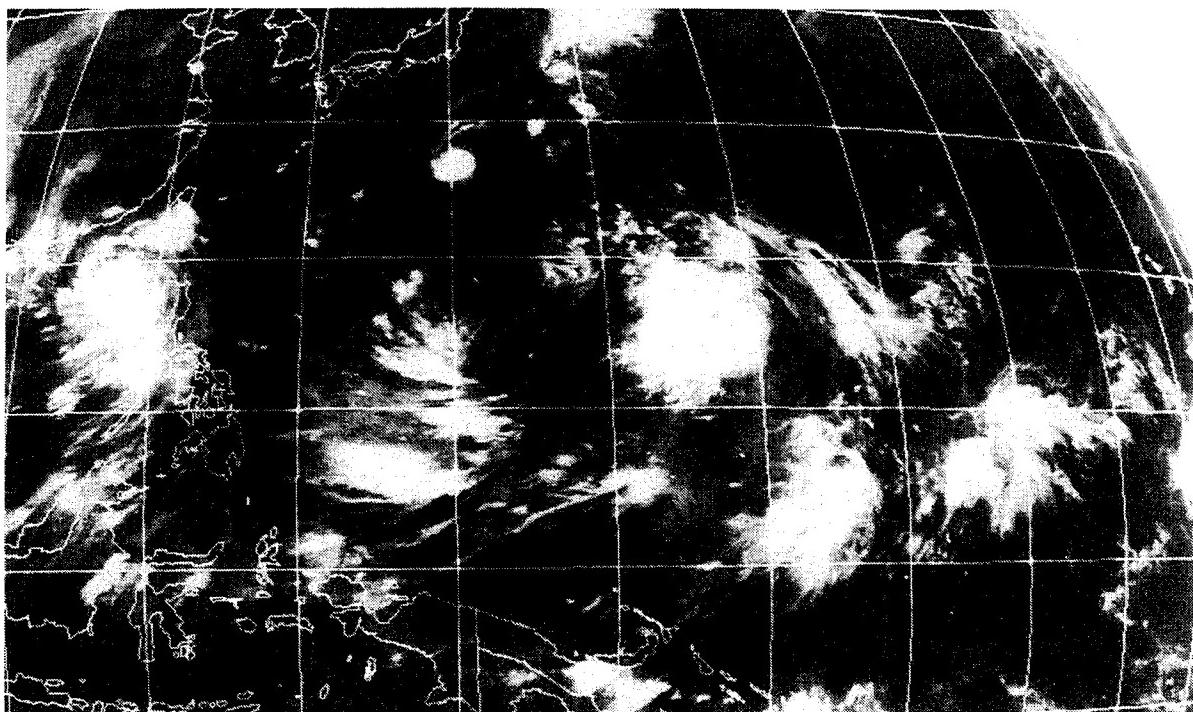


Fig. 3.13 Geostationary infrared imagery at 0000 UTC 14 August 1991 of the cloud features manifesting a large monsoon gyre centered near 15°N, 145°E. Associated with the gyre are Typhoon Ellie near 27°N, 140°E, a roughly circular cloud mass near 15°N, 155°E, and an area of weakly curved convection near 10°N, 138°E. The straight meridian is 140°E and the bottom of the image is 10°S. Fig. 3.14b is corresponding NOGAPS analysis.

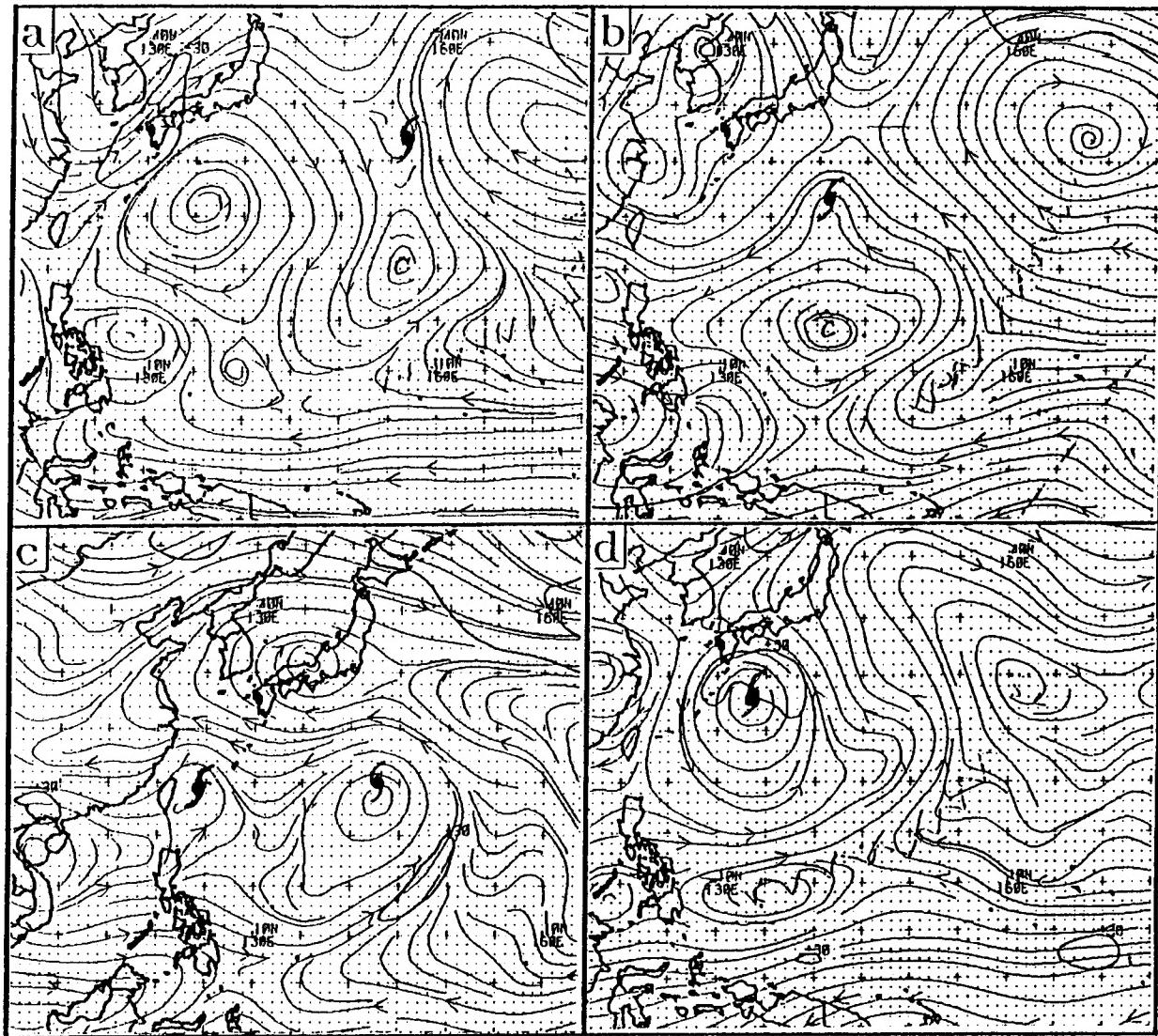


Fig. 3.14 NOGAPS analyses as in Fig. 3.6, except for 0000 UTC on (a) 10 August, (b) 14 August, (c) 17 August, and (d) 20 August 1991. TC symbols denote the positions of (a) Tropical Storm Doug, (b) Typhoon Ellie, (c) Typhoon Ellie (west) and Tropical Storm Gladys (east), and (d) Tropical Storm Gladys.

interact with the MG via the MTI transformation, which results in a merger. It will be seen later that when the MTI transformation takes place, an Environment Structure transition to another synoptic pattern, usually the N2 Pattern, must take place.

A G Pattern was present in the western North Pacific for most of the month of August 1991. By 10 August (Fig. 3.14a), a moderate size MG was well-established near

20°N, 156°E, and had already spawned a midget TC (Tropical Storm Doug; near 32°N, 156°E). By the 14th (Fig. 3.14b), the MG was near 15°N, 141°E and had spawned another midget TC (Typhoon Ellie; near 20°N, 141°E). By the 17th (Fig. 3.14c), the MG circulation had significantly increased in area, and the central pressure had decreased to the extent that JTWC was issuing warnings on the MG circulation as Tropical Storm Gladys with maximum winds of 50 kt. By the 20th (Fig. 3.14d), Gladys was just southeast of Kyushu, and a third disturbance that would become TD15 was developing near 22°N, 142°E in the confluent region between Gladys and the north-south oriented ridge circulation to the east.

*d) Multiple (M) Tropical Cyclone Synoptic Pattern* The requirements for a Multiple (M) Tropical Cyclone Synoptic Pattern are that the two TCs are:

- (i) in proximity to each other (less than about 20° lat.), but with a separation distance that would not result in a significant binary interaction, which generally occurs at less than 10-12° lat. (Brand 1970; Dong and Neumann 1983);
- (ii) oriented approximately east-west; and
- (iii) sufficiently close (north or south) to the ridge axis that the height gradient between the western TC and the eastern ridge circulation subjects the eastern TC to moderately strong (10-15 kt) and predominantly poleward steering flow (Fig. 3.15a), and/or the height gradient between the eastern TC and the western ridge circulation subjects the western TC to moderately strong, and predominantly equatorward, steering flow (Fig. 3.15b).

However, it is possible for additional TCs to be present to the southeast of the eastern TC and to the southwest of the western TC without setting up competing M Patterns, as long as they are well south of the ridge axis.

In a M Pattern, the eastern TC is acting to inhibit the recurvature of the western TC, and the western TC is concurrently acting to encourage the recurvature of the eastern TC. The "and/or" terminology in criterion (iii) above, allows for variations in the mutual influence as determined by the relative outer wind strengths of the TCs and the strengths of the ridge circulations. The two extremes would be a one-way influence of the eastern TC-western ridge pair on the western TC, and vice versa.

If criteria (ii) and (iii) are satisfied, but (i) is not satisfied due to insufficient separation, then a M Pattern still exists. However, a binary TC interaction, which falls within the Interactions (TCIs) category of the TC-Environment Transformations conceptual models (Table 3.3) may also be superposed on the M pattern depending on the sizes of the TCs. A binary TC interaction arises when the circulations of two vortices are mutually advecting.

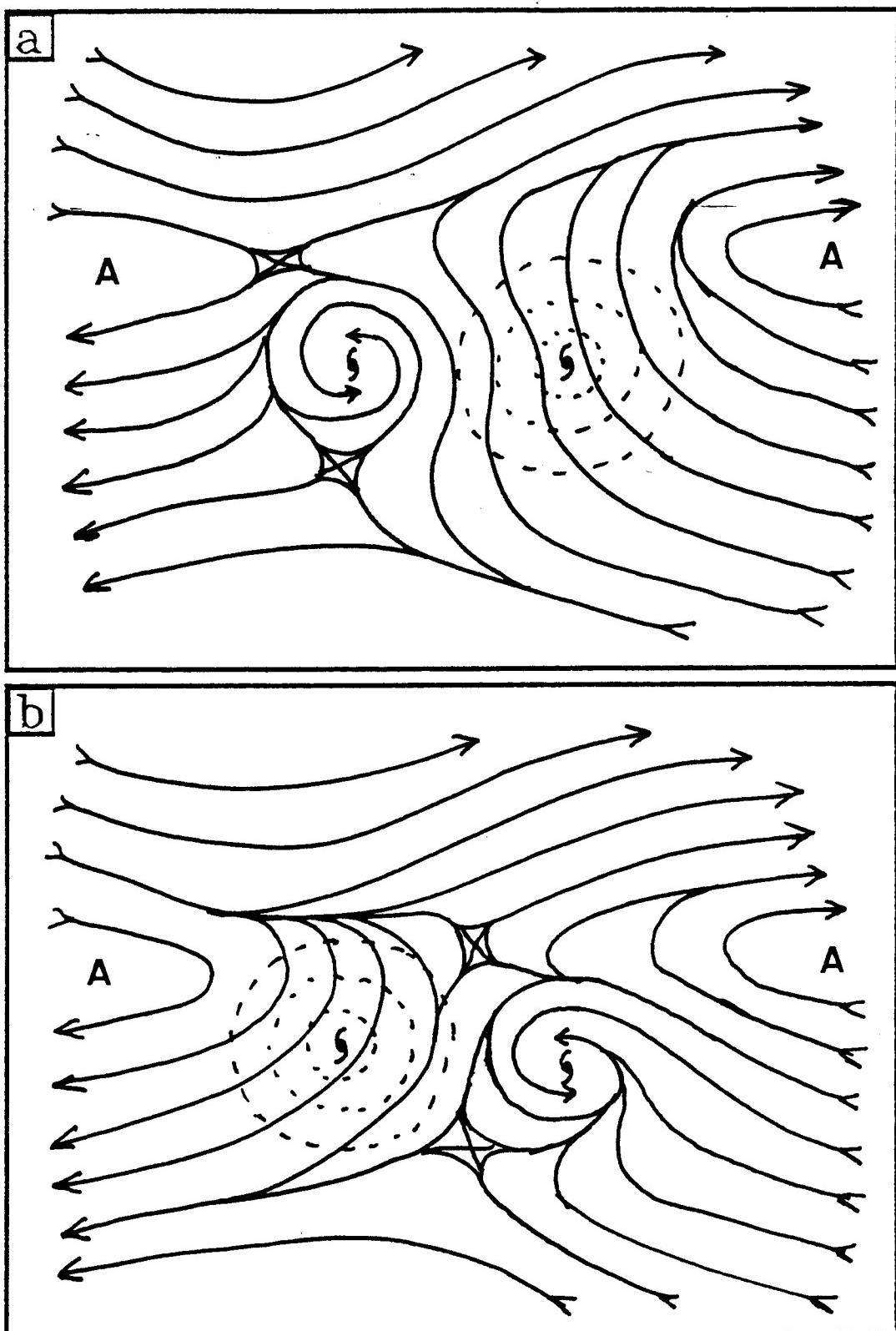


Fig. 3.15 As in Fig. 3.5, except for Multiple (M) Tropical Cyclone Synoptic Pattern.

That is, the separation distances and circulation sizes of the two TCs are sufficient to cause mutual track changes in the absence of any background flow. If a background flow does exist, its influence is then combined with the binary TC interaction.

The M Pattern concept is related to the binary TC interaction in the sense that the presence of each TC circulation is having an influence on the circulation of its counterpart. However, the key conceptual distinction between the binary TC interaction and the M Pattern is in the role of the environment. In the M Pattern, the presence of the environment, specifically the subtropical ridge, is necessary for the two TCs to have a mutual influence on each other within the separation distance range given by criteria (i).

A M Pattern existed in conjunction with Typhoons Yancy and Zola on 21 August 1990 (Fig. 3.16a), and in conjunction with Typhoon Seth and Tropical Storm Verne on 08 November 1991 (Fig. 3.16b). In each case, the 500 mb streamlines of the TC pairs are quite distinct, which implies negligible mutual advections by the "closed" circulations of the TCs. However, the asymmetric isotach patterns around Zola in Fig. 3.16a and Seth in Fig. 3.16b manifest the enhanced steering flow between their counterpart TCs and their adjacent ridge circulation. In the case of Zola (Fig. 3.16a), the large, closed 30-kt isotach to the northeast has no counterpart to the southwest, which implies strong southeasterly steering across Zola as in Fig. 3.16a. In the case of Seth (Fig. 3.16b), the area of the closed 30-kt isotach to the west is significantly larger than the isotach to the east, which implies northerly environmental steering across Seth as in Fig. 3.16b.

In the NOGAPS analyses of both the Seth/Verne and Yancy/Zola cases, an apparent extension of the eastern ridge circulation exists over the eastern TC, which a forecaster would normally consider a hindrance to recurvature. However, the ridge extension is merely a byproduct of the presence of the circulation of the eastern TC, and disappears when the circulation of the eastern TC is removed as in Fig. 3.15a. Conversely, the presence of a neutral point to the north of the western TCs in the analyses, particularly in the case of Seth, would normally suggest that recurvature is at least possible, if not probable. The observed position of the neutral point is in fact an artifact of the presence of the western TC circulation, and shifts substantially to the east when the circulation of the western TC is removed as in Fig. 3.15b. Despite appearances to the contrary, recurvature of the eastern TC is unhindered and quite probable, and recurvature of the western TC is either improbable or may be significantly delayed.

It is instructive to consider two examples of large-scale patterns that involve two TCs, but that do not satisfy one of the criteria (i) through (iii) above. The pattern involving Typhoon Ed and Supertyphoon Flo at 1200 UTC 16 September 1990 (Fig. 3.16c) meets criteria (i) and (ii), but fails to meet criterion (iii). Although the orientation of Ed and Flo is more zonal than meridional, the departure from zonality is sufficient to place Ed far enough south of the ridge axis to be outside the northerly flow between Flo and the ridge circulation to the north of Ed. The pattern involving Typhoon Nat and Supertyphoon Mireille at 1200 UTC 24 September 1991 (Fig. 3.16d) meets criteria (ii) and (iii), but fails

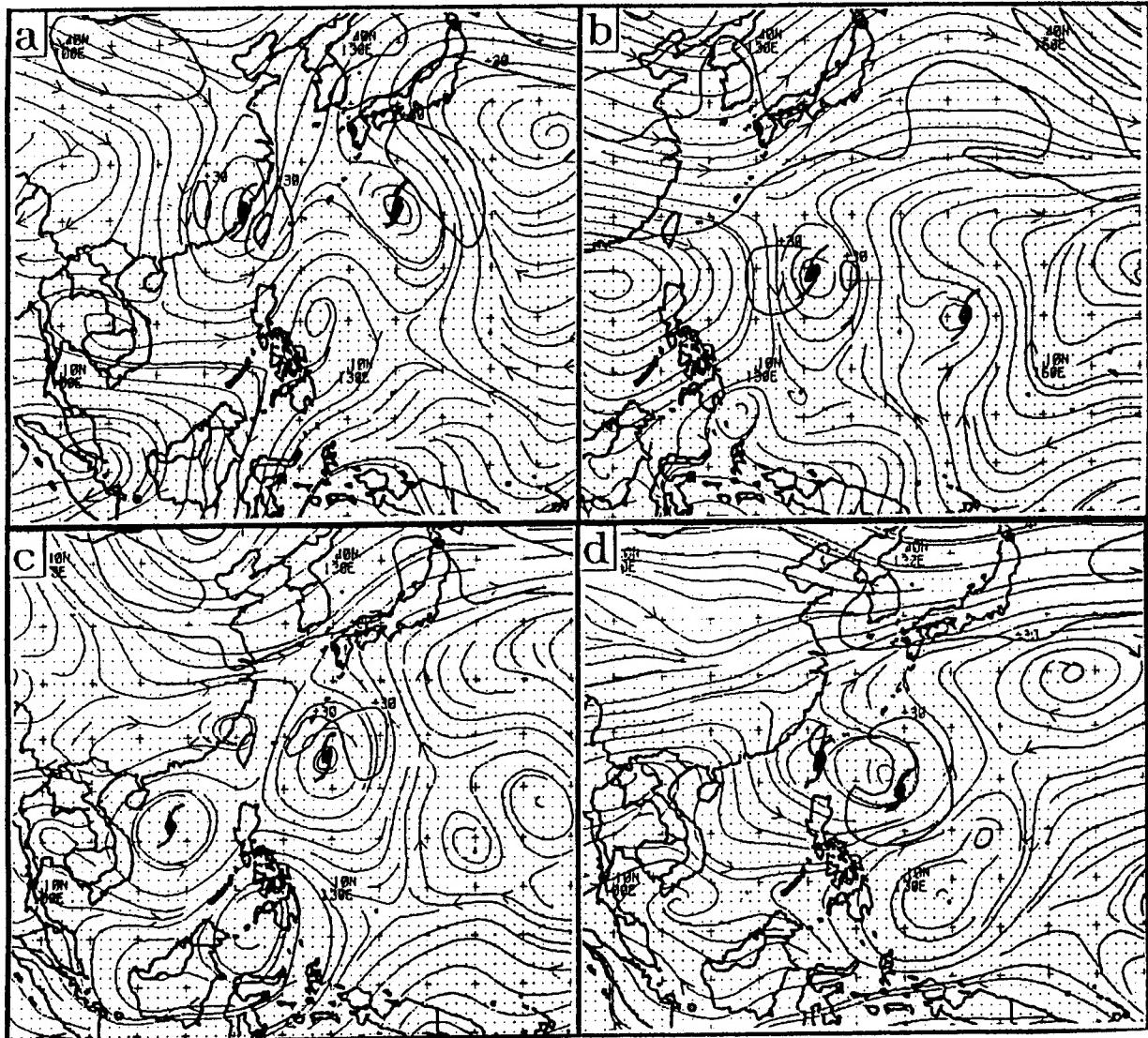


Fig. 3.16 NOGAPS analyses as in Fig. 3.6, except for 0000 UTC on (a) 21 August 1990, and (b) 8 November 1991, and for 1200 UTC on (c) 16 September 1990 and (d) 24 September 1991. TC symbols denote the positions of (a) Typhoons Yancy (west) and Zola (east), (b) Supertyphoon Seth (west) and Tropical Storm Verne (east), (b) Typhoon Ed (west) and Supertyphoon Flo (east), and (d) Typhoon Nat (west) and Supertyphoon Mireille (east).

to meet criterion (i) due to insufficient separation distance. Mireille and the ridge circulation to the west of Nat are properly positioned to produce northerly flow across Nat, in agreement with the M pattern conceptual model (Fig. 3.15b). At this time Nat (near  $22^{\circ}\text{N}$ ,  $118^{\circ}\text{E}$ ) and Mireille (near  $21^{\circ}\text{N}$ ,  $129^{\circ}\text{E}$ ) are about  $10^{\circ}$  long. apart, which is near the accepted threshold for significant binary TC interaction. However, Mireille is a large TC and the circulation of Nat appears only as a trough to the west of Mireille, rather than as the distinct circulation that appeared in the NOGAPS analyses during the preceding 72 h. Recall the TC circulations in the above M Pattern examples (Fig. 3.16a-b) remained quite distinct. This information, and the rather sudden turn by Nat from a westward to a southward track between 0600 UTC and 1200 UTC 24 September indicates that a one-way influence of Mireille's circulation on Nat is indeed occurring in concert with the M Pattern.

2) Synoptic Regions. Recall that the synoptic pattern conceptual models are adaptable templates to classify and characterize the large-scale environment of the TC. Similarly, the synoptic region conceptual models are adaptable templates to classify areas within the synoptic patterns that determine the environmental steering influence on the TC. A basic concept is that an unbroken, east-west oriented ridge may be viewed as a barrier to the northward movement of the TCs by virtue of its deep layer of dry, subsiding air, and the absence of any steering at the ridge axis. In the absence of TC-independent environmental evolutions to produce a break in the ridge, or TC-environment transformations that alter the ridge structure, the ridge circulation will dominate TC motion by constraining it to be roughly westward in the tropics. It is for this reason that the synoptic region will generally be in a specific orientation relative to ridge circulations.

The synoptic region models will be depicted with well-defined boundaries. However, since the environment of the TC is a continuum of flow features, the synoptic regions are actually smoothly blended via transition zones. Since synoptic region transitions (as well as pattern transitions) can depend on TC-environment transformations, discussion of this topic will be deferred to Section 3.d.

a) Regions within the Standard (S) Synoptic Pattern. Recall from Table 3.1 that the Standard (S) Synoptic Pattern is comprised of the Dominant Ridge (DR), Weakened Ridge (WR), and Accelerating Westerlies (AW) Synoptic Regions. The approximate boundaries of these Regions in the S Pattern are shown in Fig. 3.17.

The DR Region of the S Pattern consists of all locations that satisfy the following criteria: (i) poleward of the monsoon or equatorial trough axis, or poleward of about 5° lat. if no trough axis exists; (ii) equatorward of the axis of an east-west oriented ridge circulation that tends to dominate the motion of the TC by producing roughly easterly steering of about 10-15 kt; and (iii) not in the vicinity of a "significant" break along the ridge axis (usually associated with a midlatitude trough) that weakens the steering flow and makes it more southerly. In general, stronger and more zonally extensive ridge circulations have greater potential for the associated easterly steering to dominate TC motion. However, it is emphasized that whether or not a ridge steering actually will dominate TC motion, and whether or not a weakness/break in the ridge is "significant," depends greatly on TC size, and on any TC-environment transformations.

Various TC positions in the DR Region are illustrated in Fig. 3.17, and NOGAPS analyses in Fig. 3.6a-d give specific examples. The position of Yuri (Fig. 3.6a) could correspond to TC symbols 1, 2, or 3 in Fig. 3.17, since it is equatorward of an extensive unbroken ridge. The positions of Ed and Flo (Fig. 3.6b) are southwest of the break in the ridge, which is similar to TC symbol 3 in Fig. 3.17. Amy (Fig. 3.6c) is well below a break in the ridge, which corresponds to TC symbol 2 in Fig. 3.17.

In a persistent S Pattern, a TC can remain continually in the DR Region if it forms sufficiently close to the equator and eventually makes landfall before gaining enough

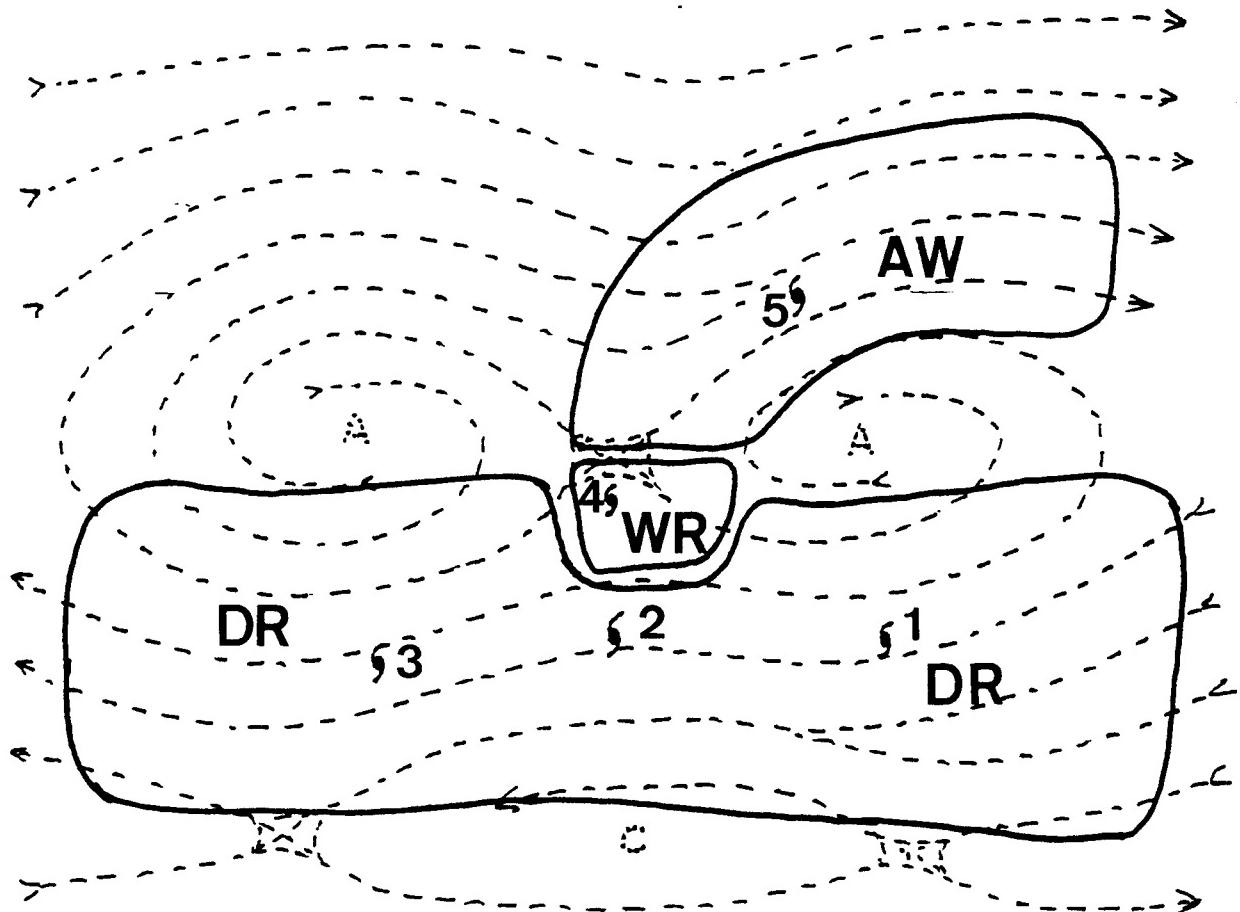


Fig. 3.17 Idealized schematic of the Standard (S) Synoptic Pattern conceptual model, except with the boundaries of the associated synoptic region conceptual models added. DR denotes the Dominant Ridge Region, WR the Weakened Ridge Region, and AW the Accelerating Midlatitude Westerlies Region.

latitude to encounter the ridge axis. Within the context of the systematic approach, the traditional "straight runner" TC is continually dominated by the ridge. For example, the non-recurring tracks of Typhoons Ed and Amy (Fig. 3.18a-b) are indicative of TCs that remained in DR Regions similar to those depicted for a single time in Figs. 3.6b and c, respectively. However, these tracks illustrate the variability of track direction among straight-runners, which is partially a function of the S Pattern variant in which they are embedded. Ed's westward to west-southwestward track is consistent with the similarly sloping orientation of the ridge axis in variant (ii) of the pattern in (Fig. 3.6b). Amy's significant gain in latitude is consistent with the east-southeasterly steering associated with the east-to-west taper of variant (iii) of the S Pattern-Dominant Ridge (Fig. 3.6c).

The Weakened Subtropical Ridge (WR) Synoptic Region (Fig. 3.17) is unique to the S Pattern (recall Table 3.1). The WR Region consists of all locations within the S Pattern that are: (i) equatorward of the subtropical ridge axis; (ii) east of the center of a break in the ridge; and (iii) close enough to the break to be in relatively weak (5-8 kt) and southeasterly-to-southerly steering. TCs are found in the WR Region of the S Pattern in two

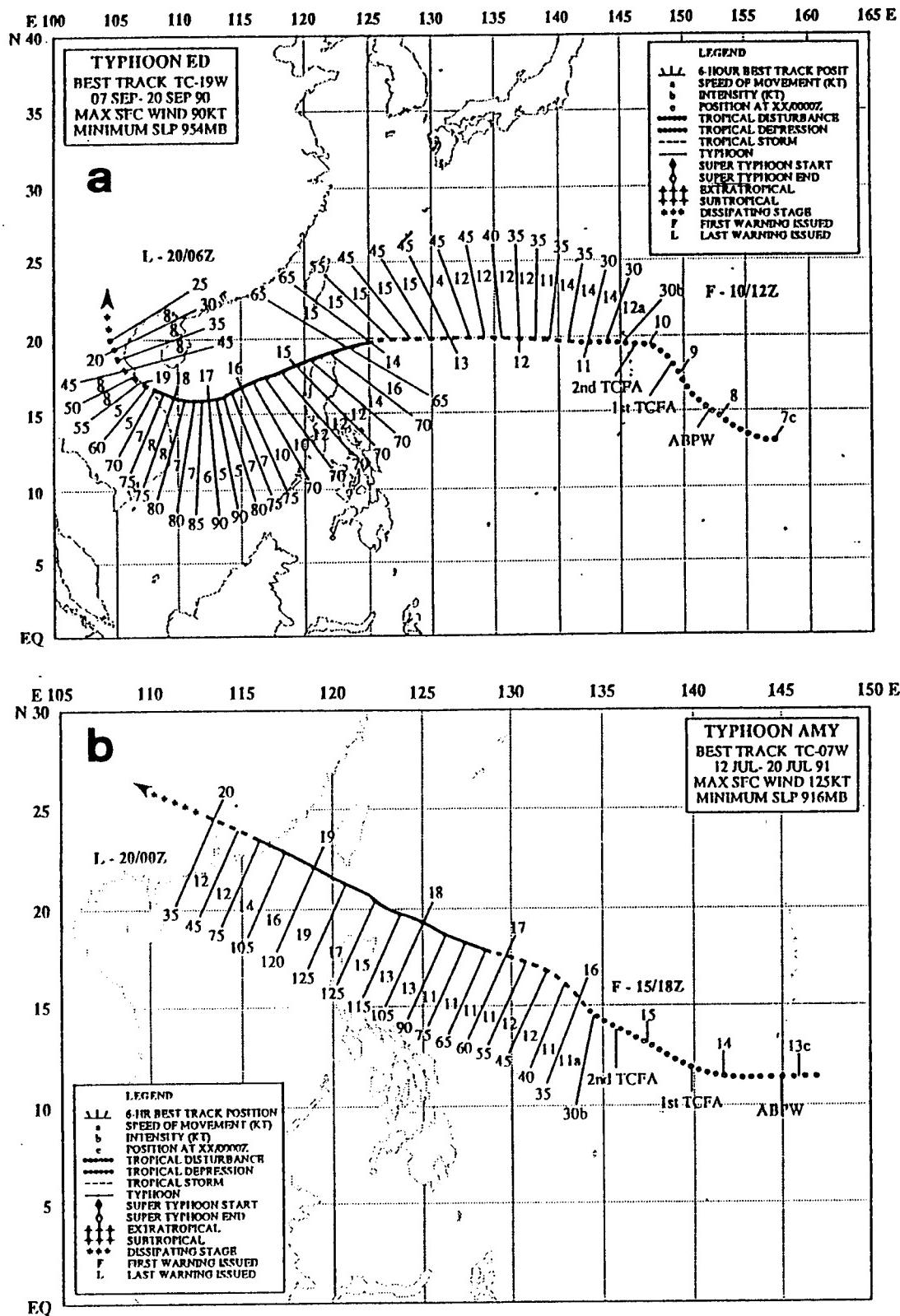


Fig. 3.18 As in Fig. 3.1, except for (a) Typhoon Ed, and (b) Typhoon Amy.

situations: (i) after leaving the DR region and before entering the AW Region (discussed next) during recurvature (Fig. 3.17; TC symbol sequence 1-4-5); or (ii) after leaving the DR Region and before returning to it during a "stair-step" maneuver (Fig. 3.17; TC symbol sequence 1-4-3). The first situation is illustrated in Fig. 3.6d with Supertyphoon Flo in the WR Region of a S Pattern enroute to recurvature. At that time, Flo is moving slowly north at about 6 kt (Fig. 3.19a). In the 24-h period beginning 1200 UTC 15 September, the translation speed of Flo has slowed from 12 to 8 kt, which is a typical indication of a transition from the DR Region to the WR Region of a S Pattern.

The Accelerating Midlatitude Westerlies (AW) Synoptic Region in Fig. 3.17 consists of those locations within a synoptic pattern that are: (i) poleward of the ridge axis, and generally within about  $10^{\circ}$  lat. of the ridge axis; and (ii) east of the ridge-break neutral point. In the S Pattern pictorial, the AW Regions are zonally oriented, and have associated steering flows that are predominantly zonal. In nature, the orientation and flow within the AW Region can vary greatly depending on the structures of the ridge and adjacent midlatitude trough and associated midlatitude troughs/ridges (e.g., low versus high index situations). On 19 September 1990 (Fig. 3.20a), Supertyphoon Flo was in a prominent short-wave trough in the AW Region of a S pattern with a ridge circulation to the east that extends far north of Flo's latitude. The motion of Flo (Fig. 3.19a) at this time is north-northwestward to northwestward due to the predominantly southerly steering generated by the meridionally broad ridge. By contrast, Tropical Storm Verne is depicted in Fig. 3.20b as a weak short-wave trough in the AW Region of a S Pattern with a meridionally-narrow, zonally-oriented ridge circulation to the east and south. Thus, the track of Verne at this time (Fig. 3.19b) is more zonal due to the predominantly westerly steering generated by the zonally-oriented ridge.

As suggested by its name, the AW Region usually causes TCs to undergo significant translational accelerations. Accelerations of 20 kt/day are common, and translation speeds can exceed 40 kt. In the case of Supertyphoon Flo (Fig. 3.19a), the translation speed increased rapidly from 12 kt in the 6-h period ending 0000 UTC 19 September to 32 kt in the 6-h period ending 0000 UTC 20 September 1990. Determining the timing and magnitude of the acceleration period continues to be one of the more serious challenges confronting the TC forecaster.

The WR Region in Fig. 3.17 is comparatively small relative to the DR and AW Regions. An alternate approach might be to omit the WR Region, and consider it as an example of a Region "transition zone" (i.e., from the DR to AW Region) as defined in the introduction to this chapter. However, the WR Region in the S Pattern is important for two reasons. First, because of the shift from relatively strong and predominantly easterly steering in the DR Region of the S Pattern to weak and increasingly southerly flow in the WR Region, a "bifurcation" in TC tracks is possible. That is, the subsequent track of the TC is sensitive to TC structure, Environment Structure, and TC position while the TC is in the WR Region. Subtle differences in these parameters may lead to two quite different tracks, i.e., only a temporary poleward deflection and then a track equatorward of the ridge axis,

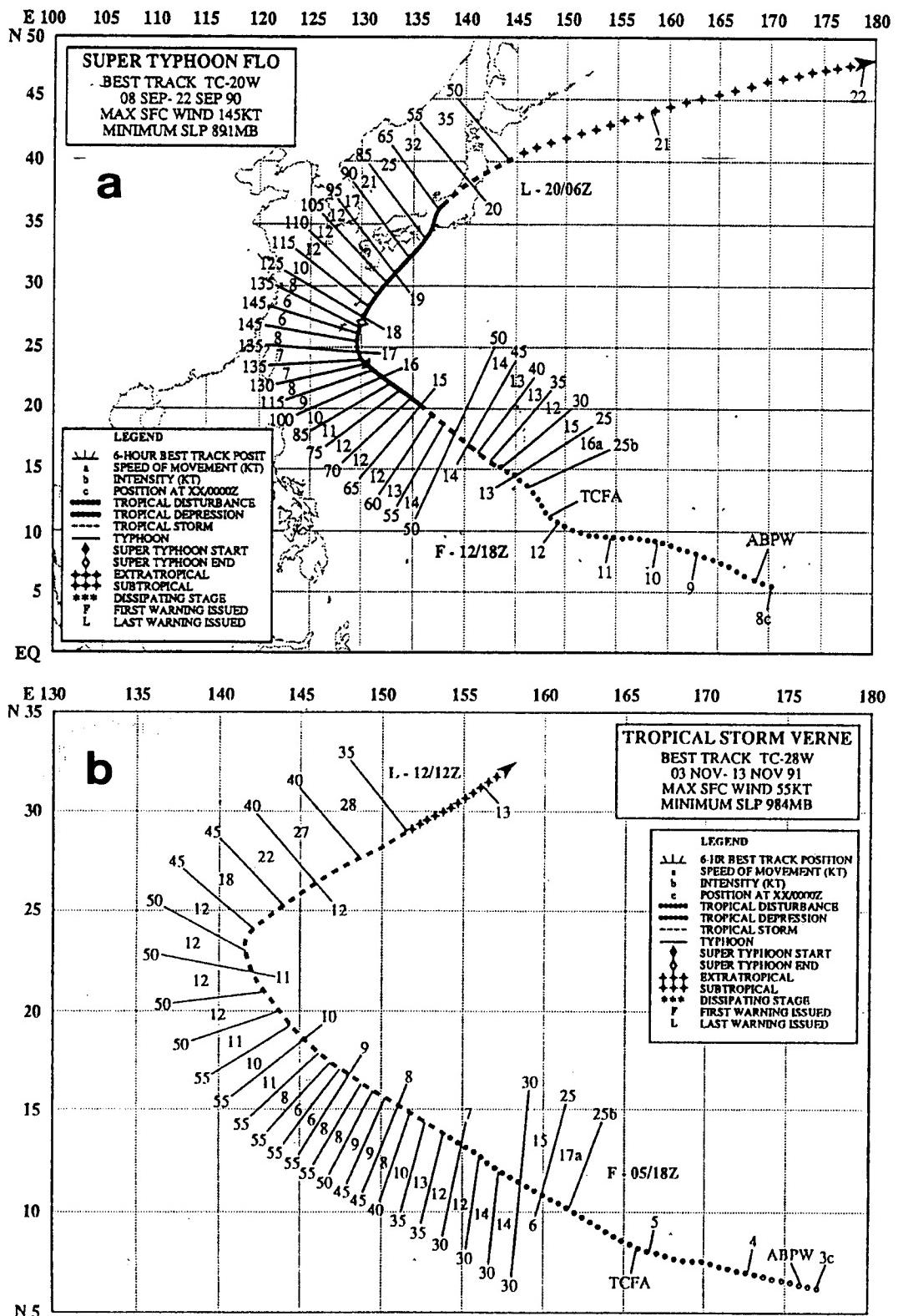


Fig. 3.19 As in Fig. 3.1, except for (a) Supertyphoon Flo, and (b) Tropical Storm Verne.

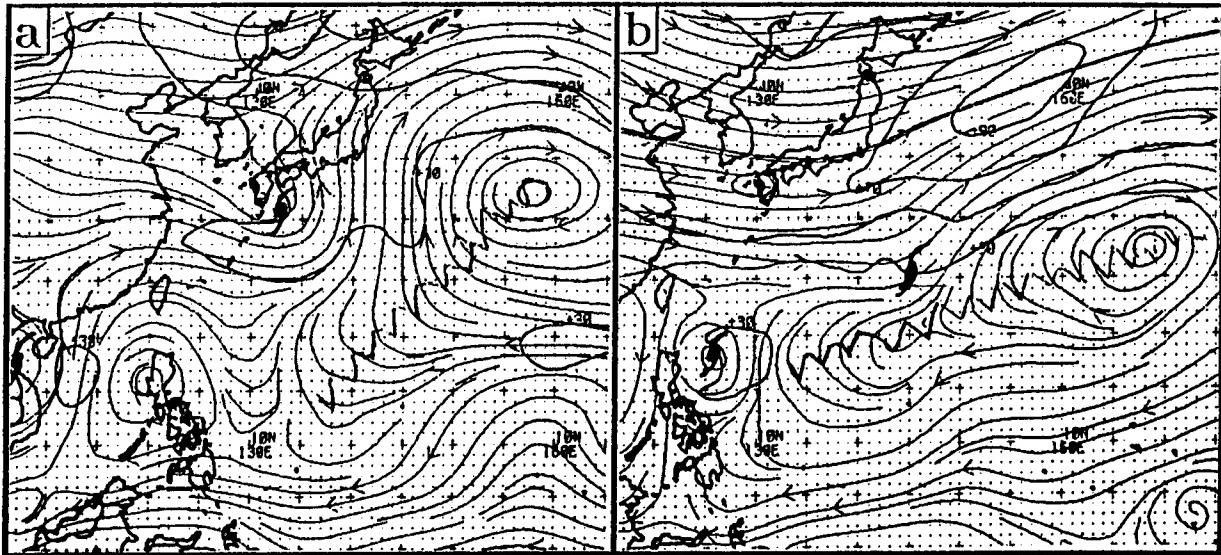


Fig. 3.20 NOGAPS analysis as in Fig. 3.6, except for 0000 UTC on (a) 19 September 1990, and (b) 12 November 1991. TC symbols denote the positions of (a) Typhoon Ed (west) and Supertyphoon Flo (east), and (b) Supertyphoon Seth (west) and Tropical Storm Verne (east).

or a recurvature followed by an acceleration into the westerlies. Second, subtle errors arising from inadequate observation, or numerical model initialization and integration properties, may have a magnified effect on TC track forecasts for storms in the WR Region. As a result, the numerical and objective model error traits (recall the upper and middle right boxes in Fig. 2.1) may differ distinctly for TCs in WR Region as compared to the DR or AW Regions of a S Pattern. This possibility will be addressed in Part II of this report.

*b) Regions within the North-Oriented (N) Synoptic Pattern.* According to the definition of the N Pattern, an anomalous, primarily north-south oriented ridge must exist to the east through south of the TC. As a result, TCs in either the N1 or the N2 Patterns (Figs. 3.21a and b, respectively) must be in either the North-Oriented (NO) or Accelerating Westerlies (AW) Synoptic Regions.

The North-oriented (NO) Synoptic Region consists of locations that are in the predominantly southerly flow to the west of the anomalous, meridionally-broad ridge circulation. Typhoons Steve and Vernon occupy the NO Region of the N1 Pattern on 0000 UTC 28 July (Fig. 3.8c) and 1200 UTC 30 July 1990 (Fig. 3.8d). The tracks of Steve and Vernon (Fig. 3.22a and b, respectively) during that period exhibit the predominantly northward direction of motion as expected. Notice that Steve and Vernon are moving through the NO Region, which is consistent with the location of the NO Region in the N1 Pattern not being dependent on the TC. Notice also that the tracks of Steve and Vernon are not straight, as might be expected from a rigid interpretation of the N1 Pattern conceptual model (Fig. 3.21a). Rather, the tracks are sinuous due to evolution of the N1 Pattern, which is modulated by surrounding environmental features, particularly the passage of midlatitude troughs and ridges. This comparison emphasizes that the synoptic pattern/region models are

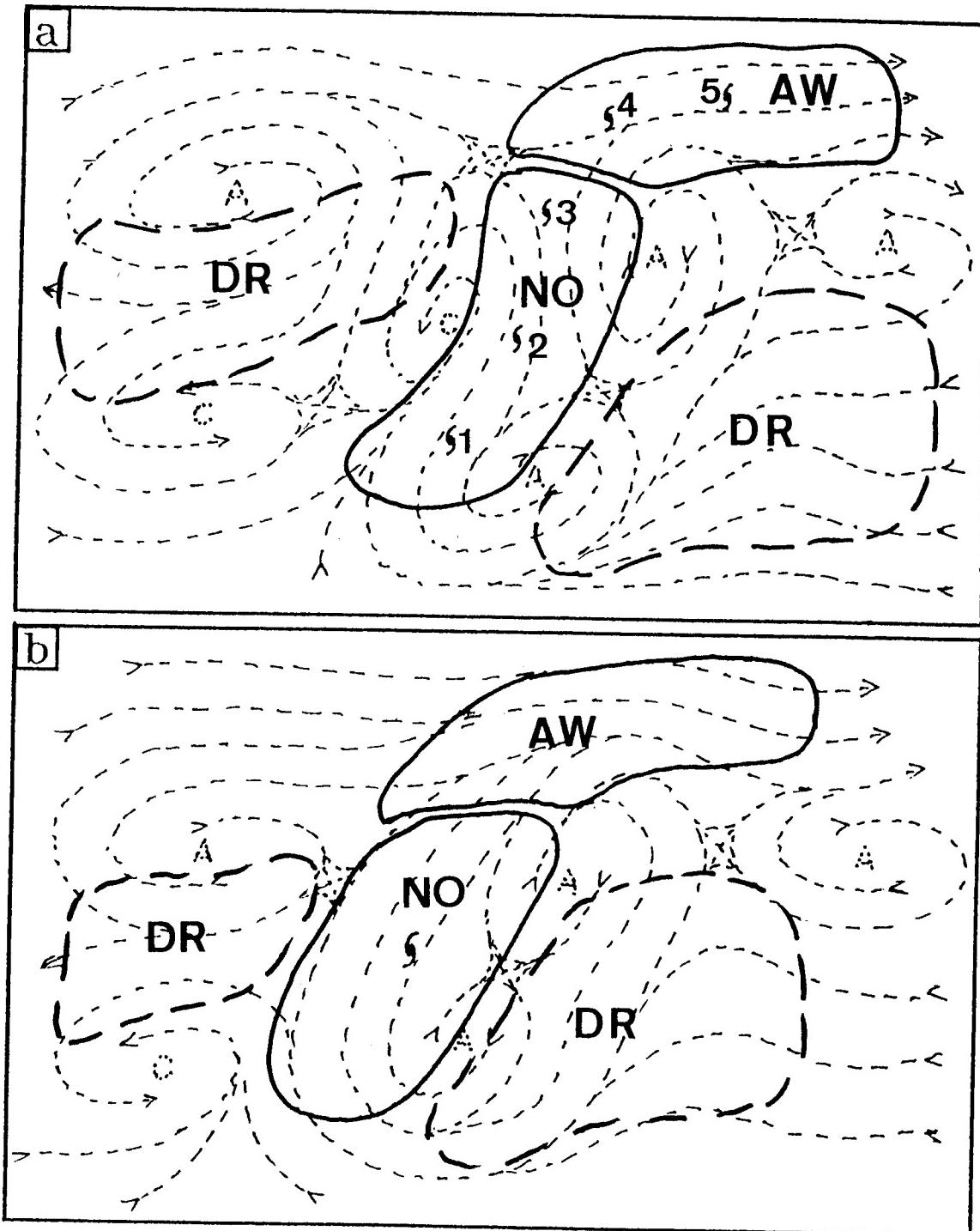


Fig. 3.21 As in Fig. 3.17, except for the North-oriented Patterns (a) N1 and (b) N2 and associated synoptic regions (solid lines). NO denotes the North-oriented Synoptic Region. The adjoining DR Synoptic Regions (heavy dashed) are not considered to be a part of the N Patterns.

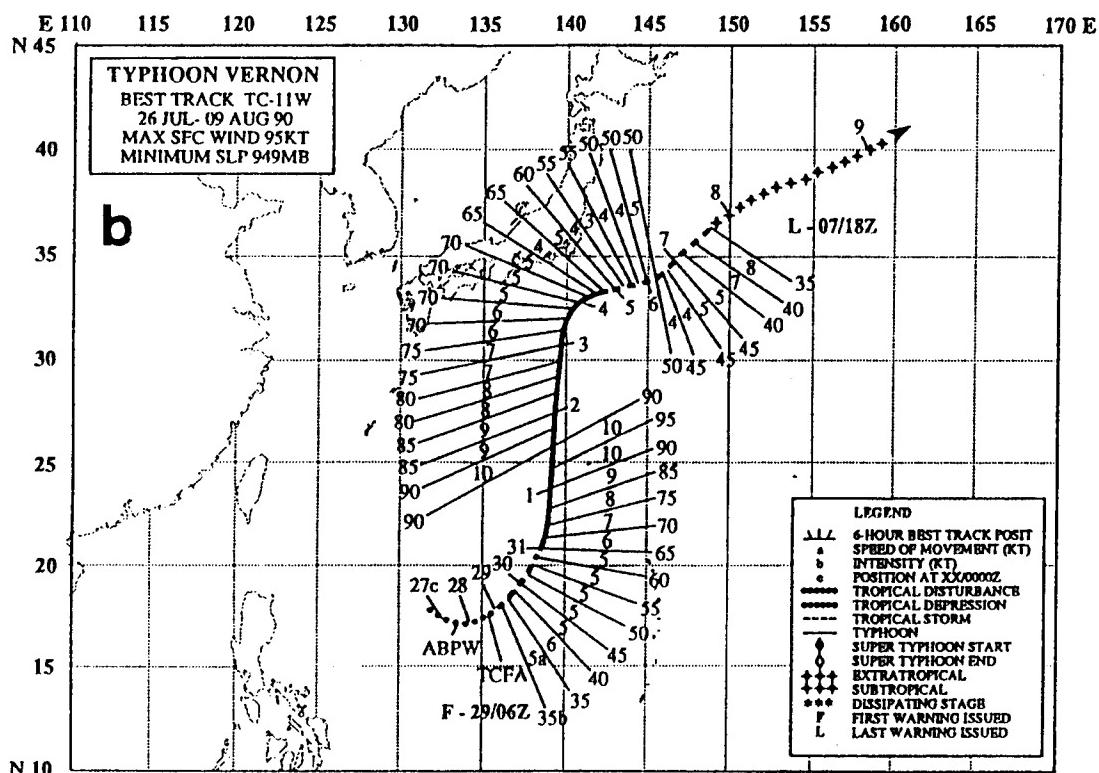
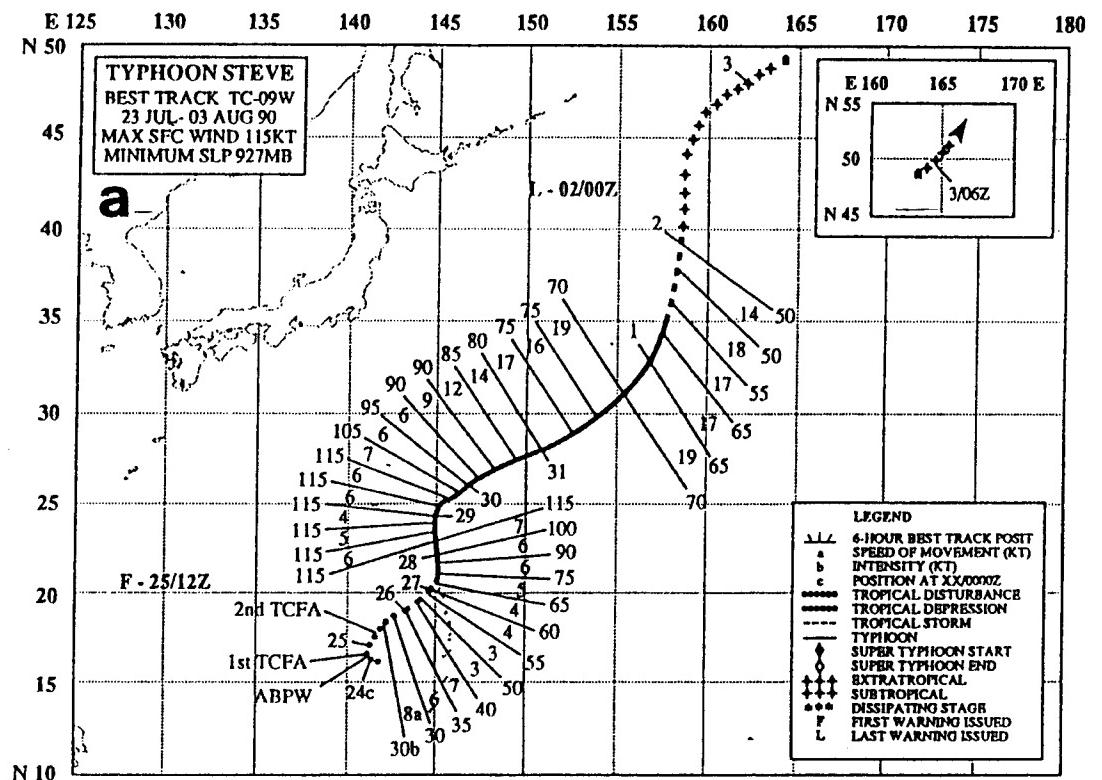


Fig. 3.22 As in Fig. 3.1, except for (a) Typhoon Steve, and (b) Typhoon Vernon.

only templates that must be adapted to the complex, evolving environments of actual TCs.

Supertyphoon Yuri is a large TC in the NO Region of a N2 Pattern (Figs. 3.11a-b). Typhoon Sarah and Tropical Storm Tip are in the NO Region of a N2 Pattern (Fig. 3.11 c-d) arising from a MG-TC interaction. A comparison of the streamline patterns around Tip (the east TC symbol) in Figs. 3.11c-d reveals how the N2 Pattern and the associated NO Region tend to move with the TC over a 24-h period.

The AW Region of N Patterns is not fundamentally different from the AW Region of the S Pattern in terms of the effect on TC motion. For reasons that will be discussed later, the entry of the TC into the AW Region may sometimes be delayed. Notice that the WR Region is not included between the NO and AW Regions in the N Patterns schematics (Fig. 3.21). The reason is that the southerly environment flow in the NO Region ensures that a TC in a persistent N Pattern *must eventually recurve*. That is, no bifurcation of TC tracks is expected in persistent N Patterns as described above for the S Pattern. Similarly, no distinctive numerical model or objective aid error traits are expected that would dictate the inclusion of a WR Region in either of the N Patterns.

Finally, there are two separate DR Regions in Figs. 3.21a-b: one the southeast of the anomalous ridging, and another to the west of the reverse-oriented monsoon trough or coalesced MG-TC. TCs that may be present in either of these DR Regions will *not* be classified as being in the N Pattern. In the N1 Pattern, the confluent area between the monsoon trough and the ridge to the east is a highly preferred TC formation area, and these TCs will be in the NO Region. Because extensive convective activity in the confluent area produces significant subsidence in the adjacent areas, the presence of TCs in either of the DR Regions adjoining the N1 Pattern is rare. The same argument hold for the western DR Region adjoining the N2 Pattern. However, the large TC or coalesced MG-TC associated with the N2 Pattern often generates a Rossby wave train (RWT) of such intensity that the associated mid-level cyclonic tendencies east to southeast of the wave train anticyclone may contribute to genesis of a second TC in the eastern DR Region.

Two examples of TC genesis in conjunction with a RWT are the formation of Supertyphoon Mireille to the southeast of Tropical Storm Luke (Fig. 3.23a) and the formation of Typhoon Percy southeast of Typhoon Ofelia (Fig. 3.23b). Mireille (near 16°N, 153°E) and Percy (near 8°N, 145°E) are located in DR regions to the southeast of anomalous ridge circulations associated with Luke (near 21°N, 130°E) and Ofelia (near 18°N, 121°E), respectively. At these times, Mireille and Percy had anomalous equatorward tracks (Figs. 3.24a and b, respectively), which agrees with the generally northeasterly steering in the eastern DR Region adjoining the N2 Synoptic Pattern (Fig. 3.21b). In the case of both Mireille and Percy cases in Figs. 3.23a and b, the DR Region would be part of a S Pattern owing the presence of an east-west oriented ridge to the north of each TC (in view of the absence of a north-south oriented ridge to the *east* of each TC). The ridge to the *west*, and even southwest, of both Mireille and Percy may seem to be a rather significant departure from the S Pattern conceptual model (Fig. 3.17). However, this anomalous ridge, as well as

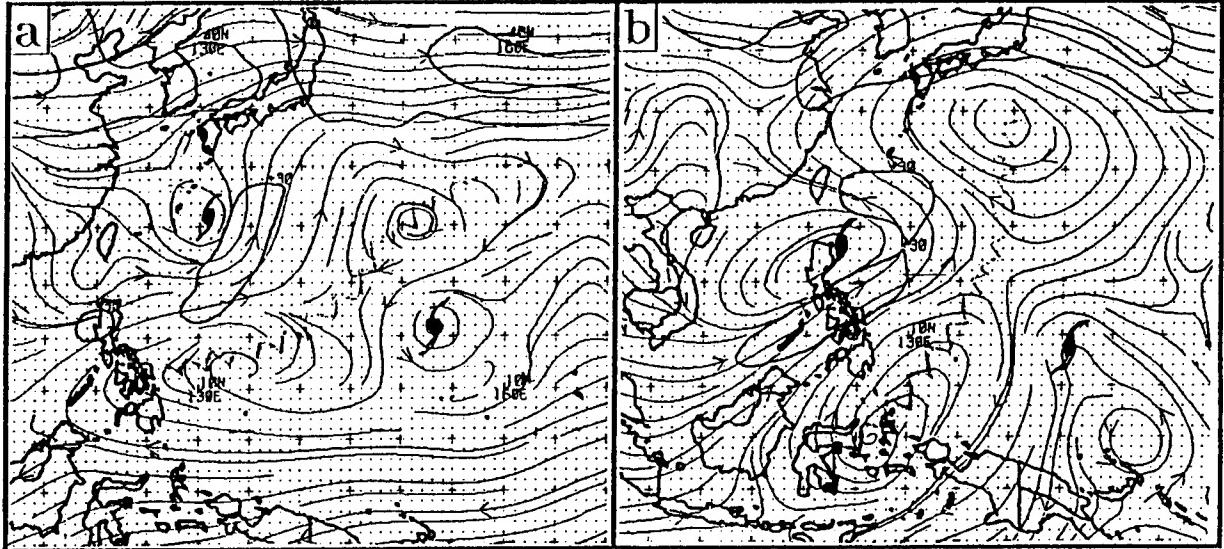


Fig. 3.23 NOGAPS analyses as in Fig. 3.6, except for 0000 UTC on (a) 18 September 1991, and (b) 22 June 1990. TC symbols denote the positions of (a) Tropical Storm Luke (west) and Supertyphoon Mireille (east), and (b) Typhoons Ofelia (west) and Percy (east).

the associated temporary equatorward excursions of Mireille and Percy, will be accounted for by the TC-Environment transformation called Tropical Cyclone Interactions (TCIs) (recall Table 3.3). In other words, the anomalous ridging will be treated as an indirect effect of Luke on Mireille, and Ofelia on Percy, respectively. The temporary equatorward excursions of Mireille and Percy ended upon the cessation of the TCI arising from the TCs farther west, and then both Mireille and Percy resumed the west-northwestward motion (Figs. 3.24a and b) expected to occur in the DR Region of a S Pattern.

*b) Regions within the Monsoon Gyre (G) Synoptic Pattern.* The Synoptic Regions associated with the G Pattern are shown in Fig. 3.25. The NO and AW Regions are fundamentally the same as in the N Patterns, although the western boundary of the NO Region curves around the large MG, which excludes a region of near the gyre center where TC formations are hindered by strong subsidence. As in the N Patterns described above, the eastern DR Region is not considered to be in the G Pattern. However, the western DR Region will be included in the G Pattern because the east-northeasterly steering in this DR Region is primarily due to the gradient between the MG and the ridge to the north. This inclusion of the western DR Region in the G Pattern distinguishes between a TC track sequence 1-2-3-4-5 and TC track sequence 1-2-6-7 in Fig. 3.25. The track of Typhoon Ellie (Fig. 3.26) is an example of the first situation, and the track of Tropical Storm Doug (Fig. 3.27) is an example of the second. Since two distinctly different TC track types are possible in the G Pattern, a track bifurcation exists depending on the radius at which the TC forms relative to the center of the MG. That is, this bifurcation does not arise from weak flow associated with the east-west ridge axis as in the WR Region of the S Pattern. Furthermore, the recurvature of Doug without any deceleration near the ridge axis (Fig. 3.27) provides further evidence that inclusion of a WR Region in the G Pattern is not necessary.

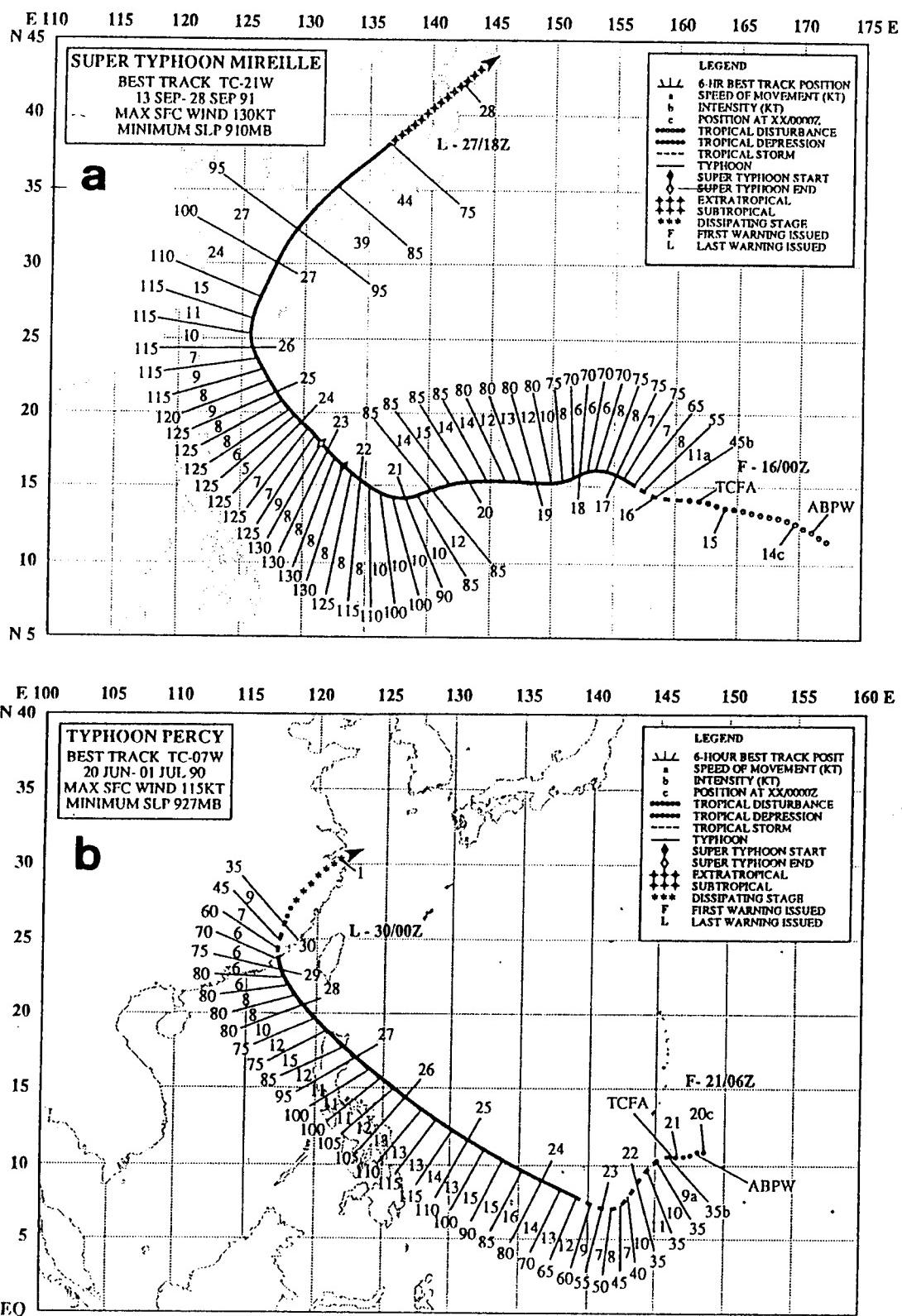


Fig. 3.24 As in Fig. 3.1, except for (a) Supertyphoon Mireille, and (b) Typhoon Percy.

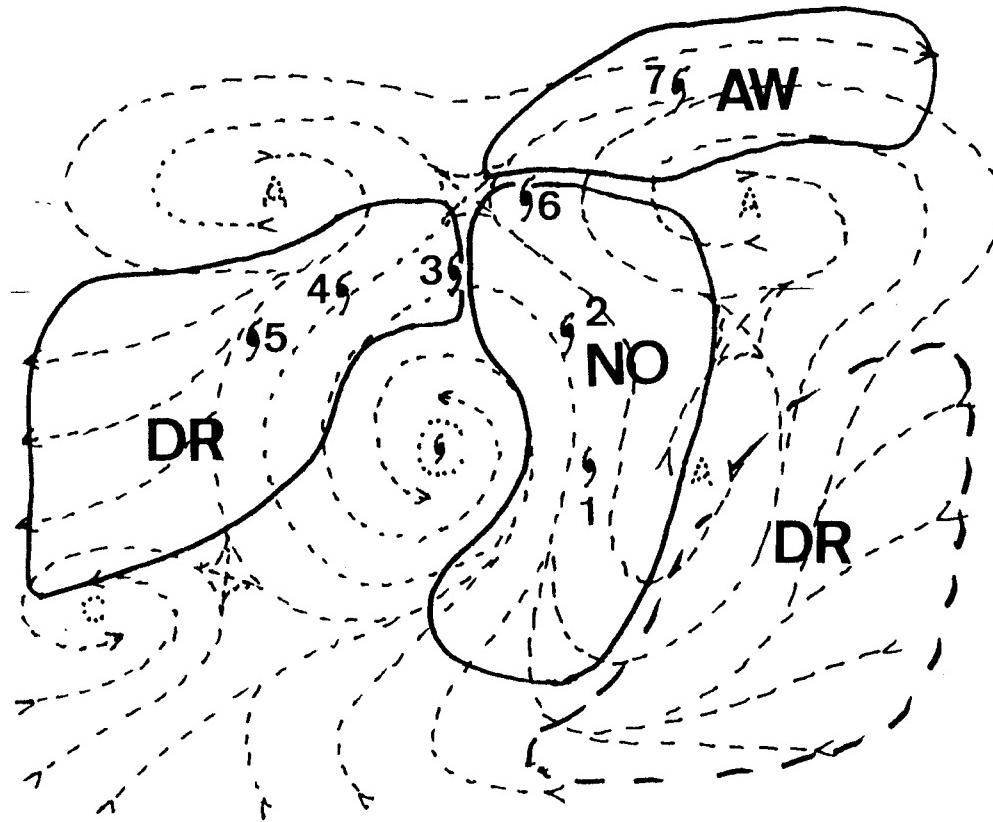


Fig. 3.25 As in Fig. 3.17, except for the Monsoon Gyre (G) Synoptic Pattern and associated synoptic regions (solid lines). The heavy dashed line has the same meaning as in Fig. 3.21.

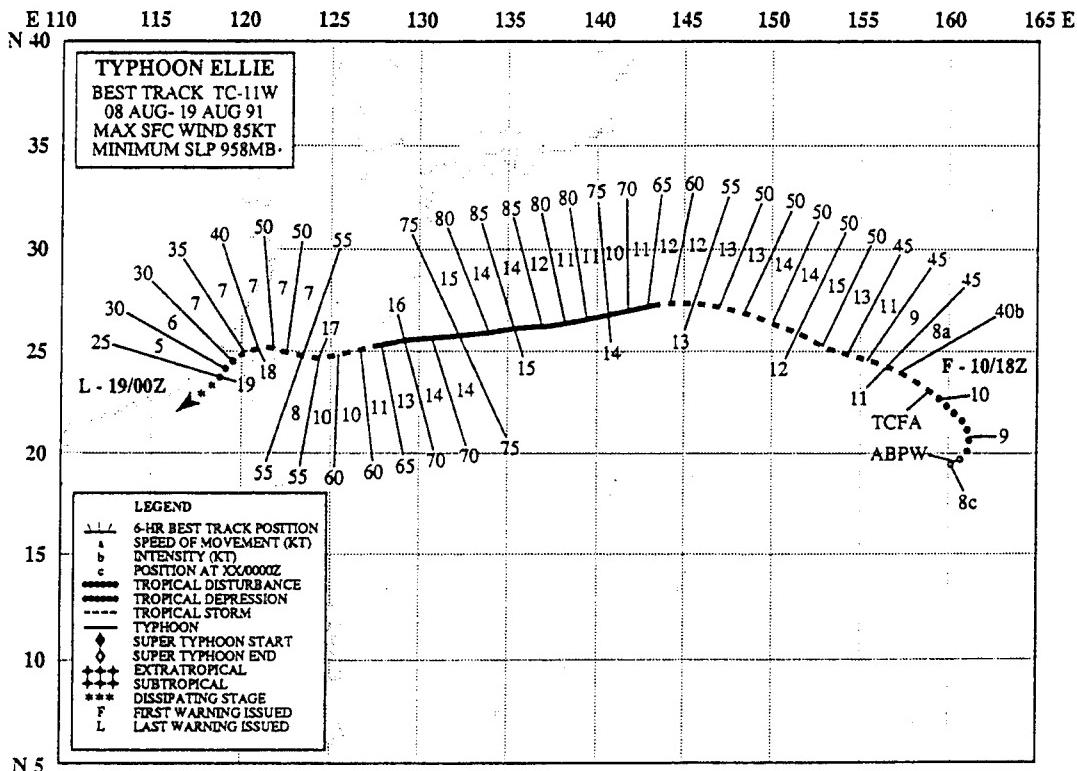


Fig. 3.26 As in Fig. 3.1, except for Typhoon Ellie.

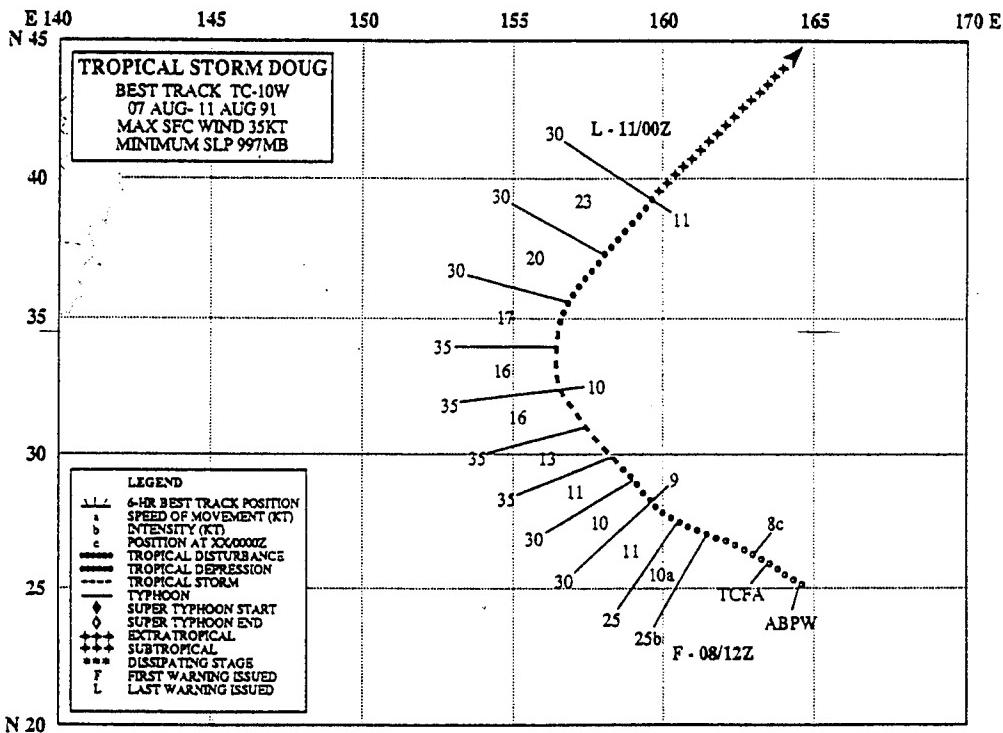


Fig. 3.27 As in Fig. 3.1, except for Tropical Storm Doug.

d) Regions within the Multiple TC (M) Synoptic Pattern. According to the conditions for a M Pattern in Section 3.b.1.d, the east and west TCs must be located in either the Southerly Flow (SF) and Northerly Flow (NF) Synoptic Region, respectively (Fig. 3.28). The SF Region consists of locations in a M Pattern that are: (i) in the predominantly southerly environmental flow in the vicinity of a line running from the center of the western TC to the center of the eastern ridge circulation; and (ii) no closer than about 10° lat. to the western TC. Conversely, the NF Region consists of locations in a M Pattern that are: (i) in the predominantly northerly environmental flow on either side of a line running from the center of the eastern TC to the center of the western ridge circulation; and (ii) no closer than about 10° lat. to the eastern TC. Since the two TCs in the idealized M Pattern are at about the same latitude and have similar circulation sizes, the SF and NF Regions are symmetric about a north-south line running through the centroid between the TCs. However, these idealized SF and NF conceptual models must be adapted to account for the variability of actual situations from the ideal.

The eastern TC will usually transition into the SF Region of the M Pattern from the DR Region of Fig. 3.28a, which will usually be part of a S Pattern, and leave via the AW Region, which will also usually be part of a S Pattern. Normally, the environment around the western TC will transition from a DR (or perhaps a WR Region) of a S Pattern to the NF Region of the M Pattern (Fig. 3.28b) due to the approach or formation of the eastern TC. The western TC will usually be prevented from moving into the AW Region from the NF Region by the equatorward flow between the eastern TC and the western ridge. The effect of the northerly flow is transitory because the eastern TC will tend to recurve. It is more likely that the western TC will transition into the DR Region of Fig. 3.28b, which will usually be part of a S Pattern.

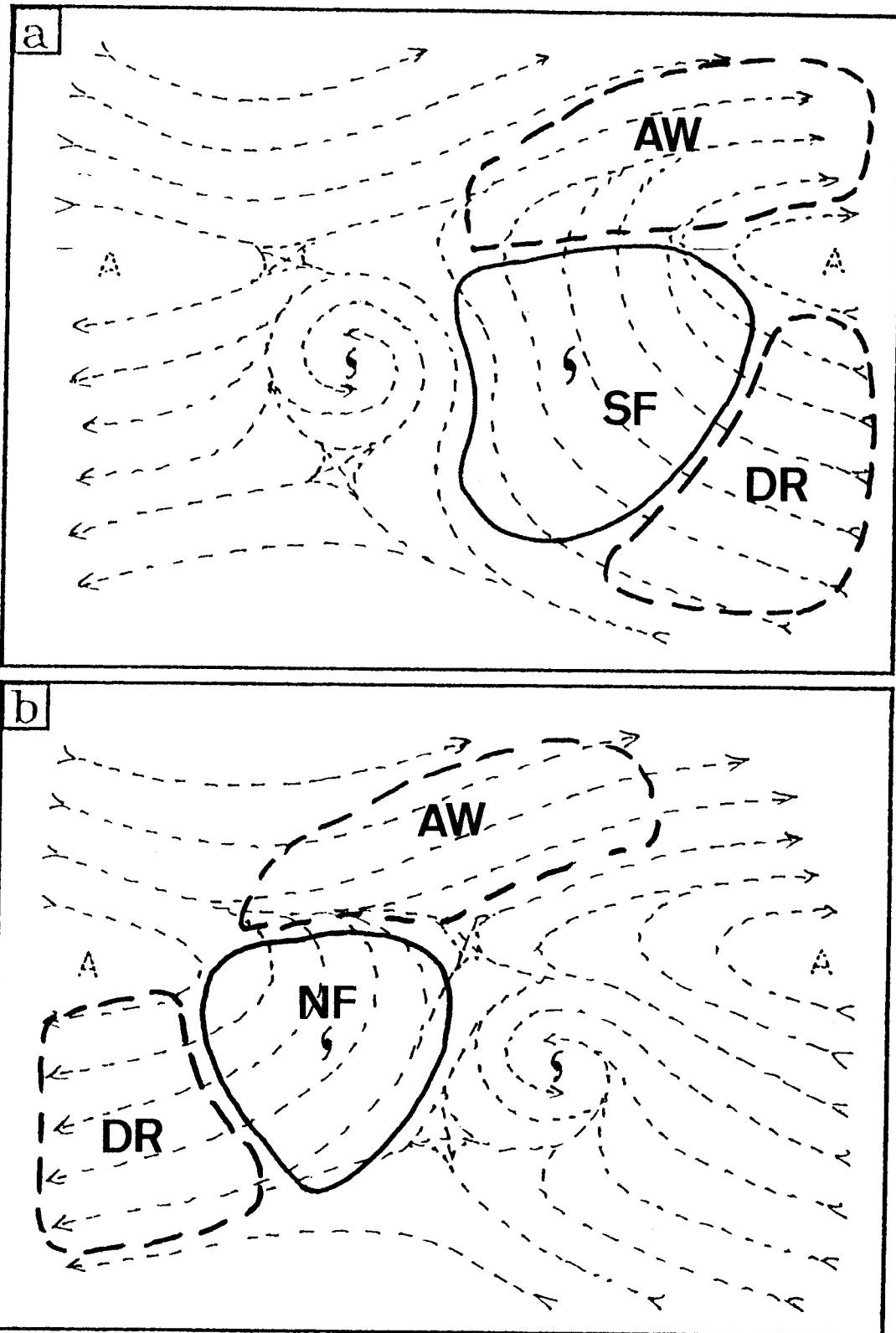


Fig. 3.28 As in Fig. 3.17, except for the Multiple (M) Tropical Cyclone Synoptic Pattern and associated synoptic regions (solid lines). SF denotes Southerly Flow Region and NF denotes NF Northerly Flow Region. The adjoining DR and AW Regions (heavy dashed) are not considered to be part of the M Pattern.

Seth/Verne on 8 November 1991 (Fig. 3.16a) and Yancy/Zola on 21 August 1990 (Fig. 3.16b) are examples of the western (eastern) TC occupying the NF (SF) Region of a M Pattern. The corresponding best tracks (Figs. 3.29 and 3.19b, and 3.30a and b, respectively) reveal modes of TC motion that are representative of the SF and NF Regions. First, notice that the translation speeds either remained about constant (Zola) or increased (Verne) during the periods between the NOGAPS analyses and the time of recurvature. Such translation speeds depart from the normal recurvature scenario in which the translation slows to a minimum of about 5-8 kt. Second, the track directions of Seth and Yancy had changed during the establishment time of the M Pattern from approximately northwestward to west-southwestward and westward, respectively. Such track direction changes at the relatively high latitudes of about 20°N and 25°N, respectively, are also unusual since TCs at such latitudes are typically turning poleward as a prelude to recurvature. The ability of the forecaster to recognize the establishment of a M Pattern and its attendant SF/NF regions is highly important, since such anomalous motion will not likely be captured by statistical track prediction techniques. In addition, numerical TC track predictions may also fail in this situation, since an accurate forecast of TC structure is needed.

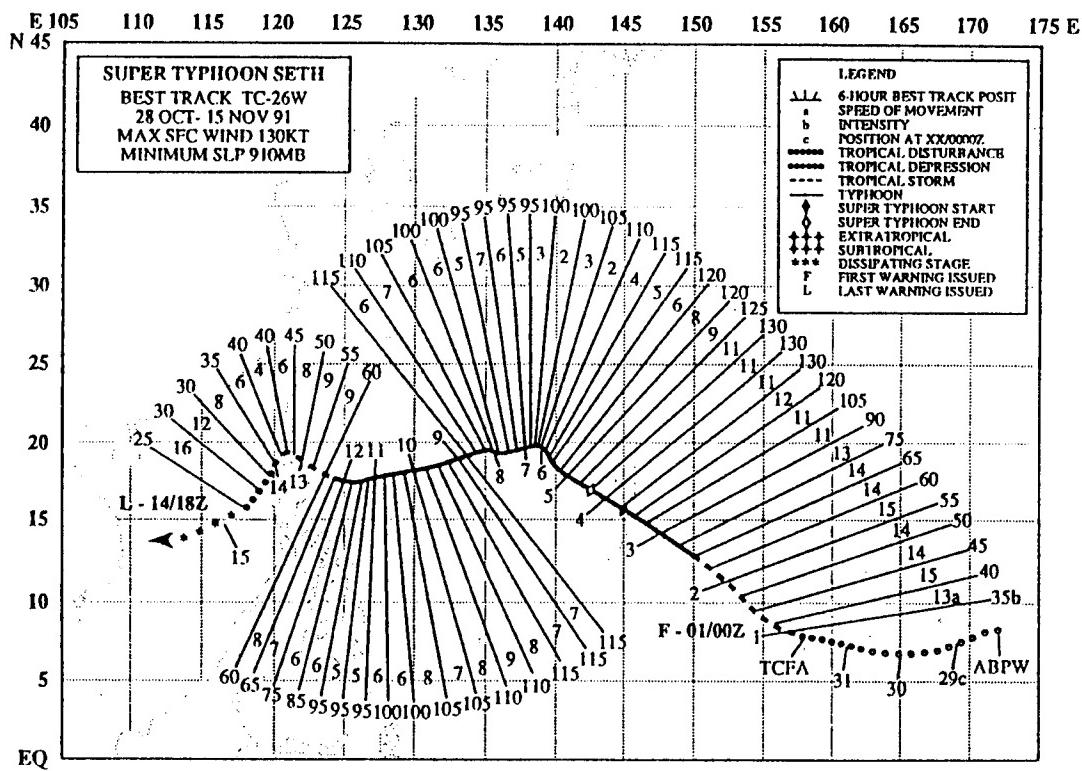


Fig. 3.29 As in Fig. 3.1, except for Supertyphoon Seth.

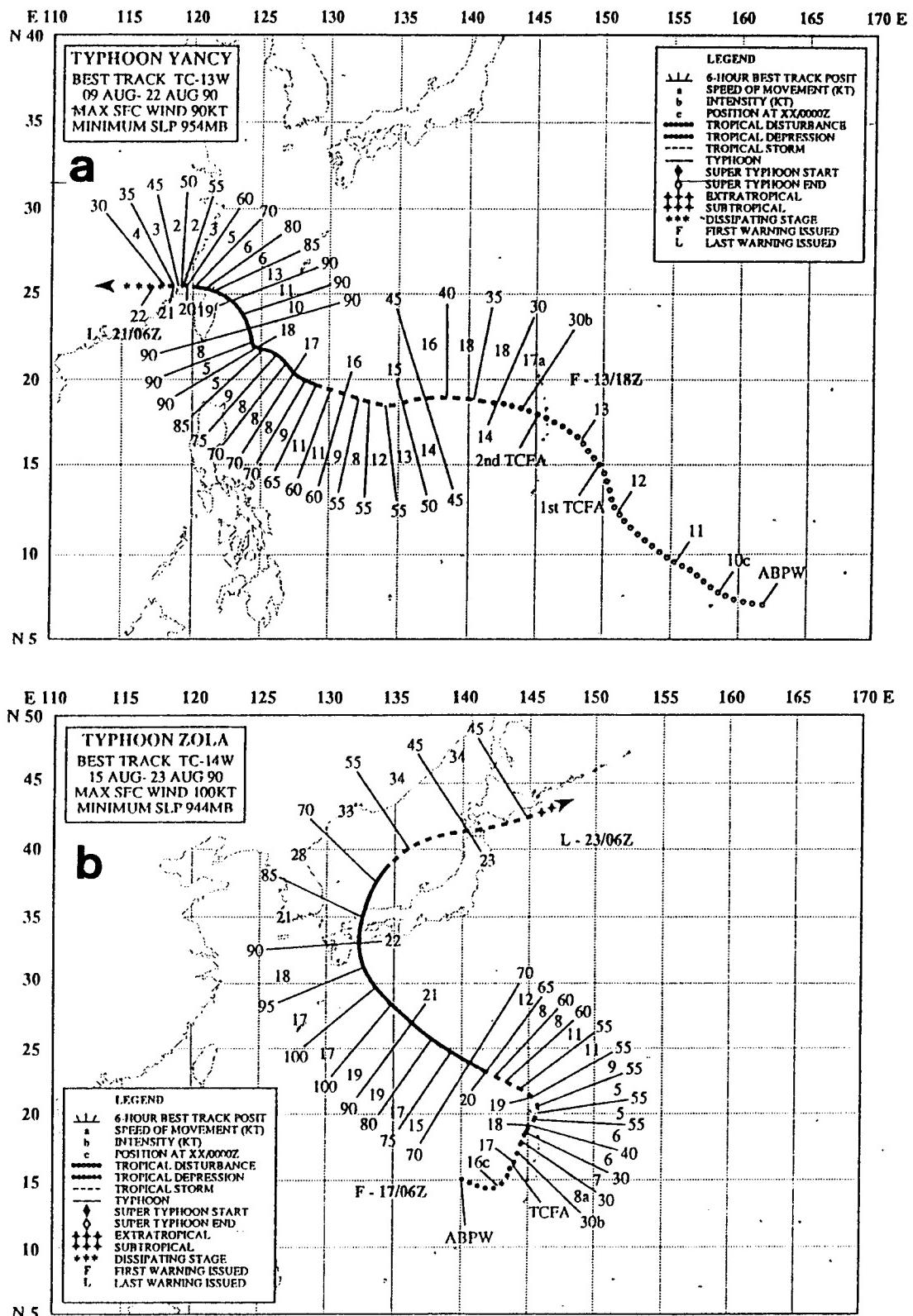


Fig. 3.30 As in Fig. 3.1, except for (a) Typhoon Yancy, and (b) Typhoon Zola.

c. *Tropical cyclone structure*

1) Tropical cyclone intensity.

a) *Intensity conceptual models.* The principal motivation for incorporating a set of TC intensity conceptual models (Table 3.2) into the TC motion forecasting knowledge base is the observed dependence of the best level or layer of environmental steering on TC intensity. Observational and modelling justifications are given in Appendix B for associating the particular intensity categories of Table 3.2 with certain steering levels.

As summarized in Appendix B, the Dong and Neumann (1986) and Velden and Leslie (1991) studies provide reasonably consistent optimal environmental steering relationships for tropical storms and typhoons. The good agreement between these studies in two distinctly different TC environments provisionally justifies application of their results to the western North Pacific region. These studies did not agree as to the relative accuracy of steering levels versus layers. However, the near-parity of steering levels and layers derived separately for tropical storms and hurricanes by Dong and Neumann is the more clearly established result. Thus, the use of steering levels for pattern interpretation is adopted for the systematic approach. Based on the discussion in Appendix B, the following set of conceptual associations between TC intensity and steering level have been developed.

*Exposed Low-level (XL).* The XL intensity model is applied to a TC with an exposed Low-Level Circulation (LLC) that is completely decoupled from the associated Convective Cloud Mass(CCM).<sup>6</sup> The optimal steering level associated with the XL model is 850 mb. Typically, this conceptual model and its associated steering level will be applied to TCs in a dissipated stage.

*Tropical Depression/Storm (TD/TS).* The TD/TS intensity model is applied to TCs with LLCs that have estimated maximum wind speeds of 60 kt or less, and that are coupled to the associated CCM. Based on the Dong and Neumann (1986) study, the optimal pattern-typing level for TDs or TSs is 700 mb. It should be noted that the TS/TD model will primarily have application in situations where weak TCs are expected to experience sustained periods of slow or no intensification due to the inhibiting influence of moderate vertical wind shear and/or proximity to land. By contrast, in situations where normal or rapid intensification is expected, TDs or minimal TSs often attain typhoon intensity in 36 h or less (*i.e.*, less than half the 72-h forecast period). In these latter situations, the TD/TS model will have minimal application.

---

<sup>6</sup> The authors are not aware of any research that has clearly established a threshold CCM-LLC separation distance beyond which decoupling may be assumed. Until such guidance becomes available, the authors suggest that forecasters use a decoupling threshold of  $1\frac{1}{4}$ ° lat., which is associated with the  $T1.5 \pm 0.5$  intensity shear pattern in the Dvorak method (Dvorak 1984; p. 27, 29).

Typhoon (TY). The TY intensity model is applied to TCs that have LLCs coupled to the associated CCM and have estimated maximum wind speeds of 65 kt or greater. Based on the Dong and Neumann study, the optimal pattern-typing level for TYs is 400 mb.

Intense Typhoon (IT). Velden and Leslie found little change in the depth of the optimal steering layer among the five typhoon intensity categories they examined (Fig. B.2 in Appendix B). Thus, an IT model does not appear to be necessary on the basis of how particularly intense TC's actually steer. Because the representation of the structure of very intense TCs by NOGAPS (to be addressed in Part II) and other similar models can be particularly poor (much too large and weak), inclusion of the IT model in the systematic approach has the benefit of signalling the forecaster to anticipate potentially large biases in the NOGAPS-predicted track. In addition, the authors believe that there is evidence for certain TC-environment transformations that appear to be associated only with very intense typhoons. Thus, it is believed that an IT model will eventually be necessary as these transformations are investigated and added to the systematic approach.

b) Steering-level selection for NOGAPS charts. Since NOGAPS (or other operational numerical models) does not have the resolution or the data to predict accurately the inner core structure of the TC, the intensity and intensity trend analyzed/forecast by NOGAPS will usually be significantly different from what actually occurs. This difference is one potential source of error in the TC motion guidance provided by the model that the forecaster must be anticipating in the second task in the numerical guidance evaluation phase in Fig. 2.1. Consequently, some guidance must be provided for selecting the appropriate NOGAPS analyses and forecasts based on the expected intensity trend of the TC being forecast.

Due to the Dong and Neumann (1986) demonstration that 500 mb is the best steering level for all TCs of greater than TS intensity, the systematic approach emphasizes using NOGAPS 500 mb streamlines and isotach fields for pattern typing. Although 400 mb has been shown to be the best steering level for typhoon intensity TCs, the 500 mb will be regarded as an acceptable substitute for several reasons. First, the paucity of rawinsondes in the western North Pacific may result in only small differences between the 400 mb and 500 mb NOGAPS wind analyses. Second, NOGAPS tends to maintain a coherent vertical structure for TCs of greater than minimal typhoon intensity. Thus, the TC movement depicted at 500 mb reflects whatever small differences may exist between the 400 mb and 500 mb NOGAPS analyses.

By contrast, if a TC is expected to remain at less than typhoon intensity for two or more days, then the 700 mb NOGAPS charts should be consulted in addition to the standard 500 mb charts. NOGAPS representations of weaker TCs tend to prematurely lose vertical coherency in moderate vertical wind shear situations, which usually do not

significantly affect the vertical coherency of the actual TC.<sup>7</sup> Thus, it is important in these situations to focus on the level at which the real TC is most likely steering. In particular, the asymmetric 30-kt isotach that is associated with the short-term motion may be found at 700 mb instead of 500 mb for the weaker TSs and TDs.

— *c) Intensity forecasting.* In view of the above discussion, the proper choice of which NOGAPS level or levels should be scrutinized for environmental steering pattern typing depends on an accurate intensity forecast, which in turn can depend on the motion of the TC as mentioned at the beginning of this report. Thus, an integrated approach to the intensity forecasting problem is an implicit requirement to the systematic motion forecasting approach addressed explicitly in this report. A detailed discussion of the many processes that affect TC inner core structure change, as well as the various objective intensity forecast techniques and subjective procedures/thumbrules that have been developed, is outside the scope of this report. For example, the intensity forecasting process (1993 ATCR, p. 8) might include elements of: (i) extrapolation (Dvorak); (ii) climatology; and (iii) subjective consideration of the positive or negative influences of upper-level environmental synoptic-scale features. If the intensity forecasting process includes element (iii), it will in turn be affected by the TC motion forecast. Thus, an iterative process between intensity and motion forecasting can be included in the Systematic Approach despite the absence of a detailed treatment of TC intensity change here. Part II of this report will provide specific procedures for iterating the TC intensity forecast into the systematic approach forecasting process.

2) *Tropical cyclone size.* The TC forecaster must for several reasons consider the actual TC size in establishing the synoptic context of the forecast situation in the first step of the numerical guidance evaluation in Fig. 2.1. First, both observational experience and basic research studies indicate that the size of the TC circulation can cause TC motion to depart significantly from that expected as a result of environmental steering. Whereas the motion of small TCs tends to conform quite closely to environmental steering, the motion of large TCs may differ significantly from, *and even alter*, such steering. The TC-environment conceptual framework of the systematic approach accounts for this TC size-motion relationship via TC size conceptual models (Table 3.3) that contribute to certain TC-environment transformations (recall Fig. 3.3), which in turn actually specify what the size-related effect on TC motion will be. In principle, application of these TC size conceptual models is straightforward since their function here is solely as an input to the TC-environment transformation models. However, the operational forecaster is confronted with a number of practical problems, including:

- (i) lack of a consistent, accepted definition of TC size;

---

<sup>7</sup> This phenomenon is discussed more thoroughly in Part II.

- (ii) available empirical wind distribution models provide no insight about physical principles that influence TC wind distribution and distribution change;
- (iii) lack of a clear distinction between the extent of the TC *surface* wind field as a component of the total TC forecast, and the extent of the TC *mid-tropospheric* wind field as a key input into the TC motion forecasting process;
- (iv) difficulty in applying any wind distribution model to actual situations owing to a lack of data; and
- (v) virtually no basic understanding of, or ability to forecast, TC size change.

All of the these issues must eventually be addressed if the motion effect of TC size is to be properly incorporated within the conceptual framework of the systematic approach.

Just as in the case of TC intensity, the present NOGAPS model does not have the data or the proper physics to predict accurately the effects of size and size change on TC motion. Recognition of this inherent shortcoming of the numerical guidance is the second reason for including assessment of storm size effects as part of the numerical guidance evaluation in Fig. 2.1.

An overview of the first three issues above that are of significance to the operational forecaster is provided in Appendix C to emphasize the need for a TC wind distribution model specifically designed for motion forecasting. A TC wind distribution model based on angular momentum considerations is then proposed and shown to have properties that are desirable for assessing the impact of TC size on TC motion. In particular, this proposed model in Appendix C includes parameters that provide a simplified, but unambiguous, measure of TC size and outer wind strength. Issue (iv) is addressed in Subsection 3.c.2.a by providing a practical technique for estimating the TC size parameter using a combination of conventional data and satellite imagery interpretation. Subsection 3.c.2.b will provide preliminary evidence that the size of most TCs changes little after initial consolidation, which simplifies the TC size input into the motion forecasting problem to a determination of the size of the TC during the formation phase. In Subsection 3.c.2.c, the four TC size conceptual models in Table 3.2 are defined based on how significant the TC propagation speed is compared to average TC forecast errors. That is, the magnitude of the  $\beta$ -effect propagation will be used to define what constitutes a midget, small, average, or large TC for the purpose of the systematic approach. This association of the four TC size conceptual models with the size parameters of the wind distribution model will be deferred until Subsection 3.d.1.

*a) Proposed TC wind distribution model.* The TC wind distribution proposed in Appendix C is

$$v^p(r) = \frac{M}{r^{0.4}} - \frac{1}{2} f_o r , \quad (3.1)$$

$$M = \frac{1}{2} f_o (R_o^p)^{1.4} . \quad (3.2)$$

In (3.1),  $v^p$  is the tangential wind in  $m s^{-1}$  at pressure level  $p$ ,  $r$  is the radius in  $m$ , and  $f_o$  is the Coriolis parameter at the latitude of the TC center. In (3.2),  $M$  is a constant of proportionality obtained from (3.1) by defining a radius  $R_o^p$  at which the azimuthally-averaged tangential wind is zero at pressure level  $p$ . Thus,  $R_o^p$  represents the maximum radial extent of the axisymmetric cyclonic circulation of the TC at a particular pressure level. Either the value of  $v$  at some particular radius  $r$ , or the value of  $R_o$ , must be supplied by the forecaster (based on external information) to determine  $M$  in (3.1).

Appendix C contains a detailed development of (3.1), in which the azimuthal momentum equation is transformed into a formula that relates changes in parcel absolute angular momentum to frictional effects. As noted in Appendix C, the value of the exponent in the first term on the right side of (3.1) was determined using aircraft reconnaissance at 700 mb. Thus, it is assumed that (3.1) reasonably approximates the azimuthally-averaged radial dependence of TC tangential wind speeds throughout the 850 to 500 mb layer.

*b) Wind distribution model application.* The proposed angular momentum model provides a dynamically-based and unambiguous measure of TC outer wind strength and size at some pressure level via the parameters  $f_o$  and  $R_o$  (see Fig. C.11). As will be seen in the discussion of BEP and RMT TC-environment transformations in Subsection 3.d.1 and 3.d.3 respectively, a knowledge of the outer wind strength or size is necessary to assess to what degree the TC will propagate relative to, or modify, its environment. Specification of  $f_o$  is hypothesized to simply be the formation latitude (45 kt intensity) of the TC, which is usually from  $10^\circ$  to  $20^\circ$  N. By contrast, specification of  $R_o$  is greatly complicated by the wide variation in TC size and comparatively little data over tropical ocean basins on which to base TC size estimates. Recall that it is the average size of the TC over the steering layer (say 850-300 mb), as approximated by  $R_o^{500}$ , that is relevant to motion forecasting, and data coverage is particularly poor at mid-tropospheric levels.

Because of the difficulty of determination by direct approach, it is proposed that  $R_o^{500}$  be estimated by first determining  $R_o^{850}$  and then making a conversion to  $R_o^{500}$  based on knowledge of the vertical variation of TC tangential winds with pressure level. This process is briefly described and illustrated below.

**Determination of  $R_o^{850}$ .** Since  $R_o^{850}$  is a radius of zero wind, it is virtually impossible to measure directly owing to the obscuring effect of the environmental winds in which the TC is embedded. However, if there are sufficient 850 mb wind reports in the vicinity of the TC so that the average radius of some non-zero TC tangential wind speed may be estimated,

then (3.1) and (3.2) may be combined to give a relationship for  $R_{\text{e}}^{850}$  as a function of Coriolis (which depends only on latitude) and the radius of this non-zero TC tangential wind speed. The results of such a manipulation of (3.1) and (3.2) are shown in Figs. 3.31a-d for which the radius of 40, 35, 30, or 25 kt winds is assumed to be known, respectively.

Analysis of two sets of 850 mb wind data during Typhoon Robyn serve to illustrate the use of Figs. 3.31a-d. At 1200 UTC 2 August 1993 (Fig. 3.32a), Tropical Storm Robyn (11W) had an intensity of 45 kt, and was located at  $9.4^{\circ}$  N,  $147.5^{\circ}$  E. This position placed Robyn midway between Guam and Chuuk at a distance of about  $5^{\circ}$  lat. (550 km). Owing to this fortuitous orientation, an average of winds at Guam and Chuuk (25 kt or  $12.5 \text{ m s}^{-1}$ ) may be used as an estimate of the axisymmetric tangential wind of Robyn at 550 km from the center. Entering Fig. 3.31a with a formation latitude of  $10^{\circ}$  N, and a 25-kt wind radius of 550 km, gives a  $R_{\text{e}}^{850}$  of about 1150 km, or about  $10.5^{\circ}$  lat. Similarly, at 0000 UTC 4 August 1993 (Fig. 3.32b), Typhoon Robyn was situated nearly midway (440 km) between Guam and Yap, which permitted a second estimate of  $R_{\text{e}}^{850}$  based on the average of the 850 mb RAOB winds reported by the two islands (37.5 kt or  $18.75 \text{ m s}^{-1}$ ). To obtain a value for  $R_{\text{e}}^{850}$  based on a formation latitude of  $10^{\circ}$  N and a 37.5 kt wind radius of 440 km, interpolation between the value of  $R_{\text{e}}^{850}$  given by Fig. 3.31c (1220 km) and Fig. 3.31d (1310 km) is required to give an average  $R_{\text{e}}^{850}$  of about 1265 km or  $11.4^{\circ}$  lat. Notice also that the curvature of the 850 mb satellite winds (Fig. 3.33a) to the north of Robyn changes from cyclonic to anticyclonic at about  $21.5^{\circ}$  N, which is an indication of the extent of Robyn's 850 mb cyclonic wind field. This latitude is about  $10^{\circ}$  north of Robyn's position, which corresponds reasonably well with the  $R_{\text{e}}^{850}$  of  $11.4^{\circ}$  given by the TC wind distribution model.

In the absence of adequate coverage by 850 mb RAOBs and/or satellite cloud-drift winds to estimate  $R_{\text{e}}^{850}$  from Figs. 3.31a-d, it is proposed that  $R_{\text{e}}^{850}$  may be inferred from the size of the total convective cloud pattern of the TC. For example, consider the imagery of Typhoon Robyn (Fig. 3.33a-b) that corresponds to the 850 mb wind reports in Fig. 3.32a-b, respectively. Recall that according to the angular momentum model, the value of  $R_{\text{e}}^{850}$  at 1200 UTC 2 August was 1150 km. A circle of this diameter corresponds well to the size of the infrared cloud pattern of Robyn in Fig. 3.33a, if all the peripheral banding features are included. This correspondence is physically plausible, since the extent of TC convection may be related to the extent of the convergent cyclonic circulation at 850 mb. Similarly, recall that according to the angular momentum model, the value of  $R_{\text{e}}^{850}$  at 0000 UTC 4 August was 1265 km. In this case, the extent of the convective cloud pattern in infrared imagery (Fig. 3.33b) is not circular owing to TUTT-induced suppression of convection to the northeast and monsoon surge-enhanced convection to the southeast. Nevertheless, a circle of 1300 km radius corresponds fairly well with the average extent of the convective cloud pattern.

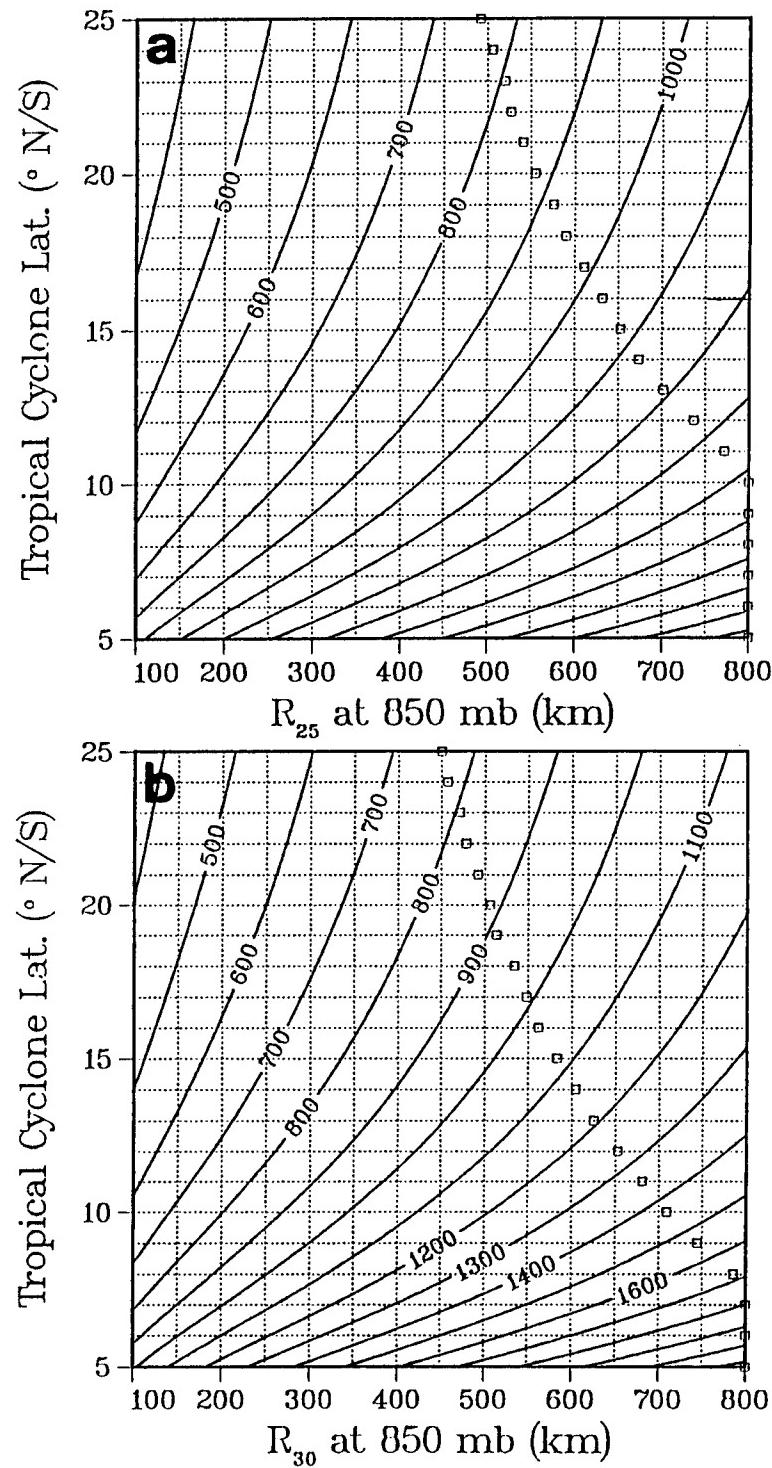


Fig. 3.31 (a-b). Values of  $R_{850}^{850}$  as a function of tropical cyclone formation latitude (ordinate) and an observed 850 mb wind radius (abscissa) of (a) 25 kt, (b) 30 kt, (c) 35 kt, or (d) 40 kt. The area of the diagrams to the right of the squares represents combinations of formation latitude and the particular wind radius that are likely unrealistic. That is, the angular momentum profiles are specified by such parameter combinations would produce maximum tangential wind speeds exceeding  $100 \text{ m s}^{-1}$  (200 kt) at a typical maximum wind radius of 20 km.

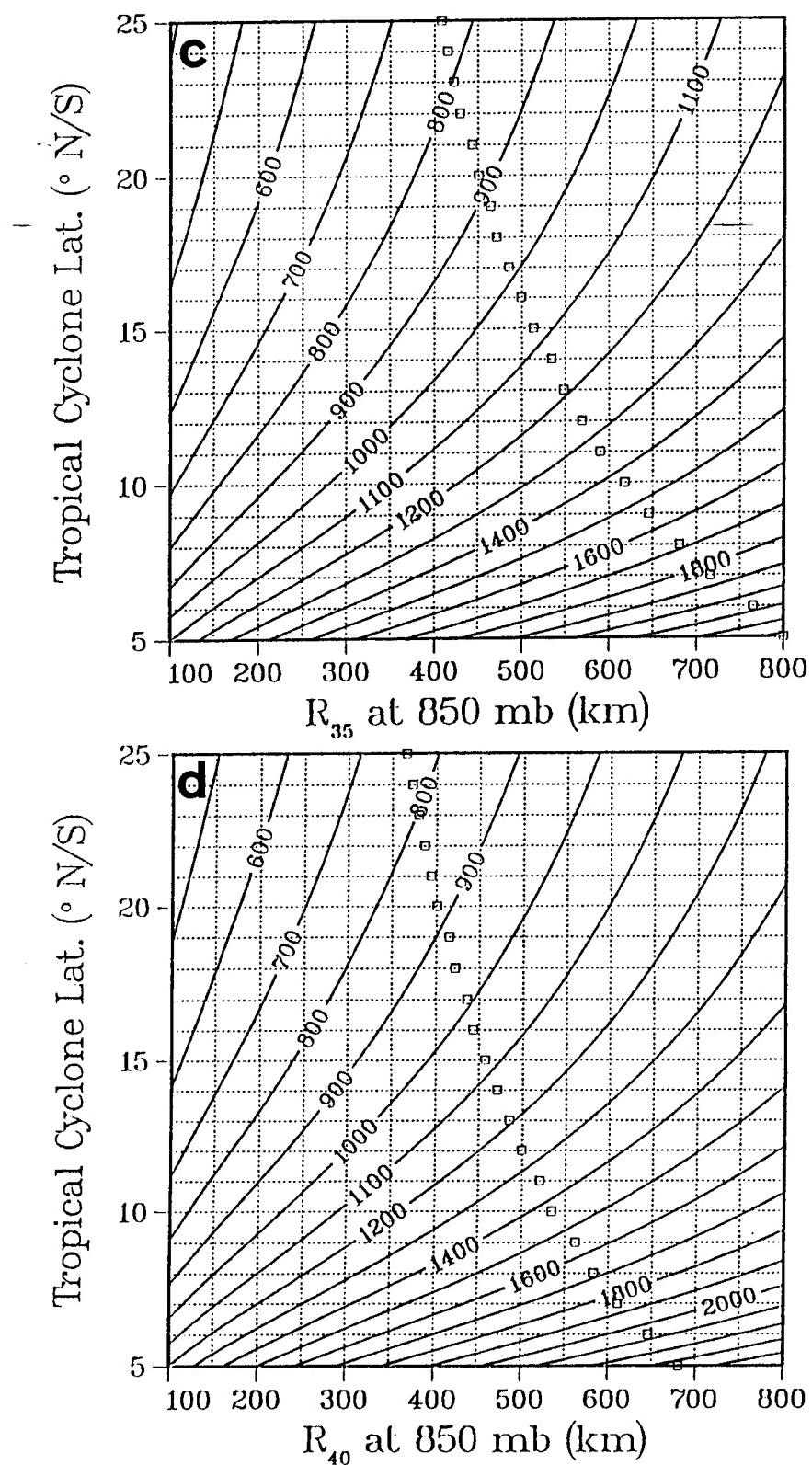


Fig. 3.31 (c-d). continued.

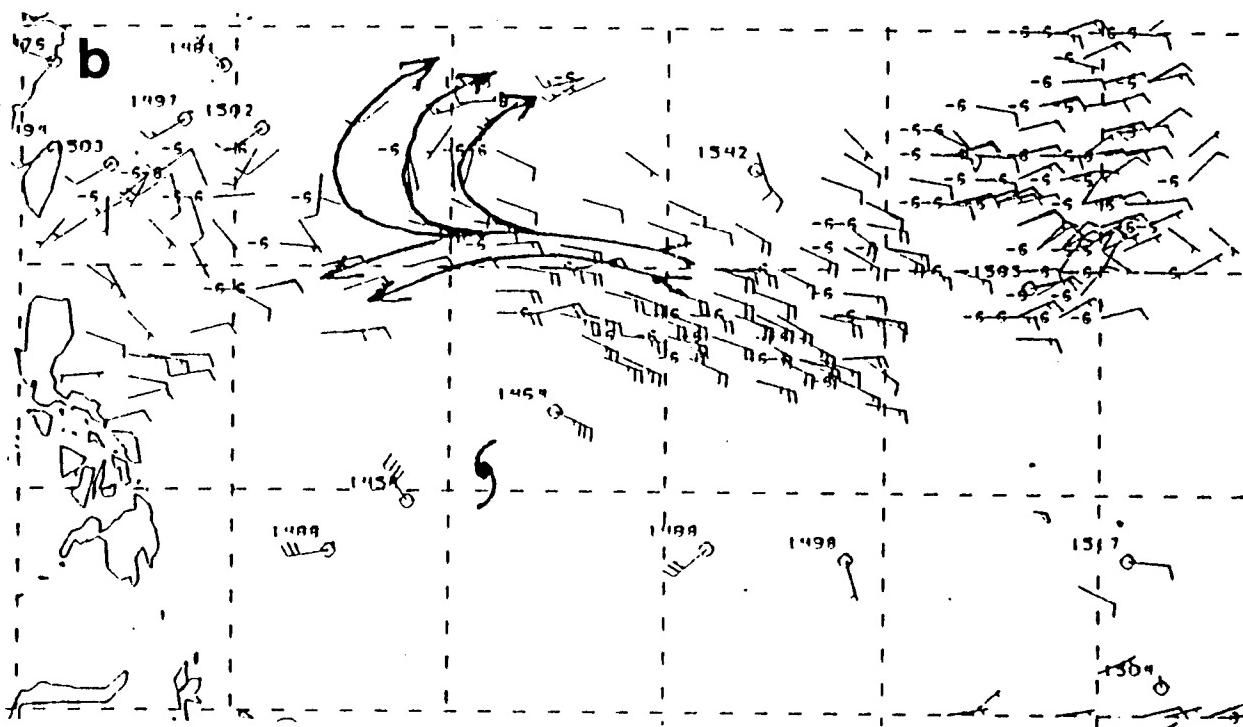
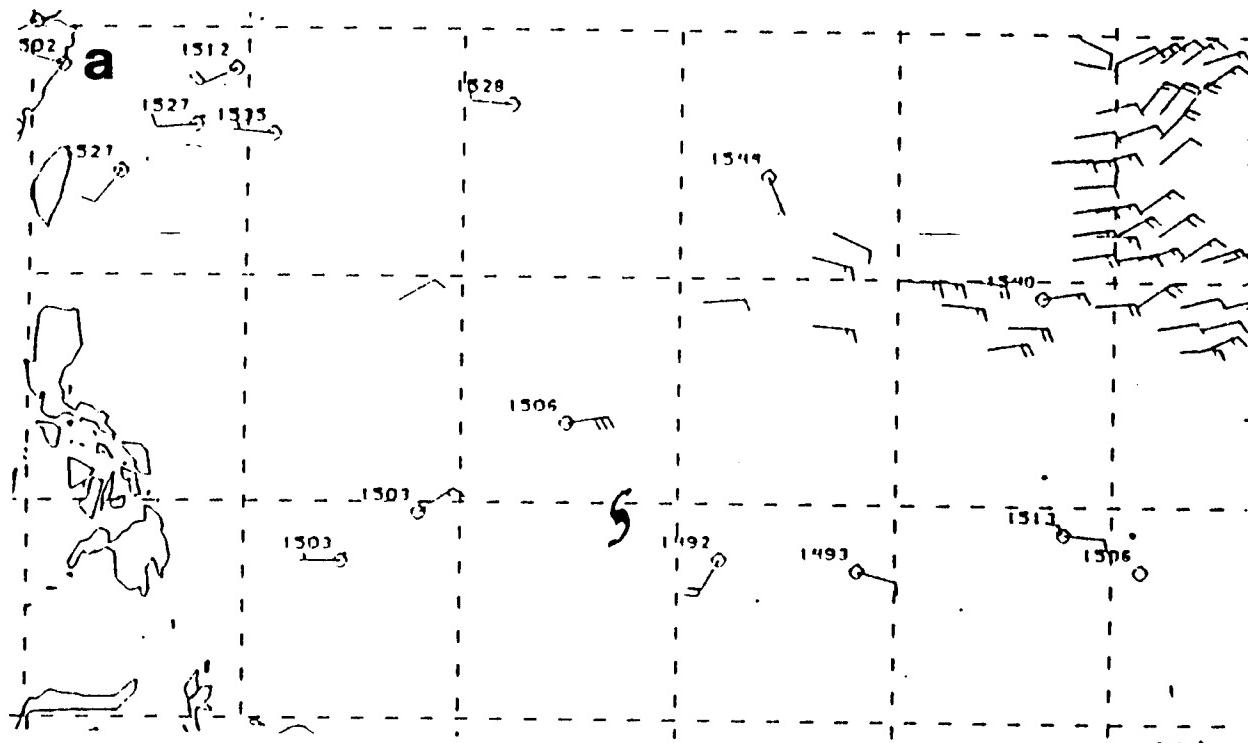


Fig. 3.32 Plots of 850 mb RAOB winds and heights and satellite cloud-drift winds (no station markers) in the vicinity of Tropical Storm Robyn (TC symbol) at (a) 1200 UTC 2 August 1993, and (b) 0000 UTC 4 August 1993. Long (short) barb is 10 (5) kt.

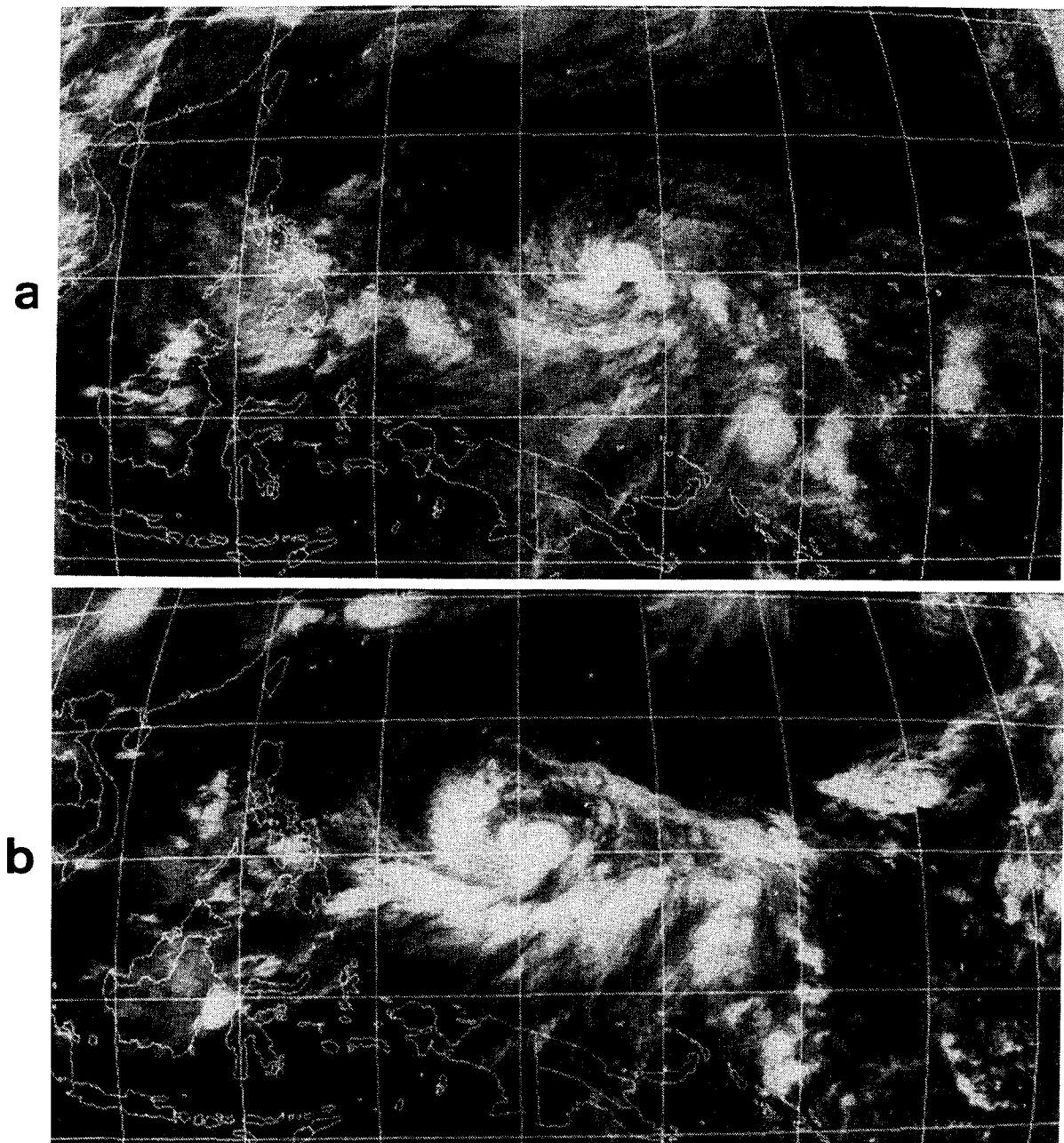


Fig. 3.33 (a)-(b). Infrared imagery of cloud pattern in the vicinity of Tropical Storm Robyn (TC symbol) for the same times as in Fig. 3.32a and 3.32b, respectively.

Given the above preliminary justification for an imagery-based technique for estimating  $R_o^{850}$ , now consider the cloud patterns of Ellie (11W; 1991), Ed (19W; 1990), Hattie (22W; 1990), and Yuri (30W; 1991) when each TC was at the tropical depression or weak tropical storm stage (Figs. 3.34a-d, respectively). Applying the imagery interpretation technique as in Figs. 3.33a-b, these TC cloud patterns imply  $R_o^{850}$  values of about 2.0° lat. (220 km) for Ellie, 5° lat. (550 km) for Ed, 7.5° lat. (825 km) for Hattie, and 12.5° lat. (1380 km) for Yuri, respectively.

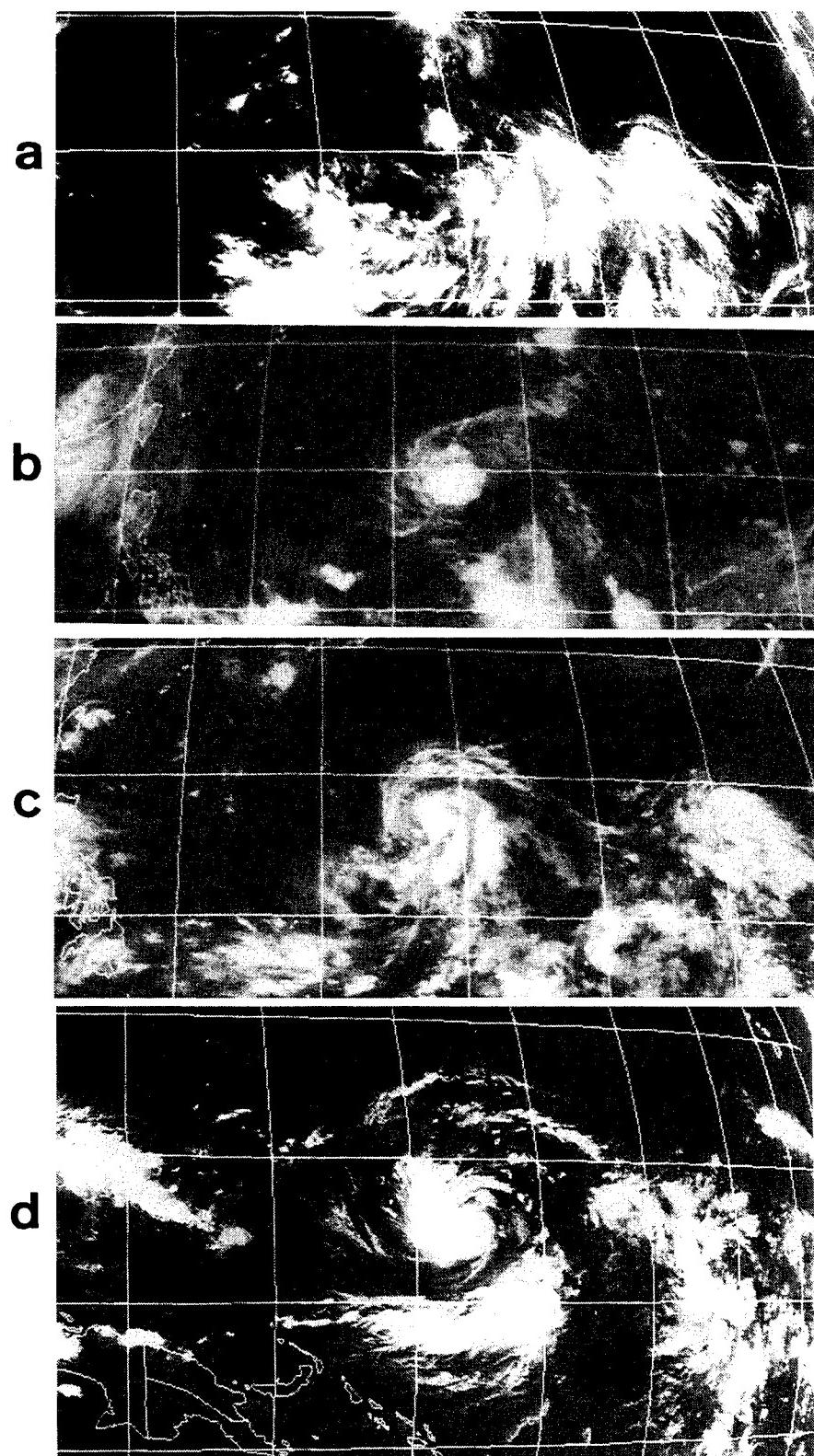


Fig. 3.34 Satellite imagery illustrating tropical cyclone sizes during the TD or TS stages for (a) small TY Ellie at 0000 UTC 10 August 1991, (b) small/average TY Ed at 1200 UTC 10 September 1990, (c) average TY Hattie at 1200 UTC 1 October 1990, and (d) large TY Yuri at 0000 UTC 24 November 1991.

The proposed imagery-based estimates of  $R_o^{850}$  for TCs as in Fig. 3.34 obviously need to be validated with a large sample, which is outside the scope of this report. In Subsection 3.d.2 on the  $\beta$ -effect propagation (BEP), a comparison will be made between the propagation behavior (and streamfunction patterns) predicted by the angular momentum model and the observed motion behavior (and NOGAPS 500 mb streamline analyses) of the three TCs in Figs. 3.34a-c. This comparison will provide additional evidence that the proposed imagery interpretation technique does give reasonable estimates of  $R_o^{850}$  over the full range of TC sizes.

**Conversion to  $R_o^{500}$ .** Since  $R_o^{500}$  is the TC size parameter that is relevant to TC motion forecasting, a relation for estimating  $R_o^{500}$  from  $R_o^{850}$  is required. The composite western North Pacific TC tangential wind of Frank (1984) will be used for this purpose (Fig. 3.35). At 500 mb, the tangential wind is zero in the Frank profile at about  $10.4^\circ$  lat. radius. The zero tangential radius at 850 mb does not appear on the diagram, and would probably be erroneously inflated in the lower troposphere by the presence of the monsoon trough in which most western North Pacific TCS are embedded. Thus, a more representative value of  $14.2^\circ$  lat. for  $R_o^{850}$  has been determined by drawing a line from the point ( $R_o^{500}$ , 500 mb) parallel to the  $4 \text{ m s}^{-1}$  isotach. Based on this assumption, the relationship between the two levels is

$$R_o^{500} = 0.73 R_o^{850}. \quad (3.4)$$

c) ***TC size forecasting.*** Whereas the above discussion provides the forecaster with a technique for estimating the present size ( $R_o$ ) of the TC circulation, it is also important that the forecaster have some basis for assessing whether the motion-relevant size of the TC is likely to change significantly during the forecast period. Forecasting TC size change is particularly difficult since: (i) virtually nothing is known about the underlying dynamical mechanisms; (ii) operational numerical models do not have any skill in forecasting TC structure change (be it intensity or size); and (iii) no objective techniques are available for predicting TC outer wind structure change. The issue may be further complicated by climatological studies that the surface wind field spreads horizontally throughout the intensification phase of the TC (e. g., the Tsui model in Fig. C.1). However, Weatherford and Gray (1988) found relatively little growth of the lower tropospheric structure of the TC during intensification (Fig. C.2).

Although a thorough study of the growth characteristics of individual TCs is outside the scope of this report, the satellite imagery interpretation technique proposed in Fig. 3.34 above offers a simple means to make a provisional assessment. Consider the infrared cloud patterns of the same TCs as in Figs. 3.34a-d at later times when each TC is at or near maximum intensity (Figs. 3.36a-d). In each case, the radius of the convective cloud pattern (and thus the implied  $R_o^{850}$ ) remained virtually unchanged during intensification across the full size range. That is, Ellie started out tiny and remained tiny, and similarly Yuri started

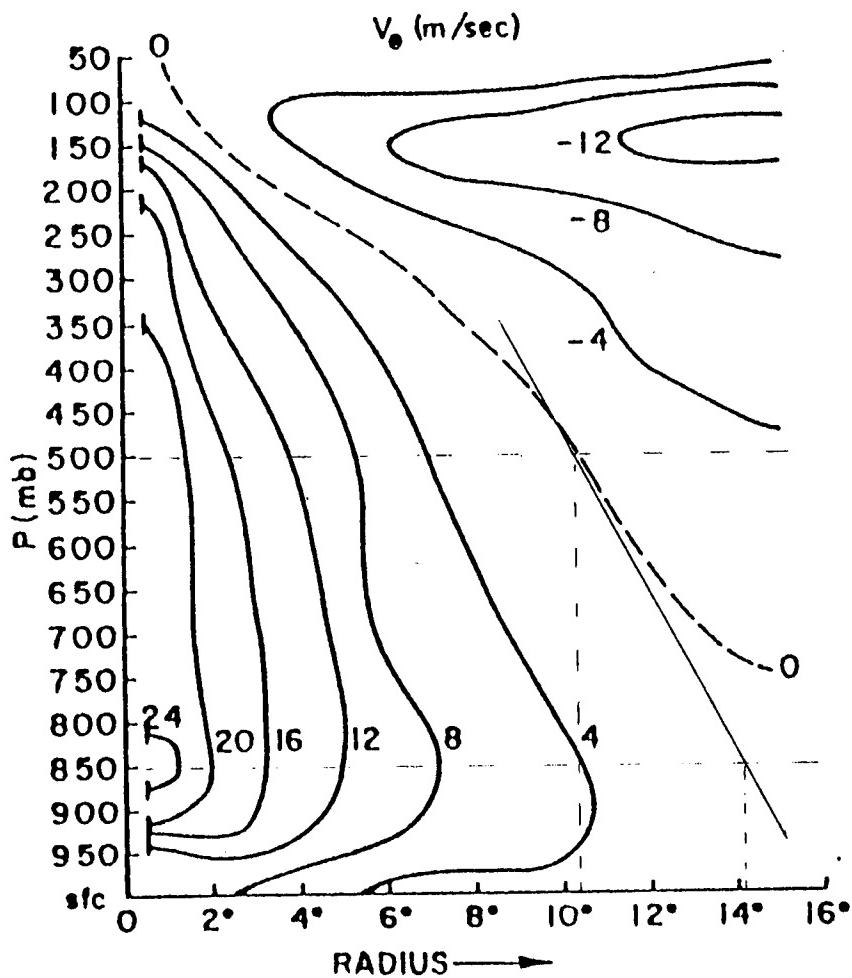


Fig. 3.35 Average tangential wind speed ( $\text{m s}^{-1}$ ; cyclonic, positive) of western North Pacific tropical cyclones (Frank 1977).

very large and remained so. A cursory examination of the cloud patterns of the 41 western North Pacific TCs in 1990 and 1991 that became typhoons indicates that only in the case of Mireille (21W; 1991) was there significant growth during intensification.<sup>8</sup> Pending future research on the subject, it will be assumed that the motion-relevant size of TC *usually* remains unchanged from that established during formation.

*d) TC size conceptual models.* For the purposes of the systematic approach, TC sizes will be grouped into four categories based on general characterizations of the

<sup>8</sup> Gradient-level wind reports from Saipan and Okinawa as Mireille passed by those islands on 19 and 26 September 1991, respectively, confirmed that Mireille grew from a comparatively small to a comparatively large TC.

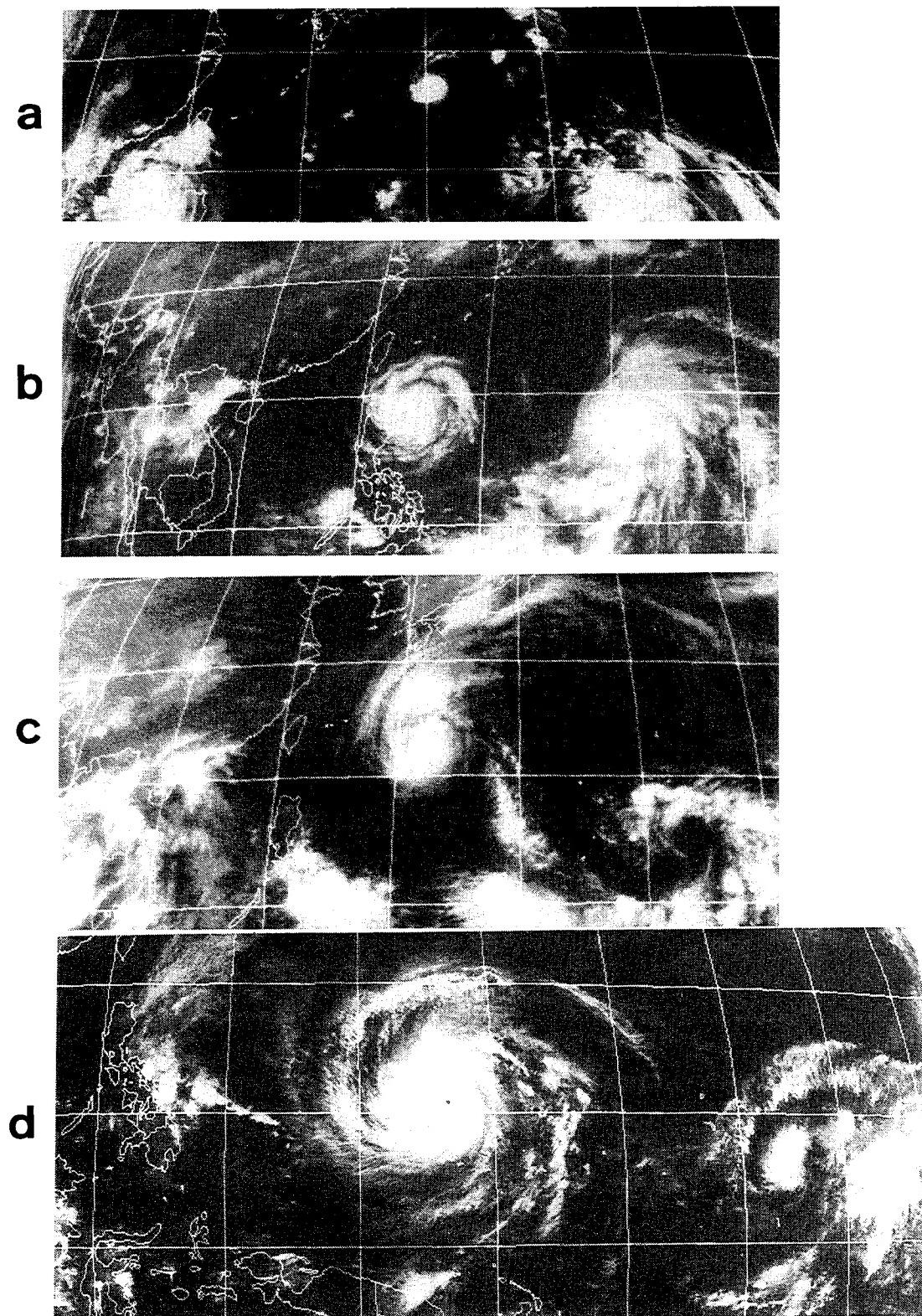


Fig. 3.36 As in Fig. 3.34, except at a later stage of development, for (a) Ellie on 4 August 1991, (b) Ed on 14 September 1990, (c) Hattie on 4 October 1990, and (d) Yuri on 27 November 1991.

degree to which the TC propagates relative to environmental steering, and/or modifies the environment structure. The model definitions are:

- **Midget TC:** Propagation relative to the environment is negligible compared to typical environmental steering in the sense that the track forecast error incurred by not accounting for the propagation is not a significant fraction of average track forecast errors. Also, the midget TC does not significantly modify its environment. Thus, the conceptualized midget TC is simply "a cork in the stream." Because of the particularly small size of the midget TC, its motion may be significantly affected by environmental features that are not well resolved by operational numerical weather prediction models initialized by routinely available data.
- **Small TC:** Similar characterization as for midget TC in terms of propagation and environment modification. For the small TC, the scale of environmental features that determine steering should be better resolved by operational numerical prediction models.
- **Average TC:** Propagates significantly relative to its environment such that the track forecast error incurred by not accounting for the propagation is a significant fraction of average error. The average TC may also moderately modify its environment to the extent that the associated change in steering is a significant fraction of average track forecast errors.
- **Large TC:** Similar characterization as for the average TC, except that the magnitude of propagation and degree of environment modification are so large that the track forecast error incurred by not accounting the propagation/environmental modification may equal or exceed average track forecasting errors. That is, major track forecast "busts" will occur if the propagation and environmental modification are not adequately anticipated by the forecaster.

To apply the above TC size definitions, it is necessary to: (i) associate each size model with a propagation speed range; and (ii) relate that propagation speed to a range of  $f_0$  and  $R_{500}$  combinations based on the angular momentum TC wind distribution model. To address the first issue, consider that the average JTWC track forecast error at 72 h is around 300 n mi (555 km), which is equivalent to about 4 kt ( $2 \text{ m s}^{-1}$ ). We now arbitrarily specify the range 50% to 100% be a "significant fraction" in the above TC size model definitions, and that the boundary between midget and small TCs is a propagation speed equal to 25% of average forecast error. Based on these stipulations, the following approximate propagation speeds may be associated with the four TC size ranges:

- Midget:  $0.5 \text{ m s}^{-1}$  or less
- Small:  $0.6$  to  $1.0 \text{ m s}^{-1}$
- Average:  $1.1$  to  $2.0 \text{ m s}^{-1}$
- Large:  $2.1 \text{ m s}^{-1}$  or more

Association of these propagation speed ranges with the corresponding ranges of the angular momentum model parameters  $f_o$  and  $R_{500}$  will be deferred until Subsection 3.d.1, which develops the  $\beta$ -effect propagation (BEP) TC-Environment transformation model.

#### d. *TC-Environment transformations*

The TC-Environment transformation models (Table 3.3) account for the mutual influence of the TC and the environment that may alter the structure of either or both in ways that affect TC motion. The TC-Environment transformation models are most challenging of the conceptual models to master and apply since they: (i) involve dynamical processes that are more complex and difficult to visualize than simple steering by a TC-independent environment; (ii) are invoked only when certain combinations of the environment and TC structure are met, which may be difficult to detect with operational data; and (iii) tend to depend sensitively (perhaps chaotically) on subtleties in the initial conditions, which results in varying degrees of change to TC and/or Environment Structure. To an even greater degree than the Environment and TC Structure models, these TC-environment transformation models must be intelligently adapted to the current forecast situation. In particular, the forecaster must combine a good understanding of the dynamical processes associated with each model with a careful evaluation of data and satellite imagery when attempting to estimate how changes in various parameters (e.g., TC size, TC location relative to a MG, etc.) may initiate and influence the transformation process, and in turn influence TC motion.

Recall also from Section 2 that TC-Environment transformations are one means by which changes in environment structure, which are called environment transitions, may be accomplished (see Fig. 3.4 and related discussion). To make use of these TC-Environment transformations, it is particularly important that the forecaster consider: (i) the possible type(s) of environment transition that may occur given the present combination of Synoptic Pattern and Synoptic Region (Table 3.1); (ii) the various conditions that determine whether the transformation process will be sufficient to accomplish the transition; and (iii) the range of TC track changes that can occur if an environment transition to another Synoptic Pattern and Synoptic Region occurs.

The discussion of each TC-Environment transformation conceptual model generally proceeds as follows. First, a synopsis of background material covering relevant basic dynamical concepts and preliminary model development will be presented in an Appendix. Next, a statement and description of the model is provided, and its impact will be described in terms of any associated environment transitions. Finally, a practical illustration of the transformation model and resulting transitions is provided using one or more case studies. If the reader already understands the background of the conceptual model, the material in the main body of the text should be adequate to understand and appreciate the role of the model within the systematic approach. If the conceptual model is not familiar to the reader, he/she is encouraged to study the material in the appendix before proceeding.

1) Beta-effect propagation (BEP). A summary of background material and preliminary development of the BEP model is provided in Appendix D.

a) BEP model description and impact. The BEP transformation model is unique among the set of TC-environment transformation models in that BEP propagation is always occurring to some extent. In Appendix D, a relationship (equation D-5) is developed for BEP speed as a function of the values of  $\beta$  and  $f_0$  at the latitude of the TC, and the value of  $R_e^{850}$ . If  $\beta$  is assumed to be a constant  $2.25 \times 10^{-11} \text{ m}^{-1} \text{ s}^{-1}$ , then a contour plot of BEP speed may be constructed as a function of  $f_0$  and  $R_e^{850}$  (Fig. 3.37). Propagation speeds of less than  $1 \text{ m s}^{-1}$ ,  $1\text{-}2 \text{ m s}^{-1}$ , and greater than  $2 \text{ m s}^{-1}$  in Fig. 3.37 correspond to the small/midget, average, and large TC size conceptual models, as defined in Subsection 3.c.2. The BEP speed versus TC size relationship in Fig. 3.37 and the observation in Appendix D that the direction of BEP is from  $320^\circ$  to  $360^\circ$  together comprise the proposed conceptual model for BEP.

Whether the BEP speed will have a significant role in causing a transition in Synoptic Pattern and Synoptic Region, and thus in the forecast track, depends not only on the TC size (as established in Appendix D), but also on the structure of the environment at the location of the TC. For TCs in the NO Region of a N or G Pattern (Figs. 3.19 and 3.25, respectively), or in the SF Region of a M Pattern (Fig. 3.24a), the prevailing steering flow is such that the TC will naturally tend to move northward, transition into the AW Region, and thus recurve. In these situations, BEP may contribute to the time of recurvature (particularly for larger TCs), and thus should not be ignored. Nevertheless, BEP propagation would not play a decisive role in the key "to recurve or not to recurve" question in these situations, since BEP will then be only a secondary effect compared to environmental steering.

For TCs located in the DR Region of any pattern, and particularly in the unbroken DR Region of a S Pattern (Fig. 3.17), the generally westward steering will tend to keep the TC in the deep tropics, so that insufficient latitude would be gained (by steering alone) to cause a transition from the DR Region into a pre-existing WR Region associated with a midlatitude trough, or create a new WR Region by poleward translation into the ridge. Even if the TC should enter the WR Region of the S Pattern, the small environment steering in the vicinity of the ridge axis tends to inhibit a further transition from the WR to AW Region, i.e., accomplish recurvature. In these cases, the poleward and westward components of the BEP vector may play a crucial role in determining not only the timing of recurvature, but whether or not recurvature will occur at all.

In view of the above, the primary importance of BEP as an environment transitional mechanism is in accomplishing the DR-WR and WR-AW region transitions within the S Pattern (Fig. 3.38). Whether the TC will gain enough latitude before landfall to accomplish these Synoptic Region transitions primarily depends on the magnitude of BEP compared to

## $\beta$ Effect Propagation Speed

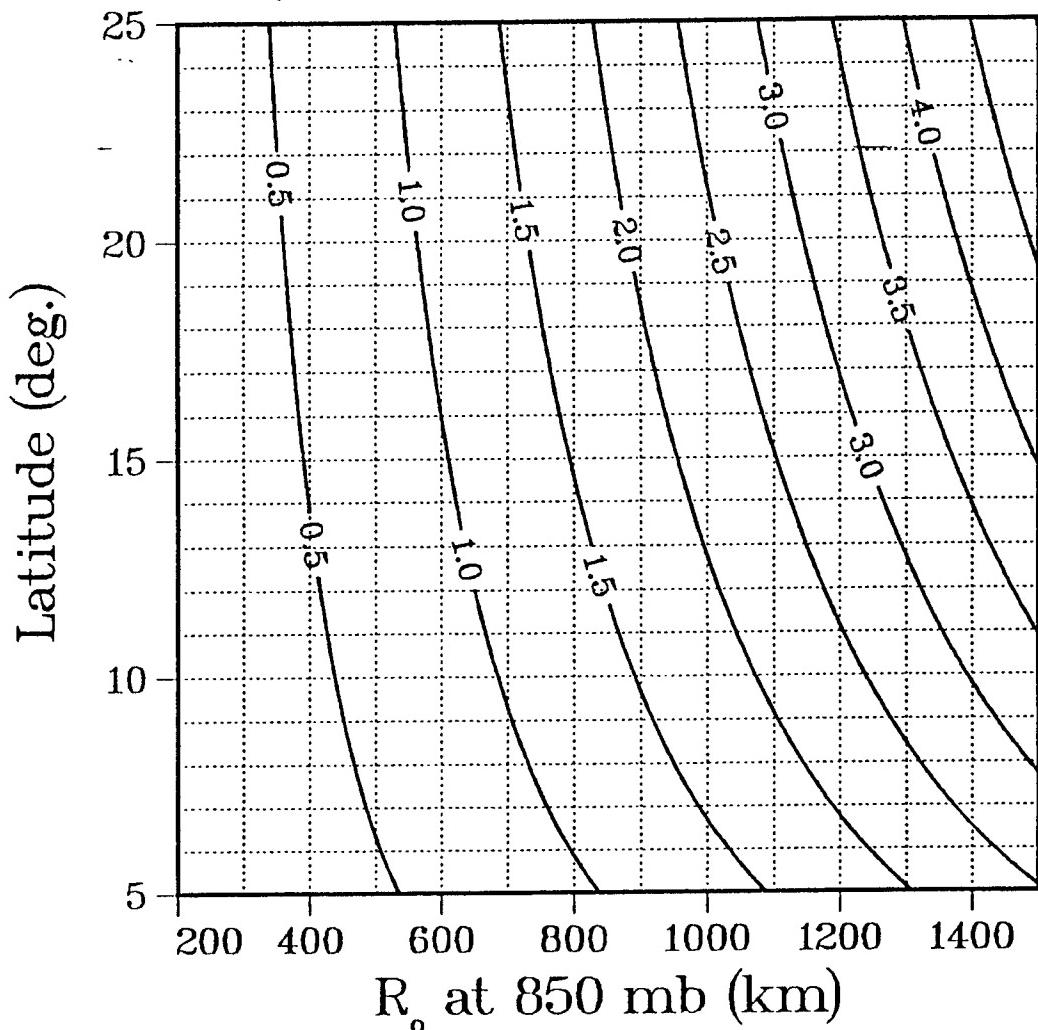
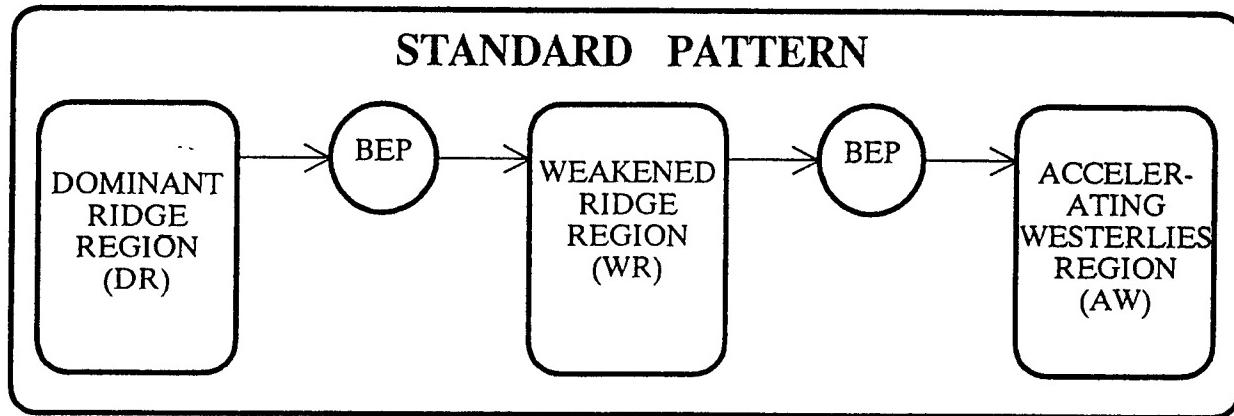


Fig. 3.37.  $\beta$ -induced propagation speed ( $m s^{-1}$ ) as a function of latitude and outer radius at 850 mb based on angular momentum profiles.

the predominantly easterly steering south of the ridge axis.<sup>9</sup> An illustration of how the motion of a borderline midget/small, an average, and a large TC propagating toward  $320^\circ$  at speeds of  $0.5$ ,  $1.5$ , and  $2.5 m s^{-1}$ , respectively, would depart from an easterly  $5 m s^{-1}$  ( $10$  kt) steering flow is shown in Fig. 3.39a. Conversely, the TC motion vectors resulting from the same steering and propagation speeds as in Fig. 3.39a, but for a propagation direction

---

<sup>9</sup> The magnitude of BEP cannot be said to solely determine whether or not the region transitions will occur because variations in the structure of the S Pattern (recall Figs. 3.6c-d) may also tend to favor or inhibit the transitions.



**Fig. 3.38.** Environmental transition in Synoptic Regions within a Standard Synoptic Pattern that may be induced by beta-effect propagation (BEP).

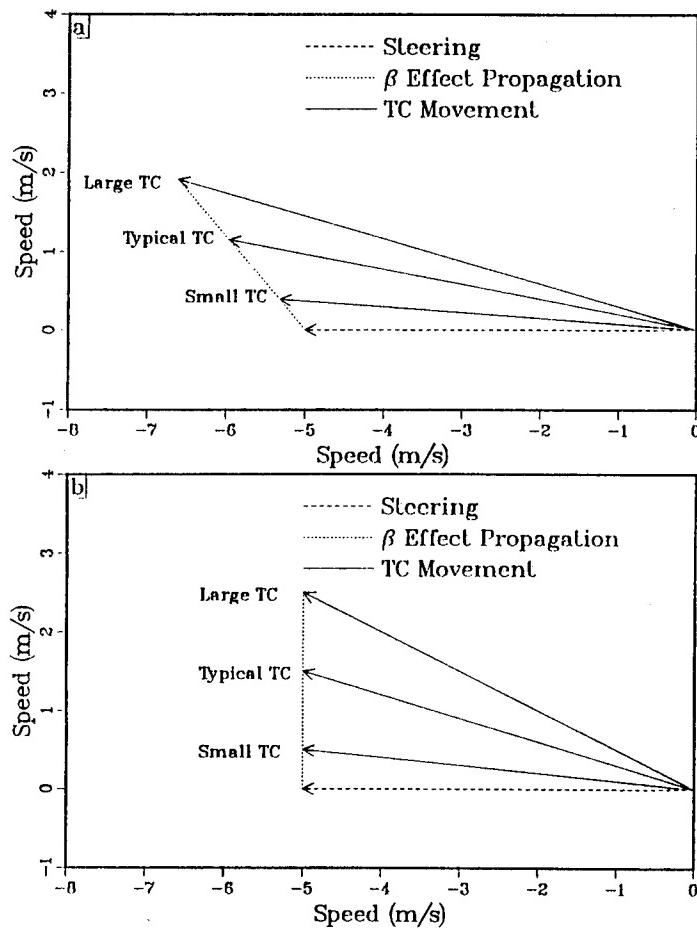


**Fig. 3.39.** Superposition of typical  $\beta$ -effect propagation speeds (dotted) corresponding to small, average, and large tropical cyclones oriented toward (a)  $320^\circ$  or (b)  $360^\circ$  on an easterly steering current of  $5 \text{ m s}^{-1}$  (dashed) to estimate direction and speed of TC movement (solid).

of north, are shown in Fig. 3.39b. Notice that the direction and speed of the small TC does not depart significantly from environmental steering in either diagram, whereas the large TC travels significantly faster (by as much as  $2 \text{ m s}^{-1}$  in Fig. 3.39a) and significantly to the right of the environmental steering (up to  $26^\circ$  in Fig. 3.39b).

Recall that the orientation of the ridge axis in the S Pattern often varies so that the corresponding steering may actually range from west-northwestward to west-southwestward (see Figs. 3.6c and 3.6b, respectively). Based on Fig. 3.39, the forecaster can anticipate that the track of a midget/small TC will conform to those steering directions quite closely, even to the extent of losing latitude in the latter case. By contrast, the forecaster should expect that large TCs will usually gain latitude, even for a west-southwest steering direction, owing to their significant BEP to the northwest (and capacity to modify environmental steering as discussed in Subsections 3.d.3 and 3.d.4 below).

Knowledge of the present TC size, and thus the likely propagation tendency, from Fig. 3.39 may assist the forecaster in selecting from widely varying fix positions. For example, assume that over the past 36 h the working best track of an ill-defined, developing TC has been showing a significant gain in latitude, although with a large fix-to-fix variability of the satellite-derived positions. Further assume that the latest satellite fix is based on infrared imagery at night, has a Position Code Number of 6 (43 n mi average error; 1992 ATCR, p. 15), and falls 40 n mi south of a persistence position based on the previous working best track. Without additional fixes to confirm a turn to a more southern heading, the knowledge that the significant BEP of large TCs tends to result in a substantial gain in latitude would guide the forecaster to choose a working best track position somewhat to the north of the latest fix. The forecaster could thus avoid prematurely "jumping on the fix" and introducing a significant and improbable left turn toward the south based on insufficient information, which could degrade objective aid performance.

*b. BEP model illustration.* The BEP TC-environment transformation model will now be illustrated via case studies of the NOGAPS 500 mb streamline and isotach analyses associated with the combinations of size ( $R_{850}$ ) and formation latitude ( $f_o$ ) for the three TCs in Figs. 3.34a-c. Based on satellite imagery (Fig. 3.34a), the  $R_{850}$  of Typhoon Ellie was estimated to be 220 km. Ellie's formation latitude (i.e., where 45 kt is first attained) was about  $24^\circ$  N (Fig. 3.24). This combination of parameters in Fig. 3.37 corresponds to a BEP speed of about  $0.5 \text{ m s}^{-1}$ . Thus, Ellie was a borderline midget/small TC, and should be expected to move in close conformity with environmental steering according to Fig. 3.39.

A comparison of NOGAPS 500 mb analyses at 0000 UTC on 14 and 17 August 1991 (Fig. 3.14b and c, respectively) with the track of Ellie (Fig. 3.26) indicates that Ellie did in fact move essentially as a "cork in the stream." On 14 August, Ellie was just entering the DR Region to the north of a large monsoon gyre in a G Pattern (Fig. 3.14b). Although no closed 30-kt isotach is present, the location of the JTWC best track position to the north of the NOGAPS circulation center indicates that the environmental steering was from the east at that time. However, the orientation of the steering flow to the west of Ellie (between the

MG to the south and the ridge circulation to the northwest) is approximately east-northeasterly. Thus, some loss of latitude would be expected as Ellie moves westward into this steering environment, assuming that Ellie has negligible propagation speed. During the next 72 h, the latitude of Ellie does in fact decrease by about  $4^{\circ}$  (Fig. 3.26), which results in a west-southwest oriented direction of motion that agrees well with the orientation of the ridge axis to the north of Ellie on 17 August 1991 (Fig. 3.14c). Thus, Ellie's track is in good agreement with theoretical expectations of only a small propagation for a very small TC.

Based on satellite imagery (Fig. 3.34b), the  $R_{850}^{850}$  of Typhoon Ed was estimated to be 550 km, and Ed's formation latitude was about  $20^{\circ}$  N (Fig. 3.21a). Entering this combination of parameters in Fig. 3.37 gives a propagation speed of  $1.0 \text{ m s}^{-1}$ . Since Ed was a borderline small/average TC, Ed might be expected to move approximately  $8^{\circ}$  to  $12^{\circ}$  degrees to the right of a typically easterly steering flow according to Fig. 3.39a and b, respectively. However, the track of Ed (Fig. 3.18a) during 11 to 14 September 1990, was actually due westward. The NOGAPS 500 mb analyses during the same period (Fig. 3.40) indicate a west-southwestward steering associated with a sloping ridge axis to the north, and also by the tendency for the JTWC position to be to the north-northwest of the NOGAPS vortex center (as in Figs. 3.40b and d). Therefore, the BEP for the small/average size of Ed would contribute to the westward track that may eventually bring Ed closer to the ridge axis, and specifically to a weakness in the ridge (note neutral point in Figs. 3.40c and d). Thus, a possibility might exist for a DR-WR region transition within the S Pattern (Fig. 3.38). However, the movement of Ed to the west and south on subsequent days (Fig. 3.18a) indicates that the BEP of this small/average size TC was insufficient to accomplish such an environment transition, and Ed remained in a DR region of a S pattern.

Based on satellite imagery interpretation (Fig. 3.34c), the  $R_{850}^{850}$  of Typhoon Hattie was estimated to be 825 km, and Hattie's formation latitude was about  $17^{\circ}$  N (Fig. 3.41). Entering this combination of parameters in Fig. 3.37 gives a propagation speed of  $1.7 \text{ m s}^{-1}$ . Since Hattie has an average size and BEP speed, Hattie might be expected to move approximately  $13^{\circ}$  to  $18^{\circ}$  degrees to the right of a typically easterly steering flow according to Figs. 3.39a and b, respectively. Notice that Hattie's direction of motion was  $300^{\circ}$  on 3 and 4 October (Fig. 3.41), despite a ridge axis that sloped east-northeast to west-southwest (Figs. 3.42a and b). The north-south extent of the ridge does diminish toward the west, which might offset the effect of the ridge slope on steering direction. In both NOGAPS analyses, Hattie is almost due north of the vortex center, which suggests nearly westward steering across the vorticity center of Hattie. Thus, Hattie's persistent gain in latitude would require a significant BEP. Notice also the distinct wave train of a trailing anticyclone and an inverted trough farther to the southeast behind Hattie in Figs. 3.42a and b. By contrast, no wave train was evident behind either of the smaller TCs Ellie and Ed (Figs. 3.14 and 3.40), which is consistent with the barotropic model streamfunction patterns in Figs. D.12a-f that the amplitude and scale of the barotropic wavetrain increase with TC size. Thus, the presence of the wave train in the NOGAPS analyses of Hattie also provides the forecaster with an important clue (if it is consistent with the size of the TC) that BEP propagation may play a significant role in the motion of this TC.

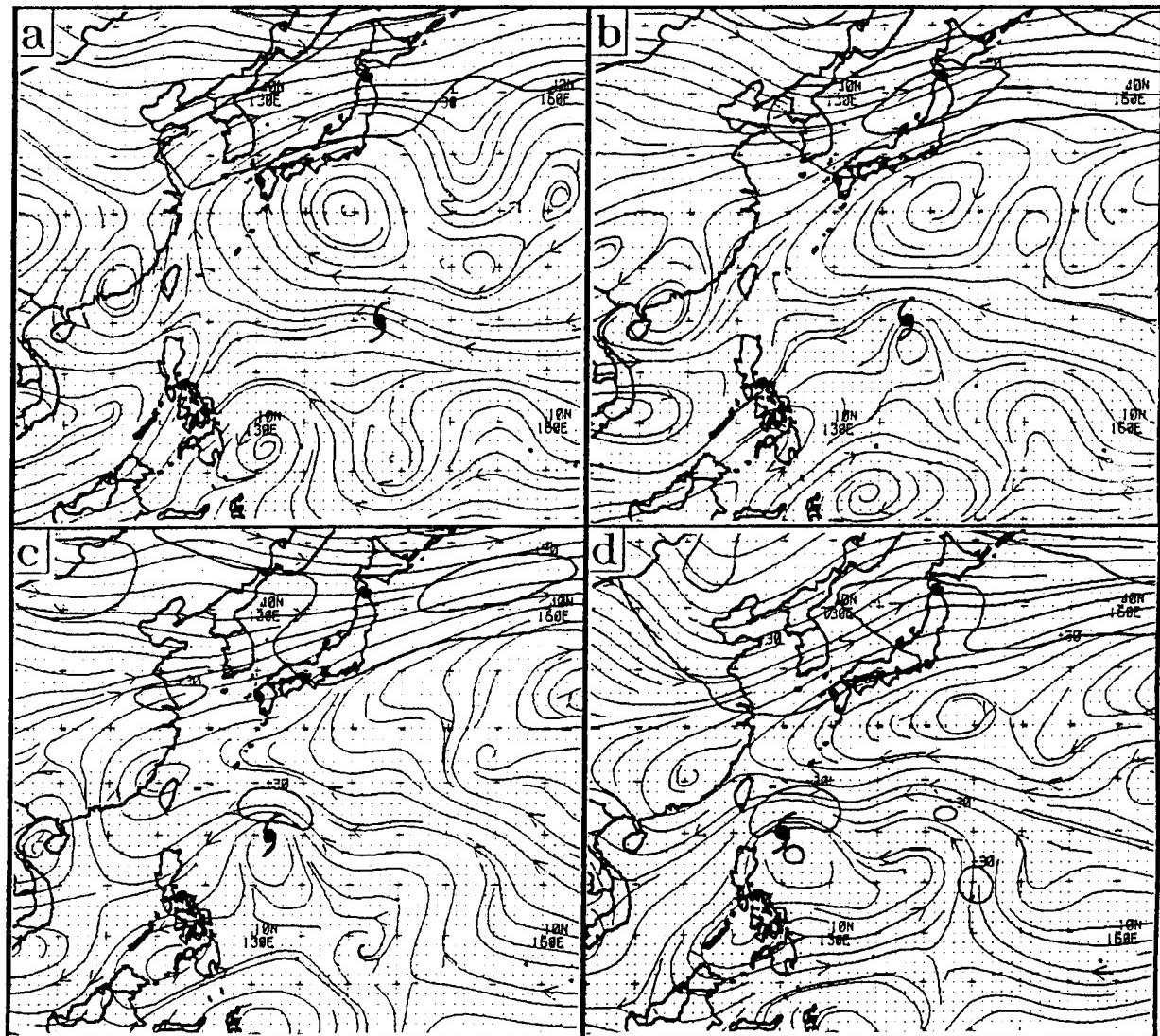


Fig. 3.40 NOGAPS 500 mb streamline/isotach analysis for 0000 UTC on (a) 11 September 1990, (b) 12 September, (c) 13 September, and (d) 14 September during Typhoon Ed.

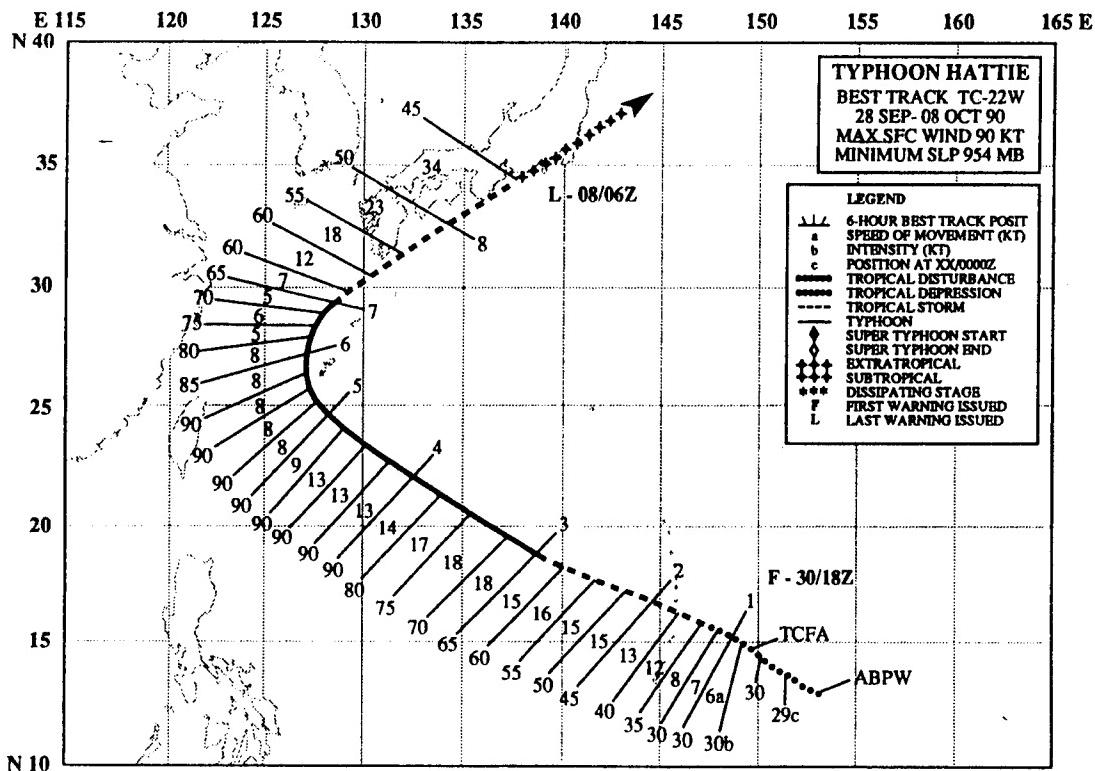


Fig. 3.41. As in Fig. 3.1, except for Typhoon Hattie during 28 September-8 October 1990.

Between 0000 UTC 4 and 5 October, the translation speed of Hattie slowed from 14 kt to 9 kt (Fig. 3.41), which is consistent with a transition from the DR Region (Fig. 3.42b) to the WR Region (Fig. 3.42c) of the S Pattern. By 0000 UTC 6 October (Fig. 3.42d), Hattie was nearly at the ridge axis, and thus was on the verge of transitioning from the WR Region to the AW Region. The environmental steering should be rather small on the ridge axis, so that the predicted 1.7 m/s (3.4 kt) BEP speed is a major contribution to the WR-AW transition. This BEP contribution is relatively larger when Hattie's translation speed slowed to only 5 kt between 0600 and 1200 UTC 6 October.

In contrast to the smaller TCs Ellie and Ed, the average size of Hattie resulted in sufficient BEP to accomplish the DR-WR and WR-AW Region transition sequence illustrated in Fig. 3.38. As a general rule, a TC well equatorward of the ridge axis in a typical Standard Pattern is most likely to recurve if it is an average or larger size, whereas recurvature is improbable for TCs of small/midget size. One example of an exception is the large TC Amy (Fig. 3.18b), which was rapidly gaining latitude but made landfall before a region transition leading to recurvature could occur.

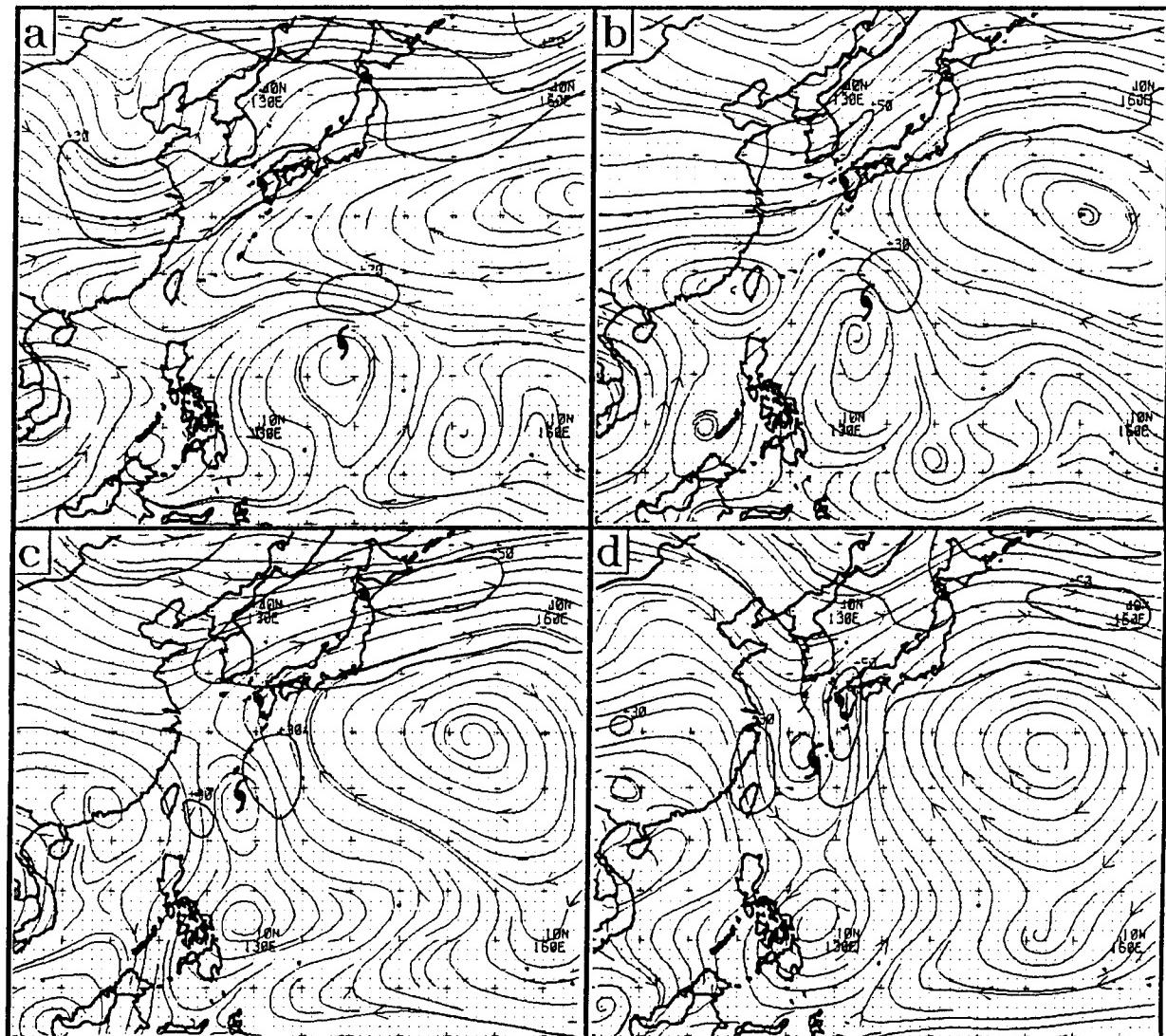


Fig. 3.42. As in Fig. 3.40, except at 0000 UTC for (a) 3 October 1990, (b) 4 October, (c) 5 October, and (d) 6 October during Typhoon Hattie.

The Hattie case also illustrates the principle that the BEP transformation process for average size (or smaller) TCs occurs without significantly altering the TC environment.<sup>10</sup> Notice that at 0000 UTC 3 October (Fig. 3.42a), the 500 mb ridge axis extends northeast from Taiwan to the Ryuku Islands (Okinawa), and then extends to the east south of Japan. Examination of the subsequent NOGAPS analyses (Fig. 3.42b-d) confirms that the basic ridge axis location and orientation did not change significantly, and that recurvature did occur where it would be expected on the basis of steering considerations alone.

The above examples illustrate that the first task of establishing a complete meteorological picture (see discussion in Section 2.c) by examination of the NOGAPS analyses and 24-72 h forecasts can not be done without consideration of the TC size. Although midget or small TCs will tend to follow a steering trajectory that may be inferred from the streamline pattern, average and larger TCs may be expected to depart significantly from a steering concept, especially if this steering is relatively weak. The purpose of the proposed angular momentum wind profiles in Appendix C and the proposed BEP conceptual model just illustrated is to provide the forecaster with a handy tool for including these factors into the meteorological analysis. This is considered to be an essential step in his/her independent meteorological assessment and this is the first step in the NOGAPS reality check, and adjustment strategy (task 2).

In summary, the sequence of steps to utilize the BEP TC-Environment transformation conceptual model is:

- (i) Determine/anticipate the formation latitude of the TC, which is where 45 kt (Dvorak T3.0) is first achieved.
- (ii) Determine  $R_{\circ}^{850}$ , which is the motion-relevant size of the TC, via a consensus of the two techniques:
  - (a) Synthesis of available 850 mb wind reports to determine one of the wind radii:  $R_{25}^{850}$ ,  $R_{30}^{850}$ ,  $R_{35}^{850}$ , or  $R_{40}^{850}$ . Then, determine the corresponding value of  $R_{\circ}^{850}$  using the appropriate diagram in Figs. 3.31a-d.
  - (b) Interpretation of available satellite imagery, wherein the extent of the total pattern of convective clouds is assumed to be approximately equal to  $R_{\circ}^{850}$ .

---

<sup>10</sup> It will be seen in Subsections 3.d.3 and 3.d.4 that the superposition principle does not apply to situations involving large TCs, in which significant modification of the subtropical ridge can occur.

Until further guidance is available, assume that this size will usually remain unchanged throughout the lifecycle of the TC (except during dissipation).

(iii) Determine the BEP speed of the TC from Fig. 3.37 using the formation latitude and the value of  $R_{850}$  determined from steps (i) and (ii) above.

(iv) Assign a BEP-based TC Size model (recall Section 3.c.2.d) according to the following criteria:

- Midget:  $0.5 \text{ m s}^{-1}$  or less
- Small:  $0.6 \text{ m s}^{-1}$  to  $1.0 \text{ m s}^{-1}$
- Average:  $1.1 \text{ m s}^{-1}$  to  $2.0 \text{ m s}^{-1}$
- Large:  $2.1 \text{ m s}^{-1}$  or more

(v) Determine the expected direction of TC motion from the combined effects of steering and BEP using the vector diagrams in Fig. 3.39, after accounting for the rotation of steering from the due easterly value in this illustration.

(vi) Recognize that, for TC of average or larger size (as measured by BEP speed in Fig. 3.37), DR-WR and WR-AW Region transitions within the Standard Pattern are likely to take place, assuming that there will be sufficient time for the TC to gain the necessary latitude before encountering land, being dissipated over water (e.g., high vertical wind shear; discussed next section), or experiencing a pattern change.

**2) Vertical wind shear.** Because the impact of vertical wind shear (VWS) on TC structure and motion is so poorly understood and little documented, little theoretical or research model-based information is available on which to base the VWS conceptual model. As a result, the format of this section departs from that suggested in the introduction of this section. Appendix E contains a brief background discussion of VWS and associated TC motion changes from an observational perspective only. The remainder of this section is then divided into two subsections: (i) a preliminary development and description of the proposed VWS conceptual model via a case study during the western North Pacific winter monsoon season; and (ii) a discussion of VWS impact that focusses on the effective Environmental Structure transitions arising from VWS-induced changes in TC structure.

**a) Proposed VWS model - Development and description.** As indicated in Appendix E, VWS can result in a variety of TC structure and associated motion changes depending on the magnitude, persistence, depth of the VWS, etc. If the magnitude of the VWS is moderate, temporary, and confined to the upper troposphere, the effect of VWS may primarily be to slow or delay intensification, as in the case of Omar in Figs. E.6 and E.7. Without a separation of the convective cloud mass (CCM) and low-level circulation (LLC) of the TC, the principal effect of the VWS on TC motion is to delay or limit the increase in elevation of the steering level (see discussion in Subsection 3.c.1) with intensity, which

generally has a relatively subtle impact on TC motion (e.g., modest direction or speed changes). In case of strong, persistent, and deep VWS, CCM-LCC separation becomes possible, and two extremely different motion scenarios may occur.

Considering the present limited understanding of VWS dynamics and difficulties in measuring the relevant parameters, it is not feasible or desirable to complicate a VWS conceptual model with too many "if-then" possibilities, particularly those that involve only subtle changes in TC motion. For the present, the VWS conceptual model developed and described below is confined to situations involving large magnitudes of VWS, and widely divergent track possibilities. The VWS model will be illustrated via a case study involving westerly VWS, since westerly VWS situations are more common, and typically involve larger magnitudes of shear.

As Typhoon Kit sheared apart and the remnants turned to the southwest in response to the northeast monsoon during 19 and 20 December 1981 (Fig. 3.43a), aircraft reconnaissance recorded the associated changes in the wind structure and central pressure. Weatherford and Gray (1988b) composited the wind data to estimate the azimuthally-averaged tangential wind field of the TC over three consecutive 12-h periods (Fig. 3.43b). During the first period from 0000-1200 UTC 19 December, Kit was a weak typhoon (75 kt), which means 400 mb was the optimal steering level according to the TY intensity conceptual model. At this time, Kit's azimuthally-averaged 35-kt wind radius was about 120 km at 700 mb (aircraft flight level), which corresponds to a  $R_{\text{opt}}^{700}$  of about 750 km based on Fig. C.5 (notice in Fig. 3.43a that Kit's formation latitude was about 11° N). Using Frank's composite profile (Fig. 3.35), the corresponding  $R_{\text{opt}}^{850}$  should be 20% larger, or about 900 km. Entering Fig. 3.37 with this  $R_{\text{opt}}^{850}$  and a formation latitude of 10°N gives a BEP speed of about 1.4 m s<sup>-1</sup>. In terms of the TC size conceptual models, such a BEP means that Kit was an average size TC that was significantly propagating relative to the environment prior to experiencing onset of the strong VWS.

By 0000 to 1200 UTC 20 December, the central pressure of Kit had filled to 1000 mb, and the horizontal extent of the 700 mb wind field had dramatically decreased (Fig. 3.43b). Satellite imagery reveals that the VWS had displaced the CCM several degrees to northeast, which left Kit with a shallow, fully exposed LLC (Fig. 3.44) embedded in a field of northeast monsoon stratocumulus. According to the exposed low-level (XL) TC intensity model, the optimal steering level of Kit should now be 850 mb. The size of Kit, as measured by  $R_{\text{opt}}^{700}$  in Fig. 3.43b, was now only 220 km, which equates to a BEP speed of about 0.2 m s<sup>-1</sup> based on Fig. 3.37 after correcting for the difference between  $R_{\text{opt}}^{700}$  and  $R_{\text{opt}}^{850}$ . As a result of large VWS, Kit was transformed into a weak, exposed LLC with an optimum steering level of 850 mb and negligible propagation.

Based on the Kit case study, a preliminary conceptual model for VWS-induced modification of TC structure may be developed for situations involving large VWS that has the potential to separate the CCM and LLC of the TC. The model is comprised of changes to TC intensity and size according to whether CCM-LCC separation occurs:

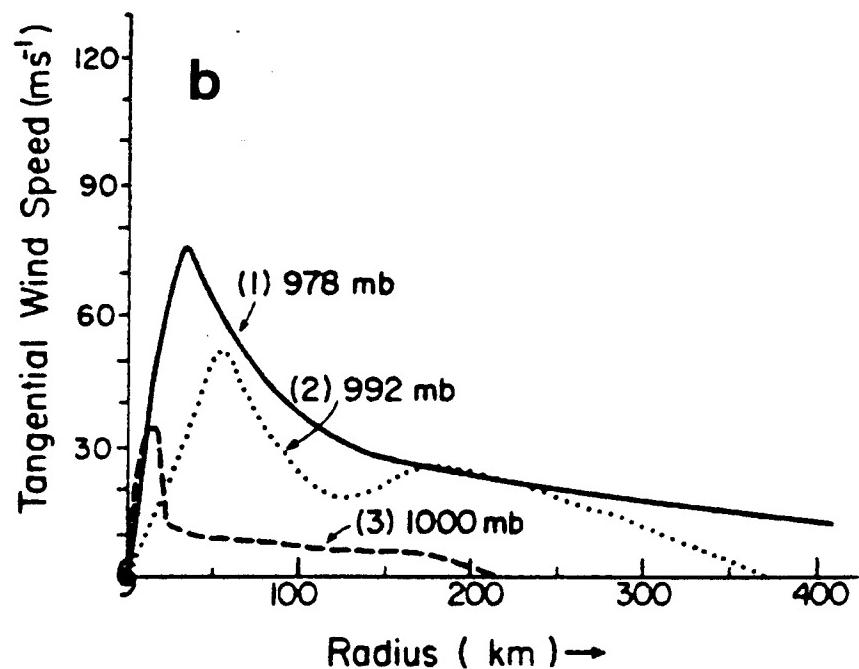
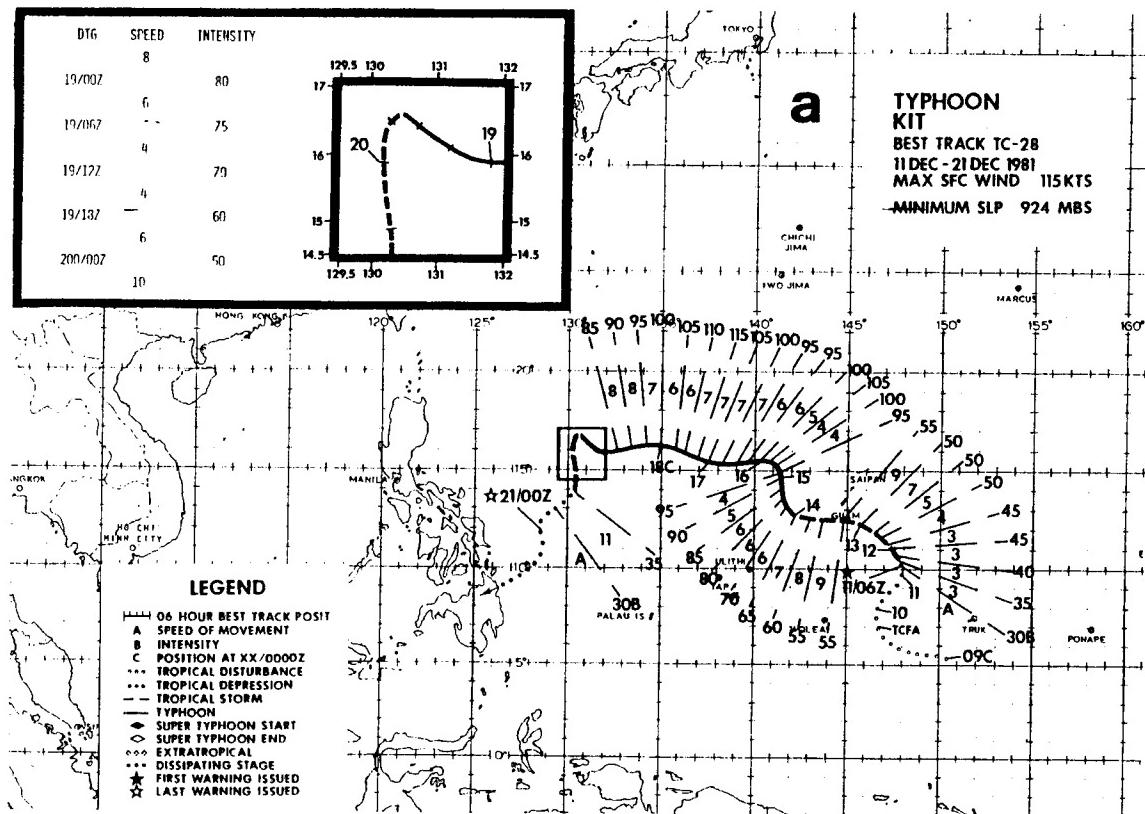


Fig. 3.43. (a) As in Fig. 3.1, except for Typhoon Kit during 11-21 December 1981. (b) Tangential wind speed (kt) for Typhoon Kit during 0000-1200 UTC 19 December (solid), 1200-2400 19 December (dotted), and 0000-1200 UTC 20 December (dashed).

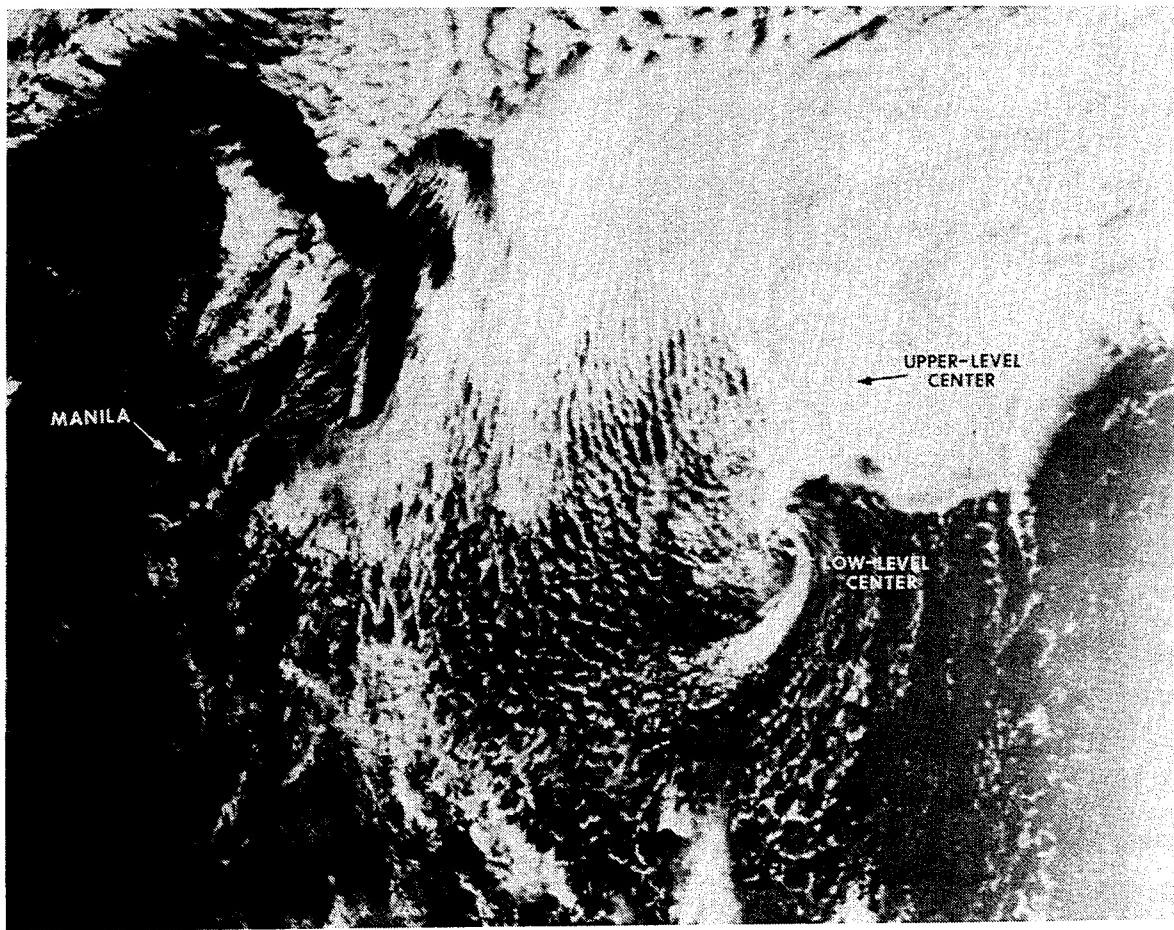


Fig. 3.44. Visible imagery of 0609 UTC 20 December 1981 indicating a weakening of Tropical Storm Kit as the low-level center is moving southward while the remnants of the deep convection are moving northeastward into a shortwave trough (ATCR 1981).

- CCM-LLC Separation:

Intensity Change: Rapid spindown of the LLC from its pre-VWS intensity to weak tropical storm intensity (35-45 kt) occurs as the CCM fully separates from the LLC. The exposed LLC then slowly weakens<sup>11</sup> to tropical depression intensity and dissipates over several days (assuming no relaxation

---

<sup>11</sup> The observed persistence of exposed LLCs against friction and horizontal shear probably results from the weak thermodynamic forcing from the eyewall-like pattern of the shallow convection near the center of the LLC (Fig. 3.44), and the high barotropic stability of small vortices.

of shear and associated reintensification). The sequence of intensity changes and associated steering level changes is schematically illustrated in Fig. 3.45.

**Size Change:** As the CCM separates, the LCC is transformed from its pre-VWS size to small or midget size owing to the loss of the intense thermodynamic forcing that maintained the original LLC against frictional dissipation. The sequence of size changes is schematically illustrated in Fig. 3.45.

- No CCM-LLC Separation:

**Intensity Change:** Various scenarios are possible, including degrees of inhibiting further intensification, arresting of intensification, or causing a weakening of the TC to tropical storm or depression intensity. However, since the CCM and LLC remain thermodynamically linked, no exposed LLC (called XL in Subsection 3.c.1) results with the attendant major decrease in steering level to 850 mb. That is, there is no transformation to the XL model as in Fig. 3.45. Rather, there may be only comparatively subtle changes in steering level between 400 mb and 700 mb.

**Size Change:** Usually no major reduction in size of outer wind structure occurs since overall thermodynamic maintenance of the LLC continues despite weakening of deepest clouds near center. In fact, forecasters have traditionally held that size increases tend to occur as the core of a TC dissipates over water as a result of the shear associated with extratropical transition. For the purposes of the systematic approach, it will be assumed that shear situations that do not involve CCM-LLC separation do not cause a significant size change to occur in the sense that a transformation among the TC size conceptual models does not take place.

As with the BEP effect, consideration of VWS shear effects enters in the first task of assessment of the synoptic context (see discussion in Section 2). That is, the first examination of the NOGAPS analyses and forecasts must consider potential VWS effects to even determine the proper pressure level to evaluate steering, storm structure, and BEP. As with the BEP transformation model, the second application of the VWS model is to assess the Environment Structure transition(s) that may be associated with VWS effects. Since upper-level wind speeds are generally higher when the westerlies are relatively zonal, the VWS transformation model will be more applicable in the Standard Pattern as opposed to the North-Oriented or Monsoon Gyre Patterns in which the westerlies tend to be weaker. Furthermore, for the TC to be sufficiently poleward to experience the VWS associated with the upper-level westerlies, it will usually be in the Weakened Ridge Region near the ridge axis at 500 mb. This situation is manifest in the tracks of both Seth (Fig. 3.29) and Kit (Fig. 3.43a) by the northward turns on 12 November 1991 and 19 December 1981, respectively, about a day prior to the sudden equatorward turn.

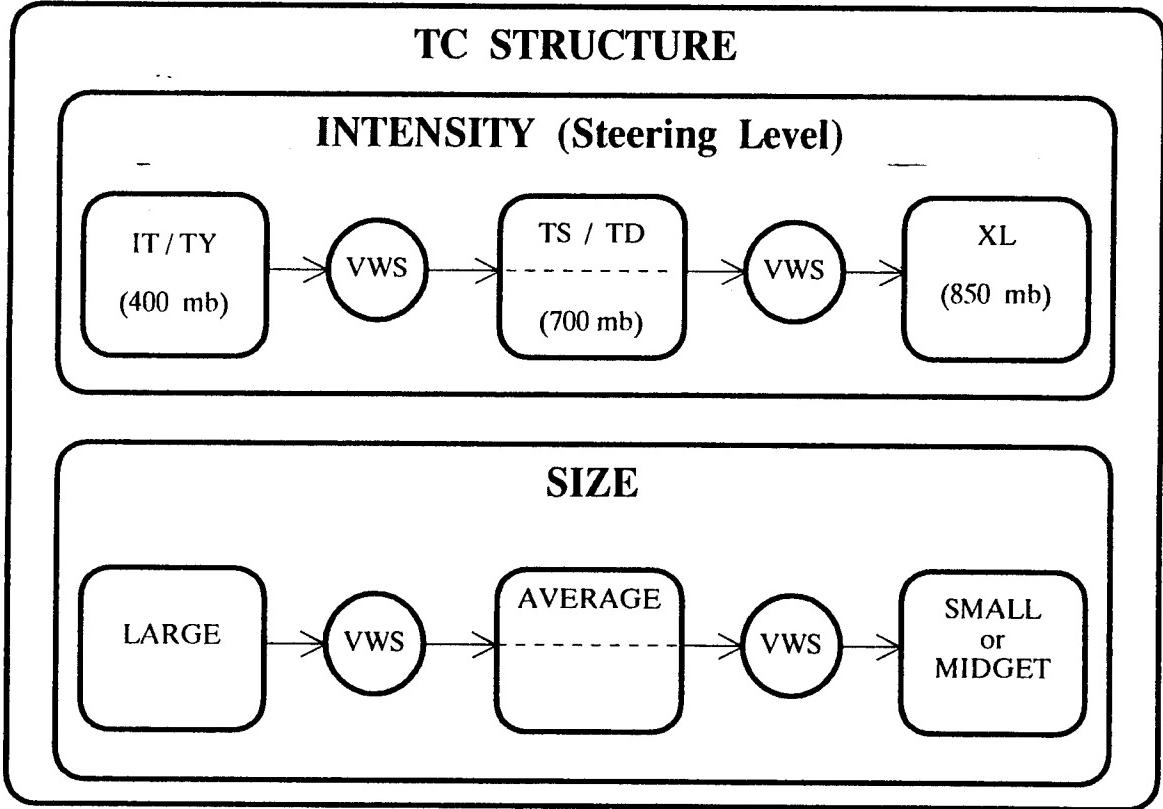


Fig. 3.45. TC Structure changes induced by vertical wind shear (VWS) that leads to a separation of the Low-Level Center (LLC) and Central Convective Mass (CCM).

*b) VWS model impact.* Consider now the environment transition implications of westerly VWS leading to a complete separation of the CCM and LLC. As the VWS transforms the TC into an exposed LLC, the optimal level of environment steering drops to 850 mb. Since the ridge normally slopes equatorward with increasing height, the exposed LLC may be equatorward of the ridge axis at 850 mb, and thus in the DR Region of the Standard Pattern at that level. As a result, the TC turns equatorward onto a westward track, as in the springtime case of Lewis (Fig. B.3a), or even a southwestward track as in the winter monsoon cases of Seth and Kit (Fig. 3.29 and 3.43a, respectively). A VWS transformation that results in an exposed LLC also produces an attendant reduction in TC size to small or midget, which reduces BEP speed to an insignificant fraction of typical steering.

A schematic of the above scenario is depicted in Fig. 3.46 in terms of the relevant TC-environment conceptual models. Notice that when CCM-LLC separation occurs, the VWS transformation model has a three-part transitional influence on the Environment Structure:

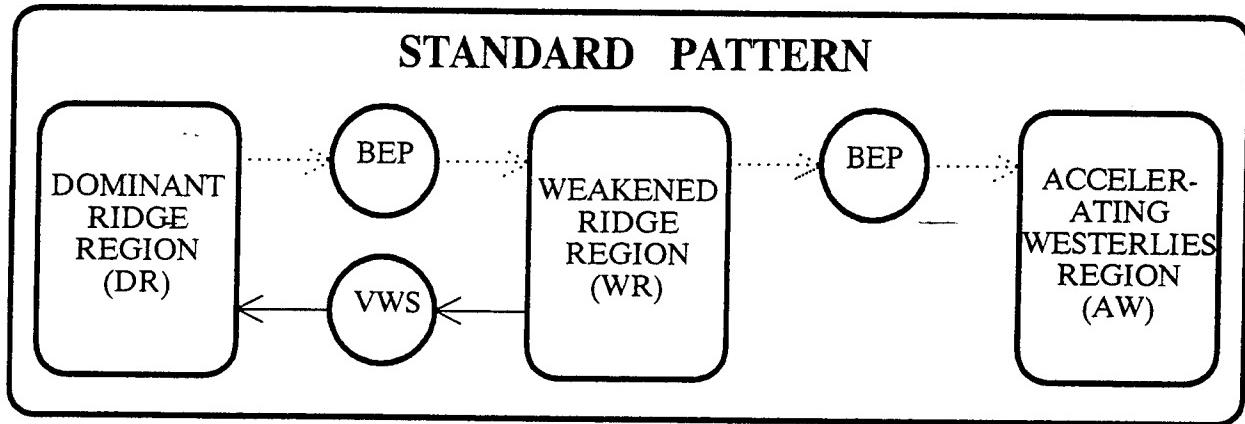


Fig. 3.46. Environment Structure transitions between Synoptic Regions within a Standard Synoptic Pattern related to vertical wind shear (VWS) that separates the low-level circulation center from the convective cloud mass.

- (i) renders BEP ineffective (dotted arrows in Fig. 3.46), and eliminates the contribution of the upper-level steering necessary to accomplish the WR-AW transition, and thus prevents recurvature;
- (ii) accomplishes a WR-DR transition by lowering the level at which the TC steers; and
- (iii) reduces the potential for latitude gain associated with BEP owing to the reduction of the TC size to small or midget, and thus diminishes the likelihood of a future DR-WR transition (dotted arrows in Fig. 3.46).

If the influence of westerly VWS does not result in a separation of the CCM and LLC, then the situation becomes more complex as to how the combined effect of TC intensity changes (and associated steering level changes), TC size (which usually does not become smaller), and environmental steering will ultimately influence TC motion. However, the important motion forecasting consideration is that only two distinctly different track forecasts are realistic: (i) a stair-step track with a return (at least temporarily) to a west-to-southwest direction of motion; or (ii) recurvature to the northeast. By contrast, persistent motion to the northwest is highly unlikely. An example of the second scenario is Ruth (Fig. 3.47), which encountered large westerly VWS associated with the northeast monsoon at nearly the same location and just two weeks before Seth (Fig. 3.29). Whereas Seth lost all of its deep convection during the VWS transformation, Ruth never lost all of its deep convection (Figs. 3.48a-d), despite the combined effect of VWS and temporary landfall over northern Luzon. That is, Ruth weakened from supertyphoon to tropical depression intensity, but did not have an exposed LLC. As a result, Ruth never steered any lower than 700 mb (Fig. 3.45), and thus recurred. Since Ruth did undergo a significant reduction in size,

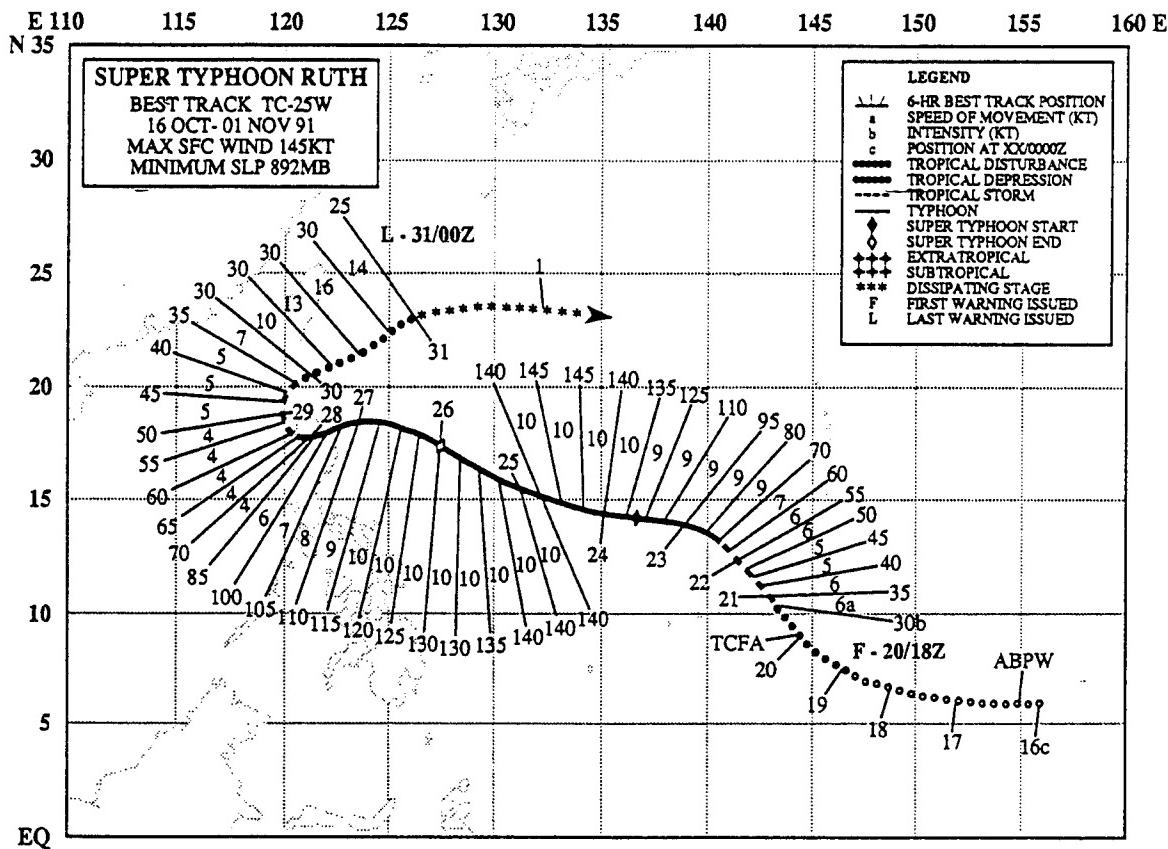


Fig. 3.47. As in Fig. 3.1, except for Supertyphoon Ruth from 16 October to 1 November 1991.

presumably because of interaction with a significant landmass, it must be concluded that steering by the west-southwesterlies of a midlatitude trough was primarily responsible for the WR-AW transition (rather than BEP).

In conclusion, it is emphasized that proper utilization of the VWS TC-environment transformation model requires an accurate TC structure change forecast, which is considered here to be a known external input to the systematic approach for TC motion forecasting. In the case of the northeast monsoon VWS situation, the scenario of LLC separation from the CCM is generally more likely than the TC successfully resisting such strong VWS. In this case, the forecaster may use the VWS model to predict a single, fairly well-defined track change. In most other VWS situations, the forecaster is faced with an alternate intensity forecast scenario that is nearly as probable as that actually forecast. The VWS conceptual model does not offer any means to discriminate between the two scenarios. However, properly applying it to both forecast possibilities will ensure that the intensity and motion components of both the official forecast and alternate scenario are internally (dynamically) consistent.

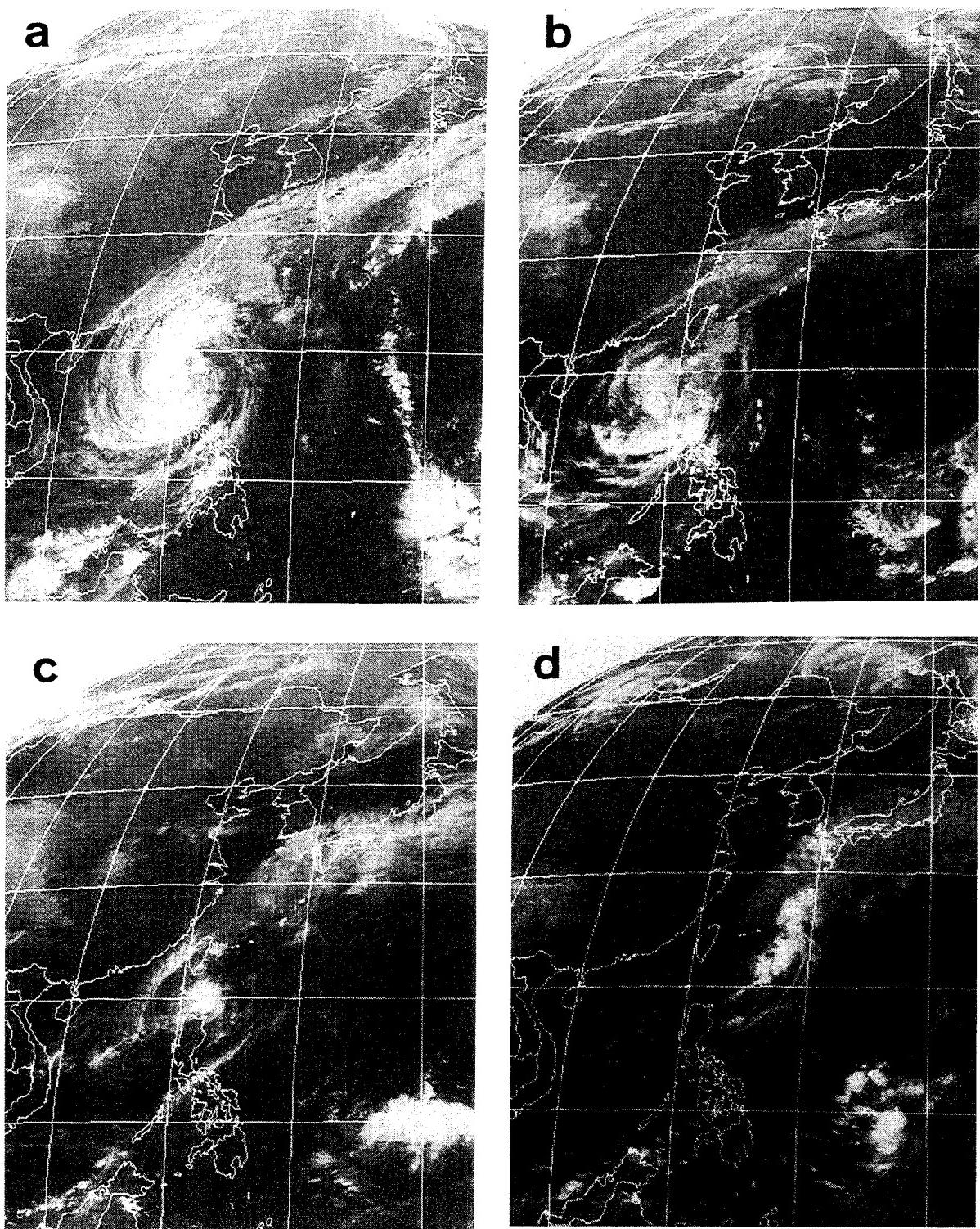


Fig. 3.48. Infrared imagery from GMS at 0000 UTC on (a) 28 October, (b) 29 October, (c) 30 October, and (d) 31 October 1991 during Supertyphoon Ruth.

3) Ridge modification by large TC (RMT). The RMT Environment Structure transformation model accounts for the observed premature recurvature of some TCs via a proposed set of mechanisms by which the TC can cause a major alteration of the structure of the subtropical ridge in its vicinity. To the authors' knowledge, this phenomena has not been addressed in the refereed literature. Because material for a background discussion is not available, Appendix F provides a preliminary development of the RMT transformation model. This subsection begins with a development and description of the RMT model, which will be centered around a case study, owing to lack of modelling work on this phenomenon. The discussion then addresses the impact of the RMT phenomenon and associated Environment Structure transitions, and finally concludes with two more case studies that further illustrate the RMT process, and the range of changes in Environment Structure and TC track that may result.

a) RMT model development and description. It was shown in Appendix D that the  $\beta$ -induced dispersion of barotropic TC-scale vortices generates a peripheral anticyclone that has a growth rate and scale that depends both on the size (Figs. D.12a-f) and outer wind strength (Figs. D.13a-b) of the TC. The advective influence of this growing anticyclone causes the motion of a TC in a quiescent environment to become more poleward over time (Figs. D.10 and D.11), which was accounted for in the BEP TC-environment transformation model by varying the propagation direction from  $320^\circ$  to  $360^\circ$  (Figs. 3.39a-b). This BEP was considered to be linearly superposed with the environmental steering, or equivalently, that the BEP transformation process did not alter the structure of the background environment. Comparisons of the tracks and associated NOGAPS streamline and isotach analyses were used to confirm that such a linear superposition of the BEP and the environmental steering does occur in nature for smaller or average TC sizes (Figs 3.40-3.42).

In the presence of a large TC, the structure of the environment, and thus the associated steering, may be altered. Supertyphoon Yuri, which had a formation latitude of about  $6^\circ\text{N}$  (Fig. 3.49), proceeded on what at first glance appears to be a rather typical recurvature track. The NOGAPS analyses during 23-26 November 1991 (Fig. 3.50a-d) indicate that Yuri was in persistent easterly steering associated with a large, quasi-steady ridge circulation extending between  $20^\circ$  and  $25^\circ\text{N}$ . In other words, Yuri was in the DR Region of a fairly steady Standard Pattern. Satellite imagery (Fig. 3.34d) indicated the size ( $R_{850}$ ) of Yuri was about 1400 km. According to the BEP model, Yuri was a large TC that should be propagating at about  $2.4 \text{ m s}^{-1}$  (Fig. 3.37). For storms such as Yuri that form at a low latitude, the barotropic model integrations initialized with the angular momentum wind distribution indicate that the expected direction of propagation would likely be a steady  $320^\circ$ , instead of turning northward toward  $360^\circ$  (Fig. D.11). Thus, Yuri should be expected to track about  $16^\circ$  to the right of a persistent  $5 \text{ m s}^{-1}$  easterly steering flow, and move at a speed of about  $7 \text{ m s}^{-1}$  (14 kt), according to Fig. 3.39a. During the period covered by Figs. 3.50a-d, Yuri had a nearly steady direction of motion of  $285^\circ$ , and after some initial acceleration maintained a translation speed of about 17 kt (Fig. 3.49). Although some north-south oriented ridging to the east of Yuri was evident by 26 November (Fig. 3.50d), the subtropical ridge circulation is clearly the dominant feature influencing the steering of Yuri.

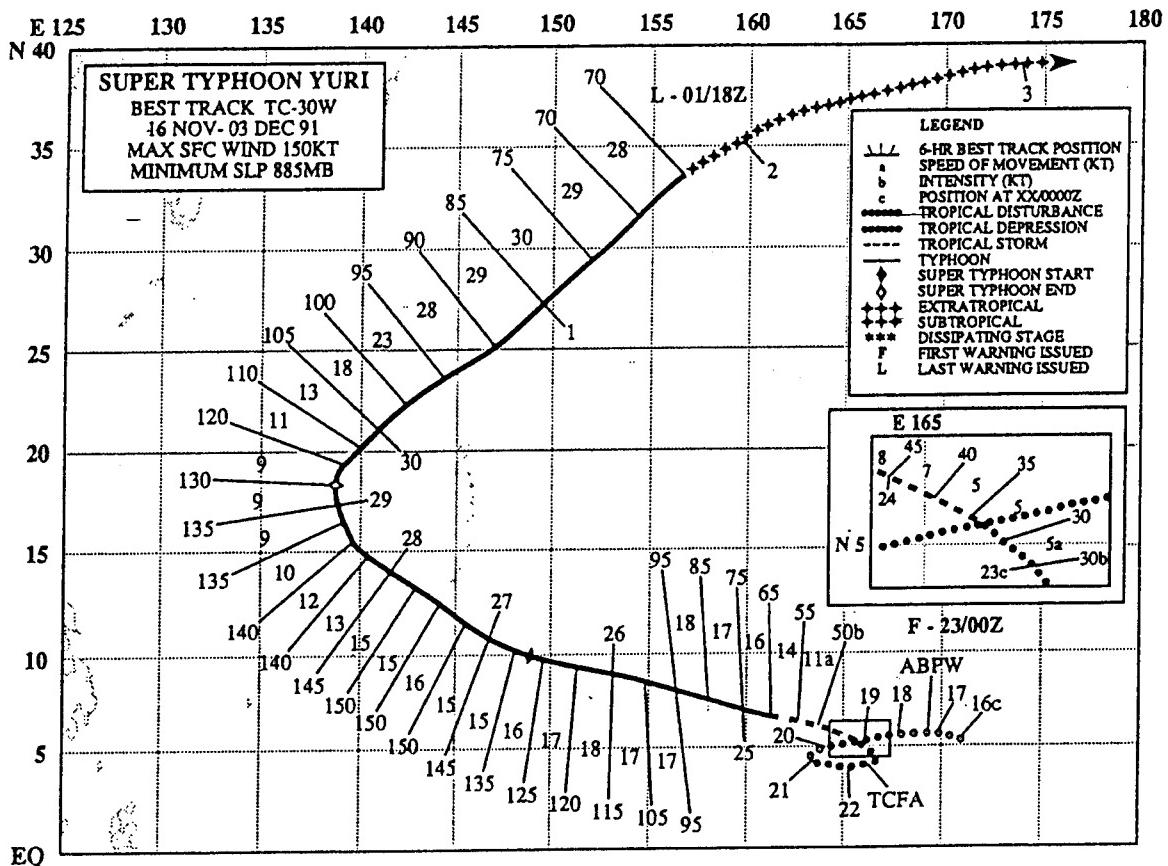
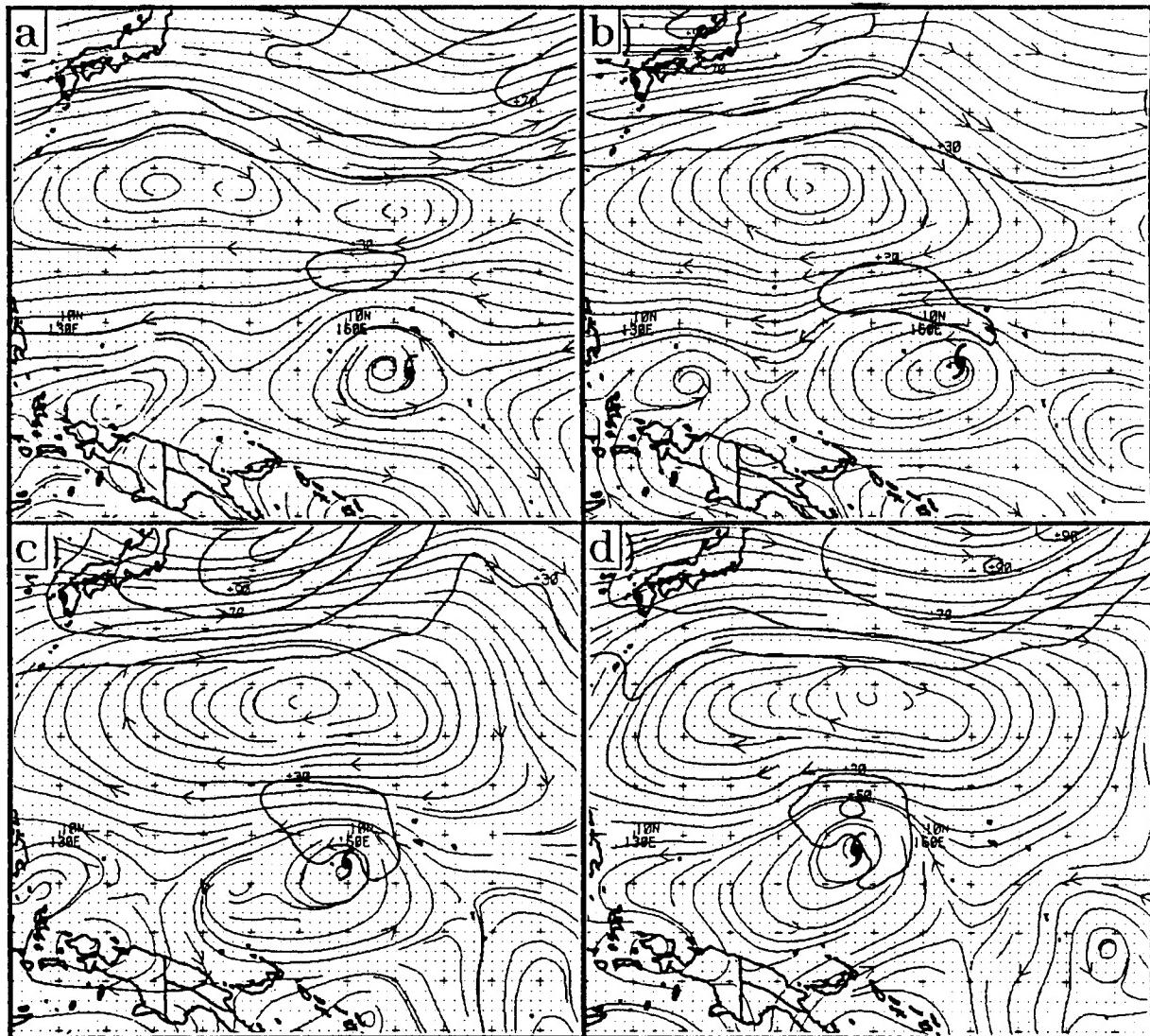


Fig. 3.49. As in Fig. 3.1, except for 16 November to 3 December 1991 during Supertyphoon Yuri.

Thus, the motion of Yuri from 23-26 November seems to conform rather closely to the BEP model of TC propagation without significant alteration of the environment. Without a significant change in the ridge pattern, the combined factors of Yuri's very low formation latitude, the modest rate of latitude gain during the four days, and the latitude and east-west extent of the ridge axis, make recurvature rather unlikely before landfall over Asia.

However, NOGAPS analyses during 27-30 November (Figs. 3.51a-d) indicate a major change in ridge structure had occurred as Yuri recurred. By 0000 UTC 27 November (Fig. 3.51a), a meridionally-oriented ridge extended from the northeast to southeast of Yuri. By 0000 UTC 28 November (Fig. 3.51b), the ridging to the east of Yuri had become more prominent and a ridge break has appeared to the northwest of Yuri, which placed Yuri in an increasingly southerly steering (notice 50-kt isotach to east of Yuri). In other words, the environment of Yuri was transitioning from the DR Region of a Standard Pattern (Fig. 3.17)



**Fig. 3.50.** NOGAPS 500 mb streamline and isotach (kt) analyses at 0000 UTC for (a) 23 November 1991, (b) 24 November, (c) 25 November, and (d) 26 November during Supertyphoon Yuri.

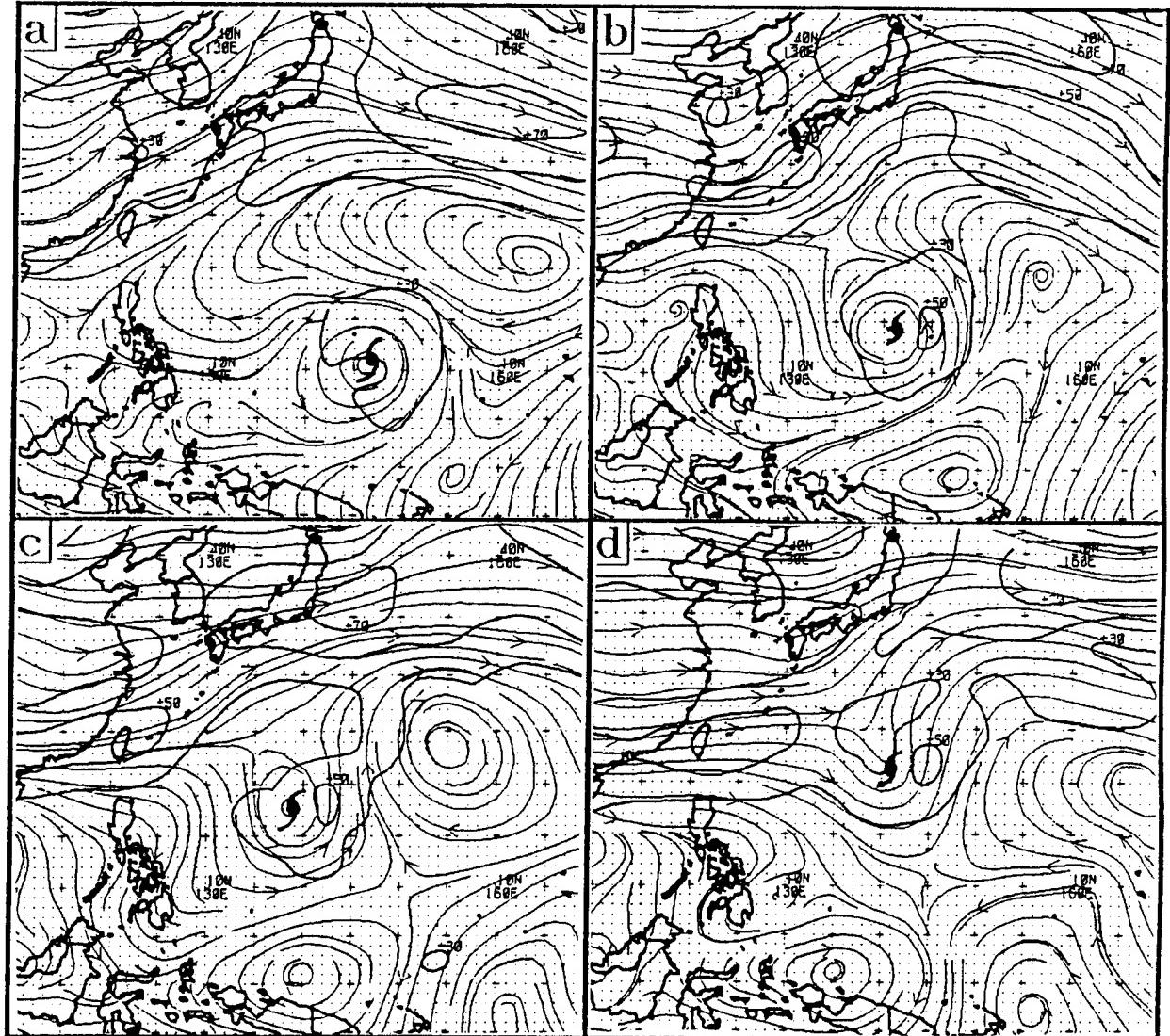


Fig. 3.51. As in Fig. 3.50, except for 0000 UTC on (a) 27 November 1991, (b) 28 November, (c) 29 November, and (d) 30 November.

to the NO Region of a N2 Pattern<sup>12</sup> (Fig. 3.119b). At 1200 UTC 28 November, Yuri turned onto a predominantly northward track (Fig. 3.49). Notice how well the structure of the environment in Fig. 3.51c agrees with the N2 Pattern schematic in Fig. 3.21b. Notice also that a weakening of the ridge circulation over the northern Philippines (Figs. 3.51b-d) allowed the midlatitude westerlies to extend south to about 15°N and expose Yuri to increasingly westerly steering. As a result, Yuri recurved on 29 November at a latitude of about 17° to 18° N.

Since the latitude of the original subtropical ridge at the recurvature longitude of 138°E was about 23°N, Yuri recurved about 5° lat. equatorward of the latitude expected based on a linear superposition of BEP and steady environmental steering. Although major structural changes in the ridge poleward of Yuri might have occurred in the absence of Yuri owing to the natural evolution of the large-scale environment, such major changes usually are associated with high amplitude midlatitude flow. As only low amplitude midlatitude circulations were present (Fig. 3.51), the premature recurvature of Yuri must be attributed to the major subtropical ridge modifications to the east and southeast. On 27 and 28 November, the flow to the southeast of Yuri resembles the  $\beta$ -induced wave train patterns in the simulated streamfunction fields for the larger vortices in Fig. D.12 (panels e and f). In a similar, but smaller, wave train trailing Hattie (Fig. 3.42a and b), the anticyclone remained significantly smaller than the subtropical ridge, and the ridge circulation was not modified. In the Yuri case, the subtropical ridge weakens and the trailing anticyclone appears to become the dominant feature that affected Yuri's motion.

The Hattie and Yuri scenarios suggest that the  $\beta$ -induced dynamical processes for TCs of sufficient size and outer wind strength may lead to the peripheral ridging that modifies the existing ridge and associated steering. As a result, the influence of the TC makes an essential contribution to its recurvature. The TC-environment conceptual framework of the systematic approach accounts for this phenomenon with the (subtropical) Ridge Modification by a Large TC (RMT) transformation model.

Based on the development in Appendix F, the proposed Ridge Modification by a Large TC (RMT) transformation model is comprised of the following elements:

- (i) Erosion of the subtropical ridge to the west and poleward of the large TC arising from  $\beta$ -induced positive relative vorticity advection;
- (ii) Building of a significant peripheral ridge equatorward and to the east of the large TC owing to intense  $\beta$ -induced negative relative vorticity advection; and
- (iii) Concomitant weakening of the subtropical ridge poleward and to the east of the TC and amplification of the  $\beta$ -induced peripheral ridge owing to a barotropically

---

<sup>12</sup> Recall from Section 3.b.1.b that N2 is the designation for a North-Oriented Pattern involving a large TC.

unstable energy conversion from the subtropical ridge to the  $\beta$ -induced ridge, which tends to result in a single extensive ridge feature with northeast-southwest (Northern Hemisphere) orientation that provides an additional southwesterly steering component to the TC.

b) *RMT model impact*. Based on the example of Supertyphoon Yuri above, the key impact of the RMT TC-environment transformation on TC motion is its tendency to alter the structure of the environment in the vicinity of a large TC from the DR Region of a Standard Pattern (Fig. 3.50a-d) to the NO Region of a N2 Pattern (Figs. 3.51a-d). In other words, the RMT transformation may function as a transitional mechanism that may result in a S to N2 Pattern transition and a DR to NO Region transition. This role of the RMT conceptual model is schematically illustrated in the lower left portion of Fig. 3.52. Once the transition to the N2 Pattern has been accomplished, the steering effect of the generally southerly flow of the NO Region will move the TC from the NO Region to the AW Region. That is, advection (ADV) will, if not interrupted, eventually result in an NO to AW Region transition within the N2 Pattern (Fig. 3.52).

Recall that a key difference between the N1 and N2 Patterns (see Section 3.b.1.b), was that TCs tend to move through the NO Region of the N1 Pattern, whereas the NO Region tends to move with the TC in the N2 Pattern. The peripheral ridging component of the RMT transformation model described in Appendix F provides the dynamical basis for this phenomenon. That is, since  $\beta$ -induced dispersion of the large TC is the source of the strong peripheral ridging to the east and equatorward of the TC, that ridging will naturally tend to follow the TC as it is steered generally poleward by the flow of the NO Region. Since the TC cannot fully recurve by moving into the AW Region until it moves poleward of the ridge to the east, the tendency for the RMT-related peripheral ridge to translate poleward with a large TC tends to forestall recurvature. Thus, the RMT transformation process includes paradoxical aspects of first inducing a S to N2 Pattern transition and a DR to NO Region transition, but then resisting the role of advection in accomplishing the NO to AW region transition within the N2 Pattern. This sequence is represented by the dashed RMT feedback loop in Fig. 3.52.

In summary, the various considerations to apply the RMT conceptual model include determining:

- (i) whether the ridge-relative size of the TC and its associated wave train are sufficient to accomplish the S to N2 Pattern transition, and if sufficient, how long will the transition process take;
- (ii) when and where the RMT-related premature recurvature (i.e., direction of motion passing through north) will occur; and
- (iii) how variations in the N2 pattern, and in the RMT feedback process that inhibits the eventual NO to AW Region transition, will affect the motion and intensity of the

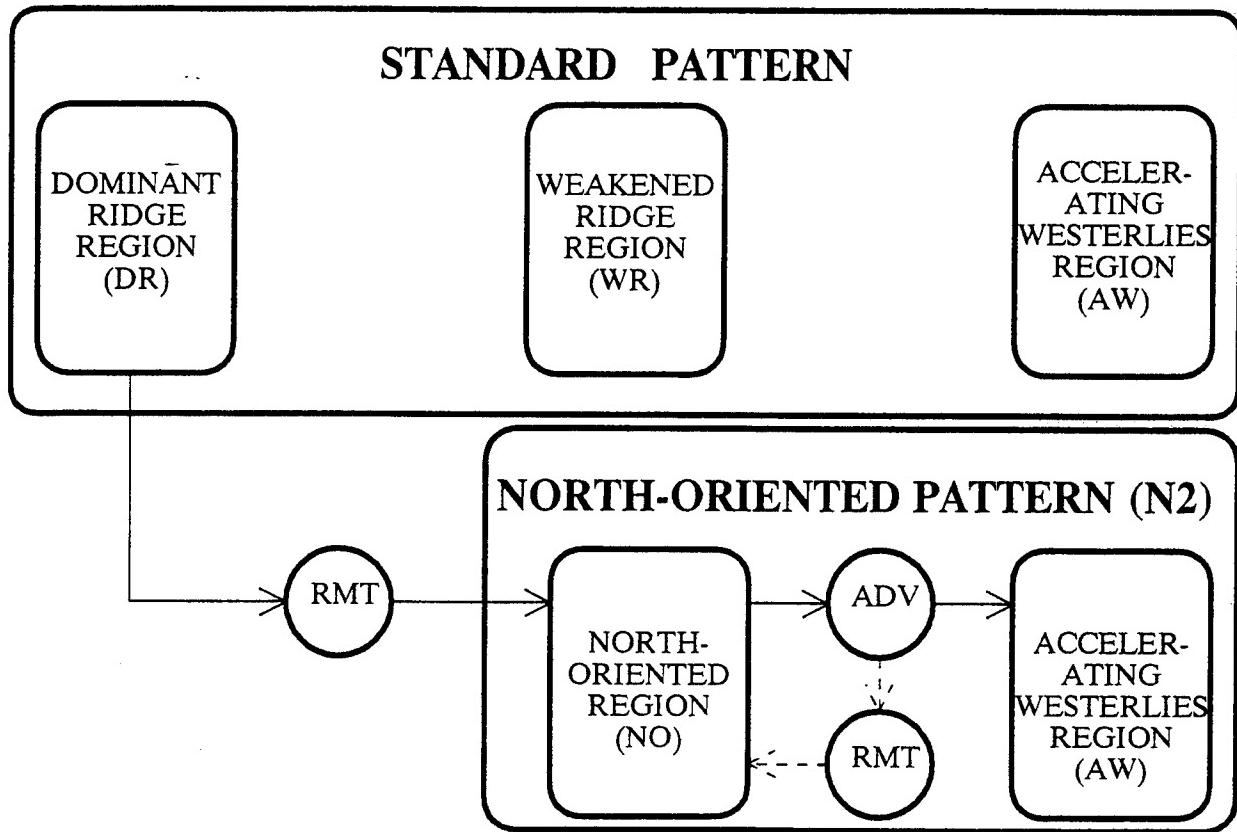


Fig. 3.52. Environment transition from a Dominant Ridge Region of a Standard pattern to a North-Oriented Pattern N2 induced by a Ridge Modification by a large TC (RMT).

TC in the NO Region. A list of the possible track and intensification anomalies that may occur during this feedback process include:

- (a) the early portion of the recurvature track of the large TC tends to be followed by a more poleward-oriented track than would be expected for a smaller TC;
- (b) a significant delay in the storm translation acceleration that is normally associated with recurvature;
- (c) a delay in turning to the east during the latter part of the recurvature; and
- (d) significant intensification after recurvature while the storm is still over warm water and is not yet exposed to strong vertical wind shear.

The case of Yuri described above illustrates a number of the above considerations. Recall that Yuri produced a very large and intensive ridging to the east of the TC, which when considered alone might imply a rapid modification of the subtropical ridge. However, the large zonal and latitudinal extent of the ridge meant that a significant period of time (0000 UTC 23 November to 1200 UTC 28 November) occurred before the combined effects of propagation and ridge erosion/building by Yuri altered the ridge structure sufficiently to accomplish the pattern transition (compare Figs. 3.49, 3.50a, and 3.51b or c). However, Yuri then spent only a day or so in the NO Region before undergoing significant northeastward acceleration, which suggests that the RMT feedback process was not particularly strong during this period. Nevertheless, the RMT feedback process probably contributed to the significant poleward component in the after-recurvature track direction of Yuri that then became slightly more poleward until about 2 December when the turn to the east ensued (Fig. 3.49).

Because of the preliminary nature of the RMT model, it is not possible to provide the forecaster with firm dynamically-based insights with which to address considerations (i) through (iii) above. Instead, two case studies are provided below to give the forecaster a sense of the range of possible TC sizes, variations in the TC track, the corresponding environmental patterns in NOGAPS streamline and isotach analyses, and clues from satellite imagery that the RMT transformation may be occurring.

c) *RMT model illustrations.* The first case study is of Typhoon Page (03W; 1994), which will be covered in some detail because it provides a particularly clear illustration of the effect of the RMT transformation processes on the environment, track, and intensity of the TC (Fig. 3.53). At 0000 UTC 11 May, Page is a tropical depression in the easterly steering of the DR Region of a S Pattern (Fig. 3.54a). The cloud signature of Page covers approximately 20° lat. by 20° long. (Fig. 3.55a), which suggests that Page has an  $R_{850}$  of about 10° lat. or 1100 km. Therefore, Page is a rather large TC that should be capable of generating a significant  $\beta$ -induced ridge. However, the NOGAPS analysis (Fig. 3.54a) still has an extensive monsoon trough to the east of Page on 11 May, and only a modest buffer eddy to the southeast at about 2°S, 152°E.

By 0000 UTC 12 May, Page has developed a more organized central cloud pattern (Fig. 3.55b), but it is still analyzed as a tropical depression (Fig. 3.53). The corresponding NOGAPS analysis (Fig. 3.54b) has a S Pattern character for the subtropical ridge, and has a more developed circulation for Page. Furthermore, the analysis has a weakening of the monsoon trough to the east, winds to the southeast of Page exceeding 30 kt, and development of a distinct buffer eddy (now near 0°N, 146°E) to the southeast of Page. All of these features appear to be consistent with the development of the peripheral ridge predicted by the barotropic simulations. Since Page has not yet attained minimal tropical storm intensity, no synthetic TC wind observations have yet been inserted in NOGAPS. So the growing ridge to the east and south of Page has been represented by the NOGAPS data assimilation cycle purely on the basis of real observations. However, the peripheral ridging has not proceeded to the point that the dominant ridge axis has shifted from the poleward

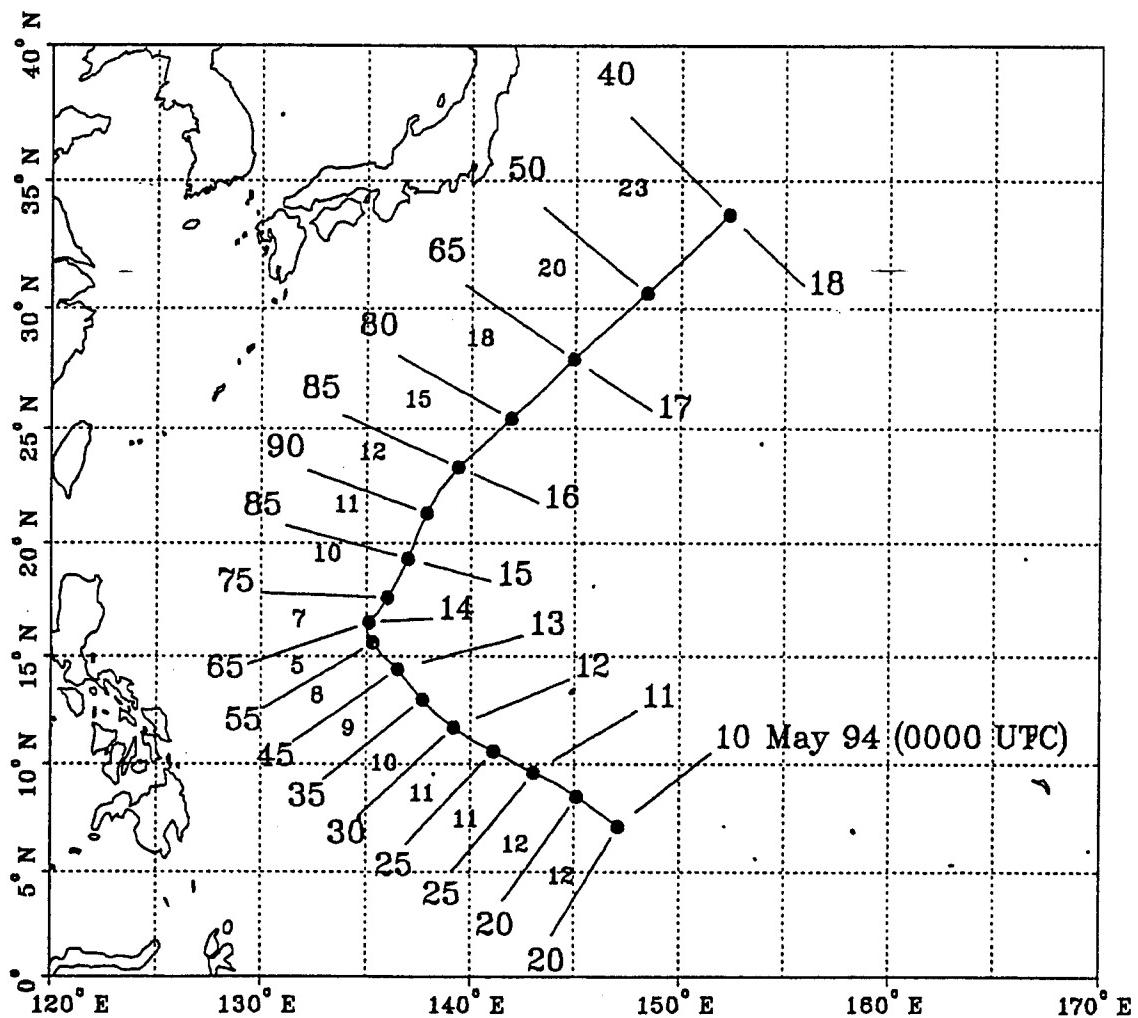


Fig. 3.53 As in Fig. 3.1, except for Typhoon Page during 10-17 May 1994, and a 12-h interval between TC positions.

side to the east side of Page. This assessment is confirmed by the significant displacement of Page to the northeast of the NOGAPS-analyzed circulation, which indicates that Page is still subject to the southeasterly 500 mb steering arising from the subtropical ridge circulation to the northeast.

By 0000 UTC 13 May, Page has attained tropical storm intensity (Fig. 3.53) and the extent of the central convection is more compact (Fig. 3.55c). This shrinking of the central cloud feature does not necessarily imply a reduction in  $R_{\text{c}}^{850}$ , since all banding features must be included. Indeed, the cumulonimbus activity approximately 10° lat. (1100 km) to the northeast of Page suggests that  $R_{\text{c}}^{850}$  has not decreased. The NOGAPS analysis now has a weaker subtropical ridge circulation to the northeast of Page (Fig. 3.54c), so that the ridge features poleward and to the east of Page appear approximately equal in strength. A weakening of the 500 mb steering and slower translation speed are consistent with the movement of the JTWC position closer to the center of the NOGAPS circulation compared

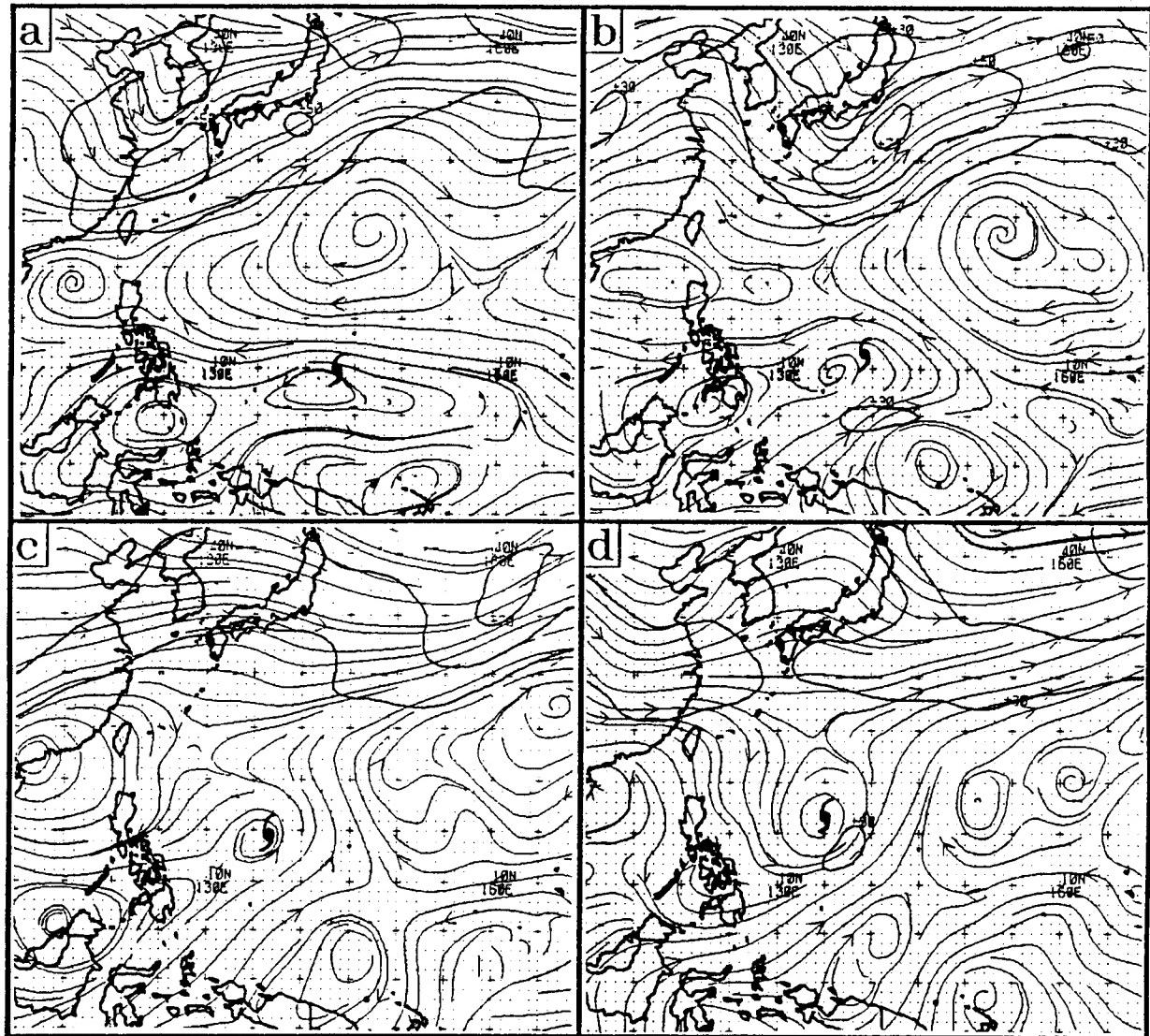


Fig. 3.54. As in Fig. 3.50, except at 0000 UTC for (a) 11 May 1994, (b) 12 May, (c) 13 May, and (d) 14 May during Typhoon Page.

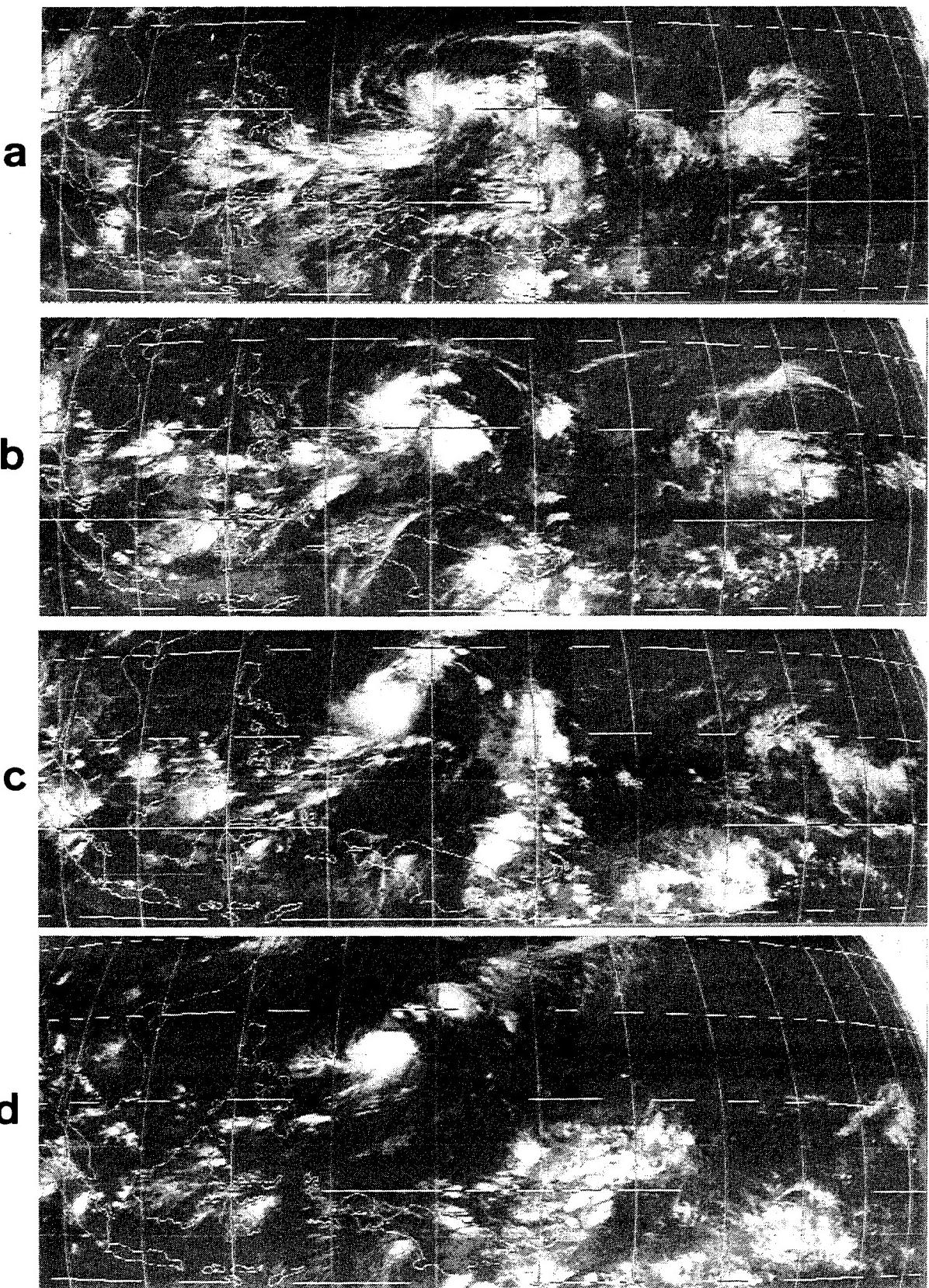


Fig. 3.55. Geostationary infrared imagery of Typhoon Page at 0000 UTC on (a) 11, (b) 12, (c) 13, and (d) 14 May 1994.

to 24 h earlier (Fig. 3.54b). All of these observations suggest that the structure of the environment conforms very well to a "transitional state" between the DR Region of a S Pattern and the NO Region of a N2 Pattern.

By 0000 UTC 14 May, Page has begun to move slowly northeast (Fig. 3.53). The structure of the ridging equatorward and to the east of Page (Fig. 3.54d) conforms well to the N2 Pattern (Fig. 3.18b) with Page now in the NO Region. The similarity of this peripheral anticyclone to the southeast of Page to that from  $\beta$ -induced dispersion of the TC in the barotropic simulation is supported by the presence of the buffer eddy farther southeast (near  $2^{\circ}$ S,  $152^{\circ}$ E), as expected for a wave train of circulations of alternating sign beginning with Page.

For about two days after recurvature near  $16^{\circ}$ N,  $135^{\circ}$ E, the translation speed of Page undergoes only a modest increase to 14 kt, and the direction of motion actually becomes more poleward (Fig. 3.53). Subsequently, the translation speed increases rapidly, and the direction of motion turns toward the east as expected for a recurring TC. Thus, the track of Page after recurvature exhibits the delayed acceleration and a poleward turn followed by an eastward turn expected in the RMT transformation model. The source of these anomalous track aspects may be revealed by comparing the evolution of the ridge structure to the east of Page in Figs. 3.54d and 3.56a-b. The latitude of Page and the ridge to the east remain about the same as Page moves from about  $17^{\circ}$ N to  $23^{\circ}$ N during the 48-h period, which is in accordance with the RMT transformation model. As a result, the transition of Page from the NO Region to the AW Region is delayed as in the RMT feedback loop portrayed in Fig. 3.52.

The satellite images during 11-14 May (Fig. 3.55a-d) reveal development of a large-scale pattern of convectively active and inactive regions that correlates well with the cyclonic and anticyclonic circulations of the wave train beginning with Page. Extensive convection appears well to the southeast of Page on 11 May (Fig. 3.55a), when no wave train is yet apparent in the NOGAPS streamline field (Fig. 3.54a). By 13 May, distinct regions of enhanced convection associated with Page and another at about  $150^{\circ}$ E are separated by an area of suppressed convection near  $10^{\circ}$ N,  $145^{\circ}$ E, which corresponds to the approximate location of the anticyclone southeast of Page near  $3^{\circ}$ N,  $145^{\circ}$ E in Fig. 3.54c. The linear convection area farther to the southeast of Page agrees remarkably well with the confluent region between the peripheral anticyclone and the trailing cyclone in the wave train near  $4^{\circ}$ S,  $159^{\circ}$ E. A similar strong correspondence between the imagery cloud patterns and NOGAPS streamline patterns is also evident on 14 May (Figs. 3.55d and 3.54d, respectively).

A similar cloud-clear-cloud pattern (Fig. 3.36d) is correlated with the wave train of Yuri on 0000 UTC 27 November (Fig. 3.51a). The minimum cloud area is bounded by  $170^{\circ}$ E to the east, and by the enhanced band of convection along  $155^{\circ}$ E, which corresponds nicely to the confluent region between Yuri and the peripheral anticyclone. Notice also that the scale of Yuri's cloud-clear-cloud pattern is considerably larger than that for Page, which is consistent with the significantly larger scale of Yuri's wave train.

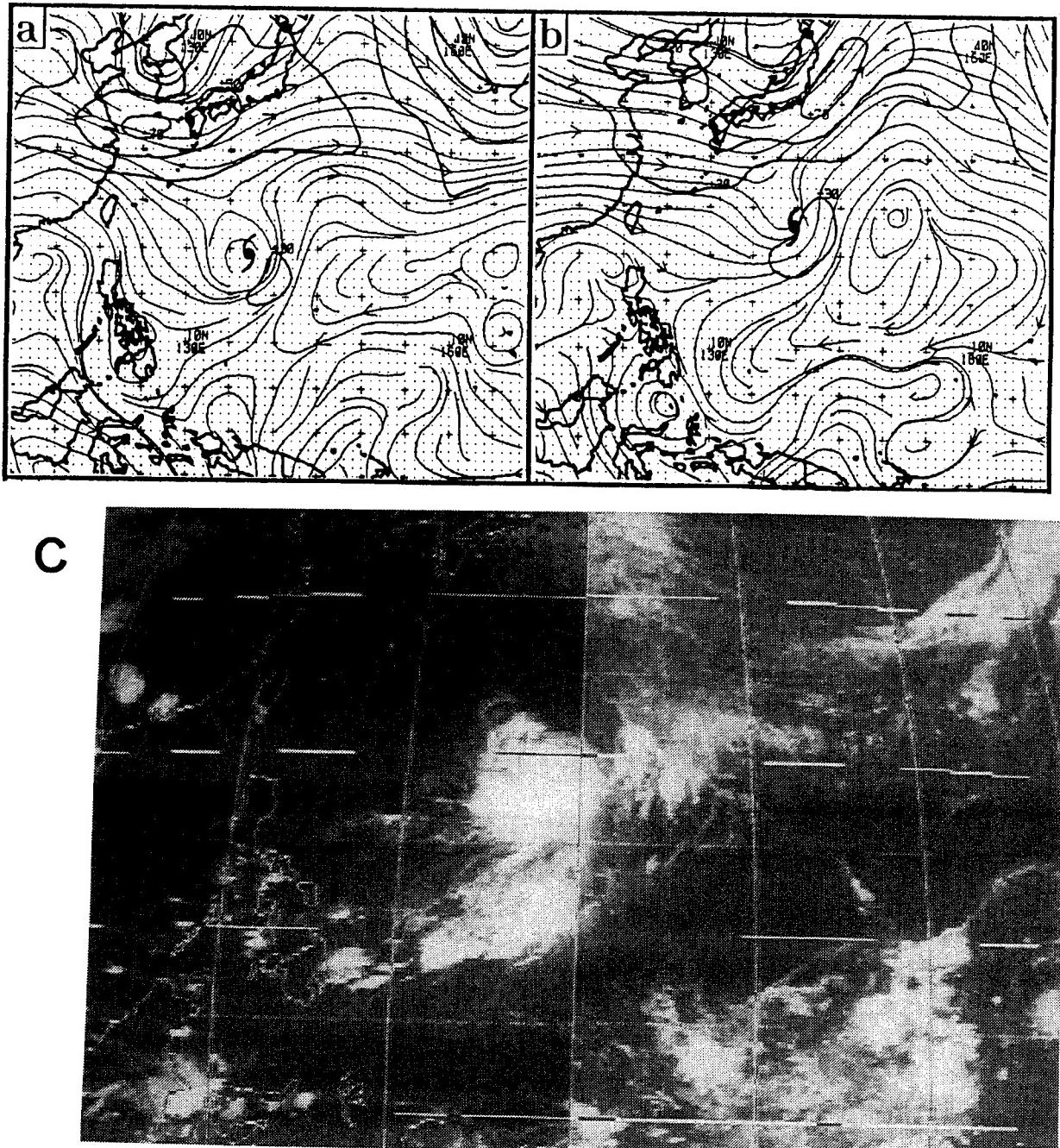


Fig. 3.56. As in Fig. 3.54, except for (a) 15 May 1994, and (b) 16 May 1994. (c) As in Fig. 3.55, except for 0000 UTC 15 May 1994.

In both the Page and Yuri cases, the cloud-clear-cloud signature in the satellite imagery and the wave train in the analysis became evident approximately two days before the track change associated with the S to N2 Pattern and the DR to NO Region transitions. These features are thus a potentially powerful tool for anticipating that a RMT-related transition may occur. However, more track change cases in association with the wave train and the cloud signatures are needed to assess the reliability of this association.

Notice also the significant intensification during and after the turn of typhoon Page to the northeast (Fig. 3.53). Such intensification is quite atypical for a recurving TC because high vertical wind shear (VWS) associated with the upper-level midlatitude westerlies would normally be expected to strongly inhibit further intensification. This VWS is usually manifest in the satellite imagery as a broad continuous plume of cirrus streaming poleward and eastward from the TC, as in the case of Ruth (Fig. 3.48a). In the case of Page, such a cirrus plume was not present a day after recurvature (Fig. 3.56c), which indicates little westerly VWS.

TC intensification after recurvature in RMT transformation situations is generally expected since:

- (i) recurvature occurs as a result of TC-induced ridge breakdown, which does not require the presence of a significant midlatitude trough and its associated jet structure;
- (ii) recurvature tends to occur at an anomalously low latitude, and thus well away from the highest winds of the midlatitude westerlies; and
- (iii) an eventual encounter with high speed westerlies as the TC gains latitude tends to be delayed by the tendency for the RMT-induced peripheral ridge (to the east of the TC) to move poleward with the TC, and thus deflect the high speed westerlies (Figs. 3.56a-b).

The second case study of Supertyphoon Yvette (23W; 1992) illustrates the importance of the ridge-relative size of the TC, and how a second TC to the east may alter the character of the RMT-related track change. At 0000 UTC 8 October 1992, Yvette was a tropical depression that had been steadily proceeding west-southwest for over two days (Fig. 3.57). The convective cloud pattern including the outer bands (Fig. 3.58a) has a  $R_{850}$  of about 660 km, which with the present latitude of 15°N would indicate an insignificant northwestward BEP (Fig. 3.37). This track and the absence of significant BEP would imply east-northeast steering. The corresponding analysis (Fig. 3.59a) has Yvette in the DR Region of a S Pattern. Notice especially that the ridge is thin in north-south extent, and also the ridge slopes toward lower latitude to the west, which is consistent with the east-northeasterly steering of Yvette inferred above.

During the next three days (Figs. 3.59b-d), the subtropical ridge weakens until a large ridge break is present poleward of Yvette. Northeasterly 500 mb flow over the South China Sea (Fig. 3.59b) on 9 October is replaced by 11 October with northwesterly flow that envelopes Yvette (Fig. 3.59d). Over the same period, a peripheral ridge develops to the east of Yvette, and together with the remaining portion of the subtropical ridge to the northeast of Yvette, forms a north-oriented ridge. That is, the S Pattern on 9 October (Fig. 3.59b) has transitioned to a N2 Pattern by 11 October (Fig. 3.59d). In response to these changes in

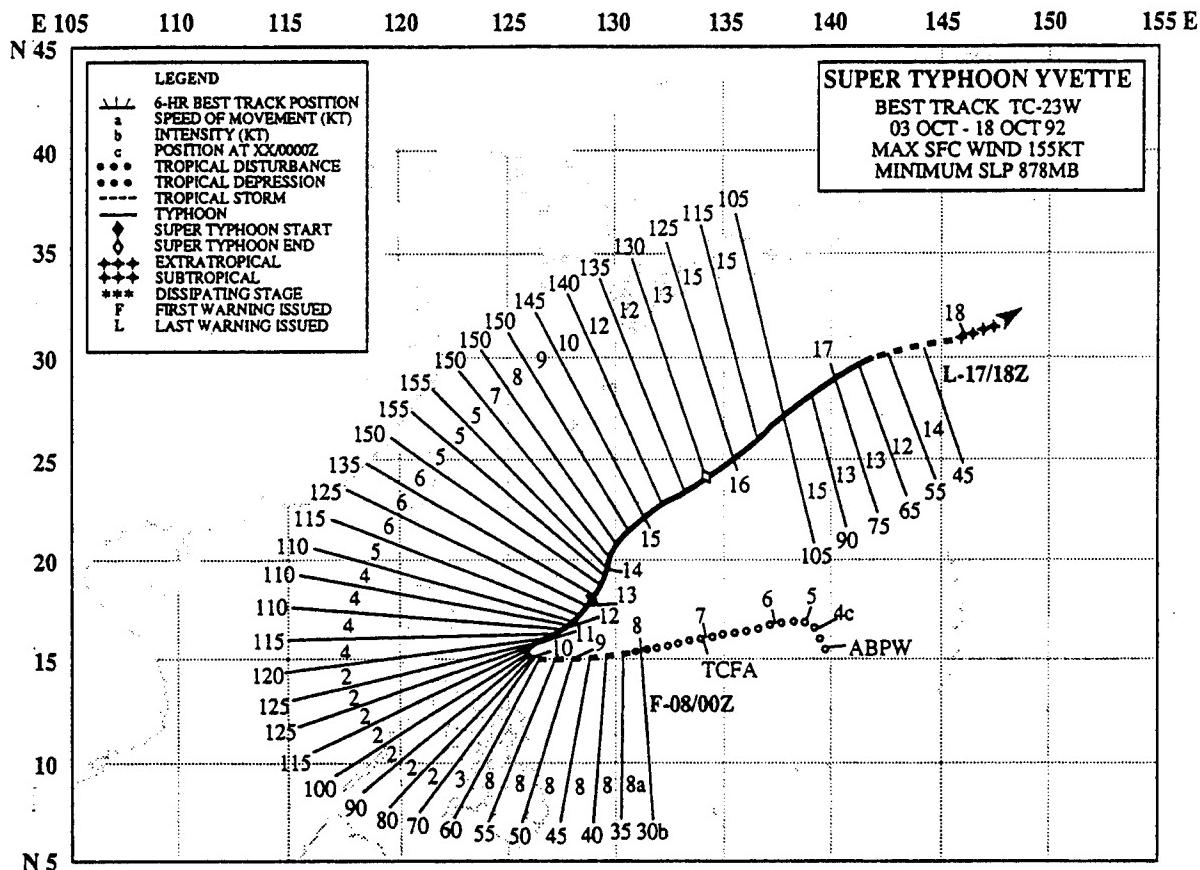


Fig. 3.57. As in Fig. 3.1, except for 3-18 October 1992 during Supertyphoon Yvette.

**Environment Structure.** Yvette slows and undergoes a dramatic change in track direction toward the northeast. Although some weakening occurs following the sharp recurvature, Yvette is still at low latitudes and re-intensification occurs (Fig. 3.57). An absence of westerly wind shear is consistent with no cirrus plume and the compact cloud pattern of Yvette in the satellite imagery (Fig. 3.58b). This intensification following a northward turn, and the delayed weakening until after an eastward turn and acceleration are consistent with Yvette being in the NO Region of the N2 Pattern until about the 14th, and then a transition into the AW Region. The north-oriented ridge to the east of Yvette weakened during 12-15 October (Figs. 3.60a-d), and by 15 October (Fig. 3.60d) the ridge to the east had decayed sufficiently to permit the eastward turn and acceleration of Yvette.

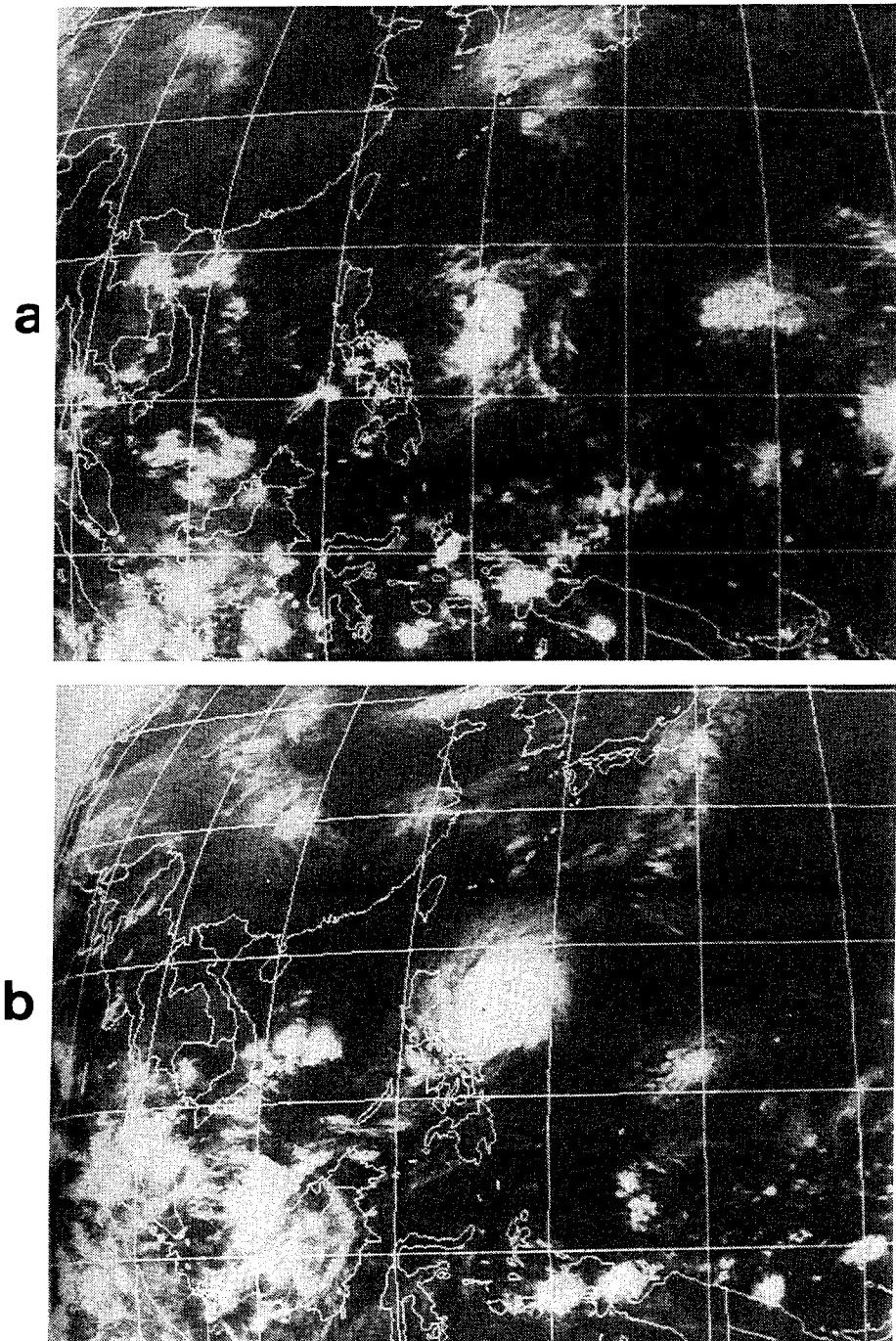


Fig. 3.58. Infrared imagery from GMS for 0000 UTC on (a) 8 October 1992, and (b) 11 October 1992 during Supertyphoon Yvette.

Since Yvette was a rather small TC, it might not have been anticipated that the RMT could accomplish the S to N2 Pattern transition. However, the key is that the subtropical ridge associated with Yvette was also substantially smaller than in either the Yuri or Page cases described above. That is, the smaller peripheral anticyclone that developed to the east

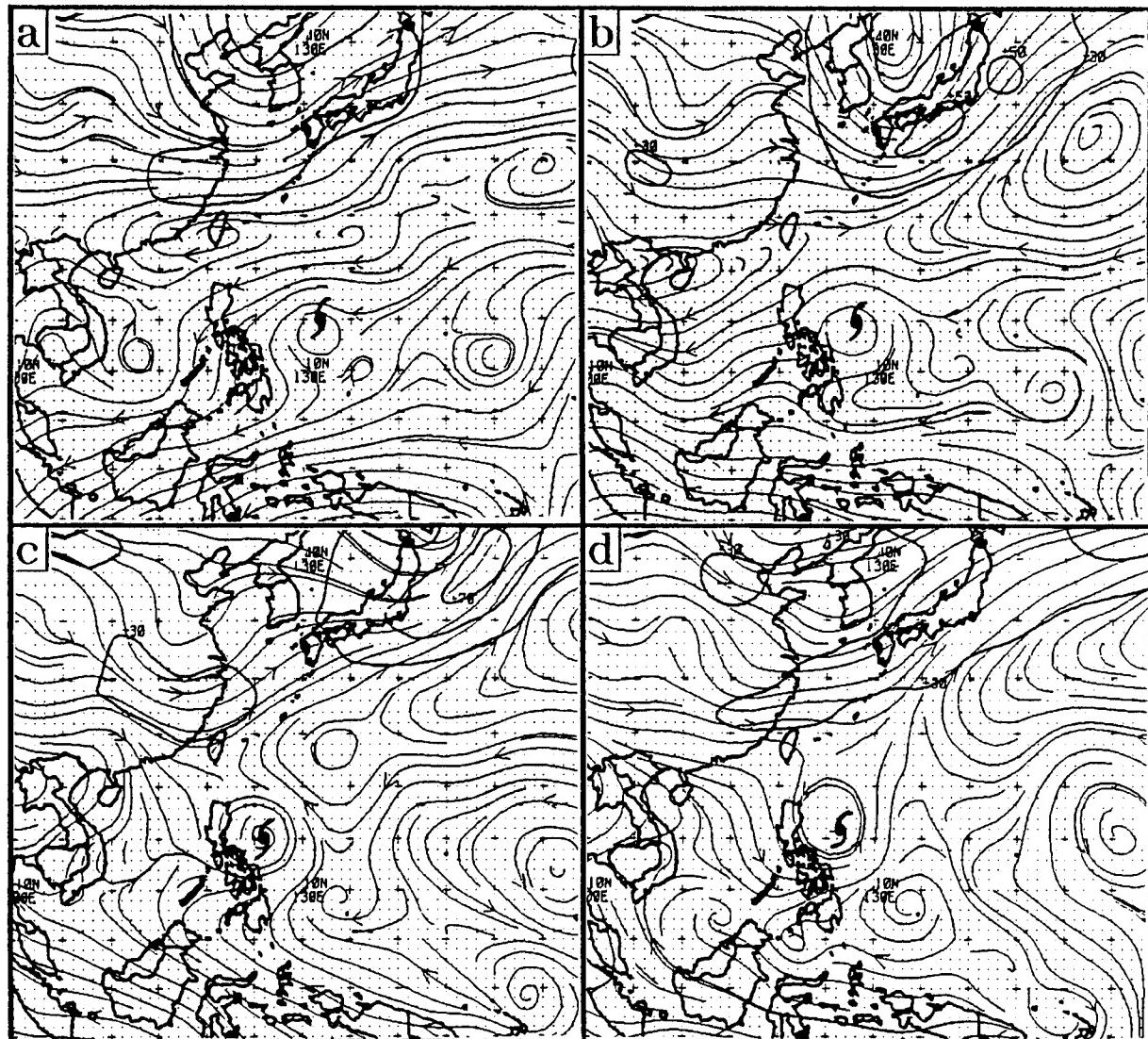


Fig. 3.59. As in Fig. 3.50, except for 0000 UTC on (a) 8 October 1992, (b) 9 October, (c) 10 October, and (d) 11 October during Supertyphoon Yvette.

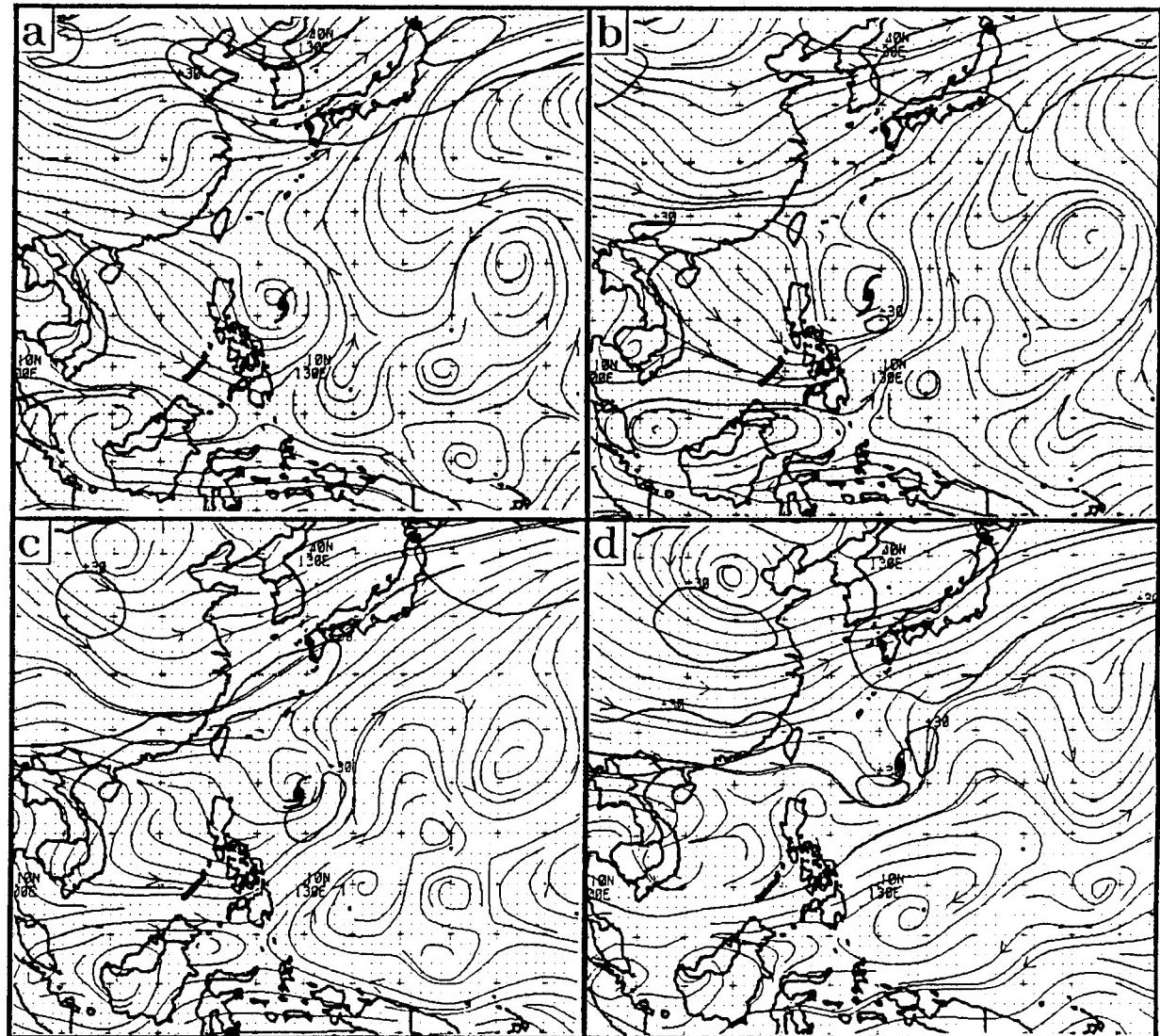


Fig. 3.60. As in Fig. 3.59, except for (a) 12 October 1992, (b) 13 October, (c) 14 October, and (d) 15 October.

of Yvette had a *similar scale* as the subtropical ridge to the north, and eventually combined with the subtropical ridge to form a north-oriented ridge. In addition, the weaker ridge-eroding PVA produced by Yvette on its poleward side evidently contributed to a breakdown of the thin subtropical ridge to the north and east. Viewed in a (subtropical) ridge-relative sense, the sizes of Yvette, Page, and Yuri were all sufficiently "large" for the associated RMT-processes to contribute to a transition in the Environment Structure. In the cases of Page and Yuri, a cloud-clear-cloud pattern in association with a wave train to the southeast was present *before recurvature* and provided a potentially useful RMT prediction tool. In the case of Yvette, no cloud pattern became evident, which suggests that the influence of the wave train was apparently too weak to influence significantly the convective activity.

4) Monsoon Gyre-TC Interaction (MTI). For the other TC-Environment transformation conceptual models, selected research results have been combined to provide the background discussion and preliminary development leading to the description and impact-analysis of the model. For the MTI case, Carr and Elsberry (1995) have provided an observational overview of, and development of a dynamically-based conceptual model of, MTI to explain a class of sudden TC track changes that they call monsoon surge track changes, and that are termed MTI track changes in the report. Because Carr and Elsberry provide a number of observational insights that are directly applicable to the utilization of the model by TC forecasters, that material appears in the first subsection below rather than in an appendix. Excerpts from the barotropic modelling of the MTI phenomenon by Carr and Elsberry serve as the development of the MTI model and appear in Appendix G. The discussion in this section is then organized into subsections that describe the MTI model and its impact on environmental structure, and illustrate the MTI transformation process via several case studies.

a) Background. During nearly every western North Pacific summer monsoon season, one or more TCs undergoes a sudden track change as in the case of Typhoon Hal (Fig. 3.61). The sudden track change of Hal occurred approximately 10° lat. equatorward of, and more than three days before, the eventual recurvature just southeast of Japan. The MTI track changes typically consist of rapid slowing of the westward movement to either quasi-stationary or a tight cyclonic looping period, and then a strong acceleration on a substantially more poleward heading. Such track changes usually occur while the TC is still in the vicinity of the monsoon trough, and are sufficiently equatorward of the mid-level subtropical ridge axis that the maneuver cannot be attributed to the influence of passing midlatitude circulations. In addition, these events routinely occur in the absence of other TCs, or occur well removed from a neighboring TC, which rules out binary TC interaction as the cause of the track change.

A sharp poleward turn as in Fig. 3.61 bears some resemblance to the track changes arising from a RMT-related transition of the environment from a S to a N2 Pattern and from a DR to a NO Region. Whereas a RMT-induced transition is associated with imminent recurvature and subsequent northeastward motion, here the post-turn heading retains a westward component so that recurvature occurs later. Because this significantly

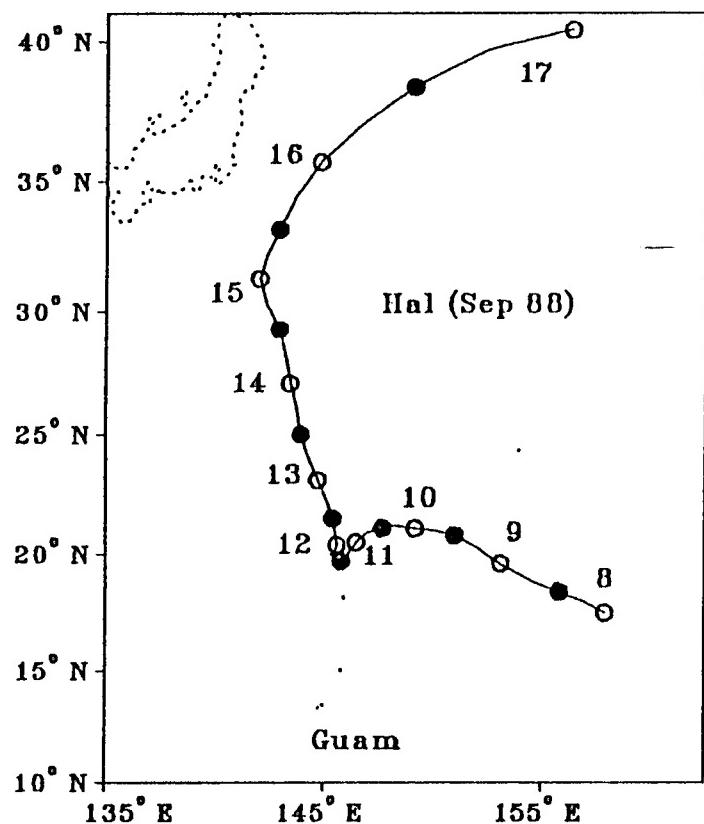


Fig. 3.61. Best track of Typhoon Hal during 8-17 September 1988 (Carr and Elsberry 1995). White and black circles denote 0000 and 1200 UTC positions, respectively.

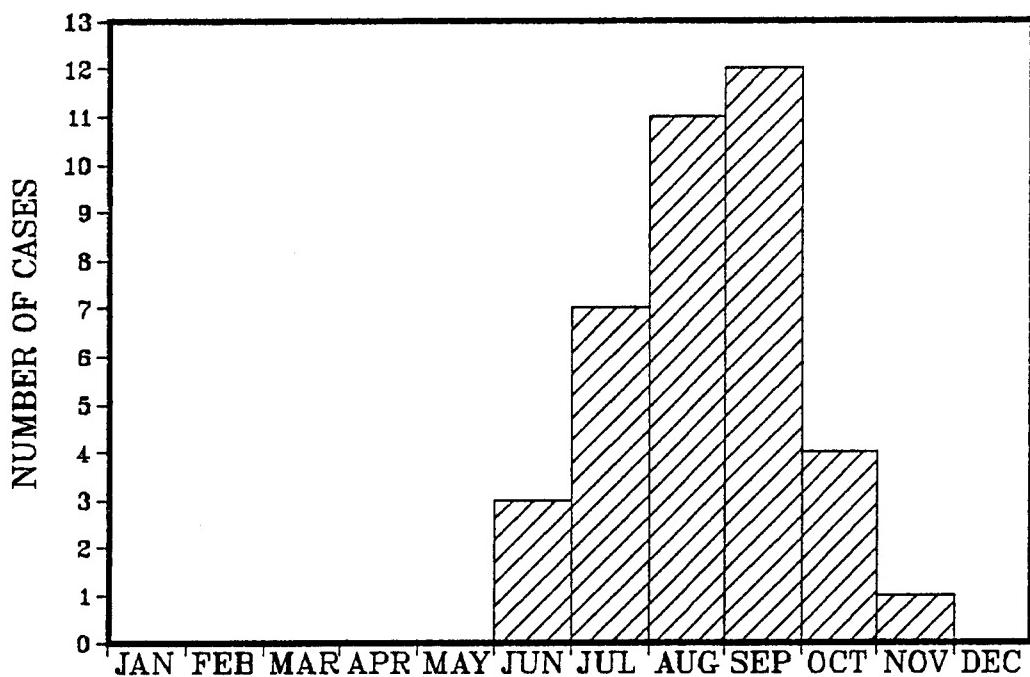


Fig. 3.62. Number of tropical cyclone cases of sudden poleward track changes during each month of 1977-91 in the western North Pacific.

different post-turn heading will be a critical aspect in the forecast, these cases will be treated as a distinct (although perhaps arising from similar dynamical processes) phenomenon from the RMT transformation.

Carr and Elsberry (1995) examined the JTWC best tracks for 1977 to 1991 for track changes similar to Hal. On average, two to three such track changes occur per year during the months of June through November (Fig. 3.62). August and September have the greatest frequency of occurrence, which corresponds to the most active portion of the southwest monsoon season.

Track changes that occurred during 1989 to 1991 are shown in Figs. 3.63a-c, respectively. The sharp poleward turn routinely approaches or exceeds  $90^\circ$ , and often appears to be part of a larger cycloid-like motion pattern in which the TC approaches and/or leaves the sudden right-turn point on a leftward-turning trajectory (cf., Mac, Sarah, and Tip in Fig. 3.63a). Although such track changes may occur throughout much of the Philippine and South China Seas, a general correlation with the monsoon trough is evident. During 1990 and 1991, the latitude at which the track change occurred was farther to the south for increasing east longitude, and thus was generally consistent with the climatological position and orientation of the monsoon trough axis. During 1989, the events generally occurred at a higher average latitude, and were in good conformity with the anomalously poleward location of the monsoon trough during the middle of that typhoon season. In addition, 10 of the 13 track changes in Fig. 3.63 occurred when the TC was 45 kt or weaker. In summary, the sudden track changes tend to occur early in the life of the TC when it is closely associated with the monsoon trough.

Several cases in Fig. 3.63 (Ken-Lola and Sarah in 1989, and Nathan and Yancy in 1990) have a track change that appears to be a temporary excursion to the left of an otherwise west-northwestward track. Whereas Sarah's excursion was quite dramatic, Yancy's was quite subtle. The remainder of the events in Fig. 3.63 resulted in a permanent change of track orientation toward the pole. For example, the poleward turns ranged from the nearly right-angle turns of Mac (1989) and Tasha (1990) to the much smaller, but nevertheless significant,  $30^\circ$  turn of Ivy (1991).

A survey of the TC descriptions in ATCRs indicated that such track changes were almost always unanticipated until they were in progress. The JTWC forecasts issued just prior to the track changes of Caitlin, Ivy, and Joel (Fig. 3.63c) are typical examples. Although the resultant forecast errors are not as large as those that can arise from a missed or false forecast of recurvature, the sudden and major modifications to the official track forecasts that are required after such unexpected turns wreak havoc with facility evacuations/preparations and ship evasive maneuvers, and erode user confidence in JTWC warnings. Thus, these sudden, below-the-ridge turns represent a significant track forecasting problem.

Discussions in the ATCRs often attribute these track changes to enhanced

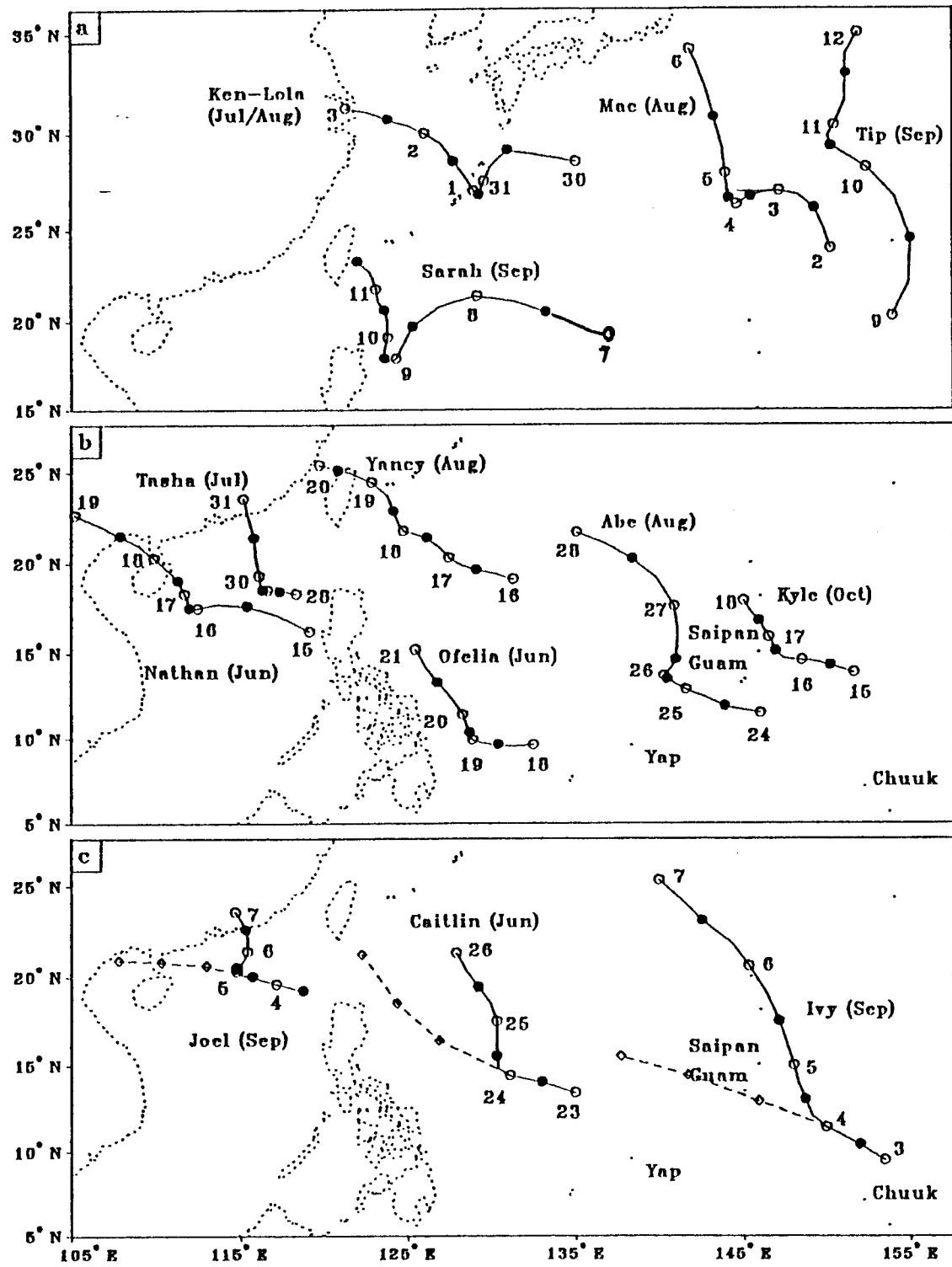


Fig. 3.63. As in Fig. 3.61, except for only 3-4 day track segments centered around all sudden, below-the-ridge tropical cyclone track changes in (a) 1989, (b) 1990, and (c) 1991. The dashed lines are JTWC track forecasts with the 24-, 48-, and 72-h positions denoted by diamonds (Carr and Elsberry 1995).

southwesterly flow located to the south and east of the TC (cf., ATCR descriptions of Tasha and Abe in 1990). This enhanced southwesterly flow may persist for several days. Although JTWC forecasters have applied a number of labels to the phenomenon, the term monsoon surge was adopted by Carr and Elsberry. It should be noted that the term monsoon surge has also been applied by Guard (1985) to describe the deep and persistent southwesterly flow associated with broad convective bands that extend equatorward from large TCs that transit the Philippine Sea during the middle of the typhoon season. However, the examples that Guard cited did not exhibit anomalous movement of the TC.

The monsoon surge associated with a sudden TC track change is accompanied by low-level winds that routinely exceed gale force ( $17 \text{ m s}^{-1}$ ) over a large area. As Typhoon Hal underwent its track change 730 km north of Guam (Fig. 3.61), enhanced southwesterly flow with gusts to  $20 \text{ m s}^{-1}$  resulted in power outages and minor property damage on the island. JTWC forecasters composited surface observations over a 60-h period preceding the track change of Typhoon Orchid in 1980 (Fig. 3.64a). The low-level structure of the monsoon surge was analyzed as a broad comma-shaped area with greater than gale-force winds that wrapped around the east side of the typhoon, and that was apparently distinct from the high winds of the typhoon (Fig. 3.64b). Since sustained gale-force winds generate fully-arisen seas of 7 m, monsoon surge gale areas associated with sudden tropical cyclone track changes represent a hazard to shipping.

The monsoon surge track change of Abe (Fig. 3.63b) occurred near enough to the islands of Guam, Chuuk, and Yap that radiosondes were being launched at 6-h intervals, which provided a greater than normal amount of data for analysis. The NOGAPS 500 mb streamline and isotach analyses valid at the peak of the surge over Guam are shown in Fig. 3.65. The surge is manifest at 500 mb as a comma-shaped 30-kt ( $15 \text{ m s}^{-1}$ ) closed isotach wrapped around the east side of Abe. Notice also the presence of what appears to be a  $\beta$ -induced wave train of alternating circulations to the southeast of Abe, similar to those discussed in the previous section in association with the RMT transformation model. This similarity of environment patterns in the vicinity of the TC further reinforces the earlier suggestion that monsoon surge and RMT-type track changes are dynamically-related phenomena.

The convection associated with the monsoon surge gale area is frequently organized into an extensive comma-shaped peripheral cloud mass (PCM) located approximately 500 to 800 km from the TC and separated by a relatively cloud-free dry slot or moat area (Fig. 3.66). The PCM usually forms to the southeast of the TC and migrates cyclonically around the TC and may eventually merge with the TC, as in the case of Abe (Figs. 3.66a-c). Alternately, the PCM may maintain a relative position roughly east to northeast of the TC, as in the case of Nathan (Figs. 3.66d-f). Although the PCM is sometimes absent or too vague to discern without the benefit of hindsight, the tendency for the PCM to appear 1-2 days *before* the sudden poleward turn may offer the forecaster an important tool for anticipating monsoon surge-related track changes.

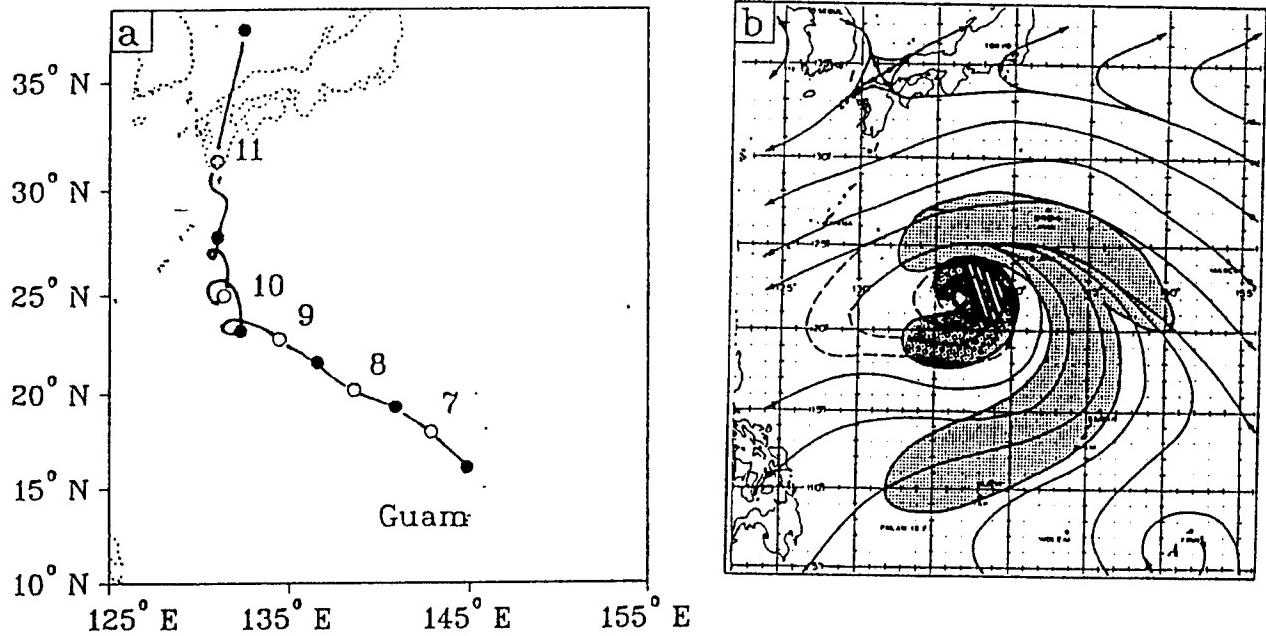


Fig. 3.64. (a) As in Fig. 3.61, except for Typhoon Orchid during September 1980. (b) Streamlines and surface gale areas around Typhoon Orchid as analyzed by JTWC based on composited surface observations from 0000 UTC 7 September to 1200 UTC 9 September 1980 that have been translated to correspond to the position of Orchid at the end of that time interval. The dotted and scalloped shading denotes the gale areas associated with the monsoon surge and Typhoon Orchid, respectively. The striped area denotes the area of maximum winds (from 1990 Annual Tropical Cyclone Report p. 67).

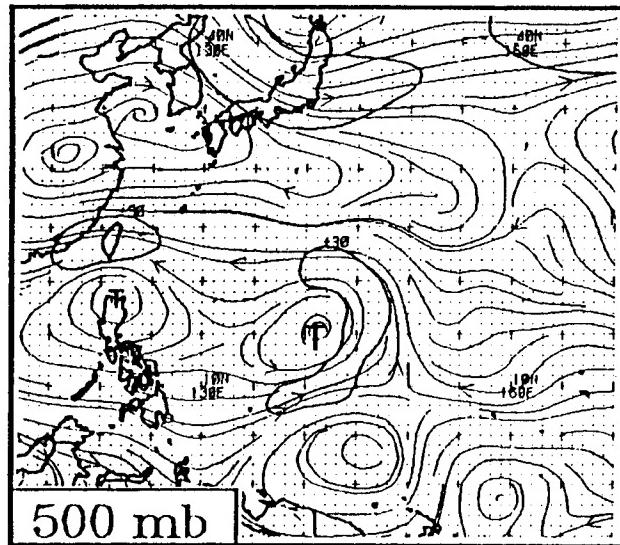


Fig. 3.65. As in Fig. 3.50, except for 1200 UTC 26 August 1990 and JTWC positions for Abe and Becky denoted by large and small T, respectively (Carr and Elsberry 1995).

A post-storm analysis by F. Wells of JTWC (ATCR 1990, pp. 51-52) provides a detailed description of the monsoon surge-type track change of Tropical Storm Nathan (Fig. 3.63b) and offers an explanation for the event. Wells attributed the sudden track change on 16-17 June 1990 to an interaction between Nathan and a synoptic-scale feature that he called a large monsoon cyclone, which has been termed a monsoon gyre (MG) in this report. On 15 June (Fig. 3.67a), the JTWC position for TS Nathan is in a region of troughing in the NOGAPS analysis to the east of the MG that is centered just off the southern coast of Vietnam. A small tropical depression (TD04W; labelled D) is located just to the northeast of the center of the MG. Because of data sparsity and resolution limitations inherent in any global model analysis, a large circulation analyzed in the vicinity of an existing tropical cyclone (in this case TD04W) is usually regarded by forecasters as a smeared-out representation of the tropical cyclone. Based on satellite imagery that indicated TD04W was a particularly small, weak, and shallow feature, Wells took the view that in this case NOGAPS was resolving a bonafide synoptic-scale cyclone.

During 16 and 17 June (Figs. 3.67b-c), the MG and Nathan moved toward each other and merged. On the 18 June (Fig. 3.67d), Nathan moved northwestward over Hainan Island. Based on these observations, Wells interpreted the curved track of Nathan prior to the sudden northward turn as a Fujiwhara-type rotation of Nathan around and into the MG, and attributed the poleward turn to a northward shift of the synoptic environment of Nathan that included the MG. Notice that the NOGAPS 500 mb analyses for Nathan have a closed 30-kt isotach on the southeastern periphery of the coalescing TC and MG (Figs. 3.67b-d) that resembles the Abe case (Fig. 3.65). Notice also that the development of the peripheral high wind region is accompanied by strong ridging to the southeast. In particular, a closed anticyclone is centered just north of the equator at 121°E on 17 June (Fig. 3.67c) that again, as in the case of Abe, appears to be part of a  $\beta$ -induced wave train. Since the cloud signatures of Abe and Nathan were not indicative of a particularly large TC, it would appear that the large circulation of the MG is the likely source of the wave train.

Based on this background, Carr and Elsberry (1995; hereafter CE) hypothesized that a monsoon surge-related TC track change is initiated by a binary interaction of a MG and a TC located to the east. This interaction consists of a rotation of the TC around the MG, followed by a coalescence of the TC with the MG, and also generates strong ridging to the east and southeast due to a nonlinear,  $\beta$ -induced dispersion of the MG. CE further hypothesized that the peripheral ridging generates the monsoon surge winds and produces a southerly steering flow across the center of the interacting MG and TC, and eventually causes northward movement of the coalesced MG/TC.

In view of the insights from the RMT transformation model, the mechanism hypothesized by CE as the impetus for monsoon surge track changes may be viewed as a variant of the southerly steering produced by  $\beta$ -induced peripheral ridge of a large TC. The essential difference is a large TC forms here from the TC-MG merger that absorbs the wind field of the parent MG. As summarized in Appendix G, selected portions from the CE modelling and observational study will serve as the basis for the MG-TC Interaction (MTI)

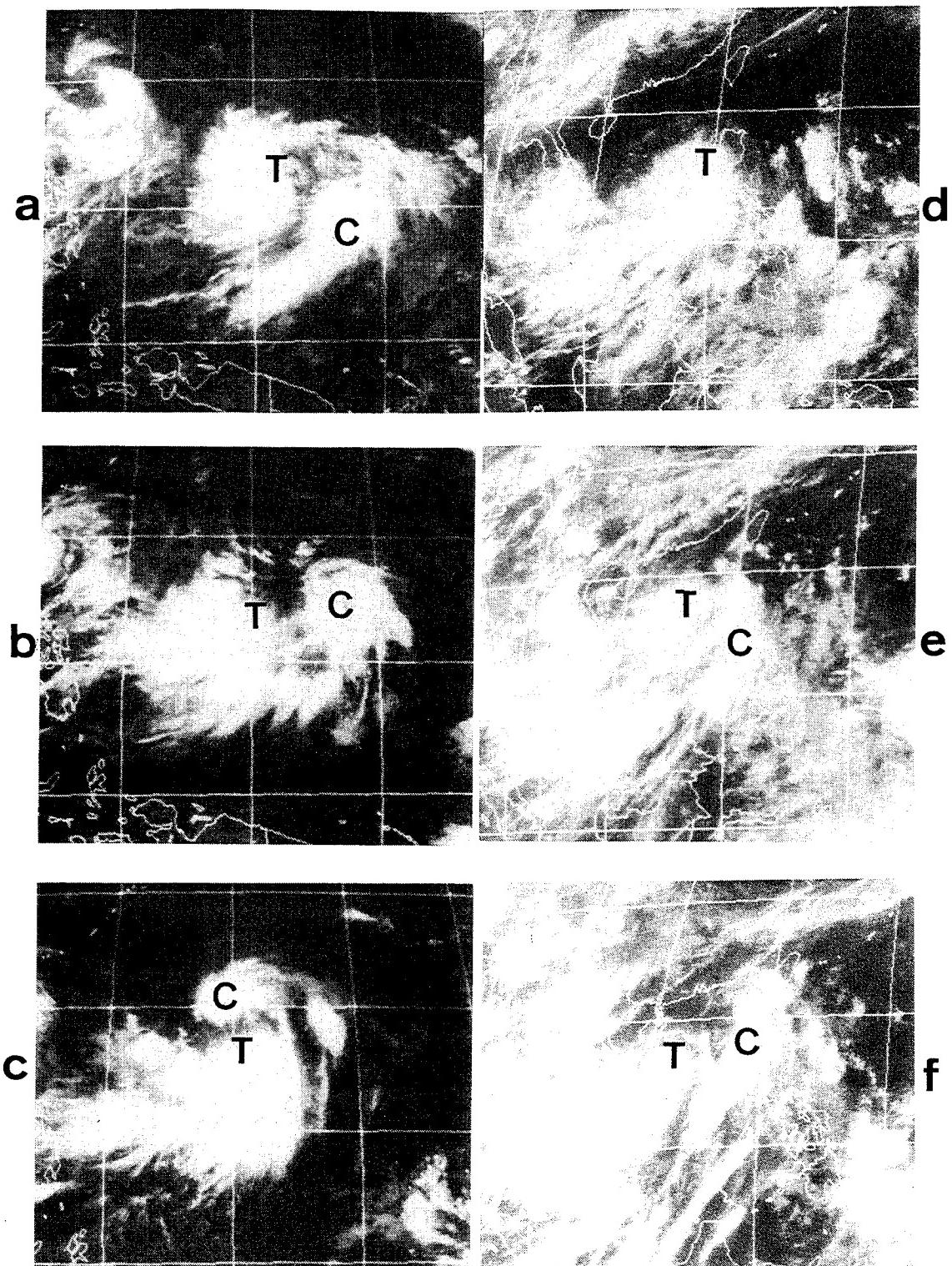


Fig. 3.66. Geostationary infrared imagery of Typhoon Abe (T), and a peripheral cloud band (C) at 2330 UTC on (a) 24 August, (b) 25 August, and (c) 26 August 1990, and of Typhoon Nathan at (d) 0000 UTC 15 June 1990, (e) 1200 UTC 15 June, and 0000 UTC 16 June.

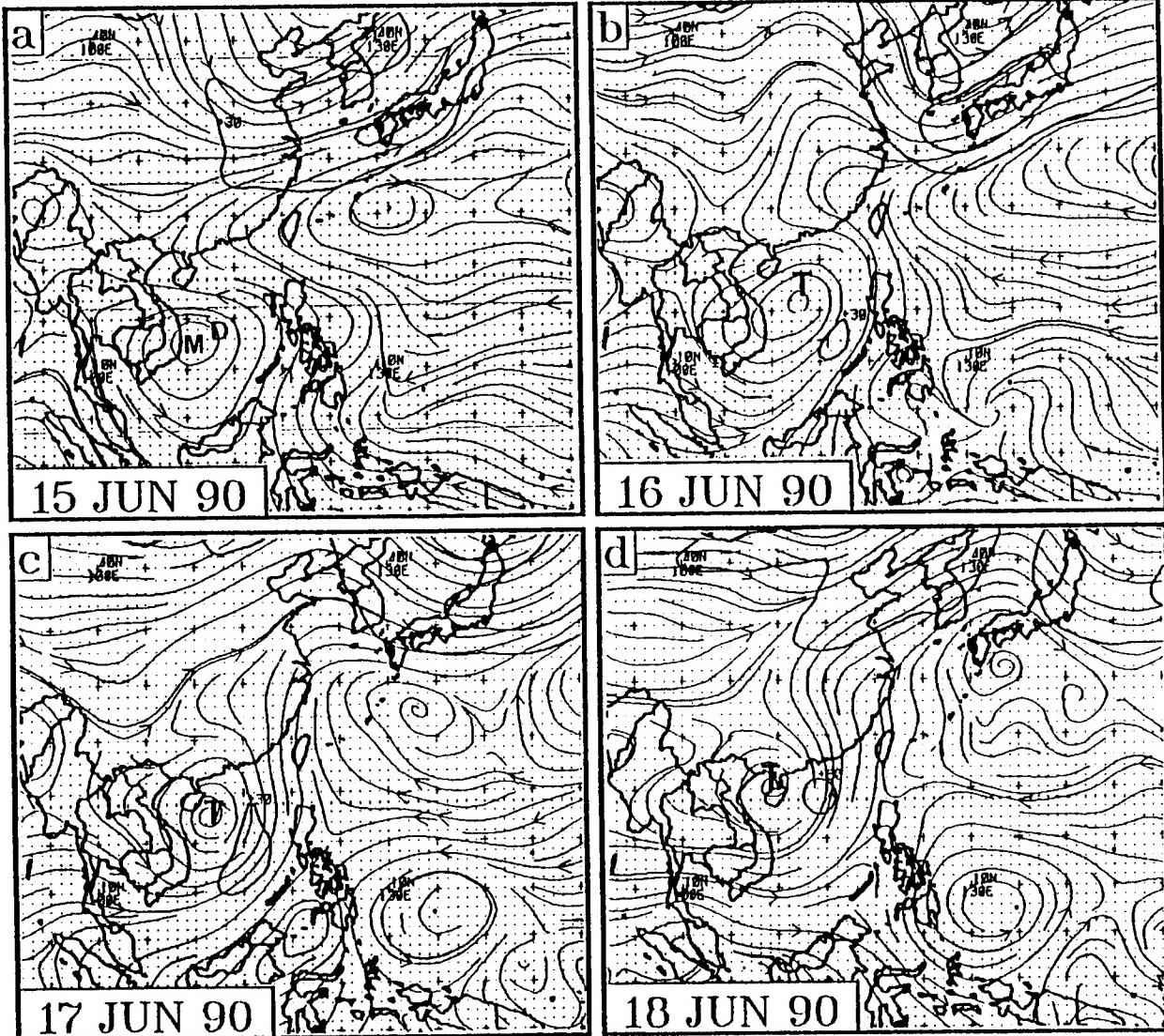


Fig. 3.67. NOGAPS 500 mb streamline and isotach analyses at 0000 UTC on (a) 15 June, (b) 16 June, (c) 17 June, and (d) 18 June 1990. The JTWC best track position of Nathan and Tropical Depression 04W are denoted by T and D, respectively. The center of the NOGAPS-analyzed "large monsoon cyclone" in (a) is denoted by M (Carr and Elsberry 1995).

TC-environment transformation model. The associated TC track changes will be henceforth referred to as MTI track changes.

b) *MTI model description and impact.* Based on the development in Appendix G, the MTI TC-Environment transformation model is comprised of the following elements:

- (i) a 24-36 h initial counter-clockwise rotation of the TC around the center of the MG may be combined with a spiralling inward, so that a TC on the poleward side of the MG may then have an equatorward curving TC track;
- (ii) a coalescence of the TC and MG circulations at about 36-48 h, which results in a quasi-stationary or cyclonic looping of TC motion, and an effective increase in the horizontal extent of the TC circulation;
- (iii) concomitant with (i) and (ii), the development of an enhanced eastern peripheral ridge circulation, which has a position that is controlled by the NVA region trailing the TC as it rotates around and into the MG, and which results in a significant poleward acceleration of the TC subsequent to the quasi-stationary period; and
- (iv) development of a crescent-shaped high wind speed region that: (a) corresponds to the confluent region between the coalescing MG-TC and growing peripheral anticyclone; (b) is distinct from the high wind speed of the coalescing MG-TC; and (c) provides a mechanism for the crescent-shaped peripheral cloud bands that tend to form in this region in MTI situations.

The impact of the MTI transformation process on Environment Structure is illustrated schematically in Fig. 3.68. In a persistent G Pattern in which no MTI transformation occurs, either a NO-to-AW or a NO-to-DR Region transition must eventually take place. However, the effect of the MTI transformation is to preclude these region transitions (denoted by dotted arrows in Fig. 3.68) within the G Pattern, and instead initiate a transition from the NO Region of the G Pattern to the NO Region of the N2 Pattern. After the MTI process has established the N2 Pattern, the southerly flow in the NO Region tends to advect the TC toward the midlatitude westerlies, and thus causes an eventual transition from a NO to a AW Region. A potential feedback loop, as in the RMT-related transitions (Fig. 3.53), that might delay the NO-AW Region transition has been omitted here to account for: (i) the somewhat smaller TC size that may result in a MTI transformation; and (ii) the tendency for the enhanced peripheral ridging that initiates the transition to decay in time, which reduces the likelihood that an anticyclonic cell in the peripheral ridge will translate poleward with the TC in the NO Region, and thus sustain the poleward motion as in the RMT cases.

c) *MTI model illustration.* The MTI conceptual model, and the range of track and associated Environmental Structure changes, will be illustrated with several case studies. Some attention must be given to distinguishing the MTI transformation from the RMT

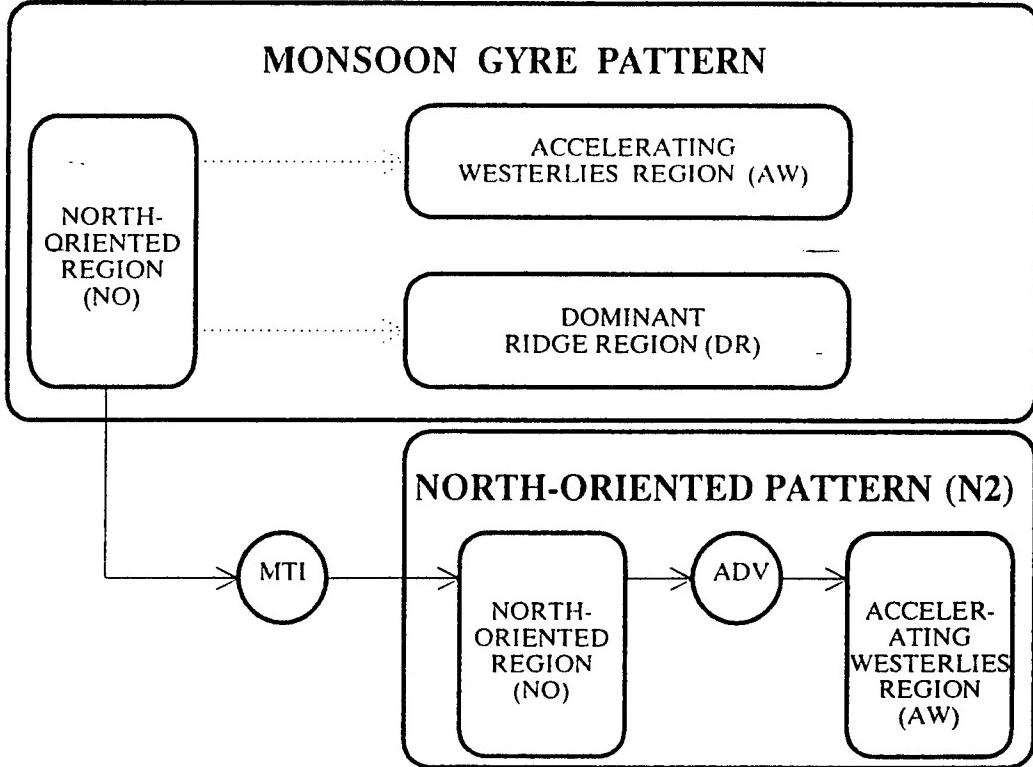


Fig. 3.68. Environment transition from a Dominant Ridge of a Standard Pattern to a North-Oriented Pattern and Region (N2) associated with a Monsoon Gyre-TC Interaction (MTI).

transformation because of the difficulty of real-time detection of some weaker monsoon gyres, and the following observational similarities between the two transformations:

- (i) both involve a large cyclonic circulation; a large TC in the RMT model, and a MG in the MTI model; and
- (ii) both result in an environment transition to the NO Region of a N2 Pattern with an associated poleward track change by the TC owing to development of a strong peripheral anticyclone.

Nevertheless, the TC tracks are different because:

- (i) the MTI case often involves a temporary period of equatorward turning before the sharp poleward turn, whereas the RMT scenario does not; and
- (ii) the RMT involves sustained poleward and eastward motion soon after the poleward turn, whereas the MTI usually involves sustained poleward and westward motion before eventual recurvature.

Because the presence of the MG may not be easily discerned at times, the forecaster must

make careful use of available satellite imagery and data when evaluating NOGAPS fields to distinguish between MTI-related and RMT-related track changes. The cloud signature of the MG, and also the formation of peripheral cloud bands (PCM) in the cases of Abe and Nathan described above, are examples of clues based on satellite imagery. The formation of a PCM alone is not sufficient to permit anticipation of MTI-related track changes, since (as will be seen below) the PCM may be absent or not appear until the track change is in progress.

A MTI-induced G-to-N2 Pattern transition and associated track change occurred with Typhoon Sarah and Tropical Storm Tip within two days during September 1989. On 7 September, Sarah is a weak tropical storm and has just completed a slight dip in a basically westward track (Fig. 3.69a). The corresponding analysis (Fig. 3.70a) has a large cyclone to the southwest of Sarah, and anomalous ridging is located to the southeast of the large cyclone, which is consistent with the G Pattern schematic (Fig. 3.12). However, the evidence from the NOGAPS analysis alone cannot conclusively establish that a G Pattern and associated MG exist. Although, Sarah has been moving from the east-northeast during the 7th, the displacement of Sarah's position from the NOGAPS cyclone center (denoted by M) could be merely a manifestation of the translation-induced shifting of a cyclone center to the left of the direction of motion, as noted previously. In corresponding satellite imagery, Sarah (denoted by the western "T" in Fig. 3.71a) is associated with a rather small convective cloud pattern that is surrounded by an extensive cloud-minimum or "moat" area within a much larger ring of convective activity. This larger cloud ring around a cloud-minimum area is a typical signature of a MG. For example, a similar, but larger scale, cloud ring and moat accompanies the very large MG of a G Pattern in Fig. 3.13. Notice that the analyzed circulation centers at about 18°N, 135°E and 18°N, 130°E in Figs. 3.70a and 3.70b respectively, agree remarkably well with the centroids of the cloud-minimum area within the larger cloud rings in Figs. 3.71a and b, which indicates that NOGAPS is accurately analyzing the position of the MG. Thus, the position displacement for Sarah in the analysis reflects that Sarah is somewhat to the north of the monsoon gyre center. This conclusion is further supported by the systematic change in the relative position for Sarah in the NOGAPS analysis and the infrared cloud pattern on 8 September (Figs. 3.70b and 3.71b). That is, Sarah has rotated cyclonically (Fig. 3.69) with respect to the circulation center in the NOGAPS analysis and the cloud ring in the satellite image. Notice especially the high translation speeds exceeding 20 kt on the 8th, which is consistent with rotation around the north side of a gyre that satellite imagery indicates is translating westward at about 5° lat. per day, or 12 kt (compare Figs. 3.71a and b).

The Sarah case illustrates how insightful interpretation of global model analyses, satellite imagery, and TC motion behavior may be used to detect the presence of a MG and associated G Pattern, and thus alert the forecaster that a MTI-induced TC track change may be in the offing, rather than a RMT-related track change. In particular, the distinctive cloud ring and moat pattern that identifies the MG is not present in the case of RMT-related track changes, because the TC is typically near the center of a convective cloud pattern that is relatively continuous (*i.e.*, moat free).

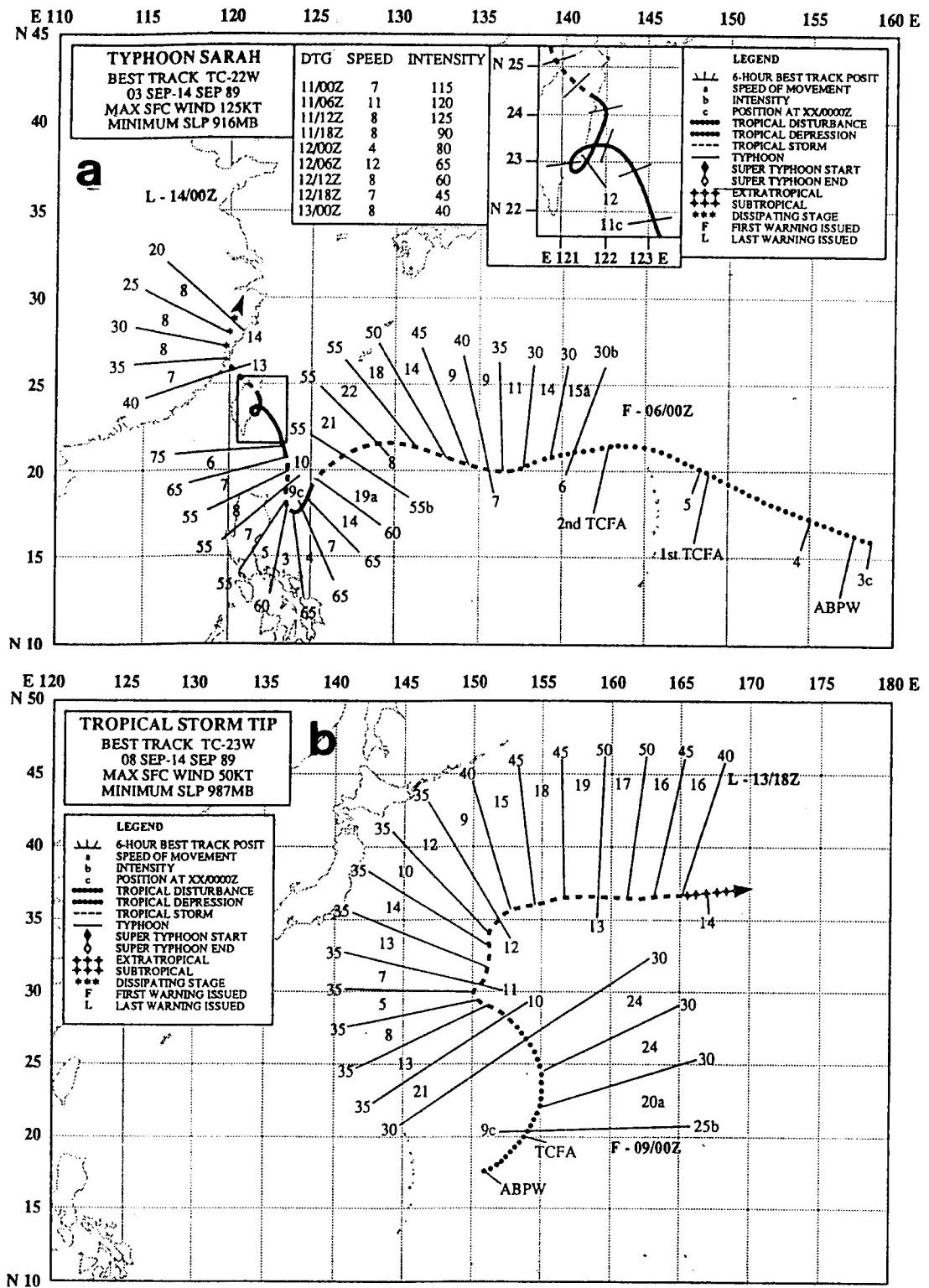


Fig. 3.69. As in Fig. 3.1, except for (a) 3-14 September 1989 during Typhoon Sarah and (b) 8-14 September 1989 during Tropical Storm Tip.

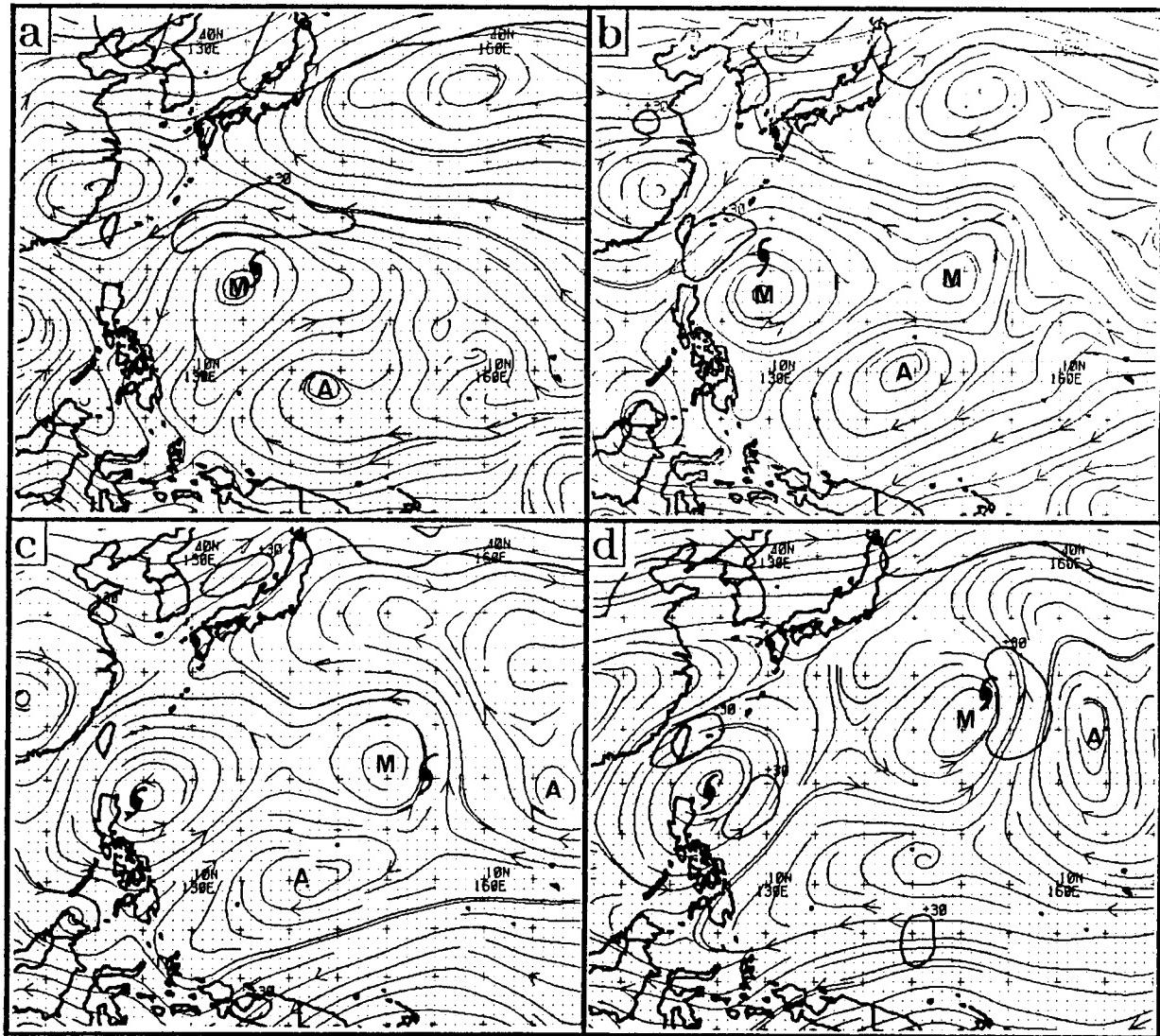


Fig. 3.70. NOGAPS analysis as in Fig. 3.67, except for Typhoon Sarah (western or only TC symbol) and Tropical Storm Tip (eastern TC symbol) at 0000 UTC on (a) 7, (b) 8, (c) 9, (d) 10, (e) 11, and (f) 12 September 1989. Positions of the monsoon gyres for Sarah and Tip and adjacent anticyclones are indicated by M and A, respectively.

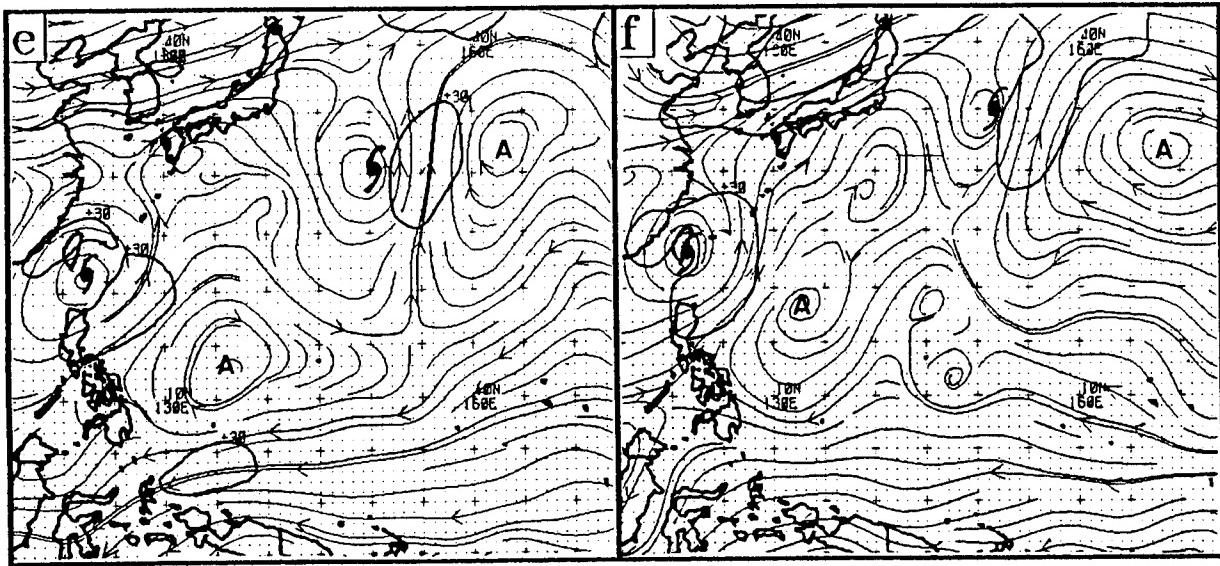


Fig. 3.70. (Continued)

By 0000 UTC 9 September, Sarah has been strongly deflected to the south (Fig. 3.69a), is nearly collocated with the analyzed center of the MG (Fig. 3.70c), and is more centrally situated in the larger cloud pattern that manifests the MG (Fig. 3.71c). All these aspects are consistent with interaction and coalescence of TC Sarah with the MG as in the barotropic simulations. For example, the extreme equatorward deflection in Sarah's track is consistent with the large deflection simulated by the barotropic model for an initial TC position to the north of the MG when interaction commences (Fig. G.7a; Track 4d). One difference in the barotropic simulation from reality is that the TC-MG interaction commences immediately, whereas satellite imagery from as early as 6 September (not shown) shows that Sarah was embedded in, but did not interact strongly with, the MG. This delay in TC-MG interaction in the Sarah case is an illustration of the uncertainty in timing of the MTI transformation process that makes the related TC track changes inherently less predictable. No peripheral cloud band forms to the east of Sarah during coalescence with the MG as would be inferred from the barotropic simulations, perhaps because Sarah was relatively small compared to the size of the large (and presumably drier) moat area of the MG.

During 10 and 11 September, Sarah moves generally northward (Fig. 3.69a), and Sarah remains nearly collocated with the NOGAPS-analyzed center of the MG (Figs. 3.70d and e). During this period, a crescent-shaped 30 kt isotach appears to the southeast and expands, which is consistent with the growth of a peripheral anticyclone in the MTI conceptual model. Enhancement of north-south oriented ridging to the east of Sarah, which should accompany a transition from a G to a N2 Pattern, is rather slow to appear, perhaps

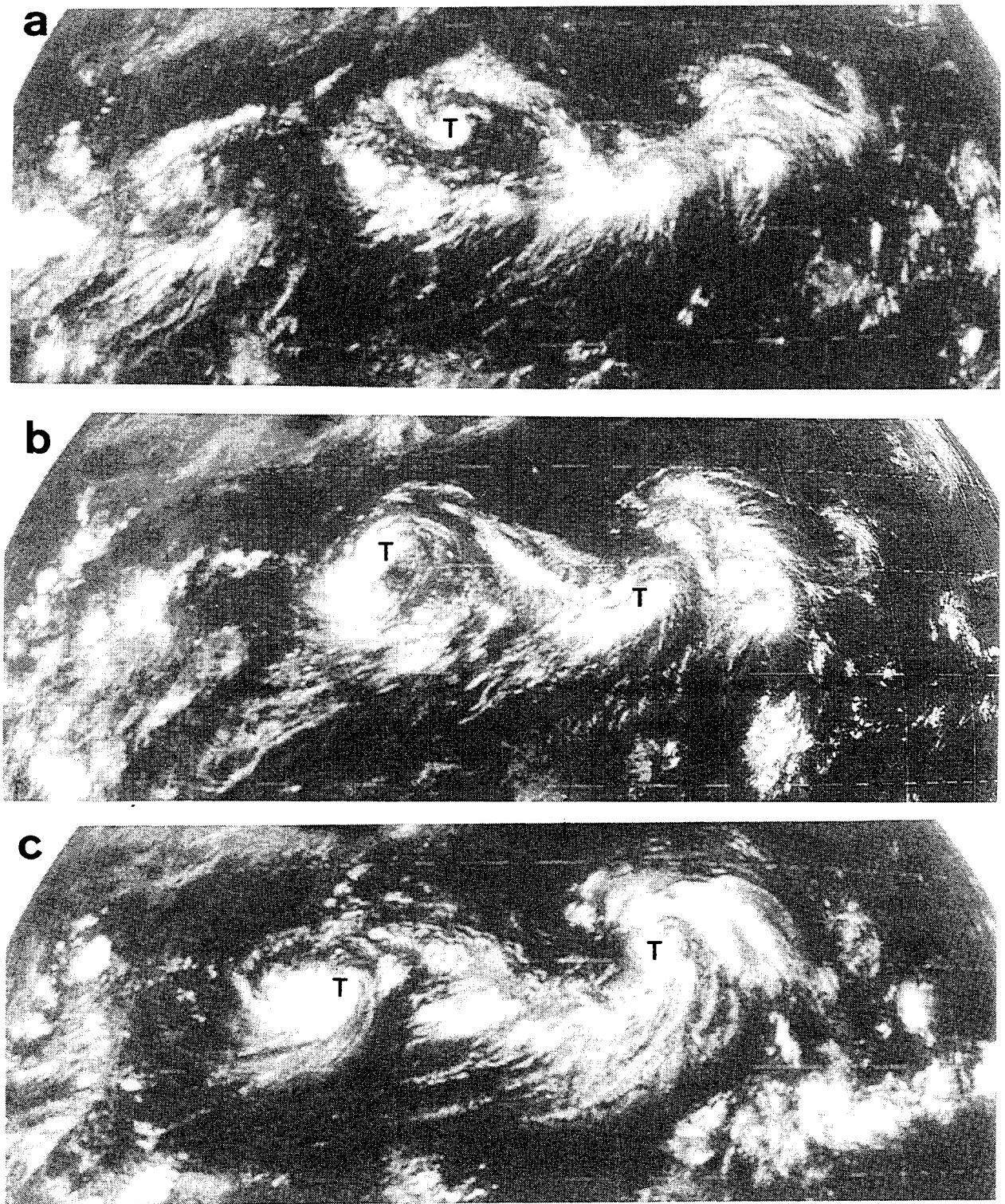


Fig. 3.71. Infrared imagery from GMS at 0300 UTC on (a) 7, (b) 8, (c) 9, (d) 10, and (e) 11 September 1989 during Typhoon Sarah (western T) and Tip (eastern T).

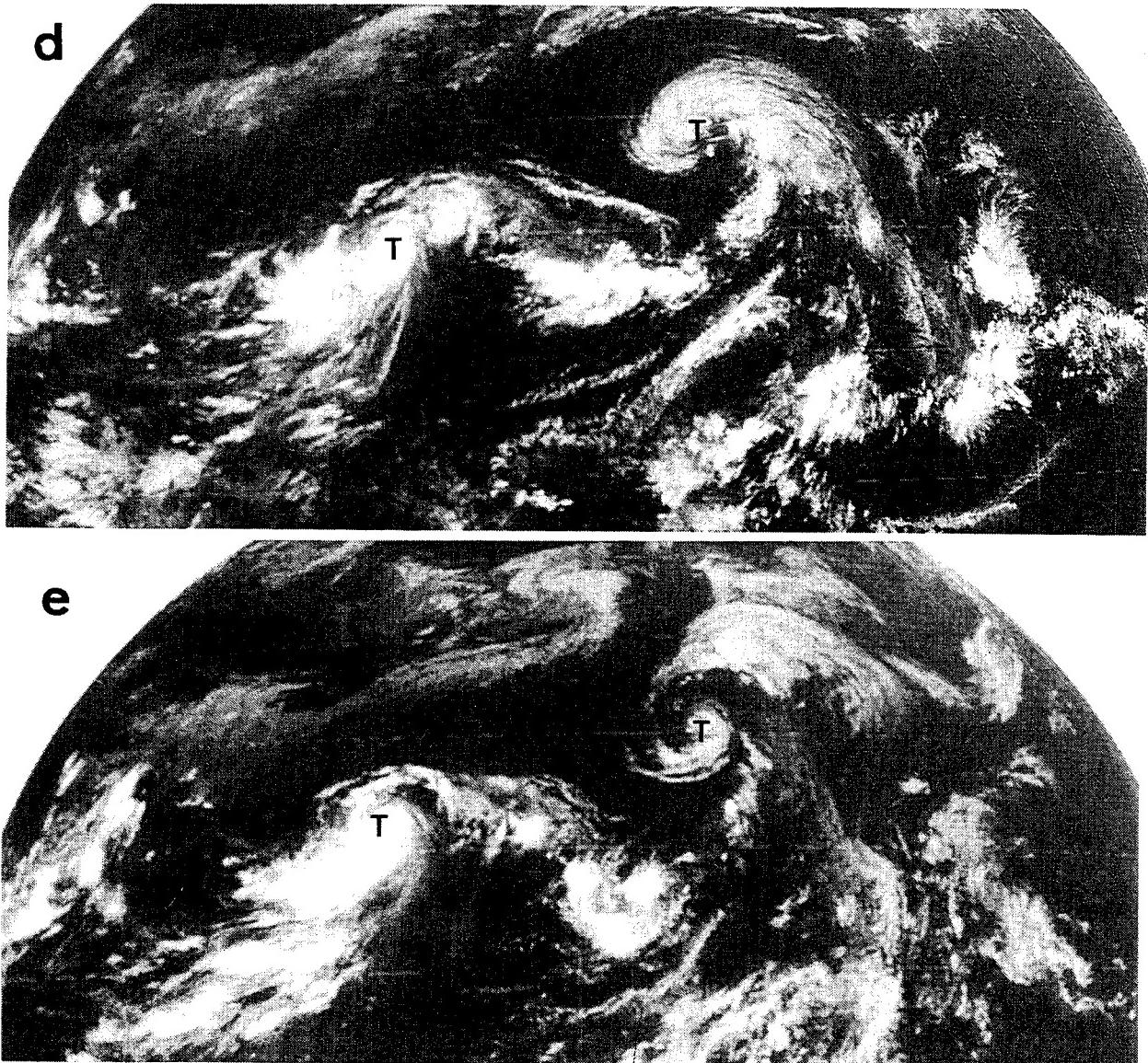


Fig. 3.71. (Continued)

due to the superposition of a second MTI-related G-to-N2 Pattern transition associated with Tropical Storm Tip to the northeast (discussed below). After Tip moves northward, a distinct north-oriented peripheral ridge becomes evident to the east of Sarah in the NOGAPS analysis (Fig. 3.70f). Whereas the cloud pattern of Sarah in the satellite images for 10 and 11 September (Figs. 3.71d-e) indicates Sarah is an average size storm, it is significantly smaller than the size of the MG cloud pattern on 7 September before the MTI transformation occurred (Fig. 3.71a). This difference suggests that considerable energy was lost from the MG circulation, which is consistent with the behavior of the barotropic simulations discussed in Appendix G.

In the case of Tropical Storm Tip, the sustained cyclonically-curved track during 9-10 September (Fig. 3.69b) bears a marked resemblance to the barotropic model track that resulted from an initial TC position south of the MG (Fig. G.7b; Track 4a). The 0000 UTC

9 and 10 September NOGAPS analyses (Figs. 3.70c and d) have the center of the MG circulation to the west-northwest and southwest of Tip, respectively, which is consistent with the motion of Tip at those times. However, the corresponding satellite images (Figs. 3.71c and d) indicate that Tip is forming in a fish-hook cloud pattern that typically wraps around the east side of a MG. Moreover, the center of the cloud minimum area (near 20°N, 150°E) in the satellite image on 9 September agrees well with the center location of the NOGAPS-analyzed circulation in Fig. 3.70c. As in the Sarah case, a combination of global model and satellite imagery interpretation may be used to identify the presence of a MG, and thus the potential for a MTI-related TC track change, perhaps a day before the track change occurs.

During 8 to 10 September (Figs. 3.70b-d), the circulation of the MG associated with Tip steadily develops (eastern M). North-south oriented ridging is evident by 9 September (Fig. 3.70c), which indicates that the G Pattern is fully established. At this time Tip is located about 4° to the east of the MG center, or in the NO Region in agreement with TC symbol #1 in Fig. 3.25. By 0000 UTC 10 September (Fig. 3.70d), peripheral ridge to the east of Tip and the MG has developed further and the subtropical ridge to the north has weakened. Since the magnitude of the peripheral ridge is similar to the subtropical ridge to the north, the structure of the environment in the vicinity of Tip is in a transition state between the G and N2 Patterns. By 0000 UTC 11 September (Fig. 3.70e), collocation of their positions in the NOGAPS analysis indicates that Tip and the MG have coalesced, and Tip is now in the NO Region of a N2 Pattern, which is consistent with the nearly concurrent turn from northwest to northward movement (Fig. 3.69b). A transition to a N2 pattern is further confirmed by the poleward displacement of the peripheral anticyclone from 26°N, 164°E on 10 September to 32°N, 163°N on 11 September (Figs. 3.70d and e, respectively), which is parallel to the movement of Tip. This tendency for the anticyclonic cell to the east of the TC in the NO Region to translate poleward with the TC is one of the defining characteristics of the N2 Pattern.

By 0000 UTC 12 September (Fig. 3.70f), the peripheral anticyclone has not moved any farther north in contrast to the 5° of lat. displacement of Tip (Fig. 3.69b), and the structure of the ridge appears to be losing the distinct north-south orientation that it had 24 h earlier (Fig. 3.70e). At this time, Tip is recurving sharply with a nearly eastward direction of motion (Fig. 3.69b), which indicates that a transition from a NO to a AW Region has occurred relatively quickly. This nearly zonal post-recurvature track of Tip is in distinct contrast to the more north-oriented tracks in the RMT cases, which is an illustration that the peripheral ridging generated by the MTI process is not sustainable, and tends to die away in agreement with the barotropic simulations.

The second case study illustrates the MTI-related track changes of Typhoon Ivy and Tropical Storm Joel, which occurred within one day during September 1991. Because the important aspects of the MTI scenario have been covered in the Sarah/Tip case, a more abbreviated discussion will be given of the Ivy/Joel case. In the Ivy case, the MTI-related poleward track change occurs during 4 September (Fig. 3.72a), and is more gradual and of a lesser magnitude than the majority of track changes shown in Figs. 3.63a-c. Furthermore,

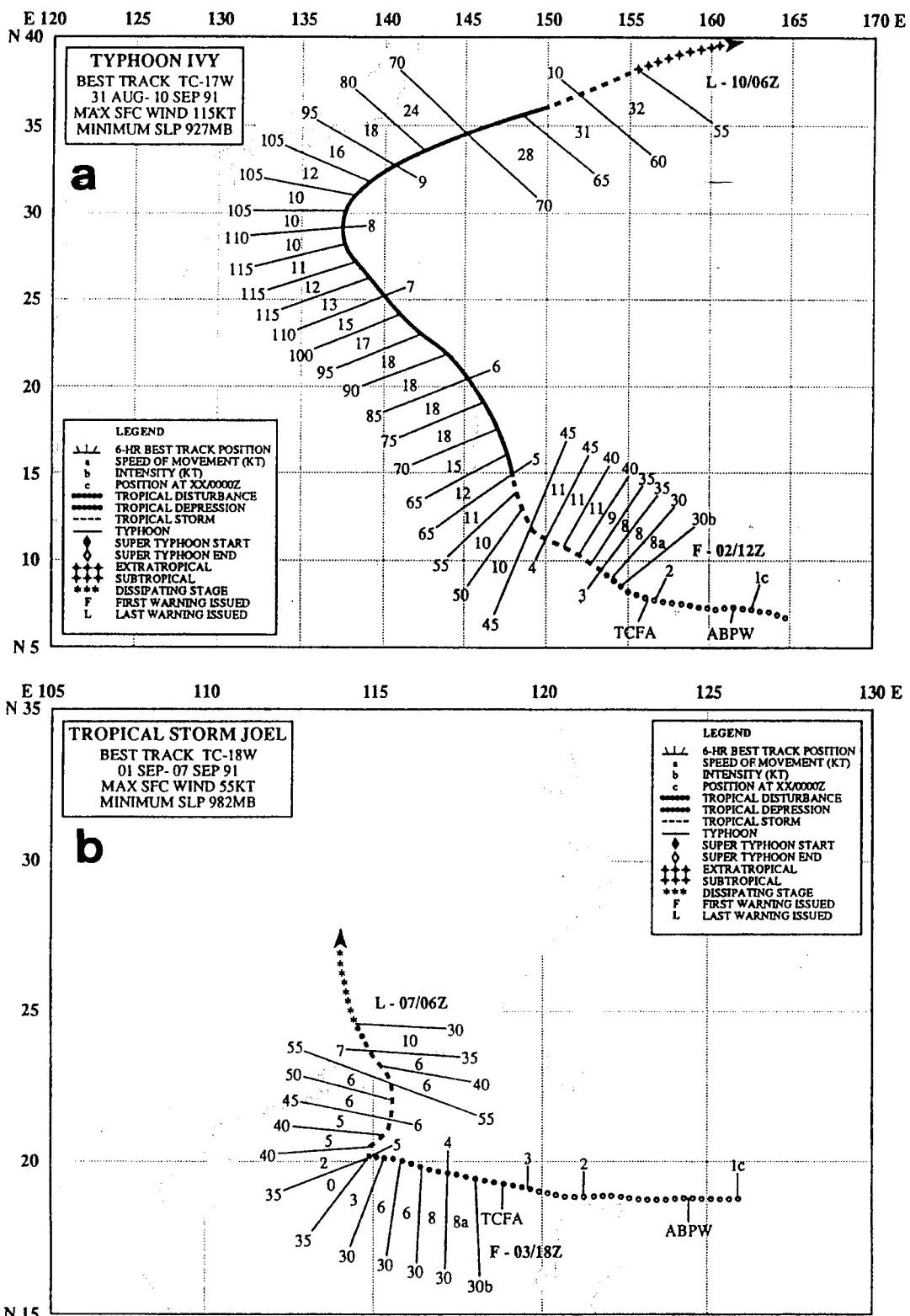


Fig. 3.72. As in Fig. 3.1, except for (a) 31 August to 10 September 1991 during Typhoon Ivy, and (b) 1 September to 7 September 1991 during Tropical Storm Joel.

the post-MTI track direction of Ivy turns from north-northwest to northwest before eventual recurvature during 8 September. The 0000 UTC analyses during 3-8 September (Figs. 3.73a-f) indicate that Ivy appeared to interact, but not fully coalesce, with the associated MG. This contention is based on the northeast-southwest elongation of the NOGAPS-analyzed circulation in Figs. 3.73a-e, and in a second circulation center at about 5°N, 136°E and 9°N, 134°E in Figs. 3.73c and 3.73e, respectively.

Convective cloud patterns in the vicinity of Ivy during 3-6 September (Figs. 3.74a-d) tend to confirm that Ivy interacted, but did not fully coalesce, with a MG. In Figs. 3.74a-c, the cloud pattern associated with Ivy is located on the eastern side of a larger cloud pattern. On 4 September (Fig. 3.74b), a ring of convection (similar to that with Sarah in Fig. 3.71a) appears to the west of Ivy with an enclosed cloud-minimum area centered at about 8°N, 140°E. This location agrees quite well with the southwestward elongation of the NOGAPS-analyzed cyclonic circulation in Fig. 3.73b, and confirms the presence of a MG. During the following two days, the cloud pattern of Ivy never becomes centrally located in the MG-related pattern of convection (Figs. 3.74c-d). By 6 September, Ivy is completely separate from the convection to the southwest that manifests the MG.

At first glance, the cyclonically-curved track of Ivy during 5-7 September (Fig. 3.72a) might be attributed to a simple advection around the MG of a persistent G Pattern. However, the significant growth of the peripheral ridge to the east of Ivy (Figs. 3.73c-e) provides strong evidence that the circulation of Ivy did interact nonlinearly with the MG, and likely generated strong NVA. Thus, Ivy represents an example of a rather weak MTI process that did not cause a definitive G-to-N2 Pattern transition, but rather resulted in an environment structure that has elements of both the G Pattern (*i.e.*, MG remained distinct) and N2 Pattern (*i.e.*, robust growth of anomalous ridge to the east, and erosion of the ridge to the north). A thorough investigation of the frequency of an Ivy-type MTI scenario has not been conducted. However, Ivy was the only case that did not involving complete TC-MG coalescence of the 14 MTI track changes that occurred in the western North Pacific during 1989-1991 (Figs. 3.63a-c), which suggests that the Ivy scenario is unusual.

Although the NOGAPS analyses during 4-6 September (Figs. 3.73b-d) have an increasingly strong peripheral ridge developing to the east of Ivy, it is not until 7 September (Fig. 3.73e) that the environment of Ivy takes on the appearance of a N2 Pattern. Thus, the transition occurred rather slowly in this case, which is consistent with Ivy's sustained northwestward track after the initial poleward turn, as opposed to more northward track in most of the cases in Fig. 3.63. Notice in the 7 and 8 September analyses (Figs. 3.73e-f) that the center of the anticyclone to the east has not followed Ivy north, which indicates that the peripheral ridging effect arising from the MTI process weakened as it did in the Tip case. As a result, the post-recurvature acceleration of Ivy is not delayed and the post-recurvature direction of movement is more eastward than poleward.

In the case of Ivy, a very distinct peripheral cloud mass (PCM) does develop to the southeast, but not until more than one day after the initial poleward motion has taken place

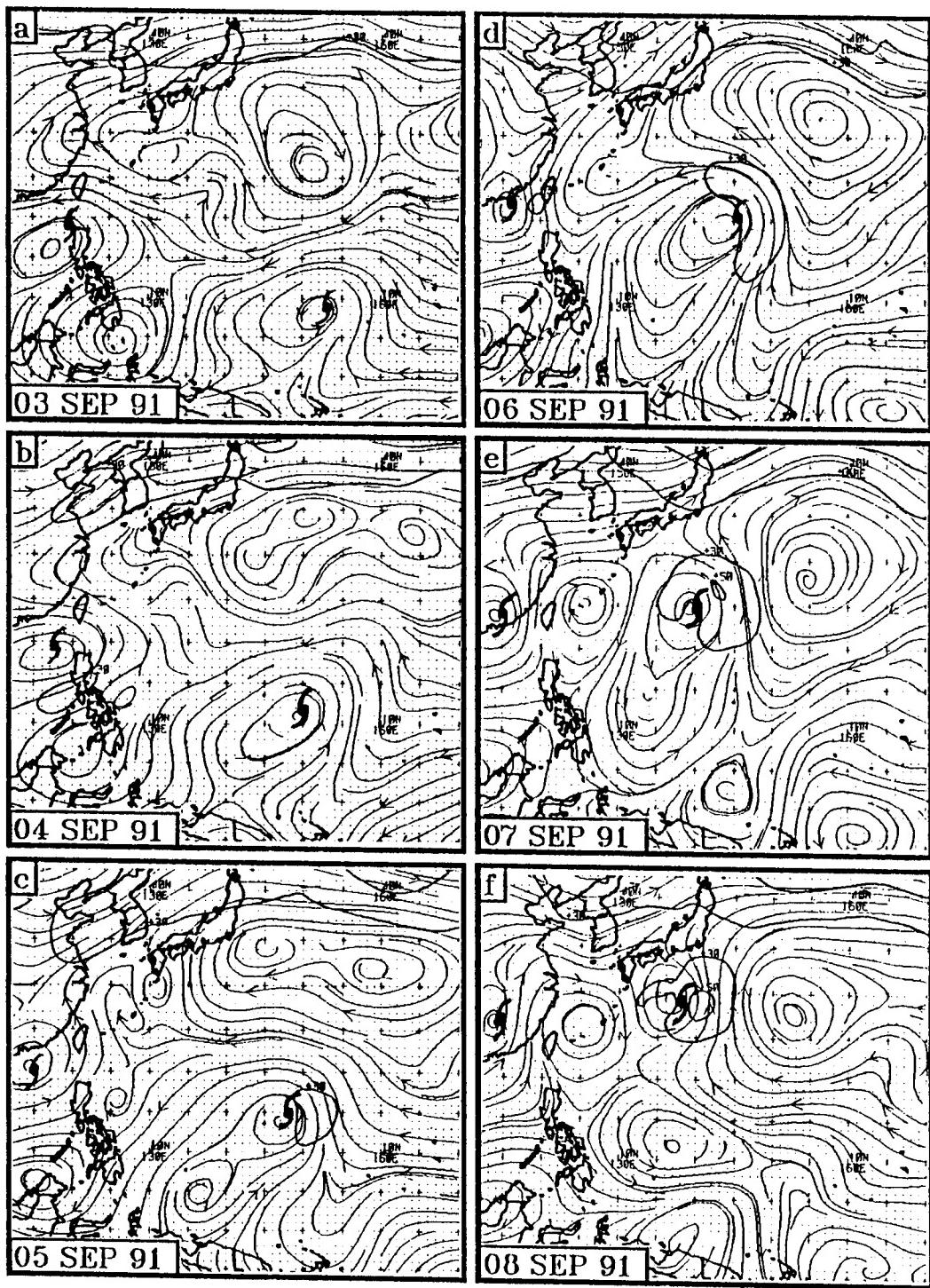


Fig. 3.73. As in Fig. 3.67, except at 0000 UTC for (a) 3, (b) 4, (c) 5, (d) 6, (e) 7, and (f) 8 September 1991 during Typhoon Ivy (eastern) and Tropical Storm Joel (western).

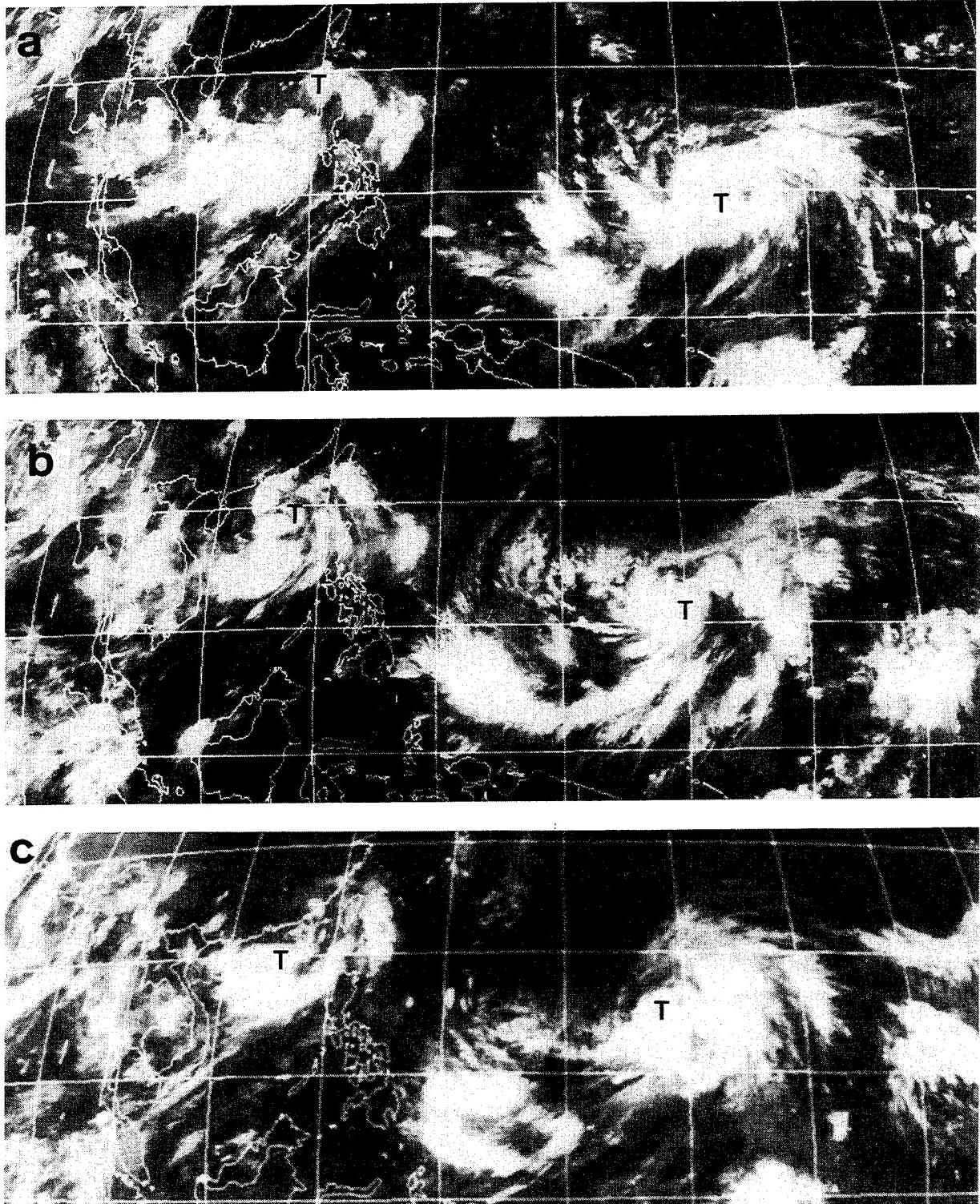


Fig. 3.74. Infrared imagery from GMS at 0000 UTC on (a) 3, (b) 4, (c) 5, and (d) 6 September 1991 during Typhoon Ivy (eastern T) and Tropical Storm Joel (western T).

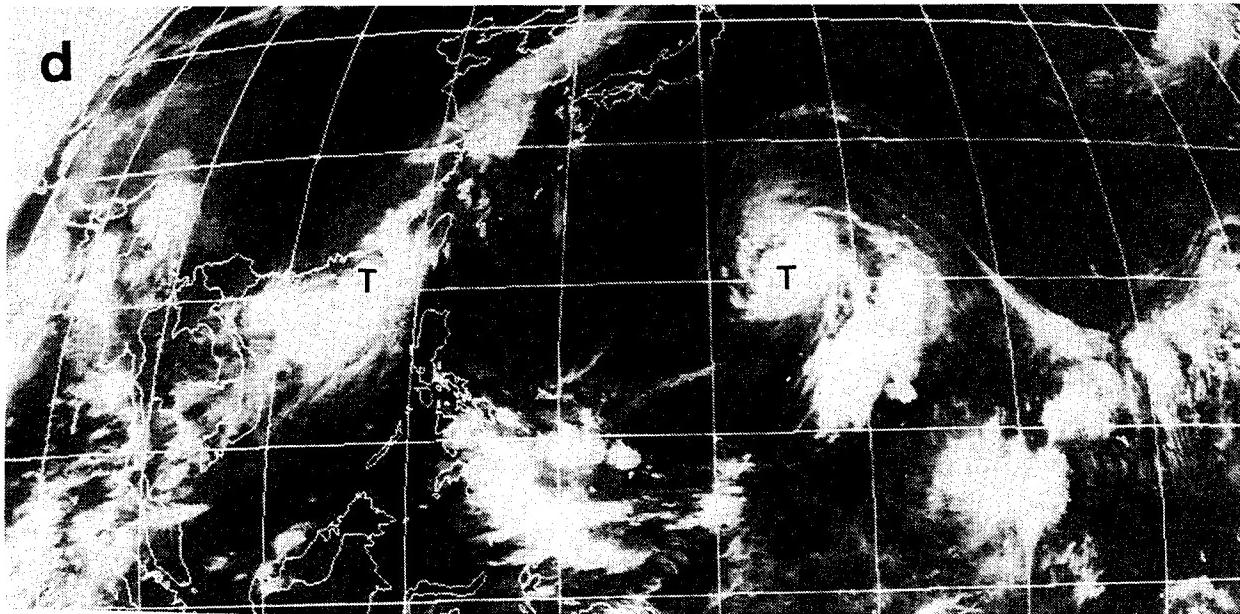


Fig. 3.74. (Continued)

(Fig. 3.74d). Although such a delayed development of the PCM thus has no prognostic utility to the forecaster, its appearance would be useful during post-storm review and analysis to identify properly that the track of Ivy resulted from a MTI scenario.

The final case of Joel conforms to the MTI conceptual model in almost every respect. At 0000 UTC 3 September, Joel is a tropical depression just to the northwest of Luzon and is traveling westward (Fig. 3.72b). The corresponding NOGAPS analysis has Joel on the northeast side of a MG over the South China Sea (Fig. 3.73a), and the corresponding satellite image (Fig. 3.74a) has the rather small cloud mass of Joel embedded on the eastern side of a large convective cloud pattern associated with the MG. At 0000 UTC 4 September, which is one day before the sudden poleward turn, Joel is collocated with the analyzed MG (Fig. 3.73b), and is also more centrally located in the large convection cloud pattern of the MG (Fig. 3.74b), which indicates that coalescence has occurred. Notice also the peripheral cloud bands to the east of Joel that subsequently maintain the same position relative to Joel for the following two days (Figs. 3.74c-d), during which time the MTI track change occurs (Fig. 3.72b). At 0000 UTC 5 September, the NOGAPS analysis has a north-oriented ridge to the east of Joel, which is consistent with a region of increasingly suppressed cloudiness to the southeast of Joel and the accompanying peripheral cloud bands in Figs. 3.74b-d.

**5) Tropical Cyclone Interactions (TCIs).** The only model that has been available to the TC forecaster for understanding binary TC interaction is the classical Fujiwhara effect (Fujiwhara 1923), which predicts the cyclonic relative rotation and possible merger of any two cyclonic vortices as a result of mutual advection by the circulations of the two cyclones. Recent research (Lander and Holland 1993; Ritchie and Holland 1993; Holland and Dietachmayer 1993) has identified some necessary modifications of the classical model when considering TCs, such as a low probability of merger, the importance of shearing

deformation as well as simple advection by the interacting TCs, and the role of variable Coriolis. Such modifications notwithstanding, the updated Fujiwhara model of TC interaction (hereafter referred to as binary TC interaction) still views the cyclonic relative rotation as essentially arising from mutual advection by the two TC circulations.

Because of the high frequency and clustering in time of TC activity during the height of the western North Pacific season, two or more TCs often exist in close proximity, and routinely appear to undergo cyclonic relative rotation (Brand 1970; Dong and Neumann 1983). Thus, the binary TC interaction model is frequently invoked as the operative mechanism by JTWC forecaster in ATCR discussions. Two examples are Typhoons Owen and Nancy in 1989 (Fig. 3.75) and Typhoons Odessa and Pat in 1985 (Fig. 3.76). Diagrams showing periods of cyclonic rotation of the TC pair relative to the midpoints between them are often constructed (Fig. 3.75b and 3.76b). Since the period of cyclonic rotation is often preceded and followed by rapid changes (called "capture" and "escape" by Lander and Holland 1993) in relative motion (e.g., Fig. 3.75b), these relative motion diagrams are essentially viewed as confirmation that mutual advection (i.e., binary TC interaction) was the impetus for the observed relative rotation of the TCs. However, the Multiple TC (M) Synoptic Pattern and the associated Northerly Flow (NF) and Southerly Flow (SF) Synoptic Regions are one circumstance in which the appearance of a cyclonic relative rotation of TCs may occur at distances that make binary TC interaction virtually impossible.

An analysis of TC tracks, NOGAPS fields, and satellite imagery for a number of cases in which cyclonic relative rotation occurred has led the authors to question such an attribution to binary TC interaction. In most cases, the combination of separation distance and small size of one or both of the TCs makes the possibility of mutual advection by the TC circulations highly unlikely. Instead, our analysis suggested other mechanisms including, but not limited to, the M Synoptic Pattern scenarios. Detailed analysis of unusual TC track segments has revealed that the  $\beta$ -induced peripheral ridges generated by larger TCs also can influence the track of a second TC in ways that may not involve cyclonic relative rotation. Based on the BEP transformation model, the temporary equatorward dips in the tracks of Mireille and Percy (Fig. 3.23a and b, respectively) appear to have been a result of peripheral ridging from Tropical Storm Luke and Typhoon Ofelia, respectively.

Consequently, the authors propose that the concept of TC interaction should be expanded from a single-mode explanation based on a mutual advection by the TC circulations to a suite of TC interaction modes. The examples in this section will indicate deficiencies of the Fujiwhara-type model, and propose other mechanisms that the authors believe are more important than the Fujiwhara effect for characterizing the observed interactions of TCs. As with the other TC-environment transformation models, this proposal is based on work by the authors that is not yet published.

a) TC Interaction (TCI) models description and impact. The TCI transformation conceptual model is comprised of six distinct modes by which the motion of a TC can be influenced by another TC, and which may occur singly or in concert. Listed roughly by

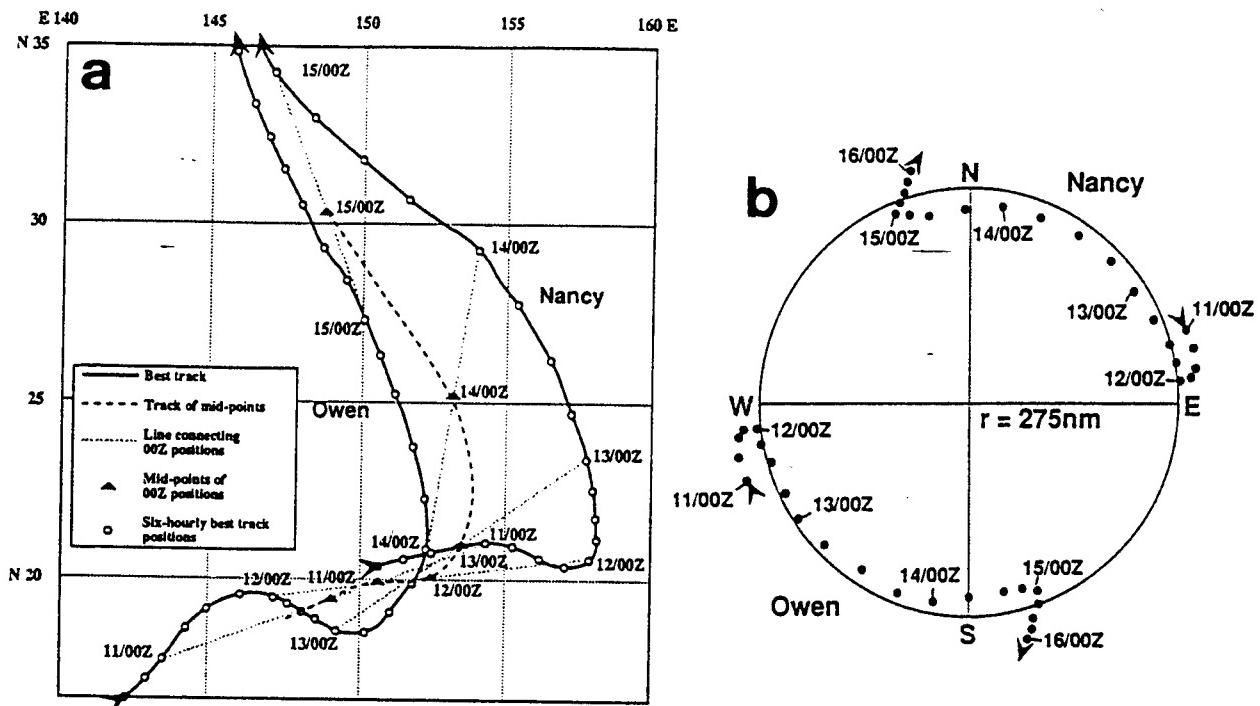


Fig. 3.75. (a) JTWC best tracks (solid) of Typhoons Owen and Nancy during 11-16 August 1989, and track (dashed) of the midpoints (triangles) of connecting lines (dots) between the TCs at corresponding times. (b) Positions of Owen and Nancy relative to the midpoints during the same period as in (a).

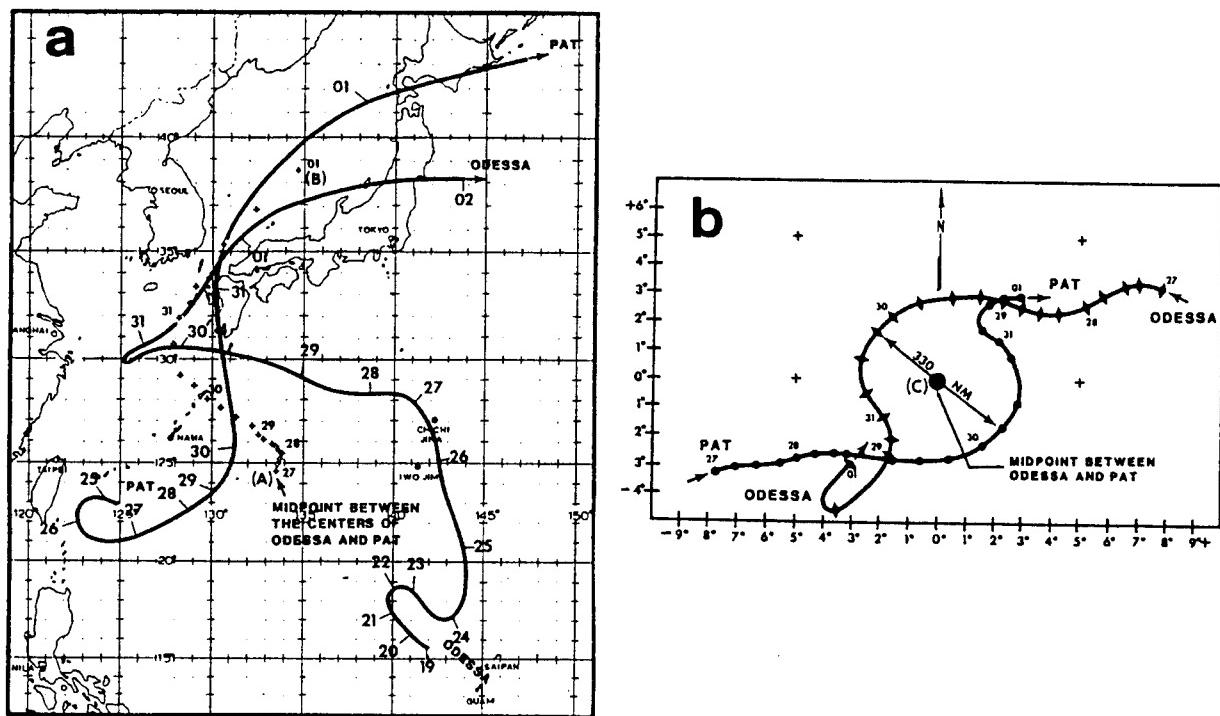


Fig. 3.76. As in Fig. 3.75, except for Typhoons Odessa and Pat in August/September 1985. In (a) the midpoint positions are denoted by asterisks beginning with 0000 UTC 27 August.

decreasing frequency of occurrence, these TCI modes are:

- (i) Establishment of a M Synoptic Pattern (TCI1). Near-simultaneous formation, or the approach of another TC within a distance from  $12^{\circ}$  to  $20^{\circ}$  lat., may establish a M pattern subject to the stipulations in Section 3.a.1. The TC is then subjected to the steering of the Northerly Flow (NF) Region or the Southerly Flow (SF) Region, which tends to inhibit or promote recurvature, respectively.
- (ii) One-way pseudo-binary influence (TCI2). A one-way influence occurs when the cyclonic circulation of a large TC advects the circulation of a significantly smaller TC. A distinction is made here from a true *interaction* in which the second (in this case, the smaller) TC would either advect or deform the first (larger) TC.
- (iii) Steering by the  $\beta$ -induced anticyclone of another TC (TCI3). The influence of the  $\beta$ -induced peripheral anticyclone of a large TC (or sometimes average size) alters the steering of another TC. Although this may result if the second TC is either east or west of the large TC, the second TC is more frequently found to the east.
- (iv) Modification of  $\beta$ -induced anticyclone of TC (TCI4). The self-induced track direction or speed modification of a large (or sometimes average size) TC associated with the development of a peripheral anticyclone is forestalled or is weakened by influence of the cyclonic circulation of another TC to the southeast or east. A typical result is that the western TC does not gain latitude as expected.
- (v) Advection of two TCs embedded in a MG (TCI5). Two TCs at different positions in a large, intense monsoon gyre of a G Synoptic Pattern may have a relative cyclonic rotation as they are advected by the circulation of the MG and its associated peripheral anticyclone. In some cases, the presence of the TC convection and associated descent may contribute to development of the MG, or at least to the maintenance of the MG, and thus prolong its existence.
- (vi) True binary TC interaction (TCI6). In contrast to (ii) above, the term *interaction* requires that the cyclonic circulations of two TCs undergo cyclonic relative rotation (and merger on rare occasions) due to mutual advection and deformation.

As with the BEP, VWS, RMT, and MTI conceptual models, these various modes of TCI may cause a transition to another Synoptic Pattern or Synoptic Region, or in some circumstances, hinder such transitions. Each of the other transformation models tended to have fairly well-defined Region or Pattern/Region transitions (i.e., Figs. 3.38, 3.46, 3.52, and 3.68 for the BEP, VWS, RMT, and MTI models, respectively). The TCI1 mode, which involves the establishment of a M Pattern with its Northerly Flow (NF) and Southerly Flow (SF) Regions, must inevitably result in an Environment Structure transition. The presence of a sufficiently close, and properly positioned, TC to the east (see Fig. 3.77) causes a transition of the Environmental Structure for the western TC from either the DR or WR

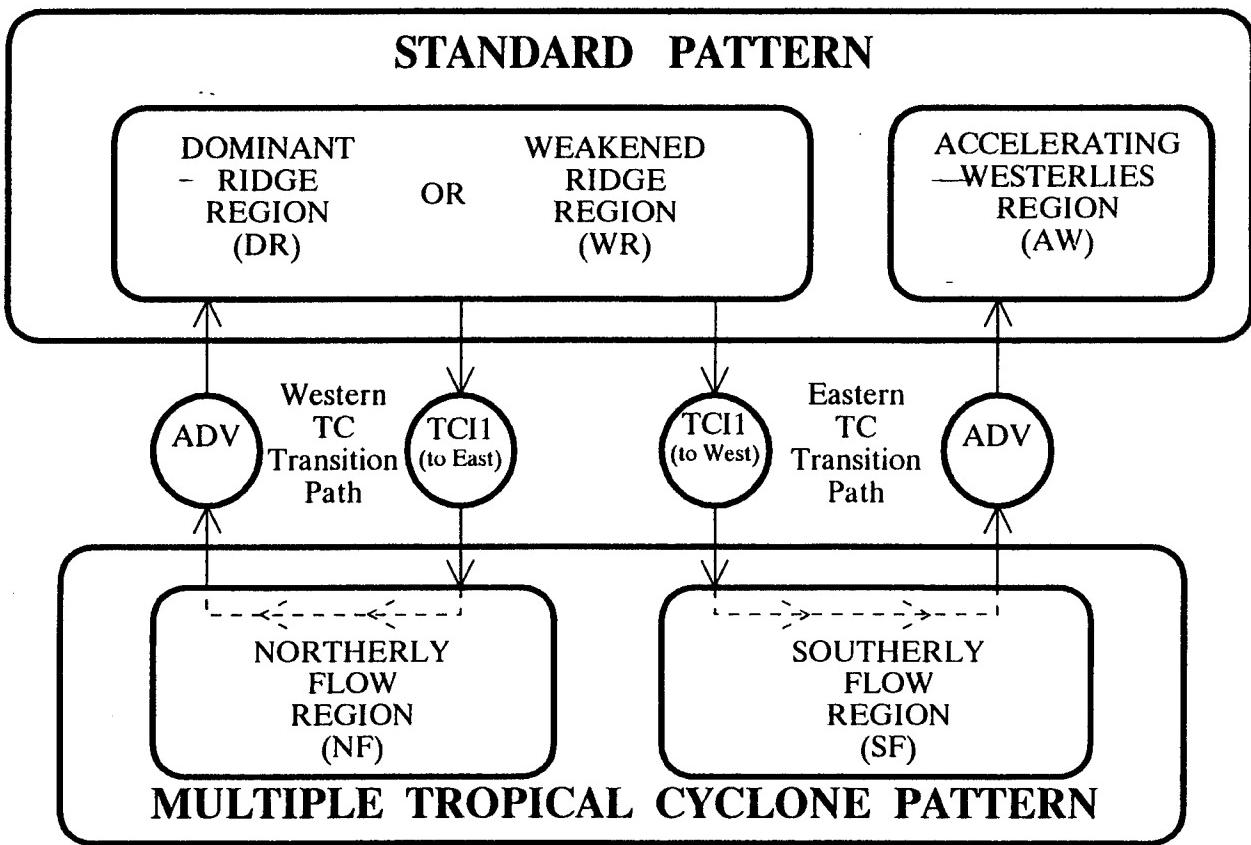


Fig. 3.77. Schematic of Environment Structure transitions between the S and M Patterns arising from the TCI1 transformation and differential advection (ADV) in the M Pattern.

Region in a S Pattern to the NF Region of the M Pattern. Conversely, the presence of a sufficiently close, and properly positioned, TC to the west (see Fig. 3.77) causes an Environment transition from either a DR or WR Region in a S Pattern to the SF Region of the M Pattern. Such a M Pattern will not be maintained indefinitely because the effect of the advection (denoted ADV in Fig. 3.77) must eventually increase the TC separation as the eastern TC moves poleward through the ridge and the western TC tends to move west and equatorward. That is, the environment of the eastern TC transitions from the SF Region in the M Pattern to the AW Region of a S Pattern, and the environment of the western TC transitions back to the DR or (less likely) the WR Region of a S Pattern.

The effects on TC motion of the TCI2-TCI6 transformation models are quite variable and may or may not result in environment transitions depending on such factors as: (i) the relative sizes of the TCs; (ii) the structure of the environment; (iii) the number of TCs; and (iv) the positions of the TCs relative to each other and the environment. As a result, the simplified schematics such as Fig. 3.77 are not always practical. Rather, five case studies

will be used to assist the forecaster in anticipating certain types of TC motion in response to various TCI modes.

b) TCI model illustrations. The case studies below are roughly arranged in order of increasing complexity. Whereas the first situations involve only two TCs and only one major TCI mode, the more complex cases involve significant contributions to TC motion by two or more TCI modes and more than two TCs.

**1. Case Study #1.** This case study involves Supertyphoon Seth and Tropical Storm Verne in November 1991. The primary purpose of this study is to illustrate the TCI1 mode, which results in the establishment of a M Pattern and associated TC motion that conform rather well to the conceptual model, and which takes place with minimal complications from external factors. Despite a separation distance too large for bonafide binary interaction (TCI6) to occur, the relative motion pattern exhibited by Seth and Verne has many of the characteristics normally attributed to binary interaction.

From 0000 UTC 2 November to 0000 UTC 5 November, Supertyphoon Seth is steadily moving out of the deep tropics on a heading of  $300^{\circ}$  (Fig. 3.78a). The corresponding NOGAPS analyses (Figs. 3.79a-d) suggest Seth is tracking through the DR Region and into the WR Region of a S Pattern, which is consistent with Seth's steady 11-kt translation early in the period, followed by a deceleration beginning late on 4 November (Fig. 3.78a). A peripheral anticyclone of moderate size is analyzed southeast of Seth (e.g., Fig. 3.79c), which is indicative of significant BEP speed and consistent with Seth's relatively rapid latitude gain (recall Fig. 3.39). The somewhat smaller size of the peripheral anticyclone relative to the subtropical ridge circulation on the poleward side does not seem to represent a potential RMT transformation. Rather, the peripheral anticyclone seems to be merely contributing to the BEP that should bring Seth to the subtropical ridge axis and imminent recurvature in about a day or so.

The inverted trough in the lower right corner of Figs. 3.79c-d appears to be a part of Seth's  $\beta$ -induced wavetrain, and represents a potential region for TC formation. NOGAPS analyses during 6 November through 9 November (Figs. 3.80a-d) do indicate Verne develops in the vicinity of the wavetrain trough of Seth and moves west-northwestward (Fig. 3.78b). As Verne develops to the southeast of Seth, a significant change in the steering flow around Seth begins to occur. First, the peripheral anticyclone southeast of Seth dissipates into a weak ridge between 0000 UTC 5 November and 0000 UTC 6 November (Figs. 3.79d and 3.80a, respectively), and is completely absent by 1200 UTC 7 November and thereafter (Figs. 3.80b-d). This is an example of the TCI4 mode, prior to the development of the M Pattern (TCI1). The isotach pattern around Seth changes from being indicative of southeasterly steering (i.e., larger closed isotach to northeast) in Fig. 3.79d to northerly steering (i.e., larger closed isotach to west). The track of Seth changes from the deceleration and poleward turn normally associated with imminent recurvature to a slow,

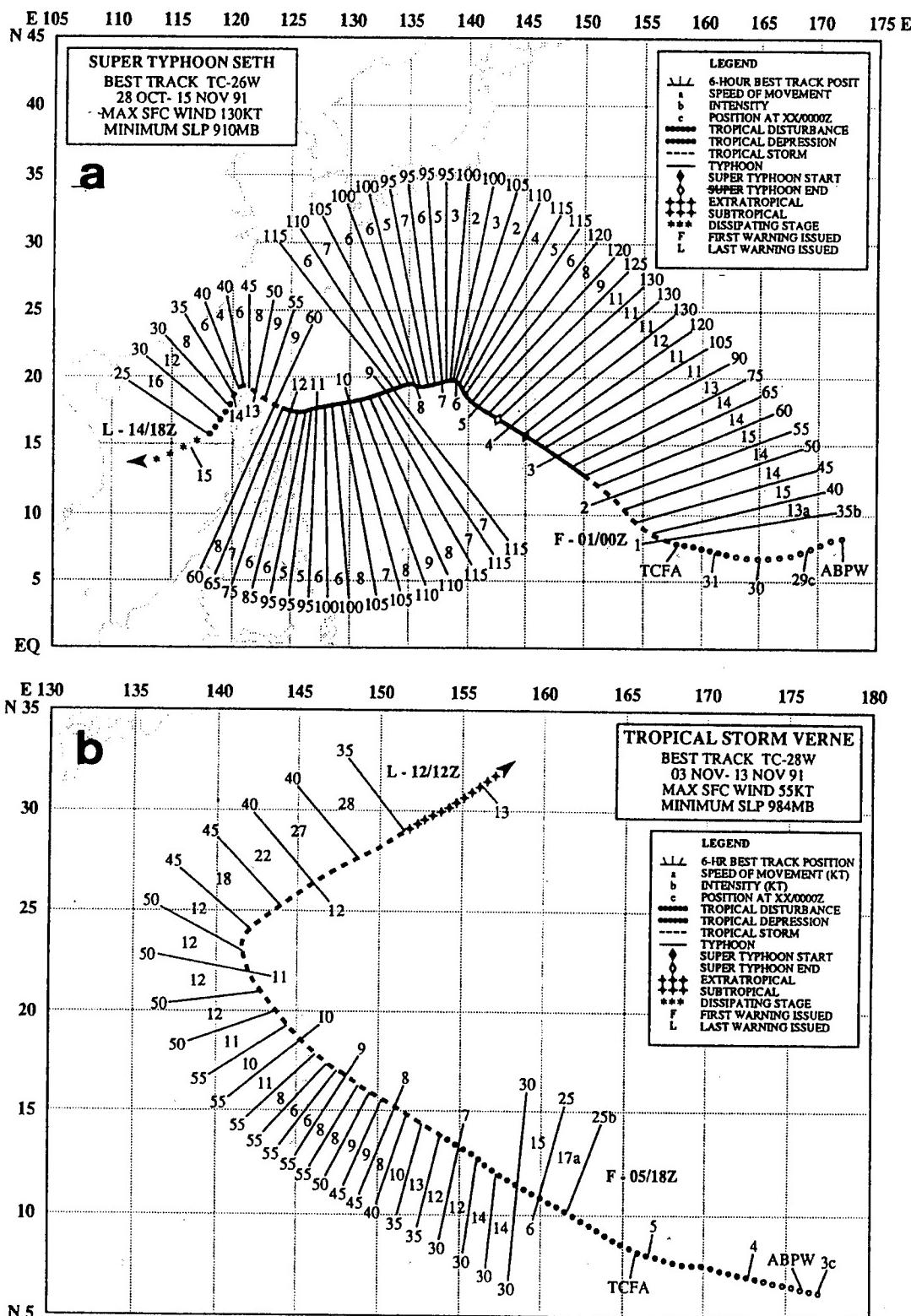


Fig. 3.78. As in Fig. 3.1, except for (a) Supertyphoon Seth during 28 October-15 November 1991, and (b) Tropical Storm Verne during 3-13 November 1991.

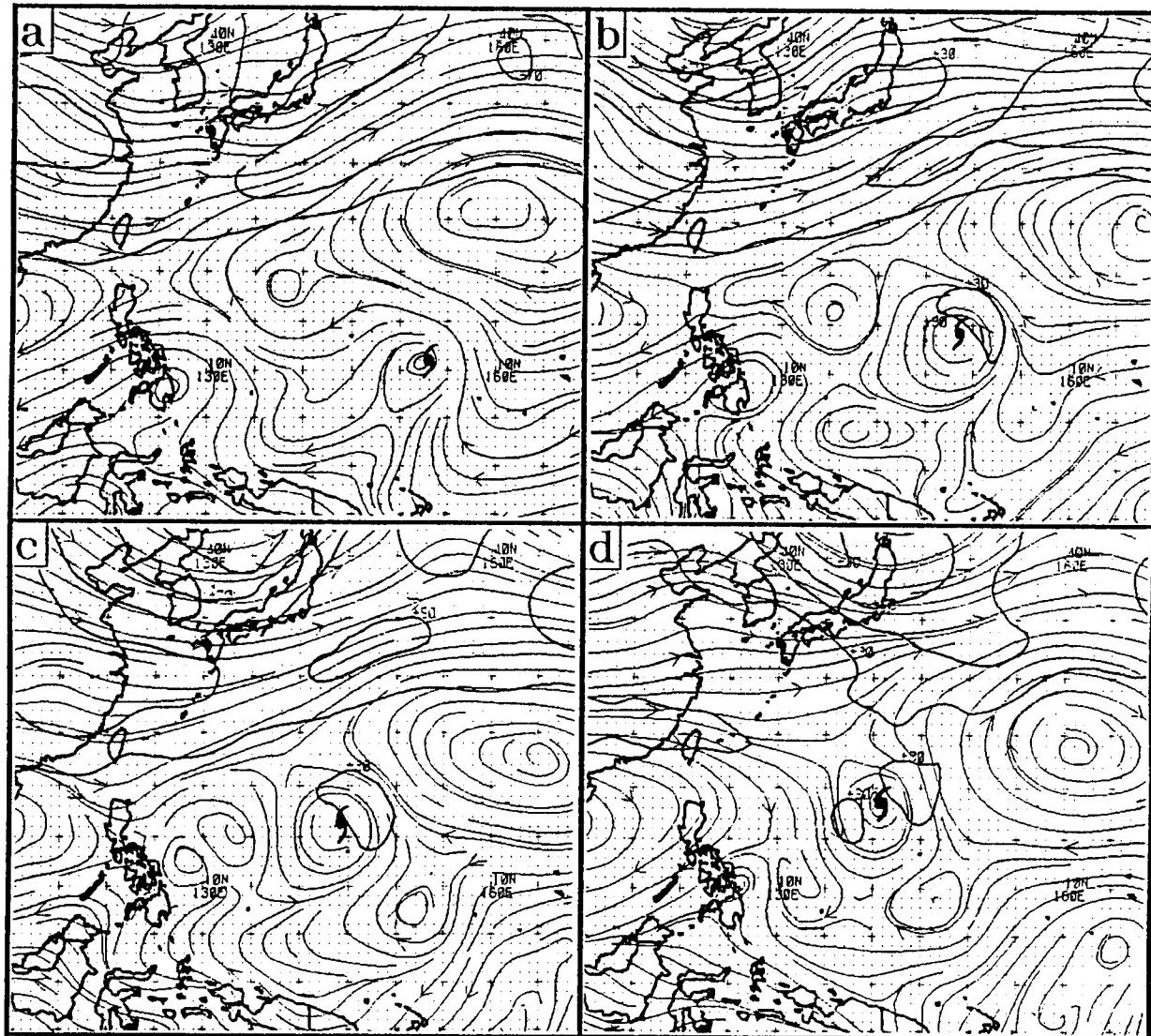


Fig. 3.79. NOGAPS 500 mb streamline and isotach analysis at 0000 UTC on (a) 2, (b) 3, (c) 4, and (d) 5 November 1991. The TC symbol denotes the position of Supertyphoon Seth.

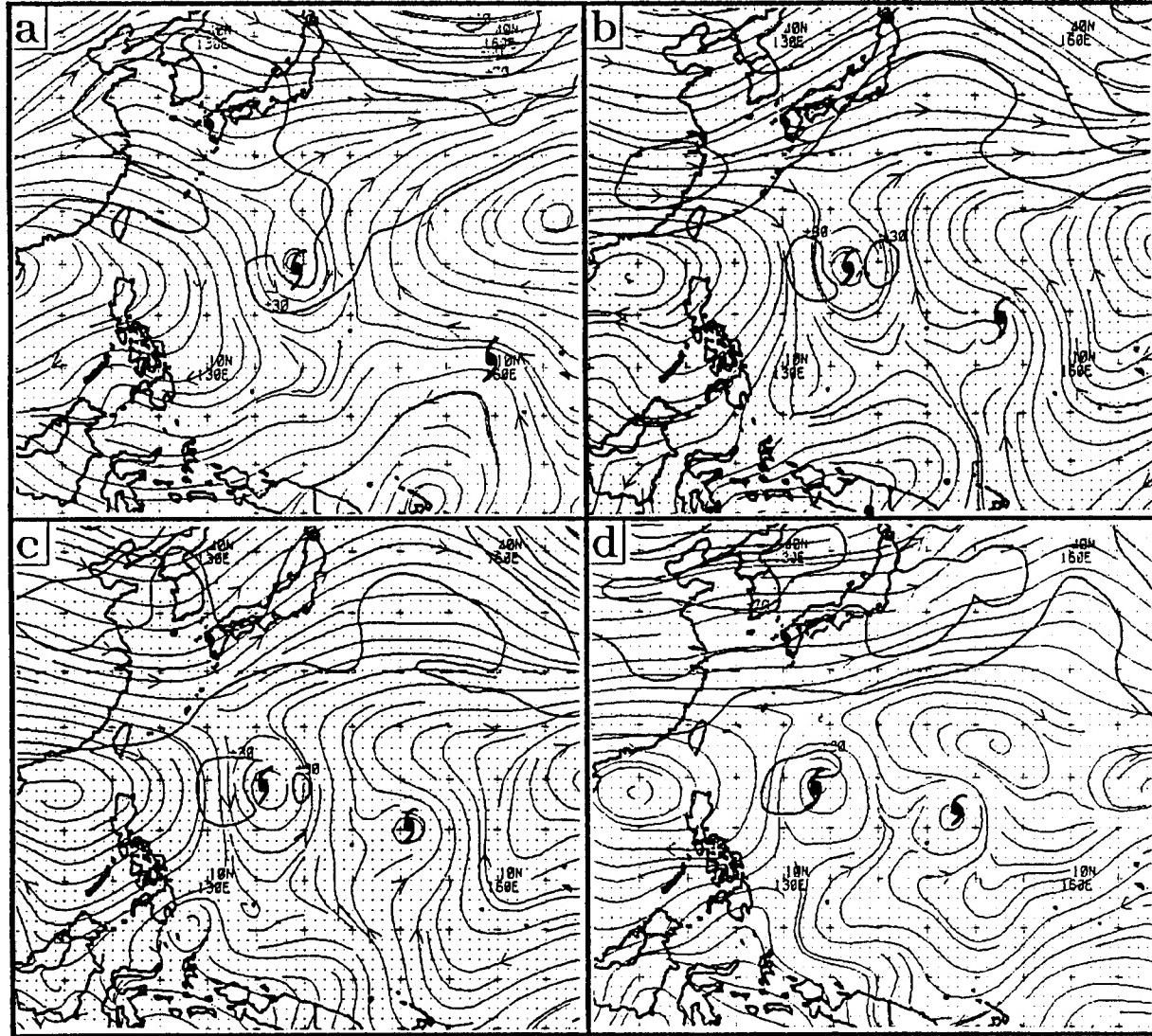


Fig. 3.80. As in Fig. 3.79, except for (a) 6, (b) 7 (1200 UTC), (c) 8, and (d) 9 November 1991. The western (eastern) TC symbol is for Supertyphoon Seth (Tropical Storm Verne).

sinuous west-southwestward motion (Fig. 3.78a). The change in the steering for Seth is proposed to be due to the weakening of the subtropical ridge circulation to the east arising from the encroachment of Verne. On 6 November (Fig. 3.80a), the encroachment is still minimal since Verne is 22° lat. (1320 n mi) distant from Seth and is still deep in the tropics. By 1200 UTC 7 November (Fig. 3.80b), the encroachment of Verne's cyclonic circulation into the peripheral ridge of Seth is evident in the streamline pattern, and is also manifest in the isotach analyses as a closed 30-kt isotach to the east of Seth that is somewhat smaller than its counterpart to the west of Seth. Since this arrangement suggests Seth is experiencing northerly steering, the structure of the environment in the vicinity of Seth appears to have nearly completed a transition from the WR Region of the S Pattern to the NF Region of a newly formed M Pattern (i.e., TCI1 mode), as depicted on the left side of Fig. 3.77.

The structure of the ridging to the north and east of Verne has clearly changed from 6 to 8 November (Figs. 3.80a and 3.80c, respectively) to that expected with a M Pattern (Fig. 3.24). However, Verne's steady direction of motion and decrease in translation speed during this period (Fig. 3.78b) suggests that the Environmental Structure in the vicinity of Verne has not yet transitioned from the DR Region of a S Pattern to the SF Region of a M Pattern. This delay is likely a result of Verne's latitude still being about 4° less than Seth's as of 0000 UTC 8 November (Fig. 3.80c). Thus, Verne is not sufficiently far north to be in the SF Region between Seth and the ridge circulation to the east.

By 0000 UTC 9 November, Verne has nearly reached the latitude of Seth (Fig. 3.80d). During 9 November, both the translation speed and poleward motion component of Verne are increasing, which indicates that the environment of Verne is undergoing the anticipated transition from a S to a M Pattern and from a DR to a SF Region as depicted on the right side of Fig. 3.77. In this case, the Environment transition affecting the eastern TC lags the transition affecting the western TC by about 36 h, which emphasizes that the transitions to SF and NF Regions in a M Pattern illustrated in Fig. 3.77 may not be simultaneous.

During 10 to 13 November (Figs. 3.81a-d), the highly dissimilar advections of the two TCs comprising the M Pattern precipitates a reverse transition back to a S Pattern, as indicated by the ADV in Fig. 3.77. As Verne recycles without decelerating (see Fig. 3.78b), the modifying effect on Seth's motion associated with the peripheral anticyclone encroachment begins to abate by 11 November (Fig. 3.81b). As a result, the subtropical ridge circulation to the south of Verne appears to build to the west, which places Seth in the WR Region and Verne in the AW of a S Pattern by 0000 UTC 12 November (Fig. 3.81c). This reestablishment of the subtropical ridge immediately to the east of Seth combined with  $\beta$ -induced peripheral ridging causes a reversal to southerly steering, with a corresponding isotach maximum to the east. Seth begins to turn northward during 12 November (Fig. 3.78a), and recurvature becomes imminent as Seth passes through the 500 mb subtropical ridge about 0000 UTC 13 November (Fig. 3.81d). Before recurvature can occur, a rapid VWS-induced weakening of Seth associated with the northeast monsoon ensues, which results in a track change to the southwest as the steering level drops to 850

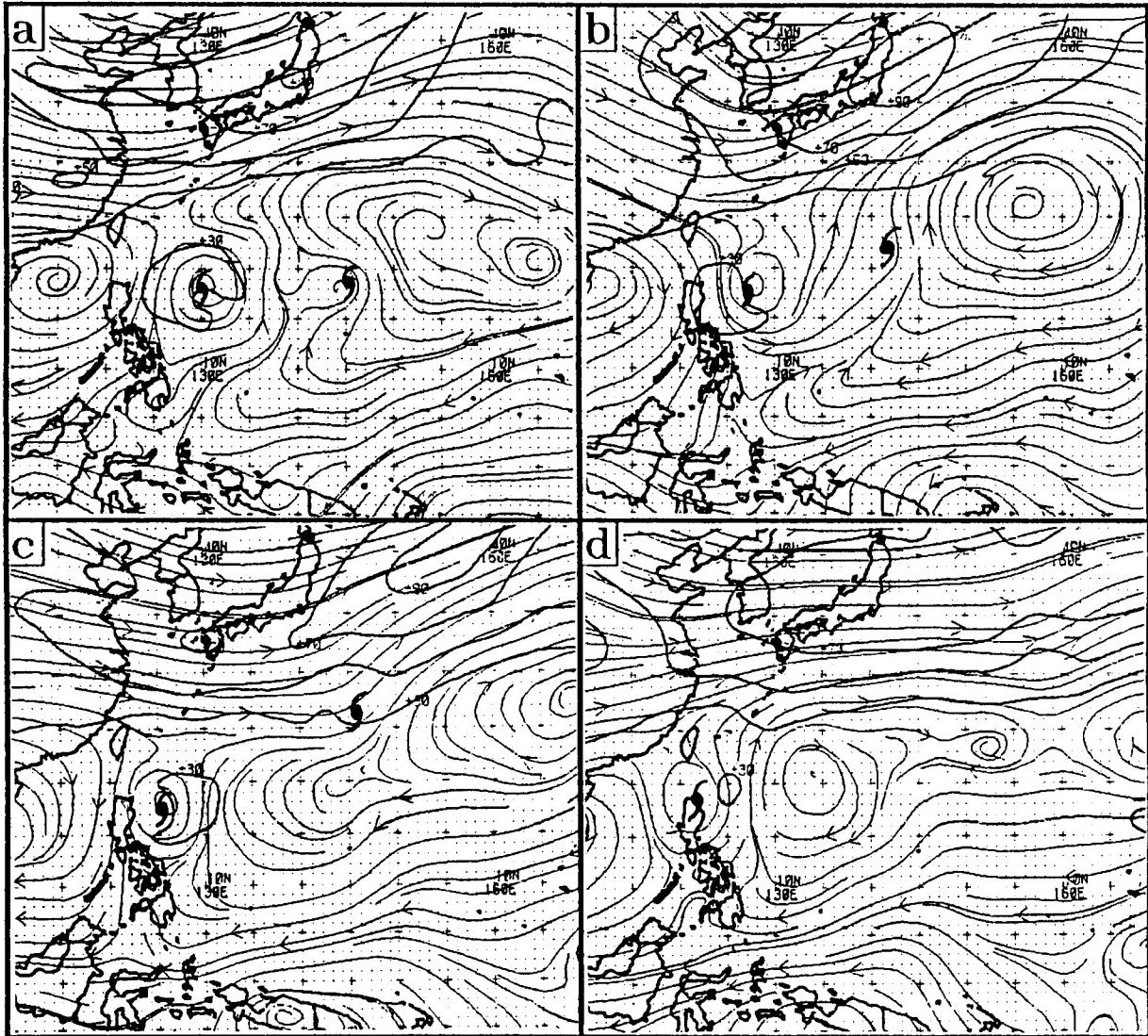


Fig. 3.81. As in Fig. 3.80, except for (a) 10, (b) 11, (c) 12, and (d) 13 November 1991.

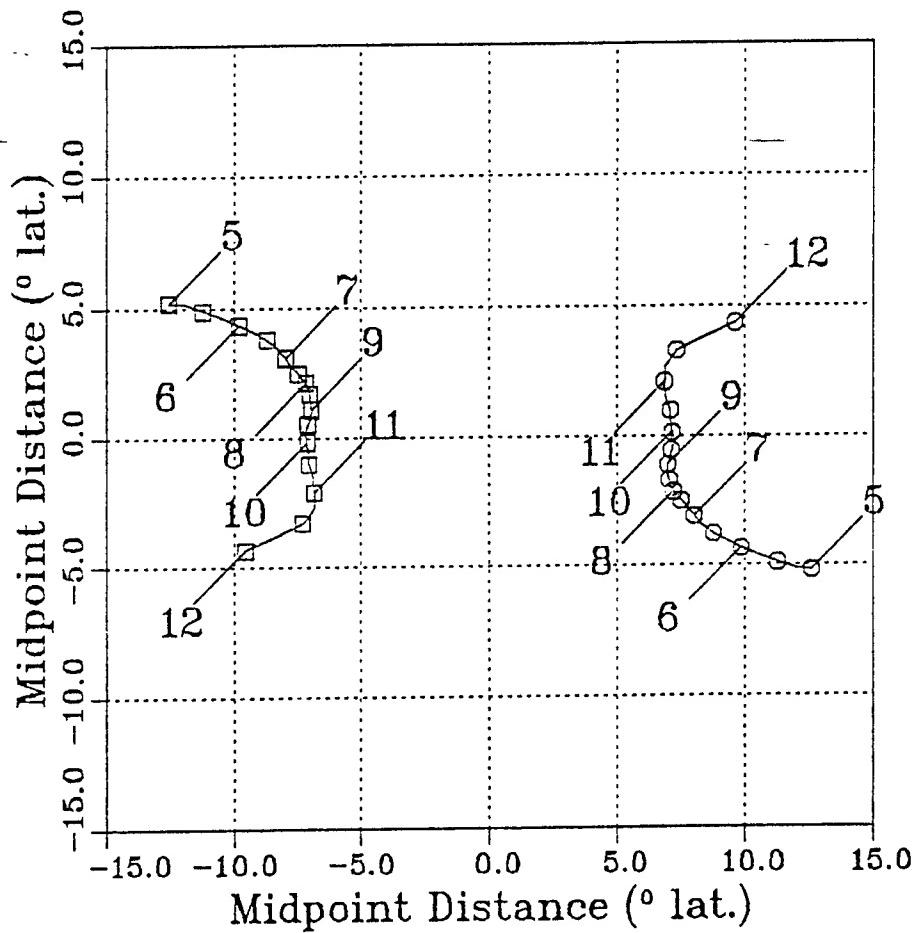


Fig. 3.82. As in Figs. 3.75b and 3.76b, except for Supertyphoon Seth (left) and Tropical Storm Verne (right) from 0000 UTC 5 November to 1200 UTC 12 November 1991.

mb (see Section 3.d.2 on the VWS transformation model).

Motion relative to the midpoint between Seth and Verne (Fig. 3.82) during the S-to-M and M-to-S Synoptic Pattern transition sequence exhibits most of the key indicators that Lander and Holland (1993) associated with a Fujiwhara-like binary interaction. After an "approach" phase with very little relative rotation, a curved "orbit" phase occurs during which a relatively constant separation distance is maintained, then a fairly sharp "escape" turn follows, and finally "departure" occurs with very little relative rotation.

The only binary TC interaction (as expected for a TCI6) indicator that is not readily evident is a sharp "capture" turn. However, this capture turn is not always readily evident

even for TCs that interact at much smaller distance, such as Odessa and Pat in Fig. 3.76b. In this case, the separation distance was never less than  $14^{\circ}$  lat. (840 n mi), which is significantly greater than the 750 n mi separation distance Brand (1970) found to be an upper limit for binary TC interaction. In addition, the angular change in orientation of the two TCs from 0000 UTC 9 to 0000 UTC 11 November is about  $7^{\circ}$  per 12 h, which would not be expected until the TCs are within 660 n mi (see Brand 1970; his Fig. 2). Furthermore, consider the size and separation of the cloud patterns of Seth and Verne at 0000 UTC on: (i) 6 November (Fig. 3.83a) when Seth begins the sharp westward turn; (ii) 8 November (Fig. 3.83b) when the M Pattern is fully established; and (iii) 10 November (Fig. 3.83c) when Seth and Verne are near their closest point of approach. At none of these times does the 850 mb circulation size ( $R_{850}$ ), or the smaller, motion-relevant mid-tropospheric size ( $R_{500}$ ), of the TCs seem to be sufficiently large in relation to the separation distance to generate a significant binary TC interaction (i.e., TCI6 mode). Thus, the Seth and Verne case illustrates that analysis of the relative motion diagram alone is insufficient to determine the mode of TCI that is causing the relative motion.

**2 Case Study #2** This case study involves Typhoons Orchid and Pat during October 1991 and illustrates a variation on the TCI1 mode for a M Pattern interaction that occurs while both TCs are recurving in the AW Region. The study also illustrates how the TCI3 and TCI4 modes may play a significant role in influencing TC motion.

During 6 to 9 October, Orchid and Pat are moving roughly in concert and make a near-simultaneous turn from a generally westward to a poleward direction of motion (Fig. 3.84a). Although Pat is approximately  $22^{\circ}$  lat. (1320 n mi) to the east-southeast of Orchid, a M Pattern may possibly develop. However, the TCs are separated by a very prominent low-latitude anticyclone that has presumably developed from the  $\beta$ -induced dispersion of Orchid (Fig. 3.85). The size of the peripheral anticyclone seems sufficiently large relative to the subtropical ridge circulation to the northeast that a RMT-generated north-oriented ridge structure is possible. Such a transition presumably does not occur because the circulation of Pat intervenes according to the TCI4 mode, and the two ridge circulations remain separate so that a north-oriented ridge does not form. However, the ridge circulation over the South China Sea erodes, presumably owing to the influence of Orchid (i.e., extensive PVA region in advance of a larger TC). As a result, Orchid is subjected to westerly steering (Figs. 3.85c-d) and begins to recurve during 8 October (Fig. 3.84a).

In the meantime, Pat is subjected to conflicting southeasterly steering associated with the subtropical ridge to the northeast and increasing west-northwesterly steering from the growing peripheral ridge of Orchid to the southwest (of Pat), which is an example of the TCI3 mode. This peripheral ridge prevents Pat from continuing westward. Instead, a slow, sinuous north-northwestward track occurs (Fig. 3.84b). This direction of motion for Pat, and the concurrent northeastward motion of Orchid beginning at 0600 UTC 8 October, results in a steadily decreasing separation distance, and thus sets the stage for the next mode of TCI.

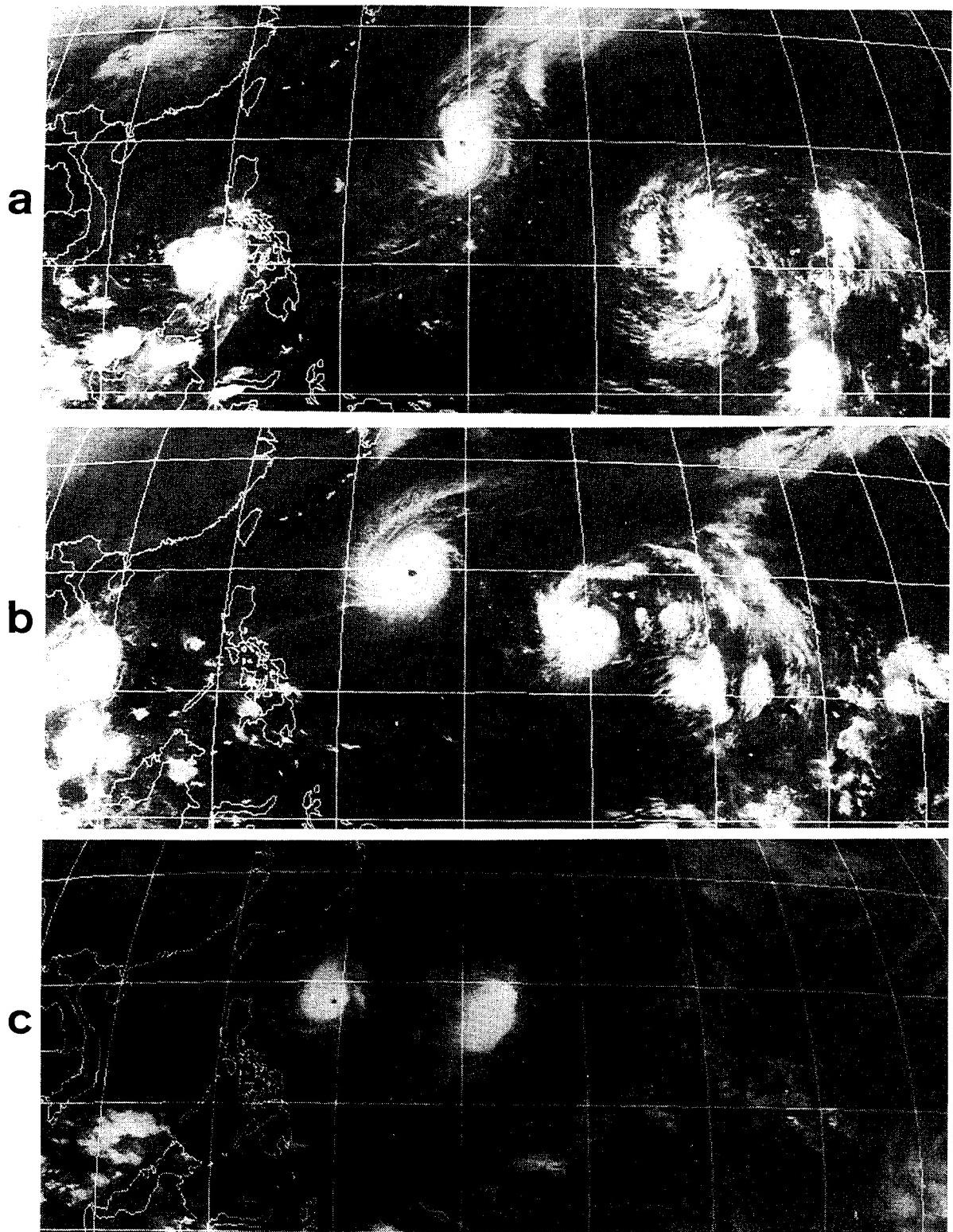


Fig. 3.83. Geostationary infrared imagery of Supertyphoon Seth (west) and Tropical Storm Verne (east) at 0000 UTC on (a) 6, (b) 8, and (c) 10 November 1991.

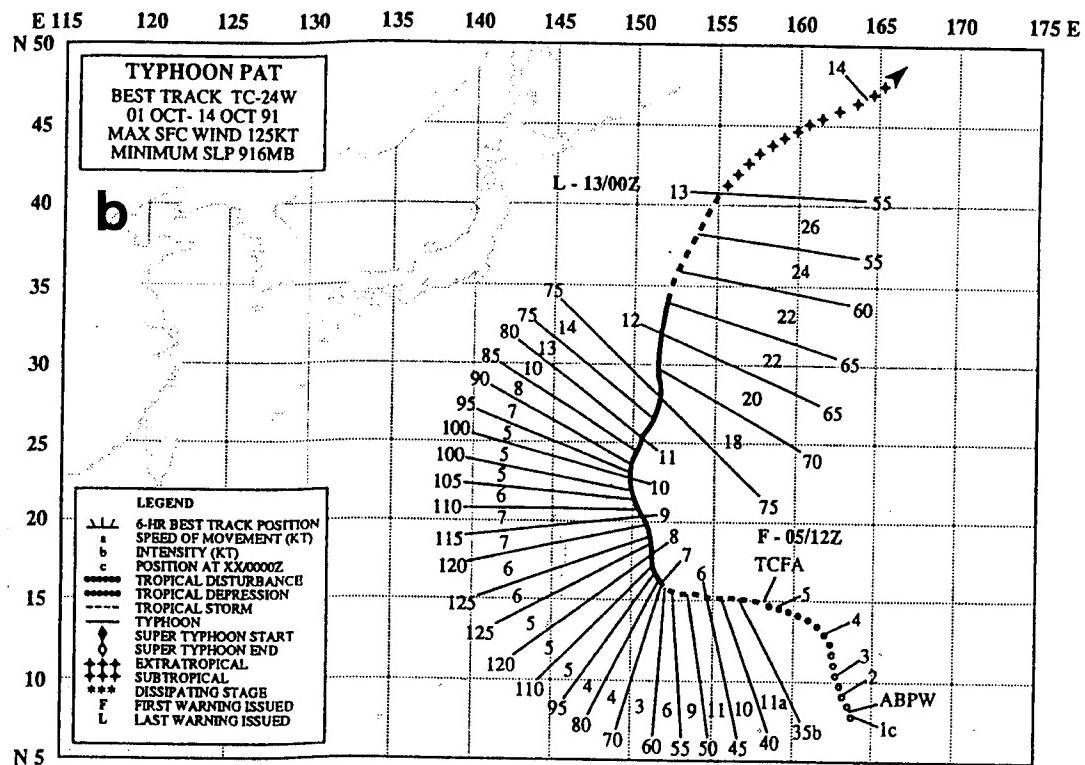
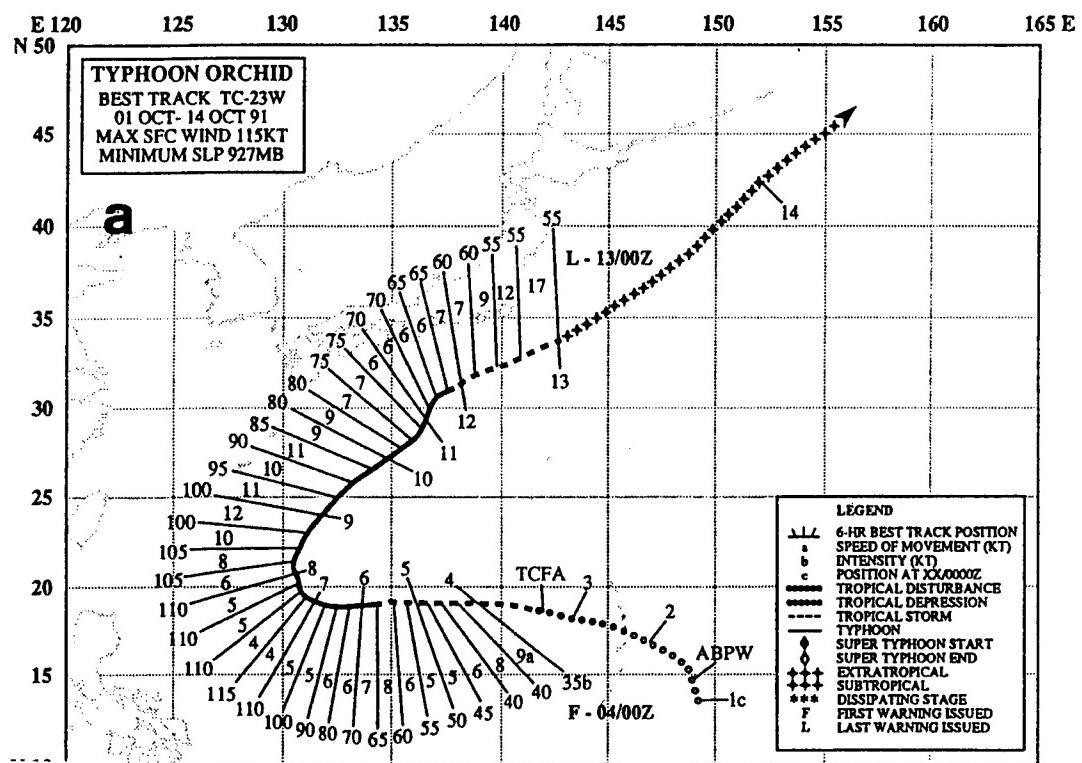


Fig. 3.84. As in Fig. 3.1, except for (a) Typhoon Orchid during 1-14 October 1991, and (b) Typhoon Pat during 1-14 October 1991.

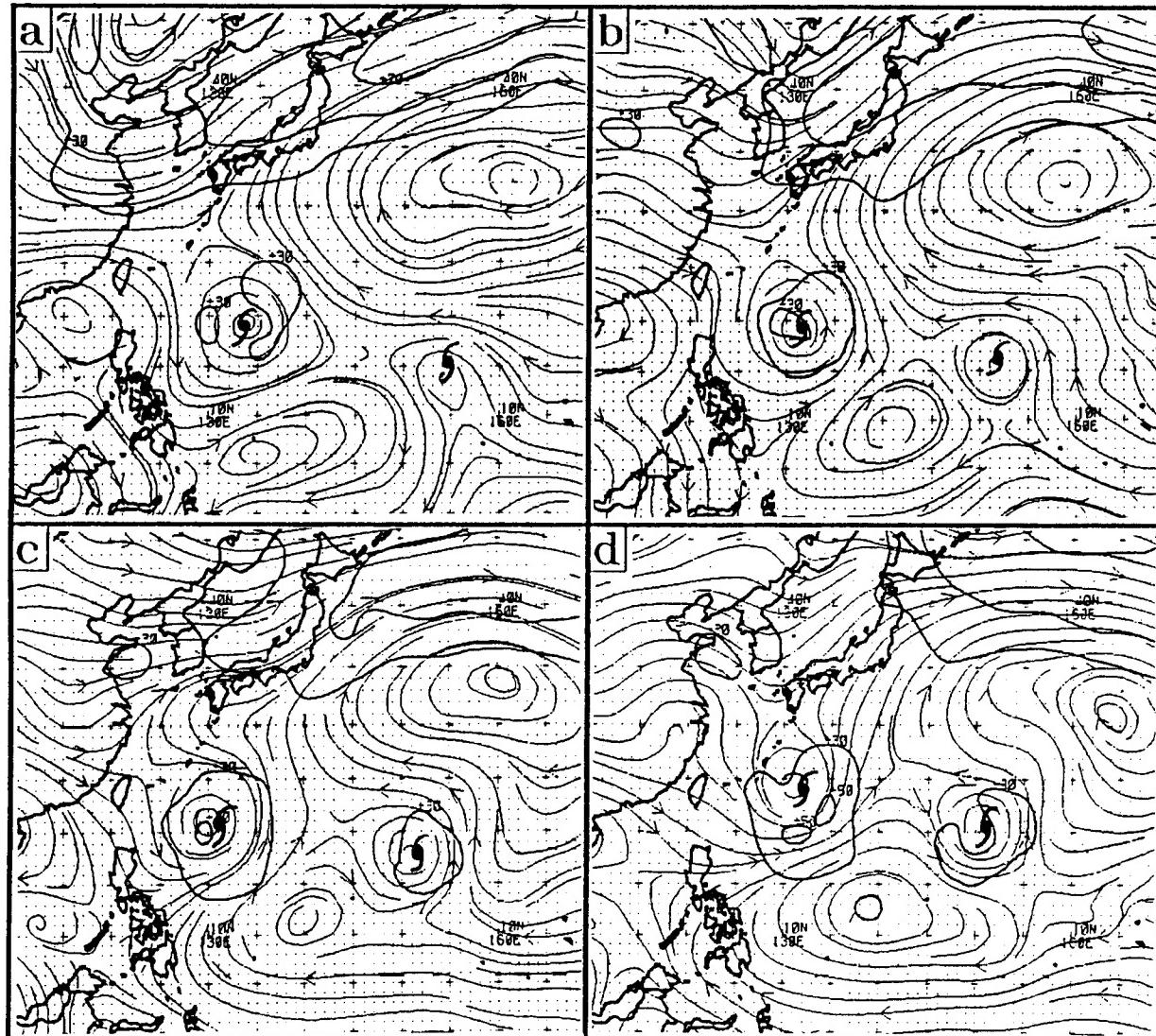


Fig. 3.85. As in Fig. 3.79, except for (a) 6, (b) 7, (c) 8, and (d) 9 October 1991. Typhoon Orchid (Pat) is to the west (east).

Late on 9 October, the post-recurvature northeastward translation of Orchid exhibits an anomalous deceleration (Fig. 3.84a) while Pat accelerates (Fig. 3.84b). In a relative motion diagram (Fig. 3.86), these motion changes have the appearance of a very sharp capture event that is followed by a 48-h orbit phase. The separation distance of 12° lat. (720 n mi) during the orbit phase is slightly smaller than the 750 n mi upper bound suggested by Brand (1970). However, the angular change during the 2-day period is 13.5° per 12 h. This rotation rate and separation distance are extreme outliers in the Brand (1970) (see his Fig. 2) distribution, for which the best fit line has a 13.5° rotation rate at 550 n mi. Thus, two very large TCs must be involved if a true binary interaction (TCI6) is indeed responsible for the relative rotation. However, the TC sizes implied by the convection patterns in the satellite imagery at 1200 UTC 10 October (Fig. 3.87), which is during the apparent capture phase, do not seem large enough to produce any mutual advection at all. Clearly, the sizes of the TCs are not large enough to explain the observed rotation rate.

Analyses during 10 - 13 October (Fig. 3.88a-d) reveal that a variant of the M Pattern is temporarily established, and this is proposed to be the explanation for the anomalous TC motions. At 0000 UTC 10 October, Pat is located at a slightly lower latitude than Orchid, and is in the southerly flow generated by the height gradient between Orchid to the west and the ridge circulation to the east. An increase in translation speed beginning at 0000 UTC 10 October confirms that Pat is indeed transitioning into the SF Region of a M Pattern. Such an environment structure in the vicinity of Pat remains in effect on 11 and 12 October (Figs. 3.88b-c), but has changed to the AW Region within a S Pattern as the southerly flow moves Pat poleward faster than Orchid (Fig. 3.88d).

As in the Seth/Verne case study above, a strong NF Region arising from the height gradient between the eastern TC and the western ridge circulation tends to keep the western TC from gaining latitude. In this case, a strong NF Region does not develop in the vicinity of Orchid because the ridge circulation over the South China Sea region has earlier been eroded by the influence of Orchid. Instead, the presence of Pat tends to reduce the large-scale, northwestward-directed height gradient across Orchid, and thus weaken the southwesterly steering in the vicinity of Orchid. This weakened steering and slowing of the motion to 6-7 kt is consistent with the near-collocation of Orchid and the NOGAPS-analyzed circulation center in Figs. 3.88a-c. As Pat subsequently moves ahead of Orchid, a strong southwesterly height gradient is restored in the vicinity of Orchid (notice the northwestward displacement of the analyzed center in Fig. 3.88d), and the translation speed of Orchid increases.

**3. Case Study #3.** This case study involves Typhoons Nancy and Owen during August 1989, which have been considered by both forecasters (ATCR 1989; p. 103-105) and researchers (Lander and Holland 1993) to represent a case of binary interaction (TCI6). Such an interpretation appears to be largely based on the relative motion diagram (Fig. 3.75b) that appears to have particularly distinct capture, rotation, and escape phases as defined by Lander and Holland. The primary purpose of this case study is to illustrate that the primary mechanism causing the relative rotation of Nancy and Owen is *not mutual*

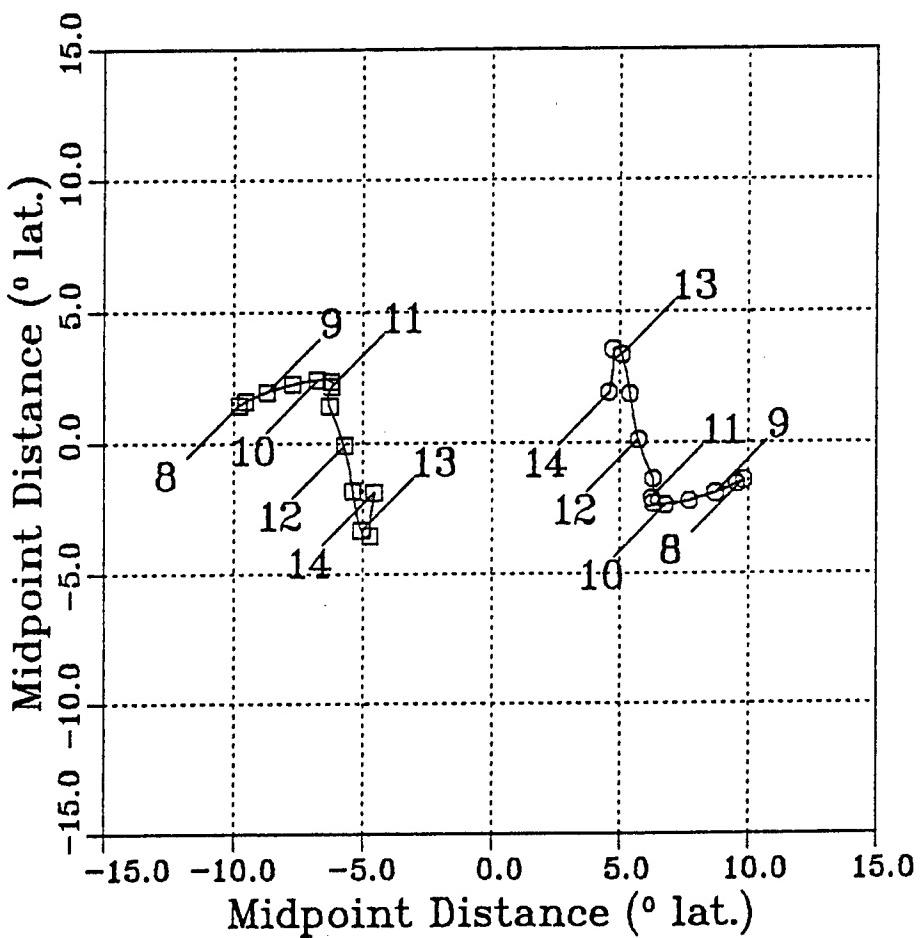


Fig. 3.86. As in Figs. 3.75b and 3.76b, except for Typhoon Orchid (left) and Typhoon Pat (right) from 0000 UTC 8 October 1991.

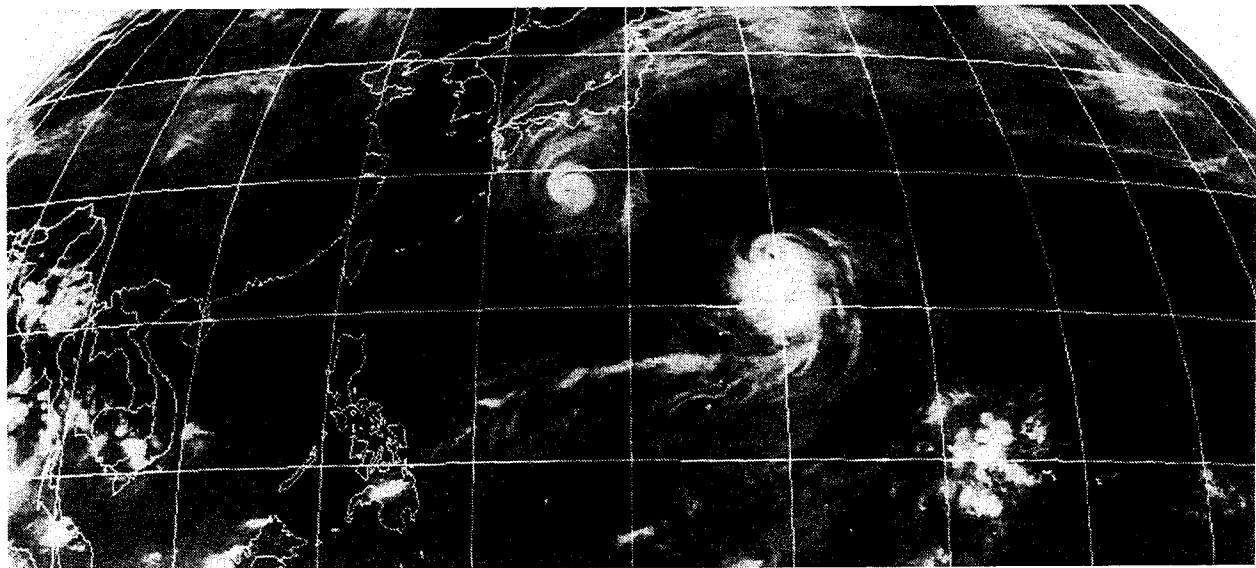


Fig. 3.87. As in Fig. 3.83, except for Typhoons Orchid and Pat at 1200 UTC 10 October 1991.

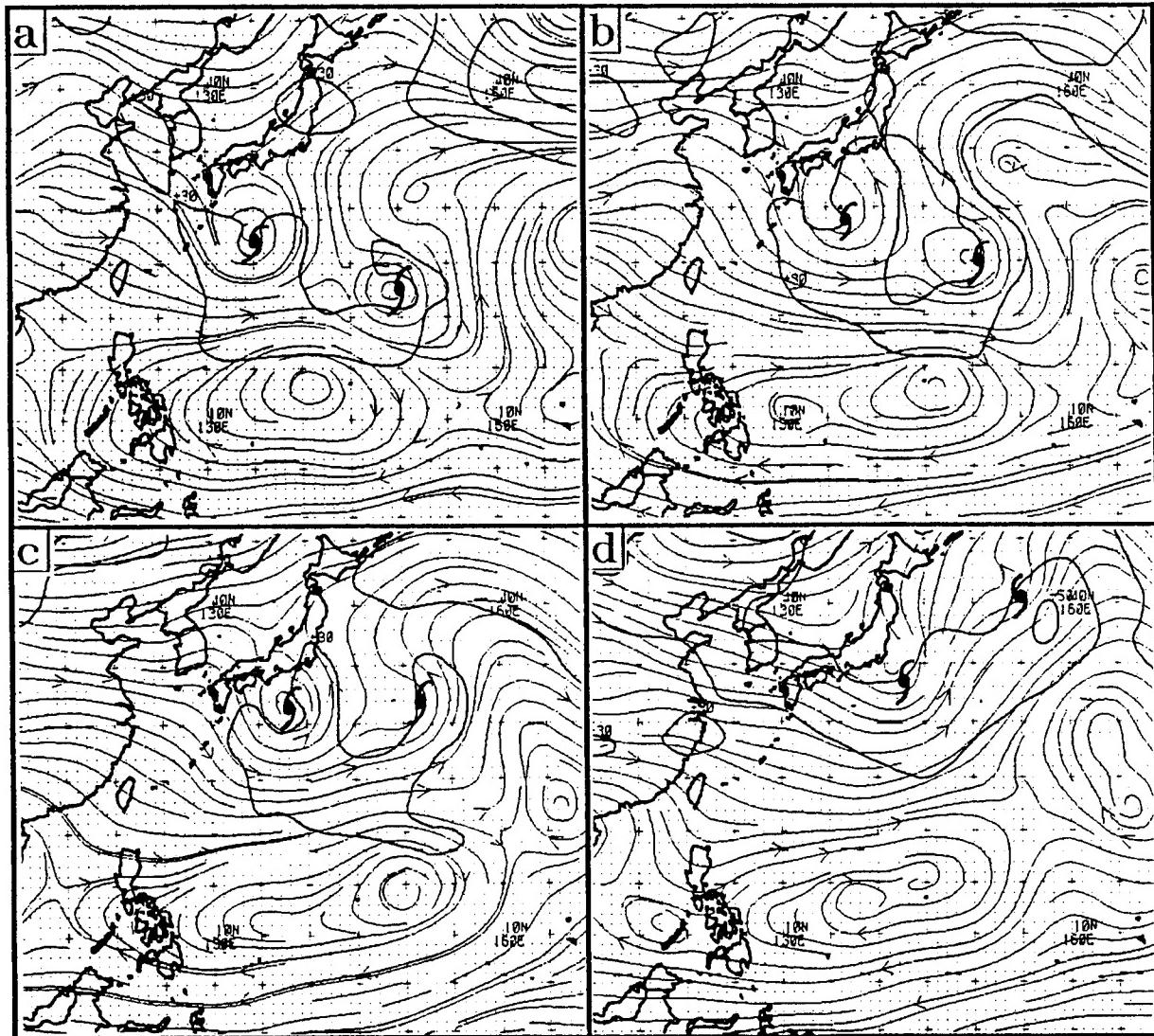


Fig. 3.88. As in Fig. 3.85, except for (a) 10, (b) 11, (c) 12, and (d) 13 October 1991.

*advection* by the TCs circulations as in the TCI6 mode. Rather, relative rotation arises from advection of both TCs by the circulation of a monsoon gyre (MG) and the associated peripheral anticyclone (i.e., TCI5 mode). The MG appears to develop partly as a result of the close proximity of Nancy and Owen, and achieves an intensity sufficient to cause an Environment Structure transition to a Monsoon Gyre (G) Synoptic Pattern.

During the period covered by Fig. 3.75b, both TCs followed sinuous north-oriented tracks (Fig. 3.89a). Such tracks may be associated with a reverse-oriented monsoon trough that defines the N1 North-Oriented Pattern (Fig. 3.7). Infrared imagery at 0300 UTC on 11-13 August (Figs. 3.90a-c) confirms that Nancy and Owen did form in a reverse-oriented monsoon trough, which is manifest by the extensive area of convection that stretches east-northeastward from the Philippines to the dateline in all three images. The initial broad and fairly continuous convection region becomes organized into alternating regions of enhanced and suppressed cloudiness, and the regions of enhanced cloudiness are clearly associated with Nancy and Owen by 13 August (Fig. 3.90c). By 13 August, the large-scale pattern of the convection including the convective signatures of Nancy and Owen has a curved "fishhook" appearance.

Subsequent imagery on 14-16 August (Figs. 3.91a-c) reveals the smaller cloud patterns of Nancy and Owen are embedded in the eastern portion of a large-scale ring of convective clouds. The large circular ring of cloudiness is particularly evident in Fig. 3.91c, because of the contrast with a distinct inner region of suppressed cloudiness centered at about 25°N, 140°E. Recall that such a cloud pattern can manifest either comparatively smaller, weaker MGs that undergo MTI transformations with TCs (cf., Fig. 3.71), or the comparatively large, intense MG that defines the G Synoptic Pattern (cf., Fig. 3.13). The cloud signature of the MG associated with Nancy and Owen is of a similar scale (25° lat. diameter in Fig. 3.17b and c) as that in Fig. 3.13, which suggests that a G Pattern is developing, rather than a MTI transformation. The presence of multiple small TCs (Nancy and Owen) further supports that a G Pattern as in Fig. 3.13 (i.e., Typhoon Ellie) is developing. In addition, a third TC develops (near 16°N, 143°E) on 15 August (Fig. 3.91b) in the southern region of the large cloud band, and then rotates cyclonically to the southeastern region (near 19°N, 148°E) by 0300 UTC 16 August (Fig. 3.91c). This TC eventually develops into Tropical Storm Peggy and follows a cyclonically curving track (Fig. 3.92) that is consistent with advection by a large MG.

Given this evidence from satellite imagery (especially Fig. 3.91) that Nancy (top), Owen (middle), and Peggy (bottom) are in the eastern semicircle of a large MG, an alternate explanation for the cyclonic rotation and poleward displacement of Owen and Nancy is proposed. That is, the relative rotation of not only Nancy and Owen, but also Owen and Peggy, may be attributed primarily to an advection of all three TCs by the cyclonic circulation of the developing MG.

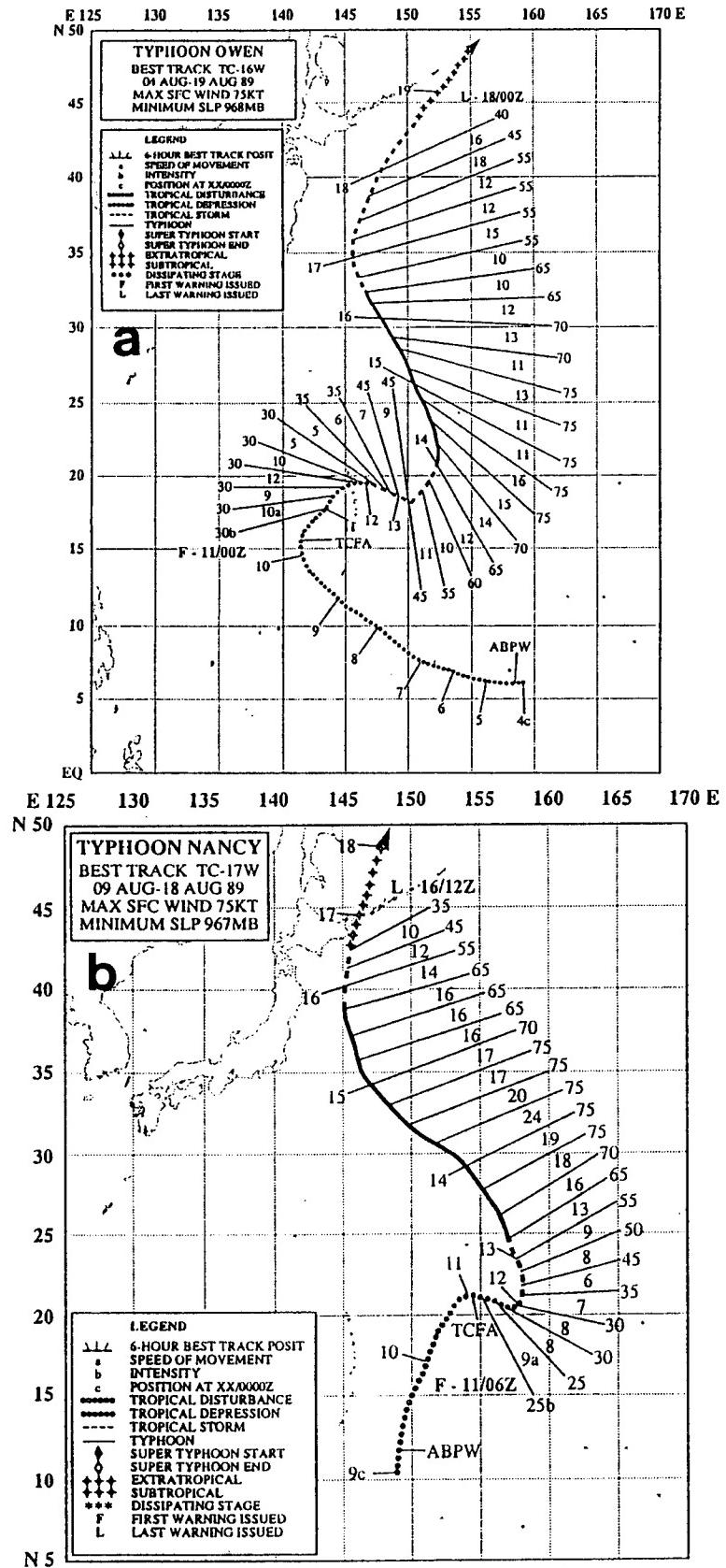


Fig. 3.89. As in Fig. 3.1, except for (a) Typhoon Owen during 4-19 August 1989, and (b) Typhoon Nancy during 9-18 August 1989.

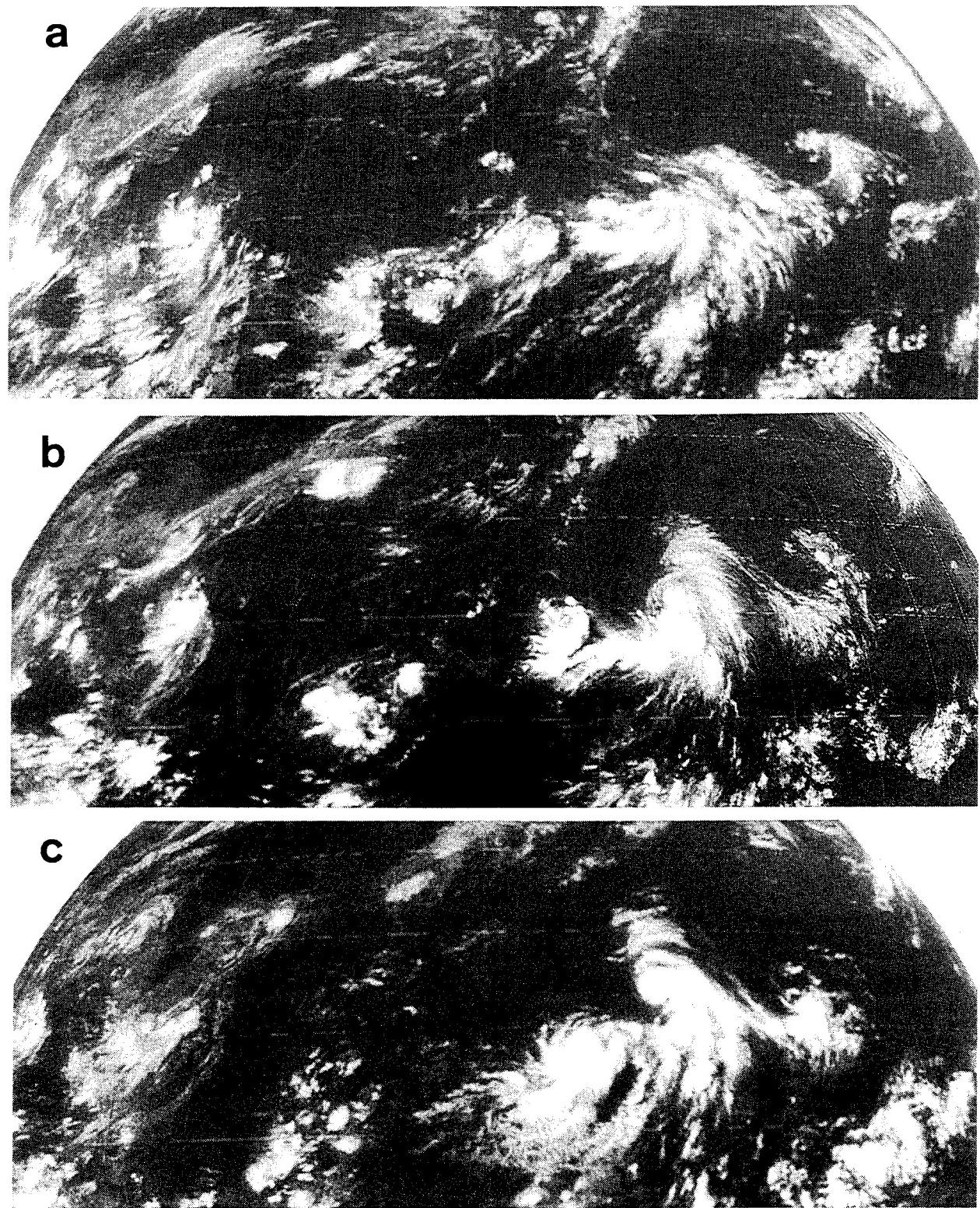


Fig. 3.90. As in Fig. 3.83, except for Typhoons Owen and Nancy at 0300 UTC on (a) 11, (b) 12, and (c) 13 August 1989.

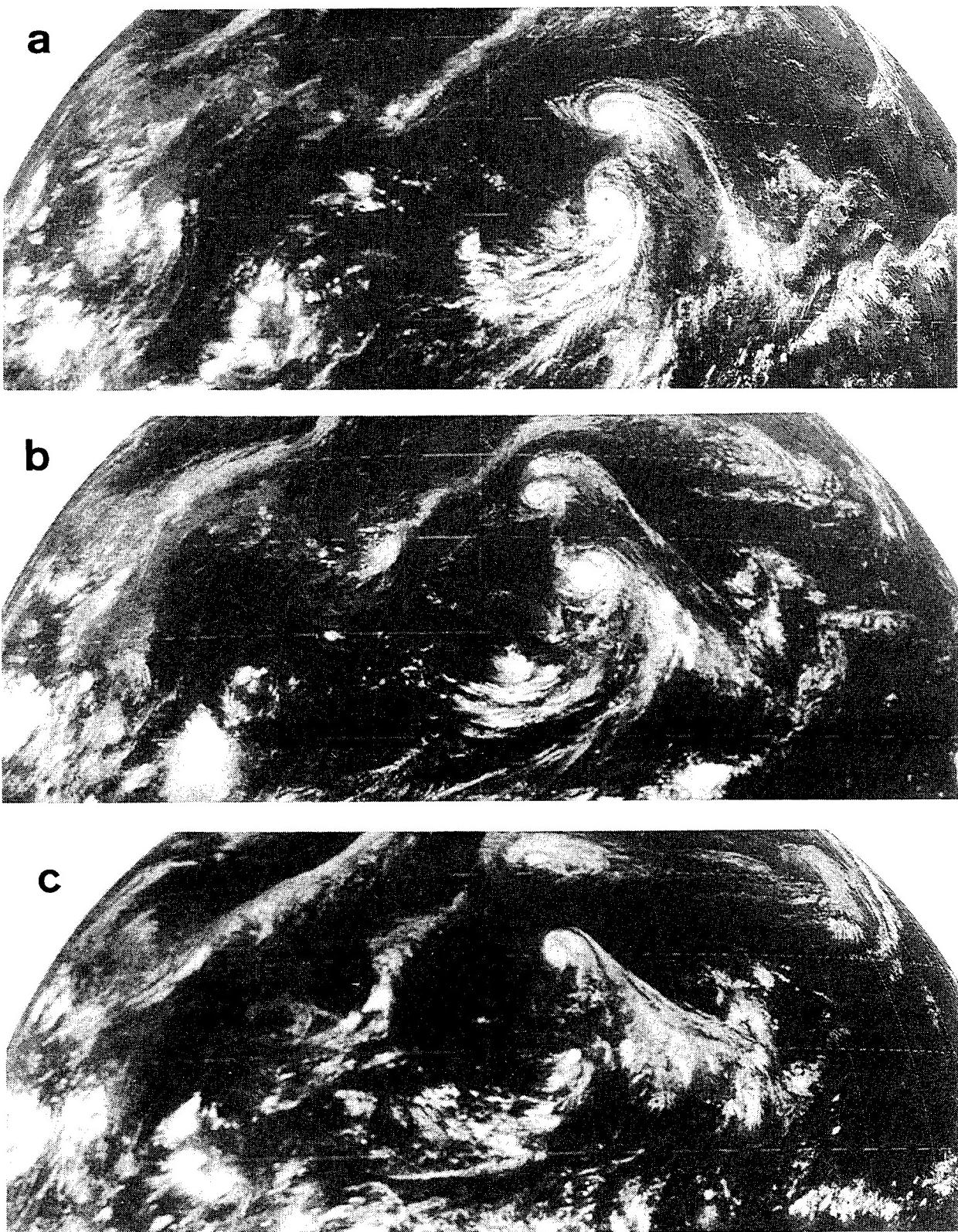


Fig. 3.91. As in Fig. 3.90, except for Typhoons Owen and Nancy at 0300 UTC on (a) 14, (b) 15, and (c) 16 August 1989.

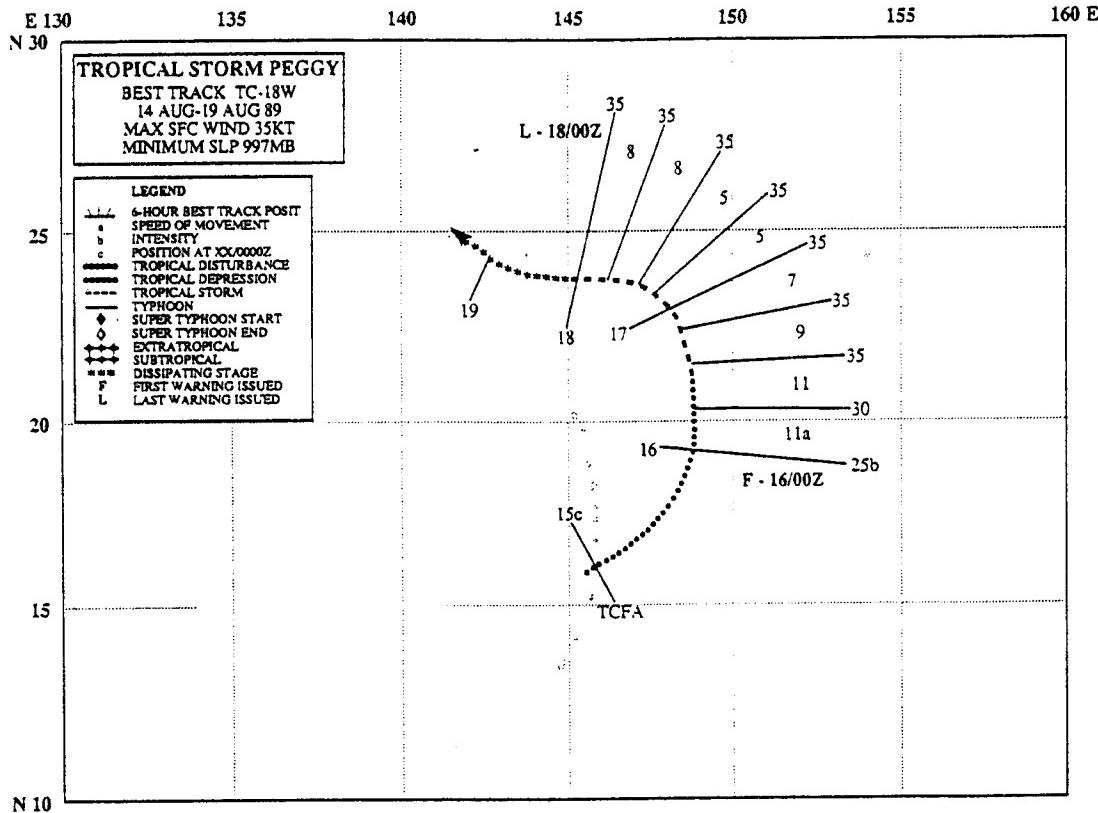


Fig. 3.92. As in Fig. 3.1, except for Tropical Storm Peggy during 14-19 August 1989.

Additional support for the G Pattern explanation for the apparent relative rotation of Nancy and Owen is available from the NOGAPS streamline analyses at 500 mb<sup>13</sup> (Figs. 3.93 and 3.94). Whereas two distinct 500 mb cyclonic circulations associated with Nancy and Owen are analyzed on 11 and 12 August (Figs. 3.93a-b), Nancy and Owen are located along the southern periphery of a single larger cyclonic circulation only 12 h later (Fig. 3.93c). Subsequent analyses through 0000 UTC 15 August (Fig. 3.94c) meet the criteria for the G Pattern: (i) a larger cyclonic circulation is evident; (ii) the JTWC positions of Nancy and Owen are on the periphery of the larger cyclonic circulation; and (iii) the TC positions rotate cyclonically around the larger circulation while maintaining the same separation distance.

<sup>13</sup> A 12-h interval has been used between the later panels in Fig. 3.93 and earlier panels in Fig. 3.94 to provide more temporal resolution during the orbiting phase of Nancy and Owen.

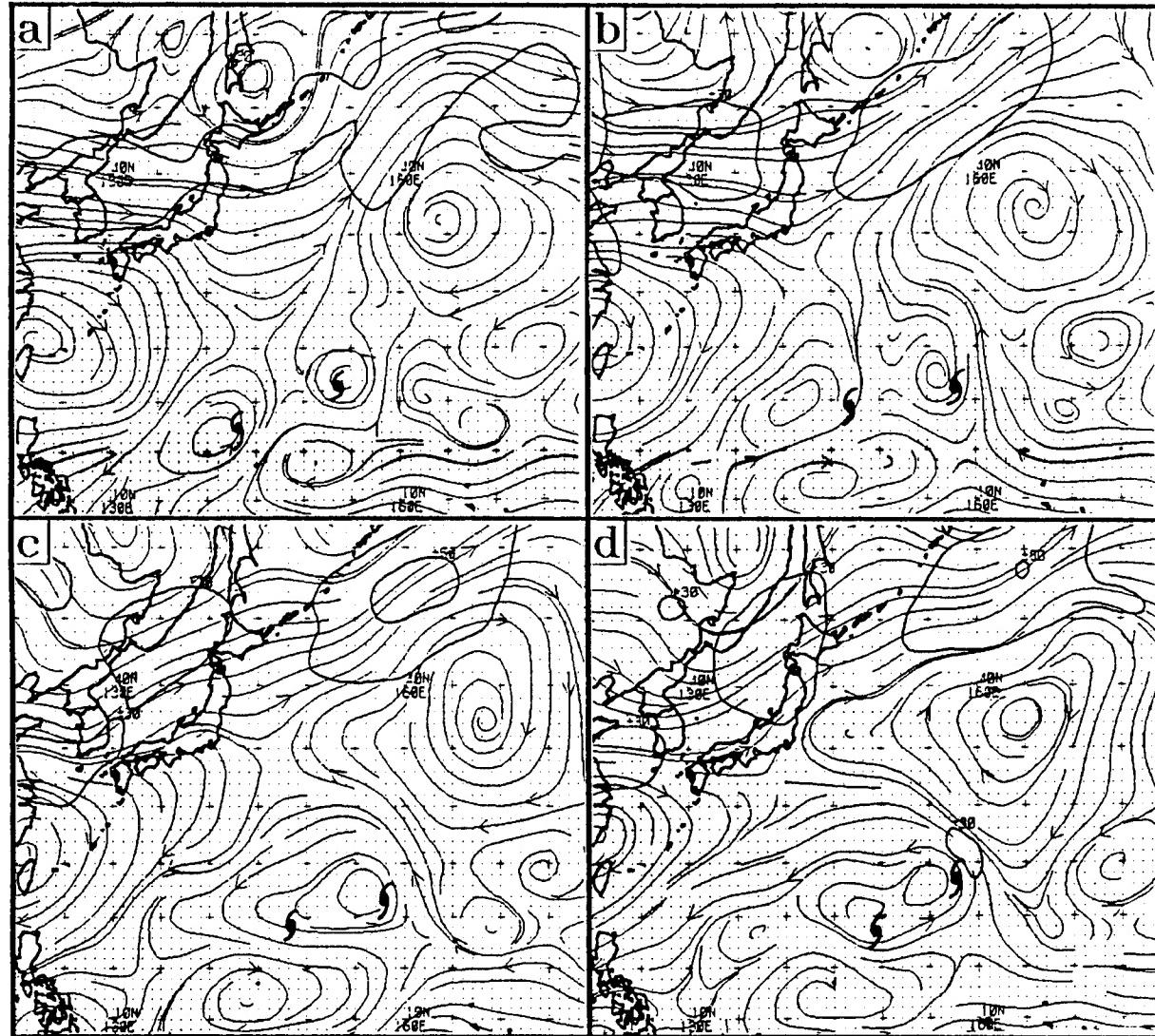


Fig. 3.93. As in Fig. 3.79, except for (a) 0000 UTC 11 August 1989, (b) 0000 UTC 12 August, (c) 1200 UTC 12 August, and (d) 0000 UTC 13 August. Typhoon Owen (Nancy) is on the west (east).

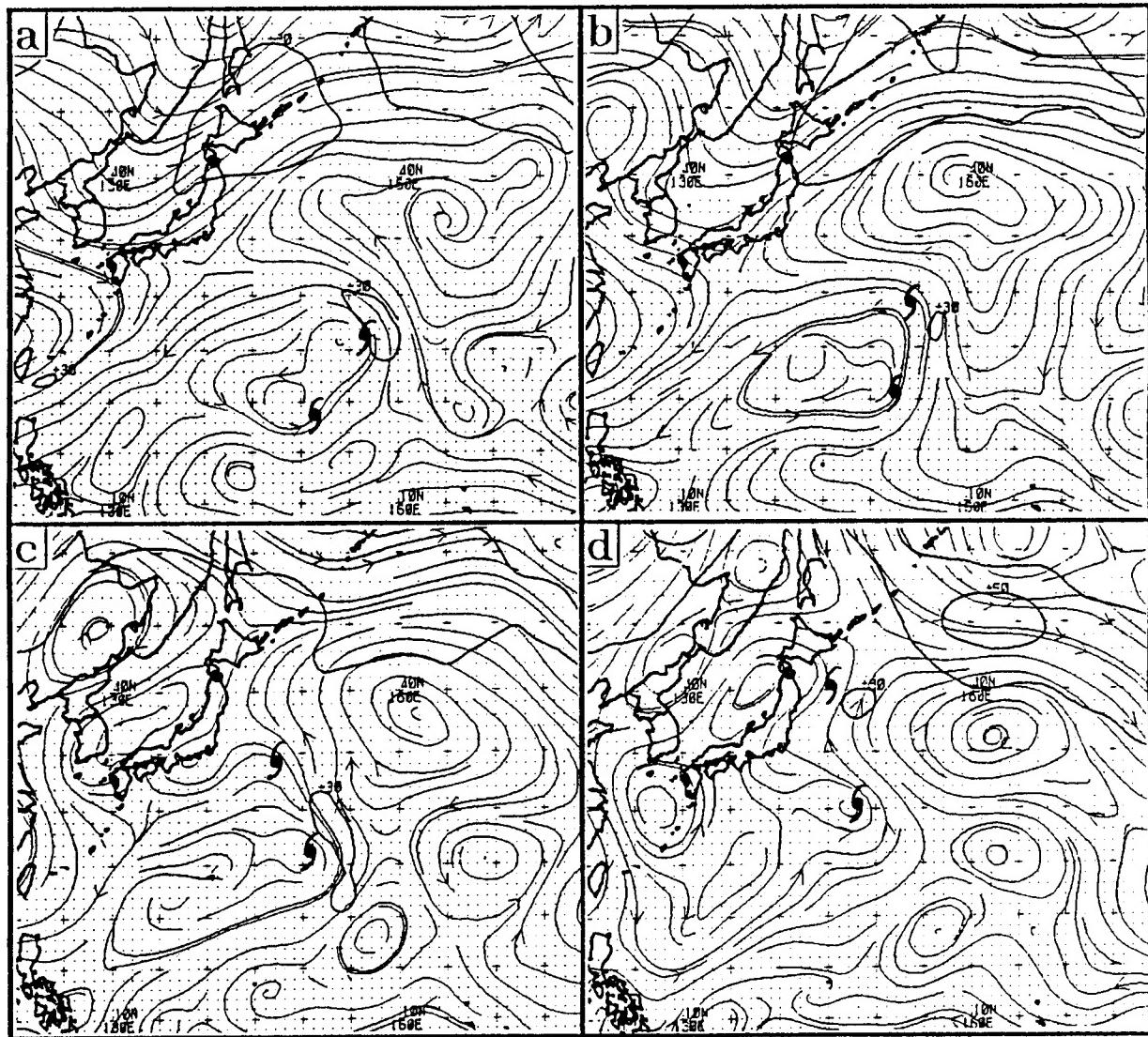


Fig. 3.94. As in Fig. 3.93, except for (a) 1200 UTC 13 August 1989, (b) 0000 UTC 14 August, (c) 0000 UTC 15 August, and (d) 0000 UTC 16 August.

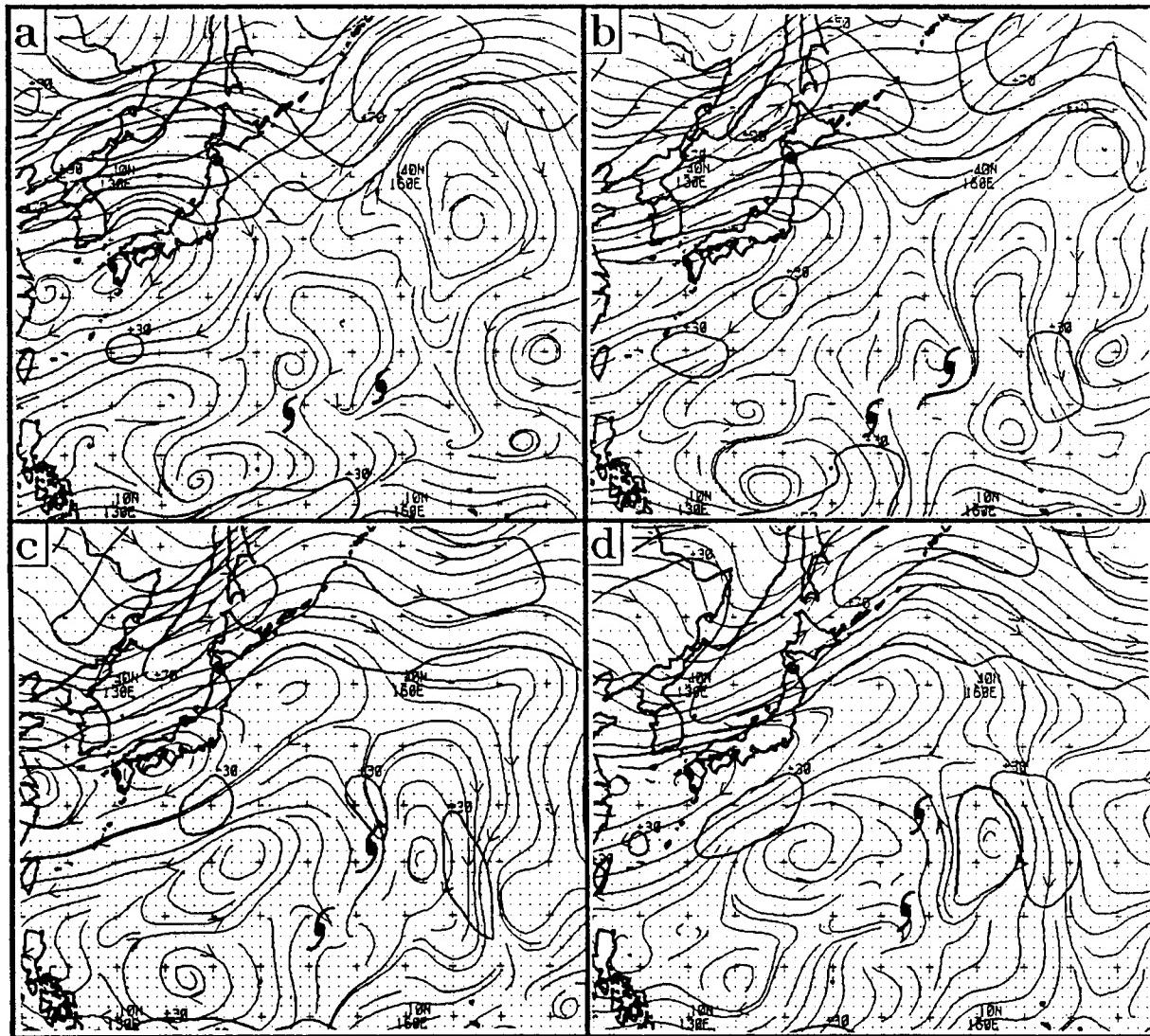


Fig. 3.95. As in Fig. 3.93, except for at the 250 mb level, and at (a) 1200 UTC 12 August 1989, (b) 0000 UTC 13 August, (c) 1200 UTC 13 August, and (d) 0000 UTC 14 August.

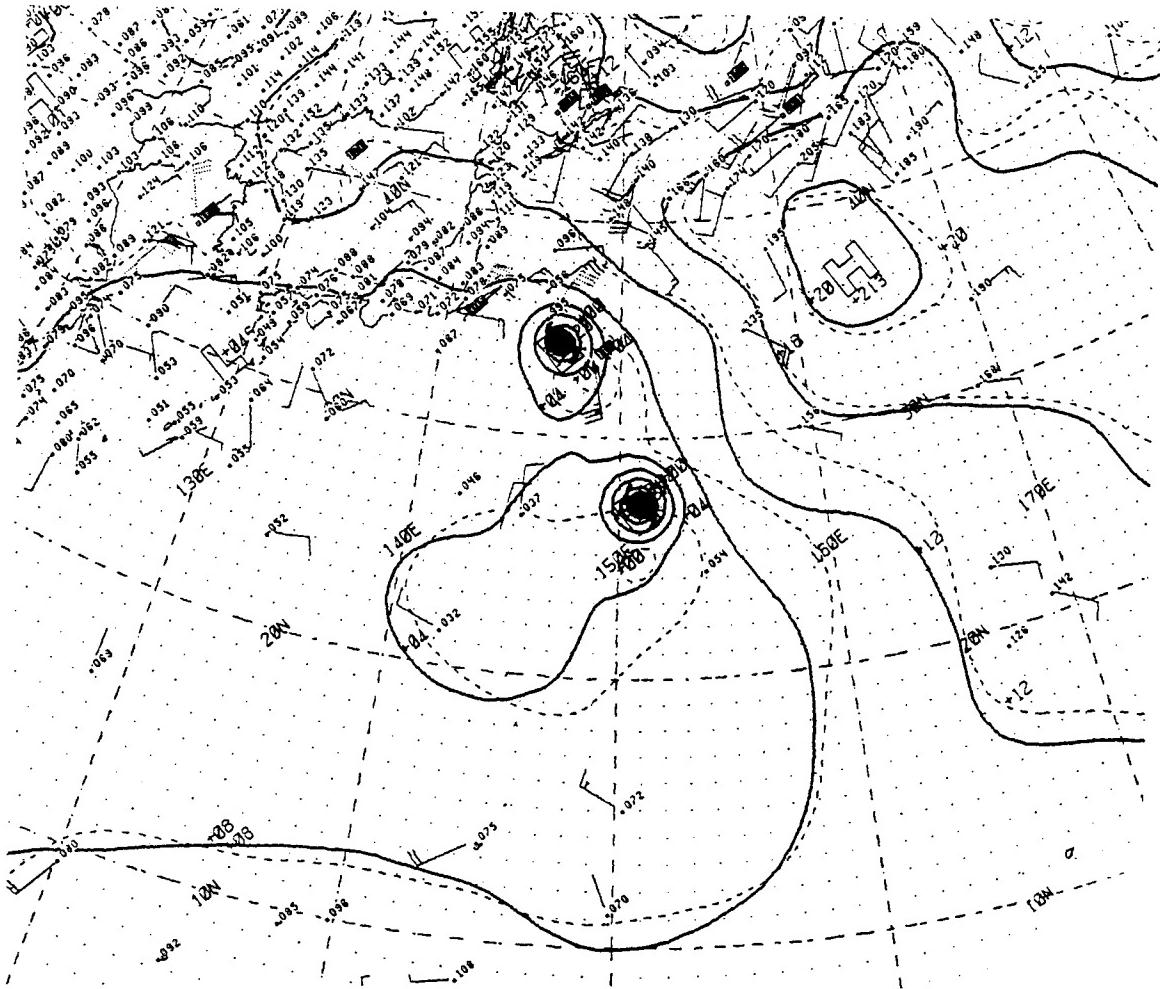


Fig. 3.96. NOGAPS surface pressure (solid, contour interval 4 mb) analysis and surface wind reports (kt) at 0000 UTC 15 August 1989.

All of the above criteria are also met at the 250 mb level (Fig. 3.95a-d), for which considerably more wind reports are available than at 500 mb. Because the size of the TC cyclonic circulation at 250 mb is so small, the large gyre in Fig. 3.95 is not likely to be an artifact of the NOGAPS data assimilation system. Finally, a manifestation of the MG also is present in the 0000 UTC 15 August surface pressure field (Fig. 3.96) in the form of a partially closed area of sub-1004 mb pressures to the southwest of Owen, which agrees with the position of the corresponding NOGAPS representation of the gyre circulation at 500 mb (Fig. 3.94c).

The 1200 UTC 12 August 500 mb analysis (Fig. 3.93c) corresponds to the beginning of the apparent orbit phase of Nancy and Owen in the relative motion diagram (Fig. 3.75b). A clear indication of the presence of a monsoon gyre circulation thus appears only 12 h after the initiation of cyclonic relative rotation by the TCs. Subsequent analyses of the gyre circulation at 500 mb suggest that advection by the developing MG was significant through the entire relative rotation phase of Nancy and Owen. In view of the relatively small circulation sizes implied by the convective cloud patterns of Nancy and Owen (Fig. 3.91), and the minimum separation distance  $8^\circ + \text{lat.}$  (about 900 km or 500 n mi), it is the authors' opinion that binary interaction (i.e., TCI6 mode) is not a plausible explanation in this case. Rather, the relative motion pattern of the two TCs appears to be primarily a result of advection by the MG. This Nancy and Owen case is best described by the TCI5 mode in which the sole impetus for the relative rotation of the TCs is advection by the MG.

In view of the above discussion, it seems fairly evident that an Environment transition from a N1 Synoptic Pattern to a G Pattern occurred with multiple small TCs developing early in the transition process. Because these TCs formed almost simultaneously and at a small separation distance, the advection of the TCs around the eastern periphery of the MG produced a very noticeable relative rotation that has been previously viewed as binary interaction (TCI6 mode), rather than the TCI5 transformation conceptual model. By contrast, the formations of Tropical Storm Doug, Typhoon Ellie, and TD13 on the eastern periphery of a MG during August 1991 (see Fig. 3.14a-d and related text) were separated in time and location so that the relative rotation was too weak to have caused forecasters to think in terms of a binary TC interaction.<sup>14</sup>

An important question is whether the development of the MG and attendant pattern transition from a N1 to G Pattern occurred essentially independent of the formation of Nancy and Owen, or whether the presence of the TCs contributed to the development and/or maintenance of the MG. The authors support the latter interpretation based on the following reasoning. Because of the reverse orientation of the monsoon trough in a N1 pattern, enhanced convergence in the upper troposphere (about 200-150 mb) is expected between the outflow of the monsoon trough convection and the northeasterly flow associated with the upper-level subtropical ridge circulation over east Asia. This situation is illustrated in Fig. 3.97a (note the prominent confluent asymptote). Because the tropopause is above this region of enhanced convergence, the converging air must subside and warm adiabatically. The resulting warm pool in the mid-to-upper troposphere will tend to cause large-scale cyclogenesis as the environmental wind field adjusts to the developing low pressure/height area. Development of a large mid-to-lower tropospheric cyclone to the northwest of the reverse-oriented monsoon trough will tend to transform the trough convection from a linear to curved pattern. Such a curved pattern of convection would

---

<sup>14</sup> Lander (1994; personal communication) has produced a relative motion diagram centered on the position of the MG that identifies the sequential rotation of the three TCs around the gyre.

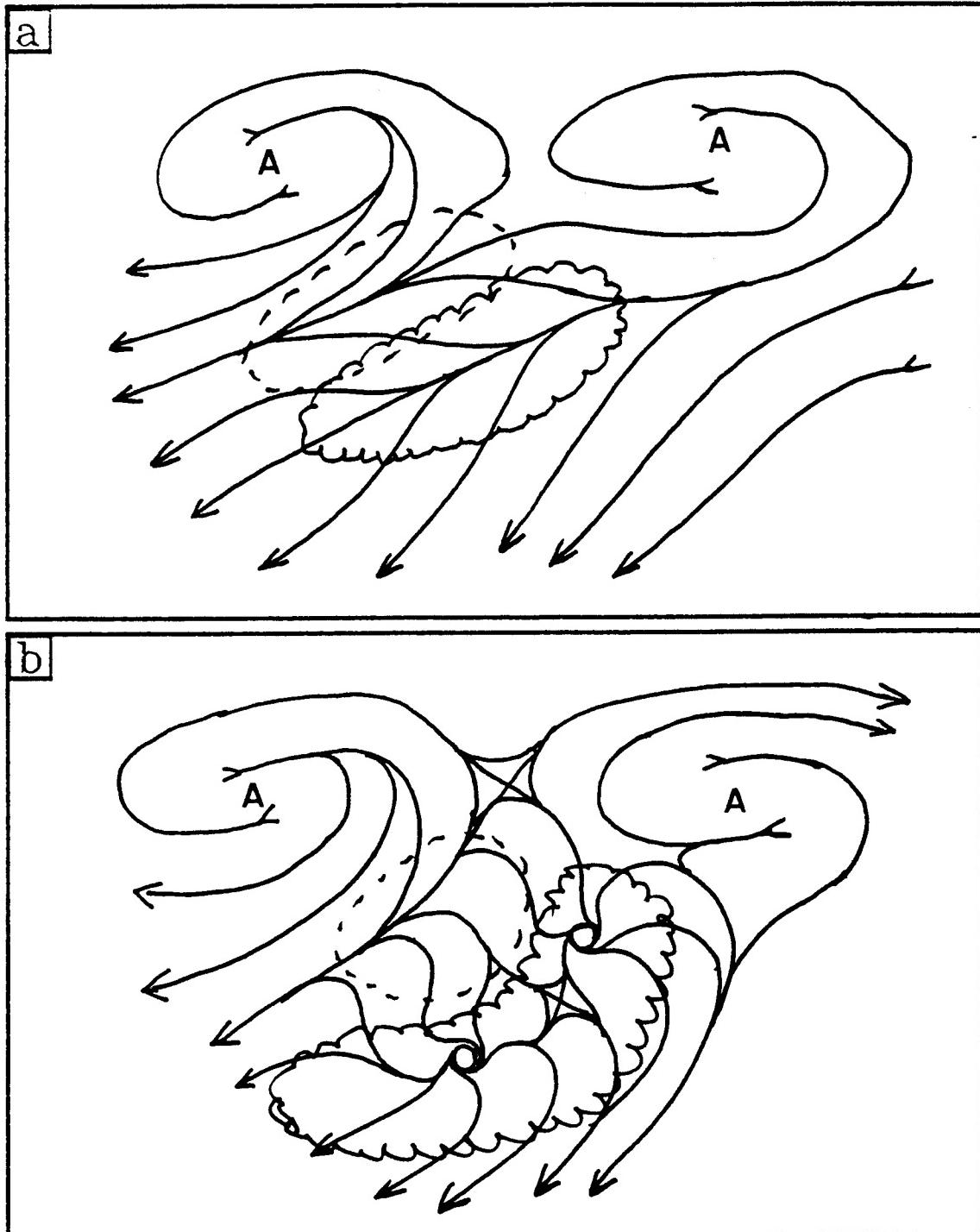


Fig. 3.97. (a) Schematic of upper-level (200-100 mb) streamline pattern depicting diffluent region associated with monsoon trough convection (scallops) and confluent region (dashed lines) between outflows of monsoonal convection to the southeast and the subtropical ridge to the northwest. (b) As in (a), except including the outflows from two tropical cyclones that have developed in the monsoon trough.

further enhance convergence to the northwest of the monsoon trough (Fig. 3.97b), and thus establish a positive feedback loop. The additional outflow generated by TCs (e.g., Doug and Ellie in August 1991) developing in the MG convection, and in close proximity with each other, would further enhance the convergence between the TCs and the anticyclone to the northwest. Such a mutual TC and MG development could significantly enhance the MG circulation and lead to the transition to a G Synoptic Pattern.

It is emphasized that the Nancy/Owen (and Peggy) example is not an isolated case of the TCI5 mode. Although a thorough review of many cases has not been conducted, the apparent binary interaction of Odessa and Pat in 1985 (Fig. 3.76a-b) is another example in which collective advection of multiple TCs by a developing MG plays a significant role. Support for this interpretation is the large ring of convection that surrounds the TCs in the satellite imagery (Fig. 3.98). Because these TCs have a much smaller separation distance than Nancy and Owen, it is possible that a bona fide binary TC interaction (TCI6 mode) may also have a role. Notice the rather small size of Odessa compared to Pat in Fig. 3.98, and that Pat moves quite rapidly north during the 30th while rotating relative to Odessa (Fig. 3.76b). It is suggested that advection by the southerly flow on the east side of the MG may be an alternate explanation for the rapid movement of Pat to the north.

In conclusion, the general nature of the tracks of Nancy and Owen in 1989 and Odessa and Pat in 1985 have a number of important similarities of which the TC forecaster should be cognizant. In both cases, the TCs tend to form in the southern region of the MG. In the case of Nancy and Owen, the formation is almost simultaneous, whereas Odessa forms earlier than Pat during the evolution of the north-oriented trough into a MG. In both cases, the TCs track around the east side of the MG, and then are "ejected" toward the pole into the midlatitude westerlies. More cases need to be examined to determine the repeatability of the general motion pattern. However, the track similarities in the two cases may provide the forecaster with a sense of the kind of TC motion to be anticipated when development of multiple TCs within a MG is observed.

**4. Case Study #4.** This case study involves Typhoons Angela, Brian, and Colleen in October 1992. The primary purpose of this case study is to illustrate that the rather complex looping motion of Colleen resulted from successive M Synoptic Patterns (TCI1 mode) that involved Colleen and the other TCs. The study also illustrates an example of one-way pseudo-binary influence (TCI2).

During 16-19 October, the track of Colleen is northwest (Fig. 3.99a). At 0000 UTC 18 October (Fig. 3.100a), Colleen is under the influence of east-southeasterly steering (note Colleen's position to northeast of NOGAPS-analyzed center) in the DR Region of a S Synoptic Pattern. Although Angela is farther west in the same pattern and near the break in the ridge, this is not considered to be a M Pattern because the ridge to the north of Colleen extends westward beyond Colleen, and thus still affects the motion of Angela.

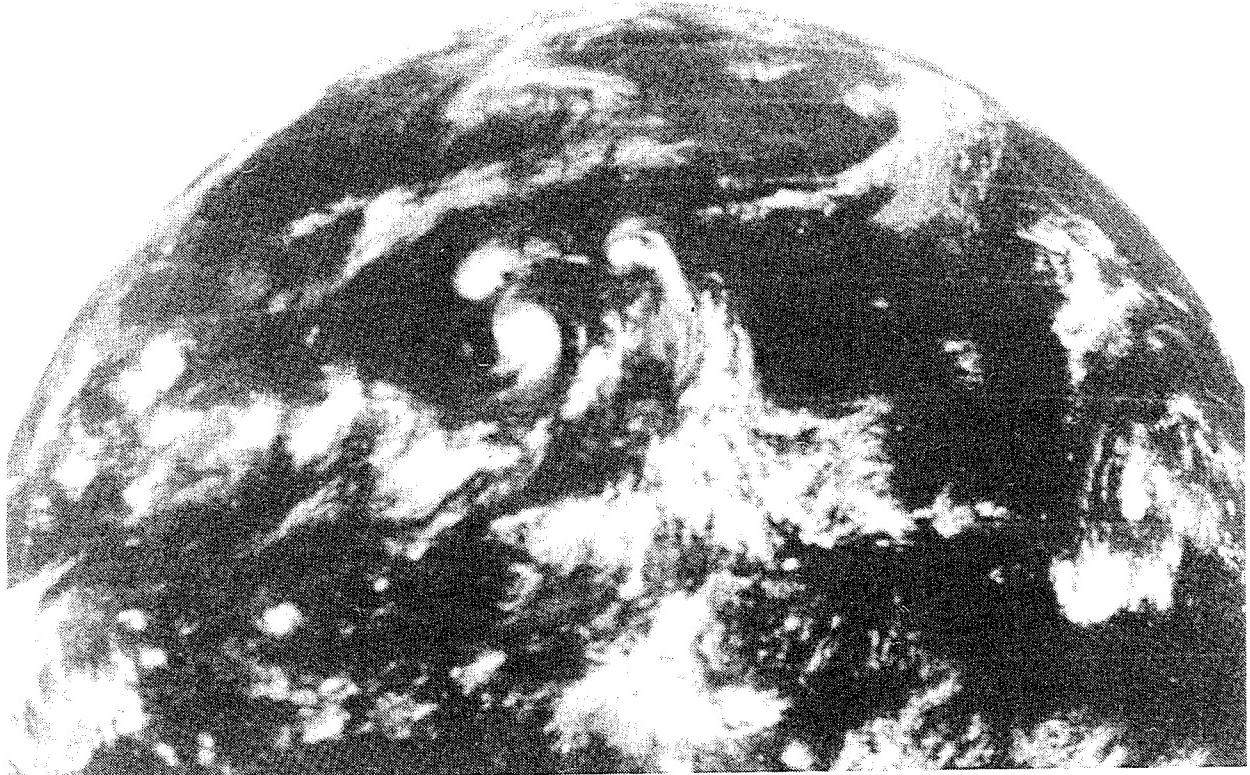


Fig. 3.98. As in Fig. 3.83, except at 0300 UTC 30 August 1985 for Typhoons Odessa, Pat, Ruby and peripheral curved convection associated with a large monsoon gyre. Pat is the larger TC with the visible eye, and Odessa and Ruby are located to the northwest and northeast of Pat, respectively.

By 0000 UTC 19 October (Fig. 3.100b), the poleward displacement of Colleen and the weakening of the ridge to the north has set up a M pattern in which Colleen is subjected to southerly flow between Angela to the west-southwest and the ridge to the northeast. Whereas the 30-kt isotach to the southeast of Angela would normally indicate a northeastward track, the M Pattern is subjecting Angela to northerly flow between Colleen to the east and the ridge circulation to the west. These offsetting influences prevent a poleward displacement of Angela, which drifts westward. Notice that Angela and Colleen are 15° lat. apart, and that satellite imagery (Fig. 3.101a) indicates that they are not particularly large, which precludes the possibility of a binary TC interaction (TCI6 mode).

By 0000 UTC 20 October (Fig. 3.100c), the northward and westward displacements of Colleen and Angela, respectively, have increased their separation by several degrees. This is expected in a M Pattern (Fig. 3.15) in which advective influences naturally tend to separate the TCs and thus destroy the pattern. As expected with the 30-kt isotach to the east (Fig. 3.100c) Angela again has a poleward displacement. Since Colleen is still well south of the ridge axis at 0000 UTC 20 October (Fig. 3.100c), Colleen might be expected

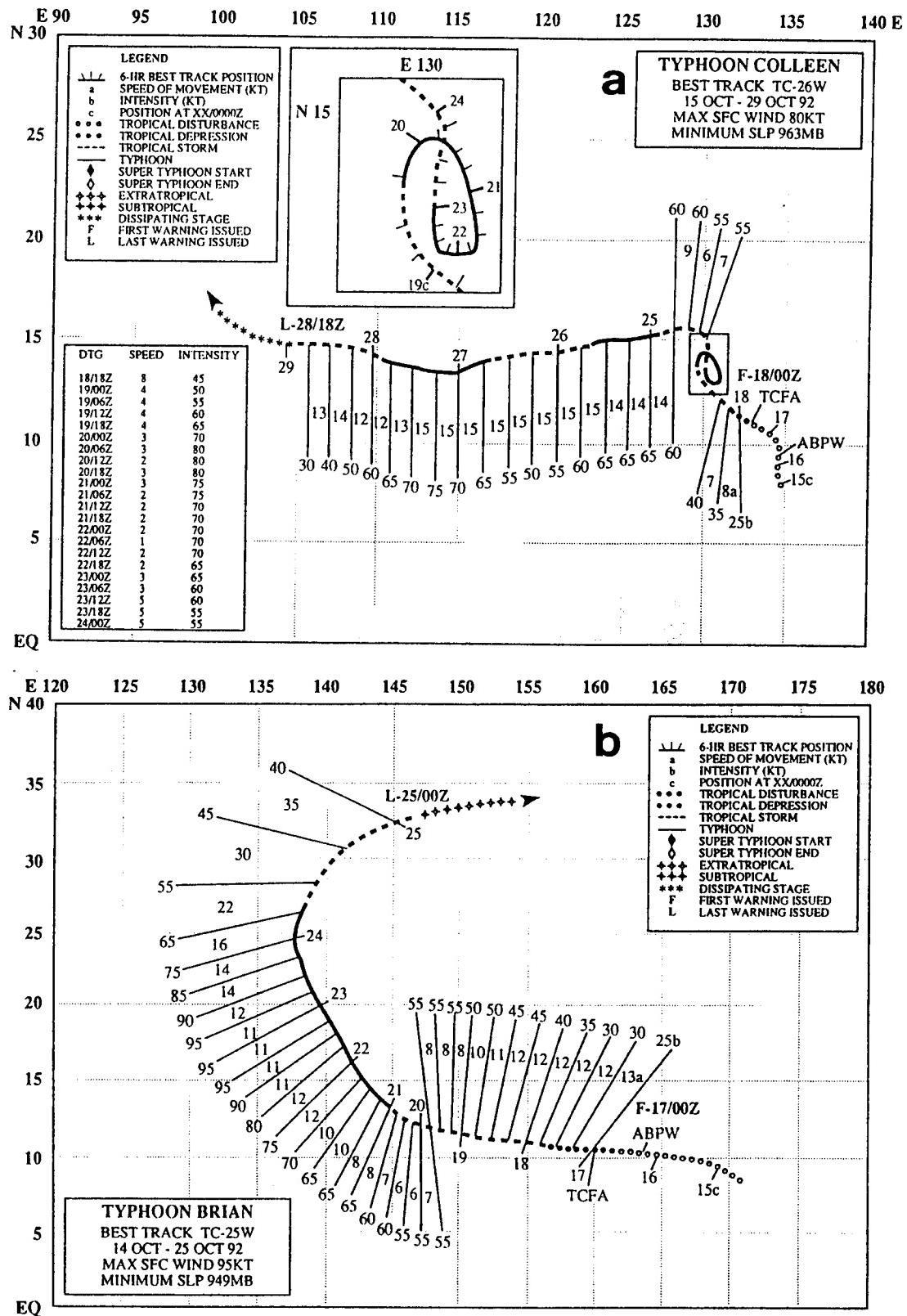


Fig. 3.99. As in Fig. 3.1, except for (a) Typhoon Colleen during 15-29 October 1992, and (b) Typhoon Brian during 14-25 October 1992.

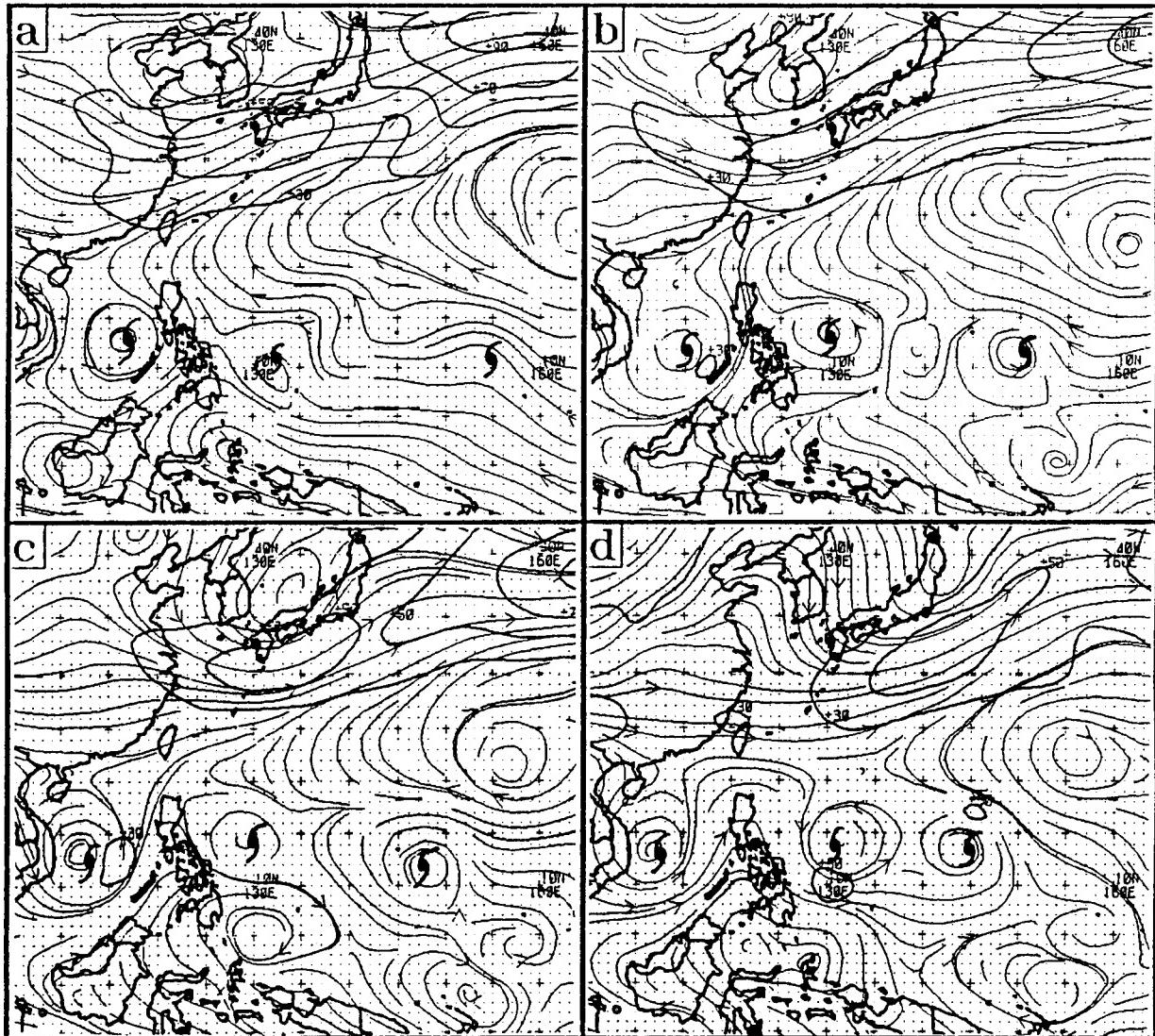


Fig. 3.100. As in Fig. 3.79, except for (a) 18, (b) 19, (c) 20, and (d) 21 October 1992. TC symbols denote Typhoons Angela (west), Colleen (middle), and Brian (east).

to have a northwestward track as Angela moves away to the west. However, Colleen begins an anticyclonic loop with an equatorward track during 20 and 21 October (Fig. 3.99a).

Colleen's equatorward track is consistent with the approach of Brian from the east, which results in the establishment of a second M pattern. By 0000 UTC 21 October (Fig. 3.100d), Brian is within 15° long. of Colleen, and has intervened between Colleen and the ridge circulation to the northeast. Notice also that the ridge to the west of Colleen has amplified, perhaps due to beta-induced dispersion from Angela. The strength of this ridge and the presence of Brian to the east appear to explain the equatorward deflection of Colleen. Notice that Brian is moving into a position between Colleen and the ridge to the northeast, which would be expected to deflect Brian poleward (Fig. 3.99b).

By 0000 UTC 22 October (Fig. 3.101c; Fig. 3.102a), the separation distance of Colleen and Brian has decreased so that the possibility of a binary TC interaction exists. However, the small size of Brian's cloud pattern in satellite imagery (Figs. 3.101b-c) indicates, and rawinsondes before and after Brian passed over Guam on 21 October (Fig. 3.99b) conclusively confirm that Brian had a mid-level circulation insufficiently large to significantly affect the motion of the much larger Colleen. Rather, the M Pattern with the ridge to the west and Brian to the northeast is expected to be the dominant influence on Colleen's motion. Notice the closed isotach to the southwest of Colleen and the analyzed 500 mb circulation center to the northeast are indicative of the northwesterly steering that would tend to offset  $\beta$ -effect propagation (BEP) toward the northwest. Colleen was nearly stationary during the 22nd (Fig. 3.99a). However, the large circulation of Colleen may have a one-way binary cyclone influence on Brian. An alternate explanation is that Brian accelerated to a 12 kt displacement (Fig. 3.99b) as a result of the M Pattern with Colleen to the southwest and the ridge to the northeast. That is, this aspect of Brian's track may have arisen from the SF Region of the M Pattern (TCI1 mode), and a one-way advective influence of Colleen on Brian (TCI2 mode).

Brian subsequently moves northward and recycles around subtropical ridge, which leaves Colleen as a single circulation system south of a southwest-northeast oriented ridge (Fig. 3.102c). Colleen resumes a poleward motion until 0000 UTC 24 October (Fig. 3.99a). A westward track then ensues after reestablishment of the ridge circulation to the north when Brian has recurved. This multiple tropical cyclone case is obviously complex because of the relative motion of the three cyclones and the ridging that develops between Angela and Colleen. Although some one-way binary influence between Colleen and Brian may have occurred on 21-22 October, the M Pattern provides an alternate explanation because of the relatively small (large) size of Brian (Colleen).

**5. Case Study #5.** This case study involves Tropical Storm Luke and Typhoons Mireille and Nat during September 1991. This study is similar to Case #4 in that three TCs are involved, and one TC (Nat) undergoes successive interactions with the other two TCs. Because of differences in orientation and relative sizes of the TCs, the resulting tracks are distinctly different. Thus, this study illustrates the range of TC motions that may

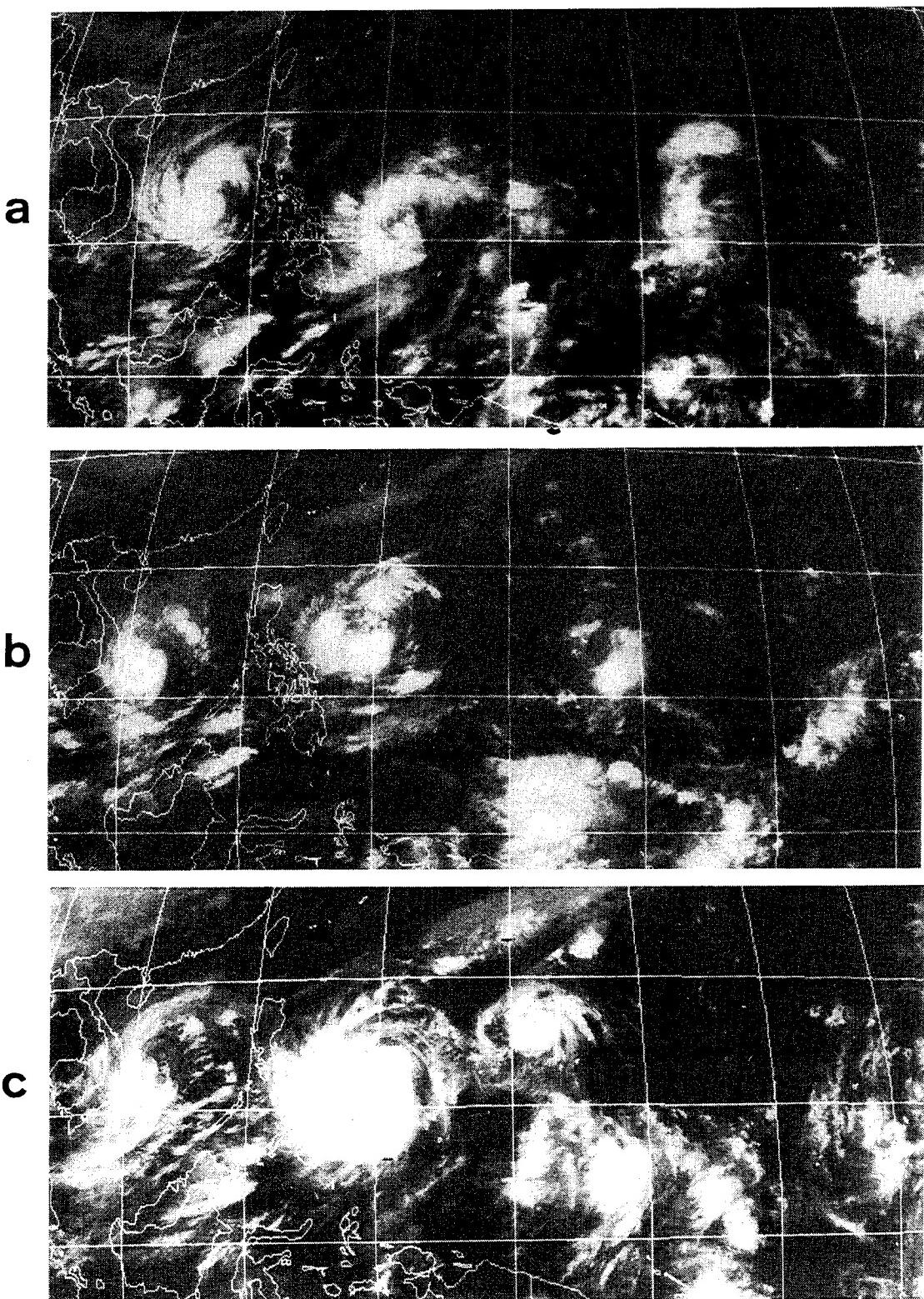


Fig. 3.101. As in Fig. 3.83, except for Typhoons Angela (west), Colleen (middle), and Brian (east) at 0000 UTC on (a) 18, (b) 20, and (c) 22 October 1992.

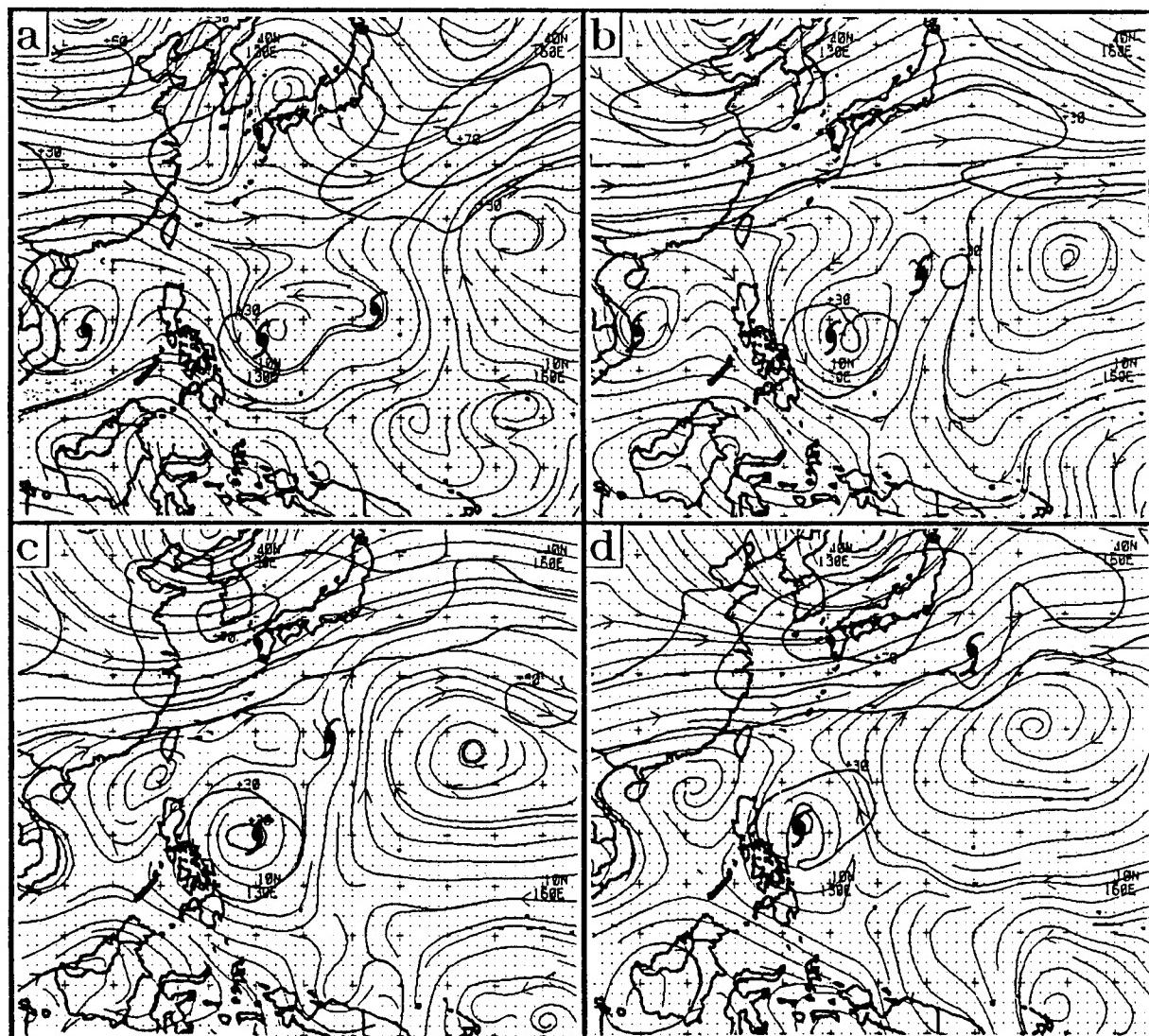


Fig. 3.102. As in Fig. 3.100, except for (a) 22, (b) 23, (c) 24, and (d) 25 October 1992.

result from various combinations of TCI modes and sizes of the TCs.

Tropical Storm Luke is a rather large monsoon depression-type system that has a rather typical recurvature track (Fig. 3.103a) during 16 to 20 September. By contrast, Mireille turns onto an atypical west-southwest track on the 17th (Fig. 3.103b), and Nat undergoes a severe track direction change from west-northwest to east-northeast during the period (Fig. 3.103c).

Luke is believed to be the cause of the track changes of the other two TCs. Because of the large size of Luke, a RMT-induced transition from a S to N2 Synoptic Pattern occurs. The  $\beta$ -induced peripheral ridge to the east of Luke subjects Mireille to east-northeasterly steering (Fig. 3.104b-c) influence that is superposed on the easterly steering arising from the S Pattern DR Region in which Mireille is located (recall Fig. 3.21b and discussion concerning eastern DR Region). Thus, the temporary west-southwestward movement of Mireille (Fig. 3.103) is an example of a TCI3 mode. Whereas the presence of Verne rapidly weakened the peripheral ridge of Seth in Case Study #1, Mireille does not appear to have a significant effect on the peripheral ridge associated with Luke, presumably owing to Mireille's small size.

As Luke recycles, the ridge to the north of Nat, which had been providing east-southeasterly steering to Nat (Fig. 3.104a), is replaced by westerly flow in the wake of Luke (Fig. 3.104c). The strength of this flow is enhanced by the strong ridge to the southeast of Nat (Fig. 3.104c-d). This ridge may have been enhanced by a  $\beta$ -induced dispersion from Luke, and this seems to be an example of a TCI3 mode with a TC to the east. Nat, which is a small TC, is swept back through the channel between Luzon and Taiwan during 17 to 21 September (Fig. 3.103c). During this period, satellite imagery shows Nat embedded in the linear convection (Fig. 3.105) of the monsoon surge that develops between the remnants of the peripheral ridge to the southeast and the lower geopotential heights to the northwest over Southeast Asia (Fig. 3.104).

During 20-23 September, the track of Mireille changes from west-southwestward to northwestward (Fig. 3.103b), and Nat undergoes another major track reversal from east-northeastward to west-northwestward (Fig. 3.103c). Since the subtropical ridge is still completely absent (Fig. 3.106a), Nat is subjected to weak west-southwesterly steering between a midlatitude cyclone to the north and the ridge to the southeast. By 21 September (Fig. 3.106b), the subtropical ridge builds from the northeast and northwest of Nat, a thin ridge extension is established to the north of Nat by 22 September (Fig. 3.106c). Since Nat is a small TC, the restoration of a thin subtropical ridge to the north is apparently sufficient to dominate the motion of Nat, and cause it to return to a westward heading on 21 September (Fig. 3.103c).

Meanwhile, Mireille has grown from a small circulation (Fig. 3.105b) to a substantially larger circulation (Fig. 3.107a) with a wave train in its wake (Fig. 3.106d). Concurrently with this increase in size, Mireille's direction of motion changes from

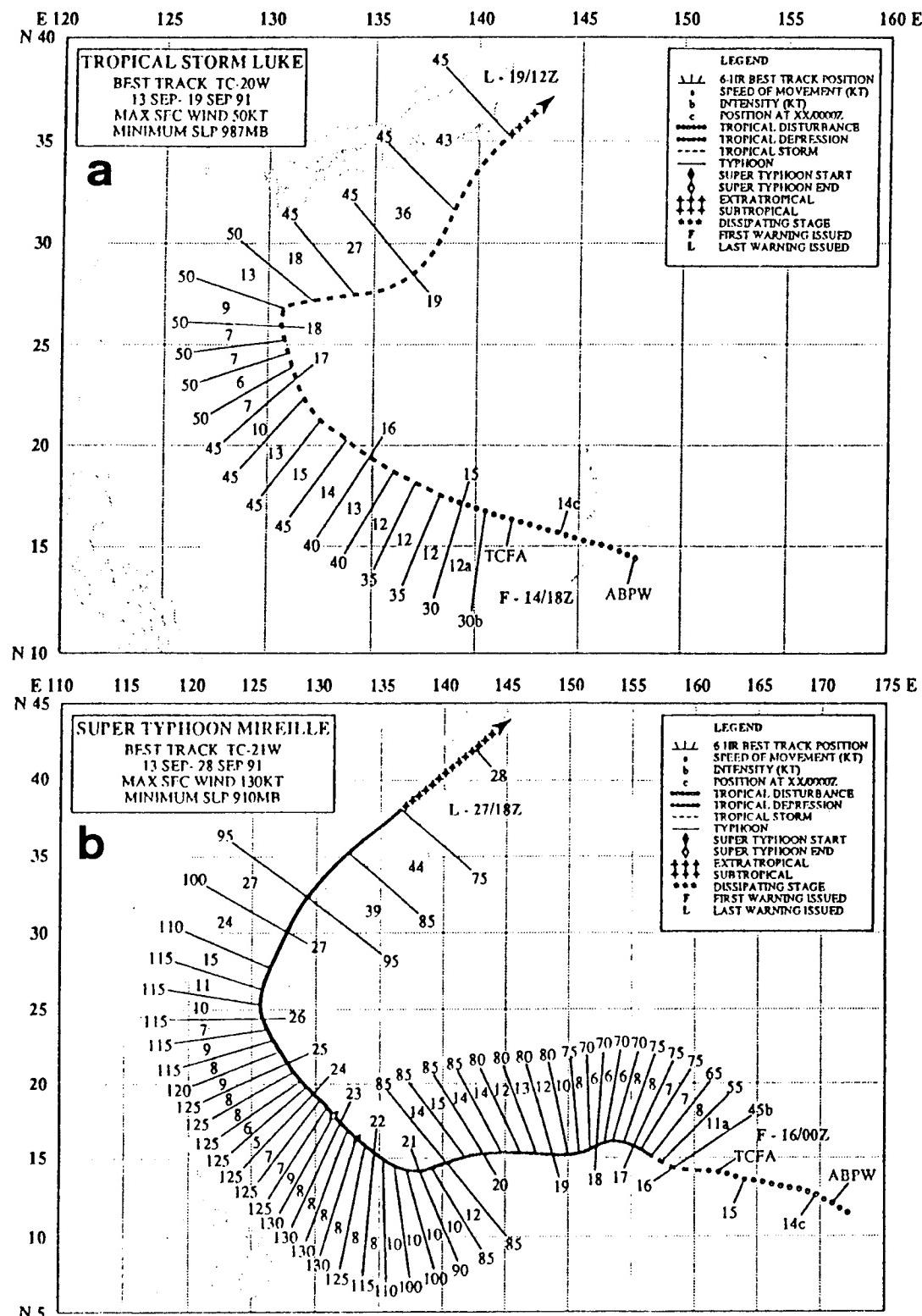


Fig. 3.103. As in Fig. 3.1, except for (a) Tropical Storm Luke during 13-19 September 1991, (b) Supertyphoon Mireille during 13-28 September 1991, and (c) Typhoon Nat during 15 September-2 October 1991.

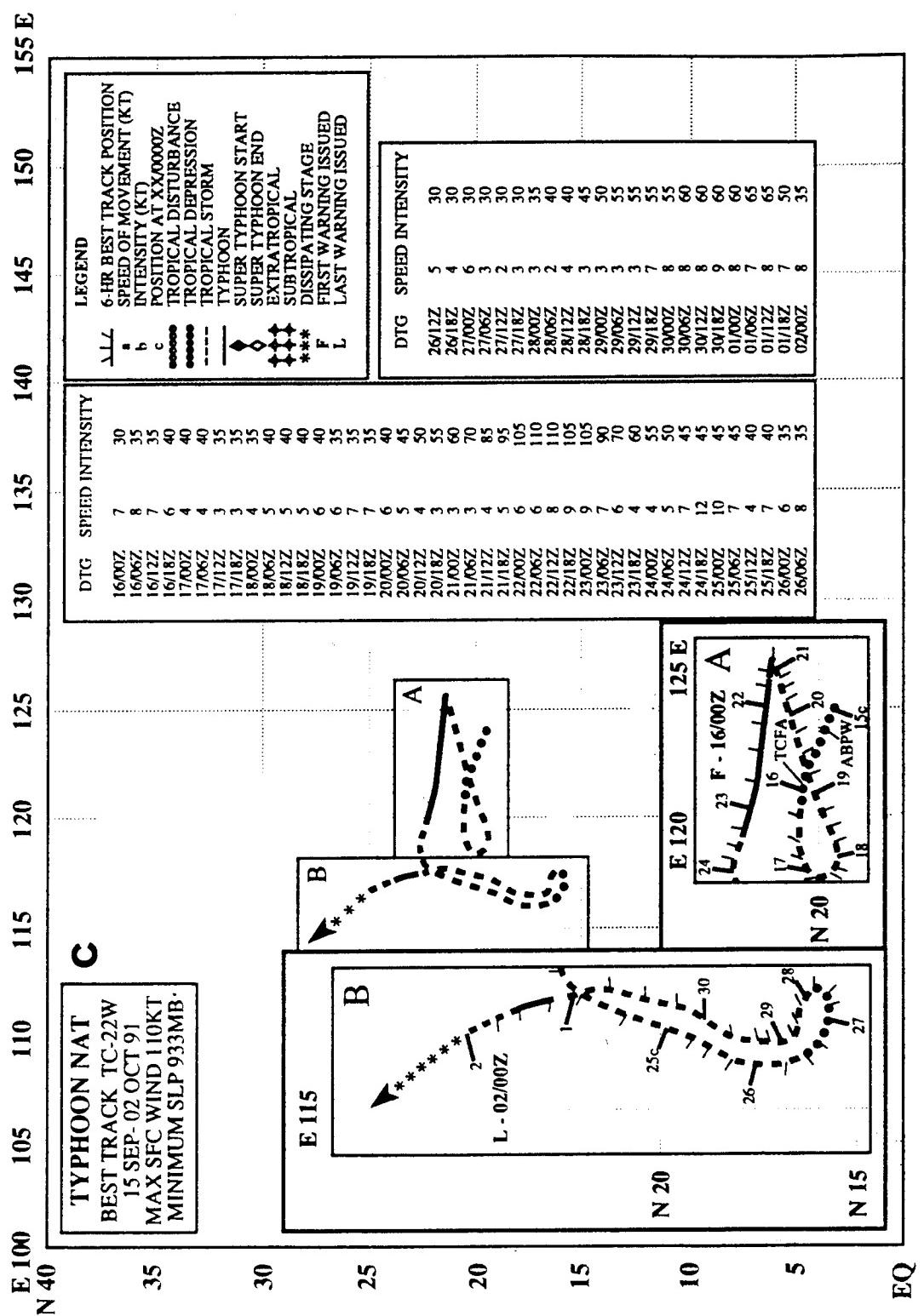


Fig. 3.103. (Continued)

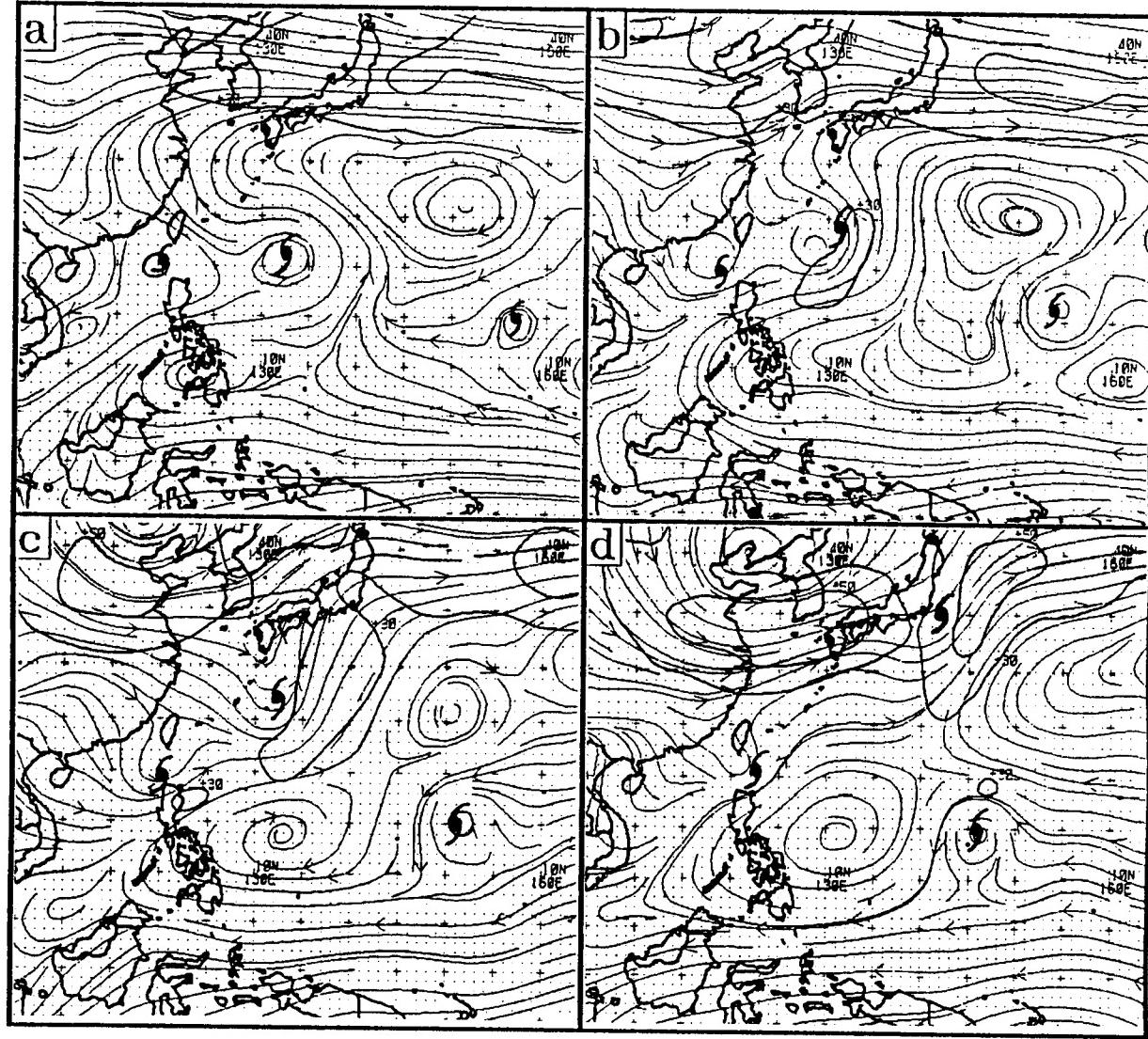


Fig. 3.104. As in Fig. 3.79, except on 1200 UTC for (a) 16, (b) 17, (c) 18, and (d) 19 September 1991. TC symbols denote Typhoon Nat (west), Tropical Storm Luke (middle), and Supertyphoon Mireille (east).

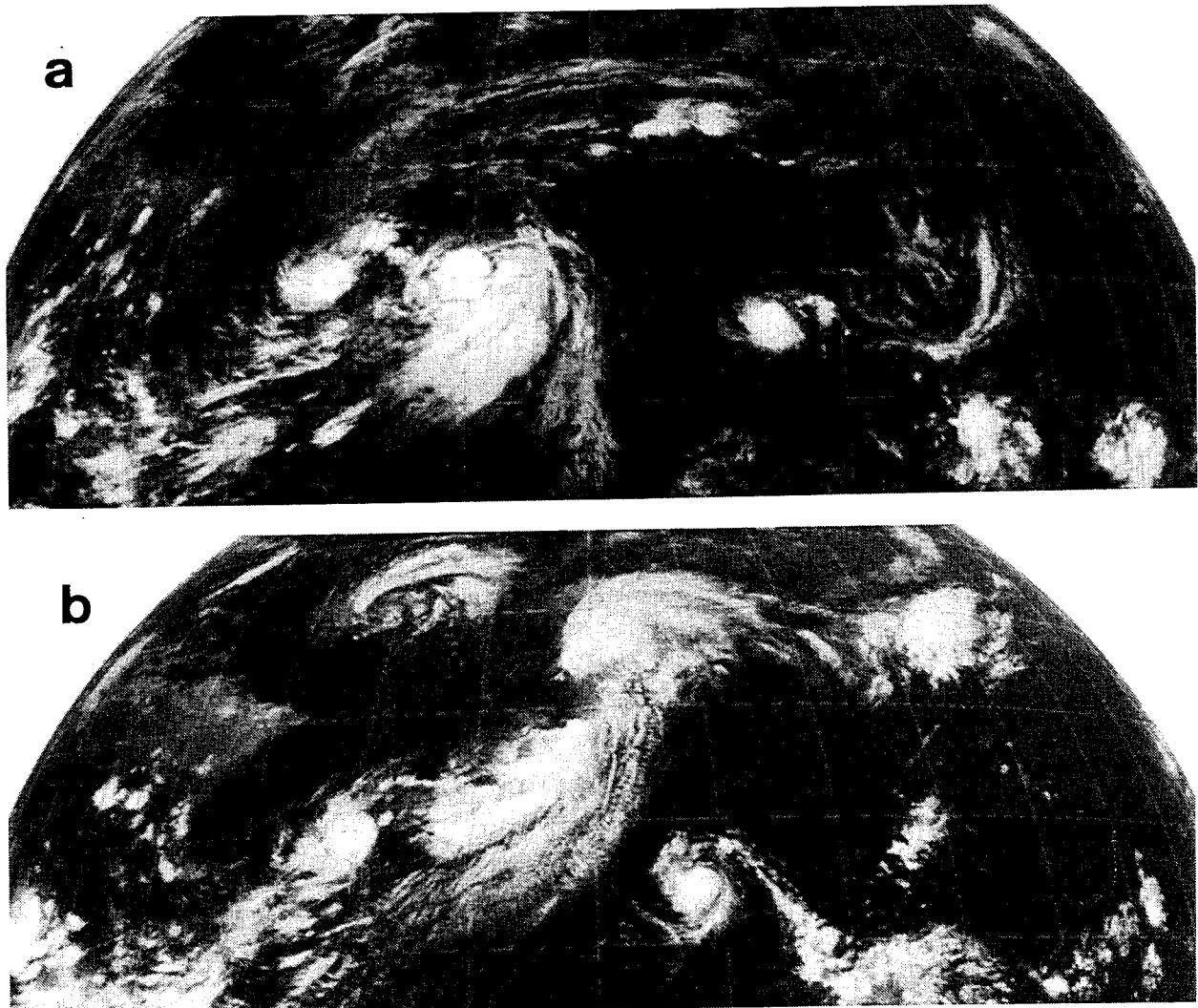


Fig. 3.105. As in Fig. 3.83, except for Typhoon Nat (west), Tropical Storm Luke (middle), and Supertyphoon Mireille (east) at 0300 UTC on (a) 17, and (b) 19 September 1991.

west-southwestward to northwestward (Fig. 3.103b), which is consistent with an expected increase in northwestward BEP. As Mireille approaches to within about 10° lat. of Nat during 24 and 25 September, Nat commences a major track change onto an equatorward heading (Fig. 3.103c). The translation speed of Mireille, which decreases from 9 to 5 kt during 23 September, then undergoes a temporary increase to about 8 kt (Fig. 3.103b). The impetus for these track changes is the establishment of a M Pattern (Fig. 3.108a-b). Because of the small size of Nat, the effect on Mireille is limited to a rather subtle change in speed on an otherwise typical recurvature track. By contrast, Nat has a rather severe track change owing to a northerly steering flow between Mireille to the east and the ridge west (Fig. 3.108b). Given the large size of Mireille and the 10° lat. separation distance, an advection of Nat by the circulation of Mireille is likely (TCI2 mode). On the 24th (Fig.

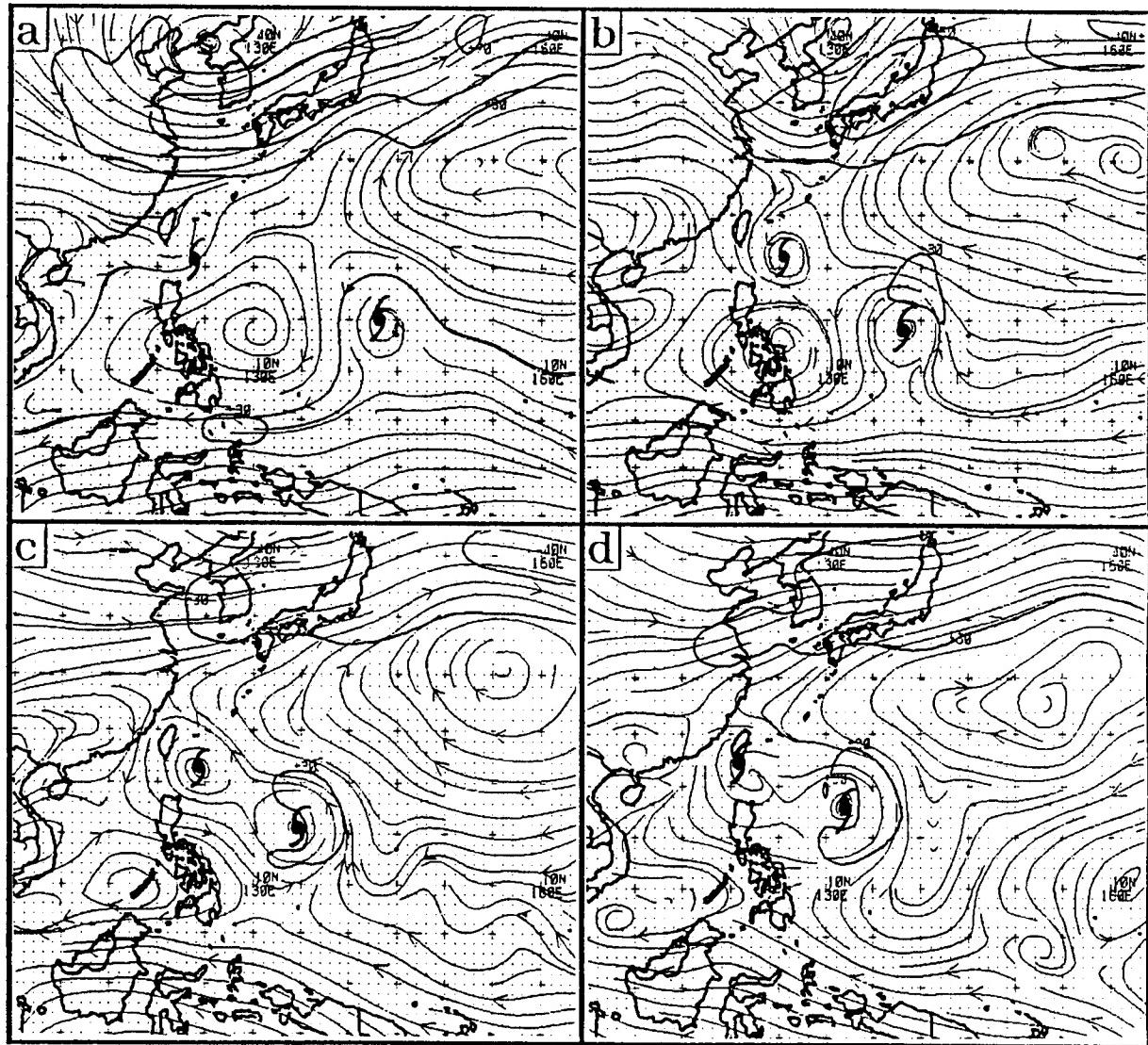


Fig. 3.106. As in Fig. 3.104, except for (a) 20, (b) 21, (c) 22, and (d) 23 September 1991, and only Tropical Storm Nat (west) and Supertyphoon Mireille (east) remain.

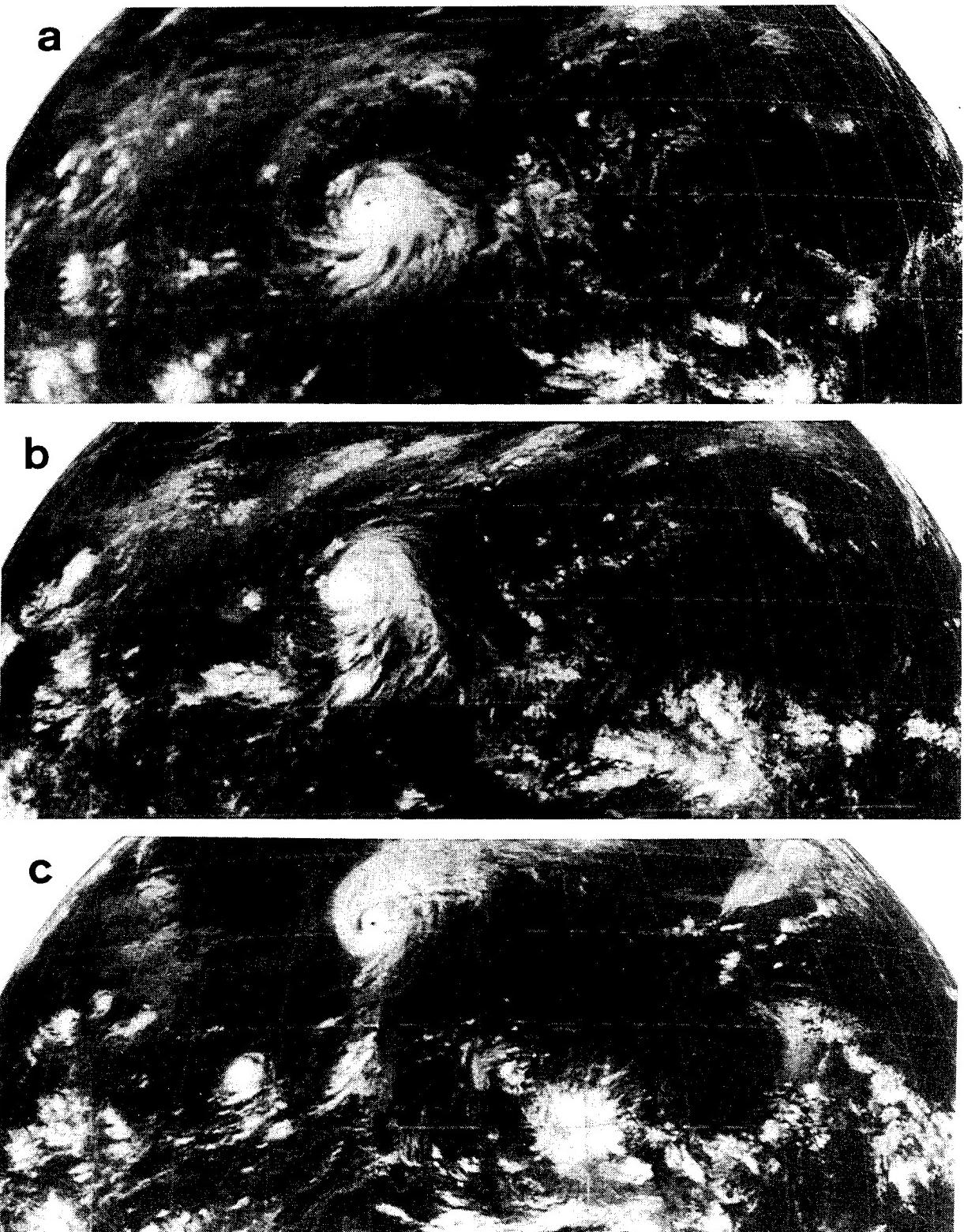


Fig. 3.107. As in Fig. 3.83, except for Typhoon Nat (west) and Typhoon Mireille (east) at 0300 UTC on (a) 24, (b) 25, and (c) 27 September 1991.

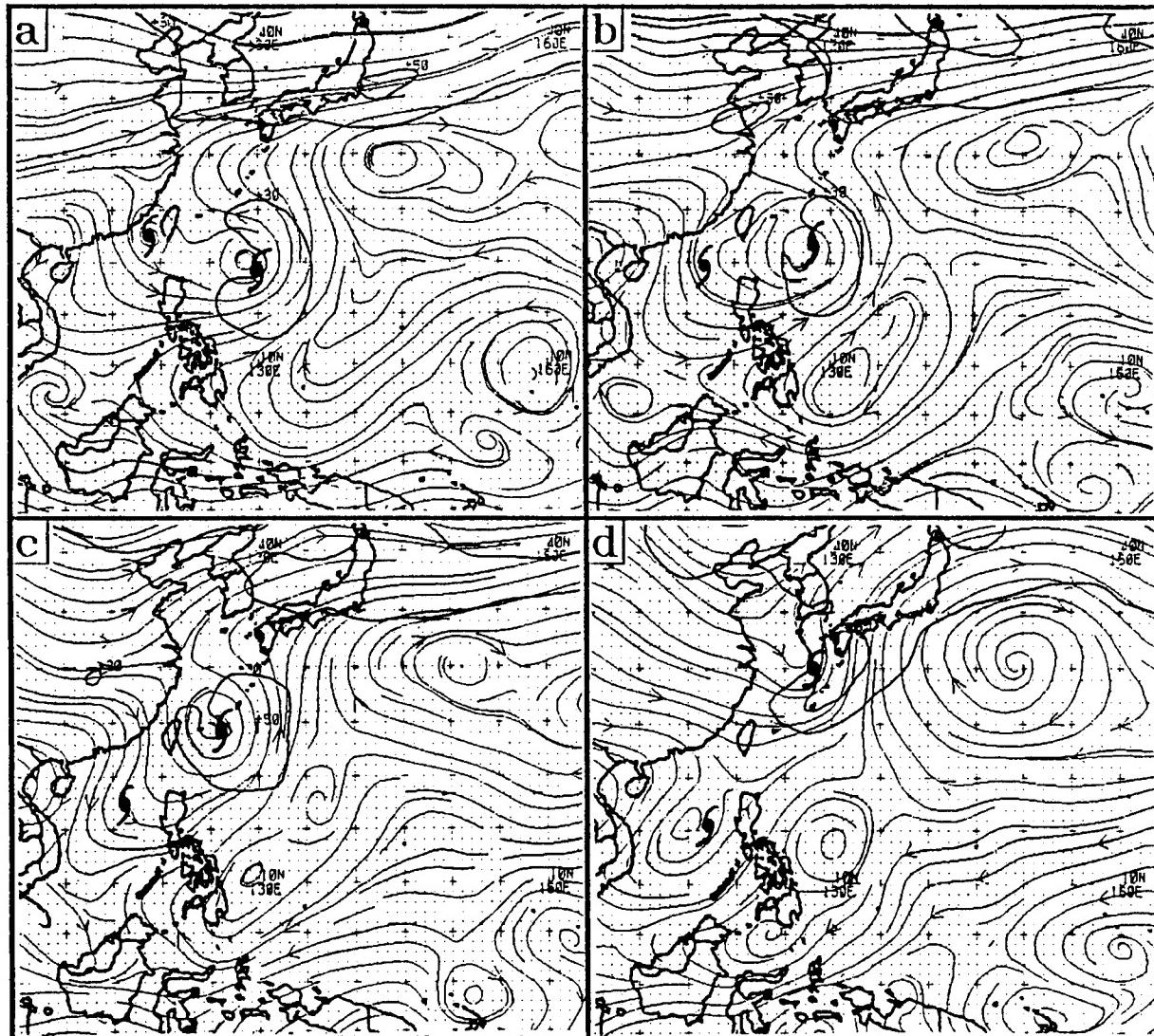


Fig. 3.108. As in Fig. 3.106, except for (a) 24, (b) 25, (c) 26, and (d) 27 September 1991.

3.107a), Nat appears to be near a band of convection spiraling into Mireille from the northwest.

The subsequent turn of Nat to the east during 26 and 27 September (Fig. 3.103c) as Mireille accelerates to the northeast is consistent with steering by the enhanced southwesterly flow between a monsoonal circulation in the South China Sea and the ridge east of the Philippines (Fig. 3.108c-d). Notice Nat is embedded in a linear southwest-northeast oriented pattern of convection trailing to the south-southwest of Mireille (Fig. 3.107c). Subsequently, Nat drifts slowly north in weak steering until landfall in Southeast Asia on 2 October (Fig. 3.103c).

In summary, the very complex track of Nat can be explained as a series of different TC interaction modes contributing to an evolving background flow:

- (i) turn to the east during 17 September in response to steering associated with the peripheral ridge remnant from Luke (TCI3 mode);
- (ii) turn back to the west during 21 September in response to a building subtropical ridge to the north (cessation of TCI3 mode);
- (iii) turn to the south during 24 September in response to northerly flow arising from the establishment of a M Pattern with Mireille (TCI1 mode). Advection of Nat by the circulation of Mireille also probably played a role in this turn (TCI2 mode);
- (iv) turn toward the east during 26 September in response to the breakdown of the M Pattern and the superposed pseudo-binary interaction (cessation of TCI1 and TCI2 modes), and initiation of advection by the enhanced southwesterlies associated with the peripheral ridge remnant from Mireille (TCI3 mode); and
- (v) turn onto the final northward leg during 28 September in response to the decay of the enhanced southwesterly flow (cessation of TCI3 mode).

The relative motion diagram for Nat and Mireille (Fig. 3.109) has been interpreted (1991 ATCR, p. 111) as a binary TC capture on 21 September. In view of (i) above and the earlier discussion, this "capture" was actually a cessation of the indirect influence of Tropical Storm Luke. By contrast, a more likely commencement time for bonafide advection of Nat by Mireille is during 24 September when the angular rotation rate between the two TCs has a significant increase.<sup>15</sup>

---

<sup>15</sup> In cases such as Mireille and Nat with an extreme size difference, a relative motion diagram in which the positions of the smaller TC with respect to the larger TC (direction and distance) are plotted relative to the fixed center of the diagram would seem to provide a more meaningful measure of the interaction.

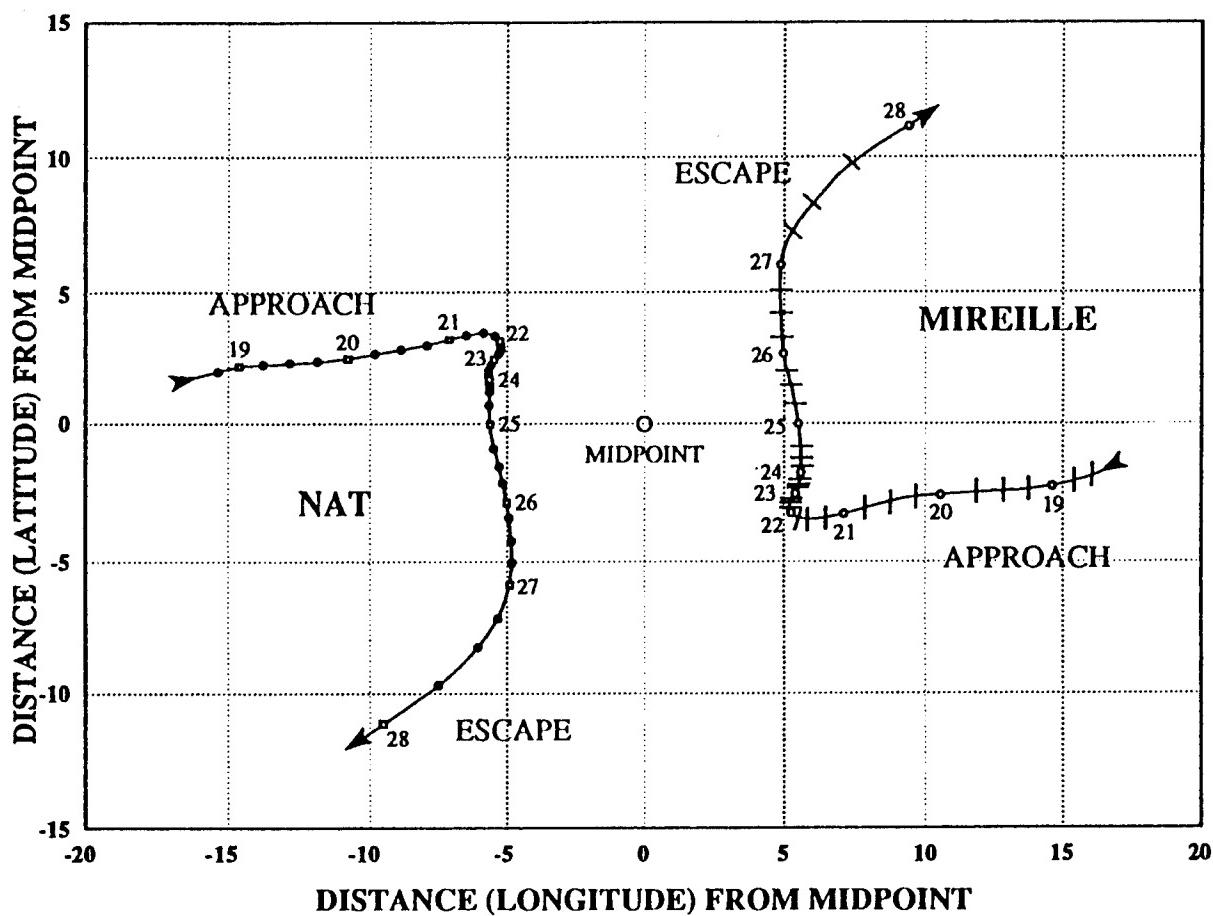


Fig. 3.109. As in Figs. 3.75b and 3.76b, except for Typhoons Nat (left) and Mireille (right) from 0000 UTC 19 September to 0000 UTC 28 September 1991.

## 6) Summary

*a) Utilization guidelines.* The preceding subsections have illustrated five TC-environment transformations that may have a significant impact on TC motion. Other synoptic circulations (which are considered as part of the TC Environment Structure) also may have a significant impact on TC motion (e.g., interactions with intense Tropical Upper Tropospheric Trough cyclones, etc.). However, these five transformations are believed to account for most TC track anomalies, and have an adequate observational and/or dynamical basis to justify their inclusion. Because some of these TC-Environment transformations are based on unpublished research, additional research is needed, particularly on the RMT transformation. In the meantime, forecasters must exercise some caution when utilizing the transformation conceptual models in the TC forecasting process.

Many of the TC-environment transformation case studies have involved complex motion processes that depend sensitively on various aspects of TC and environment structure that are difficult to specify with accuracy. It is highly unlikely that complex motion evolutions, particularly the TCI-related track changes of Colleen and Nat, will be repeated again in every detail. Thus, the forecaster should not attempt to apply the Colleen and Nat (or other past) scenarios to future situations in an unduly rigid manner. Rather, the intent of these illustrations of TC-Environment transformations has been to describe the general types of the associated TC track changes. Forecasters may use such information to:

- (i) understand the most dynamically-feasible track the TC is likely to take when a particular TC-Environment transformation is anticipated or in progress (and perhaps as importantly, where the TC is not likely to go); and
- (ii) improve forecast-to-forecast consistency by having a dynamically-based "game plan" to follow during complex transformational situations, and which can be updated and modified as warranted by changing circumstances.

*b) TC-Environment structure transformation indicators.* A number of indicators for detecting or anticipating the TC-Environment transformations have been consolidated below.

#### **Significant Beta-effect Propagation (BEP)**

##### **- Satellite imagery**

- (i) Average to Large TC size inferred from the overall extent of cloud signature.
- (ii) Cloud max-min-max pattern to southeast of TC (in conjunction with a  $\beta$ -induced wave train in the analysis).

##### **- Numerical analyses**

- (i) Average to large TC size inferred from strategically placed rawinsonde observations.
- (ii)  $\beta$ -induced wave train evident in 500 mb streamline analyses. If peripheral anticyclone is large relative to the extent of subtropical ridge, then RMT may also be occurring.

##### **- Recent TC motion**

- (i) Past motion exhibits significant deflection to right (Northern Hemisphere) of predominantly easterly steering (i.e., in DR Region).

## **Vertical Wind Shear (VWS)**

### **- Satellite imagery**

- (i) Restricted outflow on upshear side of TC.
- (ii) In case of westerly VWS, continuous cirrus streaming poleward and eastward from TC.
- (iii) Low-Level Circulation (LLC) partially or fully exposed from under Convective Cloud Mass (CCM).
- (iv) During Northern Hemisphere winter monsoon season, strong surge off Asia indicated by stratocumulus cloud streets streaming into western Philippine Sea.

### **- Numerical analyses**

- (i) Wind analyses at 200 mb have only linear divergent flow over TC instead of distinct outflow pattern. Caution: NOGAPS tends to under-analyze strength of TC outflow pattern in VWS situations, and thus over-emphasizes impact of VWS on TC.

### **- Recent TC motion**

- (i) In Northern Hemisphere winter monsoon situations, TC stalls at ridge axis prior to turning equatorward in response to winter monsoon flow.

## **Ridge Modification by Large TC (RMT)**

### **- Satellite Imagery**

- (i) Usually requires a large TC size as implied from extent of cloud signature. (Remember that an average size TC can initiate RMT if ridge circulation does not have a large meridional extent).
- (ii) A large-scale cloud max/min/max pattern extending eastward and equatorward of TC is usually present. Cloud "min" area often has a gray quasi-stratiform appearance in infrared imagery.
- (iii) Recurvature occurs *without* the characteristic broad and unbroken cirrus pattern streaming eastward and poleward that would be expected in association with a significant midlatitude trough.
- (iv) TC continues to intensify after recurvature.

- **Numerical analyses**

- (i) Growing peripheral anticyclone to east and equatorward of TC.
- (ii) Eroding subtropical ridge poleward and to west of TC.
- (iii) TC begins to recurve *without* presence of pre-existing deep midlatitude 500 mb trough that is approaching/digging.

- **Recent TC motion**

- (i) Significant slowing to possibly quasi-stationary motion south of pre-existing ridge latitude.
- (ii) Leftward curving track for up to several days after recurvature.
- (iii) Delayed acceleration for up to several days after recurvature.

### **Monsoon Gyre-TC Interaction (MTI)**

- **Satellite imagery**

- (i) TC cloud signature imbedded in or near eastern side of cloud signature of pre-existing monsoon gyre: either large- scale ring of convective cloudiness surrounding cloud minimum area, or fish-hook pattern on east side.
- (ii) Crescent-shaped peripheral cloud band forms 5-8 deg. lat. to east and equatorward of TC that does not spiral into the TC. Moat area of suppressed mid-to-high clouds usually evident between the peripheral band and the TC cloud pattern.
- (iii) Development of a cloud max/min/max pattern extending to southeast of MG in association with Rossby wave train.

- **Numerical analyses**

- (i) TC position within about 8° lat. of large cyclone at 500 mb that corresponds well with monsoon gyre cloud pattern in Section 3.d.4.
- (ii) Developing  $\beta$ -induced wave train to east and equatorward of TC as TC merges with monsoon gyre in successive analyses.
- (iii) Development of prominent crescent-shaped isotach pattern at 500 mb wrapping around east side of TC.

**- Recent TC motion**

- (i) Rapid deceleration to a quasi-stationary motion (or tight cyclonic loop) for up to a day. Deceleration is often preceded by an equatorward curving track.
- (ii) Sharp poleward turn that is usually followed by a leftward curving track and a subsequently west of poleward track until eventual recurvature. Poleward turn may be large enough to temporarily establish an east of poleward heading.

**Tropical Cyclone Interactions (TCIs)**

**- Satellite imagery**

- (i) TCI1: No obvious indicators.
- (ii) TCI2: One-way pseudo-binary influence may be expected when satellite cloud signatures indicate one TC is much smaller than the other and appropriate separation distance exists.
- (iii) TCI3: Advection of eastern TC by peripheral ridge of western TC expected when cloud signature of western TC is large, and its associated peripheral ridge is strong enough to produce a distinct cloud minimum region.
- (iv) TCI4: No obvious indicators.
- (v) TCI5: Collective advection of TCs by a monsoon gyre indicated when all TCs are embedded in, and appear to be rotating around, a larger-scale fish hook cloud pattern that wraps around the eastern side of a cloud minimum area.
- (vi) TCI6: Full binary interaction is not likely to be occurring unless low-level circulation cloud patterns of TCs in visible imagery are clearly overlapping.

**- Numerical analyses**

- (i) TCI1: Establishment of a M Pattern indicated when 500 mb isotach asymmetry of western TC shifts from east semicircle to west semicircle, or isotach pattern becomes symmetric (which indicates almost no steering and leaves the TC to propagate slowly westward and poleward).
- (ii) TCI2: One-way, pseudo-binary influence usually associated with a coalescence of a previously distinct 500 mb circulation of the smaller TC into the circulation of the larger TC.
- (iii) TCI3: Advection by peripheral ridge of another TC will not usually occur unless peripheral ridge is rather large and clearly evident in NOGAPS 500 mb streamline analyses.

(iv) TCI4: Weakening of TC peripheral ridge owing to approach of TC from east is manifest by dissipation of peripheral circulation in NOGAPS analyses or by intervention of eastern TC circulation so as to keep peripheral ridge of western TC distinct from subtropical ridge.

(v) TCI5: Collective advection of TCs by monsoon gyre indicated when TCs appear to be moving around eastern peripheral of a larger scale cyclonic circulation that is evident in streamline analyses at or above 500 mb (Check upper-level manual analyses for corroborative wind reports).

(vi) TCI6: Full binary interaction of TCs is not likely to be occurring if NOGAPS 500 analyses still represent TCs as two distinct circulations.

- Recent TC motion

(i) TCI1: Establishment of a M Pattern is evident in track of western TC by significant slowing, or reversal, of poleward movement, and is evident in track of eastern TC by failure to decelerate, or alternately to modestly accelerate, as ridge axis is traversed.

(ii) TCI2: One-way pseudo-binary influence often is indicated by rapid translation, or large track changes, by the smaller TC, particularly if smaller TC is to west and poleward of larger TC.

(iii) TCI3: Advection of TC by peripheral ridge of another TC is manifest by equatorward turn from typical westward motion if peripheral ridge is to northwest, or east-northeastward motion if peripheral ridge is to southeast.

(iv) TCI4: Weakening of peripheral ridge by the approach of another TC from the southeast is indicated by a reduction of translation speed of the western TC to a slow (4-6 kt) northwestward movement.

(v) TCI5: Collective advection of TCs by monsoon gyre is usually indicated by cyclonically curving tracks that begin with an eastward and poleward heading and have a large (about 500 km) radius of curvature. More complex movement will occur if TC separation distance decreases sufficiently to cause full binary interaction between the TCs (TCI6) that will be superposed on the collective advection by the monsoon gyre.

(vi) TCI6: Full binary interaction results in various combinations of sudden speed changes and/or track changes that may be best revealed by a relative motion diagram, plus the environmental steering of the combined binary TCs. In general, the smaller of the two TCs will experience the more severe track changes. It is the authors' opinion that full binary interaction usually does not have a significant contribution to TC motion (over and above other TCIs that usually commence first,

such as TCI1 and TCI2) until the separation distance decreases to less than 8° lat., or equivalently 480 n mi (900 km).

#### e. Knowledge base overview

1) Methodology. The preceding subsections of Chapter 3 describe the TC-Environment knowledge base that provides the meteorological foundation for the Systematic Approach. The order of presentation of the various model groups (see Fig. 3.3), and individual conceptual models in each group (Tables 3.1 - 3.3), was deliberately chosen to proceed methodically from the simpler concepts to the more complex. It is relatively straightforward to characterize steering in terms of the four Environment Structure Synoptic Patterns and associated Synoptic Regions, and to characterize the motion-relevant aspects of TC Structure (intensity and size). However, a new emphasis (and more complex problem) in the Systematic Approach is to characterize the motion-affecting interactions between the TC and its environment, which have been termed TC-Environment Structure transformations. Such a presentation methodology is believed to be the most effective for this initial introduction of TC forecasters to both the concept and components of the TC-Environment knowledge base.

Operational application of the TC-Environment knowledge base to assemble a complete meteorological TC forecast picture will actually follow the sequence illustrated in Fig. 3.110. That is, the TC Structure has to be assessed first to determine the Environment Structure because TC intensity affects the selection of the optimum steering level, and the TC size is needed to discriminate between the N1 and N2 North-oriented Patterns and to anticipate the likelihood of certain TC-Environment Structure transformations.

2) TC track characterizations. During the post-storm analysis at JTWC, forecasters have characterized TC tracks as either straight (S), recurve (R), or other (O). A S label is assigned to western North Pacific TCs that exhibit persistent westward motion that usually results in landfall over Asia. A R label is assigned to any TC that smoothly proceeds from generally westward movement to northeastward movement via a relatively brief period of northward movement through the subtropical ridge. An O track is assigned to any track that is not readily classifiable as S or R. These track characterizations provide some insight into the TC-environment affecting TC motion. For example, the S track implies persistent easterly steering equatorward of a subtropical ridge with no significant breaks, and the R track implies the presence of a ridge break, usually in association with a midlatitude trough. The O track implies some anomalous environment that affected the TC motion. However, such overall characterizations of TC tracks omit important details about the associated TC-environment situation, such as the particular circumstances surrounding recurvature in the case of an R track, or precisely what environmental anomaly caused the unusual O track.

A chronological listing of the TC-environment knowledge base conceptual models applicable during the life cycle of each TC will provide a more detailed characterization of the TC track. This will be demonstrated for the RMT case study of Yuri, and the TCI case

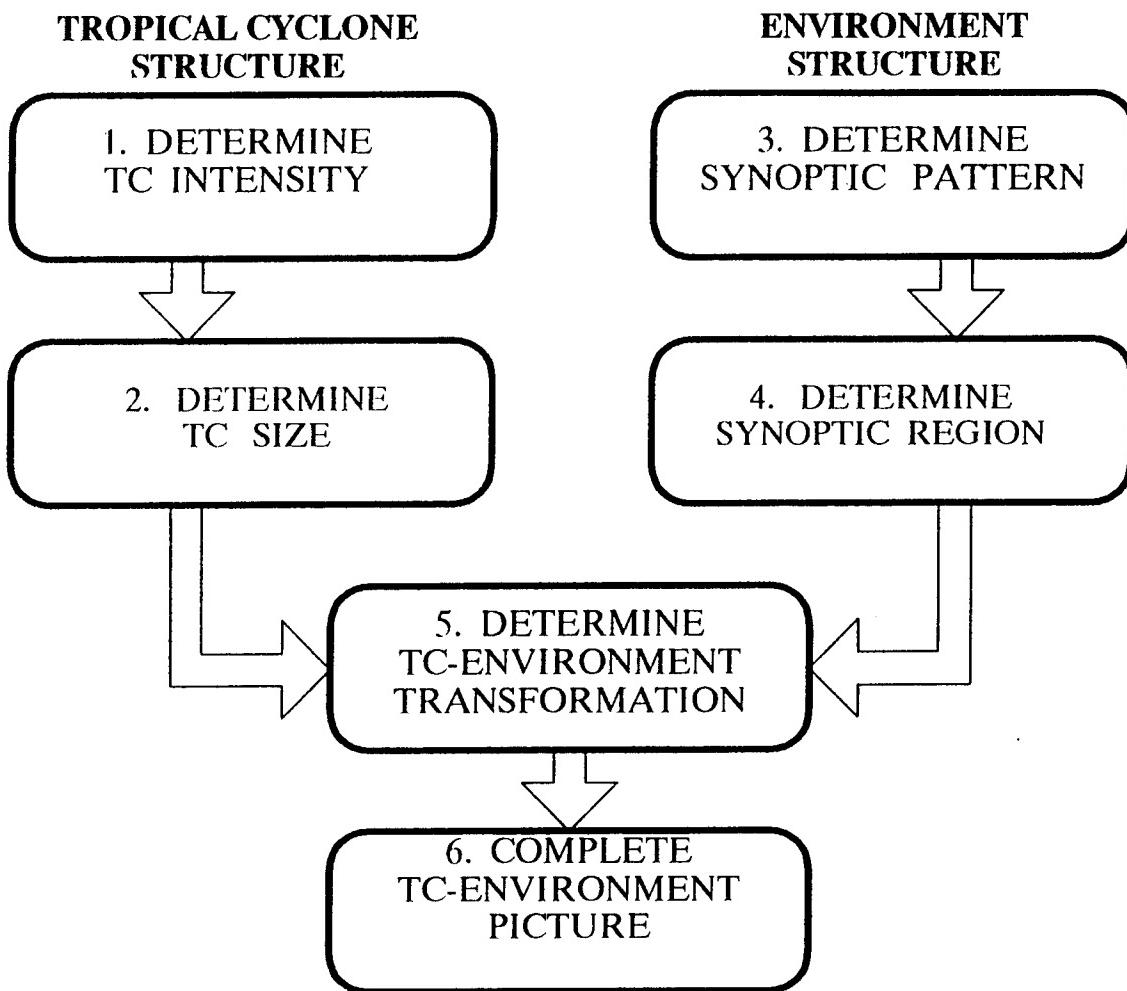


**Fig. 3.110.** Sequence of steps for combining TC Structure and Environment Structure to apply the knowledge base of conceptual models in the Systematic Approach and arrive at a complete TC-Environment picture.

studies of Seth/Verne, Owen/Nancy, and Nat presented earlier. This exercise is also a convenient demonstration of how a simple listing of the applicable TC-environment knowledge base models can provide the forecaster coming on duty a comprehensive meteorological picture, and thus contribute to shift-to-shift consistency in the forecasts.

Based on the satellite imagery to determine intensity and size, the track of Typhoon Yuri (Fig. 3.49), and the 8-day sequence of NOGAPS streamline/isotach analyses (Figs. 3.50 and 3.51), the evolution of the TC-Environment situation during 23 - 30 November 1991 is summarized in Table 3.4. Each line in the table characterizes the TC-Environment situation affecting the motion of Yuri at 0000 UTC on a particular day. The format of the table is designed to enable the forecaster to recall at a glance the evolution of the TC-Environment situation leading up to the state at 0000 UTC 30 November 1991. In conjunction with the

Table 3.4. TC-Environment characterization of Yuri during 23 - 30 November 1991. The Pattern, Region, intensity, size, and transformation notations are as given in Tables 3.1 - 3.3 (and Section 3.d.5 for modes of TCI). The slash notation denotes a Pattern transition state or Region transition zone with the transition proceeding from the condition on the left to the condition on the right.

<u>TC#</u>	<u>Date/Hr</u>	<u>Pattern</u>	<u>Region</u>	<u>Intensity</u>	<u>Size</u>	<u>Transformation</u>
30W	911123/00	S	DR	TD	L	
30W	911124/00	S	DR	TS	L	
30W	911125/00	S	DR	TY	L	
30W	911126/00	S	DR	IT	L	
30W	911127/00	S	DR	IT	L	RMT
30W	911128/00	S/N2	DR/NO	IT	L	RMT
30W	911129/00	N2	NO	IT	L	RMT
30W	911130/00	N2	AW	IT	L	

recent track of Yuri (Fig. 3.49), the information contained in Table 3.4 provides a day-by-day account of the impetus for the observed motion of the TC during the 8-day period. Notice that the Transformation column identifies the RMT transformation<sup>16</sup> and the associated S to N2 Pattern transition as the impetus for Yuri's turn to the north on 28 November, and subsequent recurvature (Fig. 3.49). The information in Table 3.4 summarizes the track of Yuri in a more complete manner than a simple Recurver (R) track classification alone.

Recall the tracks of Typhoon Seth and Tropical Storm Verne (Figs. 3.78a and b) and the accompanying 12-day sequence of NOGAPS streamline and isotach analyses (Figs. 3.79 - 3.81). Based on these figures and the related discussion in Section 3.d.5, the evolution of the TC-Environment situation affecting the motion of Seth and Verne during 2 - 13 November 1991 is summarized in Tables 3.5 and 3.6, respectively. As indicated in these tables, transitions from the S to the M Pattern are associated with the TC Interaction transformations TCI4 and TCI1 for Supertyphoon Seth, and with transformation TCI1 for Tropical Storm Verne. Notice that the S to M Pattern transition occurs at different times in Tables 3.5 and 3.6. As discussed in Section 3.d.5, Seth came into the NF Synoptic Region about 36 h prior to Verne's entry into the SF Region. The key to a successful track forecast will be the detection and timing of the transitions that lead to the sudden equatorward turn of Seth and the accelerating recurvature of Verne. In these two examples, Yuri and Verne

---

<sup>16</sup> Since Yuri was a large (L) TC, significant BEP propagation must have been contributing to Yuri's gain in latitude. However, it is not necessary to indicate this under the Transformation column in Table 3.4 since significant BEP is implicit in the "L" TC size annotation.

Table 3.5. As in Table 3.4, except for Typhoon Seth during 2 - 13 November 1991.

<u>TC#</u>	<u>Date/Hr</u>	<u>Pattern</u>	<u>Region</u>	<u>Intensity</u>	<u>Size</u>	<u>Transformation</u>
26W	911102/00	S	DR	TS	A	
26W	911103/00	S	DR	TY	A	
26W	911104/00	S	DR	IT	A	
26W	911105/00	S	DR	IT	A	
26W	911106/00	S	DR	IT	A	TCI4
26W	911107/12	S/M	DR/NF	TY	A	TCI1
26W	911108/00	M	NF	TY	A	TCI1
26W	911109/00	M	NF	IT	A	TCI1
26W	911110/00	M	NF	IT	A	TCI1
26W	911111/00	M	NF	TY	A	TCI1
26W	911112/00	S	WR	TY	A	
26W	911113/00	S	WR	TS	A	

Table 3.6 As in Table 3.4, except for Tropical Storm Verne during 2 - 13 November 1991. The notation ET denotes extratropical transition.

<u>TC#</u>	<u>Date/Hr</u>	<u>Pattern</u>	<u>Region</u>	<u>Intensity</u>	<u>Size</u>	<u>Transformation</u>
28W	911103/00	S	DR	TD	A	
28W	911104/00	S	DR	TD	A	
28W	911105/00	S	DR	TD	A	
28W	911106/00	S	DR	TD	A	
28W	911107/12	S	DR	TS	A	
28W	911108/00	S	DR	TS	A	TCI1
28W	911109/00	S/M	DR/SF	TS	A	TCI1
28W	911110/00	M	SF	TS	A	TCI1
28W	911111/00	M	SF	TS	A	TCI1
28W	911112/00	S	AW	TS	A	
28W	911113/00	S	AW	ET	A	

would be classified during post-storm analysis as having type R tracks. The summaries in these tables provide the forecaster or researcher with much more information about the significantly dissimilar TC-Environment Structure evolutions affecting Yuri and Verne, and indicate that the recurvatures of these two TCs occurred for distinctly different reasons.

The tracks of Typhoons Owen and Nancy are given in Figs. 3.89a and b and corresponding NOGAPS streamline and isotach analyses are in Figs. 3.93 and 3.94. Based on the discussion in Section 3.d.5, the evolutions of the TC-Environment for Owen and Nancy during 11 - 16 August 1989 are summarized in Tables 3.7 and 3.8, respectively. In this case, the TC-Environment transformation TCI5 is identified simultaneously for both storms.

Table 3.7. As in Table 3.4, except for Typhoon Owen during 11 - 16 August 1989. The notation under the Transformation column for the last two times denotes that the TCIS contribution to the maintenance of the G Pattern MG is occurring between Owen and Peggy (18W).

<u>TC#</u>	<u>Date/Hr</u>	<u>Pattern</u>	<u>Region</u>	<u>Intensity</u>	<u>Size</u>	<u>Transformation</u>
16W	890811/00	N1	NO	TD	S	
16W	890812/00	N1/G	NO	TD	S	TCIS
16W	890812/12	G	NO	TS	S	TCIS
16W	890813/00	G	NO	TS	S	TCIS
16W	890813/12	G	NO	TS	S	TCIS
16W	890814/00	G	NO	TY	S	TCIS
16W	890815/00	G	NO	TY	S	TCIS (w/Peggy)
16W	890816/00	G	NO	TY	S	TCIS (w/Peggy)

Table 3.8 As in Table 3.4, except for Typhoon Nancy during 11 - 16 August 1989.

<u>TC#</u>	<u>Date/Hr</u>	<u>Pattern</u>	<u>Region</u>	<u>Intensity</u>	<u>Size</u>	<u>Transformation</u>
17W	890811/00	N1	NO	TD	S	
17W	890812/00	N1/G	NO	TD	S	TCIS
17W	890812/12	G	NO	TS	S	TCIS
17W	890813/00	G	NO	TS	S	TCIS
17W	890813/12	G	NO	TY	S	TCIS
17W	890814/00	G	NO	TY	S	TCIS
17W	890815/00	G	NO	TY	S	TCIS
17W	890816/00	G	NO/AW	TS	S	

With the recognition of the presence of the monsoon gyre (MG), the Environment Structure changes to the G Synoptic Pattern for both of these small TCs. In a post-storm analysis, both Owen and Nancy would probably be classified as O under the current track characterization scheme. By contrast, the listings of TC-Environment Structure evolution in Tables 3.7 and 3.8 clearly reveal that these non-climatological tracks arose in conjunction with a N1 to G Pattern transition. As indicated in Section 3.d.5, this complex case included a TCIS transformation that initially involved Owen and Nancy, but later involved Owen and Peggy.

As a final example, consider the track of Typhoon Nat (Fig. 3.103c) and the associated 12-day sequence of NOGAPS streamline/isotach analyses (Figs. 3.104, 3.106, 3.108). Based on the discussion in Section 3.d.5, the evolution of the TC-Environment situation causing the complex motion of Nat during 16 - 27 September 1991 is summarized in Table 3.9. The first transformation listed in the table (TCI3) results in a Dominant Ridge (DR) to Accelerating Westerlies (AW) Region transition during 17 September 1991 when Nat is at only 20°N, which is a remarkable 10° equatorward of the latitude of the ridge axis 24 h earlier (see Fig. 3.104a). As a result, the westerlies are quite weak at Nat's low latitude,

Table 3.9 As in Table 3.4, except for Typhoon Nat during 16 - 27 September 1991. The notation "E" denotes that the TCI3 is arising from a TC to the east, which is Luke in the first instance and Mireille in the second.

<u>TC#</u>	<u>Date/Hr</u>	<u>Pattern</u>	<u>Region</u>	<u>Intensity</u>	<u>Size</u>	<u>Transformation</u>
22W	910916/12	S	DR	TS	S	
22W	910917/12	S	DR/AW	TS	S	TCI3E
22W	910918/12	S	AW	TS	S	TCI3E
22W	910919/12	S	AW	TS	S	TCI3E
22W	910920/00	S	AW	TS	S	TCI3E
22W	910921/00	S	AW/WR	TS	S	
22W	910922/00	S	WR	IT	S	
22W	910923/00	S	DR	IT	S	
22W	910924/00	S/M	DR/NF	TS	M	TCI1;TCI2
22W	910925/00	M	NF	TS	M	TCI1;TCI2
22W	910926/00	M/S	NF/DR	TS	M	
22W	910927/00	S	DR	TD	M	TCI3E

and Nat's movement to the east was much slower (see Fig. 3.103c) than for a typical recurvature. As Luke recurves and moves away from Nat, an unusual transition from AW to WR (Weakened Ridge) on 21 September is identified in Table 3.9, as the subtropical ridge reforms to the north of Nat (recall Fig. 3.106d). Subsequent transformations TCI1 and TCI2 involving Supertyphoon Mireille result in a transition to the M Synoptic Pattern with Nat in the Northerly Flow (NF) Region. Finally, a transition back to the S Pattern occurs as Mireille recurves and moves away (*i.e.*, cessation of TCI1 and TCI2). In this most complex situation discussed in this report, the characterization in Table 3.9 provides a much more useful summary of the track of Nat than the O label, which would be assigned under the current post-storm track characterization system.

These illustrations demonstrate that real-time characterizations of the TC-Environment situation using the conceptual models of the meteorological knowledge base of the Systematic Approach would have operational utility. In addition to continually refocussing the attention of the forecaster on the complete TC-Environment picture (including transformations), these characterizations discriminate among similar looking tracks that are in fact caused by highly dissimilar TC-environment evolutions. Thus, it is recommended that such a characterization system be considered for adoption as part of the daily operational routine, and well as for post-storm analysis.

#### **4. Conclusion to Part I**

This proposed Systematic and Integrated Approach to Tropical Cyclone Track Forecasting is based on four fundamental premises:

- (i) that TC forecasting is an integrated problem wherein TC track affects TC structure (intensity and wind distribution) and vice versa;
- (ii) that the inherently integrated nature of sophisticated dynamical track prediction models potentially make them the most useful source of TC forecast guidance;
- (iii) that at present (and for the foreseeable future), numerical TC forecast models do not consistently provide track forecasts of acceptable accuracy, because limitations in model physics and initialization, as well as data deficiencies, result in imprecise treatment of the coupling between the TC environmental flow and the TC structure; and
- (iv) that a significant fraction of numerical model forecast error is not random (or chaotic), but depends systematically on the particular TC-Environment situation.

Given the above premises, the forecaster should be able to improve significantly upon these numerical forecasts. This proposed Systematic Approach will provide the forecaster with:

- (i) a TC-Environment meteorological knowledge base of conceptual models that classifies various TC-Environment situations into a relatively small number of recurring combinations of Environment Structure and TC Structure, and especially emphasizes the conditions under which a TC-Environment change may be anticipated;
- (ii) a numerical model traits knowledge base that identifies certain types of recurring TC track forecast errors that may be associated with the various TC-Environment combinations; and
- (iii) an implementing methodology for applying these two knowledge bases to any TC forecast situation.

The objectives of Part I have been to introduce the Systematic Approach via an overview in Chapter 2 (see especially Fig. 2.1) and to present the first knowledge base in item (i) above. Chapter 3 provides this knowledge base in terms of conceptual models of Environment Structure, TC Structure, and interactions between the TC and Environment called TC-Environment transformations. It is believed that this set of models accounts for most of the types of TC motion in the western North Pacific, and in other TC basins dominated by large-scale monsoonal environments. However, the forecaster will almost

certainly encounter particular cases in which the TC-Environment situation and associated TC motion will be difficult to classify in terms of the present set of conceptual models. Communication to the authors of these situations is strongly encouraged so that new conceptual models may be incorporated as warranted.

As summarized in Fig. 2.1, the TC-Environment knowledge base and a Numerical Model Traits knowledge base are applied to the TC track forecasting problem in the Numerical Guidance Analysis Phase. Part II of this report will commence with the development of the Numerical Model Traits knowledge base (item (ii) above) and the related Objective Techniques knowledge base. Finally, the implementing methodology (item (iii) above) is of course the entire Systematic Approach.

Part II will conclude with several proof-of-concept demonstrations that illustrate how the various components of the proposed Systematic Approach may be applied to enable the forecaster to formulate an official TC track forecast that improves upon objective and numerical guidance. Adoption of this proposed Systematic and Integrated Approach to TC track forecasting is expected to improve TC warnings because: (i) the forecasts will be based on dynamical meteorological reasoning that makes optimum use of numerical and objective guidance; and (ii) the forecasts will have better temporal consistency since all forecast shifts will be working from the same "game plan."

## APPENDIX A

### A Historical Review of TC Forecasting at JTWC

The formal requirement for forecasting of TC activity in WESTPAC by the U.S. military began at the end of World War II, and was precipitated by two disastrous encounters with typhoons by Admiral Halsey's Third Fleet (Guard *et al.* 1992). In the early post-war years, the TC forecasting knowledge base consisted of only one quantitatively useful concept: that TC movement is primarily due to advection by the background environmental flow over the depth of the TC circulation (see Riehl and Burgner 1950 for an overview). Such an environmental "steering" layer was often approximated by the best single steering level. Rossby (1948) had provided a brief theoretical explanation for a poleward propagation of cyclones relative to their environment that would seem to explain departures of TC motion from steering. However, contemporaneous observational studies contended that apparent discrepancies between TC motion and the steering concept were simply due to the use of steering levels, and could be reduced to the order of measurement error by an appropriate choice of depth for the steering layer (Jordan 1952).

Various classes of objective motion forecasting techniques were developed to supplement the approach of subjectively modifying persistence and climatology tracks based on the current synoptic situation. In the late 1950's, statistical regression techniques that related 24-h TC motion to past motion and current synoptic conditions in the vicinity of the TC began to be applied in WESTPAC (e.g., Wang 1960; Miller and Moore 1960; Arakawa 1963). By the early 1960's, numerical barotropic model predictions of environmental steering were begun using smoothed analyses of upper-air data as initial conditions (ATCR 1962, 1963). Steering predictions initially used only 500 mb data, but other levels were soon added to apply the emerging understanding that the optimal steering level or layer depends on the depth of the TC circulation, and thus intensity (Miller and Moore 1960). A variant of this approach was to use the geostrophic steering computed from smoothed height fields in techniques called Hurricane Tracking (HATTRACK; Hardie 1967) and Modified HATTRACK (MOHATT; Renard *et al.* 1973). In 1977, an explicit numerical prediction of TC motion was achieved using a 3-layer primitive equation model called the Tropical Cyclone Model (TCM; Harrison 1973; Ley and Elsberry 1976), in which a synthetic TC vortex circulation (commonly called a TC bogus) was inserted at 850 mb.

Improvements in computer storage and retrieval techniques also permitted the development of a TC analog model called TYFOON-70 (Jarrell and Somervell 1970). Potential analogs that had TC parameters (movement, intensity, size, etc) and environmental parameters (positions, date, etc) similar to the present TC were extracted from the climatological database and averaged to produce a 72-h track.

Thus, four classes of objective track forecasting techniques were developed over a two-decade period: statistical, steering, climatological, and numerical TC prediction. All four classes have been improved over the years. The present statistical models include:

WESTPAC Climatology and Persistence (CLIP; Xu and Neumann 1985); the statistical-dynamical Colorado State University Model (CSUM; Matsumoto 1984); and the statistical-dynamical JTWC-92 model (JT92), which is an adaptation of the Atlantic basin NHC83 (Neumann 1988). The climatological models are Climatology (CLIM) and the Typhoon Analog (TYAN; Yogi *et al.* 1975). Three steering models are the Fleet Numerical Meteorology and Oceanography Center (FNMOC) implementation of the Beta and Advection Models for a shallow (SBAM), a medium (MBAM), and a deep (FBAM) layer. A limited-area numerical TC prediction model is the 3-layer, One-way influence TC Model (OTCM; Hodur and Burk 1978; Shewchuk and Elsberry 1978). In addition, the Navy Operational Global Atmospheric Prediction System (NOGAPS) is supplied with synthetic TC observations so that it can provide explicit numerical TC track predictions (NGPS; Goerss *et al.* 1991; Goerss and Jeffries 1994).

In contrast to the intensive and relatively successful effort over nearly four decades to develop objective techniques for TC motion forecasting, the approach to intensity forecasting has remained essentially unchanged. It has long been known that encounters with "non-tropical" air, frontal boundaries, and land had a negative influence on intensification, and that intensification apparently depended on TC orientation relative to upper-level synoptic features. However, lack of understanding of TC intensification dynamics dictated a purely subjective application of these observed TC intensity-environment associations. A highly subjective blend of climatology and persistence based on satellite interpretation (Dvorak 1975, 1984; Hebert and Poteat 1975) is modified by the anticipated effects of future synoptic patterns. Although an operational statistical intensity forecast scheme was listed in the 1974-1978 ATCRs, it was dropped in 1979 without comment, apparently due a lack of appreciable skill. The Naval Research Laboratory, Monterey is currently adapting for WESTPAC the Statistical Hurricane Intensity Forecast (SHIFOR) model recently developed by the Hurricane Research Division of NOAA based on the original work of Jarvinen and Neumann (1979).

Although there have been recent advances in understanding the impact of TC size on TC motion, the mechanisms governing the structure and structure change in the outer parts of TCs remain poorly understood. Furthermore, currently available techniques to estimate the analysis-time distribution of TC winds are much less accurate than intensity estimation techniques, and no objective scheme is currently available to predict the wind distribution of TCs in WESTPAC. The closest approach is the operational Holland-Martin model (ATCR 1990) that uses the Holland (1980) analytic wind profile to compute 100-kt, 50-kt and 30-kt wind radii using estimates of TC intensity and maximum wind radius derived from subjective interpretations of satellite imagery, and adjusted for TC translation speed. Wind radii predictions are accomplished by using future values of intensity that are obtained via the subjective intensity forecasting process described above.

## Appendix B

### Summary of Intensity Effects on TC Motion

Unfortunately, the literature contains no studies that identify optimal steering levels or layers as a function of TC intensity for the western North Pacific region. Dong and Neumann (1986; hereafter DN) and Velden and Leslie (1991; hereafter VL) have conducted the desired type of analysis in the Atlantic and Australian regions, respectively. Thus, these studies will be adopted for use in the systematic approach.<sup>16</sup>

Using 13 years (920 cases) of Atlantic TC tracks and National Meteorological Center (NMC) geopotential height analyses, DN determined optimal geostrophic environmental steering levels and layers separately for TCs of tropical storm intensity, hurricane intensity, and all TCs (tropical storm plus hurricane intensity). By definition, the optimal level/layer minimized the forecast error for a simple model that included only the advection by the geostrophic environmental winds of the level/layer. Differences between the 24-h forecast errors for the optimal levels and the optimal layers were not statistically significant, regardless of the TC intensity category (Table B.1). This result suggests that windfields at individual levels may be used for pattern interpretation in the systematic approach. High vertical wind shear situations are one exception, which will be described below.

The DN study found that the optimal steering level depended directly on the intensity of the TC: 700 mb for tropical storms; and 400 mb for hurricanes, irrespective of steering direction (Table B.1). Optimum levels for tropical storms and hurricanes correspond to well-defined minima in the 24-h forecast errors (Fig. B.1). The optimal steering levels for all TCs (tropical storm or higher) in the easterlies and westerlies were found to be 400 mb and 500 mb, respectively, which may be due to decreasing tropopause height with increasing latitude. Note in Fig. B.1 that the 500 mb level was associated with a fairly distinct minimum in forecast error for all TCs in the westerlies. By contrast, the 24-h forecast error at 400 mb for TCs in the easterlies is probably not significantly different from the 500 mb error. Thus, 500 mb is taken to be an appropriate single steering level for all TCs of greater than minimal tropical storm intensity. Additional support for this view comes from the George and Gray (1976) finding that the average direction of TC motion in the western North Pacific is mostly closely matched by the 500 mb environmental steering defined in an

---

<sup>16</sup> Although it would be preferable to use an appropriate WESTPAC study, there are good reasons to believe that the dependence of TC vertical structure, and thus steering level, on TC intensity is for the most part basin-independent. The degree of agreement between the DN and VL studies shown below is a particularly compelling reason. In addition, the Dvorak TC intensity estimation technique (developed in the Atlantic) based on cloud-top temperatures in infrared imagery has been successfully used in all TC basins with modifications.

Table B.1 Optimum steering levels, correlation coefficients between storm steering and Atlantic TC motion, and resultant 24-h forecast errors for the various stratifications (after Dong and Neumann 1986).

Classification (number of cases)	Optimum level (mb)	Correlation coefficients meridional/zonal	Dependent data 24 h forecast error (km)	Optimum deep-layer (mb)	Correlation coefficients meridional/zonal	Dependent data 24 h forecast error (km)
In the easterlies						
Hurricanes (258)	400	0.67/0.61	180	1000-100	0.66/0.60	182
Total tropical cyclones (515)	400	0.56/0.52	201	1000-150	0.58/0.54	199
Tropical storms (257)	700	0.50/0.51	213	1000-400	0.51/0.53	213
In the westerlies						
Hurricanes (191)	400	0.73/0.78	300	1000-150	0.72/0.81	295
Total tropical cyclones (358)	500	0.63/0.76	302	1000-200	0.66/0.79	295
Tropical storms (167)	700	0.58/0.71	293	1000-300	0.60/0.73	288

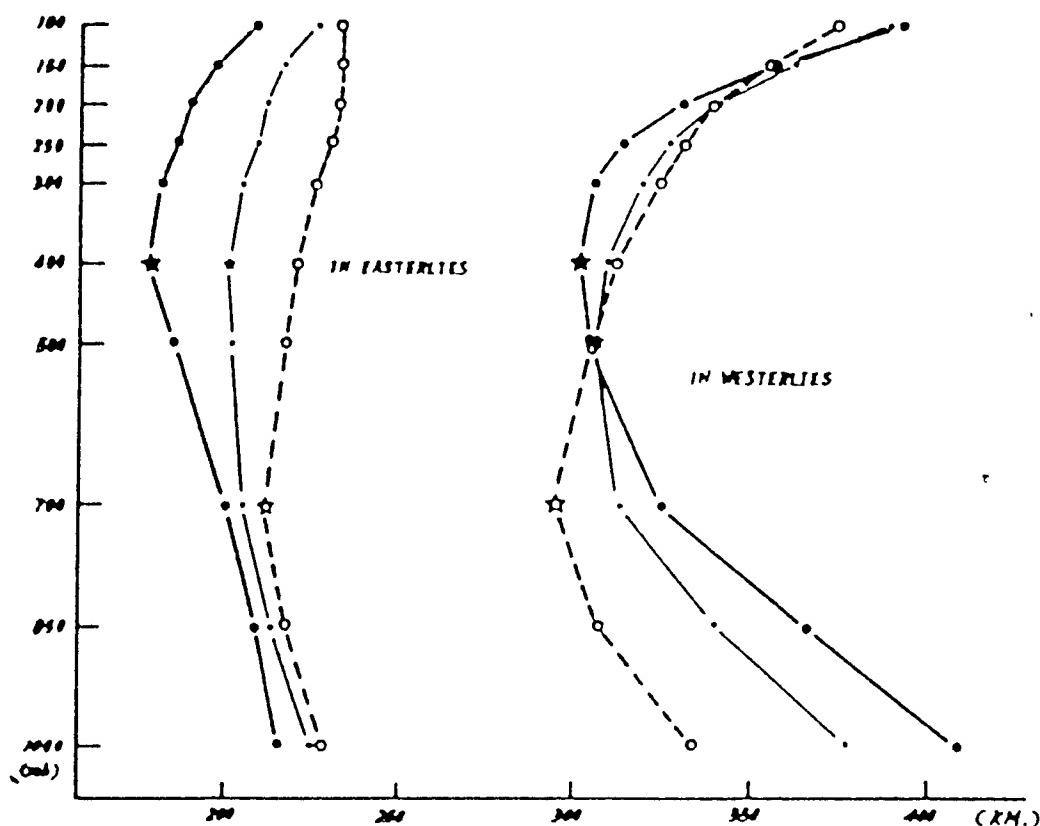


Fig. B.1 Forecast errors between Atlantic TC motion over 24 h and steering at all mandatory levels between 1000 and 100 mb. The large dots, circles, and small dots denote that forecast error is for hurricanes only, tropical storms only, and all tropical cyclones of tropical storm intensity or greater, respectively. The stars denote the optimum steering level (after Dong and Neumann 1986).

annulus of  $1^{\circ}$ - $7^{\circ}$  lat. radius about the TC. Based on this evidence, NOGAPS streamline and isotach analyses at 500 mb are predominantly used for both illustration and application of the systematic approach.

More recently, VL compared 20 years of Australian TC tracks (300 cases) with 48-h motion forecasts from a nondivergent barotropic model initialized with wind fields that had the TC circulation removed. For TCs of all intensities, VL found that forecast errors associated with the best steering layer were about 12% smaller than those associated with the best steering level. Unlike DN, VL did not separately compare steering layer and level forecasts accuracies for TC of different intensities. In agreement with DN, VL identified a direct dependence between the depth of the optimal steering layer and the intensity of the TC (Fig. B.2). In addition, for the five most intense TC intensity categories (central pressure  $\leq$  975 mb) in the VL study, the average pressure of the optimal steering layers is 595 mb, which agrees well with the 550 mb average pressure for the DN optimal steering layer for hurricanes. Similarly, the VL average layer pressure of 675 mb for the central pressures from 995 mb to 975 mb is very close to the DN average pressure level of 650 mb for TCs of tropical storm intensity.

VL included in their analysis 48-h track segments that began with the TC at tropical depression intensity (first two categories in Fig. B.2). Interestingly, the optimal steering layer (850-500 mb) was the same as for the TS categories, rather than shallower as might be expected. One explanation is that the VL results are biased by the use of 48-h track segments, since the TDs usually would have intensified significantly during this interval. However, careful analysis of the motion of Tropical Storm Lewis (Fig. B.3a) tends to confirm the VL result. Prior to 1 May 1990, Lewis followed a sinuous, poleward track while never exceeding minimal TS intensity. During 1 May, high vertical wind shear associated with upper-level westerlies began to separate the low-level circulation (LLC) of Lewis from the convective cloud mass (CCM)(Fig. B.3.b). Notice how the low sun angle in the DMSP image reveals that the cloud tops in the CCM are quite high compared to those in the LLC. Shortly after the time of the DMSP image, the LLC became completely decoupled from the CCM, and the track of Lewis turned sharply to the west (Fig. B.3.a). This motion of the LLC conformed to the easterly flow south of the 850 mb ridge (ATCR 1990, p. 38). This analysis suggests that: (i) as long as the CCM is coupled with the LLC, even quite weak TCs respond to flow over a rather deep steering layer (850-500 mb as in VL); and (ii) the 850 mb level or the 1000-700 mb layer winds provide the best estimate of steering after the LLC is decoupled from the CCM in strong vertical wind shear cases.

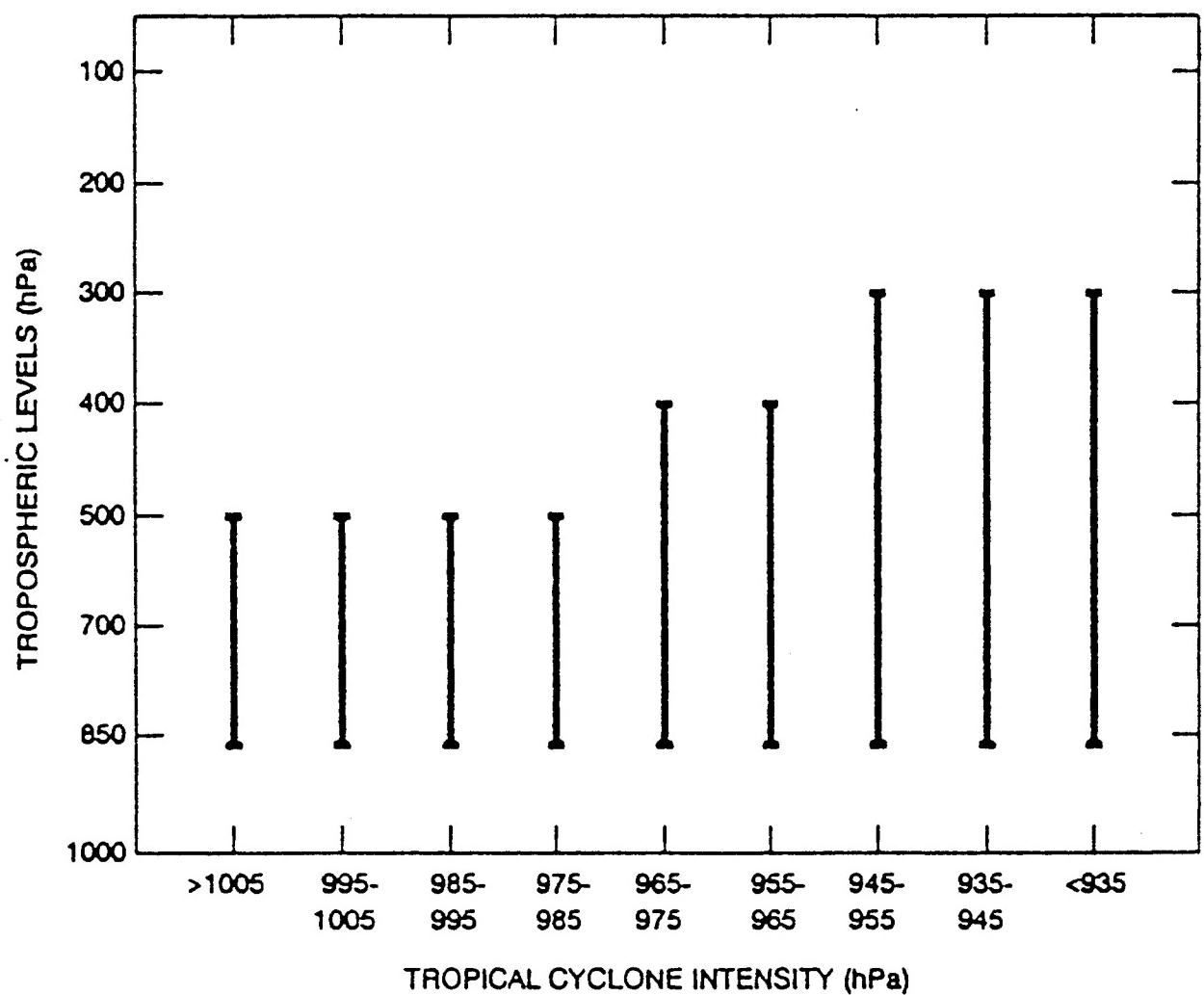


Fig. B.2 The depth of optimum steering layers based on 48-h barotropic model track forecasts as a function of TC intensity (central mean sea-level pressure) for TCs in the Australian region (after Velden and Leslie 1991).

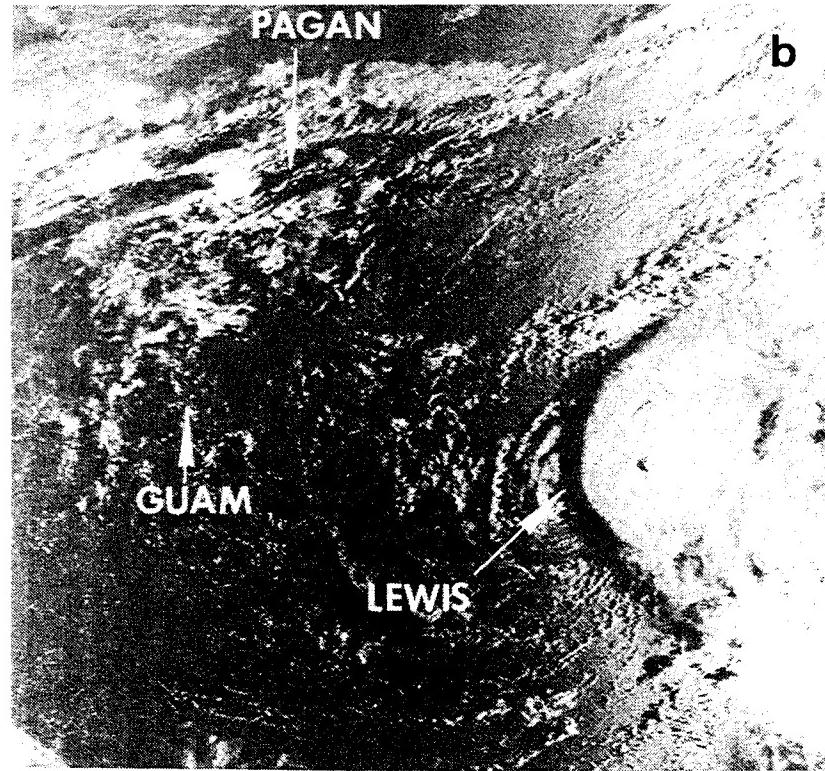
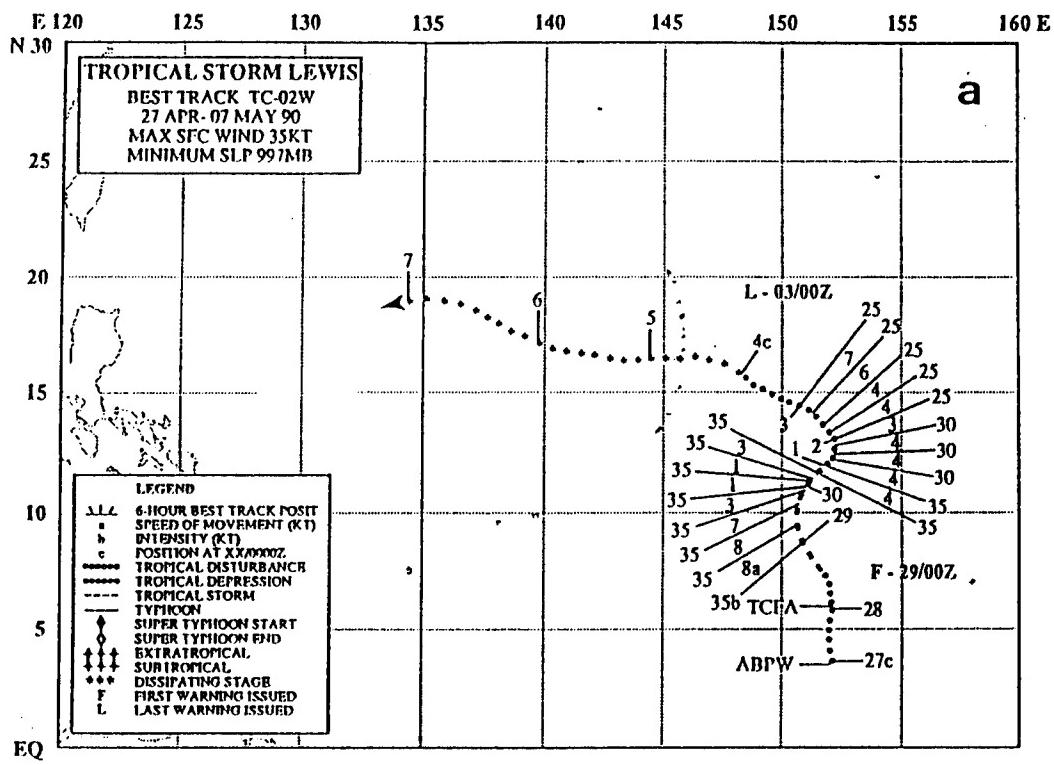


Fig. B.3 (a) As in Fig. 3.1, except for Tropical Storm Lewis during 27 April - 7 May 1990.  
 (b) Defense Meteorological Satellite Program polar orbiter visual imagery at 2022 UTC 1 May 1990. High westerly vertical wind shear has pushed the convective cloud mass to the east, and exposed the low-level circulation of Tropical Storm Lewis.

## Appendix C

### A Proposed Tangential Wind Distribution Model

**1. Measures of TC size.** As noted in Chapter 1, TC size has been traditionally associated with the average radius of the outer closed isobar (ROCI), or the average radius of some threshold surface wind speed (gale force is currently used by JTWC; hereafter  $R_{35}$ ). The radius of gale force winds is always substantially smaller than the ROCI. Western North Pacific TCs vary greatly in horizontal scale, and the radial dependence of TC outer tangential wind fields is rather variable. As a result, it is not likely that a fixed relationship exists between the two size measures.

A surface wind  $R_{35}$  or surface pressure (ROCI) distribution may not be a proper measure of TC size as it relates to TC propagation. Fiorino and Elsberry (1989) have demonstrated that the propagation speed of TC-scale vortices in a barotropic model on a  $\beta$  plane is primarily dependent on the strength of TC tangential winds outside 300 km. Because the value of  $R_{35}$  is often 300 km (160 n mi) or less, barotropic model simulations would suggest that  $R_{35}$  is not a particularly useful measure of TC size. By contrast, the ROCI should provide a more meaningful measure of TC size. Although the ROCI typically encompasses most of the outer circulation of the TC, the tangential wind strength depends on the radial pressure gradient, rather than an arbitrary isobar at some radius.

The lack of a consistent and dynamically meaningful measure of TC size is a serious impediment to TC motion forecasting. The motivation for the proposed TC wind distribution model developed below is that it provides a dynamically meaningful, albeit simplified, measure of TC size in terms of the outer wind strength believed to be important for TC propagation.

**2. Current TC wind distribution models.** The empirical wind distribution models at JTWC were developed to estimate the distribution of TC *surface* winds as required in the JTWC warning bulletins. By contrast, the TC tangential wind averaged over some deep tropospheric layer (or at the steering level as a proxy) is dynamically relevant to TC motion. It is very important that forecasters understand this distinction between the TC surface wind distribution and the TC mid-tropospheric wind distribution as the key input into the TC motion forecasting process. Thus, a brief overview of the current wind distribution models available to JTWC is presented below to illustrate their limited usefulness for motion forecasting.

The statistical model of Tsui *et al.* (1982) was developed from a 1966-1977 climatology of TC intensities and the 30-, 50-, and 100-kt surface wind radii as reported in the JTWC warnings. Given the TC intensity, the model provides the climatological, azimuthally-averaged 30-, 50-, and 100-kt radii, which are then adjusted to account for the effect of TC translation. A number of aspects of this model make it unsuitable for use in motion forecasting. First, the model provides the climatological mean TC size for a

particular intensity, and thus cannot account for the observed variations of TC size at the same intensity. Second, the model predicts a continuous growth of the 30-, 50-, and 100 kt wind radii as the TC intensifies (Fig. C.1).

This second property of the Tsui *et al.* model is inconsistent with Weatherford and Gray's (1988) composite analyses of aircraft reconnaissance 700 mb winds for various intensity categories (Fig. C.2). Whereas the outer winds are increased between the tropical storm and minimal typhoon profiles (compare lower two panels), no further increase outside a radius of 1° lat. is apparent among the three typhoon intensity ranges as an increasingly intense and tight high-wind core develops. Hence, Weatherford and Gray's results suggest that the average 700 mb wind distribution of western North Pacific TCs experiences little growth once minimal typhoon intensity is attained. Weatherford and Gray's results do not necessarily mean that Tsui's model is wrong, since the surface wind distribution may depend on other factors (e.g., changes in the vertical structure of the TC in the lower troposphere during intensification) besides changes in the size of the mid-tropospheric circulation of the TC.

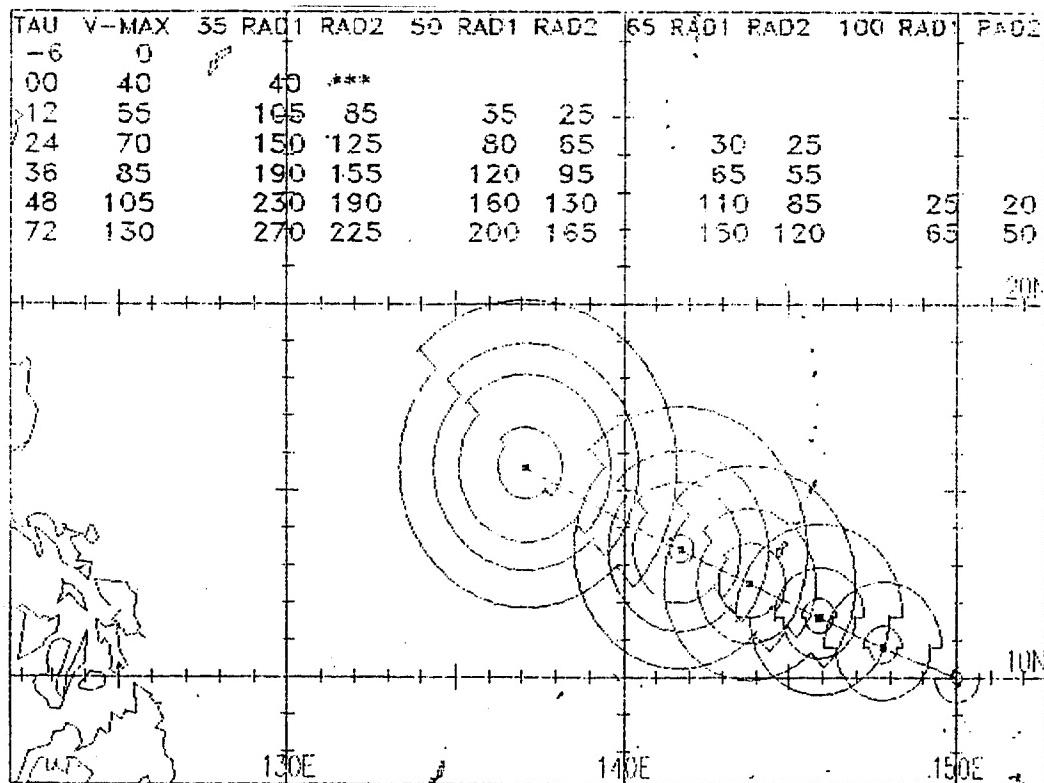


Fig. C.1 Wind radii from the Tsui *et al.* (1992) statistical wind distribution model for a hypothetical TC moving west-northwest and intensifying from 40 to 130 kt in 72 h.

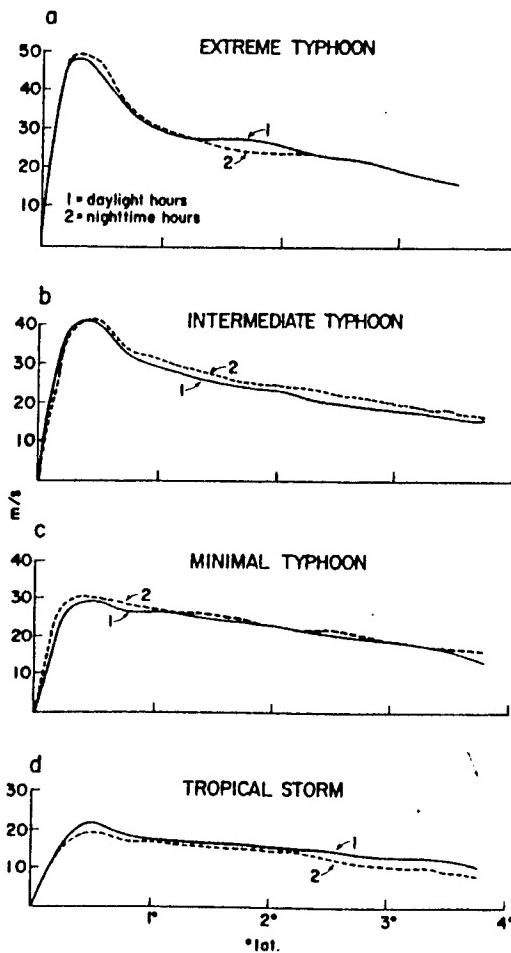


Fig. C.2 Radial profiles of western North Pacific TC tangential winds derived from composited aircraft reconnaissance flight-level wind estimates and stratified into the intensity categories shown. The average minimum sea-level pressure ranges for the tropical storm, minimal typhoon, intermediate typhoon, and extreme typhoon are 999 to 977, 976 to 950, 949 to 920, and less than 920 mb, respectively (after Weatherford and Gray 1988a).

The Huntley (ATCR 1980, p. 121) and Holland-Martin (ATCR 1988, p. 183) models supply 35-, 50-, and 100-kt wind radii using the Holland (1980) tangential wind profile

$$v(r) = \left[ AB(p_n - p_c) \frac{\exp(-A/r^B)}{r^B} + \frac{r^2 f^2}{4} \right] - \frac{rf}{2}, \quad (C-1)$$

where  $\rho$  is the surface density of air,  $p_n$  is the ambient surface pressure around the TC,  $p_c$  is the surface central pressure of the TC, and the constants A and B are related to the maximum wind speed ( $V_m$ ) and the radius of maximum wind speed ( $R_m$ ), respectively. In the Huntley model, the outer wind profile given by (C-1) depends very sensitively on the value of  $R_m$  that must be supplied by the forecaster. The Holland-Martin model overcomes this problem via a statistical association between the parameter B in (C-1) and the diameter of the  $-65^\circ\text{C}$  cloud shield in the satellite infrared image. The rationale is that this cloud shield diameter is a fairly consistent indicator of the TC size, which is in turn correlated with

eye size (Weatherford and Gray 1988b; see their Table 2), and thus  $R_m$ . The Holland-Martin model also includes an adjustment of the symmetric profile (C-1) for the effect of TC translation.

Holland derived (C-1) by approximating the pressure profile of a TC as a rectangular hyperbola, and then solving the gradient wind equation for the tangential wind. Although the Holland profile provides internally consistent and reasonably accurate 35-, 50-, and 100-kt surface wind radii if the parameters A and B can be accurately estimated, it is not appropriate as a conceptual model of TC wind distribution for motion forecasting. Because of its complexity and empirical nature, the profile provides no insight to the forecaster as to the processes that are controlling the wind distribution of the TC, or how the wind distribution will change in the future. In addition, the tangential wind profile specified by (C-1) is cyclonic out to infinity, and thus provides no inherent, unambiguous measure of TC size. The dynamically-based model for TC wind distribution and evolution proposed below does not possess these weaknesses.

The complete tangential momentum equation in polar, pressure coordinate form is

$$\frac{dv}{dt} + \frac{uv}{r} + (f_o + \beta r \sin \theta)u = -\frac{1}{r} \frac{\partial \phi}{\partial \theta} + F_\theta, \quad (C-2)$$

where  $u$  and  $v$  are the wind speeds in the  $r$  and  $\theta$  directions, respectively,  $\phi$  is the geopotential,  $f_o$  is the Coriolis parameter at the latitude of the TC,  $\beta$  is the linearized rate of change with latitude of the Coriolis parameter, and  $F_\theta$  represents frictional effects. If the azimuthal averaging process

$$\bar{A}(r) = \frac{1}{2\pi} \int_0^{2\pi} A(r, \theta) d\theta$$

is applied to (C-2), and only the terms involving symmetric variables are retained (i.e., assume asymmetric effects are negligible), then (C-2) simplifies to

$$\frac{d\bar{v}}{dt} + \frac{\bar{u}\bar{v}}{r} + f_o \bar{u} = \bar{F}_\theta, \quad (C-3)$$

where

$$\frac{d}{dt} = \frac{\partial}{\partial t} + \bar{u} \frac{\partial}{\partial x} + \bar{v} \frac{\partial}{\partial y} + \bar{\omega} \frac{\partial}{\partial p}.$$

Multiplying both sides of (C-3) by  $r$  gives

$$r \frac{dv}{dt} + uv + f_o ur = r F_\theta = T_\theta , \quad (C-4)$$

where  $T_\theta$  is the torque due to frictional effects, and the bar notation has been omitted for simplicity. All subsequent variables and operators in the following mathematical development may be assumed to be azimuthally-averaged. The left side of (C-4) may be simplified using the following identities

$$\frac{d}{dt}(rv) = r \frac{dv}{dt} + uv \quad (C-5)$$

and

$$\frac{d}{dt}\left(\frac{1}{2}r^2\right) = ur . \quad (C-6)$$

Applying (C-5) to the first two terms on the left side of (C-4), and (C-6) to the third term on the left side of (C-4) results in the simplified expression

$$\frac{dM_a}{dt} = T_\theta , \quad (C-7)$$

where  $M_a$ , the absolute angular momentum of a parcel, is given by

$$M_a = rv + \frac{1}{2}f_o r^2 . \quad (C-8)$$

The first and second terms on the right side of (C-8) are the angular momentum contributions due to: (i) tangential velocity within the earth-relative polar coordinate system; and (ii) the rotation of the coordinate system (*i.e.*, the earth). According to (C-7), the absolute angular momentum following a parcel in an axisymmetric vortex is changed only by frictional torque.

The effect of frictional torque in (C-7) is normally to decrease parcel angular momentum over time. Since friction also causes parcels in the cyclonic circulation of the TC to spiral inwards (*i.e.*, negative radial velocity), the momentum of those parcels must also be decreasing as their radial distance from the center decreases. This suggests that (C-8) should be rewritten as

$$v(r) = \frac{M_a(r)}{r} - \frac{1}{2} f_o r . \quad (C-9)$$

to account for the effect of friction on the TC tangential wind distribution at any time.

Actual TC tangential wind profiles in the lower troposphere have large  $M_a$  increases with increasing radius just outside the radius of maximum winds, and more slow increases at greater radial distances (Fig. C.3). These TCs have a radial dependence of  $M_a$  in the inflow layer that may be reasonably approximated by

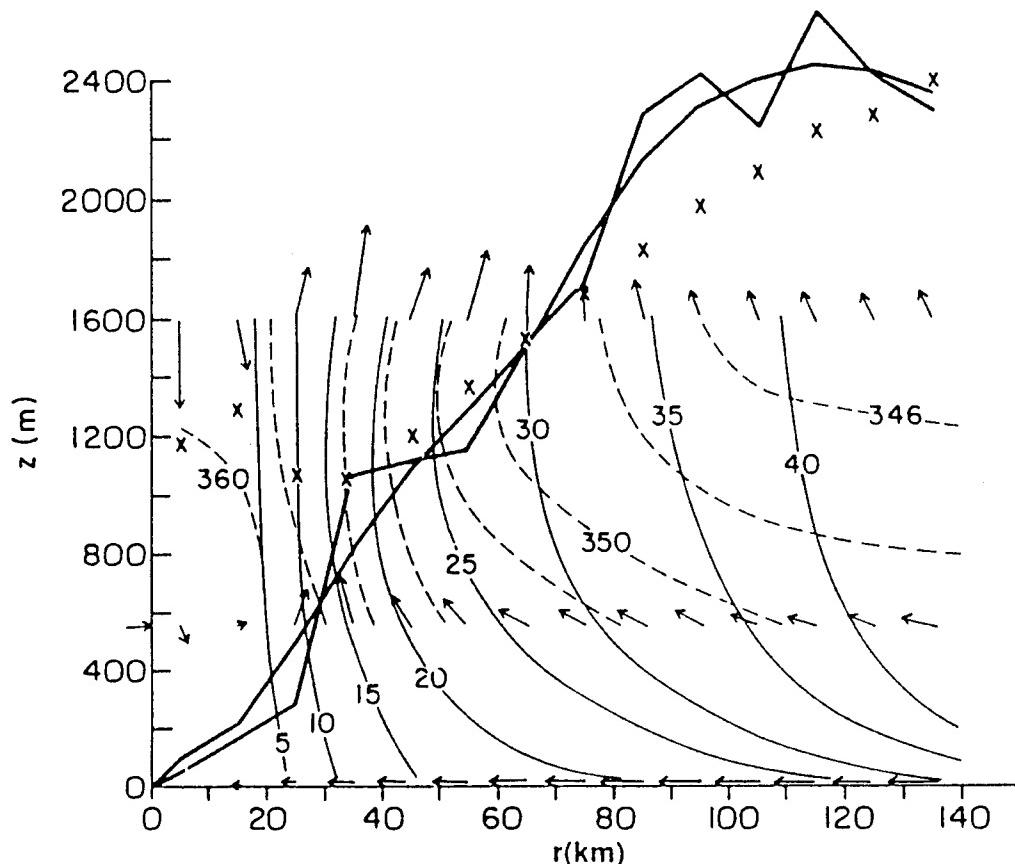


Fig. C.3 Composite azimuthally-averaged cross-section of the inflow layer in Hurricane Frederic. The heavy lines are unsmoothed and smoothed top of the inflow layer. The light solid lines are isopleths of constant absolute angular momentum ( $10^6 \text{ m}^2 \text{s}^{-1}$ ). Dashed lines are isopleths of constant equivalent potential temperature (K) (after Frank 1984).

$$M_a(r) = Mr^{1-X}, \quad (C-10)$$

where M and X are positive constants, and  $X \leq 1$ . Substituting (C-10) into (C-9) gives

$$v(r) = \frac{M}{r^X} - \frac{1}{2}f_o r, \quad (C-11)$$

which may be used as the TC tangential wind distribution if suitable values for the parameters X and M may be found.

Since the second term of (C-11) becomes negligible near the center, (C-11) asymptotically approaches

$$v(r) = \frac{M}{r^X}, \quad (C-12)$$

for small radii. The tangential wind profile given by (C-12) is known as Modified Rankine flow. Riehl (1963) found that  $X = 0.5$  may be derived via some idealized theoretical considerations, and also found that for such a value the tangential wind profile given by (C-12) agrees quite well with observations from 700 mb aircraft reconnaissance within about a  $2^\circ$  lat. radius of the TC center. However, such a value for X is not suitable for use in (C-11). The additional effect of the Coriolis term causes the wind profile given by (C-11) with  $X = 0.5$  (Fig. C.4; chain-dashed curve) to diverge significantly from the wind profile given by (C-12) with  $X = 0.5$  (Fig. C.4; dashed curve) at a radius of  $2^\circ$  lat. (222 km). Thus, to bring (C-11) into approximate agreement with observed TC tangential wind profiles near the center, a value of  $X = 0.4$  will be used in (C-11) (Fig. C.4; solid curve). It will be assumed that this value of X is reasonably accurate throughout the 850 to 500 mb layer of the TC.

Now consider that a TC must have a finite cyclonic circulation, and thus at any pressure level p there must exist an average radius at which the cyclonic tangential winds are zero; that is,

$$v(R_o^p) = 0. \quad (C-13)$$

Substituting (C-13) into (C-11) specifies the constant M to be

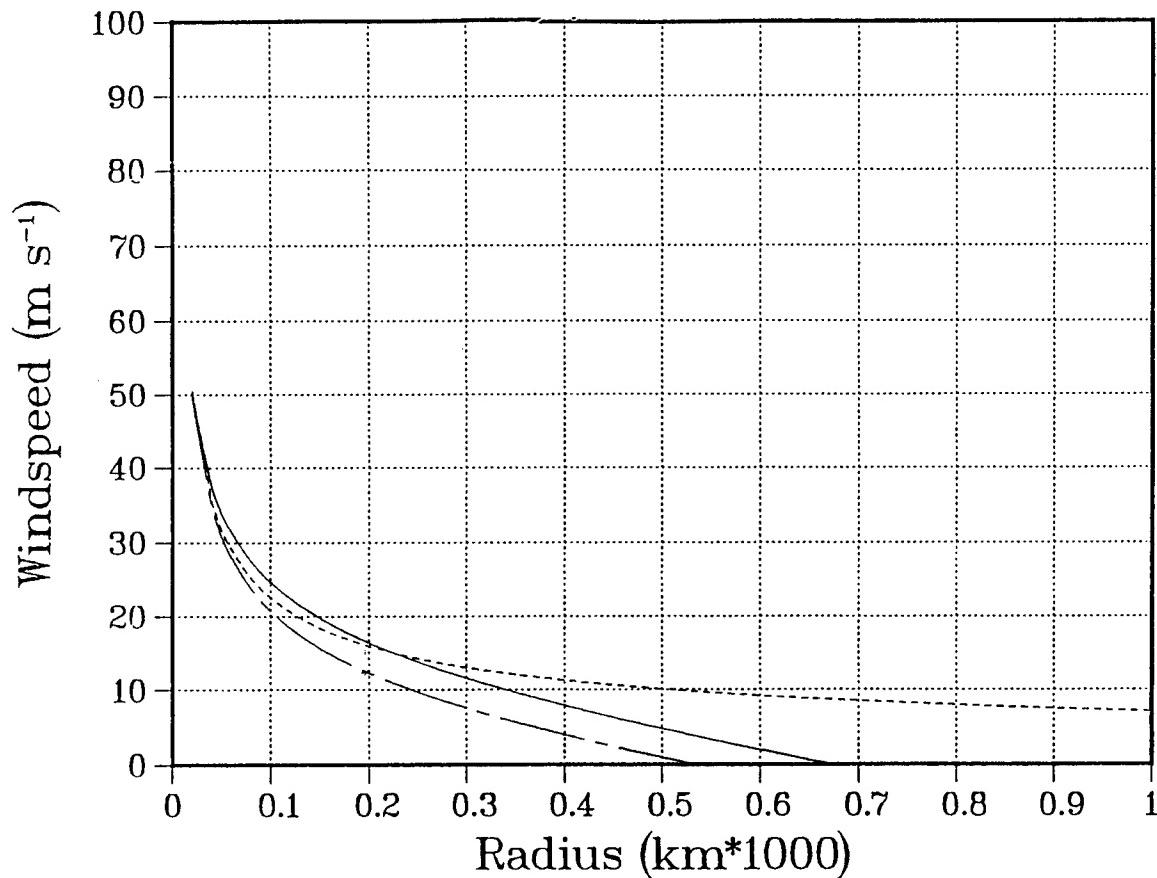


Fig. C.4 Radial profiles of tangential wind resulting from using  $X = 0.5$  in equation (C-11) (chain-dashed);  $X = 0.5$  in equation (C-12) (dashed); and  $X = 0.4$  in equation (C-11)(solid).

$$M = \frac{1}{2} f_o (R_o^p)^{1+X} . \quad (C-14)$$

Together with the stipulation  $X=0.4$ , (C-11) and (C-14) provide a model of the axisymmetric cyclonic tangential wind structure of a TC at pressure level  $p$  from 850 to 500 mb, and inside of the radius  $R_o^p$ . The limitations of the model are that: (i) asymmetric effects are ignored; (ii) the effect of friction on the radial dependence of the tangential wind speed may not be adequately approximated by the Modified Rankine flow model at small radii; and (iii) the value of  $X$  is assumed to change little over the 850 to 500 mb layer.

The first term on the right side of (C-11) represents the contribution to the parcel tangential wind speed due to the *partial* conservation of *relative* angular momentum, *i.e.*, ignoring the rotation of the earth. The influence of friction is accounted for by using a value of 0.4 for the exponent in the denominator, rather than a value 1.0, as would be the case for conservation of angular momentum in the absence of friction. That is, friction limits the

increase in tangential wind speed to about 30% for a reduction in radius by a factor of two, as opposed to the 100% wind speed increase (i.e., a doubling of windspeed) that would occur with conservation of angular momentum. The second term on the right side of (C-11) accounts for the influence of earth rotation during radial displacements of the parcels. As the radius decreases, this term becomes less negative (i.e., makes less of an anticyclonic contribution), and thus acts to increase tangential velocity in a cyclonic sense. This cyclonic spin-up as parcels converge toward the center of the TC is simply a polar-coordinate manifestation of Coriolis "force" acting to the right of parcel motion in the Northern Hemisphere. Therefore, the two terms on the right side of (C-11) give the increase in tangential wind speed that would occur due the combined effects of inertial (momentum conserving) and frictional (momentum dissipating) effects as parcels spiral cyclonically in toward the center of the TC.

Since this TC wind distribution model is based on a partial conservation of absolute angular momentum, it will hereafter be referred to as the angular momentum model. For the purpose of general discussion,  $R_o^P$  and  $v^P$  will usually be written simply as  $R_o$  and  $v$ , respectively, with the dependence on pressure implied. The superscript notation will be used only where necessary for clarity (e.g.,  $R_o^{700}$  will denote  $R_o$  at 700 mb). The discussion below illustrates a number of physically realistic properties of the angular momentum model that the authors believe make it appropriate for use in a TC motion forecasting context.

Radial profiles of tangential wind speed from (C-11) for a fixed  $R_m$  of 20 km to various  $R_o$  (100 km increments) are given in Figs. C.5, C.6, and C.7 for latitudes of 10°, 15°, and 20°N, respectively.<sup>17</sup> These profiles have a number of characteristics that are basically consistent with the composite TC profiles derived by Weatherford and Gray (1988) based on aircraft reconnaissance flights at 700 mb (Fig. C.2). For a fixed latitude, an increase in  $R_o$  (maximum radial extent) in the angular momentum model results in an increase in the tangential wind speed at all radii, with the largest increase at small radii. That is, the proposed model requires that TC intensity and TC outer wind strength be proportional to the size of the TC. Weatherford and Gray observed a similar property in their composite of aircraft winds first stratified by eye size, and then by  $V_m$  (Fig. C.8). Although the relationship between  $V_m$  and their definition of TC strength is more variable for the composite data than in the angular momentum model, a positive correlation is particularly evident for the small and medium eye stratifications (Fig. C.8; upper panels).

---

<sup>17</sup> The horizontal dashed lines at 50, 25, and  $17.5 \text{ m s}^{-1}$  in these figures have been added to give the reader some perspective of the surface wind radii reported in JTWC warning bulletins. However, recall that these profiles were developed to approximate TC tangential wind structure at pressure levels between 850 and 500 mb for the purpose of motion forecasting. It may be possible to adapt these profiles for use in TC surface wind distribution analysis, say by attempting to develop some empirical correction factor between 850 mb and surface tangential wind structures. However, caution should be exercised.

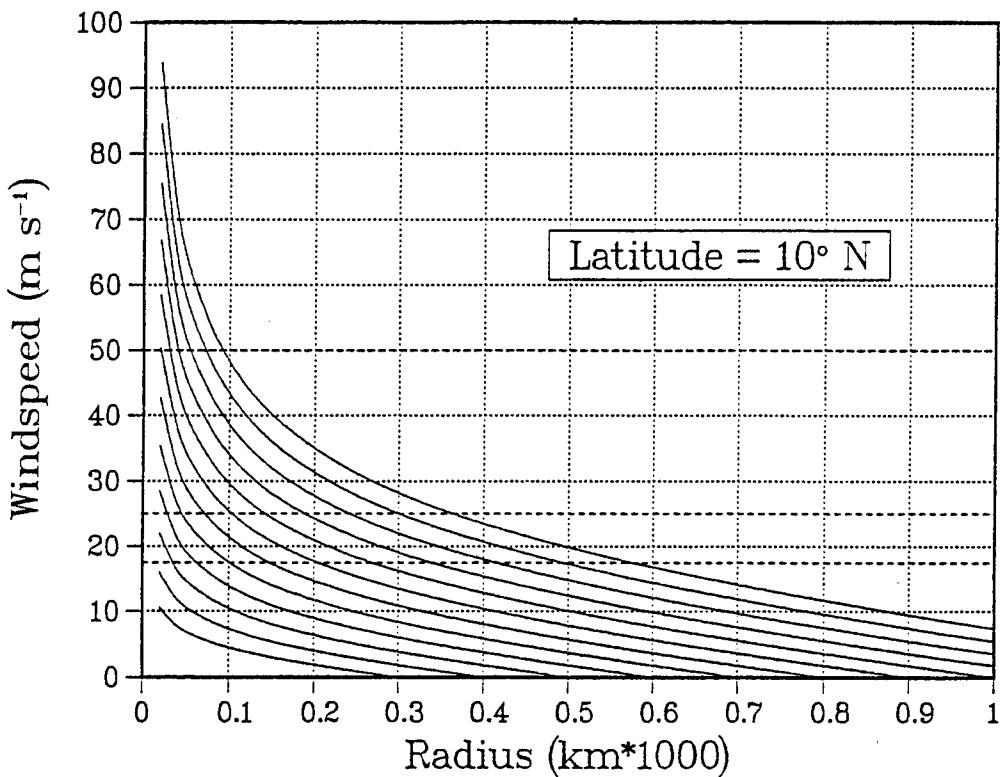


Fig. C.5 Profiles of tangential winds given by equation (C-11), holding latitude constant at 10°N, and varying  $R_0$  from 300 to 1400 km in 100 km increments.

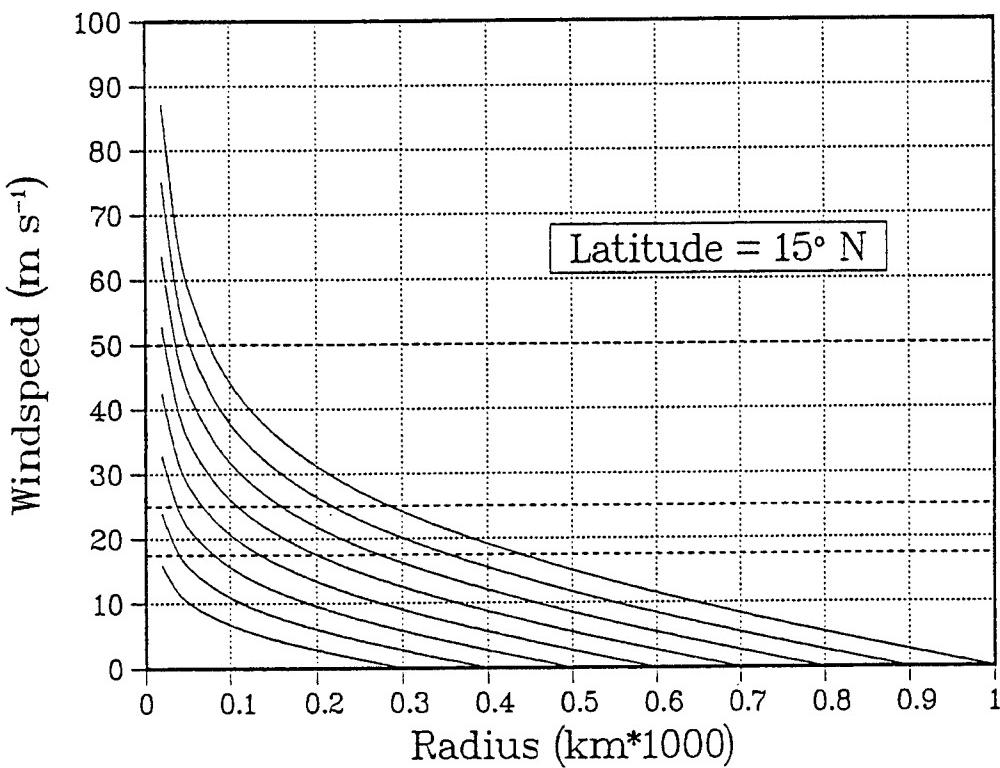


Fig. C.6 As in Fig. C.5, except for latitude 15°N and varying  $R_0$  from 300 to 1000 km.

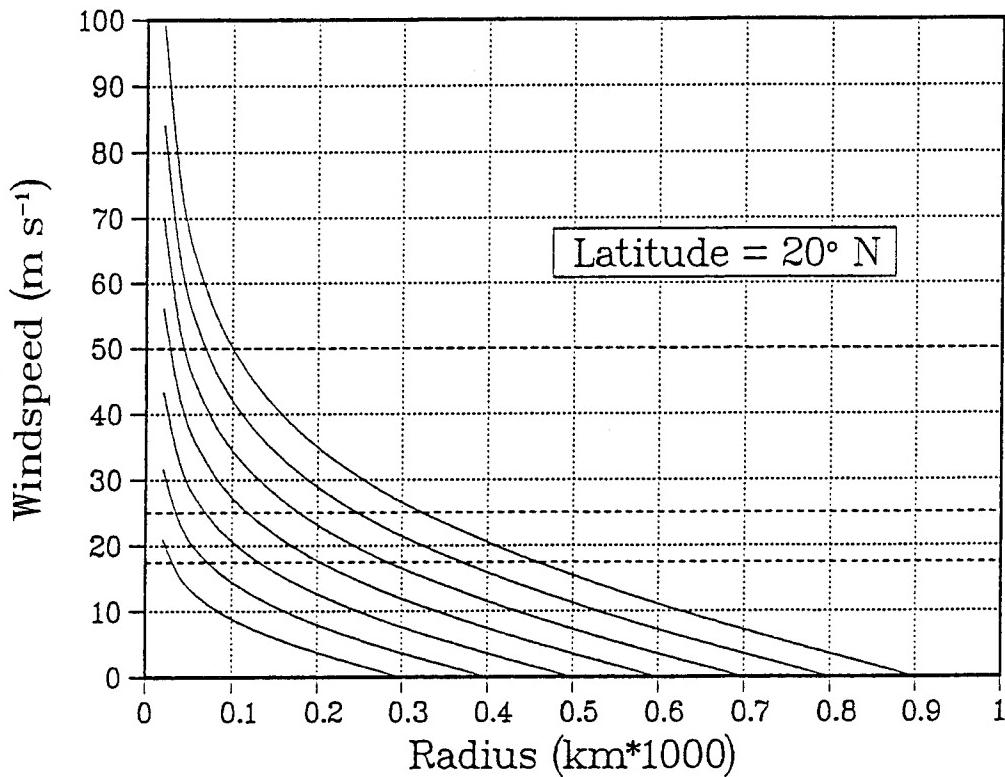


Fig. C.7 As in Fig. C.5, except for latitude 20°N and varying  $R_e$  from 300 to 900 km.

Another aspect of the angular momentum model is the positive correlation between  $R_m$  and  $R_e$  for the same  $V_m$ . For example, a wind speed of 50 m s<sup>-1</sup> (upper horizontal dashed line in Fig. C.6) is attained at about 35, 55, and 75 km for  $R_e = 800, 900$ , and 1000 km, respectively. Similar results were obtained by Weatherford and Gray for composites of TC winds stratified first by  $V_m$  (via minimum surface pressure), and then by eye size (Fig. C.9). Although the eye size-TC size correlation for fixed  $V_m$  is more variable in these composites, a positive correlation is particularly evident for the minimal typhoon category (Fig. C.9; upper right panel).

The effect of the Coriolis parameter  $f_0$  in (C-11) is that the lower average value of cyclonically-directed Coriolis torque on converging air parcels at relatively low latitudes will cause the tangential wind speed to increase more slowly as the radial distance of the parcels decreases. This effect is manifest by the smaller slopes of the outer portions of the profiles in Fig. C.5 as compared to Fig. C.7. It is also instructive to compare the influence of Coriolis changes on the wind distribution given by (C-11) when other model parameters are held constant. For TCs with the same core structure ( $V_m$  and  $R_m$ ), the angular momentum model

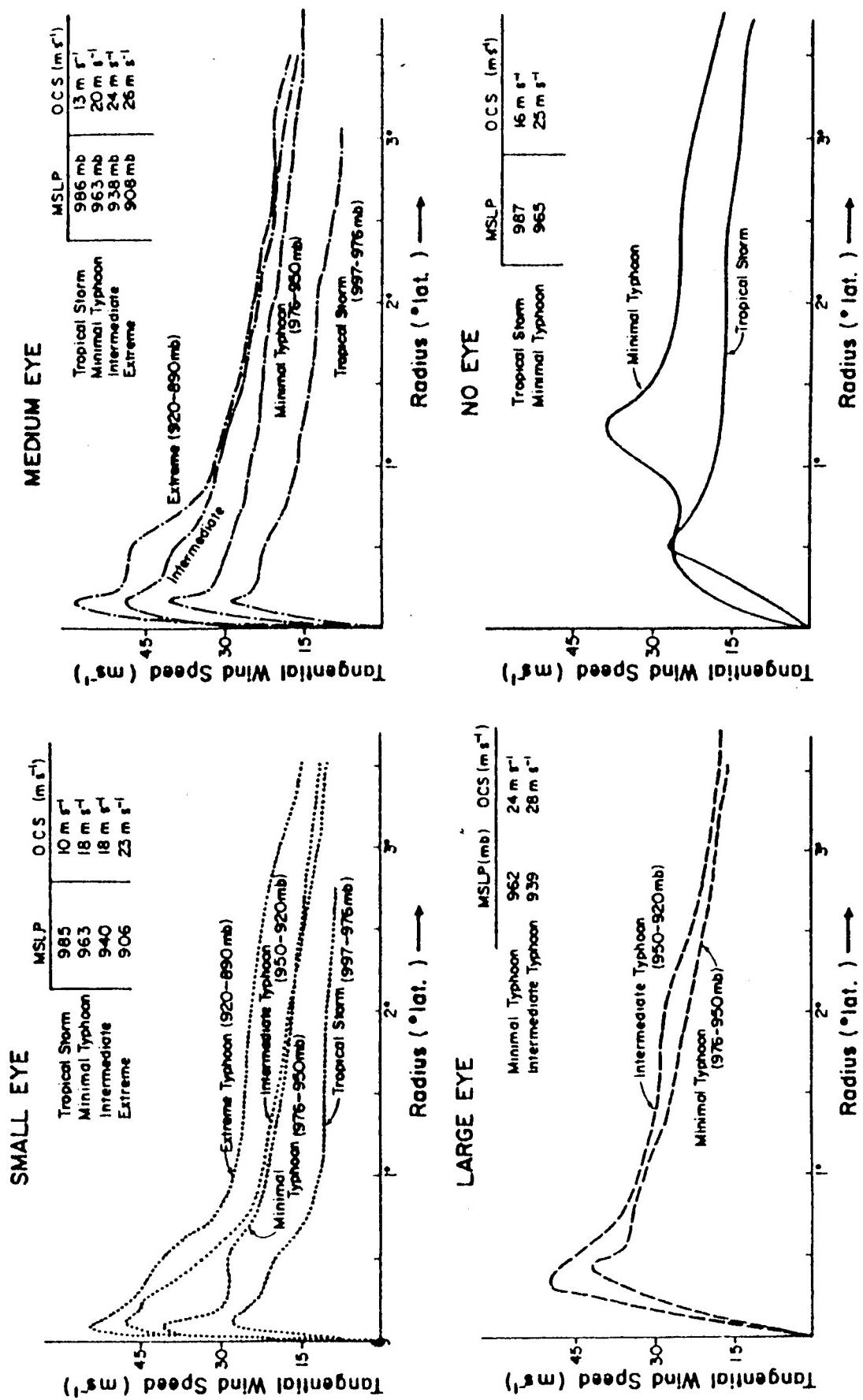


Fig. C.8 As in Fig. C.2, except for stratifying first by eye size, and then by intensity. The ranges in km for the small, medium, and large eye sizes are less than 15 km, 15 to 28 km, and greater than 28 km, respectively (after Weatherford and Gray 1988b).

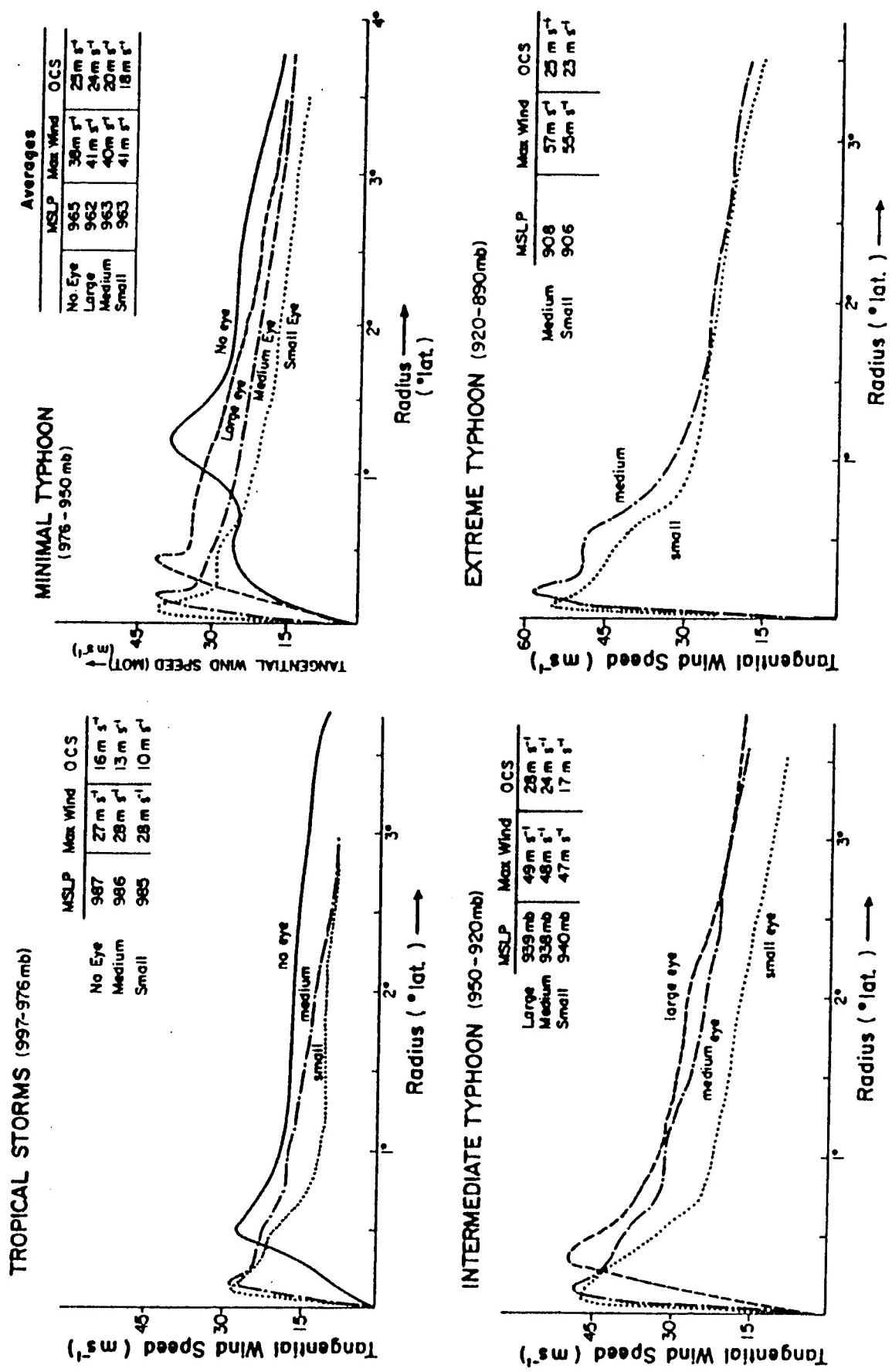


Fig. C.9 As in Fig. C.2, except for stratifying first by intensity, and then by eye size (after Weatherford and Gray).

requires that a TC at lower latitude will have a larger and stronger wind field than a TC at higher latitude (Fig. C.10). This model property is consistent with the fact that large western North Pacific TCs usually form at low ( $5^{\circ}$ - $15^{\circ}$ N) latitudes, whereas higher latitude systems are decidedly more compact. For TCs with identical radii of  $17.5 \text{ m s}^{-1}$  winds, the lower latitude TC has a larger outer circulation strength, but a weaker inner circulation strength, than a TC at higher latitude (Fig. C.11). For TCs with identical sizes ( $R_o$ ), the model requires that a TC at lower latitude will have smaller wind speeds at all radii than a TC at higher latitude (Fig. C.12). Comparison of Figs. C.5-C.7 reveals a particularly interesting aspect of the influence of latitude on the angular momentum model. For a latitude of  $10^{\circ}$ N (Fig. C.5), the model-predicted tangential wind speed at 20 km remains within observed limits (about 170 kt or  $85 \text{ m s}^{-1}$ ) for values of  $R_o$  as high as 1300 km. For a latitude of  $20^{\circ}$ N (Fig. C.7), the windspeed at 20 km attains the  $85 \text{ m s}^{-1}$  limit for an  $R_o$  of only 800 km. That is, the range of admissible TC sizes ( $R_o$ ) must be restricted to smaller values at higher latitudes to keep the model-predicted maximum tangential wind speed reasonable. Thus, the proposed angular momentum model incorporates the latitudinal dependence of Coriolis as a contributing mechanism in determining TC wind structure.

It will be assumed (without proof) that TCs do not decrease noticeably in size as they move to higher latitude, although the environmental background flow does change. If the magnitude of Coriolis does influence the TC tangential wind distribution as suggested by the angular momentum model, then it is the value of Coriolis early in the evolution of the TC that is most important. Such a situation is consistent with the principle of inertial stability. As a TC intensifies, the circulation becomes more and more inertially stable, and thus becomes resistant to influences that would tend to change the wind distribution. Although this hypothesis needs to be investigated further, it is convenient for the present to assume that the latitude at which the TC becomes a mid-range tropical storm (approximately 45 kt or Dvorak T3.0) should be used to determine  $f_o$  in (C-11) and (C-14). This latitude will be referred to as the formation latitude.

The above comparisons serve to emphasize that no single radius of wind speed, such as  $R_{ss}$  or  $R_o$  can uniquely determine the outer wind strength (area under the curves in Figs. C.5-C.7) of a TC. However, the angular momentum model parameters  $f_o$  and  $R_o$  together fully specify the outer wind strength since  $f_o$  controls the slope of the outer tangential winds and  $R_o$  acts as an outer boundary condition. It is important to establish that the profiles in Figs. C.5-C.7 agree with observations of individual TCs. Typhoon Bill became a minimal tropical storm on 3 September 1980 at about  $22^{\circ}$ N. The tangential wind speeds on 4 September were about  $40$  and  $10 \text{ m s}^{-1}$  at  $30$  and  $300 \text{ km}$ , respectively (Fig. C.13; right panel). Both of these values lie along the model wind profile for  $R_o = 500 \text{ km}$  in Fig. C.7. Typhoon Kit became of minimal tropical storm on 11 December 1980 at about  $10^{\circ}$ N. During 0000-1200 UTC 19 December, tangential wind speed of about  $37 \text{ m s}^{-1}$  and  $7 \text{ m s}^{-1}$  were present at  $35$  and  $400 \text{ km}$ , respectively (Fig. C.14; solid line). Both of these values are consistent with the  $R_o = 800 \text{ km}$  profile in Fig. C.5. Finally, notice that the outer wind profile of Typhoon Kit ( $f_o = 10^{\circ}$  lat.) has a weaker dependence on radius than the outer wind profile of Typhoon Bill ( $f_o = 22^{\circ}$  lat.), which is consistent with the dependence of the

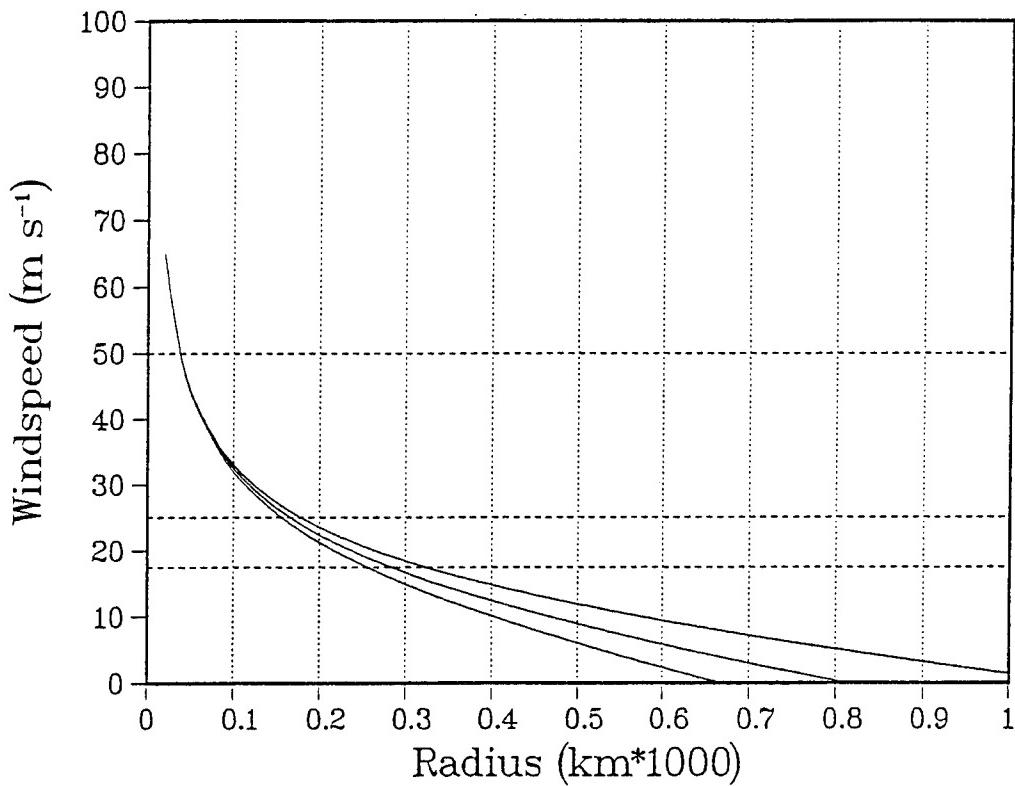


Fig. C.10 As in C.5, except  $V_m$  and  $R_m$  held constant at  $65 \text{ m s}^{-1}$  and  $20 \text{ km}$ , respectively, and latitudes of  $10^\circ\text{N}$  (largest profile),  $15^\circ\text{N}$  (intermediate profile), and  $20^\circ\text{N}$  (smallest profile).

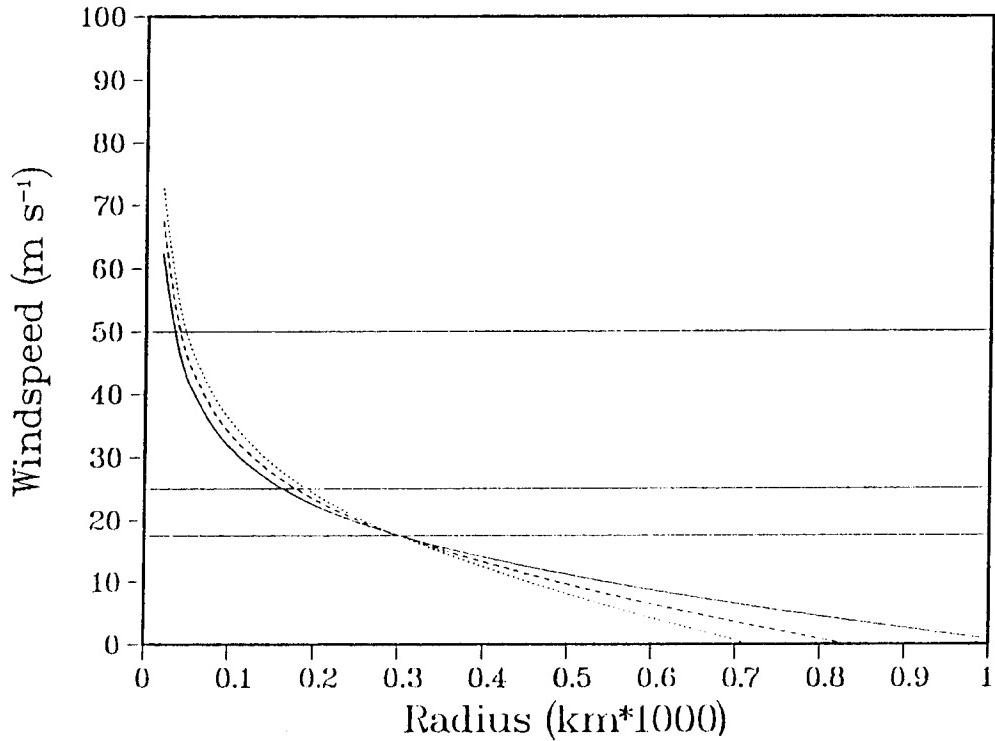


Fig. C.11 As in Fig. C.5, except with the radius of  $17.5 \text{ m s}^{-1}$  wind speed held constant, and latitudes of  $10^\circ\text{N}$  (largest profile),  $15^\circ\text{N}$  (intermediate profile), and  $20^\circ\text{N}$  (smallest profile).

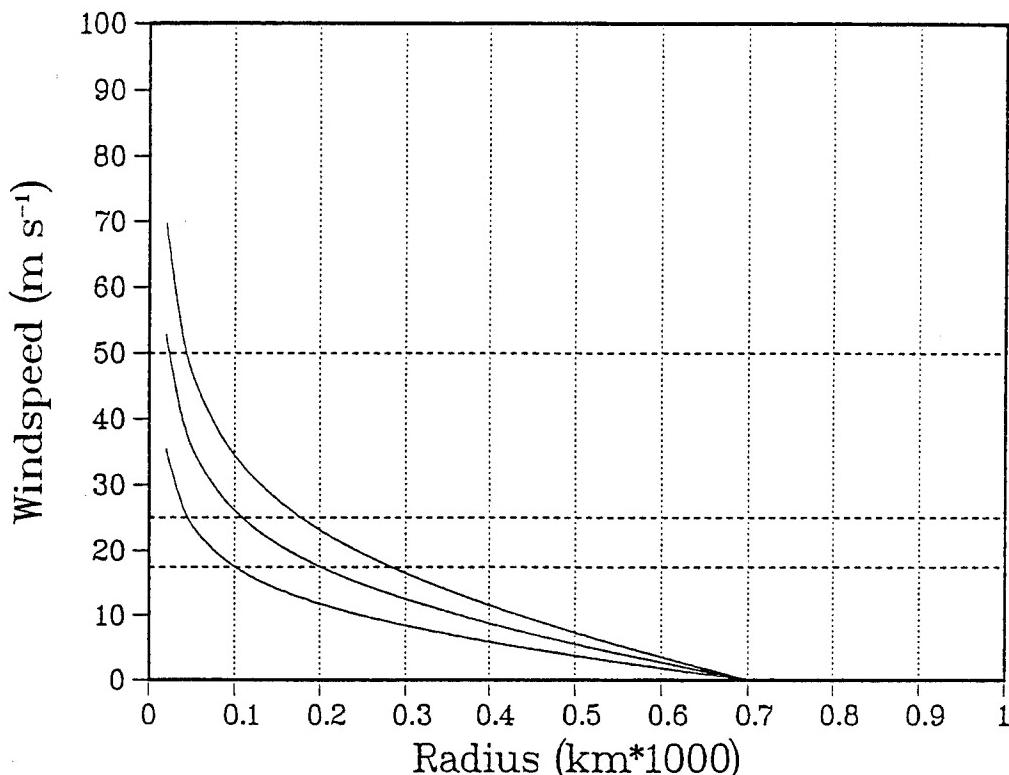


Fig. C.12 As in C.5, except with  $R_o$  held constant at 700 km, and latitudes of 10°N (weakest profile), 15°N (intermediate profile), and 20°N (strongest profile).

angular momentum model wind distribution on formation latitude  $f_o$  (Fig. C.12).

These two successful comparisons of model-predicted wind profiles with observations do not constitute a definitive test of the model, and should not be construed to imply that the model will be accurate in all situations. Examples of situations that cannot be addressed by the proposed model include: (i) the presence of multiple eyewalls (Willoughby 1990); (ii) interactions of TCs with monsoon gyres (MTI in Table 3.3); and (iii) abnormal structural changes after a TC encounters high vertical wind shear (VWS in Table 3.3), as in the case of Typhoon Kit (Fig. C.14; dotted and dashed lines). The last two situations involve TC-environment transformations, and are discussed in detail in Subsection 3.d.3.

Although the angular momentum model in Eqs. (C-11) and (C-14) provides no information about how fast a TC may change structure during intensification and/or growth, the model may at least provide a baseline for expected changes in structure. Consider two idealizations of the profiles in Fig. C.2 that indicate TCs do not experience significant growth after attaining *minimal* tropical storm intensity: (i) no outer wind increase at any

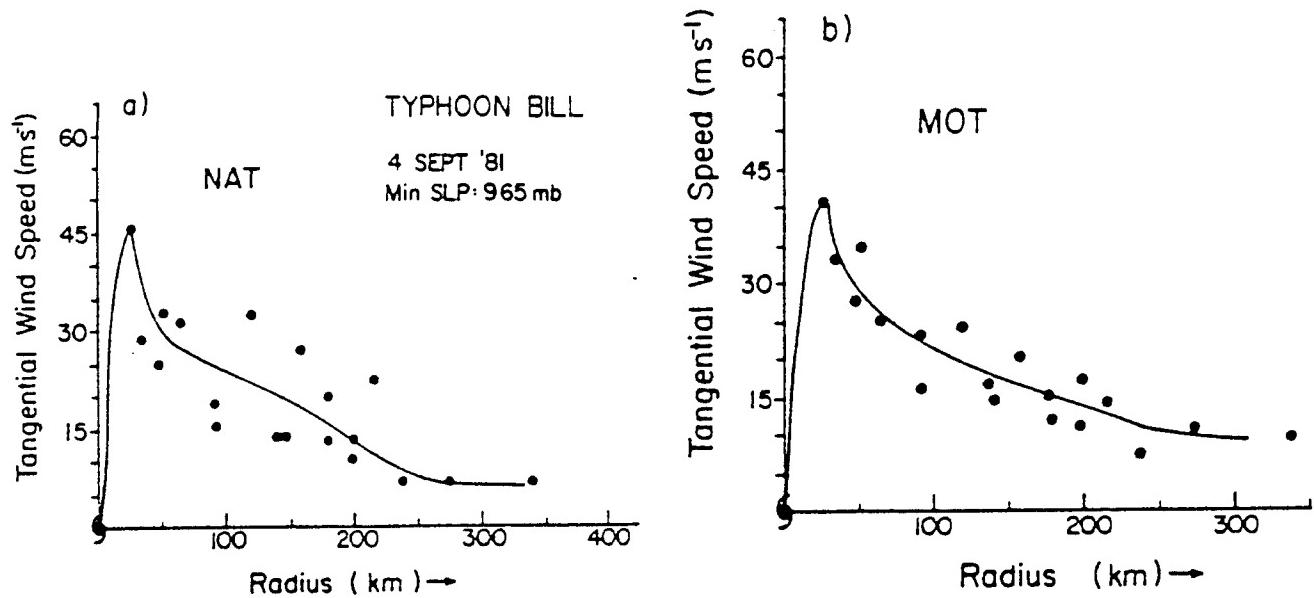


Fig. C.13 Azimuthally averaged tangential winds for Typhoon Bill from aircraft reconnaissance on 4 September 1981 in a coordinate system moving with (a) the earth, and (b) the TC.

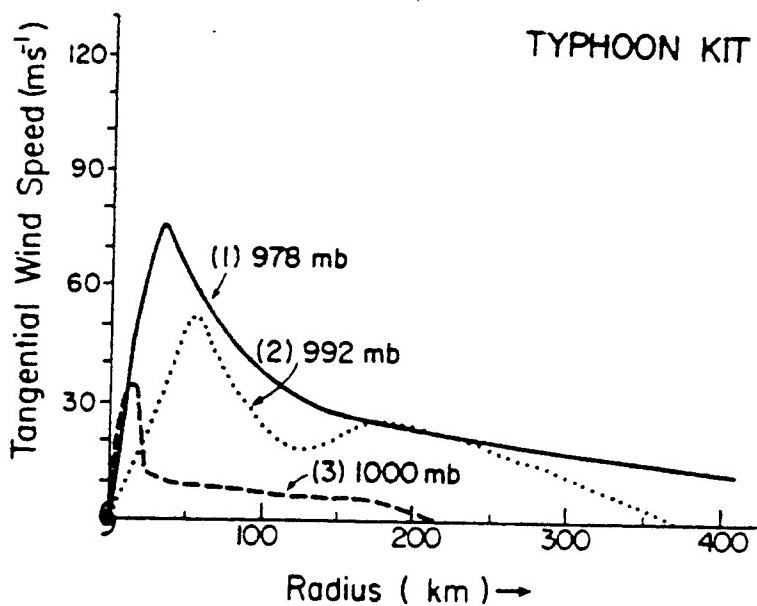


Fig. C.14 As in Fig. C.13a, except for Typhoon Kit in 1981 during the periods 0000-1200 UTC 19 December (solid), 1200-2400 UTC 19 December (dotted), and 0000-1200 UTC 20 December (dashed).

time during intensification (Fig. C.15); and (ii) outer wind increase only during the tropical storm stage (Fig. C.16). In the first situation, the sequence of six wind profiles have the same size ( $R_o = 900$  km), but a contraction of  $R_m$  with time is imposed by functions that decrease rapidly to zero beginning at various distances from the origin. This set of profiles illustrates how the maximum wind speed might increase from minimal tropical storm to supertyphoon as the ascent region of the TC contracts from just under 300 km to 20 km. During this sequence, the 17.5, 25, and 50 m s<sup>-1</sup> wind radii at the pressure level of interest would not increase significantly after first appearing. In the second situation (Fig. C.16),  $R_o$  is increased from 700 to 900 km during the "growth" phase of the TC, and then is held constant. Although a significant expansion of the 17.5 (25) m s<sup>-1</sup> wind radii occurs in the first three (two) profiles, these wind radii do not expand during the subsequent period of intensification from minimal typhoon to supertyphoon.

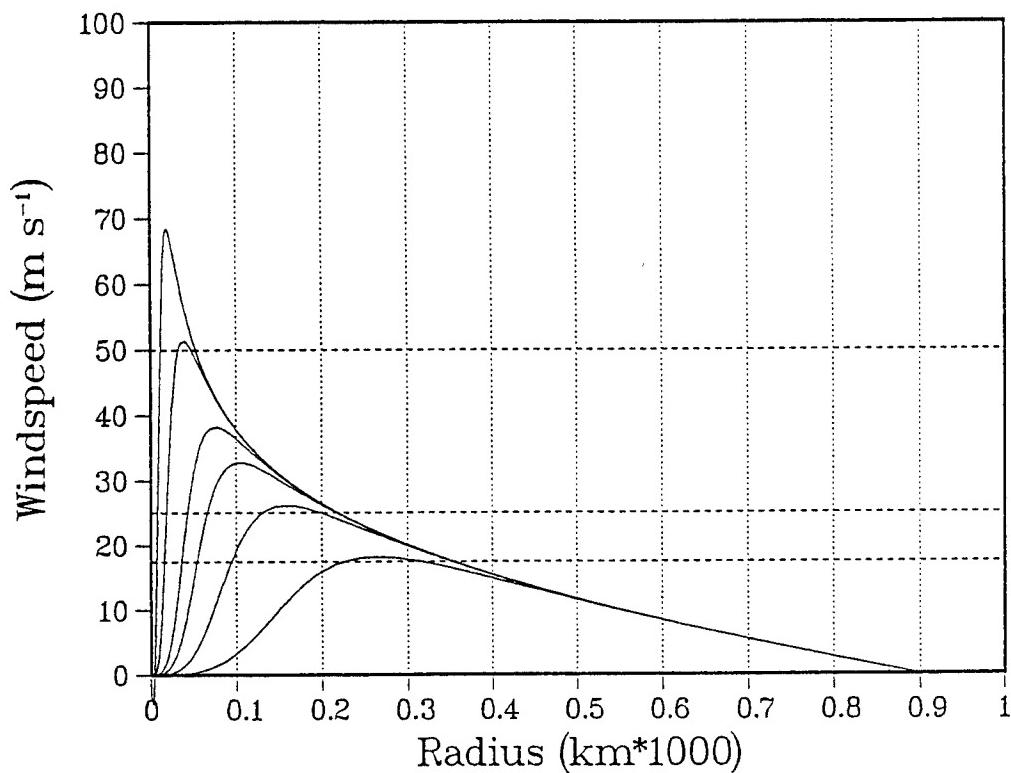


Fig. C.15 An idealized sequence of six tangential wind profiles during an intensification of a TC without an outer wind increase. The profiles were produced from equation (C-11) by holding latitude and  $R_o$  fixed at 15°N and 900 km respectively, and including an adjustable multiplicative function that can produce a radius of maximum winds ( $R_m$ ) by forcing the tangential wind to go to zero at the origin.

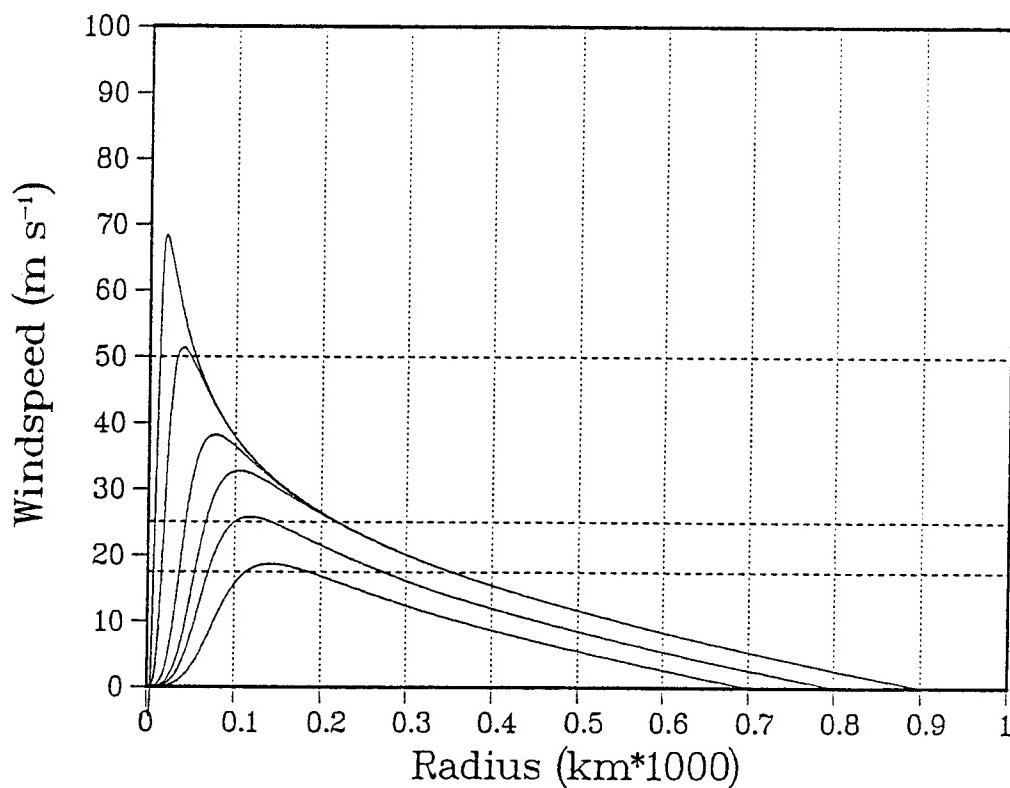


Fig. C.16 As in Fig. C.15, except that  $R_0$  is increased in 100 km increments from 700 to 900 km, and then held constant to provide an idealized TC wind distribution evolution that has both an outer wind increase and intensification during the tropical storm stage, but has no outer wind increase during intensification to the typhoon stage.

## Appendix D

### Beta-Effect Propagation (BEP) Background and Preliminary Development

**1. Background** Analytical and numerical modelling studies have focussed on the barotropic dynamics of a TC-like vortex on a  $\beta$ -plane that propagates relative to various idealized environments. In the simplest case, TC propagation occurs in a quiescent environment owing only to the variation of the Coriolis parameter with latitude ( $\beta$ ). The phrase "beta-effect propagation" (denoted BEP here) is commonly used to denote such movement of the vortex relative to the environment. A  $\beta$  plane (i.e., constant variation with latitude) approximation has traditionally been employed to approximate the sinusoidal variation of Coriolis with latitude.

A consensus exists as to the roles of the physical processes that contribute to BEP of barotropic TC-like vortices in quiescent or uniform environments. Although recent research studies (DeMaria 1985; Evans *et al.* 1992; Smith 1991; Williams and Chan (1994) have also investigated how BEP is modified by the relative vorticity gradient or the linear shear associated with a horizontally variable environmental flow, some inconsistencies remain to be resolved.<sup>18</sup> Furthermore, Williams and Chan (1994) indicate that such modifications to the quiescent-environment BEP (hereafter basic BEP) appear to be relatively minor in terms of their impact on TC forecasting. Thus, only the influence of basic BEP on TC motion will be addressed below.

Consider the barotropic vorticity equation

$$\frac{\partial \zeta}{\partial t} = -\beta v - \vec{V} \cdot \nabla \zeta - (\zeta + f) \nabla \cdot \vec{V}, \quad (D-1)$$

*A*      *B*      *C*      *D*

where the symbols have their usual meaning. According to (D-1), the local time tendency of relative vorticity (term A) depends on the linear effect of earth vorticity advection (term B), the nonlinear effect of relative vorticity advection (term C), and the nonlinear effect of the convergence/divergence of parcels that have a nonzero absolute vorticity (term D). If

---

<sup>18</sup> Recently, researchers have also examined various baroclinic mechanisms that may result in TC propagation. Such studies have typically utilized numerical models with coarse vertical resolution and highly simplified representations of important physical processes. Predictions of TC propagation are sensitive to model specification, particularly the depth of the TC outflow layer. In addition, significant inconsistencies exist among the results of the various baroclinic TC propagation studies. For these reasons, the authors believe that it would be premature to incorporate possible baroclinic contributions to TC propagation into the present version of the systematic approach.

term D is omitted for a deep, nondivergent layer, Eq. (D-1) is a statement of conservation of absolute vorticity following parcel trajectories.

Chan and Williams (1987) used a nondivergent, barotropic model on a  $\beta$  plane to identify the individual influences of earth and relative vorticity advects of a TC-scale vortex in a quiescent environment. Using a linear version of the model (i.e., term C in (D-1) excluded), Chan and Williams showed that the advection of earth vorticity (term B) caused the outer part of the TC circulation to stretch significantly toward the west, but produced negligible movement of the center of the TC (Fig. D.1). Including only terms A and B in Eq. (D.1) describes linear Rossby wave motion, for which the phase speed is proportional to the square of wavelength. Thus, the larger scale outer circulation of the TC propagates westward more rapidly compared to the smaller scale inner core of the TC. As a result, the effect of the linear  $\beta$  term in (D.1) is to distort and eventually disperse the TC.

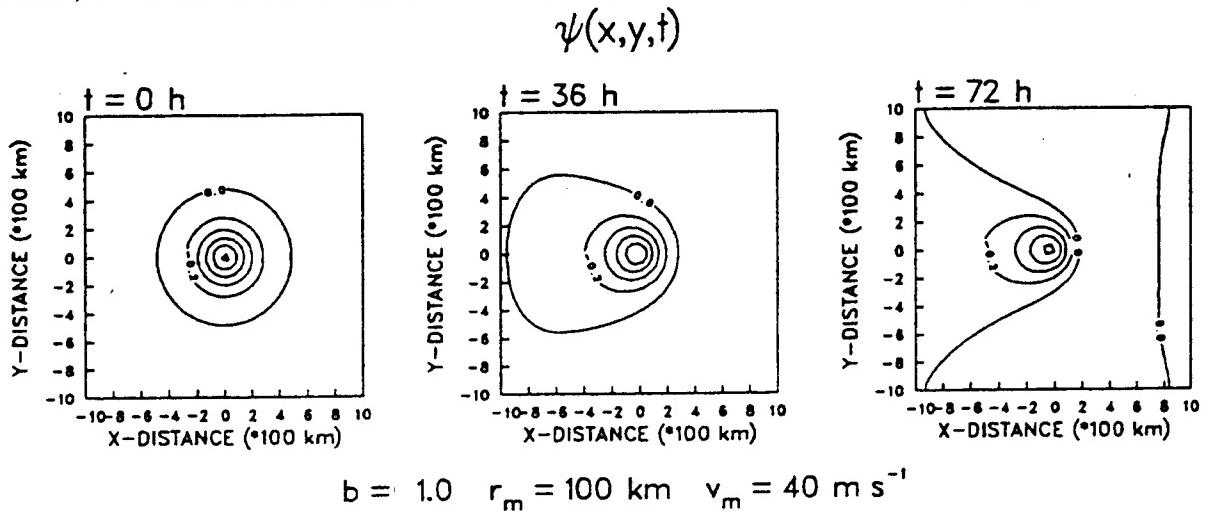


Fig. D.1 Streamfunction fields ( $\psi$ ) at 0, 36, and 72 h for the model of Chan and Williams (1977) for a vortex profile with  $V_m = 40 \text{ m s}^{-1}$ ,  $r_m = 100 \text{ km}$ , and  $b = 1.0$ . The contour interval is  $0.2 \times 10^6 \text{ m}^2 \text{ s}^{-1}$ .

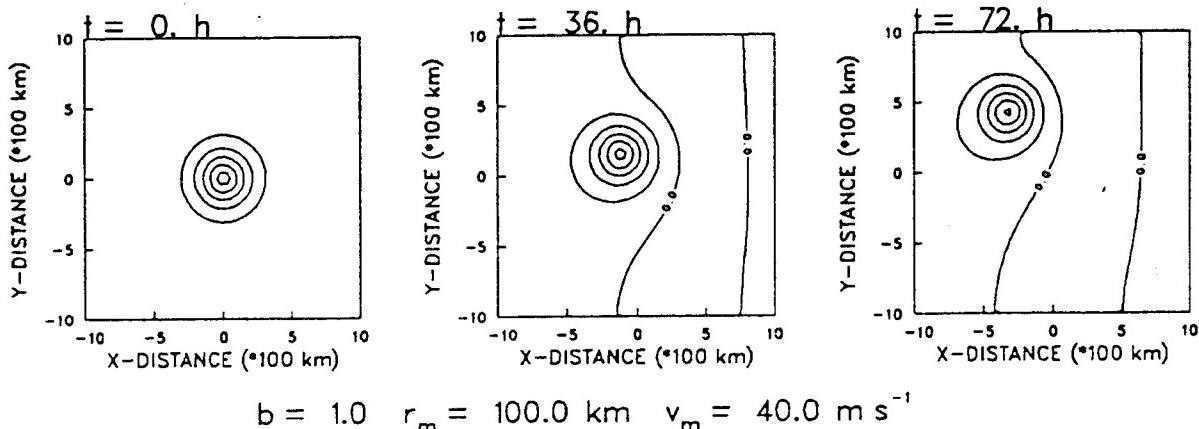


Fig. D.2 As in Fig. D.1, except for nonlinear numerical simulations of Chan and Williams (1987). The contour interval is  $0.1 \times 10^6 \text{ m}^2 \text{ s}^{-1}$ .

When Chan and Williams included the nonlinear advection of relative vorticity (term C), the TC moved northwestward in 72 h (Fig. D.2), which demonstrated that nonlinear vorticity advection is necessary for significant TC propagation relative to the environment. Because Chan and Williams initialized the barotropic model with a symmetric vortex (first panel in Fig. D.2), nonlinear relative vorticity advection was initially zero and could not contribute to TC motion until the axisymmetry of the TC was disturbed. Thus, Chan and Williams concluded that the linear earth vorticity advection has an essential role of distorting the vortex as in Fig. D.1 so that motion-inducing, nonlinear vorticity advection can occur.

An illustration of how nonlinear vorticity advection causes vortex propagation on a  $\beta$  plane in a quiescent environment was given by Fiorino and Elsberry (1989), who separated the TC circulation into symmetric and asymmetric components. They showed that the northeast-southwest orientation of the TC asymmetry evident in Fig. D.2 at 36 and 72 h is manifest as pair of gyres: an anticyclone to the northeast and cyclone to the southwest (Fig. D.3). These gyres are now commonly referred to as " $\beta$  gyres." Fiorino and Elsberry noted that the  $\beta$  gyres generate a nearly uniform flow across the center of the symmetric TC circulation, and that the speed and direction of this flow agree closely with the propagation speed and direction of the TC-scale vortex at all times during the model integration. Term C of Eq. (D-1) may be expressed as a sum of contributing advections by the asymmetric (A) and symmetric (S) components

$$-\vec{V} \cdot \nabla \zeta = -(\vec{V}_A \cdot \nabla \zeta_S + \vec{V}_S \cdot \nabla \zeta_A + \vec{V}_A \cdot \nabla \zeta_A). \quad (\text{D-2})$$

Thus, Fiorino and Elsberry showed that TC propagation on a  $\beta$  plane is almost completely accounted for by the advection of the symmetric component relative vorticity by the flow of the asymmetric component; that is, by the first term on the right side of (D-2).

Notice that the dispersive effect of  $\beta$  distorts the shape of the TC vortex in Chan and Williams's nonlinear model (Fig. D.2) from axisymmetry at 0 h to become slightly elongated to the southwest at 36 h. However, the degree and orientation of the distortion does not change significantly from 36 h to 72 h. In addition, the elongation effect is confined to the outer part of the vortex (note concentric streamlines near the center). By contrast, the degree of distortion continues to increase between 36 h and 72 h in Chan and Williams's linear model (Fig. D.1), and this distortion is evident in both the inner and outer regions of the vortex. Therefore, nonlinear vorticity advection also tends to make the vortex resistant to  $\beta$ -induced dispersion, particularly at small distances from the center. Carr and Williams (1989) demonstrated that the advection of the asymmetric component of the TC by the tangential wind of the symmetric component of the TC (i.e., the second term on the right side of (D-2)) is the source of such resistance to horizontal distortion of the vortex. In particular, they noted that radial shear of the tangential wind of a TC outside the radius of maximum winds exerts a down-shear tilting, and thus damping, effect on TC asymmetries

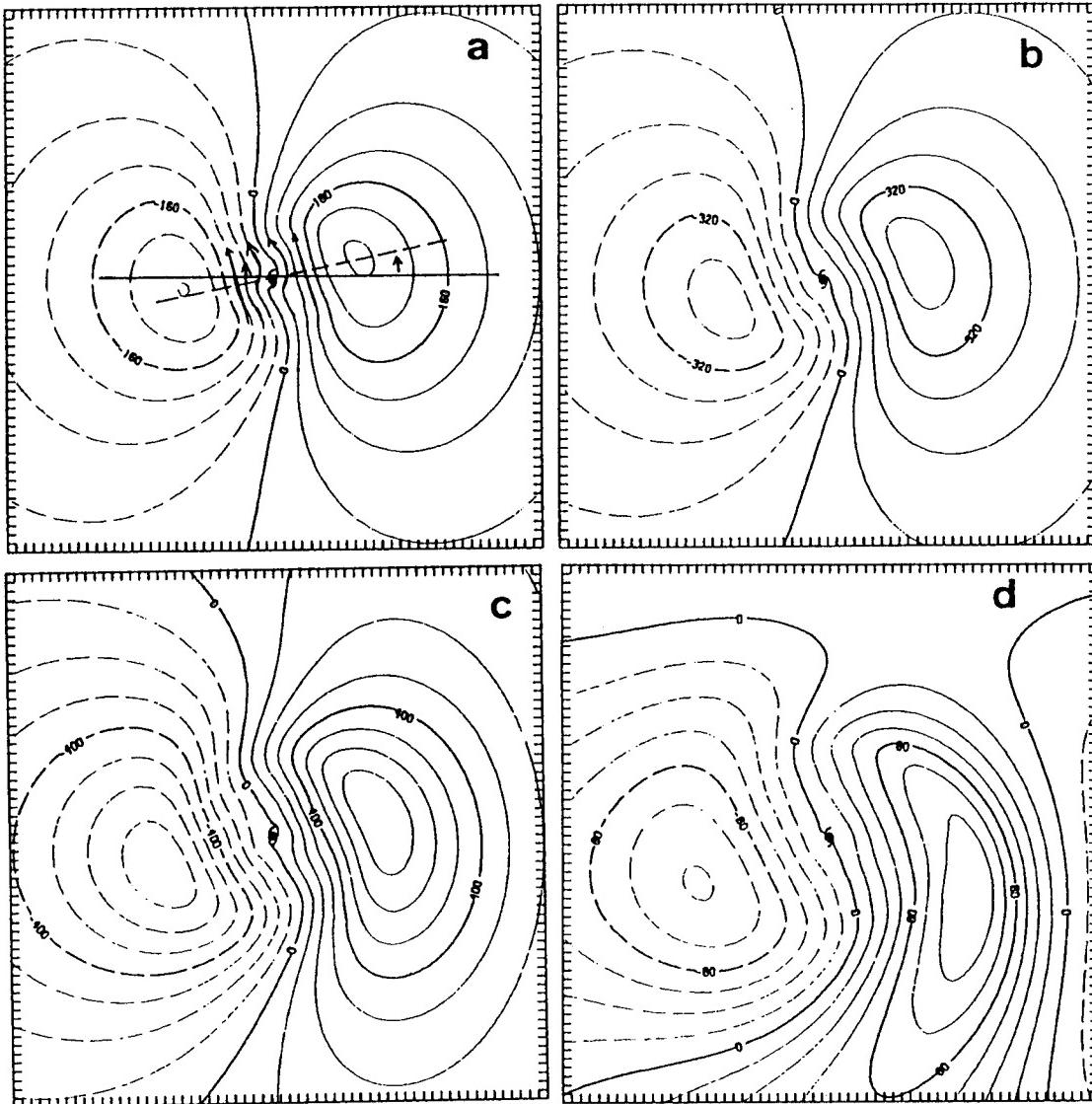


Fig. D.3 Temporal evolution of the asymmetric streamfunction  $\psi_a$  ( $m^2 s^{-1}$ ) at (a) 6 h; (b) 12 h; (c) 24 h; and (d) 72 h in the numerical simulation of Fiorino and Elsberry (1989). The plot domain is 61 x 61 points (with  $\Delta x = 40$  km, 2400 x 2400 km) centered on the vortex. The tick marks indicate the location of the grid points. Positive (negative) values indicate anticyclonic (cyclonic) streamfunctions. Contour intervals are 4, 8, 10, and 20 ( $10^4$ ), and the maximum absolute values of  $\psi_a$  are 2.5, 4, and 7 ( $\times 10^6$ ), respectively.

(Fig. D.4b), which is analogous to the down-shear tilting and damping of weak disturbances by a linearly sheared, zonal environmental flow (Fig. D.4a). In other words, TC-scale vortices tend to be barotropically stable with respect to small perturbations from axisymmetry, which explains why the inner region of TCs is nearly circular. Carr and Williams demonstrated this stabilization process by imposing a large amplitude azimuthal

wavenumber one asymmetry (similar in structure to a  $\beta$  gyre) as an unforced initial condition on a axisymmetric, steady Rankine vortex ( $v \propto r^{-1}$ ) (Figs. D.5a and d). Notice how the asymmetry damps with time (Fig. D.5b and c) as it is tilted down-shear. By 36 h, the Rankine vortex has nearly regained a symmetric shape, particularly at small radii where the radial shear of the Rankine flow is the greatest.

Shapiro and Ooyama (1990) offered an alternate perspective on barotropic vortex stability to dispersive effects. As the  $\beta$  gyres develop from the initially symmetric TC-scale vortex, the relative vorticity of the gyres is wrapped around and stretched to form a complex pattern of increasingly smaller scale filaments of positive and negative relative vorticity. This filamentation process continues without any lower-scale bound in analytical models (e.g., Smith et al. 1990; their Figs. 2 and 3). Owing to the limited resolution of Shapiro and Ooyama's numerical model (which they noted is something of a proxy for turbulent diffusion in nature), the smallest scales of these vorticity filaments are eliminated with time. The net effect of this smoothing process is the formation of a quasi-steady, nearly-uniform, and equatorward-directed relative vorticity gradient within 400 km of the vortex center (Fig. D.6). Because the magnitude of this asymmetric relative vorticity gradient is nearly equal to  $\beta$  and is in the opposite direction, a zero absolute vorticity gradient exists across a large area of the vortex (Fig. D.6b). As a result, the vorticity pattern of the growing  $\beta$  gyres tends with time to neutralize the background vorticity gradient that initiated such growth, which in turn tends to arrest gyre growth and produce near-steady propagation.

Chan and Williams (1987) noted that the magnitude of BEP increased as the overall strength and extent of the tangential winds of the TC were increased. Fiorino and Elsberry (1989) refined the relationship between TC structure and the magnitude of BEP via a set of experiments in which the inner and outer structures of the TC were independently varied. They found that changes in the wind distribution of the TC inside 300 km (Fig. D.7a) had virtually no effect on either BEP direction or speed (Fig. D.7b). By contrast, changes in the wind distribution outside 300 km (Fig. D.8a) significantly affected both the direction and speed of the BEP (Fig. D.8b). In particular, a stronger outer TC wind structure resulted in a significantly larger BEP speed.

In summary, BEP can be described as a nonlinear advection of the symmetric component of the TC by a much weaker ( $1\text{-}3 \text{ m s}^{-1}$ ) asymmetric component. Because this effect occurs with no environmental flow to advect the vortex, this process may be viewed as a "self-advection" phenomenon. The magnitude of the asymmetric flow component is determined by an approximate balance between: (i) the asymmetry-generating effect of linear advection of the earth vorticity by the TC; and (ii) the asymmetry-damping nonlinear advection of the asymmetric flow component by the radially sheared flow of the TC. In barotropic simulations, the self-advection process is significantly affected by the outer structure of the TC, but is insensitive to the inner structure of the TC. Finally, recent research suggests that the effects of horizontal shear and relative vorticity gradients in the environmental flow modifies basic BEP in a relatively minor way that generally should not have great significance to the operational forecaster.

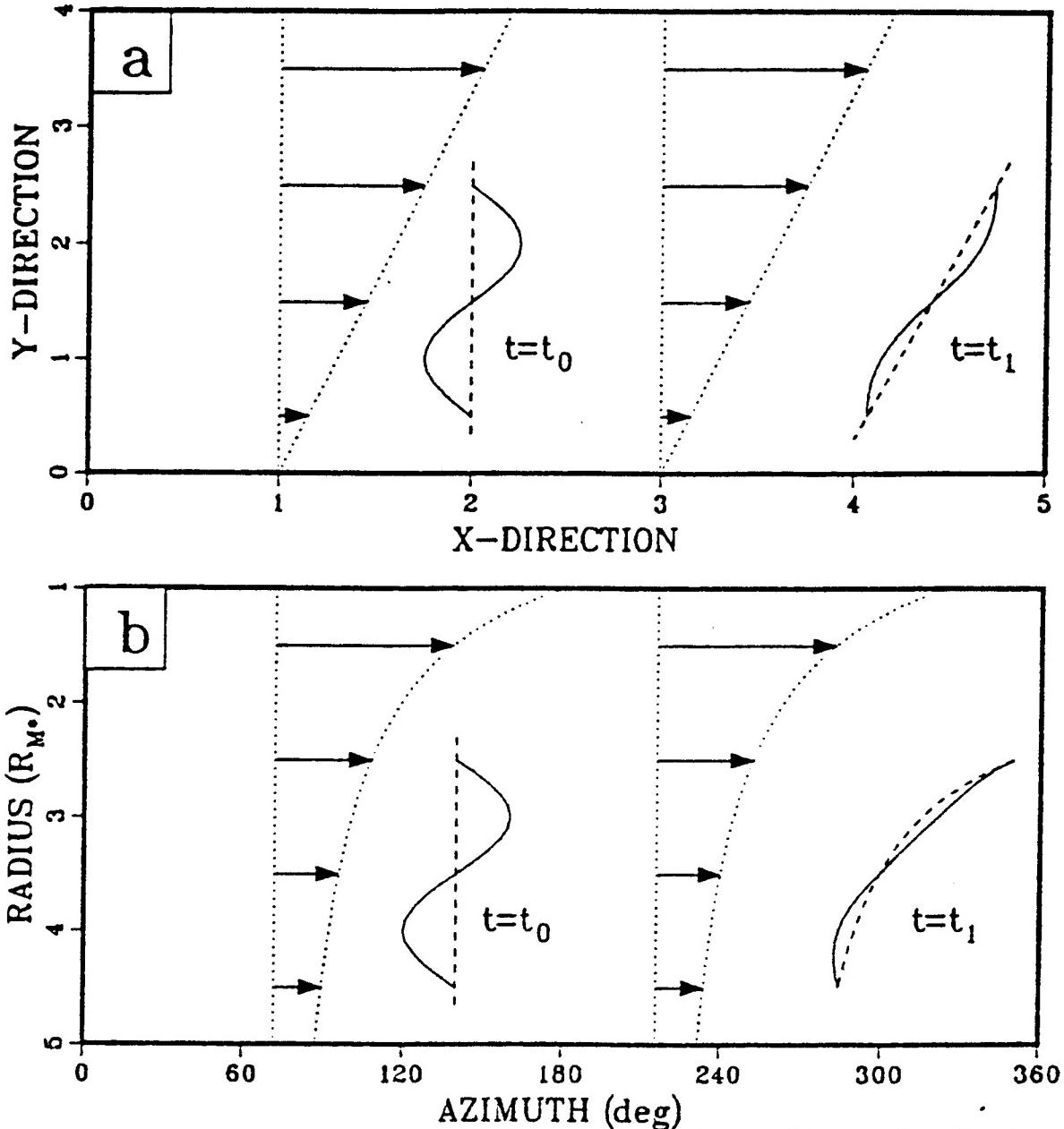


Fig. D.4 Schematic of perturbation damping with time due to (a) meridionally sheared Couette flow, and (b) a radially sheared axisymmetric vortical flow (Carr and Williams 1989).

**2. Preliminary Development.** The BEP speed versus TC size relationships identified in the literature review above may not be directly applied by the TC forecaster, since the researchers represented the TC tangential wind profile with simple functions chosen more for modelling convenience than for a close agreement with observations. The angular momentum TC wind profile developed in Subsection 3.c.2 does provide for a dynamically meaningful variation of TC size and outer wind strength, and thus may be used to develop a quantitatively useful BEP propagation versus TC size relationship.

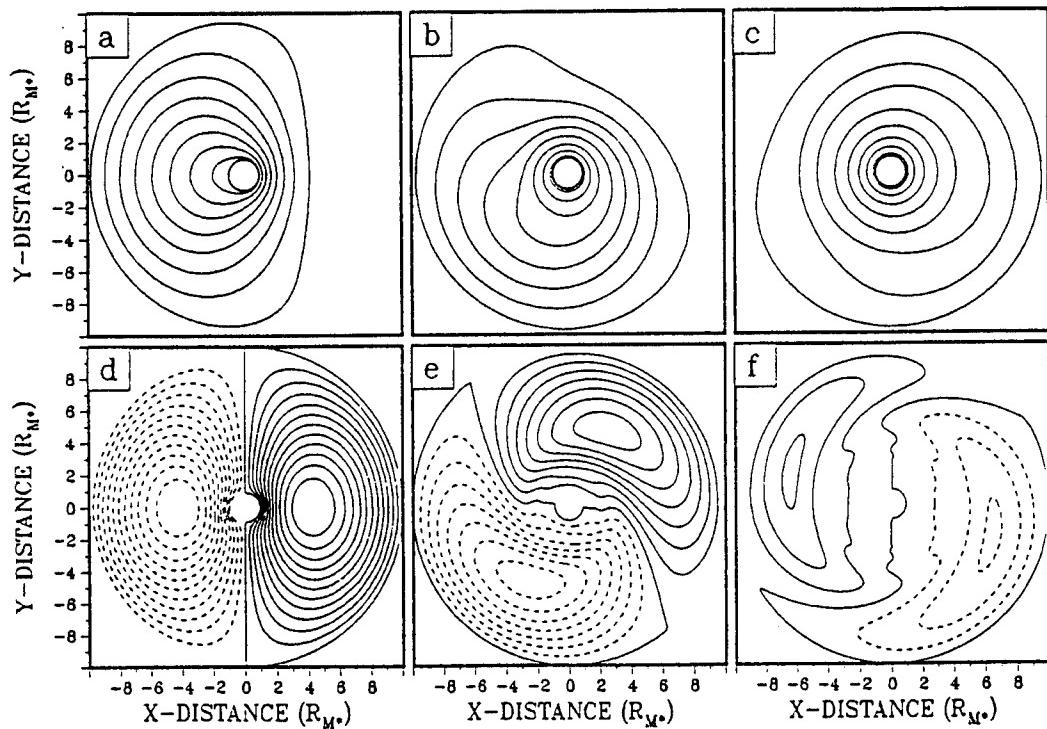


Fig. D.5 (a)-(c) Perturbation plus symmetric streamfunction for  $\beta$ -induced asymmetry at  $t=0, 8$ , and  $36$  hours, respectively. Contour interval is  $7.4 \times 10^5 \text{ m}^2 \text{ s}^{-1}$ . (d)-(f) Same as (a)-(c), except showing just the perturbation streamfunction (solid, positive; dashed, negative), and using a contour interval of  $1.7 \times 10^5 \text{ m}^2 \text{ s}^{-1}$  (Carr and Williams 1989).

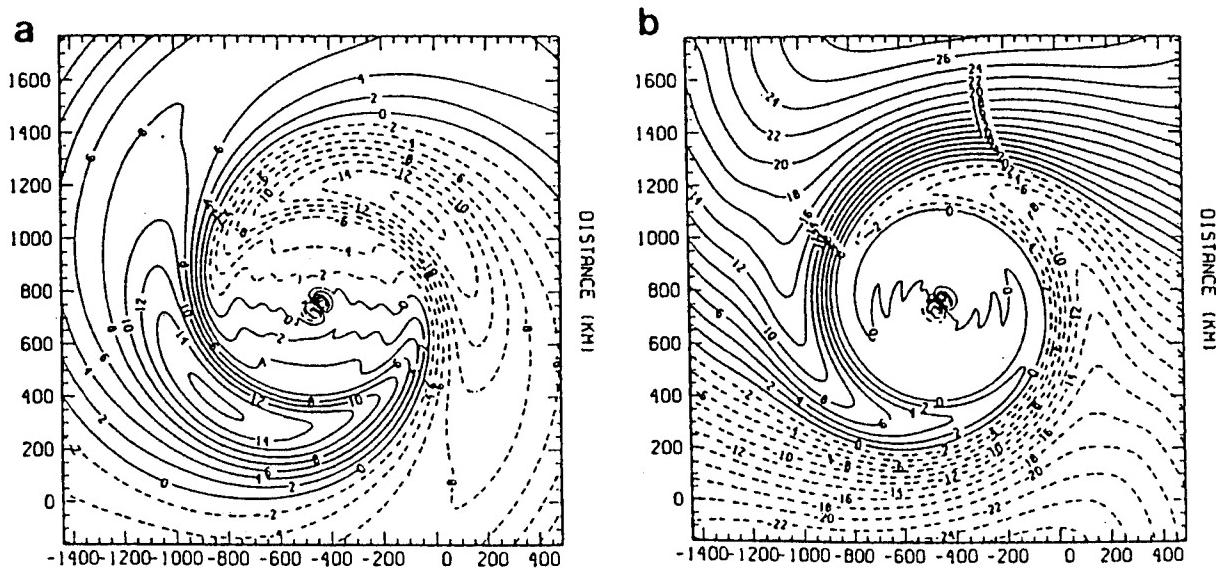


Fig. D.6 Wavenumber 1 asymmetric component in Shapiro and Ooyama (1990) beta-effect experiment at 120 h. (a) Vorticity with contour interval of  $2 \times 10^{-6} \text{ s}^{-1}$ , and (b) absolute vorticity with contour interval of  $2 \times 10^{-6} \text{ s}^{-1}$ .

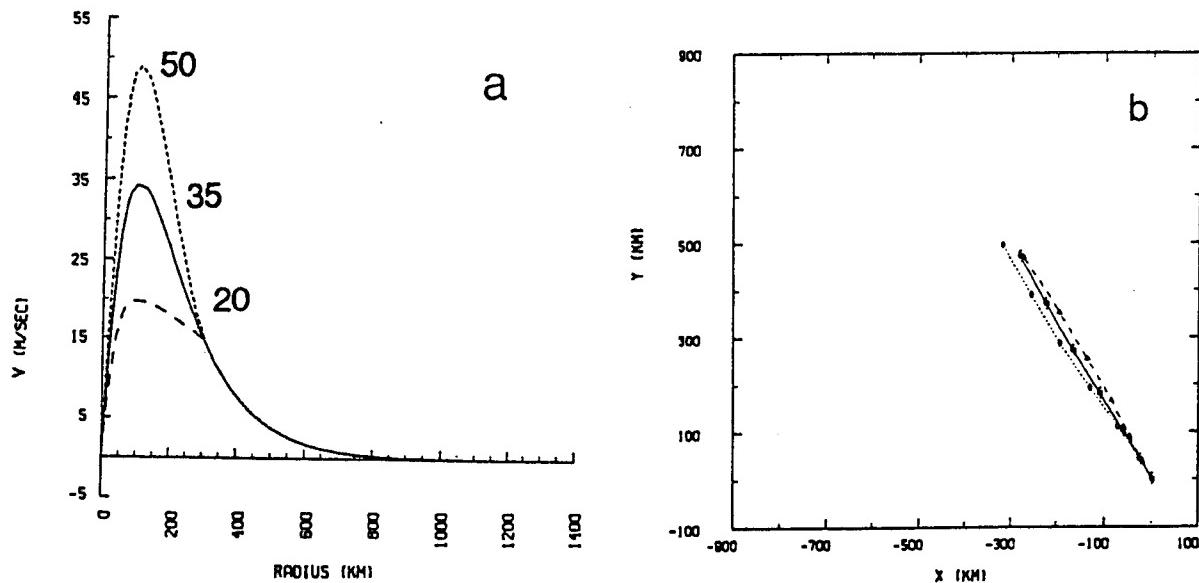


Fig. D.7 (a) Tangential wind profiles with identical outer profiles and maximum intensity of  $50 \text{ m s}^{-1}$  (short-dashed),  $35 \text{ m s}^{-1}$  (solid), and  $20 \text{ m s}^{-1}$  (long-dashed) and (b) corresponding tracks 72 h with the same line pattern as used in (a) and symbols along the tracks each 12 h (Fiorino and Elsberry 1989).

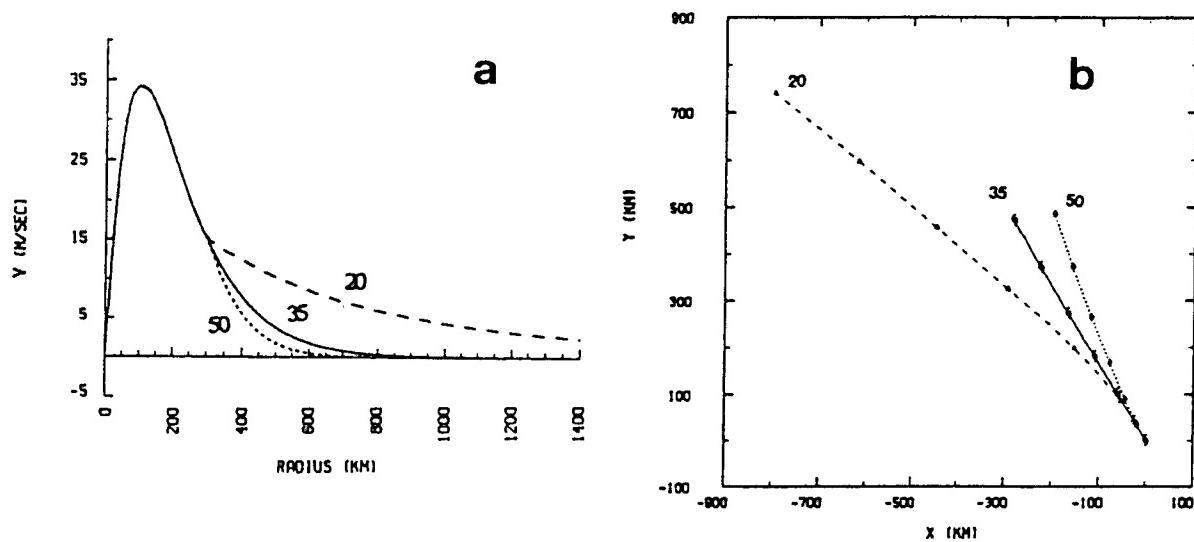


Fig. D.8 As in Fig. D.7, except for different outer profiles with identical inner profiles.

Consider the TC wind profiles in Fig. D.9, which are identical to those in Fig. C.5, except that (C-2) has been multiplied by a function that forces the wind speed to zero for radii inside 100 km, but leaves the profiles essentially unchanged outside 100 km. Also included in Fig. D.9, is the analytical exponential TC tangential wind profile

$$v(r) = V_m \frac{r}{R_m} \exp\left[\frac{1}{b}\left(1 - \left(\frac{r}{R_m}\right)^b\right)\right] \quad (D-3)$$

used by Chan and Williams (1987) with  $b=1$ . Notice that the analytical profile given by (D-3) has the same maximum wind as the largest angular momentum profile, but the outer part of the analytical profile cuts across many of the angular momentum profiles. Thus, it is difficult to assign the BEP speed of  $2.8 \text{ m s}^{-1}$  calculated by Chan and Williams to any particular size ( $R_o$ ) of TC based on one of the angular momentum profiles. An adaptation of (D-3) also was used by Fiorino and Elsberry (1989) to relate changes in BEP to changes in outer wind structure (Figs. D.7 and D.8). Thus, it is also difficult to relate quantitatively their calculated propagation speeds to the TC outer structure implied by the angular momentum profiles.

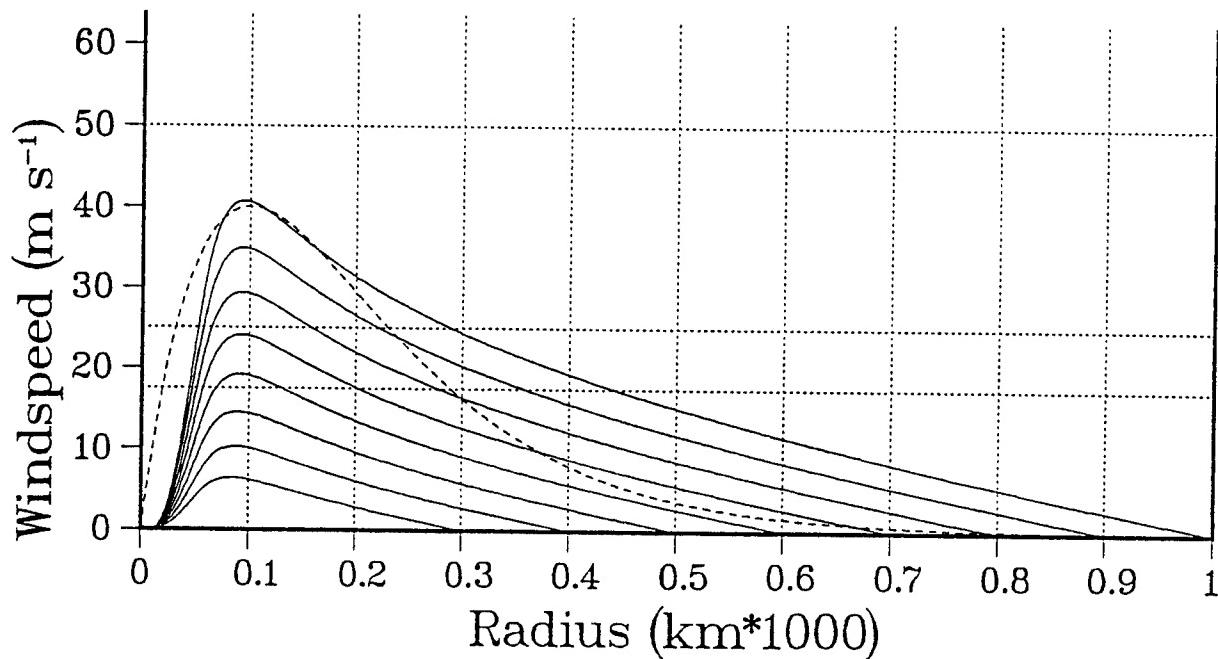


Fig. D.9 Tangential wind profiles defined with angular momentum profiles (solid) with outer radii ranging from 300 km to 1000 km (see text). An analytical profile from Eq. (D-3) with  $b = 1$  is given by dashed line.

To determine the propagation properties of vortices with tangential winds given by the angular momentum profiles in Fig. D.9, the Chan and Williams (1987) nondivergent, barotropic numerical model was integrated for 120 h on a  $10,000 \times 10,000$  km  $\beta$  plane with those wind profiles as initial conditions (Fig. D.10). Notice that the magnitudes of the 120-h displacements to the north and west smoothly increase with larger outer wind speeds (recall that the inner wind speeds within 300 km contribute little to BEP) throughout the entire range of realistic TC sizes. After an initial 12- to 24-h adjustment period, the direction of propagation is about  $320^\circ$  until about 72 h, regardless of TC size. After 72 h, the direction of propagation gradually turns to a more northward heading. Two additional integrations with  $R_o = 800$  km and  $f_o$  computed for  $10^\circ$  and  $20^\circ$  N (versus  $15^\circ$  N for the tracks in Fig. D.10) show that the  $320^\circ$  direction of propagation early in the integration is insensitive to TC formation latitude (Fig. D.11). Consequently, this  $320^\circ$  propagation direction will be treated as a baseline property of barotropic BEP, regardless of the values of  $f_o$  and  $R_o$  in equations (C-2) and (C-3), respectively.

Examination of the streamfunction fields (Figs. D.12a-f) corresponding to the  $R_o = 500$  km to 1000 km tracks in Fig. D.10 suggests that it is the development of an anticyclone to the southeast of the TC that alters the direction of the BEP at later times by imposing a strengthening southwesterly steering across the TC. The clockwise rotation of the  $\beta$  gyres, is manifest by a change in the orientation of the major axis of the propagating TC from west-southwest/east-northeast as at 48 h in Fig. D.12f to east-west as at 96 h in Fig. D.12f.

A comparison of the streamfunction fields in Figs. D.13a and b with the corresponding TC tracks in Fig. D.11 (triangle and diamond symbols, respectively), highlights the dependence of TC motion on the amplitude of the anticyclone to the southeast. The relatively straight (curved) track in Fig. D.11 departs little (greatly) from the baseline direction of  $320^\circ$ , which is consistent with the development of a relatively weak (strong) peripheral anticyclone by 96 h in Fig. D.13. Although the TC-scale vortices at low and high latitudes in Figs. D.13a and D.13b respectively, have the same circulation size initially ( $R_o = 800$  km), the straight track occurred for the TC profile with the flatter outer wind profile, and thus weaker outer wind speeds (Fig. C.4). This result agrees well with the Chan and Williams (1987) and Fiorino and Elsberry (1989) studies (among others) in which straight TC propagations tracks and little peripheral ridging were obtained using exponential TC tangential wind profiles (Fig. D.9; dashed line) that have flat profiles and weak outer wind speeds.

The curving TC tracks in Figs. D.10 and D.11 may be regarded as the superposition of two effects: (i) a baseline BEP propagation process that has a constant propagation direction (about  $320^\circ$ ), and that results from "self-advection" by an asymmetric flow largely contained within the circulation of the TC; and (ii) an time-dependent advection by the peripheral anticyclone that has an influence proportional to the strength of the wave train generated by the TC. Effect (ii) may be considered a model artifact or may be realistic. Recall that anticyclones are observed to develop to the east and south of TCs, as in the case of the large Supertyphoon Yuri between 25 and 28 November 1991 (Figs. 3.6a and 3.11a, respectively), and so this aspect of the barotropic simulations is considered to be realistic.

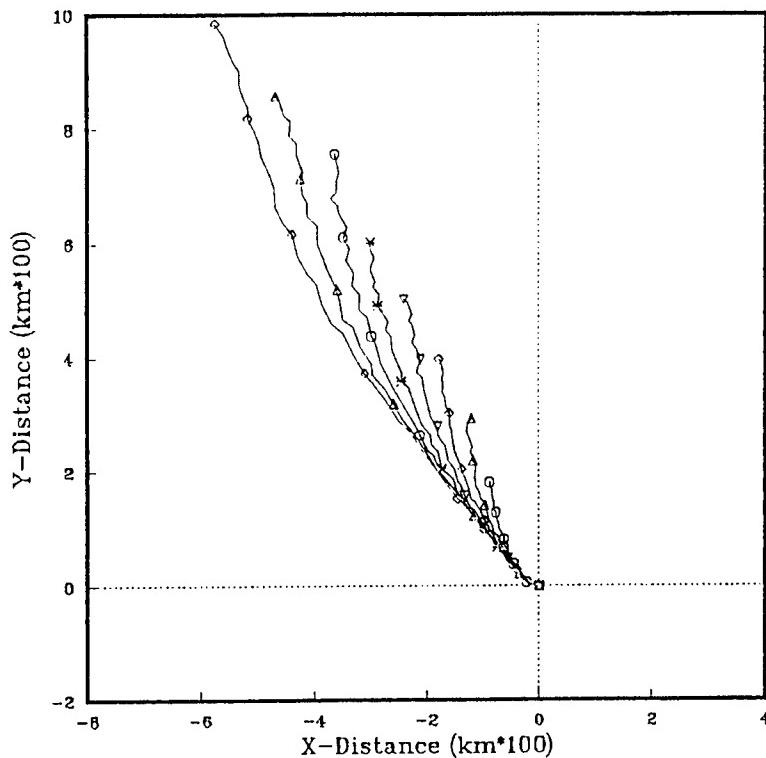


Fig. D.10 Vortex tracks to 120 h from the nondivergent, barotropic model for the angular momentum profiles at 15° lat. in Fig. D.9 with shortest (longest) track for an outer radius of 300 (1000) km. Symbols along the tracks indicate 12-h intervals.

The peripheral anticyclone is viewed here as a TC modification of the environment since the anticyclone forms sufficiently far from the circulation of the TC to be clearly distinct from it. However, the influence of peripheral anticyclone in the barotropic model simulations results in only a relatively modest variability (*i.e.*, 320° to about 360°) of the direction of BEP. Furthermore, the scale of the peripheral anticyclone associated with most TCs is sufficiently smaller than the scale of synoptic features (such as the subtropical ridge) that determine the steering by the "larger-scale" environment. Thus, the effect of the peripheral anticyclone is usually to add an additional steering component without significantly altering the structure and associated steering of the background environment. Thus, it will usually be appropriate for the forecaster to incorporate the direct advective effect of the peripheral anticyclone into the BEP conceptual model.<sup>19</sup>

---

<sup>19</sup> Under certain circumstances involving large TCs and a monsoon gyre, the peripheral anticyclone and other dynamical processes associated with  $\beta$ -induced dispersion of a large vortex can affect TC motion in ways that are quite significant and quite different from the relatively minor modification of BEP propagation that is described here. These other affects are introduced in the Ridge Modification by Large TC (RMT) and Monsoon Gyre-TC Interaction (MTI)(see Table 3.3) TC-Environment transformations in Subsections 3.d.3.a and 3.d.4.a, respectively.

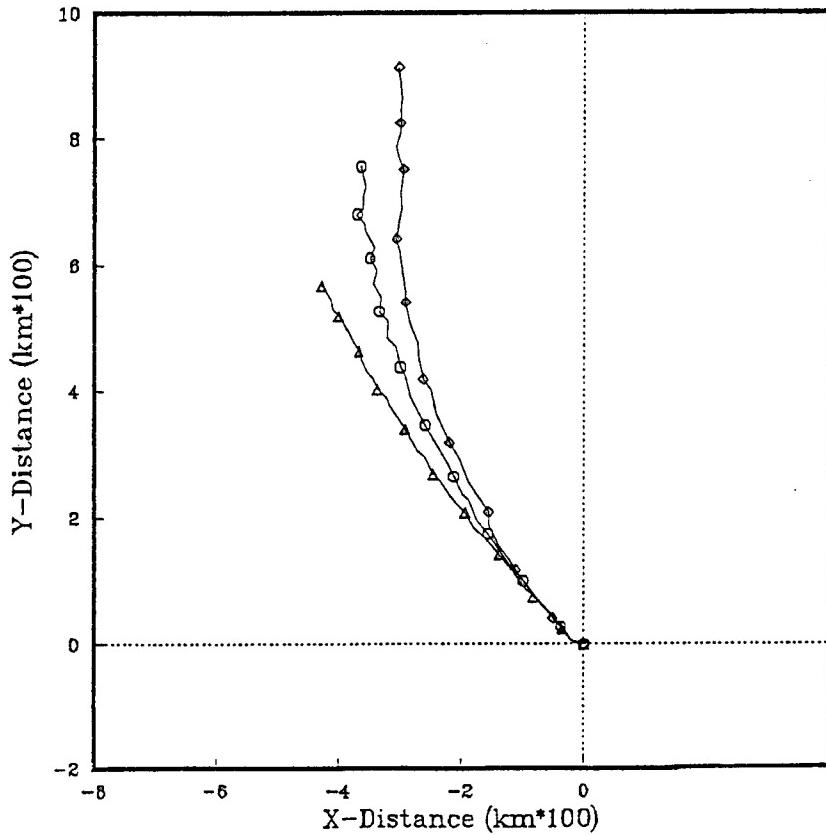


Fig. D.11 As in Fig. D.10, except for outer radius of 800 km and latitudes of 10°, 15°, and 20° (shortest to longest) tracks respectively.

The variations of BEP speed with time for the tracks in Fig. D.10 (including some profiles with intermediate values of  $R_o$ ) are shown in Figs. D.14a and b. The initial increase of BEP speed from zero is a result of initializing the barotropic model with a symmetric TC wind profile that must be deformed by the influence of  $\beta$  before self-advection can begin. Whereas the BEP speed of the smallest TCs (Fig. D.14a) tends to increase throughout the entire 120-h integration, the BEP speeds of the larger TCs (Fig. D.14b) have distinct maxima. These maxima occur earlier as the size of the TC increases, because an increasingly greater amount of the TCs outer circulation is dispersed over time to form the wave train feature to the southeast (Fig. D.12a-f). The transfer of energy weakens the outer circulation of the TC, which in turn causes the decrease of BEP speed later in the integrations. Because the rate of energy dispersion depends on the magnitude of the outer circulation of the TC, the BEP speed attains a maximum value earlier in the integration, and subsequently decreases faster, for a larger initial size of the TC. Conversely, the smallest TCs ( $R_o \leq 400$  km) are so barotropically stable to  $\beta$ -induced dispersion that no significant reduction in BEP speed occurs in integrations up to 168 h (not shown). Low-level circulations of real TCs do not exhibit such a tendency to decrease in size with time, which is presumably because the thermodynamically-driven convergence of angular momentum tends to compensate for any weakening of the cyclonic tangential wind field arising from  $\beta$ -induced dispersion. Thus,

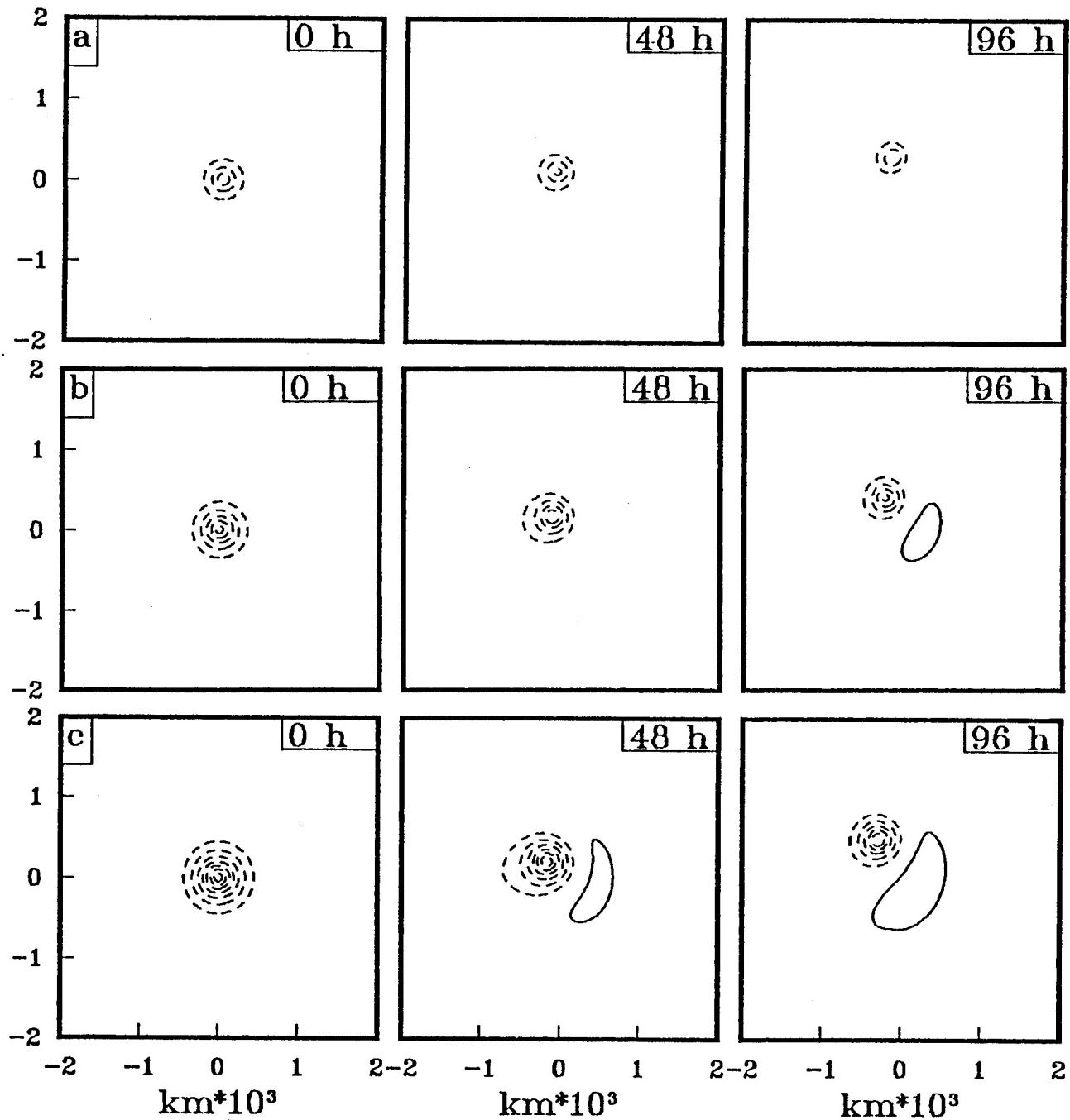


Fig. D.12 Streamfunction fields at 0, 48, and 96 h for a vortex defined by the angular momentum profiles in Fig. D.9 with outer radii of (a) 500 km, (b) 600 km, (c) 700 km, (d) 800 km, (e) 900 km, and (f) 1000 km. Negative (positive) values are dashed (solid).

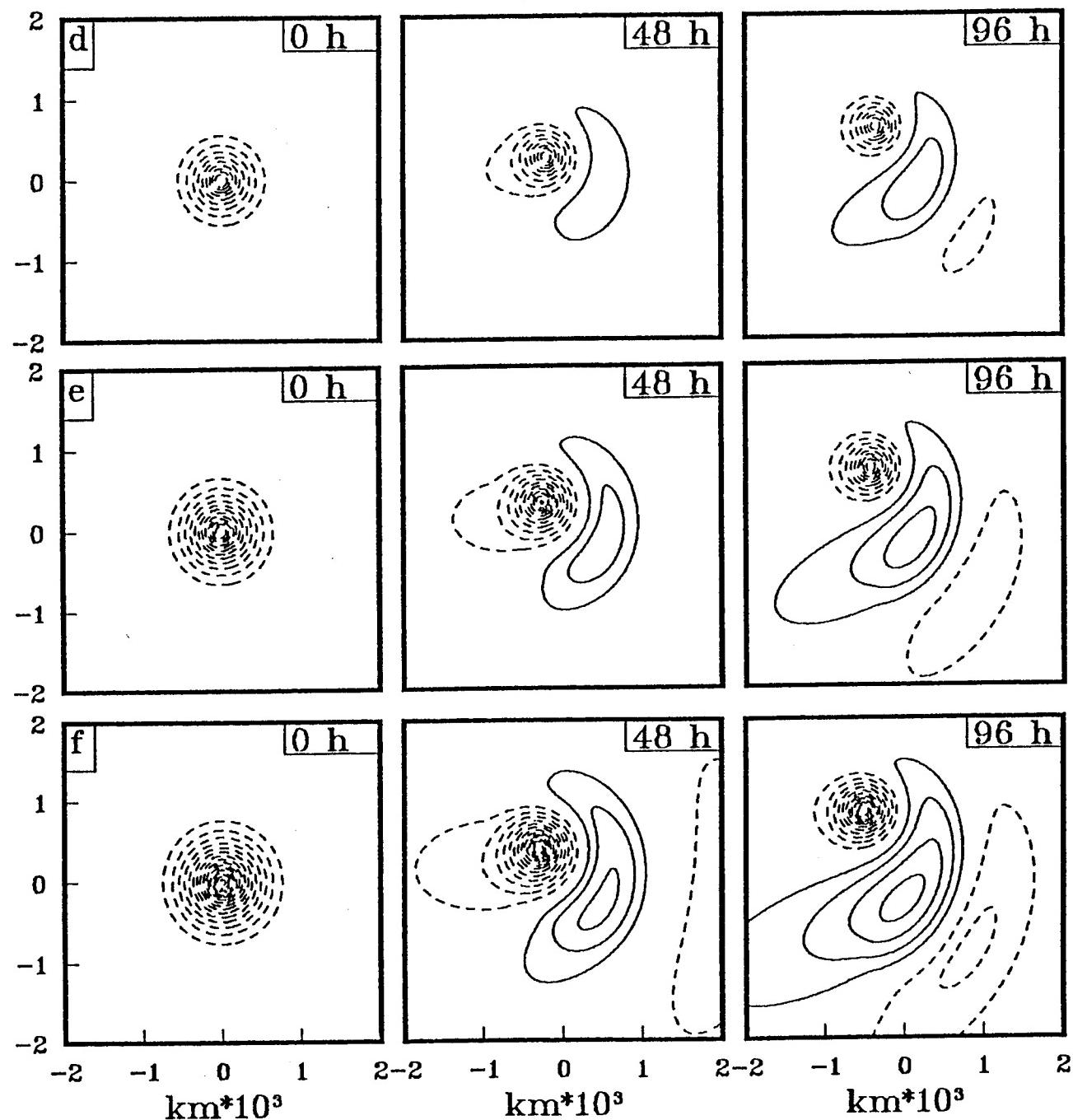


Fig. D.12 (continued)

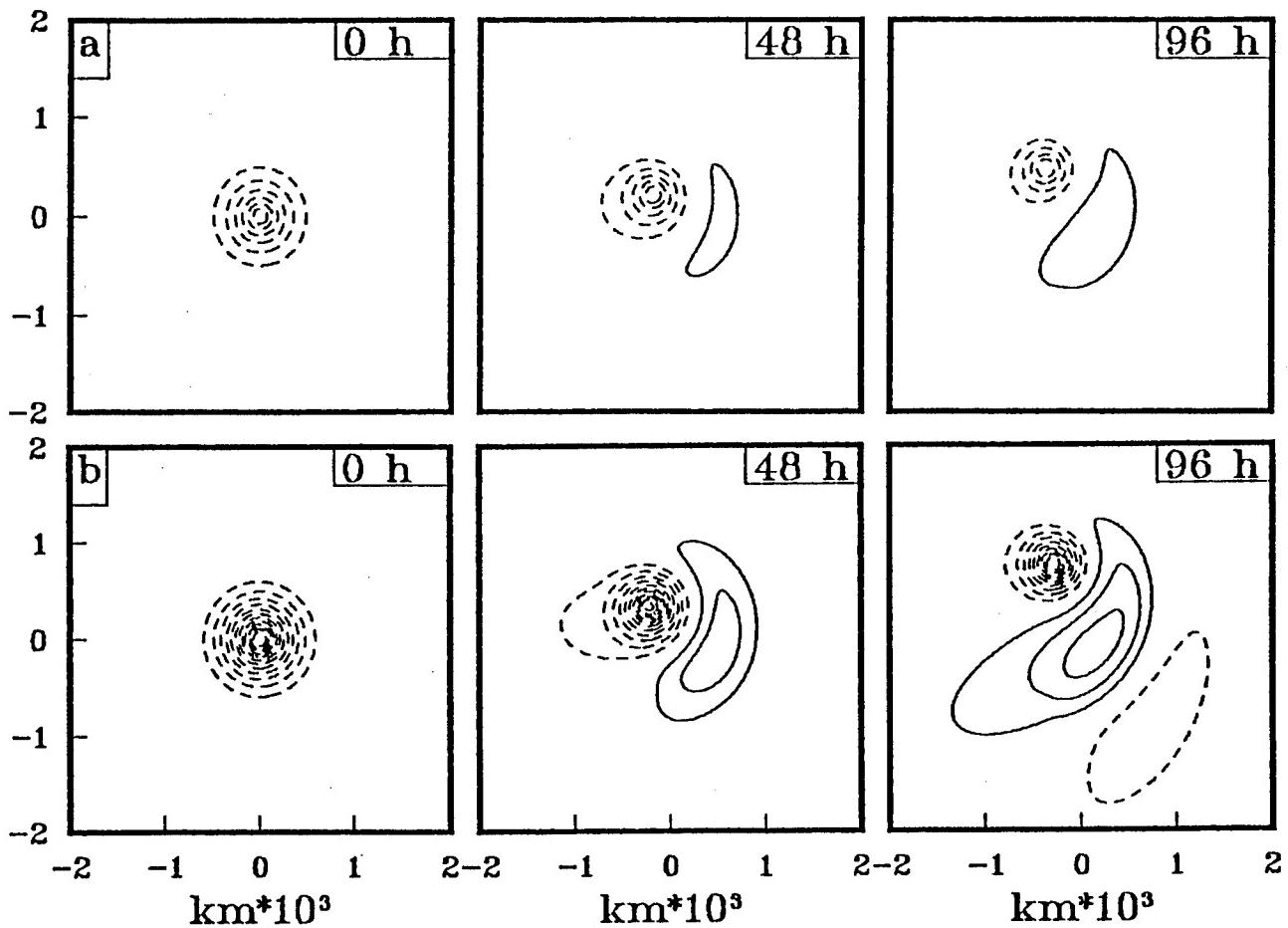


Fig. D.13 As in Fig. D.12, except for cases in Fig. D.11 with (a) 10°N and (b) 20°N and outer radius of 800 km.

some of the decay of TC size and associated BEP speed in the later hours of barotropic model simulations may be considered an unrealistic artifact of the unforced barotropic model.

Since real TCs have generally existed sufficient time for the beta-induced gyres to come into equilibrium, it will be assumed that a real TC with such a 500 mb wind structure will propagate with the peak BEP speed attained in each barotropic model integration (Fig. D.14). These maximum BEP speeds and associated TC sizes (as represented by  $R_{500}$ ) are shown in Fig. D.15 for all the BEP speed profiles in Fig. D.14. Although a clear relationship between TC size and BEP speed is indicated, two additional problems need to be overcome to develop an operationally useful BEP speed versus TC size rule based on these angular momentum profiles. First, recall that the wind profiles in Figs. C.4 to C.6 have a latitudinal dependence due the Coriolis parameter ( $f_o$ ) in equation (C-2), which has a significant effect on the outer wind distribution of the angular momentum profile. This dependence is not

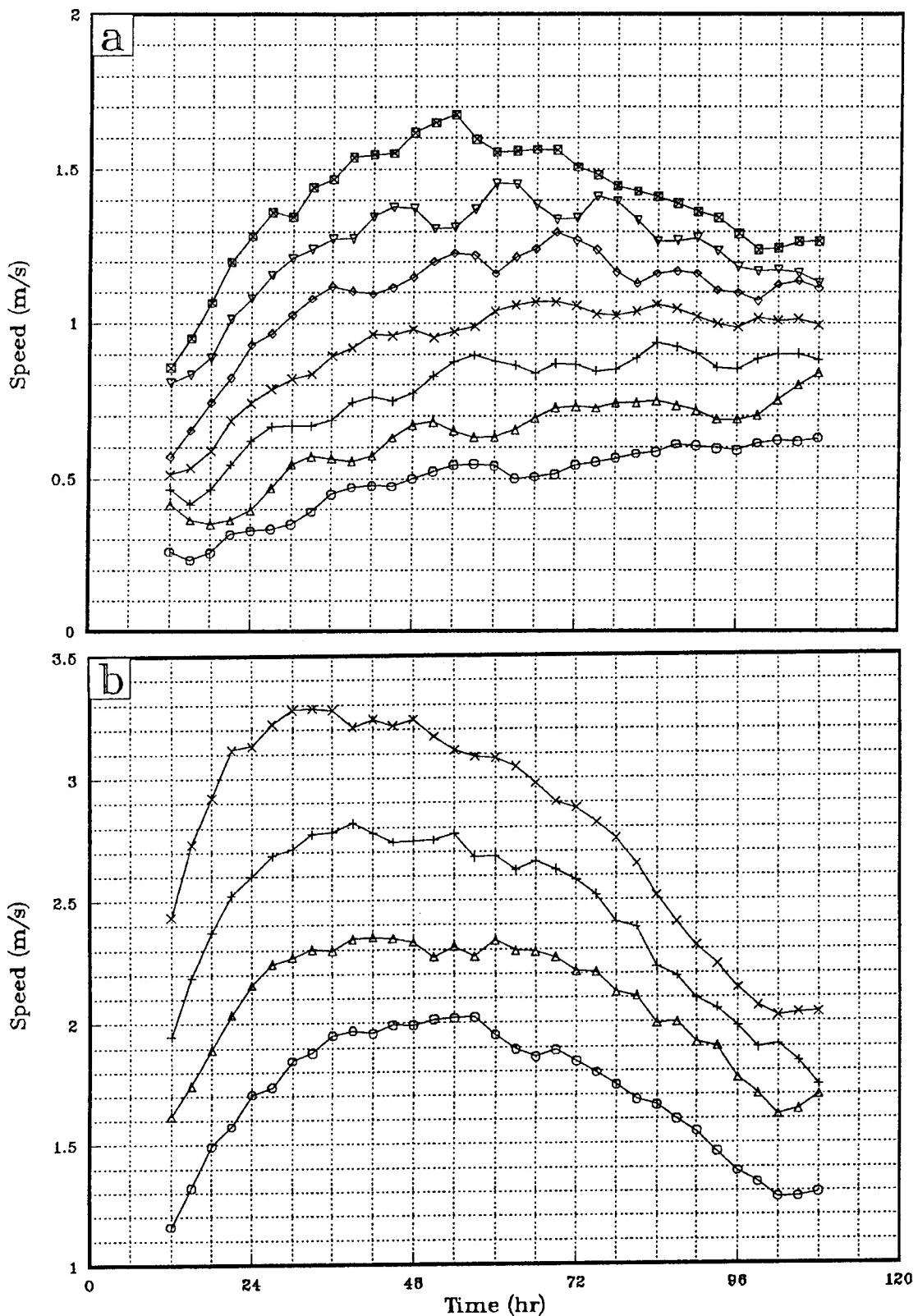


Fig. D.14 Vortex translation speeds as function of time for initially axisymmetric angular momentum wind profiles with outer radii ranging from (a) 300 km (lower) to 600 km (upper) by 50 km increments, and (b) 700 km (lower) to 1000 km (upper) by 100 km increments.

included in Fig. D.15 since all the model integrations were at 15°N. Second, Fig. D.15 relates BEP speed to  $R_o^{500}$ , rather than to  $R_o^{850}$ , which is comparatively easier to estimate via available wind data, or the alternate satellite imagery interpretation technique developed in Section 3.c.2.b.

Performing model integrations to cover the full range of expected values for parameters  $R_o^{500}$  and  $f_o$  is not a practical method to address the first problem. Thus, the technique of dimensional analysis described by Smith (1993) has been applied to develop a comprehensive BEP speed versus TC outer wind structure law based on the results in Fig. D.15 and the functional forms of equations (C-2) and (C-3). The resulting "β-drift law," to use the terminology of Smith, is

$$v_d(\beta, f_o, R_o^{500}) = 0.12 \beta^{0.55} f_o^{0.45} (R_o^{500})^{1.55}, \quad (D-4)$$

where  $v_d$  is the BEP "drift" speed in  $\text{m s}^{-1}$ . The TC propagation tracks in Fig. D.11 may be used to test the accuracy of the dependence of (D-4) on the Coriolis parameter. The corresponding BEP speed versus time plots (Fig. D.16) give a numerically-derived maximum drift speed of about  $2.0 \text{ m s}^{-1}$  at  $10^\circ\text{N}$  and  $2.7 \text{ m s}^{-1}$  at  $20^\circ\text{N}$ . The respective drift speeds of  $2.0$  and  $2.9 \text{ m s}^{-1}$  given by the β- drift law (D-4) agree within 10% with the numerical results, which confirms the accuracy of (D-4).

Adapting (D-4) to use the more readily available  $R_o^{850}$  is accomplished by substituting equation (3.4) into (D-4) to give

$$v_d(\beta, f_o, R_o^{850}) = 0.074 \beta^{0.55} f_o^{0.45} (R_o^{850})^{1.55}, \quad (D-5)$$

which will serve as the mathematical basis for the BEP conceptual model.

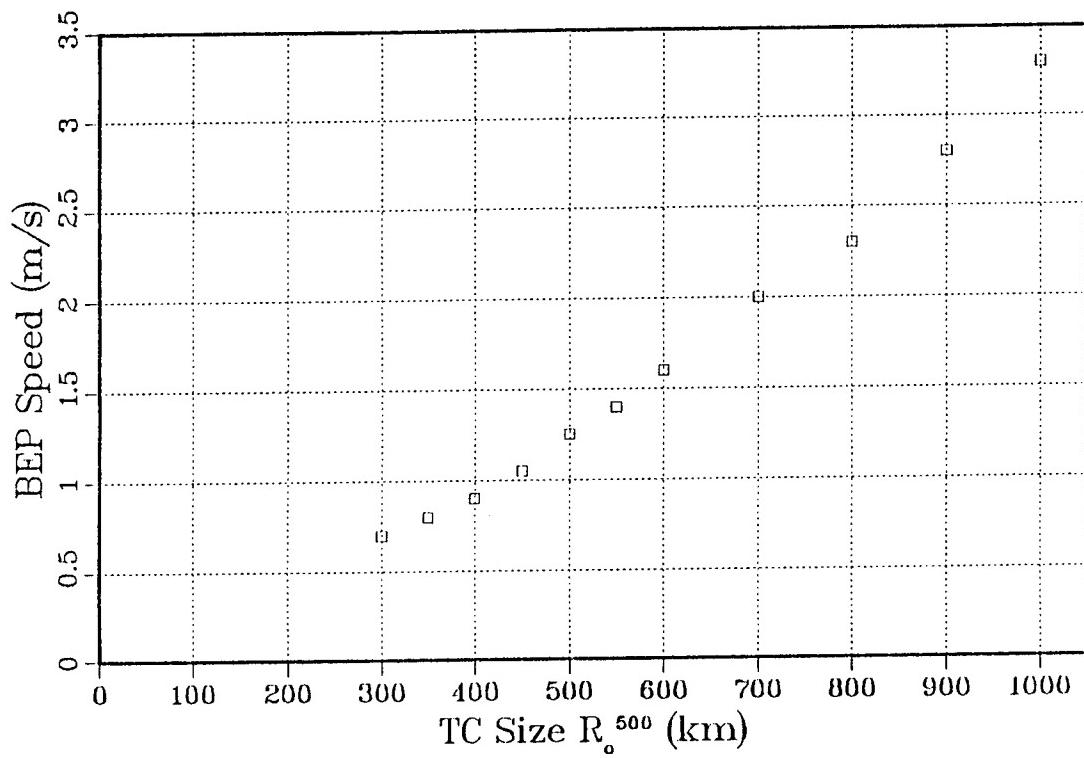


Fig. D.15 Beta-induced propagation speed of vortices with initial 500 mb angular momentum profiles at 15°N with outer radii (sizes) ranging from 300 km to 1000 km.

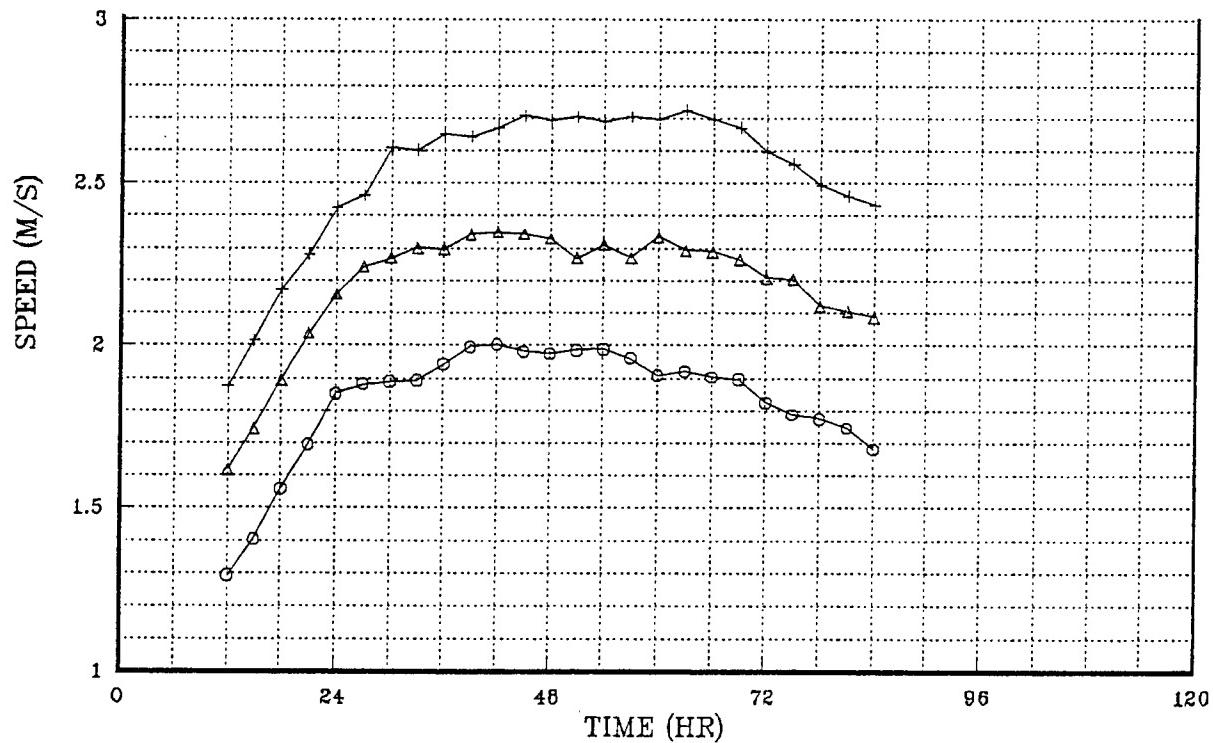


Fig. D.16 Vortex translation speed as in Fig. D.14, except for outer radius of 800 km and latitudes of 10° (lower), 15°, and 20° (upper).

## Appendix E

### Background for Vertical Wind Shear (VWS) Model

It has long been known (e.g., Gray 1968) that a small vertical wind shear (VWS) between the upper and lower troposphere is a favorable climatological condition for TC formation. After a deep cyclonic circulation and central convection exist, a TC may exhibit considerable resistance to VWS, presumably owing to large vertical transports of horizontal momentum. If the VWS is sufficiently strong, the deep convective cloud mass (CCM) may become separated from the low-level circulation (LLC) of the TC, which will result in rapid weakening and often significant changes in motion (recall Fig. B.3). VWS situations may be classified into three categories based on whether the upper-level flow contributing to the shear arises from: (i) midlatitude westerly flow poleward of the subtropical ridge axis; (ii) tropical easterly flow south of the ridge axis; or (iii) the outflow from another TC.

The first and most common category of VWS situations involves TCs approaching recurvature at the axis of the mid-level subtropical ridge, where they are routinely subjected to moderate-to-strong westerly VWS associated with the baroclinic structure of the midlatitude jetstream. The separation of the LLC and CCM of Tropical Storm Lewis (Fig. B.3b), and the associated significant change in track direction (Fig. B.3a) occurred as a result of such westerly shear.

Particularly severe westerly VWS occurs in the vicinity of the northern Philippines during October through December. Climatologically, the northeast monsoon extends over the South China Sea at low levels (Fig. E.1a), whereas a semi-permanent long-wave trough at upper levels is anchored along the east coast of Asia, which brings west-southwesterly winds as far south as 20°N (Fig. E.1b). In extreme cases, these west-southwesterly winds extend as far south as 15°N, and enhanced northeasterlies (called monsoon surges) may be occurring concomitantly at low levels. The net effect is very large VWS for TCs nearing the axis of the mid-level subtropical ridge in the vicinity of the Philippines. Such large vertical wind shear, and the relatively dry/cool air at low levels in the northeasterly monsoon, usually shears apart and weakens the TC. The LLC remnants are then advected to the south and west by the northeast monsoon flow, while the CCM recycles into the upper-level westerlies. During 13 November 1991, Supertyphoon Seth was sheared apart in a northeast monsoon VWS regime, and the exposed LLC followed the characteristic southwest track thereafter (Fig. 3.29).

The second category of VWS situations involves enhanced tropical easterly-to-northeasterly flow south of the upper-level subtropical ridge. Climatologically, the deep easterly environmental flow between the subtropical ridge and the monsoon trough decreases with height, which would subject a TC embedded in such flow to weak westerly VWS. However, very intense upper-level anticyclones occasionally develop that may have easterly winds exceeding 40 kt on the equatorward side of the ridge. Given a typical TC translation speed of about 10-12 kt in the tropics, such an upper-level flow would subject the

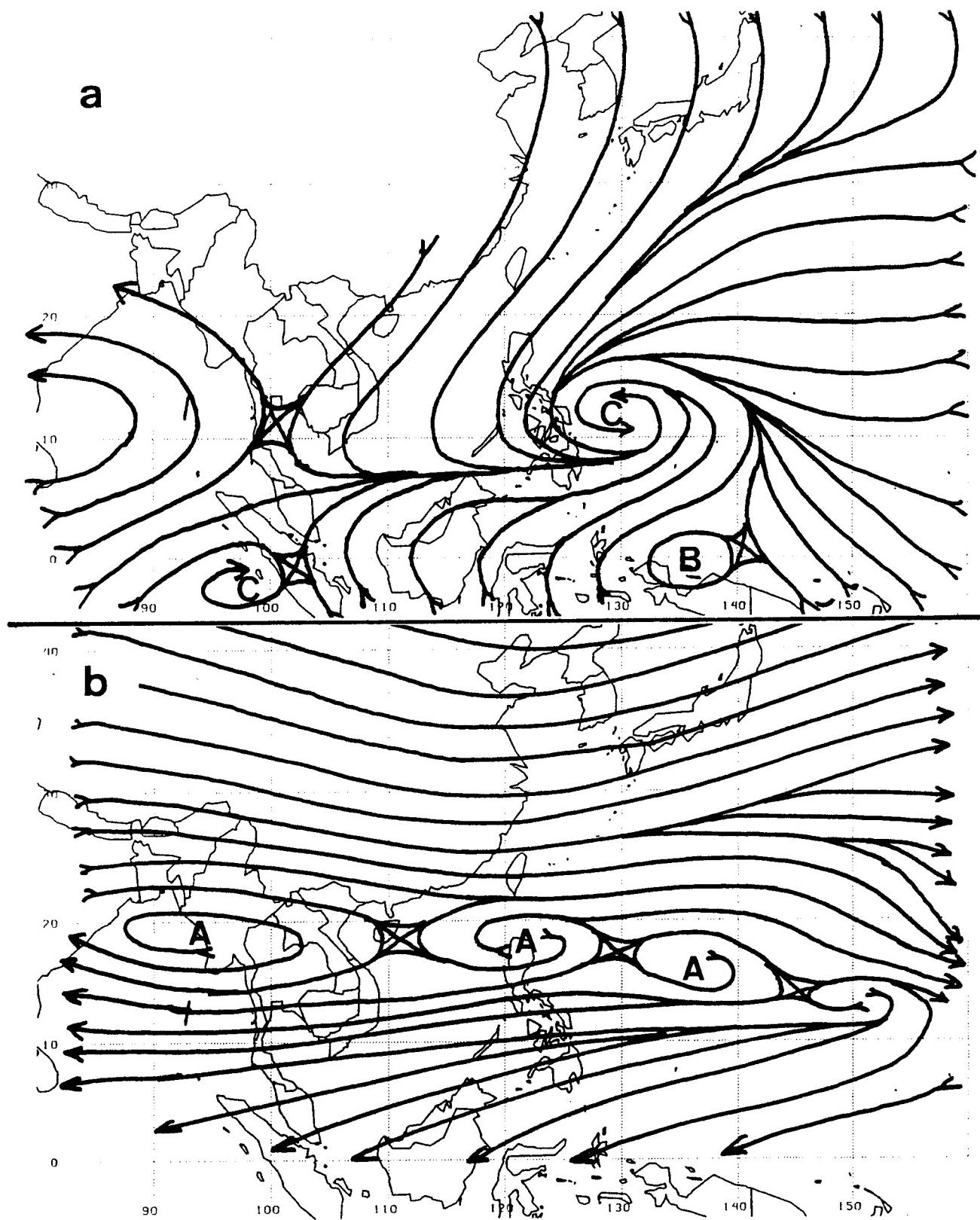


Fig. E.1 Mean (a) low-level and (b) 200 mb streamlines/isotachs during October (adapted from Sadler 1975).

TC to 30 kt or more of easterly vertical wind shear. Persistent easterly shear from such an upper-level anticyclone migrating eastward along 17°N on 28 November 1990 (Fig. E.2) contributed to a fairly rapid weakening of Supertyphoon Owen (Fig. E.3). After the LLC became fully exposed (not shown) following 30 November 1990, Owen subsequently turned to a southwest heading (Fig. E.3), which is consistent with the LCC being embedded in the low-level northeasterly flow of the winter monsoon.

The midget Typhoon Yunya experienced a similar rate of weakening (Fig. E.4a) between 14 and 15 June in response to east-northeasterly VWS arising from an upper-level anticyclone extending eastward from Southeast Asia (Fig. E.4b). In this case, the LLC remnant turned onto a northwest heading because it was embedded in the southwesterly low-level flow of the summer monsoon and no longer was responding to a deep-layer steering that included the upper-level northeasterlies. Even when Yunya was at maximum intensity (Fig. E.5), the effect of the strong upper-level flow had begun to expose the LLC along the northeast sector. Although the upper-level flow patterns in the Owen and Yunya cases were quite similar, the TC tracks after the shear-induced separation of the LLC and CCM were quite different owing to the different directions of the low-level monsoonal flow, which became the dominant steering after separation.

The final VWS category is somewhat related to the second in that the VWS arises from an upper-level anticyclone that includes the outflow pattern from another TC. Large northwesterly-to-northerly VWS is imposed on the trailing TC, which is typically located about 15° lat. to the southeast. At 1200 UTC 25 August 1992, the CCM of the precursor to Supertyphoon Omar was distorted into a wedge-shaped pattern (Fig. E.6a) by strong upper-level flow arising from the outflow of Tropical Storm Polly (14° lat. to the northwest) and flow around a TUTT cyclone (about 15° lat. to the northeast). As a result, Omar had intensified by only 20 kt (45 to 65 kt) by 0000 UTC 27 August (Fig. E.7a). Subsequently, the greater translation speed of Polly (Fig. E.7b) increased the separation distance to about 19° lat., which weakened the VWS and the associated distortion of Omar's CCM (Fig. E.6b). As a result, Omar intensified by 50 kt (65 to 115 kt) from 0000 UTC 27 August to 1200 UTC 28 August. Since the outflow from Polly did not dissipate Omar, but rather only temporarily inhibited the rate of intensification, Omar did not undergo any sustained change in track direction in response to the VWS.

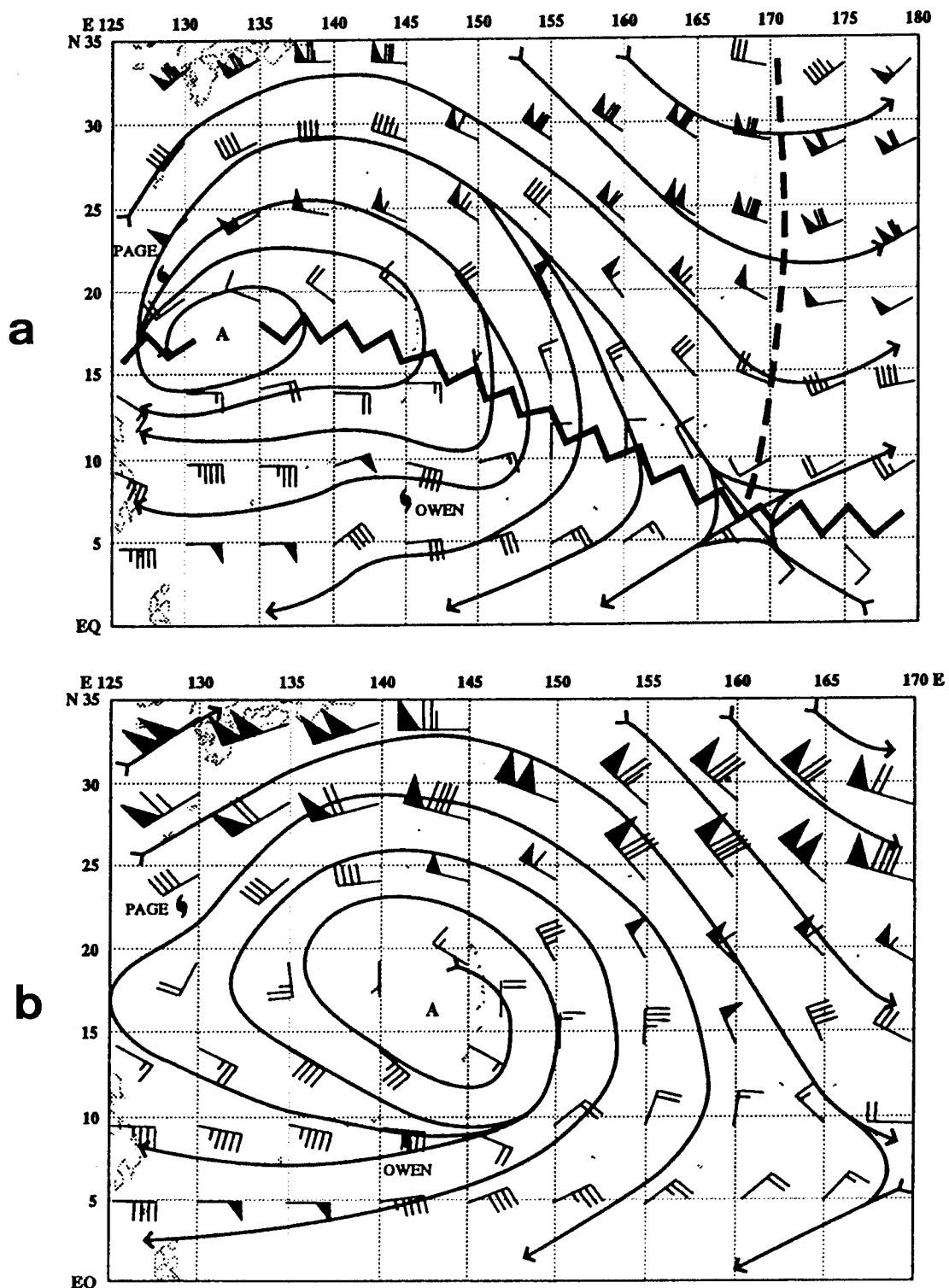


Fig. E.2 NOGAPS 200 mb analyses (a) for 1200 UTC 28 November 1990 showing Page (29W) and the center of the anticyclone to the northwest of Owen, and (b) 0000 UTC 29 November showing the relocation of the center of the anticyclone to the north of Owen (ATCR 1990).

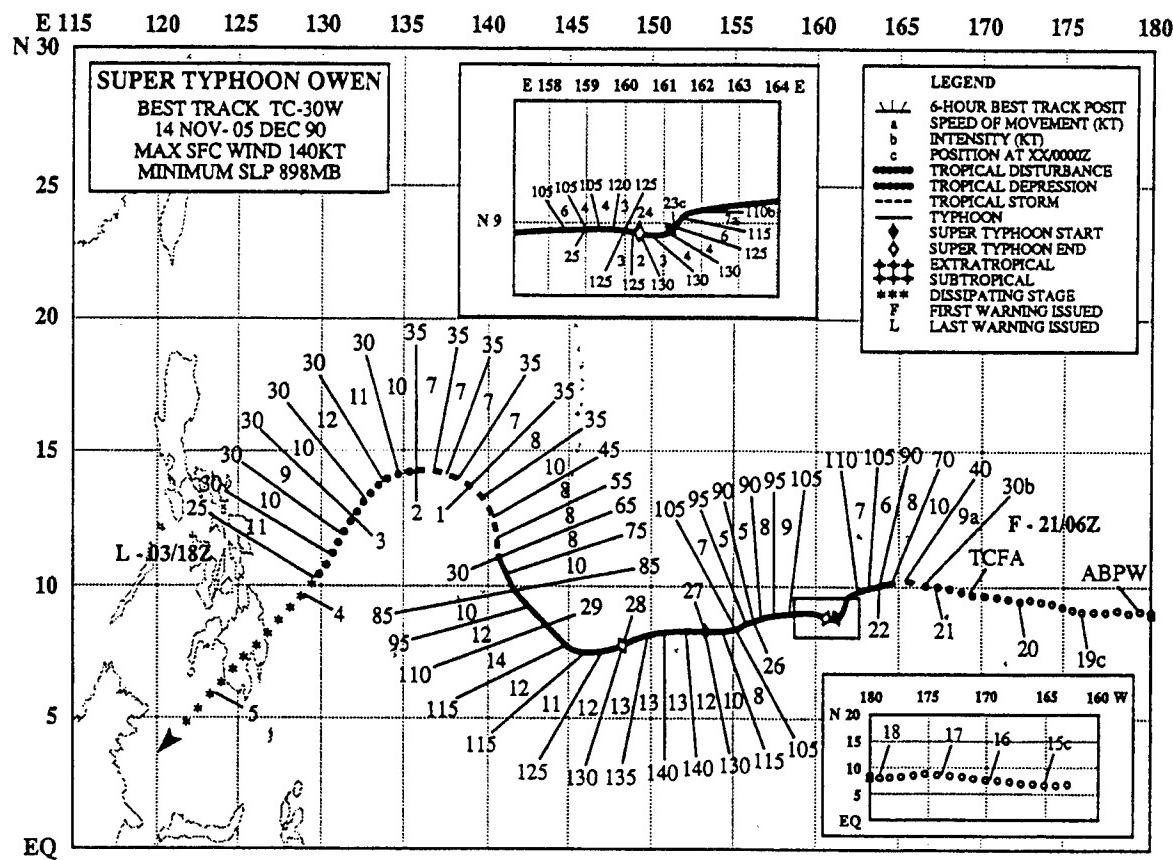


Fig. E.3 As in Fig. 3.1, except for Supertyphoon Owen on 14 November to 5 December 1990.

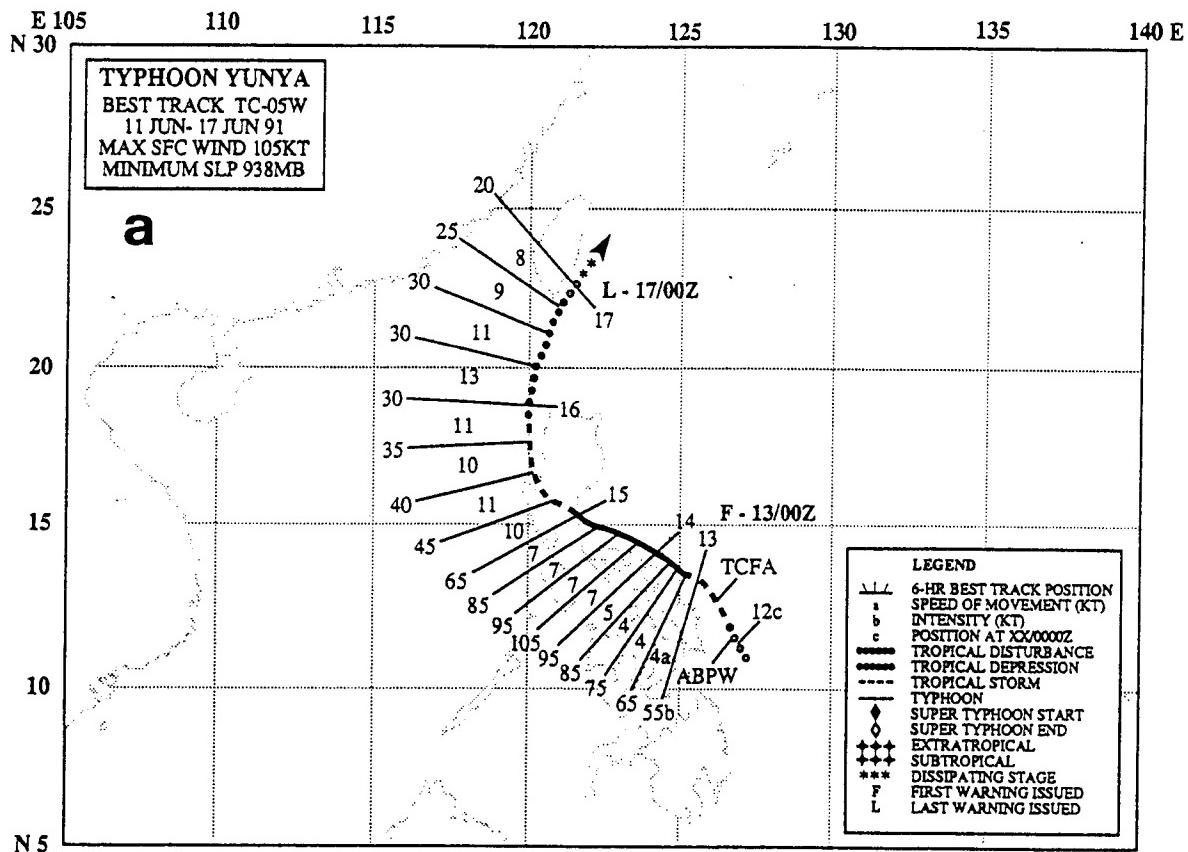


Fig. E.4 (a) As in Fig. 3.1, except for Typhoon Yunya from 11-17 June 1991. (b) As in Fig. E.2, except for 0000 UTC 15 June 1991. Notice the 40 kt ( $20 \text{ m s}^{-1}$ ) winds over Yunya, and general region exceeding 30 kt ( $15 \text{ m s}^{-1}$ ) that is shaded.

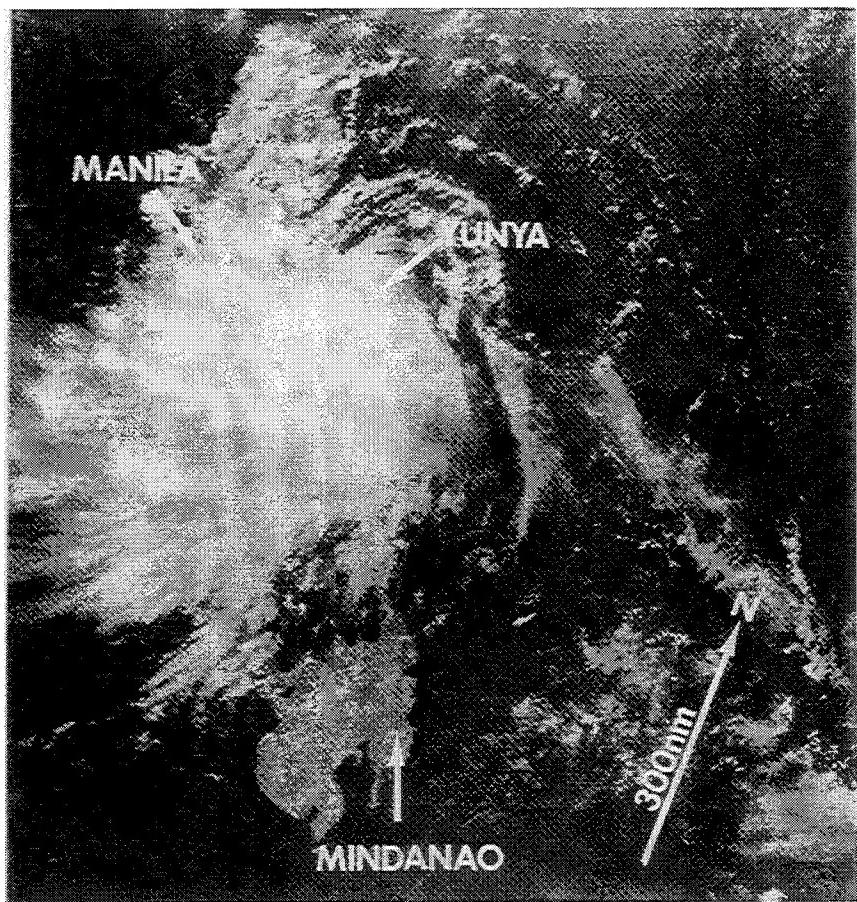


Fig. E.5 Visible imagery at 0534 UTC 14 June 1991 showing Typhoon Yunya at peak intensity nearing the Philippines. Notice the distortion of the cloud signature owing to increasing upper-level north-northeasterly winds associated with a building subtropical ridge (ATCR 1991).

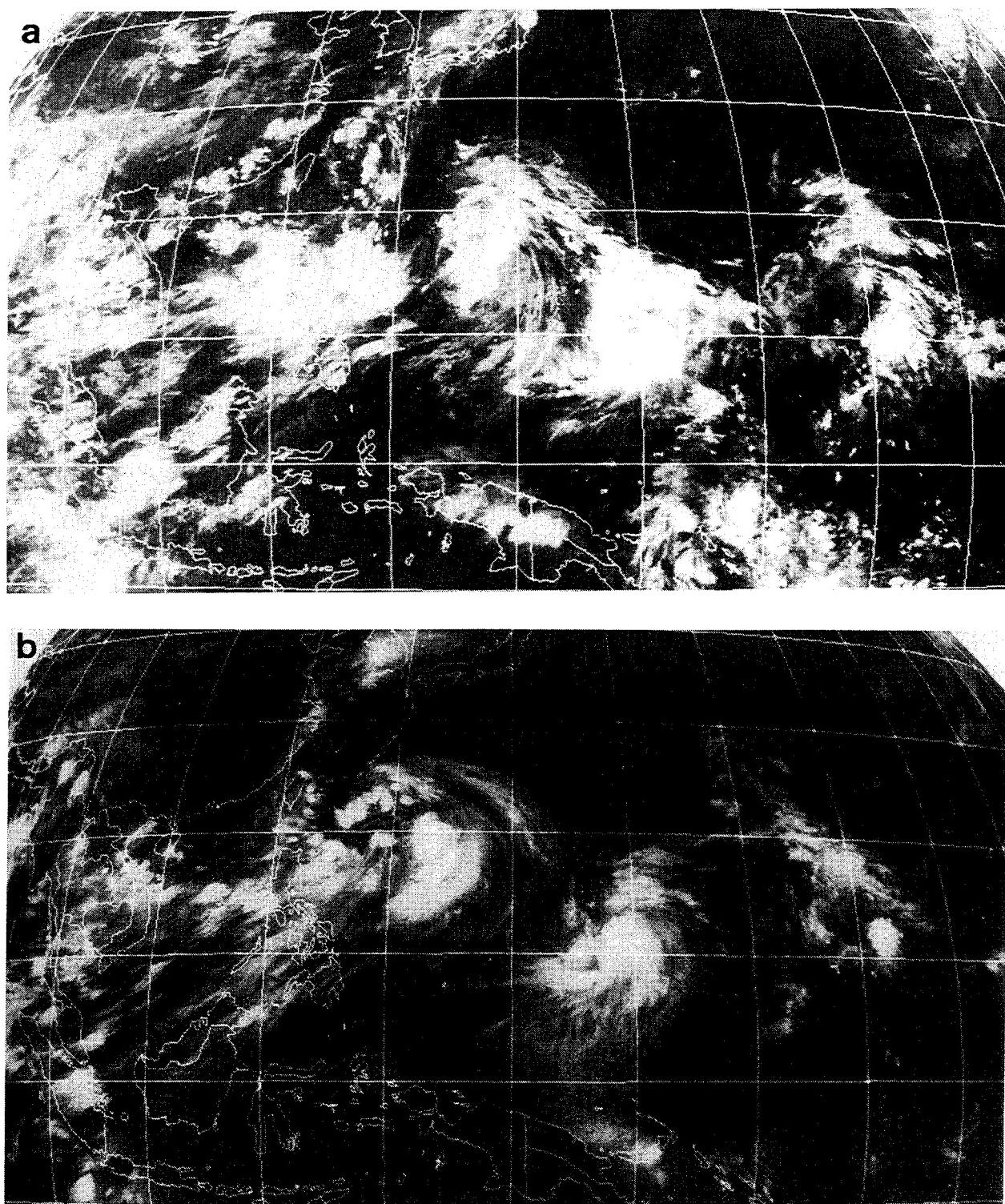


Fig. E.6 Infrared imagery from GMS at (a) 1200 UTC 25 August 1992 and (b) 0000 UTC 27 August indicating cloud patterns associated with Typhoon Omar (eastern storm) and Tropical Storm Polly (western storm).

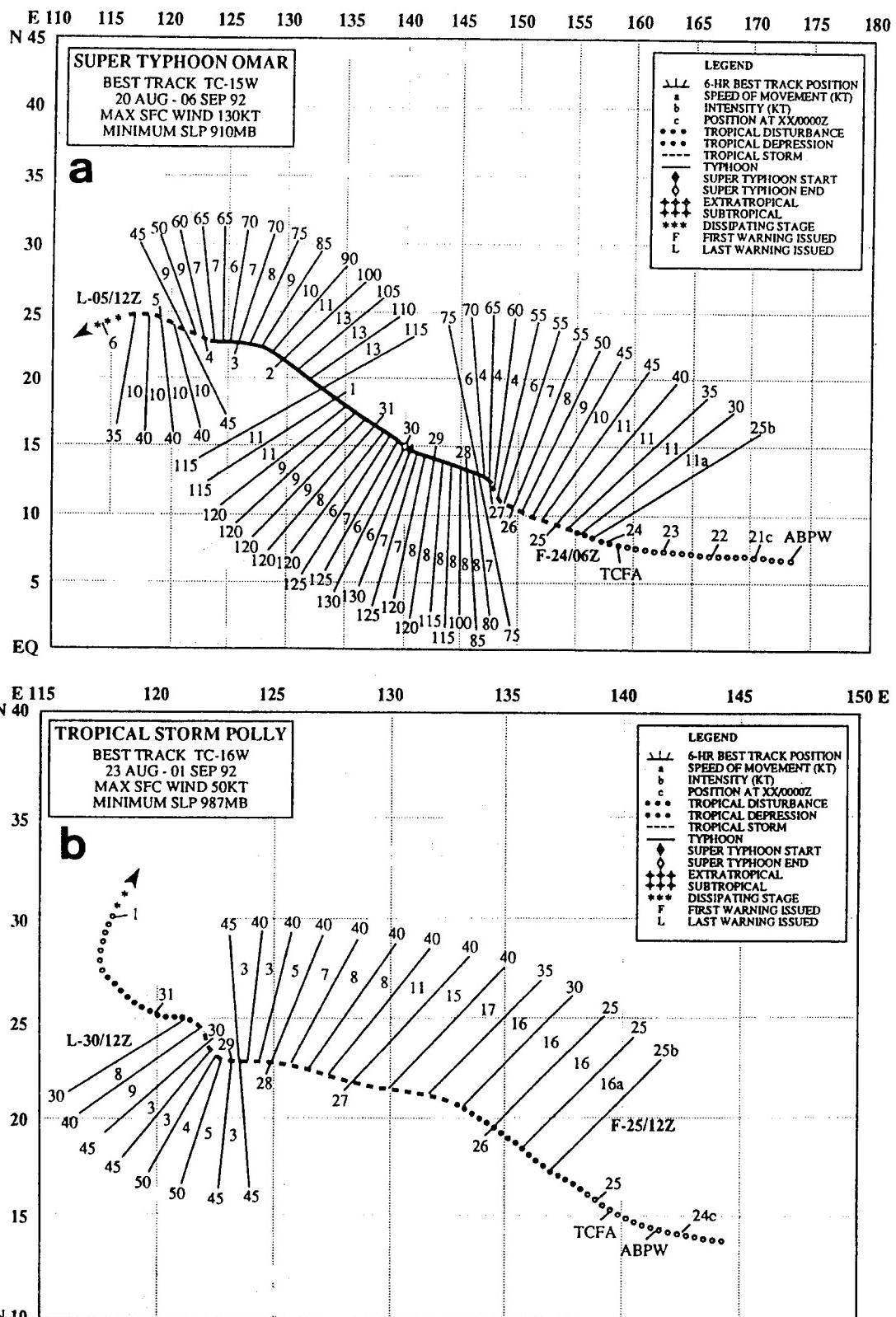


Fig. E.7 As in Fig. 3.1, except for (a) Supertyphoon Omar from 20 August - 6 September, and (b) Tropical Storm Polly from 23 August - 1 September 1992.

Appendix F  
 Preliminary Development of the Proposed Ridge Modification  
 by a Large TC (RMT) Conceptual Model

Using a barotropic model, Carr and Elsberry (1995) noted that a small vortex (Fig. F.1; dashed) generated only a weak peripheral ridge in response to  $\beta$ -induced dispersion (Figs. F.2a-c). By contrast, significant peripheral ridging (Figs. F.2d-f) resulted from the dispersion of a large, weak vortex (Fig. F.1; solid) that represents a monsoon gyre (MG) or the outer part of a large TC. Both the scale and orientation of the peripheral anticyclones produced by the MG in the Carr and Elsberry simulations (Figs. F.2e-f) are similar to those associated with the  $R_o = 900-1000$  km angular momentum profiles (Figs. D.12e-f at 48 and 96 h, respectively). Such agreement is consistent with the roughly similar initial outer wind speeds of the MG and  $R_o = 900-1000$  km TC profiles (Fig. F.1). Thus, the dynamical processes leading to the formation of the ridge southeast of the MG vortex in the Carr and Elsberry simulations will be considered representative of those leading to the formation of the ridging associated with the angular momentum wind profiles of the larger TCs.

Carr and Elsberry compared patterns of streamfunction, vorticity, and vorticity tendency for the MG vortex at 0 and 48 h (Fig. F.3) to show that  $\beta$ -induced linear dispersion and nonlinear vorticity advection together generate the peripheral anticyclone to the southeast of the MG. Since the initially axisymmetric MG vortex has concentric isolines of streamfunction and relative vorticity (Fig. F.3a), no nonlinear relative vorticity advection

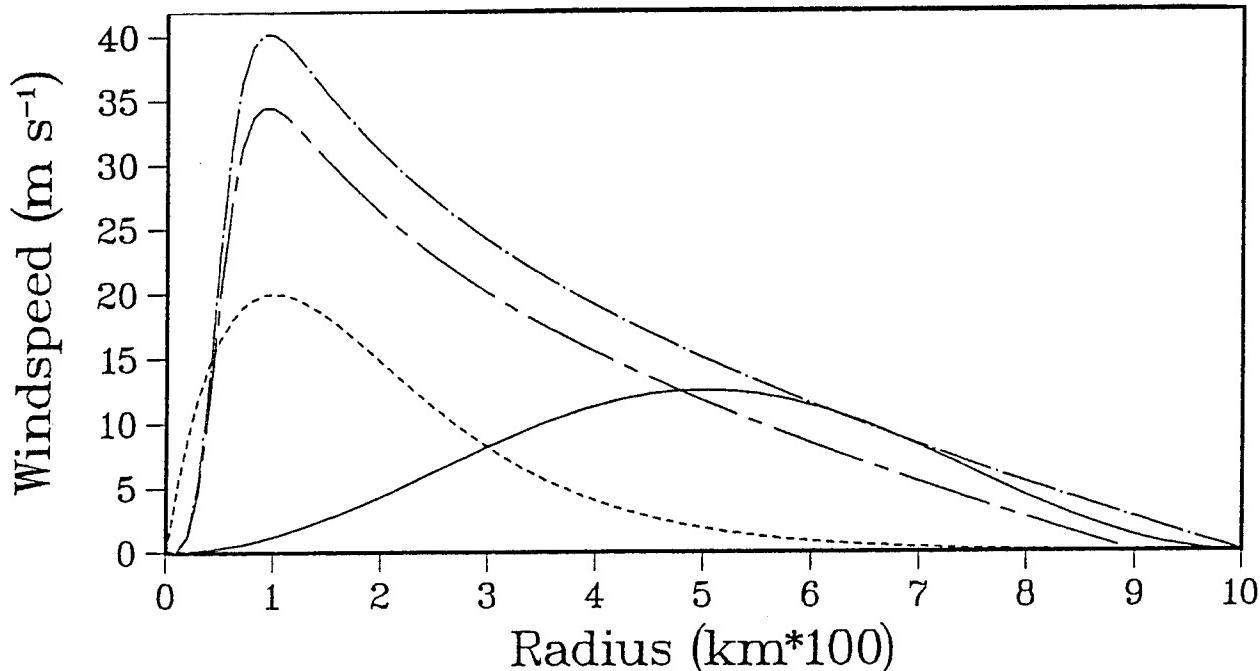


Fig. F.1 Tangential wind profiles representing large TCs with outer radii of 900 km and 1000 km (chain-dashed), an analytical profile with  $b = 1$  (dashed) used to represent a small TC, and a monsoon gyre with maximum winds at 500 km (solid).

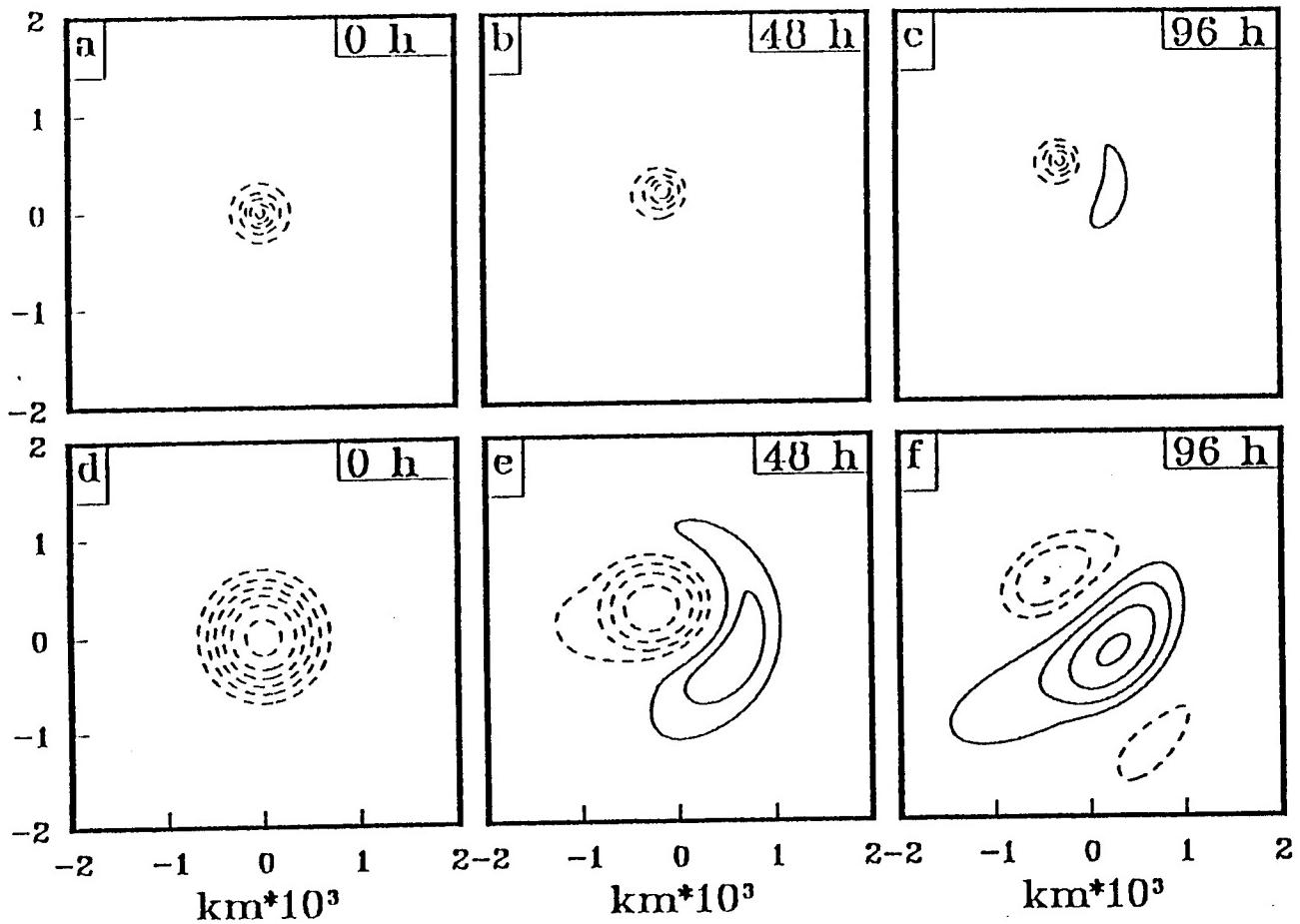
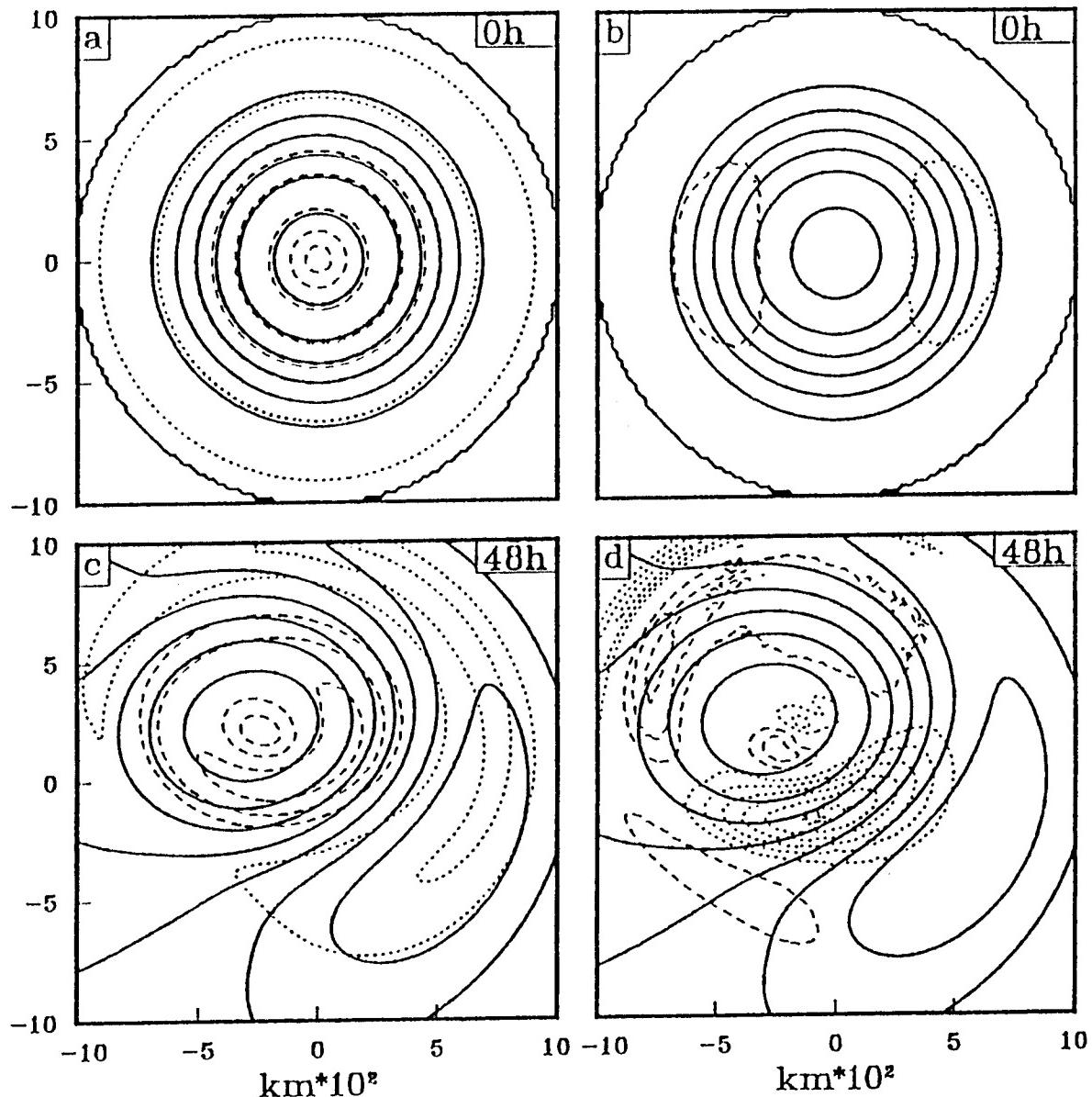


Fig. F.2 (a) - (c) Model streamfunction fields for the TC-only numerical simulation of Carr and Elsberry (1995) with the TC-only control Experiment 1a at times indicated. Contour interval is  $1 \times 10^6 \text{ m}^2 \text{ s}^{-1}$ , negative (positive) contours are dashed (solid), and the zero contour has been suppressed for clarity. (d) - (f) As in (a) - (c), except for the MG-only control Experiment 1b.

(term C in Fig. F.1 equation D-1) occurs at 0 h. As a result, only linear advection of earth vorticity (term B in equation D-1) is present initially, which results in a vorticity tendency pattern that is oriented east-west (Fig. F.3b). The initial negative (positive) vorticity tendency to the east (west) causes ridging (troughing) that distorts the streamfunction pattern of the vortex more than the relative vorticity pattern (Fig. F.3c) such that negative (positive) relative vorticity advection occurs to the south (north) of the vortex (note the intersecting streamlines and vorticity lines approximately 500 km north and south of the vortex center). By 48 h, the maximum negative relative vorticity advection is about four times larger than the linear term, and has caused the maximum negative vorticity tendency to shift from east to southeast of the MG (Fig. F.3d). As a result, the maximum ridging now



**Fig. F.3** (a) Model streamfunction (solid) and vorticity (positive dashed; negative dotted) fields of numerical simulation by Carr and Elsberry (1995) for MG-only control Experiment 1b at 0 h. Streamfunction contour interval is  $1 \times 10^6 \text{ m}^2 \text{ s}^{-1}$ , and vorticity contour interval is  $2 \times 10^5 \text{ s}^{-1}$ . (b) As in (a), except for dashed (dotted) lines denote positive (negative) local time tendency of relative vorticity contoured at an interval of  $2 \times 10^{-10} \text{ s}^{-2}$ . (c) As in (a), except for 48 h. (d) As in (b), except for 48 h.

occurs to the southeast of the MG and is manifest by the anticyclone farther southeast. The influence of positive relative vorticity advection in the Carr and Elsberry MG simulation results in a weaker, but broad, region of positive vorticity tendency that extends over most of the northern sector and out to about 700 km from the center of the MG.

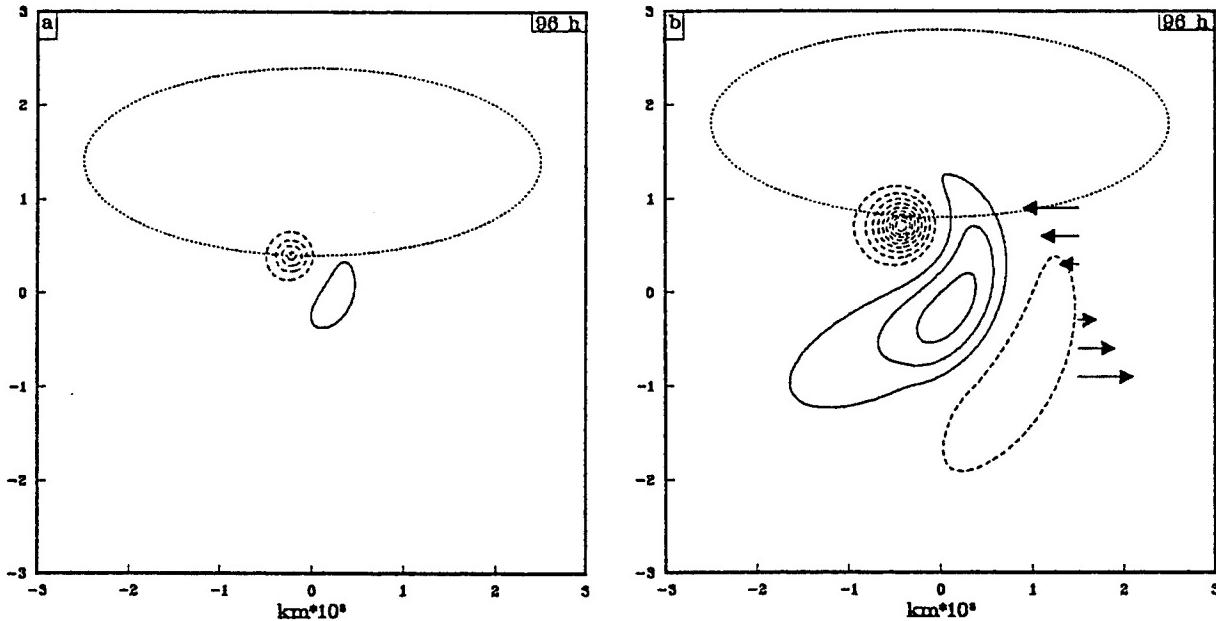


**Fig. F.4** Schematics of the relative sizes of a large subtropical ridge cell (dotted) and a (a) tropical TC with an outer radius of 830 km at 850 mb at 15° lat. and (b) large TC with an outer radius of 1230 km (dashed) after 96-h integration. The peripheral anticyclone (solid) and trailing cyclone to the southeast (panel b only) for these TC sizes indicate the differences in horizontal scale relative to the subtropical ridge cell. The arrows in (b) indicate cyclonic shear of the background flow between the subtropical ridge and monsoon trough (see text).

Based on these MG simulations, it is proposed that a sufficiently large TC in a typical tradewind easterly flow may alter its environment by: (i) building a new ridge circulation to the east-to-southeast; and (ii) eroding the pre-existing structure of the subtropical ridge to the north. The key question is how large is "sufficiently large?" A qualitative answer may be provided by comparing the size of an extensive idealized subtropical ridge feature in Figs. F.4a-b with the extent of streamfunction fields resulting from 96-h integrations of the nondivergent barotropic model initialized with the TC profiles  $R_{\text{c}}^{500} = 600$  and 900 km in Fig. D.9, respectively. Using equation (C-4), the equivalent values of  $R_{\text{c}}^{850}$  for these TCs are 830 and 1230 km, which in turn at a latitude of 15° correspond to TC sizes of typical and large, respectively (Fig. 3.37).

Whereas the peripheral anticyclone of the typical size TC (Fig. F.4a) is only a small fraction of the scale of the subtropical ridge circulation, the peripheral anticyclone of the large TC (Fig. F.4b) is similar in scale to the subtropical ridge circulation. As a result, it is proposed that the subtropical ridge erosion on the poleward side and peripheral anticyclone building equatorward and to the east of the large TC will contribute significantly to a transformation of the subtropical ridge structure from a Standard to a North-Oriented Pattern. It is emphasized that it is the *relative* size of TC wave train compared to the

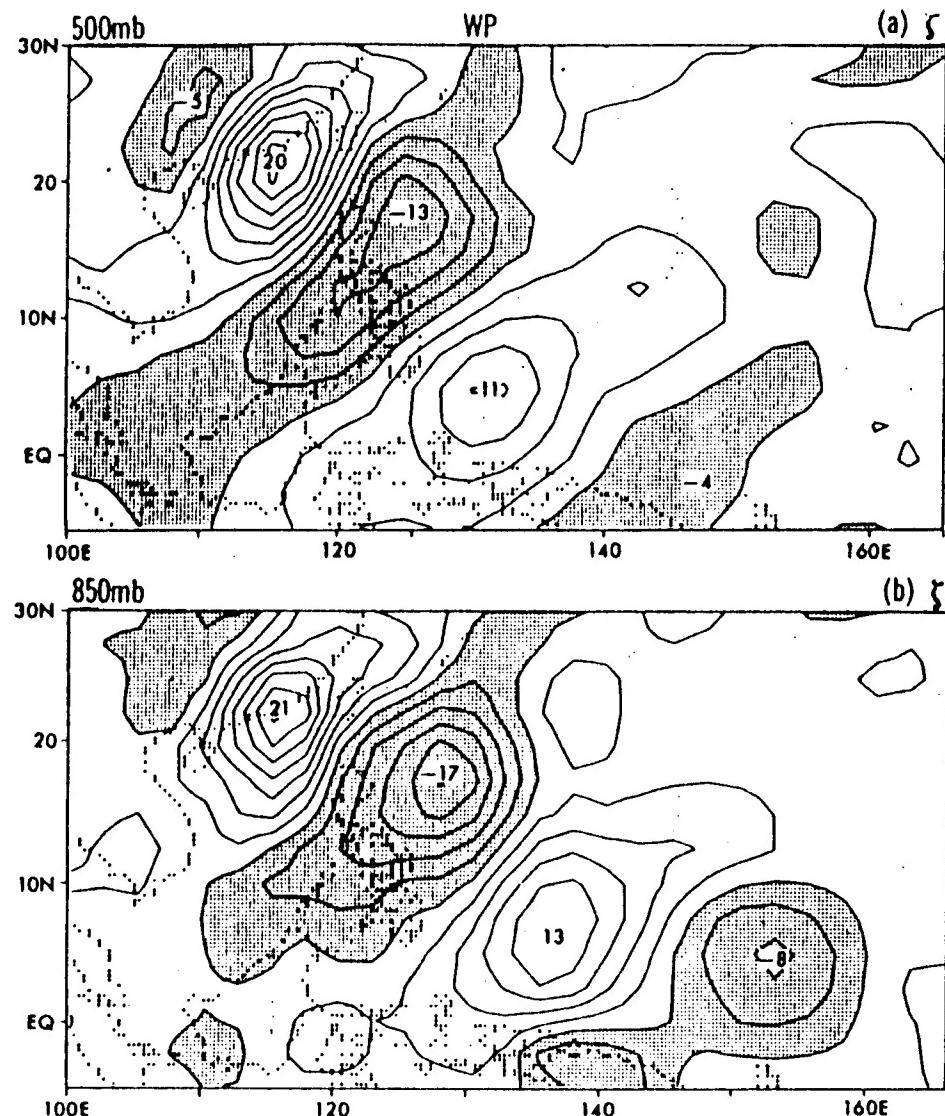


Fig. F.5 Composite patterns of bandpass-filtered relative vorticity at (a) 500 mb and (b) 850 mb indicating an equivalent barotropic structure of a large-scale wave train from China to the Equator during the summer monsoon season (Lau and Lau 1990).

subtropical ridge that matters here. Thus, it is possible for even a typical size TC to significantly modify a ridge feature that is substantially smaller than that shown in Fig. F.4.

Notice that both the peripheral anticyclone and the cyclone farther southeast in Fig. F.4b have a barotropically unstable up-shear orientation (southwest-northeast major axis) relative to the large-scale, cyclonic horizontal shear (idealized by the wind vectors in Fig. F.4b) expected between the axis of the monsoon trough and the maximum easterlies south of the subtropical ridge. Growth of a barotropically unstable eddy occurs at the expense of

this environmental horizontal shear. For similar sizes of the subtropical ridge and wave train, a significant alteration of the structure of the subtropical ridge via a barotropic energy transfer from the subtropical ridge (i.e., the environment) to the wave train (i.e., the eddy) is possible. In conjunction with the ridge building poleward and to the east and the erosion mechanism on the poleward side associated with a large TC, barotropically-induced growth of the peripheral anticyclone and associated weakening of the subtropical ridge is proposed as a scenario for premature recurvature of a large TC.

The existence and energetics of wave trains associated with large TCs have not been explicitly addressed in the literature. However, Lau and Lau (1990) have noted that: (i) similarly-oriented wave train patterns appear in composite analyses during the summer monsoon season in the western North Pacific (Fig. F.5); (ii) such wave trains have an equivalent barotropic structure in the mid-to-lower troposphere as indicated by in-phase vertical orientation of the composite wave train vorticity fields at 500 and 850 mb (Figs. F.5a and b, respectively); and (iii) an enhanced cyclonic shear in the region between the monsoon trough and the subtropical ridge exists during periods when tropical disturbances are active (Fig. F.6b), as compared to inactive periods (Fig. F.6a). Thus, Lau and Lau not only identified wave trains that have similar vertical and horizontal structures as those in barotropic model simulations, but also provided indirect evidence that barotropic growth of the wave trains may occur during active TC periods. Lau and Lau (1992) re-examined the same composite data set, and determined that a barotropic conversion of kinetic energy from the background flow to the wave train eddies does indeed occur (Fig. F.7).

Recently, Chang *et al.* (1994) have used canonical correlation analysis to reveal the structure of the wave train phenomena investigated by Lau and Lau, and then compared periods of enhanced meridional winds in the wave train with TC locations (Fig. F.8). TC locations were strongly clustered near the axis of the cyclonic feature of the wave train, so that the enhanced anticyclone is about 10° lat. to the east-southeast of the TC,<sup>20</sup> such as in the case of Yuri (Fig. 3.51a-b). This result suggests that the TCs may be responsible for the enhanced wave train phenomenon studied by Lau and Lau (1992), and that TCs may extract kinetic energy from, and thus weaken, the background flow.

Chang *et al.* noticed that the wave train arising from the  $\beta$ -induced dispersion of the MG-scale vortex in the barotropic model of Carr and Elsberry (Figs. F.2d-f) had a orientation that is more meridional than observed, such as in the case of Yuri (Figs. 3.51b-c). They hypothesized that this difference may result from the presence of a large-scale cyclonic shear in the region between the subtropical ridge and monsoon trough, whereas the Carr and Elsberry experiment had a quiescent environment. When Chang *et al.* repeated the

---

<sup>20</sup> Notice also that a secondary clustering of TC positions occurs in the northwest quadrant of the cyclonic feature of the wave train that trails the anticyclone, which is consistent with secondary TC cyclogenesis that tends to occur in the N2 Pattern associated with a large TC.

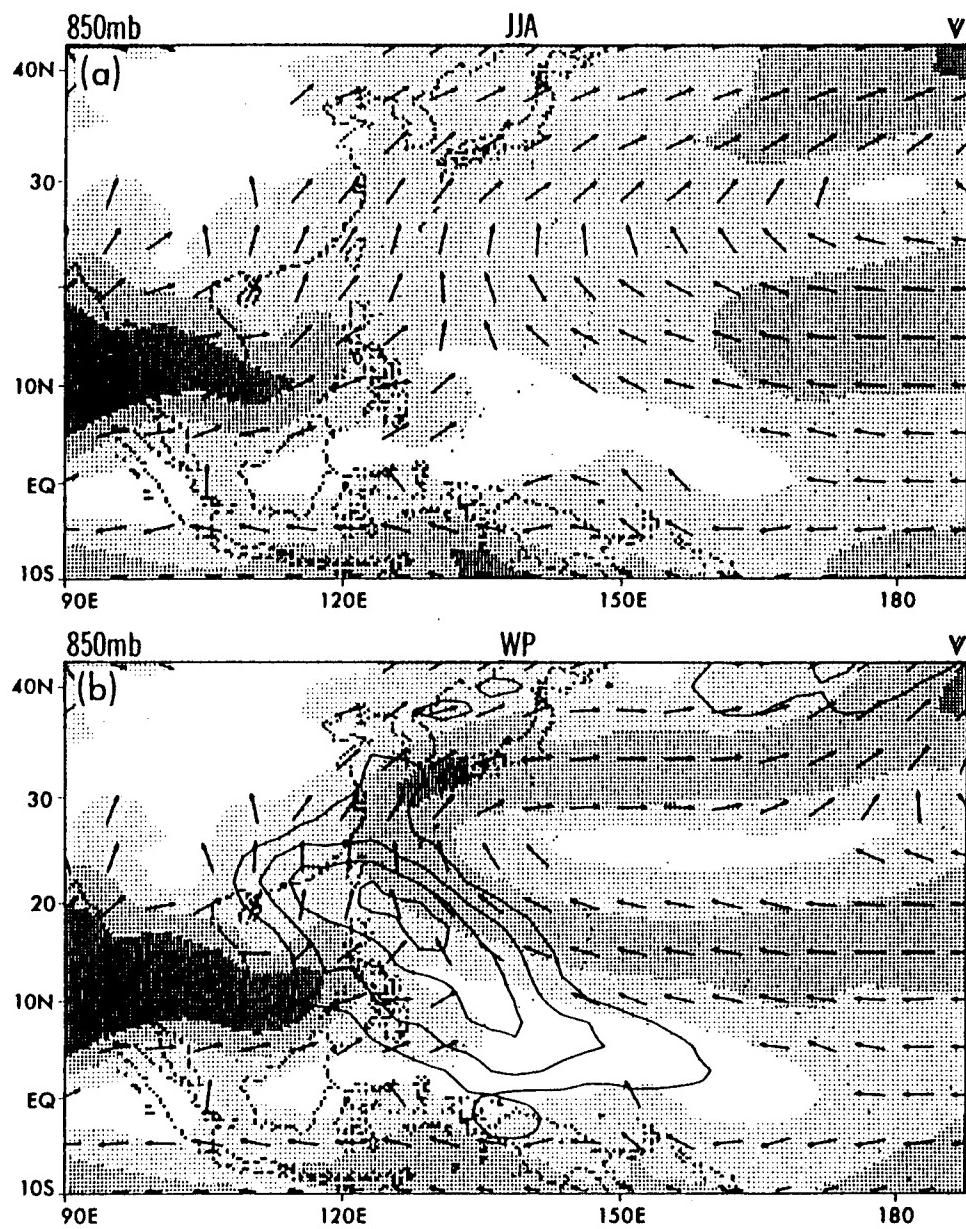


Fig. F.6 (a) Distribution of 850 mb horizontal wind in the western Pacific, as averaged over eight summers. Light stippling for wind speeds between  $2-5 \text{ m s}^{-1}$ , medium stippling for  $5-8 \text{ m s}^{-1}$ , and dense stippling for speeds larger than  $8 \text{ m s}^{-1}$ . Wind speeds less than  $2 \text{ m s}^{-1}$  are not stippled, and the corresponding directional arrows are not shown. (b) Similar to (a), except averaged only over the time intervals when WP disturbance are active. The closed contours indicate the distribution of the RMS of the phase composites of bandpass-filtered 850 mb vorticity for a complete cycle (Lau and Lau 1990).

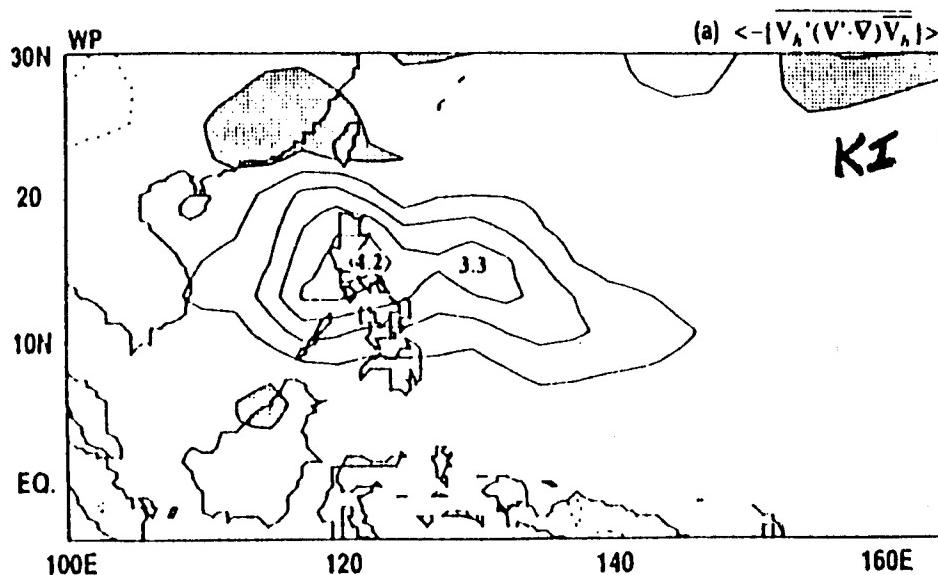


Fig. F.7 Conversion of kinetic energy of the background flow to kinetic energy of the wave train eddies in Fig. F.5 (Lau and Lau 1992).

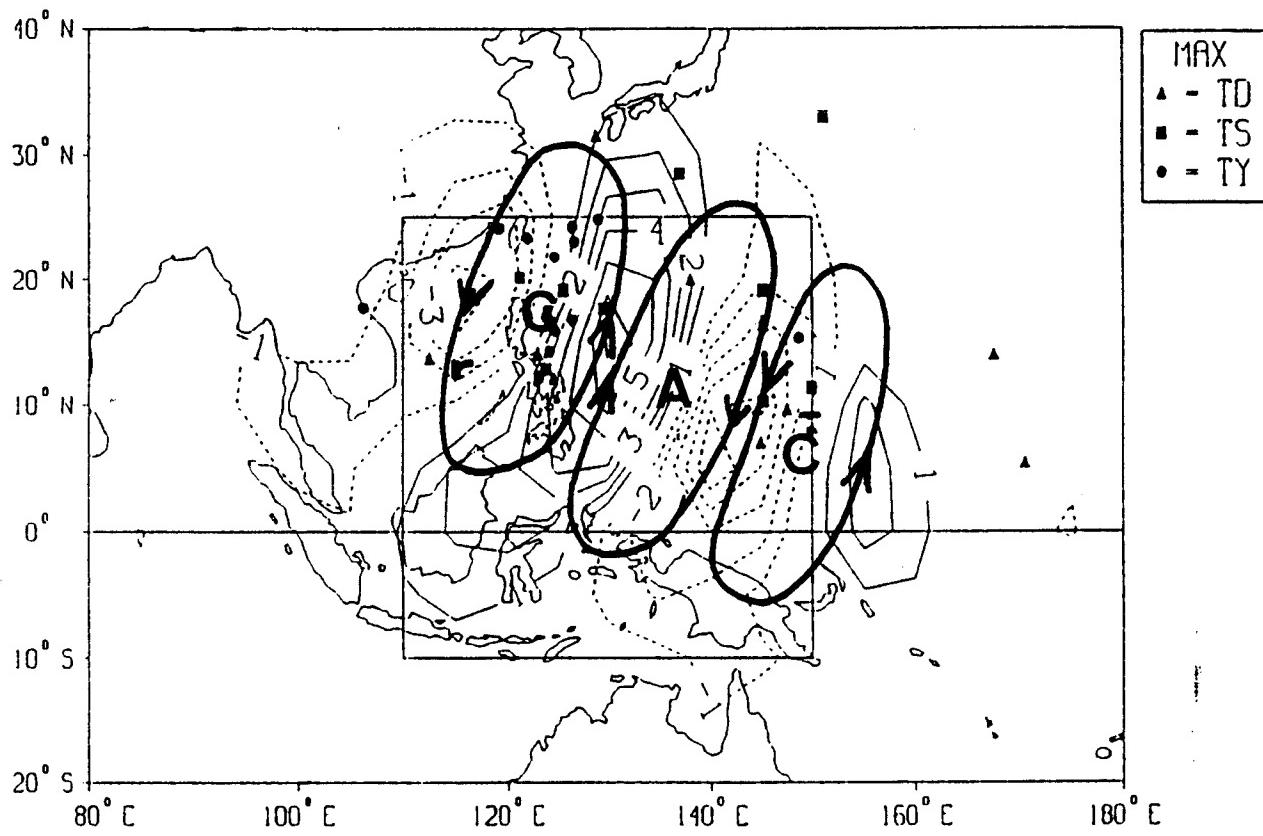


Fig. F.8 Meridional wind components (positive, solid, is poleward) in wave train from China to Equator as in Fig. F.5. Corresponding streamlines of cyclonic (C) and (A) circulation are indicated by solid lines with arrows. Positions of TD (triangle), TS (box), and TY (circle) relative to the wave train are shown (Chang *et al.* 1994).

Carr and Elsberry experiment with a zonally-uniform, linear shear flow of  $2.5 \text{ m s}^{-1}$  per 1000 km (Fig. F.9a), the orientation of the resulting wave train (Fig. F.9c) more closely resembled the observations. The authors have extended the Chang *et al.* result by removing the imposed background zonal flow to reveal the structure of the wave train that resulted from this barotropically unstable situation (Figs. F.9d-f). A comparison of Figs. F.9e and f (without environmental shear) with Figs. F.2e and f reveals significant wave train amplification that must have come at the expense of the mean shear flow.

Energetic analysis of individual TC cases will be required to validate the simulated barotropic energy conversion from the subtropical ridge to the wave train anticyclone southeast of a large TC. Based on the preliminary evidence presented above, it is assumed that the barotropic energy conversion process plays an important role.

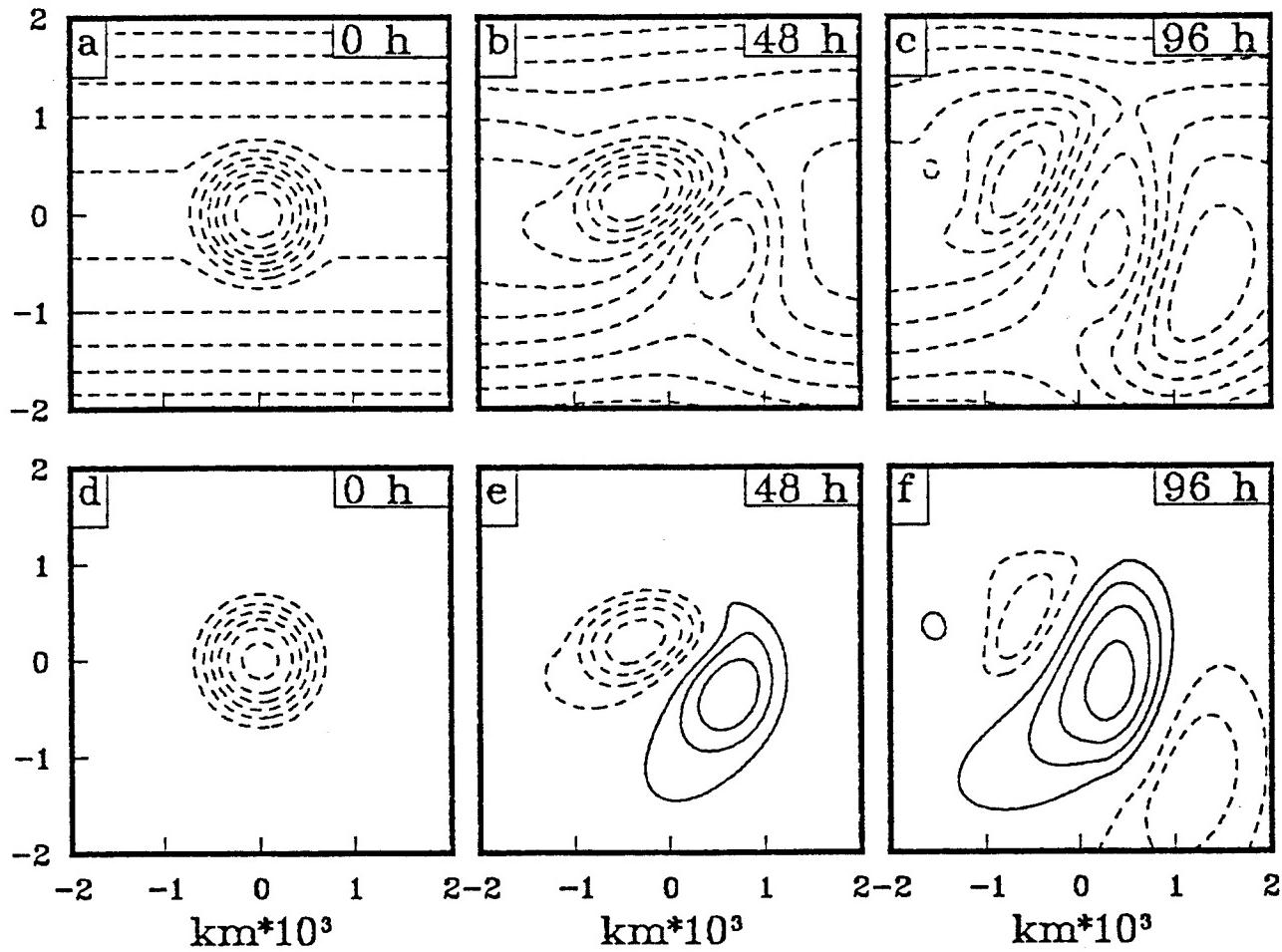


Fig. F.9 As in Figs F.2 (d-f), except with addition of a zonally-uniform linear shear of  $2.5 \text{ m s}^{-1}$  per 1000 km. Panels (d-f) are the streamfunctions in (a-c) after subtracting the initial streamfunction associated with the background linear shear, and may be compared directly with Figs. F.2 (d-f).

## Appendix G

### Preliminary Development of Monsoon Gyre-TC Interaction (MTI) Conceptual Model

The modelling component of the Carr and Elsberry (1995; hereafter CE) study consisted of 96-h integrations of a nondivergent, barotropic,  $\beta$ -plane model, which was initialized with various combinations of a large, weaker vortex that represents the MG and a small, more intense vortex that represents the TC. The TC is initially an axisymmetric vortex with a radial dependence given by equation (D-3), with  $V_m$  values ranging from  $10 \text{ m s}^{-1}$  (20 kt) to  $30 \text{ m s}^{-1}$  (60 kt), and  $R_m$  is fixed at 100 km. These values were chosen to be representative of the typical TC as it undergoes a monsoon surge track change, and to determine the effect of TC intensity on the track change process. The radial profile given by (D-3) for  $V_m = 20 \text{ m s}^{-1}$  is shown in Fig. F.1.

The MG is also initially axisymmetric with a radial dependence given by

$$v_\theta(r) = \frac{V_m}{2} \left[ 1 - \cos\left(\frac{\pi r}{R_m}\right) \right] \quad 0 \leq r \leq 2R_m , \quad (\text{G-1})$$

where  $V_m$  and  $R_m$  have the same meaning as in (D-3), and range from  $10$  to  $15 \text{ m s}^{-1}$  and from  $300$  to  $700$  km, respectively. As shown in Fig. F.1, this wind profile with  $V_m = 12.5 \text{ m s}^{-1}$  and  $R_m = 500 \text{ km}$  represents an idealized monsoon circulation that might be generated by a broad region of relatively unorganized convective heating. This value of  $R_m$  gives a circulation extent similar to the MG associated with Nathan (Fig. 3.67), which had an average circulation radius of approximately 1000 km. Although a  $V_m$  of  $12.5 \text{ m s}^{-1}$  appears to exaggerate the strength of Nathan's MG as analyzed by NOGAPS, it compensates for a probable underestimation of the actual circulation strength by the model due to lack of data over the South China Sea.

As noted earlier, when the model was initialized with only the TC-scale vortex very little peripheral ridging appeared (Figs. F.2a-c). When the MG alone was the initial condition, a  $\beta$ -induced wave train developed (Figs. F.2d-f) similar to that seen for the larger angular momentum TC wind distribution profiles (Figs. D.12e-f). Thus, CE concluded that the wind field of the initially distinct MG in a MTI track change situation is the energy source of the wave train. CE used the diagnostic diagram (Fig. F.3) to establish that the peripheral anticyclone arises primarily from intense nonlinear negative relative vorticity advection (NVA) to the southeast of the MG, but also that this NVA is made possible by linear  $\beta$ -induced distortion of the MG from its axisymmetric initial condition.

When CE added the TC-scale vortex in the model initial conditions at a location 400 km to the east of the MG (Fig. G.1a), a binary interaction of the TC and MG results, which is comprised of cyclonic rotation of the TC around the north side of the MG (Fig. G.1a-c),

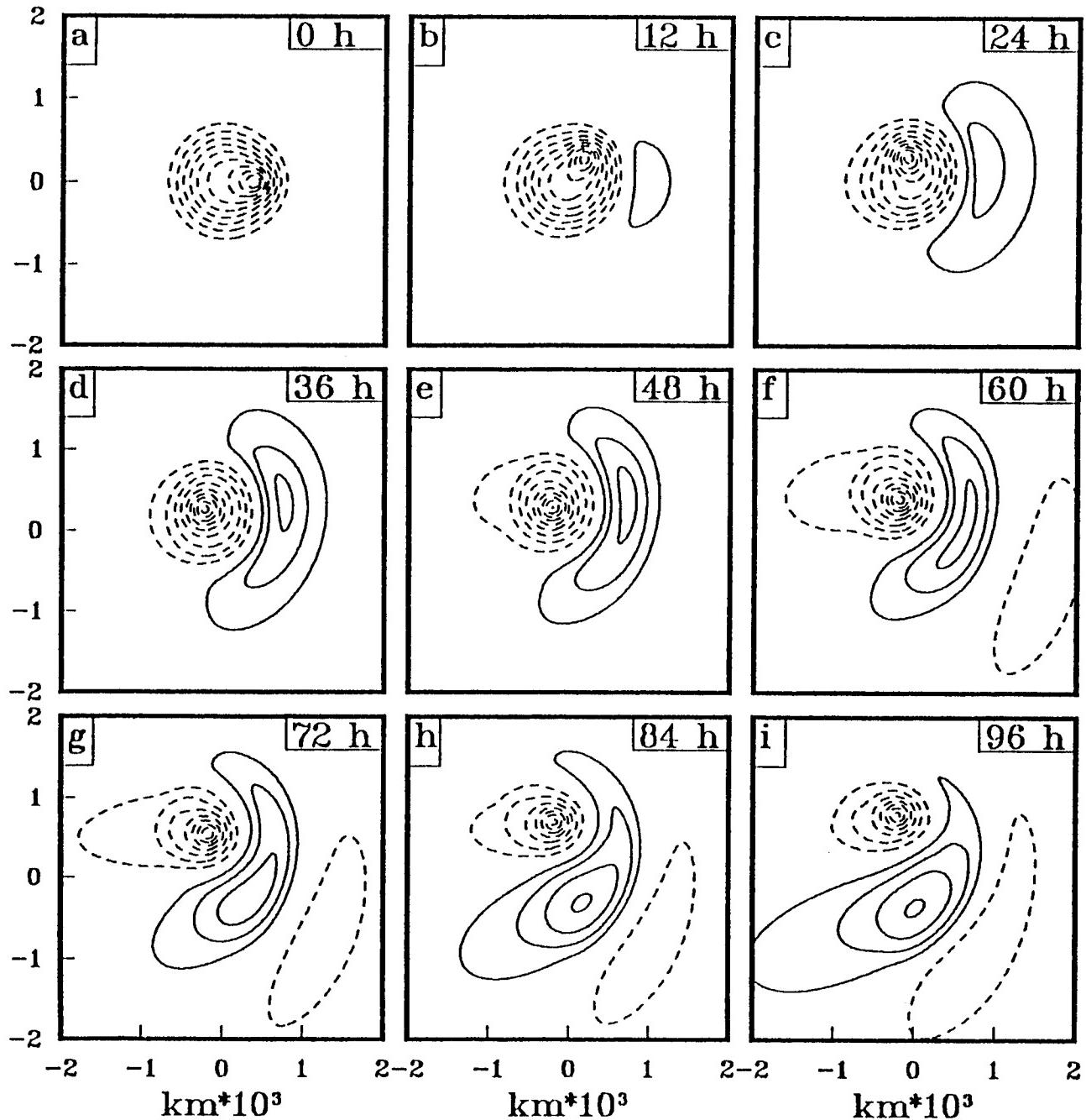


Fig. G.1 Streamfunction each 12 h to 96 h in the Carr and Elsberry (1995) model with the TC initially 400 km east of the MG center.

and a subsequent coalescence of the initially distinct TC and MG circulations into one circulation by about 36 h (Fig. G.1d). The MG and TC remain coalesced for the remainder of the integration (Figs. G.1e-i), and thus the MTI process has not only altered the track of the TC, but also has effectively caused a significant increase in the size of the TC.

A  $\beta$ -induced wave train develops in Fig. G.1 that generally resembles the one arising from the MG alone (Figs. F.2d-f), but that is also different in several important details. By 48 h, the maximum amplitude of the peripheral anticyclone has shifted from east to southeast of the MG by 48 h in the MG-only integration (Fig. F.2e). By contrast, the location of the developing anticyclone remains to the east for nearly 60 h (see Fig. G.1f), before shifting clockwise to the south-southeast by 96 h (panel i). In addition, the amplitude of the anticyclone is significantly greater at 48 h in the MG-TC integration (Fig. G.1e). Additional variations in anticyclone amplitude and orientation resulted when CE positioned the TC at 600 km east, 400 km southeast, and 400 km northeast of the MG (Figs. G.2a-c, d-f, and g-i, respectively). Notice the tendency for the orientation of ridging at 48 h to be correlated with the initial position of the TC relative to the MG in Fig. G.2. For example, the peripheral ridging is concentrated to the southeast when the TC is initially positioned to the southeast (compare Figs. G.2d and e), but is stretched out to the northeast when the TC is initially northeast of the MG (compare Figs. G.2g and h). Notice also that the ridging is comparatively weaker (stronger) by 48 h when the TC is initially positioned 400 (600) km to the east of the MG (compare Figs. G.1b and G.2b, respectively). Since neither linear advection of earth vorticity or nonlinear relative vorticity advection generated significant peripheral ridging in the TC-only case, CE inferred that TC position-dependent variations in nonlinear advection of the MG relative vorticity by the TC must be responsible for the variations in peripheral ridging among the different integrations.

An alternate interpretation that explains more precisely the connection between initial TC location and the distribution of peripheral ridging is to view the superposed TC and MG initial circulations as forming a single distorted circulation. On the TC side of the MG vortex, the streamfunction spacing is compressed, and on the opposite side, the streamfunction spacing is expanded. Recalling the discussion of Fig. F.3, such a distortion tends to produce NVA (PVA) to the right (left) of a line drawn along the major axis of the vortex from the stretched side to the compressed side (Fig. G.3). Maximum NVA is located at about the 1 to 2 o'clock position relative to the axis owing to the higher winds on the compressed side of the vortex, and the magnitude of the NVA is much higher for the highly distorted TC-MG vortex than for the moderately distorted MG-only case. The average location of the intense maximum NVA region during the first 24 to 36 h until the TC and MG coalesce (thus reducing the distortion) then determines the preferred location for the peripheral ridging to form in the barotropic model simulations.

According to the above interpretation, the NVA-related growth rate of the peripheral anticyclone depends on the degree to which the TC location distorts the combined MG-TC vortex, which explains the greater (smaller) anticyclone amplitude at 48 h for the TC initially 600 (400) km to the east of the MG (compare Figs. G.2a and b with Figs. G.1a and

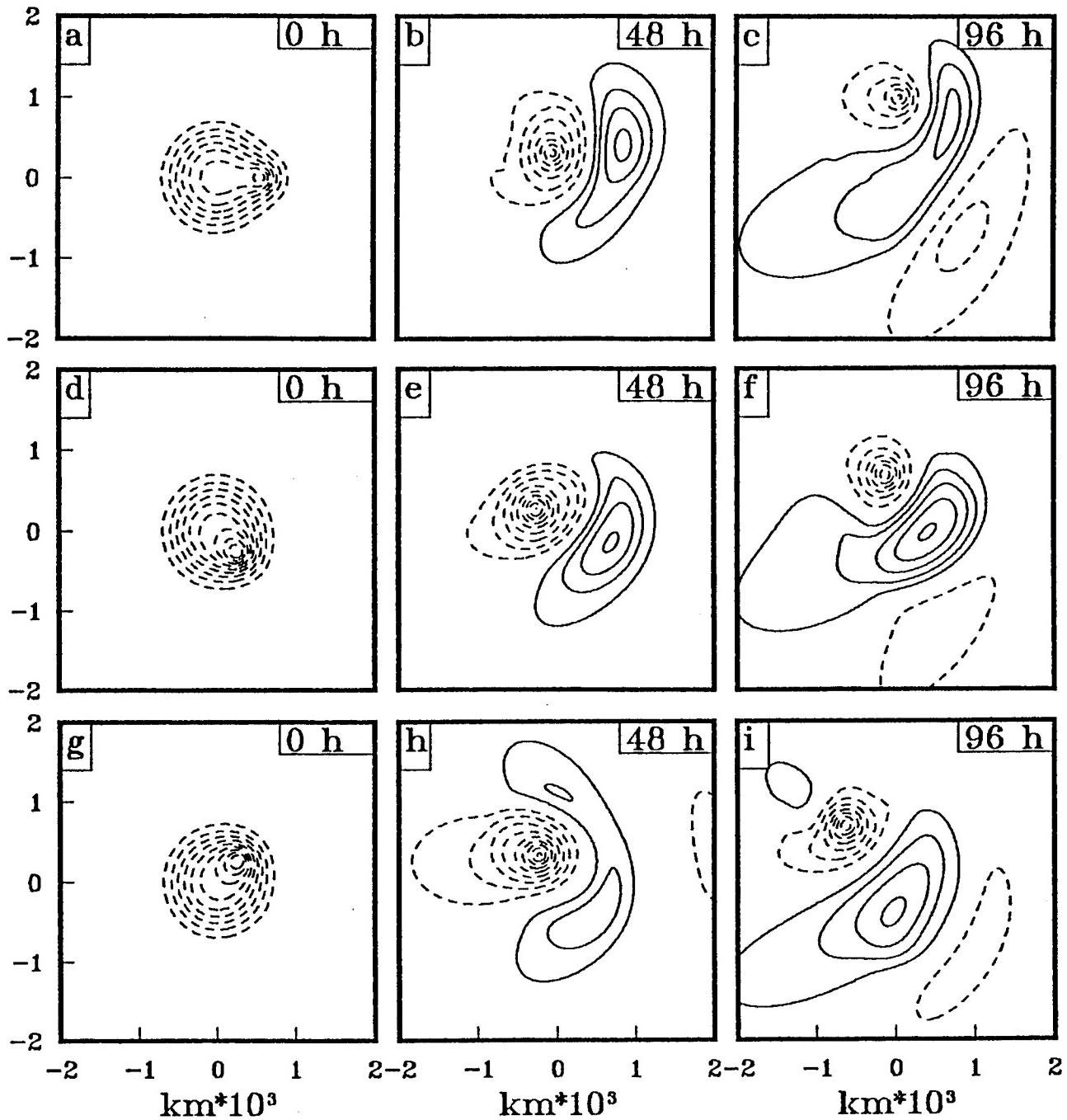


Fig. G.2 (a)-(c) Streamfunction fields as in Fig. G.1, except for every 48 h. (d)-(i). As in (a)-(c), except with (d)-(f) the TC initially 400 km southeast of the MG, and (g)-(i) the TC initially 400 km northeast of the MG.

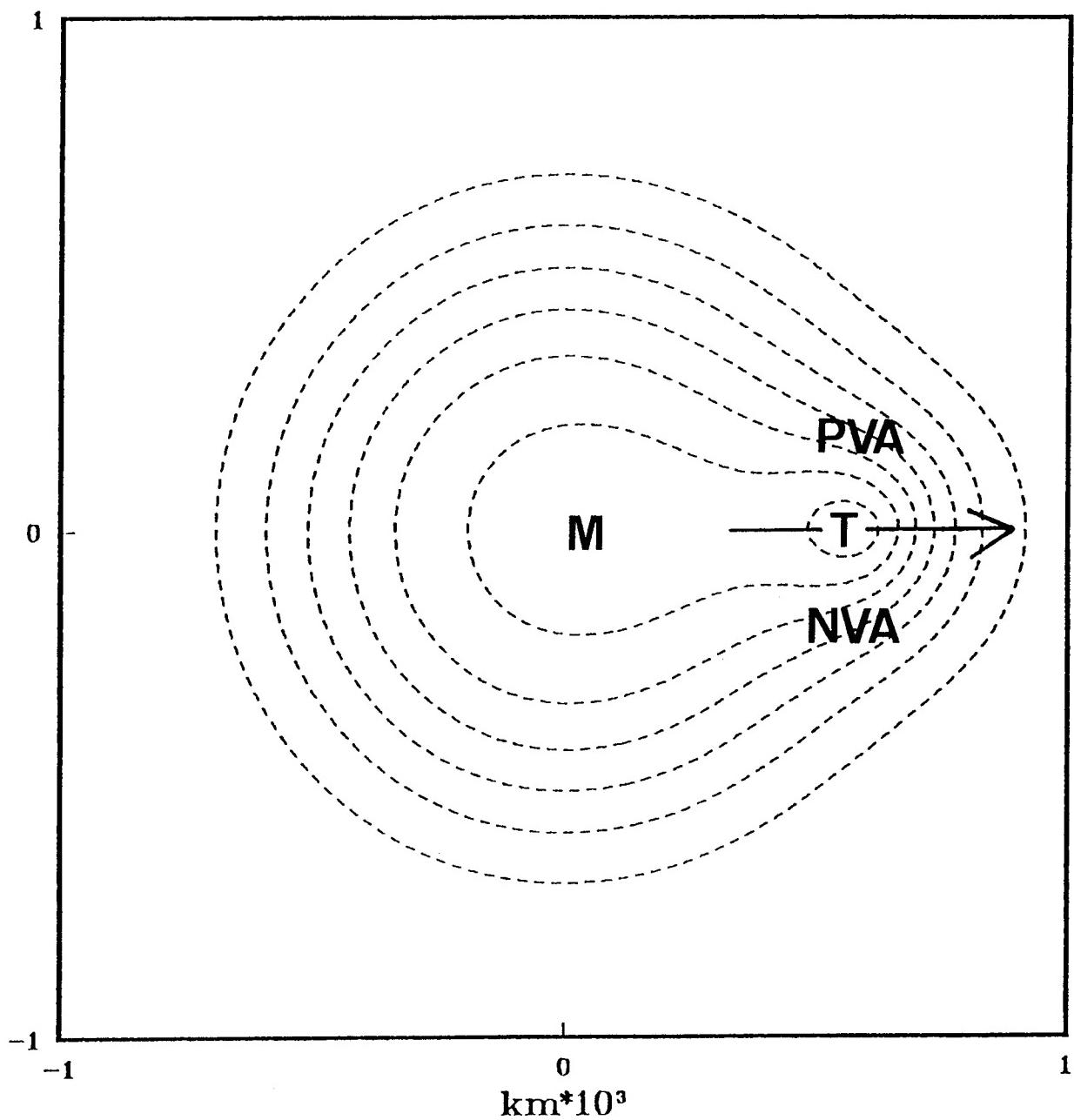


Fig. G.3 Expanded view of streamfunction with a TC (center at T) embedded within a MG (center at M). Regions of Positive Vorticity Advection (PVA) and Negative Vorticity Advection (NVA) are located to the left and right of an eastward directed arrow through the centers of the MG and TC.

e, respectively). In both the TC 400 km east and 600 km east experiments (Fig. G.4a-c and G.4d-f, respectively), crescent-shaped isotach maxima are found in the high streamfunction gradient regions between the coalesced MG-TC and peripheral anticyclone. Notice that the

location of these wind maxima agrees well with the location of the peripheral cloud band associated with actual track changes (compare Fig. G.4e with 3.66b and d). That is, the confluent region (presumably convergent in 3-D situations) in the entrance of the wind maximum should provide an impetus for upward motion and enhanced convection. It is hypothesized that dependence of the intensity of this confluent region on the position of the TC relative to the MG may provide an explanation for why the peripheral cloud band is very distinct in some MTI scenarios and entirely absent in others.

After the TC fully coalesces with the MG in the barotropic simulations, the generally northward-oriented peripheral anticyclone tends to weaken and shift to a position to the southeast of the TC-MG. After the TC has coalesced with the MG, the distorting, and thus NVA-producing, effect of the TC is removed. However, the induced peripheral anticyclone continues to distort the MG by compressing the streamfunction to the east, which results in NVA to the southeast. As a result of this NVA, the largest anticyclonic vorticity tendency tends to be equatorward of a line from the TC-MG center to the peripheral anticyclone center, so that the peripheral anticyclone is weakening to the northeast and strengthening to the southeast, which results in a clockwise rotation around the coalesced TC-MG. The rate at which the anticyclone shifts clockwise and weakens appears to be inversely related to its maximum strength. For example, the very strong anticyclone produced by a TC initial position 600 km to the east (Fig. 3.71a-c) has less weakening and a small shift. Consequently, the distorting effect of the peripheral anticyclone on the coalesced TC-MG is sustained, which results in faster and more sustained poleward TC motion, and hence a greater potential that a transition to another synoptic pattern/region will occur.

During the coalescence of the TC and MG, the effective size of the TC increases significantly. However, a significant fraction of the MG's energy is dispersed via TC-induced distortion to form the enhanced peripheral ridging. Thus, the coalesced TC-MG circulation should not be expected to have as large an outer wind strength as the circulation in a model integration in which the MG and TC are initially collocated (Fig. G.5). That is, the outer wind strength at 48 and 96 h in Figs. G.1 and G.2 is generally weaker (wider streamline spacing at equivalent radii) than in this collocated case.<sup>21</sup> This aspect of the model simulations suggests that the apparent TC growth as a result of coalescence with an MG does not result in as large a TC circulation as would occur if the TC had formed in the center of the same monsoon gyre. It will be shown below that this result has important

---

<sup>21</sup> Recall that a similar reduction in the outer wind strength of the angular momentum TC wind profiles arising from  $\beta$ -induced dispersion was believed to be excessive because other physical processes that would sustain the outer wind profile were not included in the barotropic model. The reason that these outer wind strength reductions in the TC-MG coalescence cases are viewed as potentially realistic is that the strength reductions are significantly greater than the analogous wind strength reduction in the initially axisymmetric case. As will be seen in the next subsection, observations tend to confirm this aspect of the barotropic simulations.

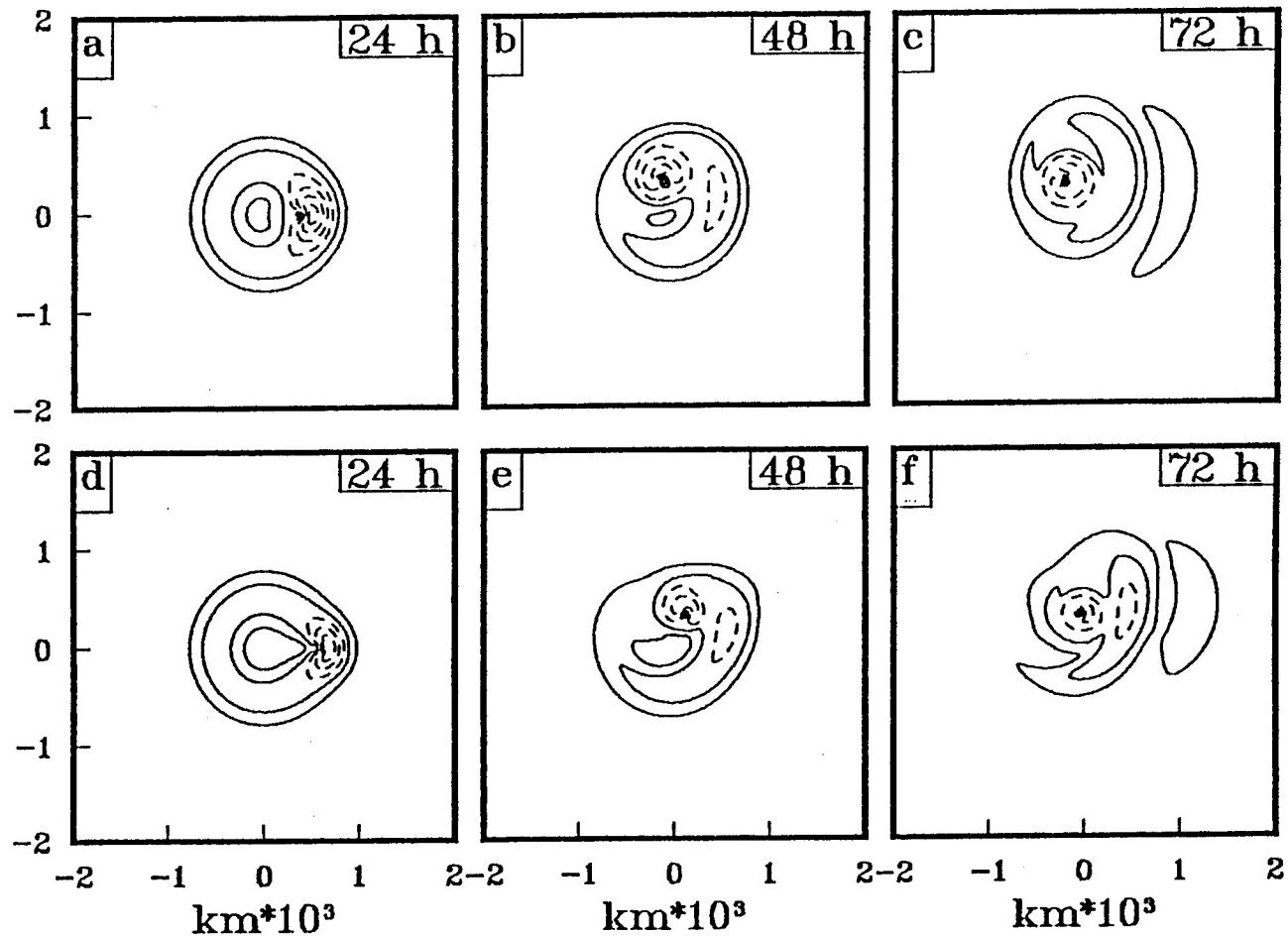


Fig. G.4 Isotachs corresponding to the streamfunction fields at 24 h, 48 h, and 72 h in Fig. G.1 (a)-(c) and for simulation with the initial TC position 600 km east of the MG (d)-(f) rather than 400 km east (Carr and Elsberry 1995). Contour interval is 5 m s<sup>-1</sup>, and contours of 15 m s<sup>-1</sup> and greater are dashed.

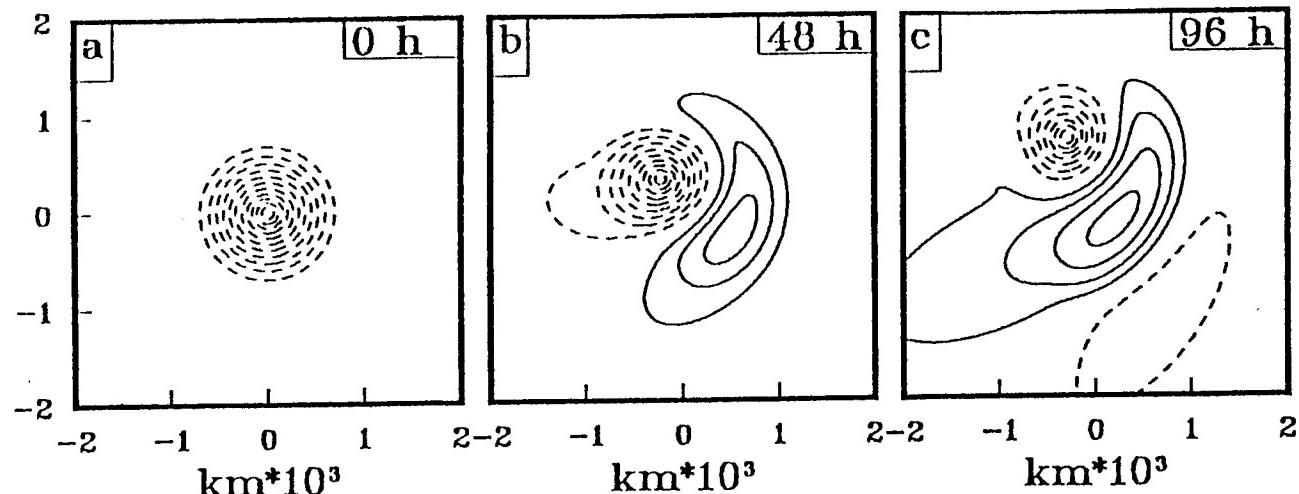


Fig. G.5 Model streamfunction as in Fig. G.1, except with TC initially collocated with the MG.

implications for the role of the MTI process as a transitional mechanism.

CE found that the initial position of the TC and MG has a profound impact of the subsequent track of the TC. All of the model tracks starting on the west side of the MG (Fig. G.6a; Tracks 3a-3d) have relatively smooth looping shapes. With one exception, all of the model tracks starting on the east side of the MG (Fig. G.6b; Tracks 2b-2e) have a distinct cycloidal shape similar to the observed tracks in Figs. 3.61 and 3.63. The initial translation velocities for all tracks agree well with the tangential wind speed of the MG at that radius. Thus, the motion of the TC in the early hours of the integration is primarily a result of advection by the flow of the MG.

Track 2f (Fig. G.6), which starts 800 km east of the initial position of the MG, is distinctive in that sustained, nearly northward motion occurs throughout the 96-h integration. Since a starting position only 100 km to the west (Track 2e) results in distinctly cycloidal motion, a bifurcation point, which markedly affects the character of the TC tracks in the model, appears to exist somewhere between 700 to 800 km east of the center of the MG. Such a bifurcation point is analogous to the binary TC situations simulated by Lander and Holland (1993).

CE found that among the four initial positions to the east that result in a cycloidal track (Fig. G.6b; Tracks 2b-2e), a direct relationship exists between the initial location of the TC and the location where the sudden slowing and poleward turn occurs. The farther the TC is to the east of the MG, the farther to the east and north is its northward turn point. The vigor of the northward acceleration of the TC after the poleward turn is also related to the initial location. The TCs that start 600 and 700 km from the center of the MG attain higher poleward translation speeds (up to  $5 \text{ m s}^{-1}$  for Track 2d) after the turn and maintain those speeds longer than the TCs that start 200 and 400 km from the MG center. It should be noted that such translation speeds are more than twice that attained by the TC owing to BEP alone. Thus, the poleward motion of the coalesced TC-MG must primarily manifest advective steering by the peripheral anticyclone in a manner similar to that occurring in the RMT transformation model. A distinct difference here is that the location of the peripheral anticyclone, and hence the direction of the associated steering, depends sensitively on the initial position of the TC relative to the MG when interaction commences. This fact explains the greater variability of TC track directions after the poleward turn for the MTI cases compared to the RMT-related situations, and also implies that MTI track changes are inherently less predictable.

An initial separation distance of 400 km places the TC just inside the  $R_m$  of the MG. Actual TC development would seem to be particularly favored here because this is where the relative vorticity of the MG has the largest positive value. The tracks in Fig. G.7 are for a constant distance of 400 km while varying the initial direction of the TC from the MG. Notice that tracks originating southeast counterclockwise through north (Northern Hemisphere) of the MG are distinctly cycloidal in shape, whereas tracks northwest counterclockwise through southwest produce relatively smooth looping motion. On the basis

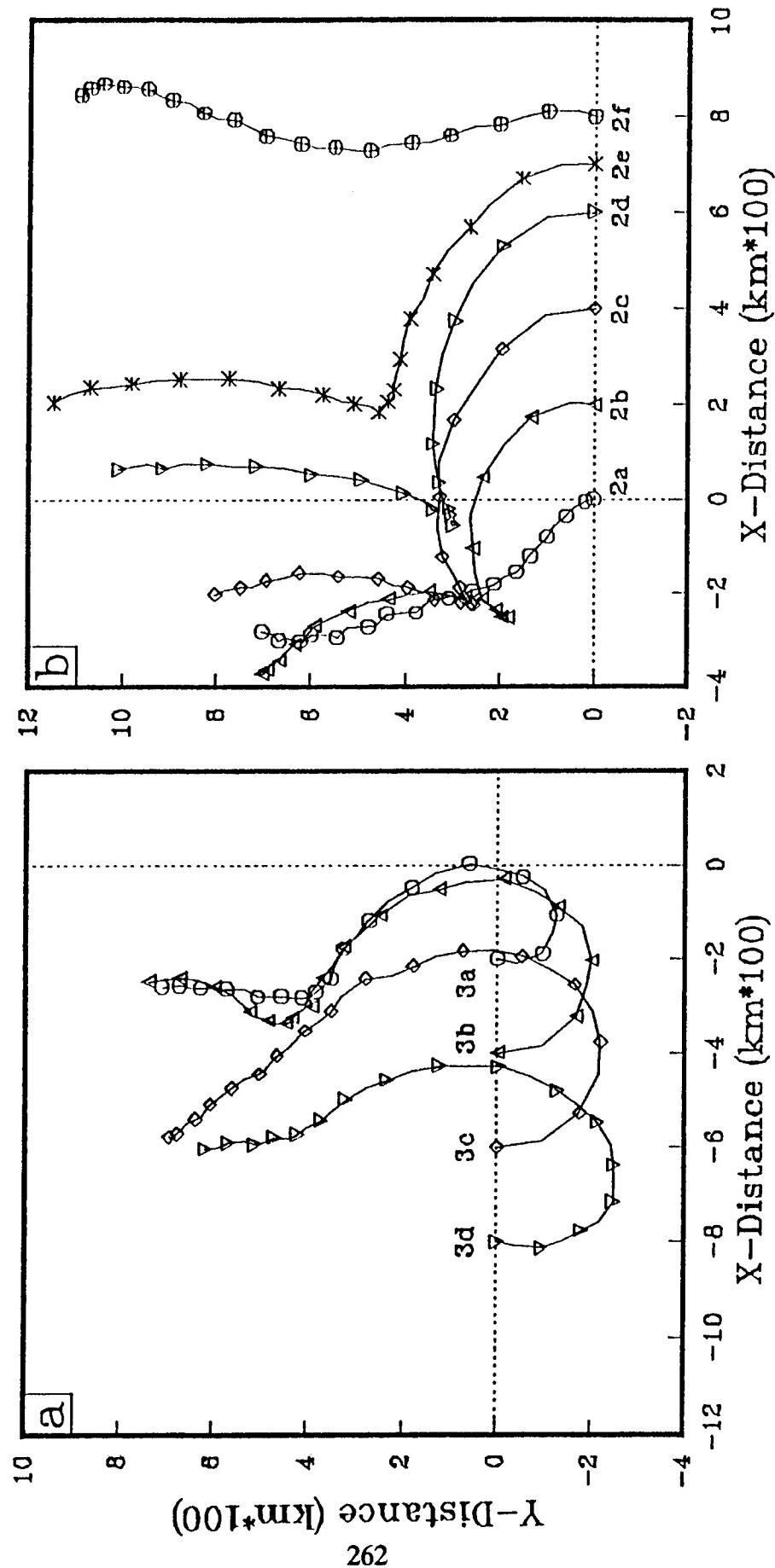


Fig. G.6 Model-simulated tropical cyclone tracks for (a) the TC to the west of the MG center at (0, 0) and (b) with the TC to the east of the MG (Carr and Elsberry 1995). The experiment labels appear at the beginning of each track.

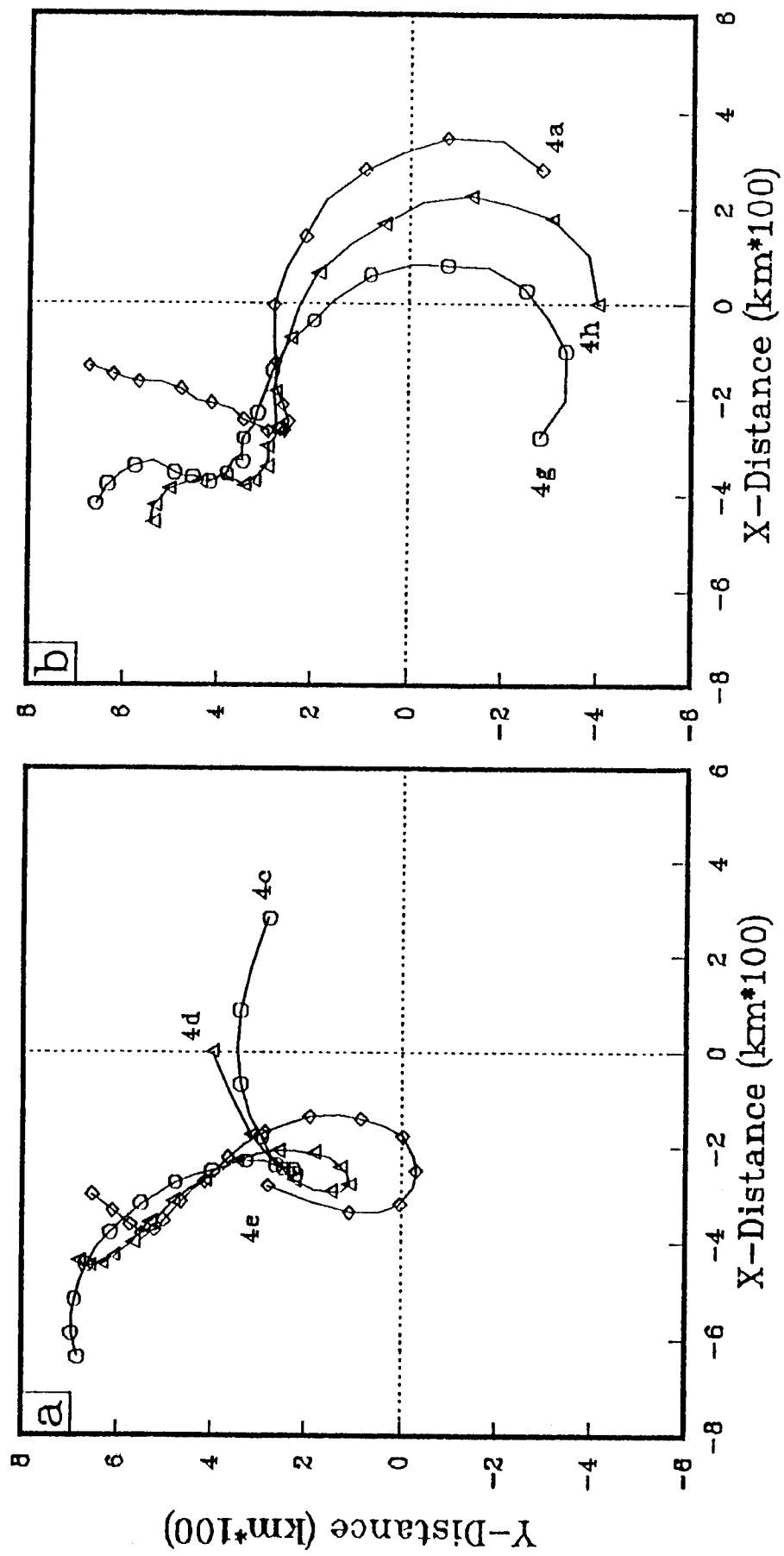


Fig. G.7 Tropical cyclone tracks as in Fig. G.6, except with constant MG/TC separation of 400 km and TC direction from the MG in the (a) poleward and (b) equatorward quadrants.

of these nondivergent, barotropic simulations, monsoon surge track changes would be expected for TC positions in the eastern semicircle of the MG.

CE also tested the sensitivity of the cycloidal track change to variations in the structure of the MG and TC with a fixed initial TC position 400 km to the east. Both the sharpness of the cycloidal maneuver and the magnitude of the subsequent poleward acceleration depend directly on the intensity of the MG (Fig. G.8). Whereas TC intensities of less than  $20 \text{ m s}^{-1}$  have a significant effect on the TC track (Fig. G.9a), TC intensities greater than  $20 \text{ m s}^{-1}$  have very little effect on the TC track (Fig. G.9b). If the MG size is varied with the initial position of the TC adjusted to maintain approximately the same relative position inside the  $R_m$  of the gyre, the shape of the TC track varies quite dramatically (Fig. G.10). Whereas multiple cycloids appear in the track of the TC interacting with a smaller MG (Fig. G.10; Track 7a), a broad and sustained arcing track with a sudden poleward turn at 72 h results when the MG is larger (Fig. G.10; Track 7c).

The model tracks simulated by CE reproduce many aspects of the MTI track changes illustrated in Figs. 3.61 and 3.63. The particularly severe model TC track change resulting from an initial position 600 km to the east of the MG (Fig. G.6b; Track 2d) closely resembles the observed tracks of Hal (Fig. 3.61) and Mac (Fig. 3.63a). The similarity of the tracks, despite significant differences in intensity at the time of the track change ( $20 \text{ m s}^{-1}$  for model TC;  $37.5 \text{ m s}^{-1}$  for Mac;  $52.5 \text{ m s}^{-1}$  for Hal), is consistent with the model-based result that TC intensities above a threshold value of  $20 \text{ m s}^{-1}$  have a minimal effect on track. Both model Track 2d and the Mac/Hal tracks have distinctly curved segments of very similar duration (36 to 48 h) and radius (about 500 km). In addition, Hal's poleward acceleration to a maximum translation speed of 11 kt ( $5.5 \text{ m s}^{-1}$ ) 24 to 36 h after the sudden slowing and poleward turn is well simulated by the model Track 2d. The only major discrepancy in the CE model simulations is the anomalously high TC translation speed in the first 6-12 h of the integration, which is attributable to initializing the model with a perfectly circular MG. Actual MGs are typically elliptical with a longer zonal axis and higher winds on the northern and southeastern quadrants due to the influence of the subtropical ridge and confluent southwesterly monsoonal flow, respectively.

Typhoon Abe (Fig. 3.63b) is an interesting example of a quite sharp poleward turn that was followed by a relatively weak and transient (instead of strong and persistent) poleward deflection, and then a return to west-northwestward movement equatorward of the subtropical ridge. Track 4c (Fig. G.7a), in which the TC was positioned 400 km to the northeast of the MG, is consistent with the track of Abe. The turn to the west in the latter half of the model simulation is remarkable since significant westward translation is occurring despite the expected tendency for the TC to propagate northwestward on a  $\beta$ -plane.

The atypical examples of Sarah and Ken-Lola (Fig. 3.63a) that had particularly pronounced equatorward dips, and Tip (Fig. 3.63a) that had a particularly sustained and cyclonically curved track segment prior to the poleward turn, are well simulated by the model for TC positions on the poleward (Fig. G.7a; Track 4d) and south Fig. G.7b; Track

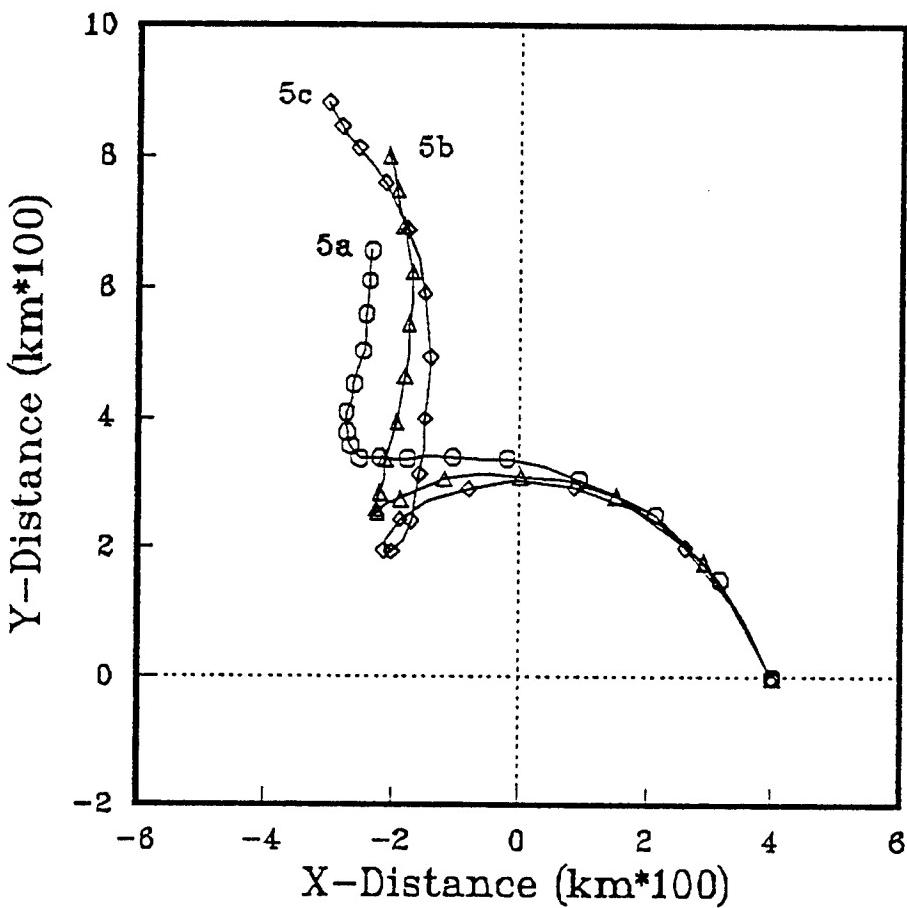


Fig. G.8 Tropical cyclone tracks as in Fig. G.6. except for Experiment 5 of Carr and Elsberry (1995) with increasing MG intensities.

4a) of the MG, respectively. Interestingly, even the highly peculiar, double looping track of Orchid in 1980 (Fig. 3.64a) is well simulated in scale and duration by the Track 7a (Fig. G.10) with a smaller MG.

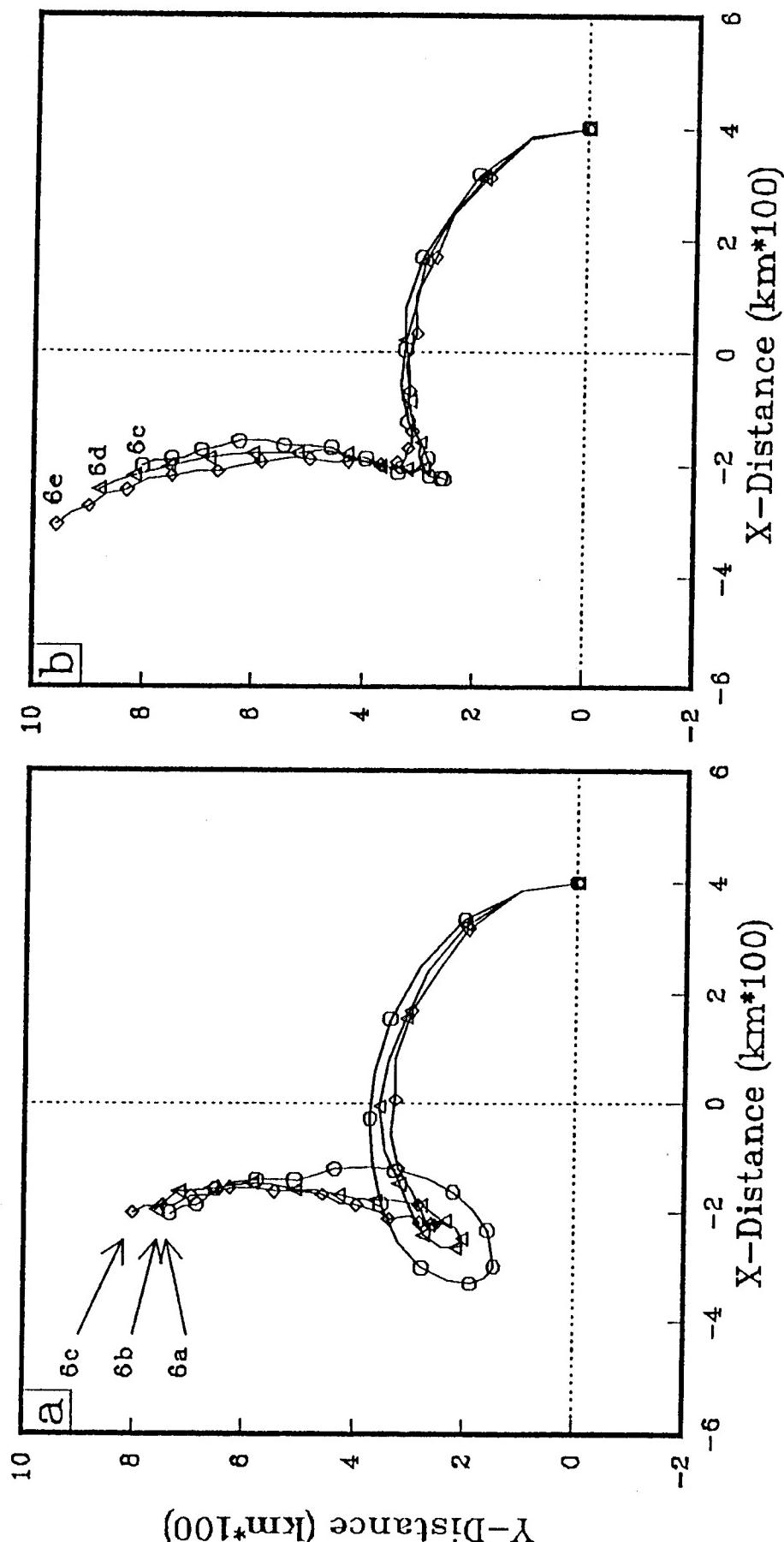


Fig. G.9 Tropical cyclone tracks in Fig. G.6, except for Experiment 6 of Carr and Elsberry (1995) with TC intensities of (a) 10, 15, and 20  $\text{m s}^{-1}$ , and (b) 20, 25, and 30  $\text{m s}^{-1}$ .

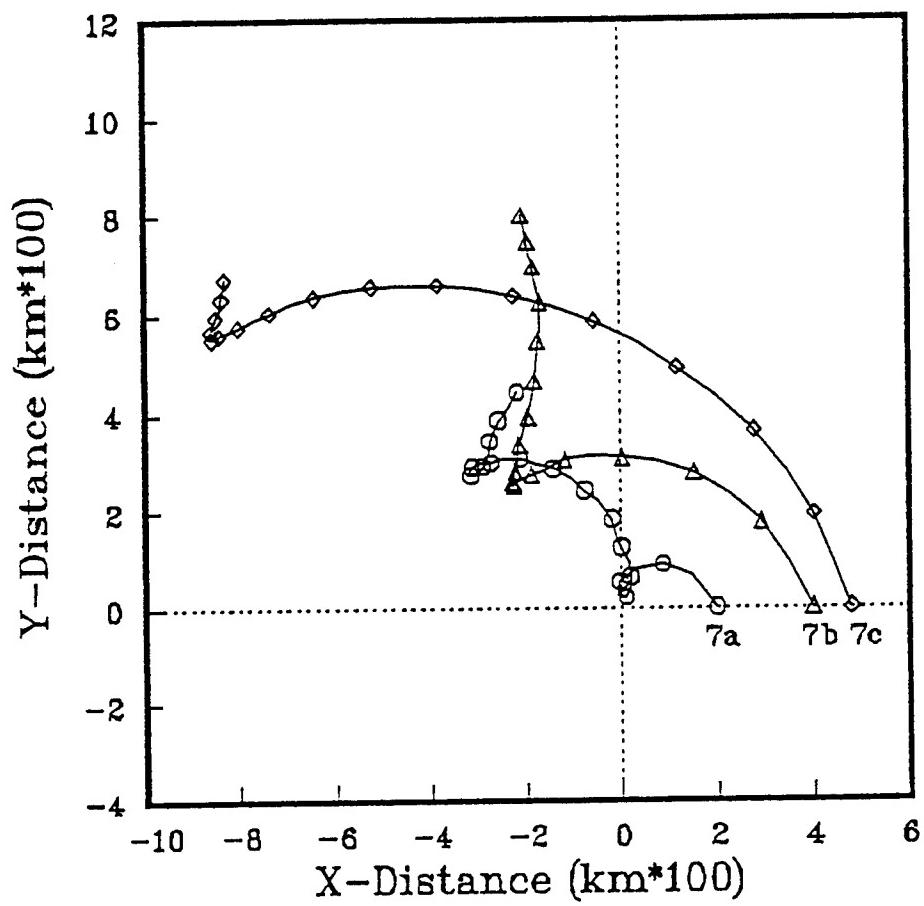


Fig. G.10 Tropical cyclone tracks as in Fig. G.6, except for Experiment 7 of Carr and Elsberry (1995) with the  $R_m$  of the MG at 300, 500, and 700 km.

## REFERENCES

- Arakawa, H. 1952: *Mame Taifu* or midget typhoon (small storms of typhoon intensity). Geophysical Magazine, **24**, 463-474.
- \_\_\_\_\_, 1963: Statistical method to forecast the movement of and central pressure of typhoons in the western North Pacific. Meteorological Research Institute Final Report, Japan Meteorological Agency.
- Brand, S., 1970: Interaction of binary tropical cyclones of the western North Pacific. J. Appl. Meteor., **9**, 433-441.
- Carr, L. E., III, and R. L. Elsberry, 1995: Monsoonal interactions leading to sudden tropical cyclone track changes. Mon. Wea. Rev., **123**, 265-289.
- Chan, J. C.-L., and W. M. Gray, 1982: Tropical cyclone movement and surrounding flow relationships. Mon. Wea. Rev., **110**, 1354-1374.
- Chan, J. C.-L., and R. T. Williams, 1987: Analytical and numerical studies of the beta-effect in tropical cyclone motion. Part. I: Zero mean flow. J. Atmos. Sci., **44**, 1257-1265.
- Chang, C.-P., J. M. Chen, P. A. Harr, L. E. Carr III, 1994: Northwestward propagating synoptic wave patterns over the tropical western Pacific and the periodicity of tropical cyclone activity during northern summer. Mon. Wea. Rev. (submitted)
- DeMaria, M., 1985: Tropical cyclone motion in a nondivergent barotropic model. Mon. Wea. Rev., **113**, 1199-1210.
- Dong, K., and C. J. Neumann, 1983: On the relative motion of binary tropical cyclones. Mon. Wea. Rev., **111**, 945-953.
- \_\_\_\_\_, and \_\_\_\_\_, 1986: The relationship between tropical cyclone motion and environmental geostrophic flows. Mon. Wea. Rev., **114**, 115-122.
- Dvorak, V. F., 1975: Tropical cyclone intensity analysis and forecasting from satellite imagery. Mon. Wea. Rev., **103**, 420-430.
- \_\_\_\_\_, 1984: Tropical cyclone intensity analysis using satellite data. NOAA Technical Report NESDIS 11, 46 pp.
- \_\_\_\_\_, 1994: A workbook on tropical clouds and cloud systems observed in satellite imagery. Volume II. Tropical cyclones. NAVEDTRA 40971, Naval Oceanographic Office, Stennis Space Center, MS 39522-5001.

- Elsberry, R. L., 1987: Tropical cyclone motion. Chapter 4, A Global View of Tropical Cyclones, Office of Naval Research, 91-131.
- \_\_\_\_\_, and P. H. Dobos, 1990: Time consistency of track prediction aids for western North Pacific tropical cyclones. Mon. Wea. Rev., **118**, 746-754.
- Evans, J. L., G. J. Holland, and R. L. Elsberry, 1991: Interaction between a barotropic vortex and an idealized subtropical ridge. Part. I: Vortex motion. J. Atmos. Sci., **48**, 301-314.
- Fiorino, M., and R. L. Elsberry, 1989: Some aspects of vortex structure related to tropical cyclone motion. J. Atmos. Sci., **46**, 975-990.
- Frank, W. M., 1984: A composite analysis of the core of a mature hurricane. Mon. Wea. Rev., **112**, 2401-2420.
- George, J. E., and W. M. Gray, 1976: Tropical cyclone motion and surrounding parameter relationships. J. Appl. Meteor., **15**, 1252-1264.
- Gray, W. M., 1968: Global view of the origin of tropical disturbances and storms. Mon. Wea. Rev., **96**, 669-700.
- Guard, C. P., 1983: A study of western North Pacific tropical storms and typhoons that intensify after recurvature. First Weather Wing Technical Note-83/002, 22 pp.
- \_\_\_\_\_, L. E. Carr, F. H. Wells, R. A. Jeffries, N. D. Gural, and D. K. Edson, 1992: Joint Typhoon Warning Center and the challenges of multibasin tropical cyclone forecasting. Wea. and Forecasting, **7**, 328-352.
- Goerss, J. S., L. Brody, and R. Jeffries, 1991: Assimilation of tropical cyclone observations into the Navy Operational Global Atmospheric Prediction System. Preprints Ninth Conf. Num. Wea. Prediction, Amer. Meteor. Soc., Boston MA 02108, 638-641.
- \_\_\_\_\_, and R. A. Jeffries, 1994: Assimilation of synthetic tropical cyclone observations into the Navy Operational Global Atmospheric Prediction System. Wea. and Forecasting, **9**, 557-576.
- Hardie, J. S., 1967: Tropical storm steering using geostrophic winds derived from smoothed 700 mb and 500 mb height fields. M. S. Thesis, Naval Postgraduate School.
- Harr, P. A., R. L. Elsberry, E. A. Ritchie, H. E. Willoughby, M. A. Boothe, L. E. Carr III, and R. A. Jeffries, 1993: Tropical Cyclone Motion (TCM-93) Field Experiment Summary. Tech. Report NPS-MR-93-004, Naval Postgraduate School, Monterey, CA, 93943, 120 pp.

- Harrison, E. J., Jr., 1973: Three-dimensional numerical simulations of tropical systems utilizing nested finite grids. J. Atmos. Sci., **30**, 1528-1543.
- Hebert, P. H., and K. O. Poteat, 1975: A satellite classification technique for subtropical cyclones. NOAA Technical Memorandum NWS SR-83, 25 pp.
- Hodur, R. M., and S. D. Burk, 1978: The Fleet Numerical Weather Central tropical cyclone model: Comparison of cyclic and one-way interactive boundary conditions. Mon. Wea. Rev., **106**, 1665-1671.
- Holland, G. J., 1980: An analytical model of wind and pressure profiles in hurricanes. Mon. Wea. Rev., **108**, 1212-1218.
- \_\_\_\_\_, 1994: Scale interaction in the western Pacific monsoon. Meteor. and Atmos. Phys. (submitted)
- \_\_\_\_\_, and G. S. Dietachmayer, 1993: On the interaction of tropical-cyclone-scale vortices. III: Continuous barotropic vortices. Quart. J. Roy. Meteor. Soc., **119**, 1381-1398.
- \_\_\_\_\_, T. McGeer, and H. Youngren, 1992: Autonomous Aerosondes for economical atmospheric soundings anywhere on the globe. Bull. Amer. Meteor. Soc., **73**, 1987-1990.
- Jarrell, J. D., and W. L. Somervell, Jr., 1970: A computer technique for using typhoon analogs as a forecast aid. NAVWEARSCHFAC Tech. Paper No. 6-70, 47 pp.
- Jarvinen, B. R., and C. J. Neumann, 1979: Statistical forecasting of tropical cyclone intensity. NOAA Technical Memorandum NWS NHC-10, 22 pp.
- Jordan, E. S., 1952: An observational study of the upper wind-circulation around tropical storms. J. Meteor., **9**, 340-346.
- Lander, M. A., 1994: Description of a monsoon 'gyre' circulation and its effects on the tropical cyclones in the western North Pacific during August 1991. Wea. and Forecasting., **9**, 640-654.
- \_\_\_\_\_, and G. J. Holland, 1993: On the interaction of tropical-cyclone-scale vortices. I: Observations. Quart. J. Roy. Meteor. Soc., **119**, 1347-1361.
- Langford, J. S., and K. A. Emanuel, 1993: An unmanned aircraft for dropwindsonde deployment and hurricane reconnaissance. Bull. Amer. Meteor. Soc., **73**, 367-375.
- Lau, K.-H., and N.-C. Lau, 1990: Observed structure and propagation characteristics of tropical summertime synoptic scale disturbances. Mon. Wea. Rev., **118**, 1888-1913.

- \_\_\_\_\_, and \_\_\_\_\_, 1992: The energetics and propagation dynamics of tropical summertime synoptic-scale disturbances. Mon. Wea. Rev., **120**, 2523-2539.
- Ley, G. W., and R. L. Elsberry, 1976: Forecasts of Typhoon Irma using a nested-grid model. Mon. Wea. Rev., **104**, 1154-1161.
- Matsumoto, C. R., 1984: A statistical method for one- to three-day tropical cyclone track prediction. Atmospheric Science Paper 379, Colorado State University, Fort Collins, Colorado, 201 pp.
- Miller, B. I., and P. L. Moore, 1960: A comparison of hurricane steering levels. Bull. Amer. Meteor. Soc., **41**, 59-63.
- Neumann, C. J., 1988: The National Hurricane Center NHC83 model. NOAA Tech. Memo. NWS NHC 41, National Hurricane Center, Coral Gables, FL 33146, 44 pp.
- Renard, R. J., S. G. Colgan, and S. K. Rinard, 1973: Forecasting the motion of North Atlantic tropical cyclones by the objective MOHATT scheme. Mon. Wea. Rev., **101**, 206-214.
- Riehl, H., and N. M. Burgner, 1950: Further studies of the movement and formation of hurricanes and their forecasting. Bull. Amer. Meteor. Soc., **31**, 244-253.
- Ritchie, E. A., and G. J. Holland, 1993: On the interaction of tropical-cyclone-scale vortices. II: Discrete vortex patches. Quart. J. Roy. Meteor. Soc., **119**, 1363-1379.
- Rossby, C.-G., 1948: On the displacements and intensity changes of atmospheric vortices. J. Mar. Res., **7**, 175-196.
- Shea, D. J., and W. M. Gray, 1973: The hurricane's inner core region. I. Symmetric and asymmetric structure. J. Atmos. Sci., **30**, 1544-1563.
- Shewchuk, J. D., and R. L. Elsberry, 1978: Improvement of a baroclinic motion prediction scheme by adjustment of the initial wind field. Mon. Wea. Rev., **106**, 713-718.
- Smith, R. B., 1993: A hurricane beta-drift law. J. Atmos. Sci., **50**, 3213-3215.
- Smith, R. K., W. Ulrich, and G. Dietachmeyer, 1990: A numerical study of tropical cyclone motion using a barotropic model. I: The role of vortex asymmetries. Quart. J. Roy. Meteor. Soc., **116**, 337-362.
- \_\_\_\_\_, 1991: An analytic theory of tropical-cyclone motion in a barotropic shear flow. Q. J. Roy. Meteor. Soc., **117**, 685-714.

- Tsui, T. L., L. R. Brody, and S. Brand, 1982: A technique for prediction surface wind distributions of tropical cyclones in the western North Pacific. NAVENVRSCHFAC Tech. Report TR-82-05, 40 pp.
- Velden, C. S., and L. M. Leslie, 1991: The basic relationship between tropical cyclone intensity and the depth of the environmental steering layer in the Australian region. Wea. and Forecasting, **6**, 244-253.
- Wang, G., 1960: A method in regression equations for forecasting the movement of typhoons. Bull. Amer. Meteor. Soc., **41**, 115-124.
- Weatherford, C. L., and W. M. Gray, 1988a: Typhoon structure as revealed by aircraft reconnaissance. Part I: Data analysis and climatology. Mon. Wea. Rev., **116**, 1032-1043.
- \_\_\_\_\_, and \_\_\_\_\_, 1988b: Typhoon structure as revealed by aircraft reconnaissance. Part II: Structural variability. Mon. Wea. Rev., **116**, 1044-1056.
- Weir, R. C., 1982: Predicting the acceleration of northward-moving tropical cyclones using upper-tropospheric winds. NAVOCEANCOMCEN/JTWC Tech Note 82-2, 40 pp.
- Williams, R. T., and J. C.-L. Chan, 1994: Numerical studies of the beta effect in tropical cyclone motion. Part II: Zonal mean flow effects. J. Atmos. Sci., **51**, 1065-1076.
- Xu, Y., and C. J. Neumann, 1985: A statistical model for the prediction of western North Pacific tropical cyclone motion. NOAA Technical Memorandum NWS NHC-28, 33 pp.
- Yogi, W., J. Long, and J. Steuckert, 1975: Further development of a 3-7 day typhoon analog forecast model for the Western Pacific. NAVENVRSCHFAC Tech. Paper No. 12-75, 37 pp.

## Distribution List

<b>Office of Naval Research (Code 322MM)</b> 800 N. Quincy Street Arlington, VA 22217-5000	2
<b>Dr. Robert L. Haney, Chairman</b> Department of Meteorology Naval Postgraduate School Monterey, CA 93943-5000	1
<b>Dr. Russell L. Elsberry (Code Mr/Es)</b> Department of Meteorology Naval Postgraduate School Monterey, CA 93943-5000	132
<b>Library (Code 0142)</b> Naval Postgraduate School Monterey, CA 93943-5000	2
<b>Dean of Research (Code 08)</b> Naval Postgraduate School Monterey, CA 93943-5000	1
<b>Defense Technical Information Center</b> Cameron Station Alexandria, VA 22304-6145	2